Computer-Based Guidelines for Concrete Pavements, Volume III: Technical Appendices

PUBLICATION NO. FHWA-HRT-04-127

JANUARY 2006

U.S. Department of Transportation
Federal Highway Administration

Research, Development, and Technology
Turner-Fairbank Highway Research Center
6300 Georgetown Pike
McLean, VA 22101-2296

FOREWORD

This report documents the investigation, modeling, and validation of the enhanced High PERformance PAVing (HIPEPAV®) II software program. HIPERPAV II is a comprehensive, yet user-friendly software package. HIPERPAV II primarily incorporates as a set of guidelines for the proper selection of design and construction variables to minimize early-age damage to jointed plain concrete pavement (JPCP) and continuously reinforced concrete pavement (CRCP). In addition, the software determines the effect of early-age behavior factors. This report, Volume III of a three-volume set, is the Technical Appendices, which documents work carried out during the study. Volume I is the *Project Summary* documenting the efforts undertaken for the guidelines. Volume II is the *Design and Construction Guidelines and HIPERPAV II User's Manual*, which provides general instruction on the use and application of the HIPERPAV II.

This report will be of interest to those involved in concrete pavement mix design, as well as the design and construction of concrete pavements. Sufficient copies of this report are being distributed to provide two copies to each Federal Highway Administration (FHWA) Resource Center, two copies to each FHWA Division Office, and a minimum of four copies to each State highway agency. Additional copies for the public are available from the National Technical Information Services (NTIS), 5285 Port Royal Road, Springfield, VA 22161.

Gary L. Henderson
Director, Office of Infrastructure
Research and Development

Notice

Quality Assurance Statement

The Federal Highway Administration (FHWA) provides high-quality information to serve Government, industry, and the public in a manner that promotes public understanding. Standards and policies are used to ensure and maximize the quality, objectivity, utility, and integrity of its information. FHWA periodically reviews quality issues and adjusts its programs and processes to ensure continuous quality improvement.

Technical Report Documentation Page

1. Report No.	2. Government Accession No.	3. Recipient's Catalog No.
FHWA-HRT-04-127	N/A	N/A

4. Title and Subtitle	5. Report Date
Computer-Based Guidelines for Concrete Pavements, Volume III: Technical Appendices	January 2006
	6. Performing Organization Code N/A

7. Authors(s)	8. Performing Organization Report No.
J. Mauricio Ruiz, Robert O. Rasmussen, George K. Chang, Jason C. Dick, Patricia K. Nelson, Anton K. Schindler, Dennis J. Turner, W. James Wilde	N/A

9. Performing Organization Name and Address	10. Work Unit No. (TRAIS)
The Transtec Group, Inc. 1012 East 38 ½ Street Austin, TX 78751	N/A
	11. Contract or Grant No. DTFH61–00–C–00121
	13. Type of Report and Period Covered Final Report February 2000 to April 2004

12. Sponsoring Agency Name and Address	14. Sponsoring Agency Code
Office of Infrastructure Research and Development Federal Highway Administration (FHWA) 6300 Georgetown Pike McLean, VA 22101	

15. Supplementary Notes:

Contracting Officer's Technical Representative: Fred Faridazar, HRDI - 11

16. Abstract

This report documents enhancements incorporated in the (HIgh PERformance PAVing) HIPERPAV II software. Enhancements made within this project include the addition of two major modules: a module to predict the performance of JPCP as affected by early-age factors; and a module to predict the early-age behavior (first 72 hours) and early life (up to 1 year) of CRCP. Two additional FHWA studies were also incorporated: one that predicts dowel bearing stresses as a function of environmental loading during the early age; and a module for optimization of concrete paving mixes as a function of 3-day strength, 28-day strength, and cost. Additional functionality to the software was also incorporated by reviewing and prioritizing the feedback provided by users of the first generation of the software, HIPERPAV I.

This volume includes the following technical appendices: A) annotated outline of the references investigated during this project; B) description of the models selected for incorporation in HIPERPAV II; C) field investigation of JPCP and CRCP sites used for model validation; D) validation of the enhanced HIPERPAV II computer guidelines; and E) finite-difference temperature model validation. This is the third volume and last in a series of three volumes that document the different tasks carried out in accomplishing the objectives for this project.

FHWA No.	Vol. No.	Short Title
FHWA-HRT-04-121	Volume I	Project Summary
FHWA-HRT-04-124	Volume II	Design and Construction Guidelines and HIPERPAV II User's Manual
FHWA-HRT-04-127	Volume III	Technical Appendices

17. Key Words	18. Distribution Statement
High Performance Concrete Pavement; HIPERPAV; Jointed; Continuously Reinforced; Early Age Behavior; Long-Term Performance; Mechanistic-Empirical Models; Temperature; Hydration; Shrinkage; Relaxation; Creep; Thermal Expansion; Slab Base Restraint; Curling; Warping; Plastic Shrinkage; Cracking; JPCP; CRCP	No restrictions. This document is available to the Public through the National Technical Information Service; Springfield, VA 22161

19. Security Classif. (of this report)	20. Security Classif. (of this page)	21. No. of Pages	22. Price
Unclassified	Unclassified	361	

SI* (MODERN METRIC) CONVERSION FACTORS

APPROXIMATE CONVERSIONS TO SI UNITS

Symbol	When You Know	Multiply By	To Find	Symbol
		LENGTH		
in	inches	25.4	millimeters	mm
ft	feet	0.305	meters	m
yd	yards	0.914	meters	m
mi	miles	1.61	kilometers	km
		AREA		
in^2	square inches	645.2	square millimeters	mm^2
ft^2	square feet	0.093	square meters	m^2
yd^2	square yard	0.836	square meters	m^2
ac	acres	0.405	hectares	ha
mi^2	square miles	2.59	square kilometers	km^2
		VOLUME		
fl oz	fluid ounces	29.57	milliliters	mL
gal	gallons	3.785	liters	L
ft^3	cubic feet	0.028	cubic meters	m^3
yd^3	cubic yards	0.765	cubic meters	m^3
		NOTE: volumes greater than 1000 L shall be shown in m^3		
		MASS		
oz	ounces	28.35	grams	g
lb	pounds	0.454	kilograms	kg
T	short tons (2000 lb)	0.907	megagrams (or "metric ton")	Mg (or "t")
		TEMPERATURE (exact degrees)		
^oF	Fahrenheit	5 (F-32)/9 or (F-32)/1.8	Celsius	^oC
		ILLUMINATION		
fc	foot-candles	10.76	lux	lx
fl	foot-Lamberts	3.426	candela/m^2	cd/m^2
		FORCE and PRESSURE or STRESS		
lbf	poundforce	4.45	newtons	N
lbf/in^2	poundforce per square inch	6.89	kilopascals	kPa

APPROXIMATE CONVERSIONS FROM SI UNITS

Symbol	When You Know	Multiply By	To Find	Symbol
		LENGTH		
mm	millimeters	0.039	inches	in
m	meters	3.28	feet	ft
m	meters	1.09	yards	yd
km	kilometers	0.621	miles	mi
		AREA		
mm^2	square millimeters	0.0016	square inches	in^2
m^2	square meters	10.764	square feet	ft^2
m^2	square meters	1.195	square yards	yd^2
ha	hectares	2.47	acres	ac
km^2	square kilometers	0.386	square miles	mi^2
		VOLUME		
mL	milliliters	0.034	fluid ounces	fl oz
L	liters	0.264	gallons	gal
m^3	cubic meters	35.314	cubic feet	ft^3
m^3	cubic meters	1.307	cubic yards	yd^3
		MASS		
g	grams	0.035	ounces	oz
kg	kilograms	2.202	pounds	lb
Mg (or "t")	megagrams (or "metric ton")	1.103	short tons (2000 lb)	T
		TEMPERATURE (exact degrees)		
^oC	Celsius	1.8C+32	Fahrenheit	^oF
		ILLUMINATION		
lx	lux	0.0929	foot-candles	fc
cd/m^2	candela/m^2	0.2919	foot-Lamberts	fl
		FORCE and PRESSURE or STRESS		
N	newtons	0.225	poundforce	lbf
kPa	kilopascals	0.145	poundforce per square inch	lbf/in^2

*SI is the symbol for the International System of Units. Appropriate rounding should be made to comply with Section 4 of ASTM E380.
(Revised March 2003)

TABLE OF CONTENTS

LIST OF FIGURES

LIST OF TABLES

LIST OF ACRONYMS AND ABBREVIATIONS

AASHO: American Association of State Highway Officials
AASHTO: American Association of State Highway and Transportation Officials
AC: Asphalt concrete
ACI: American Concrete Institute
ACPA: American Concrete Pavement Association
AE: Activation Energy
AGG: Aggregate
ASCE: American Society of Civil Engineers
ASTM: American Society for Testing and Materials
ATB: Asphalt-treated base
CAM: Cement Aggregate Mixture
CCD: Central Composite Design
CEB-FIP: CEB stands for Euro-International Concrete Committee (Comité Euro-International du Béton), FIP stands for International Federation of Prestressing (Fédération Internationale de la Précontrainte)
CL: Lean Clay
COMET: Concrete Optimization, Management, Engineering, and Testing
COPES: Concrete Pavement Evaluation System
COST: Concrete Optimization Software Tool
CRCP: Continuously Reinforced Concrete Pavement
CTB: Cement-Treated Base
CTE: Coefficient of Thermal Expansion
CTR: Center for Transportation Research
CV: Coefficient of Variation
DEMEC: Demountable Mechanical Strain Gage
DOT: Department of Transportation
ER: Effective Ratio of Joint Movement to Change in PCC Temperature
ESAL: 18-kip Equivalent Single Axle Loads
FEA: Finite-Element Analysis
FEM: Finite-Element Method
FHWA: Federal Highway Administration
FWD: Falling Weight Deflectometer
GGBF: Ground-Granulated Blast-Furnace
GPS: General Pavement Studies
GW: Well-Graded Gravel
GW–GM: Well-Graded Silty Gravel
HIPERPAV: HIgh PERformance Concrete PAVing.
HMA: Hot-Mix Asphalt
HPC: High-Performance Concrete
ICM: Integrated Climate Model
IRI: International Roughness Index
ISO: International Organization for Standardization
JCP: Jointed Concrete Pavement
JPCP: Jointed Plain Concrete Pavement
JRCP: Jointed Reinforced Concrete Pavement
JTE: Joint Transfer Efficiency
k-value: Modulus of Subgrade Reaction
LCB: Lean Concrete Base

LS: Limestone
LTE: Load Transfer Efficiency
LTPP: Long-Term Pavement Performance
LVDT: Linear Variable Displacement Transducers
ML: Lean Silty Soil
NCDC: National Climate Data Center
NCHRP: National Cooperative Highway Research Program
NOAA: National Oceanic and Atmospheric Administration
PCA: Portland Cement Association
PCC: Portland Cement Concrete
PCCP: Portland Cement Concrete Pavements
PSD: Particle Size Distribution
PSI: Present Serviceability Index
PSR: Present Serviceability Rating
RH: Relative Humidity
RIPPER: Performance/Rehabilitation of Rigid Pavements
SEE: Standard Error of the Estimate
SI: International System
SMP: Seasonal Monitoring Program
SRG: Siliceous River Gravel
THMI: Thornthwaite Moisture Index
TRB: Transportation Research Board
TxDOT: Texas Department of Transportation
UCS: Unified Classification System
VST: Volumetric Surface Texture
w/c: Water-to-Cement Ratio
w/cm: Water-to-Cementitious Materials Ratio
WIM: Weigh-in-Motion

APPENDIX A ANNOTATED OUTLINE OF MODEL REFERENCES

This appendix contains a detailed annotated outline of the primary references reviewed during the information search performed in this study. The literature review is organized in four categories:

1. Currently available early-age behavior models similar to the HIgh PERformance PAVing (HIPERPAV) System.[1]
2. Early-age behavior models with potential incorporation into HIPERPAV II.
3. Literature review on jointed plain concrete pavement (JPCP) models.
4. Literature review on continuously reinforced concrete pavement (CRCP) models.

The following sections document the literature reviewed on each of the above categories.

A.1 CURRENTLY AVAILABLE EARLY-AGE BEHAVIOR MODELS SIMILAR TO HIPERPAV

In addition to HIPERPAV, four other available software programs that predict the early-age behavior of concrete were identified. These include Durability Models of Concrete (DuCOM®), HYdration, MOrphology, and STRUCture (HYMOSTRUC®), Quadrel®, and 4C-Temp&Stress®. HYMOSTRUC and Quadrel focus on developing the adiabatic hydration curves for concrete. DuCOM and 4C-Temp&Stress are more robust finite-element programs that calculate the state of stress in early-age concrete structures. These programs are similar in some aspects to HIPERPAV, but also have differences in theory and application. DuCOM, HYMOSTRUC, Quadrel, and 4C-Temp&Stress are summarized below.

[1] *HIPERPAV alone with no succeeding numeral is used to refer to the overall concrete pavement design and construction guidelines, while HIPERPAV I and HIPERPAV II are used to refer to the two different software generations.*

A.1.1 DuCOM

Maekawa, K., Chaube, R., and Kishi, T., "Modeling of Concrete Performance," Hydration, Microstructure Formation and Mass Transport, E&FN Spon, New York, NY, 1999.

DuCOM focuses on evaluating the durability of structural concrete. This program assesses the durability of concrete from the green (or fresh) state up to several years of age using a finite-element-based program. DuCOM is a lifespan simulator that can model the microscopic behavior of concrete at early ages and relate this to its long-term performance. This program considers the properties of the concrete material's mix proportions; the casting, curing, and environmental conditions; and the shape and size of the structural concrete. The concrete's mechanistic processes are divided into short and long terms. The short-term processes are related to hydration, microstructure development, moisture transport, temperature rise, shrinkage, and creep. The long-term processes include transport of external agents into the concrete and its long-term creep behavior. Research on DuCOM continues at the Concrete Laboratory of the University of Tokyo, Japan.

A.1.2 HYMOSTRUC

Van Breugel, K. Simulation of Hydration and Formation of Structure in Hardening Cement-Based Materials, Second Edition, Delft University Press, 1997.

HYMOSTRUC is designed to predict the adiabatic (and isothermal) hydration curves of concrete. It combines the fields of cement chemistry, physics, and stereology. The particle size of the cement, the water-to-cement ratio (w/c), the initial curing temperature, and the chemical composition of cement are all considered when formulating the concrete's hydration curves. HYMOSTRUC focuses on the microscopic level. The overall degree of hydration is assumed to be the sum each individual cement particle's degree of hydration. The output from HYMOSTRUC possibly can be used to predict the macroscopic behavior of hardened concrete structures. Connecting the microscopic behavior of the cement to its macroscopic properties, such as strength and stiffness, is one of HYMOSTRUC's future objectives.

A.1.3 Quadrel

Digital Site Systems, Inc. Quadrel, Information Technology Solutions for Construction.

Quadrel is a software program that makes adiabatic heat signature testing and analysis of fresh concrete possible in the laboratory. Fresh concrete samples are placed into a Qdrum calorimeter that simultaneously measures the temperature gain and heat loss. The data is processed using Quadrel, and the adiabatic heat of hydration curve is generated. Using the hydration curve, the concrete's strength can be estimated as a function of maturity. Quadrel can be used to estimate the initial set time of the concrete, evaluate the performance of chemical admixtures and pozzolans, and determine how suitable concrete mixes are in the control of thermal cracking.

A.1.4 4C-Temp&Stress

4C-Temp&Stress. Temperature and Stress Simulation During Hardening, Users Manual, Germann Instruments, Inc., Evanston, IL, 1998.

Using the finite-element method (FEM), 4C-Temp&Stress computes the time-dependent temperatures and the state of stress in concrete structures. The program considers the influence of heat of hydration, thermal boundary conditions, and casting time and temperature on the structure's state of stress. This program also calculates the influence of cooling pipes or heating wires on the concrete's thermal state. Environmental factors like wind and radiation are taken into account. Loading of the structure enters by structural supports, self-weight, point loads, line loads, and momentum. The user can define the materials properties of the system, including those of concrete, soil, or insulation. Likewise, a mix design module for concrete specifies quantities of cement, aggregate, mineral additives, chemical additives, and water. In turn, each of these constituents has its own database with additional properties. Properties of the concrete mix, including slump, air content, thermal conductivity, and density, can be defined. The adiabatic heat development in the fresh concrete can be input, as can the concrete's stiffness and Poisson's ratio. Thermal expansion, creep, and compressive and tensile strength of concrete are all properties that 4C-Temp&Stress takes into account. The concrete structures can have several geometries. For output, the maturity of every point in the structure's cross section is calculated, as are the stresses and strengths.

A.2 EARLY-AGE BEHAVIOR MODELS WITH POTENTIAL INCORPORATION INTO HIPERPAV II

The early-age properties of concrete are influenced significantly by the climatic conditions and temperatures, as well as by the concrete mix components. In this section, a literature review of early-age concrete properties is completed. The properties that are addressed are concrete maturity, drying shrinkage, moisture transport, set time, creep, and various thermal properties.

A.2.1 Concrete Hydration

This section briefly summarizes the primary references that contain candidate models that were identified to characterize the hydration of concrete at early ages.

Byfors, J. "Plain Concrete at Early Ages," Research 3:80, Swedish Cement and Concrete Research Institute, Stockholm, Sweden, 1980.

This document contains many of the models and principles used in HIPERPAV I. This document emphasizes the modeling of the following mechanical properties: compressive strength, tensile strength, ultimate tensile strain, modulus of elasticity, Poisson's ratio, and creep effects. Moisture transport and shrinkage is acknowledged, but limited information is presented. The influences of the following primary factors were studied: cement composition, cement fineness, w/c, curing temperature, moist curing, and effect of some chemical admixtures: accelerator ($CaCl_2$) and air-entraining agents. This document presents many test results, but limited mechanistic models.

The degree of hydration is used to describe the extent to which reaction between cement and water has developed, and the degree of hydration is linked to compressive strength and creep development. It is concluded that a certain critical degree of hydration is required before any strength gain can be obtained in the cement paste.

Byfors also documents a model that provides an estimate of heat of hydration as a function of time. The model defines the heat development for the four main clinker compounds at ages of 3, 7, 28, 90, and 365 days.

Knudsen, T., "Modeling Hydration of Portland Cement—The Effect of Particle Size Distribution," Conference Proceedings, Characterization and Performance Prediction of Cement and Concrete, Edited by Young, J.F., United Engineering Trustees, Inc., New Hampshire, pp. 125–150, 1983.

This paper presents a mathematical model for the development of the hydration of portland cement with time, called the *dispersion model*, which is founded on the particle size distribution (PSD) of the cement. The rate and duration of reaction of smaller particles is different from those of larger particles. During hydration, smaller particles might be fully hydrated, and the larger particles might be at a lower degree of hydration. Therefore, at any given time, the degree of hydration has a distribution that is dependent on the PSD. All cement particles are assumed to react independently of each other. It is shown that the particle size has a dominant effect on the shape of the hydration curve.

The model development is based on kinetic theory for solid-state reactions, with the assumption that spherical grains react according to the shrinkage core model. In this model, the growing reaction zone is surrounding the unreacted core. The assumed kinetic function is used with the Rosin-Rammler PSD to obtain a very simple formulation of the degree of hydration in terms of a constant that characterizes the PSD and a rate constant that accounts for the effect of temperature on the form of the hydration curve. The model is compared to data obtained by other researchers, and good agreement with the data is found.

Pinto, R.C.A., "The Effect of Curing Temperatures on the Development of Mechanical Properties of Fresh and Hardened High-Strength Silica Fume Mixtures—A Maturity Approach," Dissertation, Cornell University, Ithaca, NY, 294 pp., 1997.

In this dissertation, Pinto presents expansions on the dispersion model presented by Knudsen, and fits the shape of the strength gain to a hyperbolic model, which has been shown to provide the best fit. Because the different reactions of cement hydration can be controlled through kinetics and/or diffusion processes, Pinto states that "one would not expect a constant value for E_a for all stages of cement hydration." Diffusion-controlled processes are expected to be less temperature sensitive than kinetically-controlled ones. Therefore, a lower activation energy (AE) value is expected as the hydration process progresses. Pinto reports that "as an average, the AE of C_3S hydration, or the apparent AE of portland cement hydration, is twice as high during the early chemically (kinetically) controlled stages than at the late, diffusion-controlled stage." Pinto provides a method to select an appropriate AE value for each of the five stages of hydration. This method is called the variable E-method. Data is further presented to address the selection of the most appropriate value for the AE, and it is shown that if AE values are selected based on strength data, different AE values can be obtained depending on the shape (hyperbolic, exponential, parabolic-hyperbolic) of the strength-age relationship.

Van Breugel, K., Simulation of Hydration and Formation of Structure in Hardening Cement-Based Materials, Second Edition, Delft University Press, Netherlands, 305 pp., 1999.

This book presents a complete review of literature and available techniques to model concrete hydration and structural development in cement-based materials, and the model developed is referred to as HYMOSTRUC. The models are able to allow for the effects of cement composition, PSD, w/c, and the initial mix temperature. For simplicity, the Rosin-Rammler function is recommended to model the cement PSD. A formulation similar to the current model in HIPERAV is recommended to determine the maximum heat of hydration. The degree of hydration is defined in terms of structural formation, and

modeled as the ratio of the amount of cement that has reacted, at a certain time relative to the original amount of cement.

The ultimate degree of hydration is determined based on the amount of water available for reaction with the cement particles, and the space available for the hydration products. However, this model is rather complex, and the relative humidity within the pore structure must be modeled. The model also does not account for different cement compositions and fineness of the cement, which will most likely influence this value.

Models are presented to determine the AE of the mix design in terms of the C_3S content of the cement used, the degree of hydration of the mix, and the temperature of the concrete.

Maekawa, K., Chaube, R., and Kishi, T., Modeling of Concrete Performance—Hydration, Microstructure Formation, and Mass Transport, E&FN Spon, New York, NY, 308 pp., 1999.

Models are presented to predict the pore structure development of hydrating concrete, which then is used to determine the mechanical and physical properties of the concrete with respect to long-term durability. To determine the pore structure development, the following components are modeled: heat generation, water consumption, pore water pressure, equilibrium of pore water pressure, and moisture migration. The model described in this book is referred to as DuCOM.

A multicomponent heat of hydration model is presented, where the heat of hydration is determined through summing the heat rates of the different clinker minerals. The heat of hydration rate for each of the mineral compounds is divided into stages in terms of cumulative heat generation. The heat generation rate of the most critical stage (stage 2) was fitted according to values obtained from adiabatic tests. Stage 3 was identified as the diffusion control stage, and a slower heat generation rate was assigned to each compound. Other blending minerals, such as slag or fly ash, are incorporated as additional mineral components. The effect of the development of ettringite on the formation of C_3A and gypsum with C_4AF is accounted for in the proposed multicomponent model.

A temperature model is proposed similar to the one initially developed by Byfors, but numerous modification factors are added. These modification factors account for the reduction of probability of contact between unhydrated compounds and free pore water, the effect of mineral composition of portland cement, the reduction of the pozzolan's reaction due to the shortage of calcium hydroxide, the relative cement fineness expressed as a ratio of the Blaine fineness, and the retardation of the overall rate of cement and slag reaction caused by the presence of fly ash.

A moisture transport model for cementitious materials is presented, which considers the multiphase dynamics of liquid and gas phases. The moisture transport characteristics are dependent on the previously determined microstructure. The model can also consider the effect of wetting and drying cycles for concrete exposed to natural environments with fluctuating moisture levels.

Onken, P. and Rostásy, F.S., "A Practical Planning Tool for the Simulation of Thermal Stresses and for the Prediction on Early Thermal Cracks in Massive Concrete Structures," Proceedings of the RILEM (French acronym for Réunion Internationale des Laboratoires et Experts des Matériaux, Systèmes de Constructions et Ouvrages) Symposium on Thermal Cracking in Concrete at Early Ages, Edited by Springenschmid, R., E&FN Spon, London, pp. 289–296, 1995.

Models similar to those developed by Byfors are presented, however, the degree of hydration model is modified to only contain two parameters, compared to the three initially proposed by Byfors. It is reported that the shape of the hydration curve is a function of the clinker composition, PSD, the w/c, and

the initial mix temperature. No models are presented to define the effect of these variables on the heat of hydration.

Bentz, D.P., Garboczi, E.J., Haecker, C.J., and Jensen, O.M., "Effects of Cement Particle Size Distribution on Performance Properties of Portland Cement-Based Materials," Cement and Concrete Research, 1999.

The effects of cement PSD on a variety of performance properties are demonstrated. Laser diffraction techniques were used to determine the PSD of the two cements analyzed. It is shown that finer grinding results in enhanced hydration, heat release, and strength at all investigated ages. At later ages, the cumulative degree of hydration and heat release of the different cements are nearly equivalent. Even though the finer particles require less time to achieve set due to its increased hydration rate, it actually requires more hydration, as more particle-to-particle bridges need to be built.

Komonen, J. and Penttala, V., "Influence of Admixture Type and Concrete Temperature on Strength and Heat of Hydration of Concrete," 10th International Symposium on the Chemistry of Cement, Edited by Justnes, H., Trondheim, Norway, 8 pp., 1997.

In this paper, the authors present some valuable results that quantify the effect of different admixtures and initial concrete temperatures on the heat of hydration of concrete. Based on the variables considered, it is concluded that the mixing temperature is the most significant variable. The higher the mixing temperature, the earlier the heat gain took place. Numerous heat of hydration curves are presented for all the variables evaluated. The efficiency of the different plasticizers varied considerably at early ages.

Ma, W., Sample, D., Martin, R., and Brown, P.W., "Calorimetric Study of Cement Blends Containing Fly Ash, Silica Fume, and Slag at Elevated Temperatures," Cement, Concrete, and Aggregates, Vol. 16, No. 2, pp. 93–99, December 1994.

In this paper, the hydration of blended cements containing fly ash, silica fume, and ground-granulated blast-furnace (GGBF) slag over the temperature range of 0 degrees Celsius (°C) to 55 °C was studied by isothermal calorimetery, and the heat evolution during the first 24 hours of hydration was examined. The AE for the different blended cements were determined and the following values were obtained: 39.0, 26.7, 30.4 and 49.3 kilojoule per mole (kJ/mol) for portland cement, fly ash, silica fume, and slag blended cements, respectively.

Andersen, P.J., Andersen, M.,E., and Whiting, D., A Guide to Evaluating Thermal Effects in Concrete Pavements, SHRP–C–321, Strategic Highway Research Program, National Research Council, Washington, DC, 104 pp., 1993.

This paper briefly summarizes all the models required to determine the temperature development in concrete at early ages due to the exothermic reaction and the influence of climatic conditions. The models used are very similar to those developed by Byfors (as mentioned above) and heat transport by thermal conduction, convection, and radiation also is introduced. Based on the analysis performed, final recommendations are made to the extent of thermal cracking based on the slab thickness, concrete placement temperature, air temperatures, and the cement type used in the concrete mixture. In this project it is assumed that the problems could occur when any of the following three conditions are encountered:

- Risk of thermal cracking becomes too large when the temperature differential exceeds 20 °C.
- Risk of temperatures within the concrete slab becoming too high. Permanent strength loss can be experienced when the concrete temperatures are higher than 60 °C.

- Risk of early freezing. According to American Concrete Institute (ACI) 308, freezing must be prevented until the concrete has reached a compressive strength of 3.45 kPa.

The degree of hydration in this study is also defined in terms of two adiabatic parameters, one that defines the curvature of hydration, and the other that defines the time of hydration initiation. Typical values for different cement types are provided. In this study, activation energies for a variety of cement were determined to be as follows: Type I = 48.8 kJ/mol, Type II = 41.3 kJ/mol, Type III = 42.5 kJ/mol, Type I + fly ash = 38.2 kJ/mol, and Type II + fly ash = 36.8 kJ/mol.

Eren, O., Brooks, J.J., and Celik, T., "Setting Times of Fly Ash and Slag-Cement Concretes as Affected by Curing Temperature," Cement, Concrete, and Aggregates, Vol. 17, No. 1, pp. 11–17, June 1995.

The time of setting of different concrete pastes by penetration resistance (American Society for Testing and Materials (ASTM) C 403) is presented. Penetration resistance was determined under isothermal curing temperatures ranging from 6 ºC to 80 ºC for concrete containing up to 50 percent of fly ash or GGBF slag. At high temperatures, slag concrete has shorter setting times than Type I cement concrete. The setting times of fly ash concrete are longer than those of Type I cement concrete and slag concrete. Empirical relationships are presented for setting time as a function of penetration resistance, temperature, and cement replacement level.

Douglas, E., Elola, A., and Malhotra, V.M., "Characterization of Ground-Granulated Blast-Furnace Slags and Fly Ashes and Their Hydration in Portland Cement Blends," Cement, Concrete, and Aggregates, Vol. 12, No. 2, pp. 38–46, 1990.

In this paper, chemical analysis, PSD, heat evolution rate, total heat evolution, and strength development were studied for three GGBF slags, and two fly ashes of low and high CaO content. At all stages, the heat evolution rates and total heat evolution by the fly ashes were lower than the corresponding values for the GGBF slag.

Rahhal, V.F. and Batic, O.R., "Mineral Admixtures Contribution to the Development of Heat of Hydration and Strength," Cement, Concrete, and Aggregates, Vol. 16, No. 2, pp. 150–158, December 1994.

This paper presents a wide range of test results to quantify the benefits of adding mineral admixtures, such as natural pozzolan, fly ash, and GGBF slag, to control heat development. Blended cements were prepared using ordinary portland cement clinker, gypsum, and mineral admixtures. The percentages of mineral admixtures investigated were 0, 10, 20, 33, 40, 50, 70, and 90, by mass. Tests were performed at 3, 7, 28, 90, and 180 days. Empirical coefficients of the contribution of mineral admixtures to heat of hydration have been obtained, as well as a mathematical expression to estimate the heat of hydration of blended cements based on the mineral admixture selected, the percentage used, and the heat of hydration of the control cement. The following conclusions pertinent to the HIPERPAV II project include:

- The rate of heat evolution of blended cements containing the mineral admixtures accelerates up to 7 days, decelerates towards 28 days, and remains constant toward 180 days.
- Liberated heat at a given age decreases as replacement percentages of the mineral admixtures increase.

Each mineral has an optimum range of replacement percentage that increases mechanical strength, and lowers the heat of hydration.

Tazawa, E. and Miyazawa, S., "Influence of Cement Composition on Autogenous Shrinkage of Concrete," Proceedings on the 10th International Congress on the Chemistry of Cement, Gothenburg, Sweden, Vol. 2, June 1997.

Autogenous shrinkage is defined as the macroscopic volume reduction caused by hydration of cement. Based on the test performed by the authors, it was concluded that autogenous shrinkage was strongly influenced by the type of cement, which is due to the difference in cement composition, and especially the content of C_3A and C_4AF. Compared to normal portland cement, autogenous shrinkage is large for high early strength cement, and is lower for moderate heat cement. Autogenous shrinkage is very low for low heat cement with high C_2S contents. For the mixtures investigated, autogenous shrinkage increases with a decrease in w/c. This ratio is, therefore, the main variable in the prediction model. An empirical equation is presented to estimate the autogenous shrinkage strain of the concrete based on the time elapsed, the type of cement, and the w/c used. The prediction model is valid for concrete with w/c ranging from 0.2 to 0.56, a coarse aggregate factor of 0.55 to 0.65, and an environmental temperature of 20 °C.

Coole, M.J., "Heat Release Characteristics of Concrete Containing Ground-Granulated Blast-Furnace Slag in Simulated Large Pours," Magazine of Concrete Research, Vol. 140, No. 144, September 1988.

This paper investigates the effect of three different European sources of GGBF slag blended with ordinary portland cement. It is shown that both the peak temperature and the time to reach this temperature are influenced strongly by the slag source. Five levels of slag replacement were investigated, and with a reactive slag at a moderate replacement of cement (20–40 percent), the temperature rise at the center of the pour was higher than when an equivalent cement was used.

A.2.2 Concrete Maturity

Maturity is a technique used to estimate the strength gain of concrete based on the measured temperature history during curing. A maturity function is a mathematical expression that accounts for the combined effects of time and temperature on the concrete's strength development. This function usually is assumed to be a linear function of temperature, or to obey the exponential Arrhenius equation.

Carino, N.J., "CRC Handbook on Nondestructive Testing of Concrete, Chapter V—The Maturity Method," Edited by Malhorta, V.M., CRC Press, Florida, 1991.

This reference presents a historical review of all the widely used maturity methods. The equivalent age concept is explained, and the importance of temperature on early-age concrete properties is stressed. The maturity concept was initiated by Saul, where maturity is the sum of change in temperature multiplied by the time interval (Nurse-Saul function). Limitations of this method are that a datum temperature is needed to calculate the temperature change. The equivalent age concept was initiated in 1960 to 1977 by Arrhenius. This age conversion factor is a function of absolute temperature. Maturity is equal to the rate constant multiplied by age (where the rate constant depends on temperature). To relate strength to maturity, hyperbolic, and other empirical functions have been developed. The empirical formulas have coefficients that follow the shape of the curve. Equivalent age is the most flexible technique available to represent maturity.

Method of Testing the Strength of Portland Cement Concrete Using the Maturity Method, Iowa Department of Transportation (DOT), Materials. Iowa Method 383. Office of Materials.

The Iowa DOT uses maturity to measure the in-place strength of the concrete. Part 1 describes the destructive testing method to get the relationship between maturity and concrete strength. Part 2 describes instrumentation of the concrete to obtain in-place temperatures. The Nurse-Saul method is used.

Carino, N., Lew, H.S., and Volz, C.K., "Early-Age Temperature Effects on Concrete Strength Prediction by the Maturity Method," ACI Journal, pp. 93–101, March–April 1983.

Early-age temperature is found to influence strength-maturity relationship at later ages. Maturity is calculated using the simplified Nurse-Saul equation. Mathematical models that represent maturity can have either log or hyperbolic functions.

Marzouk, H. and Hussein, A., "Effect of Curing Age on High-Strength Concrete at Low Temperatures," Journal of Materials in Civil Engineering, Vol. 7, No. 3. pp. 161–167, August 1995.

The effect of curing age on the strength of silica fume concrete containing fly ash at cold temperatures is given. This paper describes how properties of the concrete change as a function of temperature, composition, modulus of rupture, and splitting tensile strength. The effect of pozzolans and admixtures are considered. Maturity methods are discussed. This paper states that the maturity method may not be appropriate for concrete placed under freezing temperatures.

Jensen, O. M. and Hansen, P.F., "Influence of Temperature on Autogenous Deformation and Relative Humidity Change in Hardening Cement Paste," Cement and Concrete Research, Vol. 29, pp. 567–575, 1999.

The autogenous deformation, relative humidity, and temperature changes in hardening cement paste are investigated. Maturity concepts do not apply to these phenomena. Concrete self-desiccates because of the low w/c, shrinking in bulk, which can cause cracking. Self-desiccation shrinkage is a form of chemical shrinkage that can eventually lead to failure of the entire structure.

Kim, J.K., Moon, Y.H., and Eo, S.H., "Compressive Strength Development of Concrete with Different Curing Time and Temperature," Cement and Concrete Research, Vol. 28, No. 12, pp. 1761–1773, 1998.

Previous maturity work focuses on predicting concrete strength under isothermal conditions. In practice, this is not the case. Varying temperatures must be taken into account, and this paper tries to develop a maturity model that does that.

A.2.3 Drying Shrinkage of Concrete

Drying shrinkage happens when the rate of moisture loss from the pavement surface is greater than the rate at which it can be replenished by free moisture in the slab. The desiccated concrete shrinks, and this can lead to warping and cracking of the structure. Most typically, drying shrinkage affects exposed surfaces.

Al-Sugair, F. H. and Almudaiheem, J.A., "Further Modification of the Ross Equation to Predict the Ultimate Drying Shrinkage of Concrete," ACI Materials Journal, Vol. 87, No. 3, May–June 1990.

The Ross equation is used to predict drying shrinkage. A large amount of experimental data (drying shrinkage versus time) is used, and the effect of volume-to-surface-area ratio on drying shrinkage is the focus. Its error is ±25 percent. Drying shrinkage was predicted from 1 to 28 days in some cases.

Han, M.W. and Lytton, R.L., "Theoretical Prediction of Drying Shrinkage in Concrete," Journal of Materials in Civil Engineering, Vol. 7, No. 4, November 1995.

The water potential is used to estimate the degree of drying shrinkage. Water potential is a type of stress that forces moisture to move and causes hydrated cement particles to shrink and expand. Drying shrinkage is related to water potential by a logarithmic curve.

Kim, J.K. and Lee, C.S., "Prediction of Differential Drying Shrinkage in Concrete," Cement and Concrete Research, Vol. 28, No. 7, pp. 985–99, 1998.

The effect of creep is incorporated into the drying shrinkage prediction. The drying shrinkage profile is obtained; this depends on the distance from the exposed concrete surface and on time.

Persson, B., "Experimental Studies on Shrinkage of High-Performance Concrete," Cement and Concrete Research, Vol. 28, No. 7, pp. 1023–1036, 1998.

Relationships are developed to predict the amount of autogenous shrinkage and drying shrinkage in concrete as a function of w/c, amount of silica fume in the concrete, the ratio of evaporated water to mixing water, and internal relative humidity. The focus of this paper is relating silica fume content (slurry or granular) to total, drying, and autogenous shrinkage.

Shah, S.P., Ouyang,C., Marikunte, S., Yang, W., and Becq-Siraudon, E., "A Method to Predict Shrinkage Cracking of Concrete," ACI Materials Journal, pp. 339–346, July–August 1998.

Nonlinear fracture mechanics are used in this reference to predict drying shrinkage of a ring specimen. Cracking of concrete is caused by its creep, free shrinkage, elastic modulus, tensile strength, and fracture toughness properties. Cracking results when there is a difference in the amount of free shrinkage and creep. The effect of creep on shrinkage cracking was determined using the CEB-FIP (French acronym for European Committee for Concrete-International Federation for Prestressing) model. The time dependence of concrete fracture toughness is measured. To use this model, fracture toughness and critical crack tip opening displacement are needed.

Shimomura, T. and Maekawa, K., "Analysis of the Drying Shrinkage Behavior of Concrete Using a Micromechanical Model Based on the Micropore Structure of Concrete," Magazine of Concrete Research, Vol. 49, No. 181, pp. 303–322, December 1997.

A micromechanical drying shrinkage model is developed by the researchers who developed DuCOM. This model takes into account the concrete's pore structure and microscopic phenomena, described according to simplified mechanical and thermodynamic assumptions. Drying shrinkage is determined using a four-step procedure: 1) analytical pore size distribution; 2) time-dewatering relationship; 3) dewatering-shrinkage relationship; and 4) time-shrinkage relationship. A limitation of this model is that it has been validated on only two specimens. In addition, the theoretical equations require extensive amounts of data and subsequent experimental testing.

A.2.4 Moisture Transport in Concrete

The properties of concrete are highly dependent upon the moisture conditions within. By appropriately monitoring the moisture content of concrete, it is possible to minimize the development of some distresses. Three different pavement distresses associated with moisture loss are plastic shrinkage cracking, delamination spalling, and drying shrinkage cracking. Plastic shrinkage cracking is caused by the loss of water from the surface of a concrete pavement at early ages. If the pavement is cured properly, this cracking can be prevented. Moisture lost from the surface of the concrete pavement can also cause delamination spalling and drying shrinkage. Delamination of the concrete surface results when pavement strength decreases due to insufficient moisture in the concrete at the time of curing. This weakened portion of concrete detaches from the monolithic slab to form a delamination (or flat bottom) spall. Drying shrinkage is caused by moisture lost from the pavement surface during curing. This can lead to increased levels of stress in the pavement, and to subsequent crack formation.

RILEM Bulletin, "Properties of Set Concrete at Early Ages—State of the Art Report," Materials and Structures, Vol. 14, No. 84, pp. 398–450, 1981.

Most mechanical and physical properties of concrete are affected by moisture. Concrete is a porous material, and volume changes occur due to the presence of water, such as shrinkage and swelling. All porous materials bind water from the atmosphere with a certain relative humidity or from water on contact. Water in concrete is either chemically combined or physically adsorbed. The sorption isotherm relates the material's equilibrium content of water to that of the ambient environment's humidity. To reach an equilibrium state with a higher relative humidity, an adsorption isotherm is used. To decrease the concrete's moisture, a desorption isotherm is used. These isotherms are a function of the concrete's degree of hydration, among other factors. There is no data on sorption isotherms at early ages. The transport of moisture in the concrete is governed by Darcy's law and Fick's first law. Moisture transport depends on the concrete's moisture content. For a fixed relative humidity, transport depends on the concrete's composition, age, and temperature. Age significantly affects the concrete's diffusion prior to 28 days. For mature concrete, w/c and air content are the influential factors.

Xi, Y., Baźant, Z.P. Molina, L., and Jennings, H. M., "Moisture Diffusion in Cementitious Materials," Moisture Capacity and Diffusivity, Journal of Advanced Cement-Based Materials, Vol. 1, pp. 258–266, 1995.

This paper discusses the diffusion of water in concrete. Concrete dries due to three different diffusion mechanisms. They are ordinary drying, Knudsen diffusion, and surface diffusion. An equation for moisture diffusivity is given that is highly dependent on the concrete's w/c. Increasing a concrete's w/c causes diffusivity to increase at low humidity levels.

Maekawa, K., Chaube, R., and Kishi, T., Modeling of Concrete Performance: Hydration, Microstructure Formation and Mass Transport, E&FN Spon, New York, NY, 1999.

Moisture transport in concrete is modeled by the DuCOM researchers. This model should be able to account for the effect of crack formations on water distribution in the concrete structure.

Mjornell, K.N., Moisture Conditions in High-Performance Concrete: Mathematical Modeling and Measurements, Department of Building Materials, Chalmers University of Technology, Sweden, 1997.

A moisture model has been developed for high-strength concrete that accounts for both self-desiccation and moisture transport. The effect of curing on the concrete has been studied at very early ages, as well.

A.2.5 Set Time of Concrete

Concrete set is typically divided into two stages. The first is initial set, when the concrete paste stiffens considerably. The second stage is final set, where the concrete has hardened so that it can sustain load. The setting of concrete referred to here is the final set. This parameter is very important when determining the early-age stress state of the concrete.

Byfors, J., Plain Concrete at Early Ages, Swedish Cement and Concrete Research Institute, 1980.

This paper investigates how different aggregate and admixtures affect the setting time of concrete and its time-dependent stiffness. Aggregates in the concrete that are investigated include quartzite, granite, dolomite, and andesite. Blended cements are investigated, such as ordinary portland cement with silica fume, slag, and fly ash. The linear and nonlinear growth of the concrete modulus as a function of time is recorded at early ages and at later ages.

Uchikawa, H., Hanehara, S., Shirasaka, T., and Sawaki, D., Effect of Admixture on Hydration of Cement, Adsorptive Behavior of Admixture and Fluidity and Setting of Fresh Cement Paste," Cement and Concrete Research, Vol. 22, pp. 1115–1129, 1992.

A rheological discussion on concrete setting times is presented. The yield stress is related to the mortar specimen's set time.

De Siqueira Tango, C.E., "An Extrapolation Method for Compressive Strength Prediction of Hydraulic Cement Products," Cement and Concrete Research, Vol. 28, No. 7, pp. 969–983, 1998.

The determination of concrete set time for pavements is discussed in this report. If drying shrinkage and creep of the concrete are not taken into account, the zero stress point corresponds to the zero set temperature. However, if these factors are considered, the zero stress point occurs at a higher temperature. Compressive stresses can be alleviated by shrinkage and creep effects. A novel method to determine set temperature is presented. The procedure is to fill a mold with fresh cement mix and determine the set temperature when the mix separates from the sides of the mold.

Struble, L.J. and Lei, W.-G., "Rheological Changes Associated with Setting of Cement Paste," Advances in Cement-Based Materials, Vol. 2, p. 244, 1995.

Set times can be a measure of the cement hydration's AE. The Arrhenius method is used to determine how the rate of chemical reaction depends on temperature. The thermal sensitivity of the reaction is the AE. AE is time dependent, but it is usually assumed to be a single value during all stages of hydration. The hotter the mix, the faster the setting time.

A.2.6 Thermal Properties of Concrete

Because temperature is one of the primary factors that influence the behavior of jointed concrete pavements (JCP) at early ages, the thermal properties of the concrete must be understood. HIPERPAV II incorporates seven thermal properties of concrete. They are coefficient of thermal expansion (CTE), thermal conductivity, specific heat, thermal diffusivity, convection, emissivity, and solar absorptivity. This section defines these parameters and summarizes how these properties change at early ages. Early-age factors that influence concrete's thermal properties are its degree of hydration, the amount and type of aggregate, and the water-to-cementitious materials ratio (w/cm). HIPERPAV II requires an understanding of concrete thermal properties at early ages and in the long term.

A.2.6.1 Coefficient of Thermal Expansion

CTE is defined as the relative length change of a material caused by changing its temperature one degree. In concrete, CTE is a function of the paste and the aggregate. The aggregate's CTE depends upon its mineralogical composition, and only slightly on its moisture content. The CTE of paste depends primarily on the moisture content, w/cm, and age of the paste.

> *Khan, A.A., Cook, W.D., and Mitchell, D., "Thermal Properties and Transient Thermal Analysis of Structural Members During Hydration," ACI Materials Journal, Vol. 95, No. 3, pp. 293–303, May–June 1998.*

CTE of concrete is assumed to be equal to the volumetrically weighted average of its ingredient's CTE. Concrete CTE is known to increase with increasing concrete density. CTE is highly dependent on age only during the first few hours after construction. The early-age CTE is significantly higher than the hardened concrete's CTE. After 10 hours of hydration, it decreases, then remains constant.

> *LaPlante, P. and Boulay, C., "Evolution du Coefficient de Dilation Thermique du Beton en Fonction de sa Maturite Aux Tout Premiers Ages," Materials and Structures, Vol. 27, pp. 596–605, 1994.*

CTE of concrete was measured at early ages and plotted as a function of equivalent age at 20 °C.

A.2.6.2 Thermal Conductivity

Thermal conductivity is the ratio of heat flux to temperature gradient. Thermal conductivity is defined as the amount of heat flowing per unit time between two parallel faces of unit area when the faces are unit distance apart. The plates are maintained at a temperature difference of 1 degree. All the heat entering one face leaves the opposite face.

> *Khan, A.A., Cook, W.D., and Mitchell, D., "Thermal Properties and Transient Thermal Analysis of Structural Members During Hydration," ACI Materials Journal, Vol. 95, No. 3, pp. 293–303, May–June 1998.*

Thermal conductivity varies with concrete density. Heavier aggregates typically have concrete with a higher thermal conductivity. Because thermal conductivity of water and air are different from that of the hydration products, thermal conductivity is expected to change during early hydration. Water has lower conductivity than aggregate. Concrete made with a low w/c and a higher density should have a high thermal conductivity. This is why lightweight concrete with high porosity and, therefore, low conductivity, has good insulating properties.

It is difficult to measure thermal conductivity in early-age concrete. Some researchers report a drop in thermal conductivity from 6 hours to 7 days, while others say there is no change in thermal conductivity after 24 hours. For normal strength concrete (30 megapascals (MPa)), its thermal conductivity during maturation is 33 percent higher than when hardened. For high-strength concrete (100 MPa), there is only a 2 percent difference in the thermal conductivity of maturing and hardened concrete. Thermal conductivity is typically independent of temperature within the normal climactic range. However, above 100 °C, thermal conductivity decreases linearly.

Properties of Set Concrete at Early Ages—State of the Art Report, Materials and Structures, Vol. 14, No. 84, November–December 1981.

This article reports that aggregate type is the most important factor affecting the thermal conductivity of concrete.

Brown, T.D. and Javaid, M.Y., "The Thermal Conductivity of Fresh Concrete," Materials and Structures, Vol. 3, No. 13, pp. 411–416, 1970.

These researchers report a decrease in thermal conductivity of concrete with age for fresh conventional concrete.

A.2.6.3 Specific Heat

Specific heat is defined as heat capacity. Specific heat is determined by measuring the temperature rise in a calorimeter using a predetermined supply of energy. There is limited information about specific heat of concrete in the literature, and some of it is contradictory.

Khan, A.A., Cook, W.D., and Mitchell, D., "Thermal Properties and Transient Thermal Analysis of Structural Members during Hydration," ACI Materials Journal, Vol. 95, No. 3, pp. 293–303, May–June 1998.

Specific heat is a function of time. A 15 percent drop in specific heat a few hours after casting to 5 days later for rapid hardening concrete with a w/c of 0.5 is reported. Moisture content has a significant effect on specific heat. Oven dry specimens have lower specific heat than do saturated samples. Also, specific heat increases with temperature and decreases with increasing concrete density.

Mindess, S. and Young, J. F., Concrete, Prentice-Hall, Inc., Englewood Cliffs, NJ, 1981.

Specific heat of concrete is not affected by aggregate type. It varies by only 8 percent due to a change in aggregate. Typically, specific heat ranges from 800 to 1200 joules per kilogram (J/kg) °C. It is dependent on porosity (w/c), water content, and temperature. In the reference synthesis, a decrease between 1 and 20 percent in the concrete's specific heat is reported as it hardens. Specific heat is a function of the cement's degree of hydration.

A.2.7 Creep

Knowledge of the nonlinear creep behavior is important when accurately estimating axial stresses. The behavior of young concrete under load is best modeled by including viscoelastic deformations and plastic flow. In HIPERPAV I, the effect of relaxation is accounted for empirically, and a more sophisticated model that combines the effects of creep and viscous response (relaxation) of concrete at early ages is required. This section provides a brief summary of the primary references that contain candidate models.

Umehara, H., Uehara, T., Iisaka, T., and Sugiyama, A., "Effect of Creep in Concrete at Early Ages on the Thermal Stresses," Proceedings of the International RILEM Symposium, Munich, Germany, pp. 79–86, E&FN Spon, October 1994.

This document contains the approach followed to model the creep behavior in HIPERPAV I and II. Models were developed based on tensile and compressive creep tests. The stress level, period of loading, and temperature at the test were the parameters investigated. The effective modulus method is used to

characterize the creep, and the viscoelastic nature of concrete loaded at early ages, therefore, cannot be modeled.

Bažant, Z.P., "Numerical Determination of Long-Range Stress History From Strain History in Concrete," Materials and Structures, RILEM Paris, Vol. 5, No. 27, pp. 135–141, May–June 1972.

This paper presents an efficient systematic numerical algorithm for computing the stress history from any prescribed strain history in a linear age-dependent viscoelastic material such as hardening concrete. The method is applicable for any form of the creep function. It is assumed that stress history is a series of sudden (discontinuous) stress increments, then the algebraic equations resulting from the superposition of creep responses due to all the individual stress increments are solved. The disadvantage of this method is that large storage space could be required to store the complete history of stresses for all the elements in the structure. Uncertainty exists about the applicability of the principle of superposition in the case of creep recovery. Bažant and Panula (as referenced below) address this issue more directly and provide an example of the measured creep versus predicted creep where the theory works very well.

Bažant, Z.P., and Panula, L., "Practical Predictions of Time-Dependent Deformations of Concrete," Materials and Structures, Third RILEM, Vol. 11, 1978.

In this document, the Double Power Law is developed to predict concrete creep at constant humidity and temperature from the composition of the concrete mix, strength, age at loading, and load duration. The Double Power Law is perhaps the most well known compliance function, and it has been used by many researchers since its development. With the Double Power Law, creep of concrete at constant moisture and thermal state is described by power curves for load duration ($t–t_0$), and by inverse power curves to account for the effect of the loading age t_0. The Double Power Law was modified later to the Triple Power Law (discussed next) to improve the accuracy of the long-term creep prediction.

Bažant, Z.P., and Chern, J.C., "Strain Softening with Creep and Exponential Algorithm," Journal of Engineering Mechanics Division, American Society of Civil Engineers (ASCE), Vol. 111, No. 3, 1985.

In this paper, Bažant provides an improved creep model for concrete at constant temperature and water content. It gives the creep rate as a product of power functions of the load duration, the age of loading, and the current age of the concrete. This model was called the Triple Power Law, and the Double Power Law was modified with a binomial function to provide a more accurate description of long-term creep. This model is extensively calibrated with test data obtained from literature.

Emborg, M., Thermal Stress in Concrete Structures at Early Ages, Doctoral Thesis, Luleå University of Technology, Division of Structural Engineering, 285 pp, 1989.

Emborg tested the validity of both the Double and Triple Power Laws at early ages and concluded that neither was calibrated for loading at early ages, and their use was not intended to predict creep for young concrete. Therefore, Emborg adjusted the Triple Power Law to account for loading at ages earlier than about 2 days, and the extended Triple Power Law was developed. Most of the parameters for the Triple Power Laws remained unchanged, and two additional functions were added: one that accounts for the age dependence of the instantaneous deformation, and another to increase the creep when the load has been applied at early ages.

Westman, G., Concrete Creep and Thermal Stresses. Doctoral Thesis, Luleå University of Technology, Division of Structural Engineering, 301 pp, 1999.

Westman modified the shape of the two additional functions first developed by Emborg in 1989 based on early-age creep tests performed. In this thesis, Westman provides the necessary values for each of the parameters in the extended Triple Power Law.

A.3 JPCP LITERATURE REVIEW

The literature review of JPCP models is presented in this section. The models are divided into seven sections. The first section reviews pavement structural models, such as the stresses that develop in the pavement due to temperature, moisture, and traffic loading, for example. The second section reviews available climatic models that can be used in conjunction with the structural models to account for climatic conditions at the time of pavement curing and also over the years as the pavement is subjected to long-term use. Third, the JPCP distress models are presented. These models are primarily empirical in nature. This means that the models are valid only for the pavement sections for which they were developed. In HIPERPAV II, it is preferable that mechanistic models be used that have been calibrated and validated with actual experimental data. Literature review on faulting, transverse cracking, and spalling are presented.

A.3.1 JPCP Structural Models

The JPCP structural models are used to predict the stresses acting on the pavement due to the different forms of loading, such as temperature, moisture, and traffic. Eight references are described below in the annotated bibliography.

Huang, Y.H., Pavement Analysis and Design, Prentice Hall, Englewood Cliffs, NJ, 1993.

Huang discusses KENSLABS, a finite-element program that can be used to predict pavement behavior, in detail. The types of foundations that can be accounted for are liquid, solid, and layer. Pavement layers can either be bonded or unbonded and have different or the same material properties. Likewise, the load transfer at multiple slabs can be taken into account, as can the curling/warping loading response. Arbitrary pavement dimensions, loading conditions, and shoulder conditions can all be considered. This program requires a substantial amount of computer storage.

Smith, K.D., Peshkin, D.G., Darter, M.I., and Mueller, A.L., "Performance of Jointed Concrete Pavements, Volume III—Summary of Research Findings," FHWA–RD–89–138, Federal Highway Administration (FHWA), McLean, VA, November 1990.

The ILLI-SLAB program is described in this reference. ILLI-SLAB is a finite-element program that analyzes pavements. It calculates stresses, deflections, and moments directly due to loading or temperature effects. This program is able to analyze pavements of arbitrary dimensions with any number of slab arrangements. Two layers either can be bonded or not bonded, and these layers can have the same or different material properties. The subgrade can either be a liquid or solid subgrade, and the program can account for uniform or nonuniform support due to erosion. Similarly, arbitrary loading (axle) conditions and pavement shoulder conditions can be taken into account with ILLI-SLAB. This program, however, requires large amounts of computer storage.

Lee, Y-H. and Darter, M.I., "Mechanistic Design Models of Loading and Curling in Concrete Pavements," Airport Pavement Innovations: Theory to Practice, Proceedings of the Conference. Edited by Hall, J.W. Jr., ASCE, September 1993.

FEMs are used to analyze the edge stresses on the pavement. The FEM can account for finite slab length, finite slab width, and slab curling. These correction factors can be used to correct Westergaard's solutions based on the infinite slab assumption.

Lee, Y-H. and Lee Y-M., Corner Stress Analysis of Jointed Concrete Pavements, Transportation Research Record No. 1525, Transportation Research Board (TRB), National Research Council, Washington, DC, 1996.

FEMs again are used to determine the corner stresses on a pavement, similar to the reference above. Design factors considered are widened outer lanes, tied concrete shoulders, and different loading configurations. These correction factors can be used in the fatigue equation for predicting corner cracks.

Ramsamooj, D.V., "Stresses in Jointed Rigid Pavements," Journal of Transportation Engineering, pp. 101–108, March–April 1999.

Fracture mechanics is used to determine design stresses midway between the edge of the rigid pavement and at the corner. The solutions generally agree with Westergaard, finite-element, and American Association of State Highway and Transportation Officials (AASHTO) road test solutions. However, stresses predicted by this equation are 30 percent greater than the Westergaard stresses. Pavement deflections and stresses also are calculated. When wheel load is placed at the middle of the slab, critical stresses are at the bottom. Convex curling in a pavement occurs due to thermal temperature gradients. Traffic loading is critical for this condition.

Liang, R.Y. and Niu, Y-Z., "Temperature and Curling Stress in Concrete Pavements: Analytical Solutions," Journal of Transportation Engineering, Vol. 124, No. 1., pp. 91–101, January–February 1998.

The objective of this paper is to develop a theoretical model to predict the temperature and curling stresses in a concrete pavement. Based on nonlinear temperature gradients through the slab, the authors are able to develop the equivalent temperature bending moment. If a pavement experiences a severe temperature change (10 °C in 1 hour), the nonlinear temperature gradient must be taken into account. However, for more gradual temperature changes, linear temperature gradients are sufficient.

Kuo, C.-M., "Effective Temperature Differential in Concrete Pavements," Journal of Transportation Engineering, Vol. 124, No. 2., pp. 112–116, March–April 1998.

Three-dimensional FEM code is used to evaluate curling stresses in pavements due to temperature gradient, slab self weight, and support under the concrete slab. The number of allowable traffic loads can be calculated before terminal serviceability is reached.

Grater, S.F. and McCullough, B.F., "Analysis of Jointed Concrete Pavement," Research Report 1244–10, Center for Transportation Research, The University of Texas at Austin, Austin, TX, 1994.

The mechanisms that cause cracking in JCPs are discussed in this report. Climatic factors, such as changing temperatures and moisture conditions 1 year after construction, are used in the analysis. The climatic analysis is extended from several days to 1 year. This program has been revised extensively at the University of Texas at Austin, evolving from JRCP–1 to JRCP–6.

A.3.2 JPCP Climatic Models

The JPCP climatic models are used to predict pavement temperatures and moisture conditions. Climatic conditions are especially influential during early-age curing, but are also critical to the pavement's long-term performance. In the following section, several climatic models are described.

McCullough, B.F. and Rasmussen, R.O., Fast-Track Paving: Concrete Temperature Control and Traffic Opening Criteria for Bonded Concrete Overlays, Publication No. FHWA–RD–98–167, October 1999.

This reference describes the theory behind the software package HIPERPAV I. This program predicts early-age pavement behavior caused by temperature and moisture changes during the first 72 hours after concrete placement. At its core is a finite-element temperature prediction model. The model takes into account heat generated internally due to hydration, solar absorption, convection, irradiation, and age-dependent specific heat and thermal conductivity. The early-age variations in temperature can have a significant influence on the behavior of young concrete. Thermal and moisture stresses must be controlled to minimize early-age damage to the concrete pavements.

Muller, A.L., Peshkin, D.G., Smith, M.I., Darter, M.I., Performance of Jointed Concrete Pavements, Volume VI, Appendix C—Synthesis of Concrete Pavement Design Methods and Analysis Models, FHWA–RD–89–141, FHWA, McLean, VA, July 1990.

A review of climatic models is given in this reference. The models mentioned include Climatic-Material-Structural and Liu-Lytton drainage models.

Lytton, R.L., Pufahl, D.E., Michalak, C.H., Liang, H.S., and Dempsey, B.J., "An Integrated Model of the Climate Effects on Pavements," FHWA–RD–90–033, 285 pp., FHWA, McLean, VA, November 1989.

The Integrated Climate Model (ICM) is a one-dimensional coupled heat and moisture flow program that is intended for use with pavements. Based on the location of the selected site, the structure's material properties, and the historical climatic data, the ICM internally generates weather patterns of rainfall, solar radiation, air temperature, cloud cover, windspeed, and snowfall throughout the year. The ICM determines the temperature, frost and heave zone depths, frost heave, layer elastic moduli, and pore water pressure profile at different depths throughout the pavement structure at different stages during the year. The model is the combination of three models developed during previous research efforts. They are the Climatic-Materials-Structures Model, the Infiltration and Drainage Model, and the Frost Heave and Thaw Settlement Model.

Barber, E.S., "Calculation of Maximum Pavement Temperatures from Weather Reports," Bulletin 168, Highway Research Board, Washington, DC, pp. 1–8, 1957.

This reference describes a model that could be used in pavements to determine the initial temperature profile. The model is based on air temperature, wind velocity, and solar radiation inputs, which can all be obtained from weather records. This model provides a solution to the differential equation of conduction of heat in a homogeneous isotropic material. The model has the following limitations:

- Only one pavement layer can be analyzed.
- The effect of rain, snow, and clouds on the pavement surface is not taken into account.
- The model assumes a semi-infinite mass.

A.3.3 JPCP Distresses

Guidelines have been developed in the past that relate design features to pavement distresses. These references are summarized here. Most of the guidelines are based on empirical data, so it is best not to extrapolate these models to sets of inputs outside the realm of those used in their development.

> *Smith, K.D., Wade, M J., Peshkin, D.G., Khazanovich, L.H. Yu, T., and Darter, M.I., Performance of Concrete Pavements, Volume II: Evaluation of In-Service Concrete Pavements, FHWA–RD–95–110, FHWA, McLean, VA, June 1998.*

This report synthesizes the behavior of more than 300 concrete sections. It provides critical levels of distress for the JPCP with regard to joint faulting, transverse cracking, longitudinal cracking, joint spalling, and roughness in terms of Present Serviceability Rating (PSR) and International Roughness Index (IRI). It also synthesizes the behavior of the pavements in terms of the design features. Design features that are investigated are pavement thickness, base type, subgrade type, joint spacing, joint orientation, transverse joint load transfer, joint sealant, drainage, shoulder type, widened lanes, reinforcement, and maximum coarse aggregate size. For example, an increase in pavement thickness translates to a decrease in transverse cracking and joint spalling, while there is no significant change in faulting. The mechanisms behind these trends also are discussed. For the example given, thicker slabs theoretically reduce stresses in the concrete, so the pavement will not be subjected to as severe a load. This translates to a reduction in spalling and transverse cracking. A summary of the influence of design features on pavement distresses is given in table 1.

Table 1. Summary of how pavement design parameters influence JPCP distresses.

Variable	Faulting	Spalling	Transverse Cracking	Longitudinal Cracking	Corner Breaks	Roughness	Comments
Slab thickness ↑	x	↓	↓	–	–	–	–
Joint spacing ↓ JPCP	x	–	↓	–	–	–	–
—random	–	–	↑	–	–	–	3.6-, 3.9-, 5.8-, 5.5-meter (m) joints JPCP
Joint orientation	↓	↓	–	–	↑	–	Nondoweled designs
Transverse joint load transfer	↑	–	–	–	–	–	Nondoweled joints
	↓	–	–	–	–	–	Doweled joints
Dowel diameter—small (2.54 cm)	↑	–	–	–	–	–	–
—large (3.2 cm)	↓	–	–	–	–	–	–
Dowel covering	↓	↓	–	–	–	–	Epoxy or plastic
Joint sealant—sealed	↓	↓	–	–	–	–	Preformed compression seals best
Joint sealant—none	–	–	↑	–	↑	–	–
Base type—JPCP on AGG*	–	–	↓	–	–	–	–
Base type—ATB* / CTB*	–	–	↑	–	–	–	Stabilizing >6% for benefits
No base course	↑	–	–	–	–	–	No dowels in pavements
Base type—permeable	x	–	–	–	–	–	Less moisture distress Requires good drainage
Drainage—good	↓	↓	↓	–	–	–	More pronounced effect on nondoweled sections
Shoulder type—tied PCC*	–	–	–	–	↓	–	Tied PCC better than AC* shoulders
Widened lanes	↓	–	–	↑	–	–	Reduce pavement stresses
Reinforcement—type	–	–	↓	–	–	↑	JRCP* (steel >0.17%)
—quantity	–	–	↑	–	–	–	JRCP (steel <0.10%)
Coarse aggregate—large size	↓	–	↓	–	–	–	–

*AC – asphalt concrete, AGG – aggregate, ATB – asphalt-treated base, JRCP – jointed reinforced concrete pavement, PCC – portland cement concrete

The arrows indicate the conditions that cause the distresses to increase or decrease, and the dash implies that there is no influence. Cells with an "x" indicate that no trend could be concluded or there was not enough data. This reference also examined European and Chilean concrete pavements to learn how pavements in the United States can be improved. In Europe, the four modernity categories expected to increase pavement performance are nonerodible base courses, positive pavement drainage, strengthened structure (dowel bars and CRCP), and the optimization of material use (wider lanes and trapezoidal cross section). Only 25 percent of U.S. pavements incorporate two or more of these features.

Yu, H.T., Smith, K.D., Darter, M.I., Jiang, J., and Khazanovich, L., Performance of Concrete Pavements, Volume III: Improving Concrete Pavement Performance, FHWA–RD–95–111, FHWA, McLean, VA, June 1998.

This reference develops models that predict joint faulting, slab cracking, joint spalling, pavement serviceability, and pavement roughness. Three hundred pavements were used to formulate these empirical models, and most of the pavements are located in the Upper Midwest, have carried 10 million 18-kip equivalent single axle loads (ESALs) and are 10 to 15 years old. The majority of the JPCP pavements are in the wet-freeze climatic zone and have nonstabilized bases. Trends are given for the distresses as a function of traffic, dowel bearing stress, drainage, annual precipitation, freezing index, dowel bar size, joint spacing, and stabilized bases. The distresses investigated in this report are faulting for doweled and nondoweled pavements, transverse cracking, transverse joint spalling, and roughness. Guidelines are developed that recommend the preferred pavement design for minimal pavement distress.

Titus-Glover, L., Owusu-Antwi, E B., Hoener, T., and Darter, M.I., Design and Construction of PCC Pavements Volume II: Design Features and Practices that Influence Performance of Pavements, FHWA–RD–98–127, FHWA, McLean, VA, October 1998.

This report uses canonical discriminant analysis to assess how design factors affect the performance of JPCP. The pavement distress analysis is performed for the four climatic regions of wet-freeze, wet-no freeze, dry-freeze and dry-no freeze. The distresses that are analyzed are faulting with and without dowels, transverse cracking, and pavement roughness. A summary table showing the influence of long-term factors and design parameters on pavement transverse cracking is shown in table 2. The pavements are subdivided into slabs that are less than 254 millimeters (mm) thick and those that are more than 254 mm thick. The arrows indicate the conditions that cause transverse cracking to increase or decrease, and "N/A" implies that these factors had no influence. A dash means that no trend could be concluded or that there was not enough data.

Table 2. Summary of factors affecting transverse cracking in JPCP.

Transverse Cracking	**<25.4 cm**				**>25.4 cm**			
	***DF**	***DNF**	***WF**	***WNF**	**DF**	**DNF**	**WF**	**WNF**
Freezing index (>277 °C days)	↑	↑	↑	↑	N/A	N/A	N/A	N/A
Annual average precipitation (>1 m)	↑	↑	↑	↑	–	–	–	–
Subgrade type (coarse)	↑	↑	↑	↑	↑	↑	↑	↑
Subgrade k value (>41 kPa/mm)	–	↑	↑	↑	–	–	↑	↑
Subgrade k value (<41 kPa/mm)	–	–	–	–	–	–	–	–
Joint spacing (>4.6 m)	↑	↑	↑	↑	N/A	N/A	N/A	N/A
Joint spacing (<4.6 m)	–	–	–	–	–	–	–	–
Base type (granular)	–	–	–	–	–	–	–	–
Base type (stabilized)	↑	↑	↑	↑	↑	↑	↑	↑
28 day MOR (>4.5 MPa)	–	–	–	–	↑	↑	↑	↑
28 day MOR (<4.5 MPa)	↑	↑	↑	↑	N/A	N/A	N/A	N/A
Paver type (slip form)	↑	↑	↑	↑	↑	↑	↑	↑
Paver type (side form)	–	–	–	–	–	–	–	–
Transverse joint form method (saw)	↑	↑	↑	↑	↑	↑	↑	↑
Transverse joint form method (plastic)	–	–	–	–	–	–	–	–

*DF – dry freeze, DNF – dry-no freeze, WF – wet freeze, WNF – wet-no freeze

Sensitivity Analyses for Selected Pavement Distresses, SHRP–P–393, Strategic Highway Research Program, National Research Council, Washington, DC, 1994.

This reference provides models for predicting JPCP distresses, namely joint faulting in doweled and nondoweled pavements, transverse cracking, joint spalling, and roughness of doweled and nondoweled JPCP. The models are based on mechanistic and empirical concepts, and a fatigue analysis is used to predict distress formation. A sensitivity analysis is completed for each model, and trends are given showing how the input affects the distress magnitude. Several limitations of these models are apparent. Only a limited number of pavement sections were used to develop these models, so they should not be used to extrapolate to other pavements. Likewise, the data from all four climatic regions is lumped together. The researchers rank input parameters to show the parameters' importance in influencing the performance of PCC pavements. The first parameter is age, followed by traffic loading, slab thickness, modulus of subgrade reaction (*k*-value), precipitation, percent steel tied with joint spacing, edge support tied with freeze-thaw cycles, and subgrade type.

Smith, K.D., Peshkin, D.G., Darter, M.I. and Mueller, A.L., Performance of Jointed Concrete Pavements, Volume III—Summary of Research Findings, FHWA–RD–89–138, FHWA, McLean, VA, November 1990.

This reference assesses how design features influence the behavior of 95 pavements. Trends show how each design parameter influences pavement distresses. Limitations of these models are the limited database used to develop them and their inability to account for construction-related distresses. The models were developed empirically, and because pavement performance is highly variable, these models should be used only on the pavements for which they were developed.

Titus-Glover, L., Owusu-Antwi, E.B., and Darter, M.I., Design and Construction of PCC Pavements, Volume III: Improved PCC Performance Models, FHWA–RD–98–113, FHWA, McLean, VA, January 1999.

This research report gives a history of JPCP distress model development, and lists the prediction equations. The mechanisms behind faulting, spalling, transverse cracking, corner breaks, and roughness are discussed. A mechanistic-empirical basis is used to develop these equations. The empirical data is extracted from the Long-Term Pavement Performance (LTPP) Program database. The regression equations were developed using multiple linear regression, nonlinear regression techniques, and the Statistical Package for Social Sciences. To develop the transverse and corner cracking models, a linear fracture mechanics approach is used in conjunction with the fatigue damage approach. To develop the spalling model, the spall stress is calculated using a mechanistic model. It is a function of traffic, environment, incompressibles in the joint, and the concrete properties. The IRI model depends on the initial pavement IRI, traffic loading, and pavement aging.

Darter, M.I., Becker, J.M., Snyder, M.B., and Smith, R.E., Portland Cement Concrete Pavement Evaluation System: COPES, National Cooperative Highway Research Program (NCHRP)–277, National Cooperative Highway Research Program, September 1985.

A total of 418 sections were used to develop regression models for predicting JPCP performance. Design factors, material/soil factors, climatic factors, and maintenance-related factors were examined in developing the model. Several recommendations were to use stabilized bases, PCC shoulders, increased subgrade *k* modulus, increased concrete modulus of rupture, larger dowels, and increased slab thickness.

Perera, R.W., Byrum, C. and Kohn, S.D., Investigation of Development of Pavement Roughness, FHWA–RD–97–147, FHWA, McLean, VA, May 1998.

Roughness models were developed using data taken from the LTPP databases. A model was formulated for each climatic region, and for doweled and nondoweled pavements. Correlation methods were used to find the most influential parameters affecting pavement distresses.

Hansen, W., Jensen, E.A., Mohr, P., Jensen, K., Pane, I., and Mohamed, A., The Effects of Higher Strength and Associated Concrete Properties on Pavement Performance, Volume I—Final Technical Report, The University of Michigan, Department of Civil and Environmental Engineering, July 2000.

This report subdivides pavement variables into six sections: environmental, design, concrete, subbase, traffic loading, and distress factors. It examines how each one influences pavement behavior. The distresses investigated are joint faulting, joint spalling, transverse cracking, and corner breaks. Focus is placed on examining how specific concrete properties influence the distresses. Table 3 shows how flexural strength impacts joint spalling, transverse cracking, and corner breaks, but not joint faulting.

Table 3. Influence of concrete properties on JPCP pavement distresses.

PCC Properties	Joint Faulting	Joint Spalling	Transverse Cracking	Corner Breaks
PCC flexural strength	–	X	X	X
PCC compressive strength	X	–	–	–
PCC elastic modulus	X	X	X	–
CTE	X	–	X	–
PCC shrinkage	X	–	–	–
PCC fracture energy	–	–	X	X
PCC permeability	–	X	–	–
PCC air void system	–	X	–	–
Reactive aggregate	–	X	–	–

This meets one of the study objectives: to determine the concrete properties that contribute to exceptional long-term pavement performance. The key properties with regard to pavement distress are concrete flexural strength, elastic modulus, CTE, and fracture energy. Fracture properties of the concrete are important with regard to transverse cracking and corner breaks.

A.3.3.1 JPCP Faulting

Faulting often is reported to be caused by the erosion of subbase material from under the approach side of the slab, and its deposition under the leave side. When the slab deflects on the leave side, material is pushed toward the approach slab due to hydraulic action. When the approach slab is loaded by the passing wheel, the material is pushed back to the leave side. The fines accumulate under the leave slab. Over time, there is a difference in the vertical profile of the approach and leave sides of the pavement; this is termed faulting. Erosion of the subbase is due to shear stresses induced by water at the joint. In the following section, several references are summarized that relate to pavement faulting.

Ksaibati, K. and Staigle, R., "Faulting Performance Modeling for Undoweled Plain Concrete Pavements," Transportation Research Record 1482, TRB, pp. 1–6, Washington, DC, 1995.

Faulting of nondoweled JPCP in Wyoming is modeled using an empirical regression model. Wyoming is part of the dry-freeze region of the United States. Factors incorporated into the faulting regression equation are environmental factors, average joint width, edge support, subgrade soil classification, traffic loads, and the presence of positive drainage.

Bendana, L.J. and Yang, W.-S., "Rehabilitation Procedures for Faulted Rigid Pavement," Transportation Research Record 1388, TRB, pp. 200–210, Washington, DC, 1993.

Initially, faulting is found to increase linearly with age. When the fault distance is greater than 1.6 mm, faulting increases nonlinearly. Faulting is caused primarily by traffic loading. Faulting is very difficult to correct after it has occurred. Severe faulting has been found on New York State highways, and remediation efforts are needed. Two rehabilitation methods used were to pump grout under the slab and to grind the pavement surface. If the grout is not installed evenly, or if there is too much grout or too little grout, it is possible that the JCP will blowout or crack due to uneven subbase. Installing load transfer devices is the most effective way to reduce faulting in JPCP.

Bustos, M., de Solminhac, H.E., Darter, M.I., Caroca, A., and Covarrubias, J.P., "Calibration of Performance Models for Jointed Concrete Pavements Using Long-Term Pavement Performance Database," Transportation Research Record 1629, TRB, pp. 108–116, Washington, DC, 1998.

Faulting data found in the LTPP database is analyzed for JPCP pavements. Calibration factors are presented based on the climatic region. It is found that faulting in the dry-no freeze sections is the lowest of all the regions.

Ioannides, A.M., Lee, Y. and Darter, M.I., "Control of Faulting through Joint Load Transfer Design," Transportation Research Record 1286, TRB, pp. 49–56, Washington, DC, 1990.

A mechanistic-empirical faulting model is developed for JPCP with dowels. The major influencing factor is the bearing stress at the dowel-concrete interface, which is determined mechanistically. It is a function of the modulus of dowel support, joint width, wheel load, load transfer efficiency (LTE) (assumed to be 45 percent), dowel stiffness, dowel moment of inertia, critical dowel distribution factors, and relative stiffness of the dowel-concrete system. This model uses both Westergaard and Timoshenko theory. A concern is how close the dowels must be to the joint to provide effective load transfer. In addition, an equation for the faulting of nondoweled pavements is given where the load transfer is provided by aggregate interlock.

Hansen, E.C., Johannesen, R., and Armaghani, J.M., "Field Effects of Water Pumping Beneath Concrete Pavement Slabs," Journal of Transportation Engineering, Vol. 117, No. 6, November–December 1991.

This reference investigates water pressures and velocities due to pumping under slabs. Traffic produces high pressure under the approach slab and suction under the leave slab. Frictional erosion generates loose, fine material. Water flow at the joint is generally in the opposite direction of the traffic. Pumping is more severe under pavements with upward thermal curling.

Van Wijk, A J. and Lovell, C.W., "Prediction of Subbase Erosion Caused By Pavement Pumping," Transportation Research Record 1099, TRB, pp. 45–57, Washington, DC, 1985.

This paper lists erosion tests of subbase material, such as the rotational shear device, the brush test, the jetting test, and the vibrating table. The rotational shear device can be used to investigate the erosion of clay and stabilized materials. Noncohesive materials cannot be tested with it. The jetting test is used for noncohesive materials. The brush test is primarily used for stabilized materials. The most commonly used subbases in the United States are portland cement stabilized, crushed stone, dense graded, asphalt concrete, sand, and asphalt stabilized subbases. The climatic conditions at the pavement location determine the performance of the pavement layers, especially its temperature and moisture content. Regression equations are given that relate erosion to variables such as pavement age and portland cement content. Materials that resist erosive shear stresses of 50 Pa or greater should not erode for the life of the pavement. Materials that erode for a shear stress between 25 and 50 Pa should have low erosion and those that erode at a shear stress less than 25 Pa should have high erosion.

LTPP Data Analysis: Frequently Asked Questions About Joint Faulting with Answers from LTPP, LTPP Tech Brief, FHWA–RD–97–101, FHWA, McLean, VA, 1997.

The LTPP database was mined to determine the site conditions and pavement design features that affect transverse joint faulting. Dowels are the most effective means of controlling joint faulting. Larger dowels reduce the amount of faulting because of the reduced dowel-concrete bearing stress. Increasing pavement drainage reduces faulting; this is more effective for nondoweled pavements than for doweled pavements. Short joint spacing and widened slabs also reduce faulting.

A.3.3.2 JPCP Transverse Cracking—Midslab

Cracking in JPCP pavements reduces their long-term performance. An annotated bibliography follows of references that discuss pavement design features and their relation to transverse cracking.

Bustos, M., de Solminhac, H.E., Darter, M.I., Caroca, A., and Covarrubias, J.P., "Calibration of Performance Models for Jointed Concrete Pavements Using Long-Term Pavement Performance Database," Transportation Research Record 1629, TRB, pp. 108–116, Washington, DC, 1998.

The LTPP database is used to develop correlation factors between JPCP pavement distress and climatic conditions at the pavement location. To do so, several pavement sections in the database are disregarded, such as those without a subgrade *k*-value. This decreases the reliability of the transverse cracking model. However, this study finds that transverse cracking depends on climatic conditions. The least severe cracking is found in the dry-no freeze zone, while the most severe is in the wet-no freeze region. These correlations are not obvious, but this may be because cracking is not heavily dependent on environment, as faulting is, for example.

Moody, E.D., "Transverse Cracking Distress in Long-Term Pavement Performance Jointed Concrete Pavement Sections," Transportation Research Record 1629, TRB, pp. 6–12, Washington, DC, 1998.

The mechanisms that cause midslab transverse cracking are divided into three sections. The primary ones are due to pure bending stresses, curling stresses, and subgrade friction. The secondary transverse cracking mechanisms (at the joint) are due to joint saw cutting timing, loss of load transfer, and locked transverse joints due to dowel bar corrosion or misalignment. These transverse cracks near the joint should not be considered when calibrating the midslab cracking model. The third mechanism causing transverse cracking is related to drying shrinkage. Drying shrinkage cracks do not penetrate the entire

pavement thickness. Correlations also are found between traffic loading and transverse cracking. No section with fewer than 600,000 ESALs had transverse cracks. Transverse cracks increased due to increased traffic, increased monthly temperature changes, and the use of cement-treated bases (increased curling and warping stresses). Transverse cracking decreases with thicker pavements and stronger concrete (tensile strength).

> *Frabizzio, M.A. and Buch, N.J., "Investigation of Design Parameters Affecting Transverse Cracking in Jointed Concrete Pavements (JCPs): A Field Study," paper presented at the TRB 78th Annual Meeting, Washington, DC, 1999.*

This paper investigates several design features that influence the formation of transverse cracks in pavements. This is a synthesis of experimental data; no theoretical model is developed. Aggregate interlock across joints is studied using volumetric surface texture (VST) testing. VST measures the roughness of the crack surface. VST shows that the crack propagating through aggregate results in a smoother crack surface (and therefore lower aggregate interlock) than does the crack that propagates around the aggregate (high aggregate interlock). This implies that a poor aggregate-cement bond has improved load transfer at the joint due to aggregate interlock. Four parameters commonly are used to quantify the efficiency of the load transfer across the joint for the doweled and nondoweled pavements. They are the deflection load transfer, the transferred load efficiency, the total load transferred from loaded side to unloaded side, and the aggregate interlock shear stiffness per unit length of crack. Also, it is shown that aggregate type influences the number of transverse cracks in the JPCP. Pavements reinforced with recycled aggregate have more transverse cracks than do those with good quality aggregate. Shoulder type also influences transverse cracking in the pavements, depending on type of aggregate used. Other causes of transverse cracking are plastic and drying shrinkage cracks, fatigue cracking, and induced frictional stresses due to expansion and contraction of the slabs. An increase in temperature causes the slabs to expand and the joint to close if the LTE is between 30 to 50 percent. If it is 90 percent, then increased temperature does not affect the LTE.

A.3.3.3 JPCP Spalling

Spalling of concrete pavements typically has been studied qualitatively. Researchers present possible causes of spalling based on pavement condition surveys. The majority of the models that have been developed to predict spalling are empirical in nature. They often relate rainfall, evaporation rate, and other factors to spalling. An annotated bibliography of spalling references is given below.

> *Senadheera, S.P. and Zollinger, D.G., "Framework for Incorporation of Spalling in Design of Concrete Pavements," Transportation Research Record 1449, TRB, pp. 114–122, Washington, DC, 1994.*

This reference reviews the majority of prior research on spalling, especially on CRCP. The most important factors that affect the rate of spalling are rainfall, coarse aggregate type, and subbase type. Spalling is a two-step process. First, a horizontal delamination crack forms in the pavement. Then fatigue damage accumulates due to traffic and temperature-induced strains, and the concrete spalls. Two forms of spalling have been seen in pavements—a deep spall caused by the popout of an aggregate particle, and a shallow spall due to the horizontal delamination of the concrete. The long-term performance curve for spalling has an 'S' shape and can be modeled using the Weibull probability distribution function.

McCullough, B.F. and Dossey, T., "Considerations for High-Performance Concrete Paving: Recommendations from 20 Years of Field Experience in Texas," Transportation Research Record 1684, TRB, pp. 17–24, 1999.

This reference deals primarily with CRCP, but also discusses spalling. Factors that significantly influence spalling are surface moisture evaporation at the time of placement and ambient temperatures above 0 °C. To prevent spalling, the amount of water that evaporates from the surface of the pavement must be minimized. High evaporation rates drive delamination cracking deeper into the pavement after construction. The traffic later causes the vertical fracture plane to intersect with the horizontal delamination plane, and the concrete breaks out to form a spall. Wet cotton mats are efficient at reducing surface evaporation, as are plastic sheeting, double membrane curing, and single membrane curing. Constant monitoring of surface evaporation is suggested during concrete construction.

Rollings, R.S., "Joint Spalling in Newly Constructed Concrete Pavement," Journal of Performance of Constructed Facilities, pp. 137–144, August 1998.

A review of spalling work is presented in this paper. Qualitative studies have been performed that list potential causes of spalling. On airport pavements, it appears that poor workmanship is the major cause of spalling. Other possible causes of spalling are listed, such as poor concrete properties, freeze-thaw cycles, poor consolidation and finishing of the concrete, poor repair of the pavement edges, and inadequate curing.

Bustos, M., de Solminhac, H.E., Darter, M.I., Caroca, A., and Covarrubias, J.P., "Calibration of Performance Models for Jointed Concrete Pavements Using Long-Term Pavement Performance Database," Transportation Research Record 1629, TRB, pp. 108–116, Washington, DC, 1998.

In this paper, JPCP distress models were calibrated using LTPP data. Adjustment factors are made to predict JPCP distresses for each region of the United States. Researchers found that a wet climate prevents spalling better than does a dry climate. This agrees with the hypothesis that increased evaporation causes horizontal delamination, a forerunner of spalling.

A.4 CRCP LITERATURE REVIEW

During task B of this project, a literature review of references on CRCP early-age behavior was accomplished. From this effort, a number of references have been compiled and models identified describing the early-age behavior of CRCP.

This section briefly summarizes the primary references identified, including candidate models and useful information on CRCP early-age behavior.

McCullough, B.F, Abou-Ayyash, A., Hudson, W.R. and Randall, J.P., "Design of Continuously Reinforced Concrete Pavements for Highways," Research Project NCHRP 1–15, Center for Highway Research, The University of Texas at Austin, Austin, TX, August 1975.

This document provides some history of CRCP use. To establish optimum CRCP design specifications, it is necessary to understand the major influences controlling the mechanistic behavior of CRCP at early ages. This work is one of the first studies that attempts to correlate the primary factors influencing CRCP behavior to predict theses factors' effects on pavement performance. Based on the findings of that work, a mechanistic design procedure was developed that takes into account the early-age behavior of the pavement. This mechanistic design method proved that the crack spacing and crack width could be

properly controlled to fall within certain limits to minimize undesirable conditions. Major factors influencing crack spacing and crack width are explained. A crack spacing between 1.5 and 2.4 m is considered effective in minimizing distress occurrence. Also, it is concluded that crack width should be limited to no more than 0.6 mm to minimize steel corrosion. The limiting criteria for crack spacing and crack width is based on the performance of CRC pavements in several highways nationwide and laboratory tests. Primary factors that were found to influence CRCP performance include:

- Concrete strength: It was found that concrete tensile strength plays an important roll in the development of spalling. For pavements with a concrete tensile strength less than 2756 kPa, a significant increase in spalling is observed.
- Crack spacing distribution and crack width: It was found that the larger the crack spacing, the larger the crack widths, resulting in loss of load transfer. On the other hand, for small crack spacings, load deflections tend to increase, contributing to the development of stresses that can lead to punchouts.
- Coarse aggregate type: The coarse aggregate type, and in particular its angularity, seem to have an important effect on spalling development. Since siliceous river gravel (SRG) tends to be more roundly shaped, it tends to have a lack of bond with the paste. Crushed aggregate tends to have a better bond strength at the aggregate-paste interface, and therefore, fewer spalling problems.

Palmer, R.P., Olsen, M.P.J., and Lytton, R.L., "TTICRCP—A Mechanistic Model for the Prediction of Stresses, Strains, and Displacements in Continuously Reinforced Concrete Pavements," Research Report 371–2F, Texas Transportation Institute, The Texas A&M University System, College Station, TX, 1988.

This study improves on behavior prediction models CRCP–1, CRCP–2, and CRCP–3 by better modeling bond stress distribution and stress-slip prediction. The TTICRCP software program developed under this study has the objective of better characterizing the behavior of CRCP pavements using a more sophisticated, mechanistic-based approach. The model includes the means to better simulate the interaction between the steel reinforcement and the concrete. During its development, numerous derivations were made based on engineering mechanics and energy concepts. The result was a system of linear, second-order ordinary differential equations describing the complex behavior of the CRCP system. The solution to this system of equations is conducted using a combination of matrix and iterative solution schemes. This program was developed as an analysis routine with the crack spacing as an input rather than an output, as opposed to the CRCP–8 program. In addition, it has not been fully validated and is subject to further modification. However, initial review of the model has demonstrated that it can better predict the crack widths due to the improved characterization of the slip zone between the steel and the concrete. Therefore, this program shows promise as a possible improvement to the CRCP–8 modeling system. This report also provides a literature review on bond-stress and stress-slip relationships.

Won, M., Hankins, K., and McCullough, B. F., "Mechanistic Analysis of Continuously Reinforced Concrete Pavements Considering Material Characteristics, Variability, and Fatigue," Research Report 1169–2, Center for Transportation Research, The University of Texas at Austin, Austin, TX, March 1991.

This is one of the main references for the CRCP–8 program. Although it describes the CRCP–5 program, no major improvements to the software have been made after this study. This reference briefly describes the purpose of transverse steel and why the States do not commonly use it. It also describes the factors affecting transverse cracking in CRCP. The primary purpose of this study is to provide enhanced bond stress/slip relationships for the University of Texas at Austin Center for Transportation Research (CTR)

software program CRCP series. It describes a stochastic method (Monte Carlo) to account for the effect of the variability of materials on CRCP performance variability. The report concludes that variability of steel amount, size, and depth, subbase friction, environmental conditions, slab thickness, CTE, and drying shrinkage are small compared to the variability of tensile strength. Therefore, the report concentrates on the variability of concrete tensile strength as the most significant factors affecting crack spacing. It is assumed that concrete tensile strength has a normal distribution. It is considered that the coefficient of variation (CV) of tensile strength is close to 20 percent, based on the above references. A mechanistic model to predict punchout distress is also presented, taking into account wheel loads and previously predicted crack spacing distribution. The subroutine in CRCP–8 that predicts punchouts is based on a mechanistic-empirical model. During the study, a number of ILLISLAB FEM runs for CRCP of different thicknesses and crack spacings were run. The effect of aggregate interlock and longitudinal steel on load transfer at cracks was ignored during stress calculations. The results of this analysis were used to fit a regression model predicting transverse tensile stress from thickness and crack spacing. Fatigue is then incorporated in this analysis to predict punchout development.

Zollinger, D.G., Buch, N., Xin, D., and Soares, J., "Performance of CRC Pavements Volume 6—CRC Pavement Design, Construction, and Performance," FHWA–RD–97–151, FHWA, McLean, VA, 1997.

This reference presents the FHWA CRCP punchout model. In this work, new predictive models for the behavior and performance of CRCP were developed. Although an explicit punchout prediction model was not included in this reference, several derivations were proposed to improve the prediction of the loss of load transfer across a crack, which is intuitively one of the key factors in punchout prediction. The basic framework of the proposed model includes a more mechanistic-based approach to characterizing the change in stress due to load transfer. The load transfer is comprised of a combination of aggregate interlock, base support, and reinforcement interaction. The study found that accurately characterizing the load transfer due to aggregate interlock could significantly improve the overall distress prediction. The LTE was found to be a function of aggregate interlock, support stiffness, and radius of relative stiffness. This reference also provides guidelines for designing and constructing CRCP. It also extensively describes the factors affecting cracking and describes punchout distress mechanisms. A thickness design procedure for CRCP is presented based on crack spacing, LTE, and fatigue cracking concepts. In this procedure, shear stresses at transverse cracks and curling and warping due to traffic and environmental loads are investigated to predict punchouts. A methodology to take into account design reliability is presented. The authors also present construction methods to improve CRCP crack patterns. Based on experimental test sections, the document concludes that surface crack initiation is more effective than interior crack initiation. From previous recommendations of crack spacing from 1.5 to 2.4 m, it demonstrates results of studies recommending spacings of 0.9 m as a minimum, warning about crack spacings less than 0.9 m. To minimize spalling at cracks, the maximum crack spacing is limited to 1.8 to 2.7 m.

Kim, S.-M., Won, M.C., and McCullough, B.F., "Development of a Finite-Element Program for Continuously Reinforced Concrete Pavements," Research Report 1758–1F, Center for Transportation Research, The University of Texas at Austin, Austin, TX, November 1997.

This report describes the CRCPFEM model, developed under a Texas DOT (TxDOT) effort with the objective of developing a more mechanistic-based model to predict the various responses in CRCP. The CRCPFEM model is a two-dimensional, plane-strain finite-element program developed using a sophisticated set of submodels to predict the behavior of the CRCP due to shrinkage, creep, temperature change, and slab-base restraint. Although the validation of the current version of the software is not extensive, it does show promise as a candidate model for this effort. If selected, further validation of this model can be performed. The ability for this model to account for relaxation creep makes it a worthy

candidate for incorporation into the proposed system. This effect, modeled in HIPERPAV, is quite significant for JPCP. The ability to model this important phenomenon is critical to the accuracy of the early-age prediction. Parametric studies were performed in this study to evaluate the effect of factors influencing CRCP responses. Further investigation of an accurate bond slip relationship is recommended.

Suh, Y.C., Hankins K., and McCullough, B.F., "Early-Age Behavior of Continuously Reinforced Concrete Pavement and Calibration of the Failure Prediction Model in the CRCP–7 Program," Research Report 1244–3, Center for Transportation Research, The University of Texas at Austin, Austin, TX, March 1992.

The main purpose of this study was to calibrate the failure (punchout distress) prediction model in the CRCP program. The calibration is based on data from the Texas CRCP database. The report also presents the results of test sections constructed in Houston, TX, to monitor the early-age behavior in CRCP. The effect of different factors such as concrete properties, aggregate type, steel content, concrete curing temperature, and time of day of construction was investigated, among other factors. Condition surveys were performed to monitor cracking patterns and slab movements. This report may provide some ideas for future instrumentation of CRCP sections. The model was validated for only two aggregate types: limestone and siliceous river gravel.

McCullough, B.F., Ma, J.C.M., and Noble, C.S., "Limiting Criteria for the Design of CRCP," Research Report 177–17, Center for Transportation Research, The University of Texas at Austin, Austin, TX, August 1979.

This reference provides limiting criteria for the design of CRCP. Factors considered include crack spacing, crack width, and maximum steel stresses. The limiting criteria are a function of the target pavement distresses (punchouts, spalling, steel corrosion, and steel permanent deformation). This study also recommends fatigue relationships to be used in the design procedure for CRCP. It also provides information on the CTE of various steel types.

McCullough, B.F. and Rasmussen, R.O., "Fast Track Paving: Concrete Temperature Control and Traffic Opening Criteria for Bonded Concrete Overlays: Task G, Volume 1: Final Report," Federal Highway Administration Report, FHWA–RD–98–167, Washington, DC, 1999.

This research demonstrates the importance of early-age behavior on the long-term performance of JPCP and bonded concrete overlays. The authors mention that a number of factors influence early-age behavior, and these can be placed into four different categories: pavement design, materials and mix design, environment, and construction operations. This approach is believed to be applicable to any type of concrete pavement.

"Continuously Reinforced Concrete Pavement," National Cooperative Highway Research Program, Synthesis of Highway Practice No. 16, Highway Research Board, 1973.

This document describes current CRCP construction practices. It provides a table with the primary factors affecting crack spacing and some guidelines for design and construction of CRCP. The authors emphasize the need for good subgrade support and warn about the practice of designing for less thickness than that required for JCP. They also warn about using wire fabric as reinforcement. The guidelines limit the maximum crack width to 0.5 mm and limit the steel percentage to not less than 0.7 percent where high temperature drops and deicing chemicals are used. The document warns about steel strengths greater than 60 ksi that may lead to wide cracks and loss of aggregate interlock, and questions the use of transverse steel.

Tayabji, S.D., Selezneva, O., Jiang, Y.J., "Preliminary Evaluation of LTPP Continuously Reinforced Concrete Pavement Test Sections," FHWA–RD–99–086, FHWA, July 1999.

In this reference, an attempt is made to find initial correlations of factors collected on General Pavement Studies (GPS) sections GPS–5 from the LTPP database to long-term CRCP performance. No definitive correlations were found with the available data. The study concludes that additional data, including early-age information, is required for good correlations of factors influencing pavement performance.

Lee, Ying-Haur, Darter, M. I., "Development of Performance Prediction Models for Illinois Continuously Reinforced Concrete Pavements." Transportation Research Record 1505, TRB, pp. 75–84, Washington, DC, 1995.

In this study, a failure prediction model based on regression techniques was developed. The Illinois Pavement Feedback System database was used for this purpose. The model is limited to a small range of steel content (0.60 to 0.62 percent) and slab thickness (203–229 m). According to this study, crack spacing had no effect on pavement performance.

McCullough, B.F., Hudson, W.R., and Noble, C.S., "Summary and Recommendations for the Implementation of Rigid Pavement Design, Construction, and Rehabilitation Techniques," Research Report 177–22F, Center for Transportation Research, The University of Texas at Austin, Austin, TX, March 1981.

This reference presents a supplementary CRCP design procedure for thickness, subbase, and steel reinforcement for TxDOT. Most of this material is based on the AASHTO *Pavement Design Guide.*

Won, M., McCullough, B.F., and Hudson, W.R., "Evaluation of Proposed Texas State Department of Highways and Public Transportation (SDHPT) Design Standards for CRCP," Research Report 472–1, Center for Transportation Research, The University of Texas at Austin, Austin, TX, April 1988.

The TxDOT design standards for CRCP are evaluated, taking in consideration the variability in pavement response due to different aggregate types using the software program CRCP.

Won, M., Hankins, K., and McCullough, B.F., "A Twenty-Four Year Performance Review of Concrete Pavement Sections Made with Siliceous and Lightweight Coarse Aggregates," Research Report 472–3, Center for Transportation Research, The University of Texas at Austin, Austin, TX, April 1989.

This study investigates the effect of design variables on long-term pavement performance of experimental test sections constructed in Houston, TX. Variables studied include percent steel, crack spacing, and aggregate type. The findings from that study indicated that lightweight aggregate performed better than sections constructed with standard SRG aggregate. Condition surveys and structural capacity studies were performed to observe the performance of the pavement sections at different ages. Crack spacing for the test sections was preformed, however this crack spacing was reduced with time. Preforming was found to be beneficial, because it reduces spalling and punchouts. Intermediate cracking was reduced.

Weissman, A.J., McCullough, B.F., and Hudson, W.R., "Development of Pavement Performance Models for Continuously Reinforced Concrete Pavements in Texas," Research Report 472–7F, Center for Transportation Research, The University of Texas at Austin, Austin, TX, August 1989.

Performance prediction models for CRCP are developed with the use of the Texas CRCP database. A distress index is used to describe the CRCP deterioration as a function of punchouts and patches. The

validity of the model is believed to be to limited, and therefore is not recommended for general practical use.

Aslam, M.F., Carrasquillo, L.R., and McCullough, B.F., "Design Recommendations for Steel Reinforcement of CRCP," Research Report 422–2, Center for Transportation Research, The University of Texas at Austin, Austin, TX, November 1987.

A procedure for comparing the effects of aggregate type on the requirements for steel reinforcement is developed. Lab testing of mixes with limestone and SRG aggregates are tested to determine concrete properties for those aggregate types. The CRCP–4 program is used to develop steel design methods based on the differences in concrete properties for both aggregate types.

Wei, C., McCullough, B.F., Hudson, W.R., and Hankins, K., "Development of Load Transfer Coefficients for Use with the AASHTO Guide for Design of Rigid Pavements Based on Field Measurements," Research Report 1169–3, Center for Transportation Research, The University of Texas at Austin, Austin, TX, February 1992.

This report provides procedures to measure load transfer at joints and cracks for CRCP.

Otero, M.A., McCullough, B.F., and Hankins, K., "Monitoring of Siliceous River Gravel and Limestone Continuously Reinforced Concrete Pavement Test Sections in Houston 2 Years After Placement, and Development of a Crack Width Model for the CRCP–7 Program," Research Report 1244–4, Center for Transportation Research, The University of Texas at Austin, Austin, TX, March 1992.

A model for predicting crack width for CRCP is developed based on experimental sections in Houston, TX. The principal variables having an effect on crack width are identified.

McCullough, B.F., Zollinger, D.G., and Allison, B.T., "Preliminary Research Findings on the Effect of Coarse Aggregate on the Performance of Portland Cement Concrete Paving," Research Report 1244–5, Center for Transportation Research, The University of Texas at Austin, Austin, TX, October 1993.

This report provides concrete properties of mixes made with various coarse aggregates. It summarizes findings of research reports 1244–1 to 1244–4 and describes an experiment to evaluate different curing techniques, saw cutting techniques, and skewed transverse steel on crack width, crack spacing, and concrete strength. In addition, it provides background on the development of different versions of the CRCP program. A description of drying shrinkage and moisture models also are provided.

McCullough, B.F. and Rivero-Vallejo, F., "Drying Shrinkage and Temperature Drop Stresses in Jointed Reinforced Concrete Pavement," Research Report 177–1, Center for Transportation Research, The University of Texas at Austin, Austin, TX, August 1975.

This is a research report for JRCP–1, a tool to predict the behavior of JRCP, which can be used to predict the behavior of CRCP steel in the transverse direction.

Strauss, J.P., McCullough, B.F., and Hudson, W.R., "Continuously Reinforced Concrete Pavement: Structural Performance and Design/Construction Variables," Research Report 177–7, Center for Transportation Research, The University of Texas at Austin, Austin, TX, May 1977.

Probabilistic models are used to predict pavement performance based on several factors. Models for load transfer through steel reinforcement and aggregate interlock are developed. The report describes a 1977 condition survey of CRCP pavements in Texas.

McCullough, B.F. and Ma, J., "CRCP–2, An Improved Computer Program for the Analysis of Continuously Reinforced Concrete Pavements," Research Report 177–9, Center for Transportation Research, The University of Texas at Austin, Austin, TX, August 1977.

This report presents modifications made to the CRCP–1 program to account for wheel load stresses to predict crack spacing, to modify the steel-stress model to cover conditions in which the development length for bond exceeds one-half the crack spacing, and to account for the increase in strength after 28 days for analysis of minimum temperature drop.

McCullough, B.F. and Strauss, J.P., "A Performance Survey of Continuously Reinforced Concrete Pavements in Texas," Research Report 21–1F, Center for Transportation Research, The University of Texas at Austin, Austin, TX, November 1974.

A method for performing condition surveys of CRCP is discussed. A distress index for evaluation of CRCP is developed.

Zollinger, D. and Barenberg, E., "Continuously Reinforced Pavements: Punchouts and Other Distresses and Implications for Design," Project IHR–518, Illinois Cooperative Highway Research Program, University of Illinois at Urbana-Champaign, Urbana-Champaign, IL, March 1990.

This report describes the factors affecting CRC pavement cracking behavior. It also provides an analysis of factors affecting punchout distress. The authors describe previous steel instrumentation efforts and provide mechanistic modeling for prediction of punchout distress, including load transfer mechanisms, shear, spalling on the transverse crack, and transverse bending analysis. Most of this research is also presented in FHWA publication FHWA–RD–97–151.

Wimsatt, A.W., McCullough, B.F., and Burns, N.H., "Methods of Analyzing and Factors Influencing Frictional Effects of Subbases," Research Report 459–2F, Center for Transportation Research, The University of Texas at Austin, Austin, TX, November 1987.

This report provides information on pushoff test procedures and typical friction values.

Chia, W.S., McCullough, B.F., and Burns, N.H., "Field Evaluation of Subbase Friction Characteristics," Research Report 401–5, Center for Transportation Research, The University of Texas at Austin, Austin, TX, September 1986.

This report provides information on pushoff test procedures and typical friction values for various subbase types and bond breakers.

Haque, M., Zaman, M., and Soltani, A., "Cracking Characteristics of Model CRC Pavements," TRB 77th Annual Meeting, Washington, DC, January 11–15, 1998.

The authors investigate the effect of steel reinforcement (rebar spacing) on crack spacing behavior of CRCP using numerical methods and small-scale laboratory experiments. They also evaluate the effect of skewed reinforcement.

Nishizawa, T., Shimeno, S., Komatsubara, A., and Koyanagawa, M., "Study on Thermal Stresses in Continuously Reinforced Concrete Pavement," paper presented at the TRB 77th Annual Meeting, Washington, DC, 1998.

The authors investigate development of thermal stresses in CRCP. Test sections are instrumented in the field, and measured stresses are compared to calculated stresses.

Mains, M.R., "Measurement of the Distribution of Tensile and Bond Stresses Along Reinforcing Bars," ACI Journal, Vol. 48, pp. 225–252, November 1951.

This article investigates bond stresses and bond slip of reinforced concrete. It includes experimentation with strain gauges to measure bond stress and bond slip. Bond stress and bond slip relationships are discussed.

Nilson, A.H., "Internal Measurement of Bond Slip," ACI Journal, Vol. 69, pp. 439–441, July 1972.

Similar to the above article, this reference also investigates bond stresses and bond slip of reinforced concrete.

Haque, M., Zaman, M., and Soltani, A., "Cracking Characteristics of Model CRC Pavements," TRB 77th Annual Meeting, Washington, DC, January 11–15, 1998.

This article investigates the effect of rebar spacing on crack spacing and crack patterns with the use of small-scale laboratory experiments and numerical simulation.

Zollinger, D. and Senadheera, S., "Spalling of Continuously Reinforced Concrete Pavements," Journal of Transportation Engineering, Vol. 120, No. 3, May–June 1994.

This article presents a mechanistic flat-bottom spalling model for CRCP/JCP.

Kerr, A.D., "Assessment of Concrete Pavement Blowups," Journal of Transportation Engineering, Vol. 123, No. 2, pp. 123–131, March–April 1997.

A mechanistic model for analysis of concrete pavement blowups is described. The model can be used for both CRCP and JCP.

Nishizawa, T., Shimeno, S., Komatsubara, A., and Koyanagawa, M., "Study on Thermal Stresses in Continuously Reinforced Concrete Pavement," Transportation Research Record 1629, pp. 99–107, November 1998.

A procedure for estimating the thermal stresses in CRCP is proposed. Measured thermal strains are compared with FEM-predicted strains and divided into axial, curling, and nonlinear components.

Kim, S.-M., Won, M., and McCullough, F., "Three-Dimensional Analysis of Continuously Reinforced Concrete Pavements," TRB 79th Annual Meeting, Washington, DC, January 9–13, 2000.

A three-dimensional analysis of CRCP is performed and compared with results of two-dimensional analysis performed with CRCPFEM. Nonlinear bond slip relationships are studied in this analysis. Primary conclusions include the effect of transverse steel amount and location on crack width; significant stresses at the edge on the farthest transverse steel bar from the crack; significant effect of nonlinear bond-slip relationships on concrete stress; analysis with the two-dimensional model gives a good approximation, compared to the three-dimensional model.

Schindler, A., Henry, P., and McCullough, F., "Validation of CRCP–8 to Predict Long-Term Transverse Crack Spacing Distributions in Continuously Reinforced Concrete Pavements," TRB 79th Annual Meeting, Washington, DC, January 9–13, 2000.

This paper describes validation efforts of the CRCP–8 program to predict crack spacing for experimental sections in Houston, TX.

McCullough, F., Zollinger, D., and Dossey, T., "Evaluation of the Performance of Texas Pavements Made with Different Coarse Aggregates" Research Report 3925–1, Center for Transportation Research, The University of Texas at Austin, Austin, TX, September 1998.

This report presents information on crack spacing and crack width of CRCP for sections monitored in Houston, TX, and Hempstead, TX. It presents the results of an effort to validate CRCP–8 crack spacing and presents information on delamination spalling and the thermal coefficient of concrete. The report describes practices of CRCP design and construction for the State of Texas over a 23-year period.

APPENDIX B MODELS SELECTED FOR INCORPORATION INTO HIPERPAV II

Chapter 3 of the first volume in this report series documents the models that were identified and the ones selected for incorporation into HIPERPAV II. This appendix provides a detailed description of the models that were selected. The models incorporated are divided into:

- General early-age behavior models.
- JPCP performance models.
- CRCP early-age behavior models.
- Models used in the Concrete Optimization, Management, Engineering, and Testing (COMET) module.
- Model used in the dowel analysis module.

B.1 GENERAL EARLY-AGE BEHAVIOR MODELS

A number of potential model enhancements were identified over the course of previous implementation efforts of HIPERPAV I. In this section, early-age behavior models incorporated into HIPERPAV II are presented. These models are divided in the following categories:

- PCC hydration models.
- PCC temperature prediction models.
- Drying shrinkage models.
- Relaxation-creep models.
- Nonlinear thermal gradient model.
- Nonlinear axial restraint model.

All other models in HIPERPAV I that were kept in HIPERPAV II are not presented here because they have been defined previously elsewhere.[1,2,3] Figure 1 shows a schematic of the enhancements made to the early-age behavior models in HIPERPAV II.

B.1.1 PCC Hydration Models

During the development of this project, the project team closely followed recent developments by the University of Texas at Austin on characterization of cement and admixtures. Based on these findings, improved models capable of predicting the hydration development of concrete mixes based on chemical composition of the cement and mix proportions were incorporated in HIPERPAV II. These models are based on a database of U.S. cements as shown in table 4.[4]

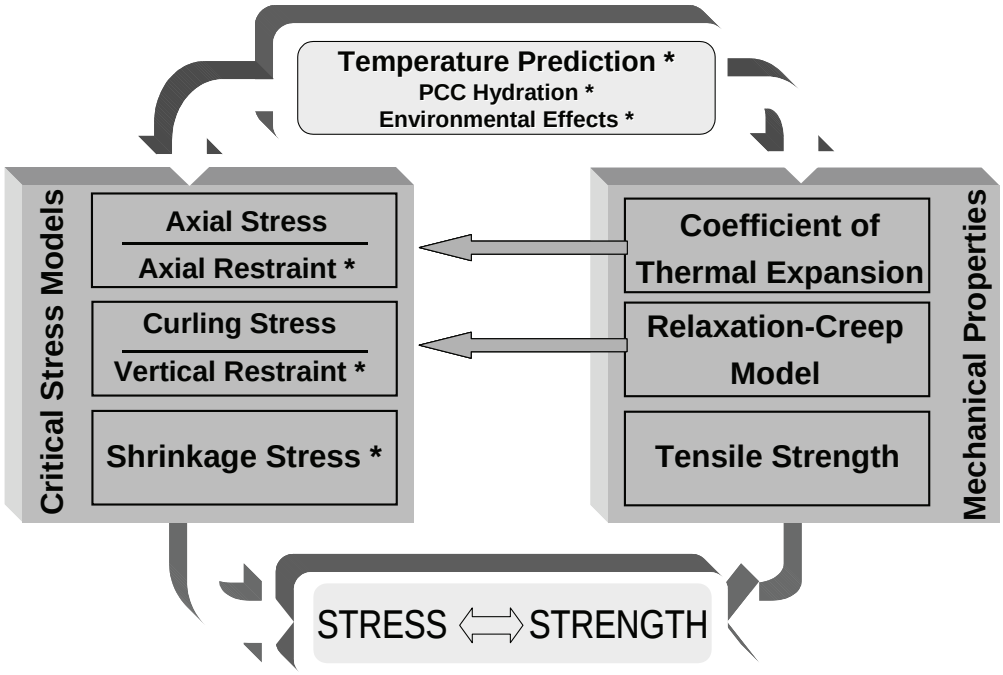

* Improved models

Figure 1. HIPERPAV early-age behavior framework showing improved models in HIPERPAV II.

Table 4. Data sources and their use in the development of the hydration models.[4]

	Portland Cement Association (PCA)—Lerch and Ford[5]	**Schindler[4] Materials Characterization Phase**
Calibration Data Sources	U.S. cements sources. Eight Type I, five Type II, three Type III, three Type IV, one Type V. All cement properties known. Well known and recognized data source. Conduction calorimeter heat of solution tests.	Texas materials. Three different cement sources. Different fineness. Class C and F fly ash. GGBF slag. All cement properties known. Semiadiabatic testing.
	Kjellsen et al.[6]	**Schindler[4] Field Work Phase**
Validation Data Sources	Swedish cements source. All cement properties known. Type I cement. Nonevaporable water calculations.	Texas materials. Typical paving mixtures. Different cements. All cement properties known. Field data collected. Mixed usage of Class C and F fly ash, and GGBF slag. Semiadiabatic testing.

The model used in HIPERPAV II to predict the hydration of a cementitious mixture is presented below. The degree of hydration is defined as in equation 1:

$$\alpha(t_e) = \alpha_u \cdot \exp\left(-\left[\frac{\tau}{t_e}\right]^{\beta}\right) \quad (1)$$

where,

$\alpha(t_e)$ = degree of hydration at equivalent age, t_e,
t_e = equivalent age at reference temperature (21.1°C), (hours (h)),
α_u = ultimate degree of hydration,
τ = hydration time parameter (h), and
β = hydration shape parameter.

The rate of heat liberation is defined as in equation 2:

$$Q_h(t_e) = H_u \cdot C_c \cdot \left(\frac{\tau}{t_e}\right)^{\beta} \cdot \left(\frac{\beta}{t_e}\right) \cdot \alpha(t_e) \cdot \exp\left[\frac{E}{R}\left(\frac{1}{273+T_r} - \frac{1}{273+T_c}\right)\right] \quad (2)$$

where,

$Q_h(t_e)$ = rate of heat liberation at equivalent age, t_e, (Watts per cubed meter (W/m^3)),
E = AE (J/mol),
R = universal gas constant (8.3144 J/mol/°C),
T_c = nodal PCC temperature (°C),
T_r = reference PCC temperature (°C),
C_c = cementitious materials content (kilogram per cubed meter (kg/m^3)), and
H_u = total heat of hydration of cementitious materials at 100 percent hydration (J/kg), defined as in equation 3:

$$H_u = H_{cem} \cdot p_{cem} + 461 \cdot p_{SLAG} + 1800 \cdot p_{FA-CaO} \cdot p_{FA} \quad (3)$$

where,

p_{SLAG} = slag mass ratio to total cementitious content,
p_{FA} = fly ash mass ratio to total cementitious content,
p_{FA-CaO} = fly ash CaO mass ratio to total fly ash content,
p_{cem} = cement mass ratio to total cementitious content, and
H_{cem} = heat of hydration of the cement, defined by Bogue as in equation 4:[7]

$$H_{cem} = 500 \cdot p_{C_3S} + 260 \cdot p_{C_2S} + 866 \cdot p_{C_3A} + 420 \cdot p_{C_4AF} + 624 \cdot p_{SO_3} + 1186 \cdot p_{FreeCa} + 850 \cdot p_{MgO} \quad (4)$$

where,

p_i = mass ratio of *i*-th component to total cement content.

To predict the ultimate degree of hydration, and time and shape parameters in equation 1, multivariate nonlinear regression models were developed as shown in equations 5, 6, and 7:

$$\tau = 66.78 \cdot p_{C_3A}{}^{-0.154} \cdot p_{C_3S}{}^{-0.401} \cdot Blaine^{-0.804} \cdot p_{SO_3}{}^{-0.758} \cdot \exp(2.187 \cdot p_{SLAG} + 9.50 \cdot p_{FA} \cdot p_{FA-CaO}) \quad (5)$$

$$\beta = 181.4 \cdot p_{C_3A}{}^{0.146} \cdot p_{C_3S}{}^{0.227} \cdot Blaine^{-0.535} \cdot p_{SO_3}{}^{0.558} \cdot \exp(-0.647 \cdot p_{SLAG}) \quad (6)$$

$$\alpha_u = \frac{1.031 \cdot w/cm}{0.194 + w/cm} + 0.50 \cdot p_{FA} + 0.30 \cdot p_{SLAG} \leq 1.0 \quad (7)$$

where,

P_{C_3A} = weight ratio of tricalcium aluminate to total cement content,
P_{C_3S} = weight ratio of tricalcium silicate to total cement content,
P_{SO_3} = sulfate weight ratio to total cement content,
Blaine = Blaine value, specific surface area of cement (m^2/kg), and
w/cm = the water-cementitious material ratio.

The above models are based on heat of solution, conduction calorimeter, and semiadiabatic calorimeter test data. From a multivariate analysis, an r^2 of 0.988 was achieved. The isothermal curing temperature considered for the test data was 21.1 °C.

The recommended AE model (*E*) is defined in equation 8:

$$E = 22{,}100 \cdot f_E \cdot p_{C_3A}{}^{0.30} \cdot p_{C_4AF}{}^{0.25} \cdot Blaine^{0.35} \quad (8)$$

where,

P_{C_3A} = weight ratio of tricalcium aluminate Bogue compound,
P_{C_4AF} = weight ratio of tetracalcium aluminoferrite Bogue compound,
Blaine = Blaine value, specific surface area of cement (m^2 /kg), and
f_E = AE modification factor for mineral admixtures, defined as in equation 9:

$$f_E = 1 - 1.05 \cdot p_{FA} \cdot \left(1 - \frac{p_{FA-CaO}}{0.40}\right) + 0.40 \cdot p_{SLAG} \quad (9)$$

where,

p_{FA} = mass ratio replacement of the fly ash,
p_{FACaO} = mass ratio of the CaO content in the fly ash, and
p_{SLAG} = mass ratio replacement of the GGBF slag.

A sensitivity analysis of the effect of temperature on the hydration of the cement was performed over a temperature range of 4.4 to 40.6 °C. From this analysis, the AE (*E*) model was found to be independent of curing temperature.

The limitations and assumptions to the model above presented are:

- Due to the nature of the model, its validity holds only for the range within it was calibrated. The model should not be used to predict hydration outside this range, as listed in tables 5 and 6. Table 5 presents the range of chemical and physical cement properties. Table 6 presents the range of mixture proportions and mineral admixtures properties.
- The effects of chemical admixtures are currently not considered in the hydration model.
- The model assumes that the same interaction between the mineral admixtures and the base cement source applies to all combinations of cement and mineral admixtures.

Table 5. Range of cement properties used to calibrate the hydration model.

	C_3S (%)	C_2S (%)	C_3A (%)	C_4AF (%)	SO_3 (%)	Free CaO (%)	MgO (%)	Alkalis	Blaine (m^2/kg)
Average	52.5	20.8	8.4	9.3	2.6	1.4	1.8	0.6	373.7
Min	20.0	9.3	3.5	5.5	1.2	0.1	0.6	0.2	289.1
Max	64.5	55.0	13.2	16.6	4.4	2.9	4.0	1.1	579.5

* Equivalent alkalis as per ASTM C150 = $Na_2O + 0.658\ K_2O$

Table 6. Range of mixture proportions and mineral admixtures properties used for model calibration.

	w/cm	Fly Ash CaO (%)	Fly Ash SiO_2 (%)	Fly Ash Alkalis (%)	Fly Ash Dosage (%)	GGBF Slag Dosage (%)
Average	0.42	–	–	–	–	–
Min	0.36	10.8	35.8	0.3	0.0	0.0
Max	0.54	24.3	54.1	1.4	45.0	50.0

Based on the empirical results reported, the degree of hydration at initial and final set are determined as shown in equations 10 and 11:

$$\text{ASTM C 403 initial set: } \alpha_i = 0.15 \text{ (w/cm)} \tag{10}$$

$$\text{ASTM C 403 final set: } \alpha_f = 0.26 \text{ (w/cm)} \tag{11}$$

where,

α_i = degree of hydration at initial set,
α_f = degree of hydration at final set, and
w/cm = water-cementitious materials ratio.

With equations 10 and 11, the equivalent age at setting can directly be determined from the hydration parameters. The closed form solutions are shown in equations 12 and 13. They are very useful, since the setting time at the reference temperature can now be obtained.

ASTM C 403 initial set:

$$t_{ei} = \tau \cdot \left(-\ln\left[\frac{0.14 \cdot w/cm}{\alpha_u} \right] \right)^{\frac{-1}{\beta}} \quad (12)$$

ASTM C 403 final set:

$$t_{ef} = \tau \cdot \left(-\ln\left[\frac{0.26 \cdot w/cm}{\alpha_u} \right] \right)^{\frac{-1}{\beta}} \quad (13)$$

where,

t_{ei} = equivalent age at initial set (hours),
t_{ef} = equivalent age at final set (hours), and
w/cm = water-cementitious materials ratio.

It is customary to express the effect of chemical admixtures on cement mixes in terms of their effect on initial set at different temperatures. With equation 12, the initial set time for the cement without a chemical admixture can be estimated. Next, the effect recommend by the supplier of the chemical admixture can be added to the calculated initial set time. In the case of retarders, the initial set time will be increased, and with accelerators, the initial set time will be reduced. With this approach, it is assumed that only the hydration time parameter is affected by the chemical admixtures. Then, the new hydration time parameter can be determined that includes the use of chemical admixtures, as shown in equation 14:

ASTM C 403 initial set:

$$\tau_{chem} = \left(t_{ei} + \Delta_{chem}\right) \cdot \left(-\ln\left[\frac{0.14 \cdot w/cm}{\alpha_u} \right] \right)^{\frac{1}{\beta}} \quad (14)$$

where,

τ_{chem} = adjusted hydration time parameter to include the effect of retarder or accelerators (h),
t_{ei} = equivalent age at initial set of the cement without chemical admixtures determined from equation 12 (h), and
Δ_{chem} = effect of mineral admixture on the time at initial set at the reference temperature (21.1 °C), where positive retards and negative accelerates.

B.1.2 HIPERPAV II Finite-Difference Temperature Model

In HIPERPAV I, a one-dimensional finite-element technique was used, but this procedure has proven to be a computational burden, and may not be appropriate for the large number of time-steps involved in

long-term analyses. The finite-difference method is another numerical technique that is available to solve the transient heat transfer problem. In HIPERPAV II, the previous finite-element procedure for heat transfer analysis was replaced with a finite-difference method after extensive calibration and validation. The finite-difference model is used for both early-age and long-term predictions of concrete temperature. A description of this model follows:

The basic equation of the heat transfer model with respect to distance, *x*, and time, *t*, can be written as shown in equation 15:[8]

$$\frac{d}{dx}\left(k \cdot \frac{dT}{dx}\right) + Q_H = \rho \cdot c_p \cdot \frac{dT}{dt} \tag{15}$$

where,

T = temperature (°C),
ρ = density (kg/m^3),
c_p = specific heat capacity (J/kg/°C),
Q_H = generated heat per unit time and volume (W/m^3), and
k = thermal conductivity (W/m/°C).

With this approach, the concrete temperature can be evaluated at discrete times after placement. Boundary conditions have to be chosen to satisfy compatibility with field conditions.

In concrete placed under field conditions, heat will be transferred to and from the surroundings, and the temperature development in the concrete structure is determined by the balance between heat generation in the concrete and heat exchange with the environment. The surroundings could either be an additional source of heat or at a lower temperature than the hydrating concrete. Heat transfer with the surroundings may take place in four basic ways: conduction, convection, irradiation, and solar absorption. Figure 2 illustrates how each of these methods exchange heat in a pavement system. The evaporation of moisture from the pavement surface causes a change in phase, which reduces the surface temperature due to the withdrawal of latent heat of vaporization. The models that will be used to model each of the heat exchange mechanisms will now be discussed in more detail. Due to the scope of this project, the parameters were not determined through physical testing, but instead parameters were obtained from published research. Therefore, normal ranges found acceptable in previous calibration efforts of these models are used.

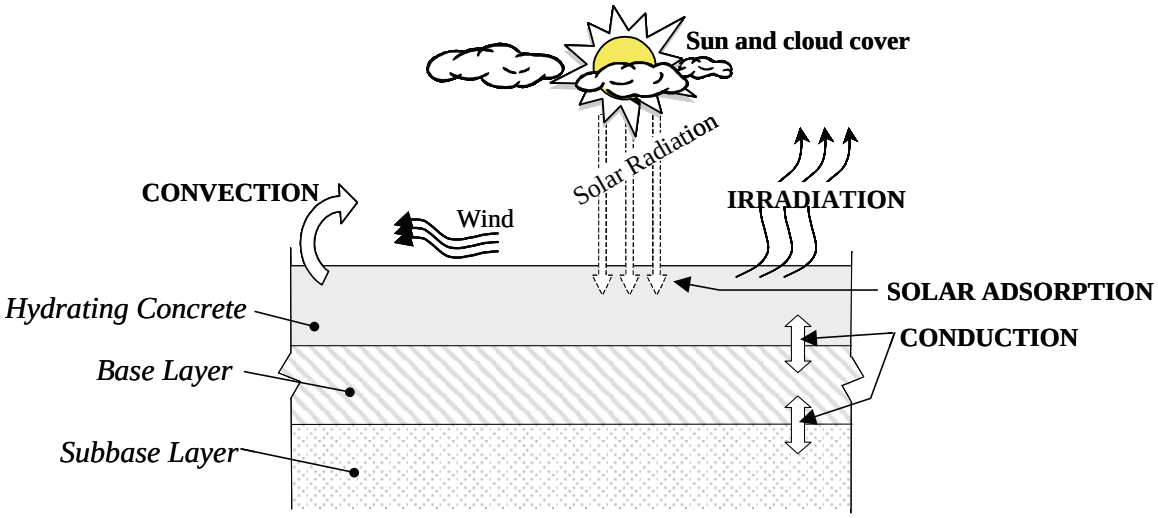

Figure 2. Heat transfer mechanisms between pavement and its surroundings.

Appropriate values for all the thermal material properties involved must be selected for the system. New methods to model early-age thermal properties and boundary conditions also were investigated.

B.1.2.1 Specific Heat

The specific heat of a material can be defined as the ratio of the amount of heat required to raise a unit weight of a material 1 °C to the amount of heat required to raise the same weight of water by 1 °C. The International System (SI) units for specific heat are J/kg/ºC, whereas the U.S. customary units are expressed in British Thermal Unites per pound per degrees Fahrenheit (BTU/lb/°F). Both the temperature of the concrete and the water content impact the specific heat of the mixture.[9,10]

Based on tests performed on hardening concrete, it is reported that the heat capacity is linear with the logarithm of time, which for common cement types is very similar to a linear decline with degree of hydration.[10,11] Test data shows a 13 percent decrease in specific heat of concrete during hardening.[11] The following model shown in equation 16 is used in HIPERPAV II, as it accounts for the effect of temperature and mix proportions, and also decreases the specific heat as the concrete hardens:[12]

$$c_p = \frac{1}{\rho} \cdot (W_c \cdot \alpha \cdot c_{cef} + W_c \cdot (1-\alpha) \cdot c_c + W_a \cdot c_a + W_w \cdot c_w) \quad (16)$$

where,

c_p = current specific heat of the concrete mixture (J/kg/ºC),
ρ = unit weight of concrete mixture (kg/m^3),
W_c, W_a, W_w = amount by weight of cement, aggregate, and water (kg/m^3),
c_c, c_a, c_w = specific heats of cement, aggregate, and water (J/kg/ºC),
c_{cef} = fictitious specific heat of the hydrated cement (J/kg/ºC), determined as 8.4 T_c + 339, where T_c is the current concrete temperature (ºC), and
α = degree of hydration.

Based on the literature reviewed, the following specific heat values are recommended for cement, aggregate, and water (table 7):

Table 7. Typical specific heat values for concrete constituents.

Material	Specific Heat (J/kg/ºC)	Reference
Cement	1140	(13)
Water	4187	(9)
Limestone/dolomite	910	(14)
Sandstone	770	(14)
Granite/gneiss	780	(14)
Siliceous river gravel	770	(14)
Basalt	900	(14)

To evaluate the proposed specific heat model, a mix design typically used in pavement construction was used.[(1)] The mix design per cubic meter consisted of 380 kg cement, 154 kg water, and 1631 kg of coarse and fine aggregate, which provided a unit weight of 2224 kg/m^3. Figure 3 was developed based on the model shown in equation 16, and it may be concluded that it provides an adequate estimate of the specific heat as it fulfills the following requirements:

- The calculated values are between the recommended range of 800 and 1200 J/kg/°C.
- The specific heat decreases linearly with an increase in degree of hydration.
- There is 8 to 14 percent difference in specific heat of the mature and hardened concrete.
- The specific heat increases with an increase in concrete temperature.
- It accounts for the effect of mixture constituents.

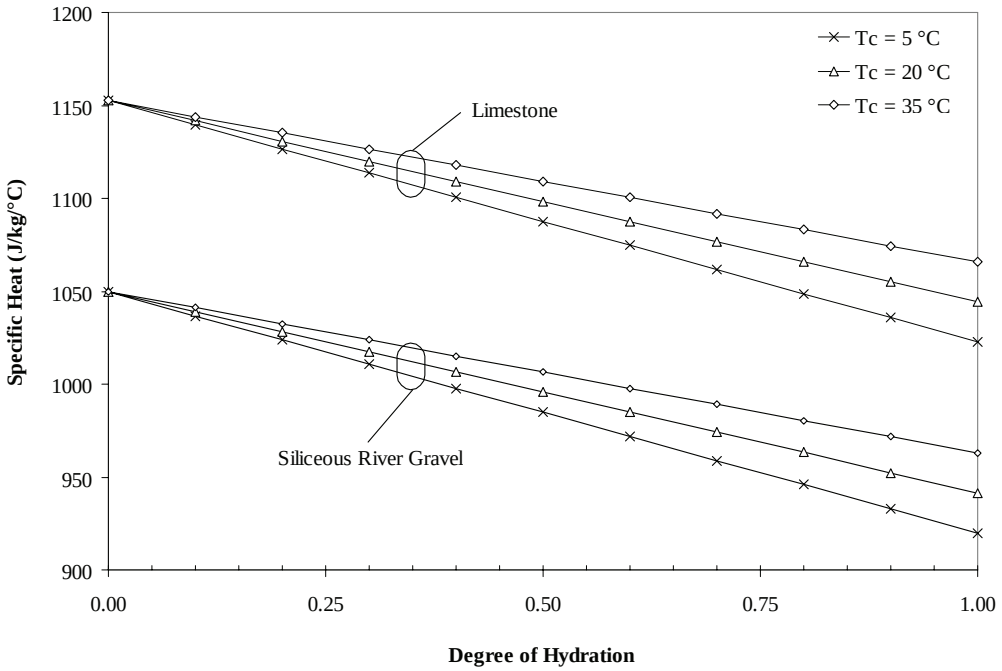

Figure 3. Concrete specific heat as influenced by the mixture constituents, temperature, and degree of hydration.

B.1.2.2 Conduction

Thermal conduction is defined as heat transport in a material by transfer of heat between portions of the material that are in direct contact with each other. In a pavement system, conduction occurs between the pavement layers, and between the surface of the concrete slab and the surface protection (insulation) used at early ages, such as water fogging, plastic sheets, blankets, and urethane foams. The governing equation for thermal conduction reveals that heat transfer is a function of the thermal conductivity, density, and specific heat of the materials in contact.

Thermal conductivity of concrete (*k*) measures the ability of the concrete to transfer heat, and is defined as the ratio of the rate of heat flow to the temperature gradient.[9] The thermal conductivity is of great importance, since it determines the rate of penetration of heat into the concrete and hence the magnitude of temperature gradients and thermal stresses.[13] The SI units for thermal conductivity are W/m/ºC, whereas the U.S. customary units are expressed in BTU/h/ft/°F.

B.1.2.2.1 Heat Conduction of Concrete

It is reported that the water content, density, and temperature of the concrete may significantly influence the thermal conductivity.[9] The conductivity of ordinary concrete depends on its composition and especially the aggregate type used. Typical values proposed for the thermal conductivity of mature concrete are listed in table 8.

Table 8. Typical values of thermal conductivity of moist mature concrete.[9]

Aggregate Type	Moist Density of Concrete (kg/m^3)	Thermal Conductivity (W/m/ºC)
Quartzite	2350–2440	4.1–3.1
Dolomite	2500	3.3
Limestone	2450–2440	3.2–2.2
Sandstone	2400–2130	2.9
Granite	2420	2.6
Basalt	2520–2350	2.0–1.9

Thermal conductivity values, similar to the ones presented in table 8, are also recommended by ACI Committee 207.[15] In contrary to the values reported above, work performed at McGill University in Canada reports for normal strength concrete, thermal conductivity values of 1.723–1.740 W/m/ºC for maturing concrete and values of 1.14–1.17 W/m/ºC for hardened concrete.[10] These values are significantly lower than those listed in table 8. It was concluded that the average thermal conductivity of maturing concrete is 33 percent higher than that of the hardened concrete. This value is in agreement with that obtained by others, which showed a 21 percent decrease in thermal conductivity from the maturing state to the hardened state.[11]

From this information, assuming that the decline in this parameter is linear with the logarithm of time, which for common cement types is very similar to a linear decline with degree of hydration, a relationship that considers these initial and final values could be expressed as shown in equation 17:

$$k_i = k_\infty (1.33 - 0.33 \cdot \alpha) \tag{17}$$

where,

k_i = current thermal conductivity of the concrete (W/m/ºC),
k_∞ = thermal conductivity of mature concrete (W/m/ºC), and
α = degree of hydration.

B.1.2.2.2 Conduction to Supporting Layers

The temperature and properties of the base underlying the concrete have a significant influence on the temperature development of the hardening concrete. Tables 9 and 10 present typical thermal characteristics of some commonly used base materials.

Table 9. Thermal characteristics of various base materials.[16]

Base Material	Density (kg/m^3)	Thermal Conductivity (W/m/ºC)	Specific Heat (J/kg/ºC)
Gravel, dry	1703	0.52	838
Gravel, moist	1898	2.42	1047
Asphalt	2302	1.38	1047

Table 10. Thermal characteristics of various pavement materials.[17]

Base Material	Density (kg/m^3)	Unfrozen Thermal Conductivity (W/m/ºC)	Unfrozen Specific Heat (J/kg/ºC)
Asphalt concrete	2371	1.21	921
Stabilized base	2339	3.32	1005
Cohesive subgrade	2066	1.59	1214

During the development of the ICM,[18] different values for the thermal conductivity and specific heat was determined based on the moisture condition of the soil and three different material conditions—unfrozen, freezing, and frozen. The soil moisture content has a great influence upon the thermal conductivity and heat capacity of the soil. In later reports on the development of the ICM, the values listed in table 11 were recommended based on the AASHTO soil type classification.

Table 11. Thermal characteristics of various soil materials.[17]

Soil Type	Dry Density (kg/m^3)	Dry Thermal Conductivity (W/m·ºC)	Specific Heat Capacity (J/kg·°C)
Stabilized	1188	1.50	1047
A–1	1188	0.90	712
A–2	950	0.81	712
A–3	1045	1.02	838
A–4	856	1.02	712
A–5	808	0.45	712
A–6	856	0.60	712
A–7	760	0.30	712

B.1.2.2.3 Conduction to Surface Protection

Conduction further transpires between the surface coverings of the concrete slab commonly placed over during construction. These include insulation blankets, curing compound, plastic sheets, urethane foams, closed cell polystyrene foam, and many patented products. Insulation blankets often are used to provide a uniform temperature gradient, to prevent concrete freezing under cold weather conditions, and where opening requirements dictate very quick strength gain.[19] The use of blankets in cold weather conditions will increase the strength gain considerably, as some of the concrete heat generated during hydration is trapped, which allows concrete hydration at increased temperatures. It is also reported that when a period of less than 16 hours is required for early opening to traffic, the use of blankets become beneficial.[19] These blankets should be placed after the sawing operation and near the time the slab temperature begins its decent from the peak temperature.

Other membranes and surface coverings are also commonly placed over the concrete during construction. These include curing compound, plastic sheets, urethane foams, closed cell polystyrene foams, and many other products. The steady state heat transfer to the surrounding, excluding any radiation, can be expressed as shown in equation 18:[20]

$$q = h_0 \cdot (T_s - T_a) \tag{18}$$

where,

q = heat flux (W/m^2),
h_0 = overall heat transfer coefficient (W/m^2/°C),
T_s = surface temperature (°C), and
T_a = air temperature (°C).

Where more than one layer of insulation is used, the overall heat transfer coefficient can be calculated, which is a single coefficient that defines the thermal resistance of all the materials. The overall heat transfer coefficient can be calculated as shown in equation 19:[20]

$$h_0 = \left(\frac{d_1}{k_1} + \frac{d_2}{k_2} + \ldots + \frac{d_n}{k_n} \right)^{-1} \tag{19}$$

where,

h_0 = overall heat transfer coefficient (W/m^2/°C),
$d_1, d_2, \ldots d_n$ = thickness of n successive layers (m), and
$k_1, k_2, \ldots k_n$ = thermal conductivity of n successive layers (W/m/°C).

Table 12 contains some properties of various insulation materials that could be encountered during concrete construction operations.

Table 12. Thermal characteristics of various insulation materials.

Base Material	Thermal Conductivity (W/m/°C)	Typical Thickness (mm)	Reference
No cover	0	0	–
Polyurethane foam	0.035	25	(21)
Plastic sheet	0.043	0.1	(22)
Water	2.168	Variable	(22)
Blankets:			
Mineral fiber: ρ = 6.4–32 kg/m^3	0.039	75	(22)
Textile organic fiber:			(22)
ρ = 12–24 kg/m^3	0.043	25	
ρ = 24–48 kg/m^3	0.033	25	
Glass fibers: ρ = 16–32 kg/m^3	0.055	25	(21)
Alumina fibers: ρ = 48–64 kg/m^3	0.058	25	(21)
Cotton wool mats: ρ = 80 kg/m^3	0.042	25	(20)
Mineral wool:			(20)
ρ = 151 kg/m^3	0.039	50	
ρ = 316 kg/m^3	0.042	50	

ρ = unit weight

B.1.2.3 Convection

Thermal convection is the heat transferred from a surface to a gas (or fluid), where convection is the movement of a mass of gas (or liquid) due to the temperature difference, and physical contact of the gas (or liquid) is the actual method of heat transfer. Convection is, therefore the mechanism of heat transfer between the concrete surface and the environment, and as illustrated above in figure 2, includes the effect of wind and evaporation. For flat surfaces such as concrete pavements, the wind velocity across the concrete surface determines whether convection is forced or free. In the case of free convection, the transport of heat is the result of temperature gradients. In HIPERPAV II convective heat transfer is modeled through the use of equation 20:[22]

$$q_c = h_c \cdot (T_s - T_a) \tag{20}$$

where,

q_c = heat transferred due to convection (W/m^2),
h_c = surface convection coefficient (W/m^2/°C),
T_s = surface temperature (°C), and
T_a = air temperature (°C).

The rate of heat flow from a horizontal surface is controlled by the magnitude of the temperature difference, the speed of the air flow, and also the surface texture of the member. As heat is transferred from the warmer horizontal plate to the adjacent air, the air is heated, its density decreases, and it tends to rise. As the heated air rises, it is replaced by cooler air, which in turn is heated and rises; this is a continuous recurring process until the heat balance is eliminated. This complex phenomenon has been thoroughly investigated by numerous researches in the heat transfer field. From combinations of experimental work from Heilman and Langmuir, a model that is also used in ASTM C 680 is available for use on a smooth horizontal surface that is valid for both forced and free convection.[21,22,23] However, this model does not include any modification due to surface roughness, and it is recommended that the surface convection coefficient above be increased by 6 percent to account for this effect.[20] Therefore, the following model (shown in equation 21) was incorporated in HIPERPAV II:

$$h_c = 3.727 \cdot C \cdot \left(0.9 \cdot \left(T_s + T_a\right) + 32\right)^{-0.181} \cdot \left|T_s - T_a\right|^{0.266} \cdot \sqrt{1 + 2.857 \cdot w} \tag{21}$$

where,

h_c = surface convection coefficient (W/m^2/°C),
C = constant depending on the shape and heat flow condition, equal to 1.79 for horizontal plates warmer than air, or 0.89 for horizontal plates cooler than air,
T_s = surface temperature (°C),
T_a = air temperature (°C), and
w = windspeed (m/s).

In some programs that model the convection boundary conditions, it is common to use equations 22 and 23 to determine the magnitude of the convection coefficient:[24,25,26]

$$\text{If } w \leq 5 \text{ m/s, then } h_c = 20 + 14 \cdot w \tag{22}$$

$$\text{If } w > 5 \text{ m/s, then } h_c = 25.6 \cdot 0.78w \tag{23}$$

where,

h_c = surface convection coefficient (kJ/m^2/h/°C), and
w = windspeed (m/s).

These equations were obtained from experimental data for the flow of air at room temperature parallel to a smooth vertical copper plate.[20] The original equation presented by McAdams is very similar to equations 22 and 23, and after converted to similar units, is as shown in equations 24 and 25:[20]

$$\text{If } w \leq 4.87 \text{ m/s, then } h_c = 20.24 + 14.08w \tag{24}$$

$$\text{If } w > 4.87 \text{ m/s, then } h_c = 25.82 \cdot 0.78w \tag{25}$$

These equations do not incorporate the fact that the surface convection coefficient is influenced by the magnitude of the temperature difference, as the tests were all performed at room temperature (21 °C). McAdams acknowledged this relationship, and recommended that the windspeed in the above equations be modified by a multiplier to account for this effect.[20] Using this form of the convection equation (equations 22 and 23) is, therefore, more appropriate to determine the effect of convection on vertical elements such as beam webs or retaining walls. However, the multiplier to the windspeed must be incorporated when the air temperature is above room temperature, and the effect of a rough concrete surface as opposed to a smooth plate must be taken into account. Figure 4 compares the surface convection coefficient associated with a vertical (equations 22 and 23) and horizontal plate (equation 21) as presented in this section. Note that with a vertical plate there is a significant increase in the amount of heat transferred as the windspeed is increased above a value of 5 m/s.

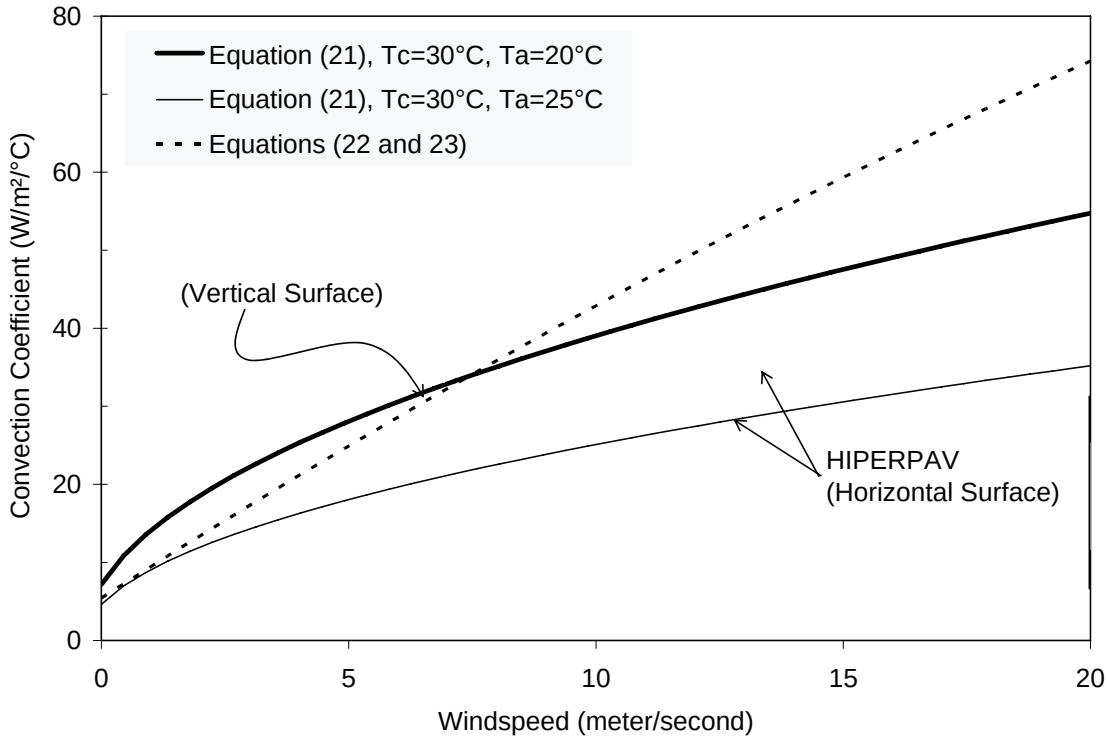

Figure 4. Comparison of different convection coefficients as influenced by the windspeed.

Because the heat transfer due to convection on the surface could occur simultaneously with the presence of surface insulations over the pavement top surface, the overall heat transfer coefficient that includes both these effects must be determined. The overall heat transfer coefficient can be calculated as shown in equation 26 (will all the parameters as defined elsewhere):

$$h_0 = \left(\frac{1}{h_c} + \frac{d_1}{k_1} + \frac{d_2}{k_2} + \ldots + \frac{d_n}{k_n} \right)^{-1} \tag{26}$$

In some cases, liquid-curing membranes, water fogging of the pavement surface, or other porous coverings are used. When evaporation of the water on the surface occurs, the energy associated with the phase change is the latent heat of vaporization. Evaporation occurs when liquid molecules near the surface experience collisions that increase their energy above that needed to overcome the surface binding energy. The energy required to restrain the evaporation must come from the internal energy of the liquid, which then must reduce in temperature. The amount of energy transferred through evaporative cooling can be determined in equation 27:

$$q_{evap} = -E_r \cdot h_{lat} \tag{27}$$

where,

q_{evap} = heat flux due to latent heat of vaporization (W/m^2),
E_r = evaporation rate (g/m^2/s), and
h_{lat} = latent heat of vaporization (W·s/g).

In metric units, the latent heat of vaporization is the quantity of heat, in joules, required to evaporate 1 gram of water, and it varies with temperature.[22] The latent heat of vaporization can be defined as shown in equation 28:[22]

$$h_{lat} = 2500 + 1.859 \cdot T_a \tag{28}$$

where,

h_{lat} = latent heat of vaporization (W·s/g), and
T_a = air temperature (°C).

Where curing membranes and water fogging are used, the duration of latent heat development can be identified by determining the evaporation rate per unit area and by knowing the thickness of the applied membrane. Most States specify the curing compound application rate, and ASTM C309[27] recommends a rate of application of 5 m²/l if the rate of application is not specified.

B.1.2.4 Solar Absorption

Solar absorption is the flux absorbed by the pavement surface through exposure to the incoming sunrays. In HIPERPAV II, the following simplified equation for solar absorption (equation 29) is used:

$$q_s = \beta_\varepsilon \cdot I_f \cdot q_{solar} \tag{29}$$

where,

q_s = solar absorption heat flux (W/m^2),
β_ε = solar absorptivity,
I_f = intensity factor to account for angle of sun during a 24-hour day, and
q_{solar} = instantaneous solar radiation, (W/m^2) as defined in table 13.

In HIPERPAV II, the solar radiation used is based on the 95 percentile value of solar radiation from historical records at any given weather station considered in the HIPERPAV II weather database. The solar radiation in the simulation varies with time of day, ranging from zero at sunrise and sunset to a peak value midday.

In table 13, the solar radiation is a function of the cloud cover, and even with an overcast sky, some of the longer wavelengths can still penetrate the sky and be a source of heat. During nighttime, the solar radiation is negligible. The intensity of solar radiation (I_f) is assumed to follow a sinusoidal distribution, with the simplifying assumption that the highest solar radiation occurs at 5 p.m.

The solar absorptivity of PCC is a function of the surface color, with typical values ranging from 0.5 to 0.6. An ideal white body would have a value of 0.0, and an ideal black body would have a value of 1.0.

Table 13. Typical peak solar radiation values used in HIPERPAV II.[1]

Sky Conditions	Solar Radiation (W/m^2)
Sunny	1000
Partly cloudy	700
Cloudy (overcast)	300

B.1.2.5 Irradiation

Irradiation is the reason that a frost occurs on a clear night even though the air temperature remains well above the freezing point. Irradiation heat transfer also affects the concrete surface, which is the heat transfer that is accomplished by electromagnetic waves between a surface and its surroundings. The Stefan-Boltzmann law is commonly used for this type of heat transfer, which is defined in equation 30:[20]

$$q_r = \varepsilon \cdot \sigma \cdot (T_c^4 - T_\infty^4) \tag{30}$$

where,

q_r = heat flux of heat emission from the surface (W/m^2),
σ = Stefan-Boltzmann radiation constant (5.67×10^{-8} W/m^2/°C^4),
ε = surface emissivity of concrete,
T_c = concrete surface temperature, (°C), and
T_∞ = surrounding air temperature, (°C).

The surface emissivity is a function of the concrete's surface color. An "idealized" black surface would have a value of 1.0. A value of 0.88 was selected for use in HIPERPAV II.[28] However, in the above equation, T_∞ is the temperature of the surrounding environment, and this value cannot arbitrarily be assumed to be equal to the ambient temperature. This equation would be valid for use in enclosed spaces, but where long wave radiation toward the open sky is involved, using this equation requires an appropriate estimate of the effective surrounding air temperature in terms of the atmosphere's ability to reflect and absorb the radiation. In figure 5, an idealized thermally black body with a surface temperature (T_s) equal to the air temperature is receiving and absorbing solar energy at a rate, q_r. Because the plate is at the same temperature as the air, there will be no heat transfer through convection, but the plate will exhibit a radiation loss in the far infrared wavelength. The loss rate (R) is defined as the difference between the black body radiation ($\sigma \cdot T_s^4$) emitted by the surface and the incoming long wave atmospheric radiation (A_R), which is striking the surface.[29]

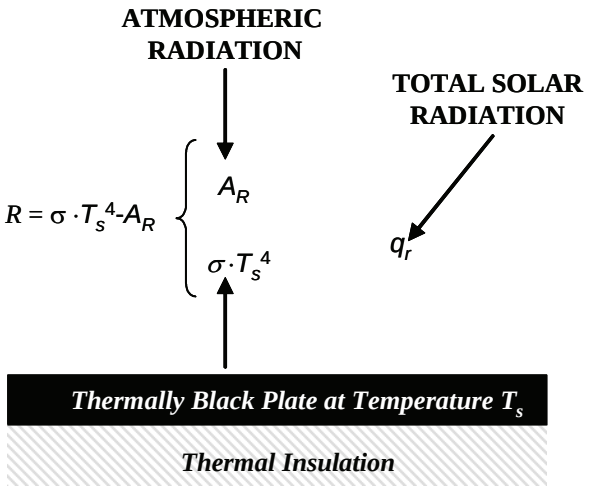

Figure 5. Radiant energy exchanges between the sky and an exposed thermally black plate.[29]

Atmospheric radiation originates from gasses in the air. When radiation at the ground level is of concern, only water vapor and carbon dioxide are the main contributors, and water vapor is the most important.[29] Only the presence of these small gases prevents the atmosphere from being completely transparent in the far infrared. Therefore, to accurately model the radiation from the atmosphere to the surface, it is essential to determine the radiation expected from the gas mixture of water vapor and carbon dioxide. The fact that the composition, temperature, and pressure of these mixtures vary with height above ground level also must be considered.

The emissivity of a particular radiating gas is a function of the number of molecules of the radiating gas in the column of air under investigation. At a given temperature, the number of molecules of the radiating gas is linearly proportional to the density-length product, $m_g \equiv p_g L_g$, where p_g is the density of the gas and L_g is the length of the gas column.[29] The total emissivity (ε_w) of a column of water vapor and nonradiating gas is primarily a function of the following: the density-length product (m_w) of the water vapor, the partial pressure (P_w) of the water vapor, the total pressure (P_T) of the mixture, and the temperature of the mixture (T).[29] However, the total emissivity is not strongly influenced by either the partial pressure of the water or the temperature of the mix. When carbon dioxide is added to the gas mixture, the radiative behavior of the gas column is only slightly changed. Based on the established work from Hottel and Egbert,[30] Bliss expressed the total emissivity of moist atmospheric air as a function of m_w, and the ratio of carbon dioxide to water vapor concentrations at a total pressure of 1 atmosphere and a temperature of 20 °C, which can mathematically be presented in equation 31 as:

$$\varepsilon_{atm} = \left(1.009 + \frac{0.2191}{\sqrt{m_w}} + \frac{1.547 \times 10^{-5}}{(m_w)^{1.5}} \right)^{-1} + 0.185 \cdot \left(\exp(-3.060 \cdot m_w) - \exp\left(-1.8 \cdot m_w \left(1.7 + 50 \cdot \frac{\rho_c}{\rho_w} \right) \right) \right) \quad (31)$$

where,

ε_{atm} = total atmospheric emissivity (unitless),
m_w = density-length product of the water vapor ($m_w \equiv p_g L_g$ = g/cm^2), and
ρ_c / ρ_w = ratio of carbon dioxide density to water vapor density (unitless).

In equation 31, the first term accounts for the emissivity of water vapor (moist air), and the second term accounts for the added emissivity caused by the presence of carbon dioxide. Figure 6 shows the individual contribution of the water vapor and carbon dioxide to the calculated emissivity of moist air. Note that the presence of carbon dioxide adds a maximum of only 0.185 to the overall emissivity. This figure further shows the effect of water vapor in the air, on the atmospheric emissivity. As the concentration of water vapor becomes less (dry air) the atmospheric radiation (total emissivity) decreases.

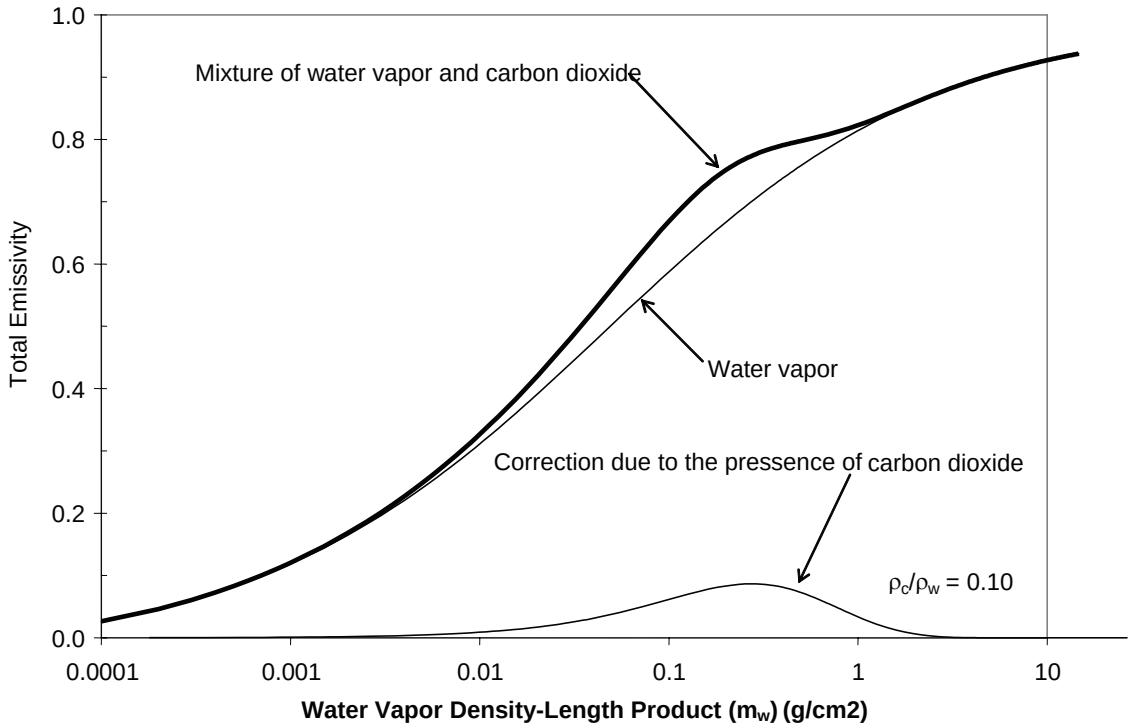

Figure 6. Emissivity of moist air at a total pressure of 1 atmosphere and a temperature of 20 °C.

The nature of the earth's atmosphere is that the pressure and temperature decreases with altitude, which, due to gas equilibrium principles, causes a change in the moisture condition of the body of gas. Therefore, to determine the total atmospheric emissivity, the earth's atmosphere should be considered as several layers, all at different temperatures, pressures, and moisture conditions. The composition of the atmosphere varies significantly, but it varies with height in typical ways. It can be shown that the variation of pressure with height above ground level can be determined by equation 32:[29]

$$P_z = P_i \cdot \exp(-1.2 \times 10^{-4} \cdot z) \tag{32}$$

where,

P_z = atmospheric pressure at height z (atm),
P_i = atmospheric pressure at ground level (atm), and
z = height above ground level (m).

As the total pressure is decreased, the emissivity of the gas is decreased. Equation 31 provided the total atmospheric emissivity at a pressure of 1 atmosphere, and by determining an adjusted density-length

product of the water vapor, the effect of different pressures on emissivity can be incorporated. The adjusted density-length product of the water vapor (m'_w) can be determined as in equation 33:[29]

$$m'_w = m_w \cdot P_z / P_0 \tag{33}$$

where,

P_z = actual pressure of the moist air (atm), and
P_0 = pressure of known emissivity versus water vapor relationship (1 atm).

The variation of temperature with height is less uniform, but it is reported that at heights above a few meters off the ground surface, it often obeys the following relationship in equation 34:[29]

$$T_z = T_i - 0.006 \times z \tag{34}$$

where,

T_z = atmospheric temperature at height z (°C),
T_i = atmospheric temperature at ground level (°C), and
z = height above ground level (m).

As the total energy of a moist air column changes with a change in temperature, a temperature correction must be applied to the calculated total atmospheric emissivity. The total energy radiated by a gas of specified water-vapor content is function of its temperature only, and is directly proportional to the fourth power of its absolute temperature.[29] The temperature adjustment factor (T_f), which can be multiplied to the emissivity determined at a temperature different than the actual condition, can be determined as in equation 35:[29]

$$T_f = [(T_i + 273) / (T_0 + 273)]^4 \tag{35}$$

where,

T_i = actual temperature of the moist air (°C), and
T_0 = assumed temperature during calculation of the emissivity (°C).

The water vapor density is variable with height, and the total precipitable water contained below a certain height (z) can be determined with the following relationship in equation 36:[29]

$$\int_0^z dm'_w = \frac{p_{wi}}{5.7\times10^{-6}}\left(1 - \exp\left[- z \cdot 5.7\times10^{-6}\right]\right) \tag{36}$$

where,

$\int_0^z dm'_w$ = total precipitable water contained below a height z (g/cm^2),
p_{wi} = water vapor density at ground level (g/cm^2), and
z = height above ground level (m).

In HIPERPAV II, the climatic conditions are defined in terms of the relative humidity and the air temperature (dry-bulb temperature). Through the use of established gas relationships, the water vapor density can be determined. The water vapor saturation pressure for a given dry-bulb temperature can be determined as in equations 37 and 38:[22]

For dewpoint range of -100 to 0 °C:

$$\ln(p_{ws}) = 0.68 \cdot \left[C_1 / T_R + C_2 + C_3 \cdot T_R + C_4 \cdot T_R^2 + C_5 \cdot T_R^3 + C_6 \cdot T_R^4 + C_7 \cdot \ln(T_R)\right] \quad (37)$$

where,

p_{ws} = the water-vapor saturation pressure (atm),
T_R = the dry-bulb temperature, (°R = °C *1.8 + 491.67),
C_1 = -10214.165,
C_2 = -4.8932428,
C_3 = -0.0053765794,
C_4 = $-1.9202377 \times 10^{-7}$,
C_5 = $3.5575832 \times 10^{-10}$,
C_6 = $-9.0344688 \times 10^{-14}$, and
C_7 = 4.1635019.

For dewpoint range of 0 to 200 °C:

$$\ln(p_{ws}) = 0.68 \cdot \left[C_8 / T_R + C_9 + C_{10} \cdot T_R + C_{11} \cdot T_R^2 + C_{12} \cdot T_R^3 + C_{13} \cdot \ln(T_R)\right] \quad (38)$$

where,

C_8 = -10440.397,
C_9 = -11.29465,
C_{10} = -0.027022355,
C_{11} = -1.289036×10^{-5},
C_{12} = $-2.4780691 \times 10^{-9}$, and
C_{13} = 6.5459673.

After the water vapor saturation pressure is determined, the water vapor pressure of the moist air can be determined from the known relative humidity (RH), as shown in equation 39.

$$p_w = \mathrm{RH} \times p_{ws} \quad (39)$$

The information above provides all the information needed to determine the apparent atmospheric emissivity with the following variables: surface atmospheric pressure (atm), dry-bulb temperature (°C), relative humidity, and the ratio of carbon dioxide to water vapor. The atmosphere is divided into different layers, and by using a step-wise procedure, the emissivity can be accumulated from each layer. After the apparent emissivity (ε_{app}) is determined, the intensity of atmospheric radiation (A_R) can be determined in equation 40 (figure 5 above):

$$A_R = \varepsilon_{app} \times \sigma \times T_a^4 \ (\mathrm{W/m^2}) \tag{40}$$

Now with the intensity of atmospheric radiation determined, the apparent surrounding air temperature (T_∞) can be solved from equation 41:

$$T_\infty = (A_R / \sigma)^4 - 273 \ (°\mathrm{C}) \tag{41}$$

As the apparent surrounding air temperature is now determined, the Stefan-Boltzmann law can be used to determine the heat transfer by irradiation (equation 30). Figures 7 to 9 illustrate the sensitivity of the effective surrounding temperature to all the various input variables with the following parameters as baseline values for the analysis: atmospheric pressure = 750 millibars, dry-bulb temperature = 30 °C, relative humidity = 20 percent, ratio of carbon dioxide to water vapor = 1.0. Under the conditions investigated, there is a significant reduction in the apparent surrounding temperature associated with a decrease in total pressure and the relative humidity. A change in the carbon dioxide content seems to have a minimal impact on the apparent surrounding temperature, and a ratio of 0.1 should be sufficient for most conditions.[29]

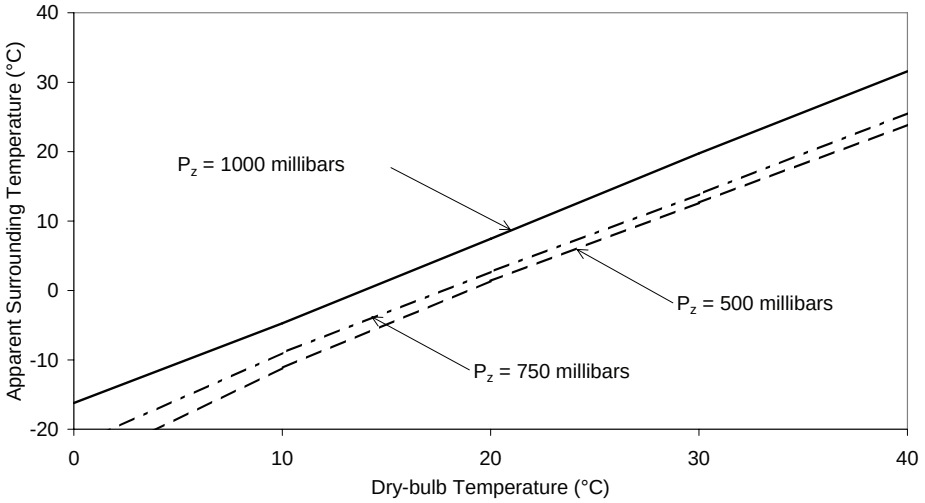

Figure 7. Sensitivity of the apparent surrounding temperature to changes in climatic conditions, atmospheric pressure.

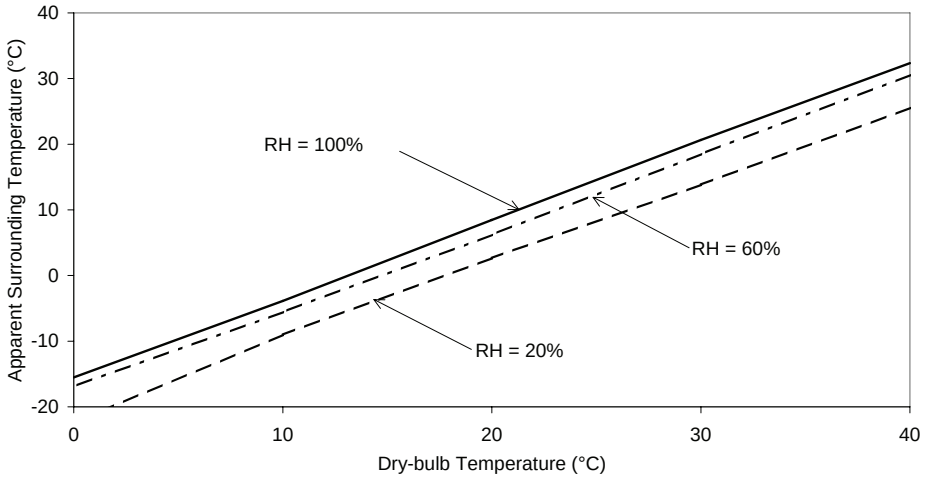

Figure 8. Sensitivity of the apparent surrounding temperature to changes in climatic conditions, relative humidity.

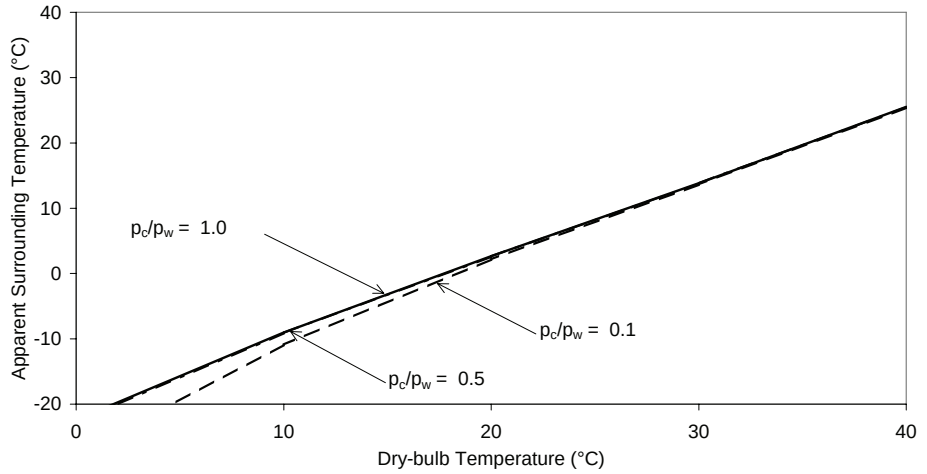

Figure 9. Sensitivity of the apparent surrounding temperature to changes in climatic conditions, ratio of carbon dioxide to water vapor.

B.1.2.6 Prediction of Initial Pavement Temperature Profile

Although the initial temperature of the mix and temperature of the subbase are required inputs in HIPERPAV II, the finite-difference temperature model used in HIPERPAV II requires as an input the complete temperature profile including depths beyond the subbase. For this purpose, HIPERPAV II uses a simple closed form solution for prediction of pavement temperatures.[31] The 24-hour periodic temperature, *T*, at a given depth, *x*, can be predicted as in equation 42:[31]

$$T = T_M + T_V \frac{H \cdot e^{-x \cdot C}}{\sqrt{(H+C)^2 + C^2}} \cdot \sin\left(\frac{\pi}{12} t - x \cdot C - arcTan\frac{C}{C+H}\right) \quad (42)$$

where,

T = 24-hour periodic temperature of the mass, ºC,
T_M = mean effective air temperature, ºC,
T_V = maximum variation in temperature from the effective mean, ºC,
t = time from beginning of cycle (one cycle = 24 h),
x = depth below surface, m,
H = h/k, where h is the surface convection coefficient, W/m^2/ºC, and k is the conductivity, W/m^2/ºC/m, and
C = $(0.131/c)^{0.5}$, where diffusivity $c = k/(sw)$, s is specific heat in J/kg/ºC, and w is density in kg/m^3.

As can be observed, the above model considers the climatic conditions and thermal properties of the materials for prediction of pavement temperature. To provide for temperature equilibrium with the environment, pavement temperatures are predicted for a total of 96 hours in advance up to the time of construction.

B.1.3 Shrinkage

HIPERPAV II has been updated to include the prediction of autogenous shrinkage as well as drying shrinkage. The chosen autogenous shrinkage model was developed by Jonasson and Hedlund.[32] Likewise, the drying shrinkage model in HIPERPAV II has been updated from the RILEM B_3 model previously used in HIPERPAV I to the Baźant-Panula model.[33] Now, shrinkage modeling is subdivided into two cases, when the w/cm is less than 0.40, and when it is greater than or equal to 0.40.

B.1.3.1 Autogenous Shrinkage and Drying Shrinkage for w/cm < 0.40

Autogenous shrinkage is defined by the Japanese Committee on Autogenous Shrinkage as "The macroscopic volume reduction of cementitious materials when cement hydrates after initial setting. Autogenous shrinkage does not include the volume change due to loss or ingress of substances, temperature variation, the application of an external force, and restraint."[34] (p. 54). The magnitude of autogenous shrinkage depends on the w/cm in the concrete. The lower the w/cm, the greater the importance of autogenous shrinkage, as compared to drying shrinkage. From a practical viewpoint, Aïtcin recommends that when w/cm < 0.40, autogenous shrinkage cannot be neglected.[34] For a w/cm of 0.30, the autogenous shrinkage can represent 50 percent of the total shrinkage, with total shrinkage equaling drying shrinkage plus autogenous shrinkage.

The shrinkage model selected for incorporation in HIPERPAV II was developed by Jonasson and Hedlund. In developing this mechanistic-empirical model, experimental test data for high-performance concrete (HPC) with a w/cm < 0.40 and 28-day compressive strength of equal to or greater than 80 MPa was used. The total shrinkage strain—autogenous shrinkage for the whole system plus drying shrinkage due to drying and wetting deformation at the surface—for the concrete's cross section is expressed in equation 43 as:[32]

$$\varepsilon_{cs}(t) = \varepsilon_{cs0}(t)\,\varepsilon_{csd}(t) < 0 \tag{43}$$

where,

t = time after casting (days),
$\varepsilon_{cs}(t)$ = total external shrinkage strain ($\times 10^6$ με),
$\varepsilon_{cs0}(t)$ = autogenous shrinkage under sealed conditions (see equation 44), and
$\varepsilon_{csd}(t)$ = additional strain due to drying/wetting caused by humidity change with the environment (see equation 45).

Autogenous shrinkage is modeled as:

$$\varepsilon_{cs0}(t) = \varepsilon_{s0\infty}\,\beta_{s0}(t) \tag{44}$$

where,

$\beta_{s0}(t)$ = time distribution of autogenous shrinkage (equation 45) and
$\varepsilon_{s0\infty}$ = final value of autogenous shrinkage (equation 46).

Autogenous shrinkage measurements were initiated 24 hours after casting. The authors state that, prior to 24 hours, the concrete is plastic, but assume that the stresses and deformations begin after this time period. This expression for the time distribution of autogenous shrinkage starts at zero, 24 hours after casting.

$$\beta_{s0}(t) = \exp\left(-\left[\frac{t_{s0}}{t - t_{start}}\right]^{0.3}\right) \tag{45}$$

where,

t_{s0} = 5 days (constant for HPC) and
t_{start} = 1 day (start time of autogenous shrinkage).

The time distribution of autogenous shrinkage is not a function of the concrete's w/cm. Instead w/cm is incorporated into the ultimate autogenous shrinkage. It is expressed in the following empirical equation as:

$$\varepsilon_{s0\infty} = \left(-0.65 + 1.3\frac{w}{B}\right)\cdot 10^{-3} \tag{46}$$

where,

w = water content (kg/m^3) and
B = cement content + silica fume content (kg/m^3).

Drying shrinkage is a surface concept. The external humidity exchange occurs only in the outer shell of the structural member, called "surface layer drying." The portion of the cross section affected by surface layer drying, α_{sd} (figure 10), is assumed to be constant with time and is calculated using equation 47:

$$\alpha_{sd} = \frac{u l_{sd}}{A_c} \leq 1 \tag{47}$$

where,

u = perimeter of the cross section in contact with environmental humidity,
A_c = cross section perpendicular to water flow, and
l_{sd} = typical length of surface for water exchange, given by equation 48:

$$l_{sd} = \frac{l_{sd,ref}}{0.5 - \frac{w}{B}} \tag{48}$$

where,

$l_{sd,ref}$ = 0.0045 m, the reference depth of surface layer drying for HPC.

This term tends to infinity when the *w/B* ratio is 0.5. It can only be used when *w/B* < 0.50, which is one of the constraints of using this model.

Figure 10. Surface layer zone subjected to drying shrinkage for a slip-formed pavement.

There are two cases, when $\alpha_{sd} = 1$ and when $\alpha_{sd} < 1$, as shown for typical pavement cross sections, $\alpha_{sd} < 1$. However, for some cylinders, $\alpha_{sd} = 1$, for example, for cylinders with diameters of 100 mm and *w/B* = 0.32.

Case I (equation 49): $\alpha_{sd} = 1$.

$$\varepsilon_{sd,all}(t) = \varepsilon_{sd,tot}\ \beta_{sd}(t)\,\beta_{sd,RH} \tag{49}$$

where,

$\varepsilon_{sd,all}(t)$ = drying shrinkage (plus autogenous shrinkage) when the whole specimen is affected by drying,
$\varepsilon_{sd,tot}$ = final drying shrinkage (see equation 51),
$\beta_{sd,RH}$ = coefficient depending on relative humidity (see equation 56), and
$\beta_{sd}(t)$ = time development of drying shrinkage, expressed by equation 50:

$$\beta_{sd}(t) = \left[\frac{t - t_s}{t_{sd} + t - t_s} \right]^{0.5} \tag{50}$$

where,

$t - t_s$ = time after start of drying and wetting (days),
t_s = age of concrete at start of drying and wetting (≥ 1 day), and
t_{sd} = 200 days, time reflecting the typical rate of humidity exchange.

This total shrinkage $\varepsilon_{sd,tot}$ is the same order of magnitude for HPC as for normal strength concrete. The empirical relationship is:

$$\varepsilon_{sd,tot} = \left(-0.1 - 0.8 \frac{w}{B} \right) \cdot 10^{-3} \tag{51}$$

Case II (equation 52): $\alpha_{sd} < 1$.

When α_{sd} is less than 1, a moisture exchange is taking place between the surface of the structural layer and the environment, and there is an inner part that is affected only by self-desiccation. Using a force balance and assuming that plane sections remain plane (equation 52),

$$\varepsilon_{csd}(t) = \alpha_{sd}\, \varepsilon_{sd,all}(t) \tag{52}$$

Combining with equation 49, equation 53 results,

$$\varepsilon_{csd}(t) = \alpha_{sd}\, \varepsilon_{sd,tot}\, \beta_{sd}(t)\, \beta_{sd,RH} \tag{53}$$

setting equation 54,

$$\varepsilon_{sd\infty} = \alpha_{sd}\, \varepsilon_{sd,tot} \tag{54}$$

yields equation 55,

$$\varepsilon_{csd}(t) = \varepsilon_{sd\infty}\, \beta_{sd}(t)\, \beta_{sd,RH} \tag{55}$$

where,

$\varepsilon_{csd}(t)$ = additional strain due to drying/wetting of the concrete with the environment,
$\varepsilon_{sd\infty}$ = final external strain due to drying shrinkage (see equation 54),
$\beta_{sd}(t)$ = time development of drying shrinkage (see equation 50), and
$\beta_{sd,RH}$ = coefficient depending on relative humidity (see equation 56).

To describe the shrinkage of HPC as a function of relative humidity:

$$\beta_{sd,RH} = \frac{RH_0 - RH}{\left|RH_{ref} - RH_0\right|} \tag{56}$$

where,

RH = actual environmental relative humidity,
RH_0 = relative humidity at sealed conditions (80 percent for w/cm ≤ 0.4), and
RH_{ref} = chosen relative humidity at a typical indoors environment (60 percent when w/cm ≤ 0.4).

In addition, it has been found for normal strength concrete, and can be applied to HPC, that when the relative humidity is less than the reference relative humidity, it can be assumed that drying shrinkage is not affected by relative humidity, as seen in equation 57.

$$\beta_{sd,RH} = 1 \quad for \quad RH \le RH_{ref} \tag{57}$$

The effect of changing the w/c on the total shrinkage according to the Jonasson model is shown in figure 11. The lower w/c, the higher the total shrinkage.

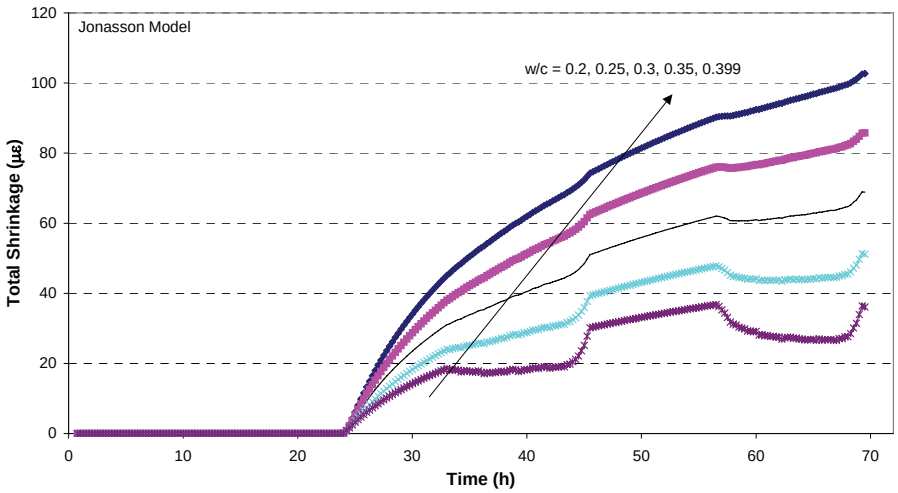

Figure 11. Influence of w/cm on total shrinkage predicted by the Jonasson model.

B.1.3.2 Autogenous Shrinkage and Drying Shrinkage for w/cm ≥ 0.40

The Bażant-Panula shrinkage model was selected to model the concrete when its w/cm ≥ 0.40. It models total shrinkage, which is autogenous shrinkage plus drying shrinkage, and it takes into account the composition of the mix and other empirical dependences.[35] It was also found to match the experimental drying shrinkage data better than the B_3 model previously used in HIPERPAV I as described in section D.3.2.

The drying shrinkage strain is expressed by equation 58:[35]

$$\varepsilon_{sh}\left(\hat{t},t_0\right)=\varepsilon_{sh\infty}k_h S\left(\hat{t}\right) \tag{58}$$

where,

ε_{sh} = shrinkage strain (με),
t = time (days),
t_0 = age when drying begins (days), assumed to be the concrete's set time,
$\hat{t}$ = duration of drying (days), $\hat{t}=t-t_0$,
$\varepsilon_{sh\infty}$ = ultimate shrinkage strain (με) (see equation 63),
k_h = humidity dependence (see equation 65), and
$S(\hat{t})$ = time dependence (see equation 59).

The time dependence is shown in equation 59:

$$S\left(\hat{t}\right)=\sqrt{\frac{\hat{t}}{\tau_{sh}+\hat{t}}} \tag{59}$$

where,

τ_{sh} = shrinkage half-time (equation 60).

The size dependence of the diffusion type is:

$$\tau_{sh}=600\left(\frac{k_s}{150}D\right)^2\frac{C_1^{ref}}{C_1\left(t_0\right)} \tag{60}$$

where,

k_s = shape factor, k_s = 1 for infinite slab, 1.15 for infinite cylinder, 1.25 for infinite square prism, 1.30 for sphere and 1.55 for cube (If the length of a cylinder or prism is 3 times its width, then it can be assumed to be infinitely long. For a finite length cylinder less than 3 times its width, its k_s can be determined by linearly interpolating between the k_s value for a sphere or prism and its corresponding k_s for an infinitely long member),
D = effective cross section thickness (mm), = 2 *v/s*, with *v* = volume and *s* = surface area, (*D* is thickness/2 based on calibrations using the HIPERPAV I field sites (see section D.3.2). The same calibration factor was also reported by Persson.[36]),
C_1^{ref} = 10 mm^2/day, and
$C_1(t_0)$ = age dependence (mm^2/day), given by equation 61:

$$C_1\left(t\right)=C_7k_T^{'}\left(0.05+\sqrt{6.3/t}\right) \tag{61}$$

where,

C_7 = empirical reference diffusivity at 7 days (mm^2/day) (see equation 66) and
k'_T = temperature dependence coefficient, given by equation 62:

$$k_T^{'} = \frac{T}{T_0}\exp\left(\frac{5000}{T_0} - \frac{5000}{T}\right) \tag{62}$$

where,

T = temperature (Kelvin) and
T_0 = reference temperature 23 °C (in Kelvin).

This model was calibrated using laboratory data. Since it will be used to model drying shrinkage that occurs in the field at temperatures that are not found in the laboratory, the effect of k'_T will be neglected. T will be set to 23 °C in the modeling.

Ultimate shrinkage is given by equation 63:

$$\varepsilon_{sh\infty} = \varepsilon_{s\infty}\frac{E(7+600)}{E(t_0+\tau_{sh})} \tag{63}$$

where,

$\varepsilon_{s\infty}$ = empirical shrinkage given in equation 67.

$$E(t) = E(28)\sqrt{\frac{t}{4+0.85t}} \tag{64}$$

where,

$E(28)$ = 28-day modulus of elasticity.

Humidity dependence is the same as it is in the B_3 model, as shown in equation 65:

$$k_h = \begin{cases} 1-h^3 & for \quad h \le 0.98 \\ -0.2 & for \quad h = 1 \\ linear \ \text{interpolation} \ for & 0.98 \le h \le 1 \end{cases} \tag{65}$$

where,

h = relative humidity ($0 \le h \le 1$).

The empirical dependences of drying shrinkage on concrete strength and composition of the mix are defined in the following equations. The reference diffusivity C_7 (mm^2/day) is shown in equation 66:

$$C_7 = 1/8 \text{ w/c } c - 12 \tag{66}$$

if $C_7 < 7$, $C_7 = 7$, and if $C_7 > 21$, $C_7 = 21$.

Final shrinkage $\varepsilon_{s\infty}(10^{-6})$ is defined as shown in equation 67:

$$\varepsilon_{s\infty} = 1210 - 880y \tag{67}$$

where, as shown in equations 68 and 69,

$$y = \left(390z^{-4} + 1\right)^{-1} \tag{68}$$

$$z = \left(\left[1.25\sqrt{a/c} + 0.5\left(\frac{g}{s}\right)^2 \right] \times \left(\frac{1 + s/c}{w/c} \right)^{1/3} \sqrt{0.145 \cdot f_c'} \right) - 12 \quad if \quad z \geq 0 \tag{69}$$

else $z = 0$, with,

c	= cement content (kg/m^3),
w/c	= w/c by weight, or w/cm,
a/c	= total aggregate (coarse + fine)-to-cement ratio by weight,
g/s	= coarse aggregate-to-fine aggregate ratio by weight,
s/c	= sand-to-cement ratio by weight, and
f'_c	= 28-day compressive strength (MPa).

Brooks investigated the effect of admixtures on shrinkage.[37] He found that shrinkage was not greatly affected by fly ash, GGBF slag, or silica fume (5–15 percent). As a result, these additives will not be added to the cementitious materials content when calculating the drying shrinkage with the Baźant-Panula model.

The Baźant-Panula model does not take into account the cement type (α_1) and the specimen curing (α_2) factors that were included in the B_3 model. They were added to equation 67, as shown in equation 70:

$$\varepsilon_{s\infty} = \alpha_1 \alpha_2 \left(1210 - 880y\right) \tag{70}$$

where, as shown in equations 71 and 72,

$$\alpha_1 = \begin{cases} 1.0 \quad for \quad Type \quad I \quad cement \\ 0.85 \quad for \quad Type \quad II \quad cement \\ 1.1 \quad for \quad Type \quad III \quad cement \end{cases} \tag{71}$$

and

$$\alpha_2 = \begin{cases} 0.75 \quad for \quad steam \quad cured \quad specimens \\ 1.0 \quad for \quad water \quad cured \quad specimens \\ 1.2 \quad for \quad sealed \quad specimens \end{cases} \tag{72}$$

As shown in figure 12, increasing the w/c causes the total shrinkage to increase, as predicted by the Baźant-Panula model.

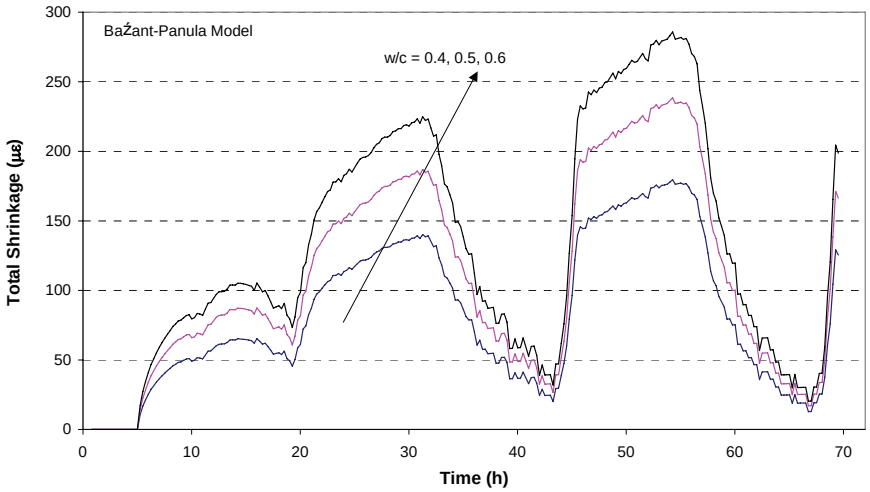

Figure 12. Effect of w/c on total shrinkage predicted by the Baźant-Panula model.

B.1.3.3 Comparison Between the Shrinkage Models

It is necessary to investigate the difference in the Baźant-Panula and Jonasson-Hedlund models when the w/cm is at and below 0.4. This is shown in figure 13. It is apparent that the shrinkage predicted by the Baźant-Panula model is greater, in some cases by 140 με. After experimental data is collected for pavement mixes with w/cm < 0.40, the Jonasson-Hedlund model can be calibrated.

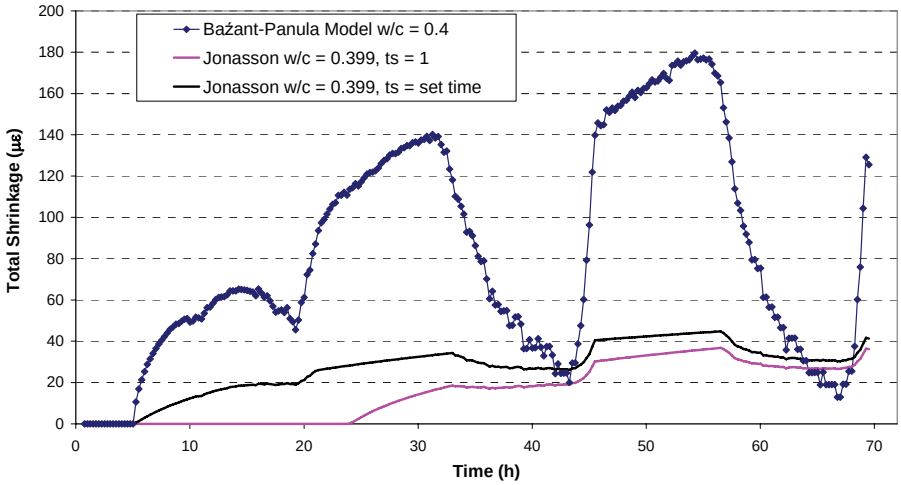

Figure 13. Comparison of the Baźant-Panula and Jonasson-Hedlund shrinkage models.

The influence of the start time on the Jonasson-Hedlund also was investigated. Changing t_{start} (equation 45) and t_s (equation 50) to the set time allows the model to predict shrinkage at times less than 24 hours. This modification was made for HIPERPAV II predictions, since autogenous shrinkage has been documented to begin at times less than 24 hours.(34)

In this new approach, the predicted total shrinkage in HIPERPAV II is the greater of the shrinkage predicted by the Jonasson-Hedlund and the Baźant-Panula models.

B.1.4 Nonlinear Restraint Model

Recognizing the nonlinear restraint effect imposed by some subbases, such as hot-mix asphalt (HMA) subbases, a nonlinear model was included in HIPERPAV II in addition to the current linear one to provide for the characterization of such behavior. The nonlinear model is of the following form, shown in equation 73:

$$\tau_f = C_2 \left(\frac{u_c}{\partial_f} \right)^{\frac{1}{n}} \tag{73}$$

where,

τ_f = friction stress (kPa),
u_c = PCC axial displacement (m),
δ_f = axial displacement at sliding (m),
C_2 = maximum friction stress (kPa), and
n = nonlinear power coefficient (dimensionless).

Typical values of the above coefficients can be obtained by performing friction tests. The procedure for these tests is described elsewhere. (See references 38, 39, 40, and 41.)

B.1.5 Nonlinear Thermal Gradient Model

Recognizing that thermal gradients through the slab depth are nonlinear for the most part, the model developed by Mohamed and Hansen is used in HIPERPAV II to determine an equivalent linear gradient as a function of a nonlinear one as follows in equation 74:[42]

$$\Delta T_{eq} = -\frac{12M^*}{\alpha h^2} \tag{74}$$

where,

ΔT_{eq} = equivalent linear temperature gradient, ºC,
h = slab thickness, m,
α = PCC CTE, m/m/ºC, and
M^* = constant dependent on the temperature distribution expressed as shown in equation 75:

$$M^* = \int_{-h/2}^{h/2} \varepsilon(z) z dz \tag{75}$$

where,

z = distance from slab midplane (z is positive downward), m, and
$\varepsilon(z)$ = strain profile, m/m.

The equivalent linear gradient from top to bottom of the slab determined with the above model was developed with the objective of producing the same curvature as the Westergaard and Bradbury linear gradient solution.[42]

In HIPERPAV II, the strain profile is determined as shown in equation 76:

$$\varepsilon(z) = \alpha(T_z - T_{z,set}) \tag{76}$$

where,

T_z = current temperature at slab depth z, ºC, and
$T_{z,set}$ = temperature at slab depth z, at time of set, ºC.

B.1.6 Creep Model

The creep model described below was not incorporated in HIPERPAV II due to lack of data for validation. However, it is presented here because researchers in this project made major efforts that could make incorporating the creep model relatively easy in the future when enough data for validation is available.

When load is applied to a concrete member, it responds with an immediate elastic deformation (ε_{el}), followed by a time-dependent creep response (ε_{cr}), which is shown in figure 14. This time-dependent

response is best modeled by viscoelastic theory.[43] To obtain a reasonably accurate estimate of the stresses at early ages, the amount of creep must be taken into account.

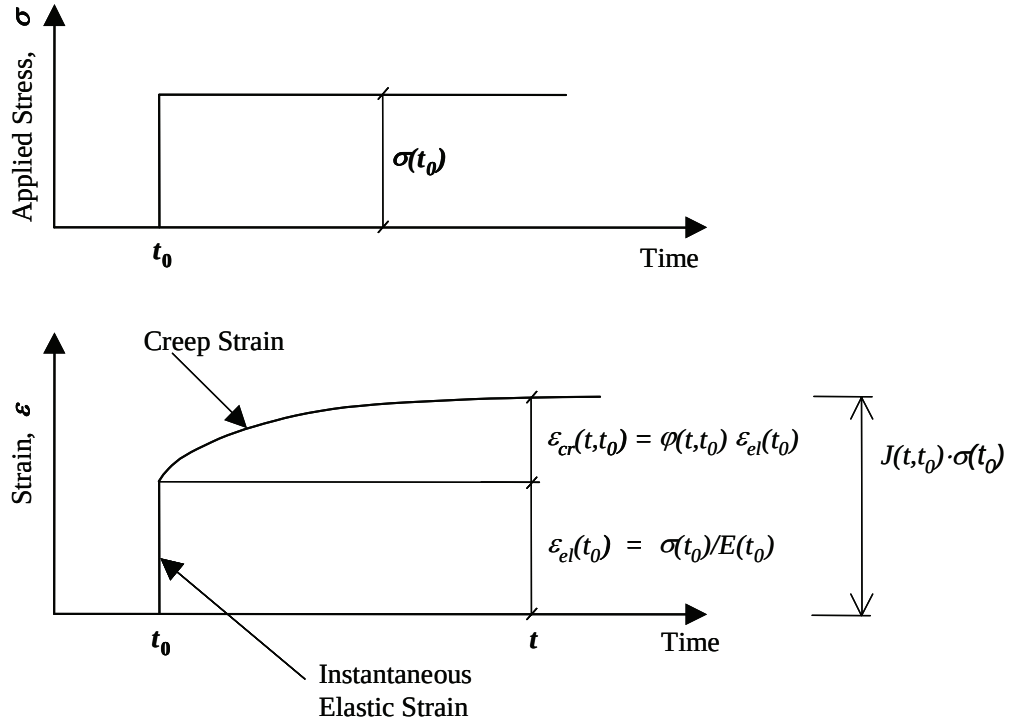

Figure 14. Time-dependent deformation at time *t*, for a loading at time t_0.[43]

In modeling of time-dependent deformation, creep compliance formulation is generally the preferred method. In this method, the total linear time-dependent deformation, $\varepsilon(t)$, is expressed as mathematically as shown in equation 77 below and illustrated in figure 14 above.

$$\varepsilon(t) = J(t,t_0)\cdot\sigma(t_0) \tag{77}$$

where,

$J(t,t_0)$ = creep compliance defined as the response at time t after loading at time t_0 and
$\sigma(t_0)$ = applied stress at time t_0.

The instantaneous and time-dependent components of the total deformation can be separated as shown in equation 78:

$$J(t,t_0) = \frac{1+\varphi(t,t_0)}{E(t_0)} = \frac{1}{E_{eff}} \tag{78}$$

where,

$E(t_0)$ = the instantaneous modulus of elasticity at time t_0,
$\varphi(t,t_0)$ = the creep coefficient (ratio of creep to elastic strain), and
E_{eff} = the effective modulus of elasticity at time t.

B.1.6.1 Creep Model Identified—Extended Triple Power Law

Few models are available to model the time-dependent deformation and creep compliance of concrete at early ages. The Extended Triple Power Law model is developed from the Double Power Law and the Triple Power Law.[35,44] The Double Power Law is perhaps the most well known compliance function, and has been used by many authors because it is based on extensive laboratory test results. The Triple Power Law was developed to provide a more accurate description of the long-term creep. As is commonly done, it will also be assumed that the creep response in tension is equal to the creep in compression.

Neither the Double nor the Triple Power Laws were calibrated for loading at early ages, and they were not intended to predict creep for young concrete.[45] Westman estimated that the Double and Triple Power Laws are only valid for loading ages larger than about 2 days.[43] Therefore, the Triple Power Law was adjusted first by Emborg[45] and then by Westman[43] to account for loading at ages less than about 2 days. The Extended Triple Power Law, as documented by Westman, provides good agreement with early-age test data, and accounts for all the factors that could influence the time-dependent deformation, such as:

- Concrete age at setting.
- Concrete age at loading (which is most important).
- Applied stress level.
- The influence of varying temperature.

B.1.6.2 Creep Model Definition

In 1989, Emborg extended the Triple Power Law with two additional functions, which Westman[43] modified in 1999. For loading ages less than about 2 days, the function $\Psi_1(t_0)$ models the age dependence of the instantaneous deformation, and $\Psi_2(t,t_0)$ models the increase of creep when the load has been applied. The purpose of the two new terms, $\Psi_1(t_0)$ and $\Psi_2(t,t_0)$, are shown schematically in figure 15. The creep compliance according to the Extended Triple Power Law is as shown in equations 79 through 90:

$$J(t,t_0) = \frac{1}{E_0} + \frac{\varphi_1}{E_0}\left(t_0^{-m} + \alpha\right)\left[(t-t_0)^n - B(t,t_0;n)\right] + \frac{\Psi_1(t_0)}{E_0} + \frac{\Psi_2(t,t_0)}{E_0} \tag{79}$$

where,

t = concrete age,
t_0 = equivalent age when the load is applied (days),
E_0 = negative asymptotic modulus of elasticity at time t_0 (psi), (1 psi = 6.89 kPa) (E_0 may be determined from the 28-day modulus, $E_0 \approx 1.5 \cdot E_{28}$),

$$\alpha = 1/40(\text{w/c}) \tag{80}$$

w/c = water-to-cement ratio,

$$\Phi_1 = 10^{3n}/2(28^{-m} + \alpha) \tag{81}$$

$$m = 0.28 + (0.145 \cdot f'_c)^{-2} \tag{82}$$

f'_c = 28-day cylinder compressive strength (MPa),

$$n = 0.12 + ((0.07 \cdot x^6)/(5130 + x^6)) \text{ if } x > 4; \text{ and } n = 0.12 \text{ if } x \leq 4 \tag{83}$$

$$x = \left[2.1\frac{(a/c)}{(s/c)^{1.4}} + 0.1\left(f_c^{'}\right)^{1.5}(w/c)^{1/3}(a/g)^{2.2} \right] \cdot a_1 - 4 \tag{84}$$

where,

a/c	=	total aggregate/cement ratio,
s/c	=	sand/cement ratio,
a/g	=	coarse aggregate/cement ratio, and
a_1	=	1.00 for Type I or II cement, 0.93 for Type III cement, and 1.03 for Type IV cement.

$B(t,t_0;n)$ is a binomial integral and may be evaluated by the following power series (equations 85 and 86):

$$B(t,t_0;n) = n \cdot t_0^n \left[\frac{\beta^{-n} - 1}{n} + \ln \beta + \sum_{k=1}^{\infty} \left(n^{-1}_{k}\right)(-1)^k \left(\frac{\beta^{k-n} - 1}{n-k} - \frac{1-\beta^k}{k} \right) \right] \tag{85}$$

with

$$\beta = t_0/t \text{ and } k = \text{summation time step} \tag{86}$$

Furthermore, if $t_0 \leq t_1$,

$$\Psi_1(t_0) = \gamma_1 \cdot \left(\frac{t_1 - t_0}{t_1 - t_s} \right)^{a_1} \tag{87}$$

if $t_0 > t_1$,

$$\Psi_1(t_0) = 0 \tag{88}$$

and if $t_0 \le t_3$,

$$\Psi_2(t,t_0)=\gamma_2 \cdot \left[1-\exp\left(-\left(\frac{t-t_0}{t_2}\right)^{a_2}\right)\right]\left(\frac{t_1-t_0}{t_1-t_s}\right)^{a_3} \tag{89}$$

If $t_0 > t_3$,

$$\Psi_2(t,t_0)=0 \tag{90}$$

where,

t_s = the apparent setting time of the concrete (days),
t_1 , t_3 = time limits for adjustment at early ages (days),
t_2 , a_2 = parameter for the development of the time function (days),
γ_1 = initial value of function $\Psi_1(t_0)$ at $t_0 = t_s$,
γ_2 = initial value of function $\Psi_2(t,t_0)$. at $t_0 = t_s$,
a_1 = parameter modifying the shape of $\Psi_1(t_0)$, and
a_3 = parameter modifying the end value of $\Psi_2(t,t_0)$.

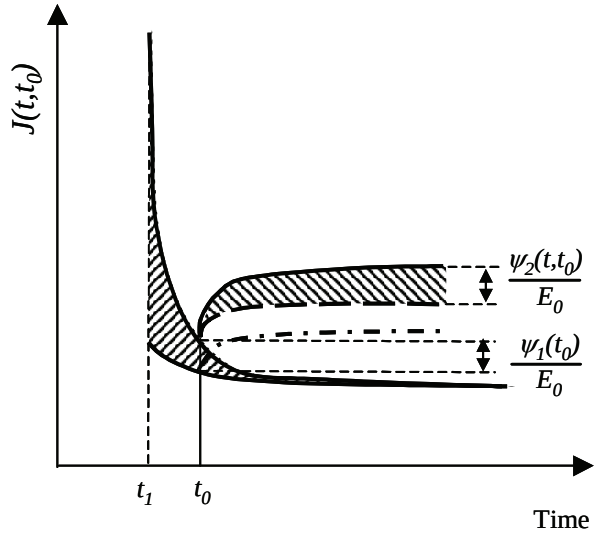

Figure 15. A schematic of the additional $\Psi_1(t_0)$ and $\Psi_2(t,t_0)$ functions to extend the Triple Power Law for the early-age creep response.[43]

The dependence of creep on different curing temperatures that are constant for the time of interest may be modeled with the coefficients n_T and φ_T instead of n and φ_1, as shown in equations 91 through 97:[35]

$$n_T = \beta_T \cdot n \tag{91}$$

where,

$$\beta_T = \frac{0.25}{1+\left(74/(T-253.2)\right)^7} + 1$$, (T measured in Kelvin), and (92)

$$\varphi_T = \varphi_1\left(1+C_T\right) \quad (93)$$

where,

$$C_T = C_{T1}\cdot\tau_T\cdot C_0 \quad (94)$$

$$C_{T1} = \frac{0.25}{1+\left(100/(T-253.2)\right)^{3.5}} - 1 \quad (95)$$

$$\tau_T = \frac{1}{1+\left(60/t_{oT}\right)^{0.69}} + 0.78 \quad (96)$$

$$C_0 = 0.125\cdot(w/c)^2(a/c)\cdot a_1 \quad (97)$$

where,

t_{oT} = age of the concrete when the temperature T is applied.

The age of the concrete at time of loading, t_0, is here expressed as shown in equation 98:

$$t' = t'_e = \int_o^{t'} \beta'_T\left(t''\right)dt'' \quad (98)$$

where,

t'_e = equivalent hydration period, and equation 99,

$$\beta'_T = \exp\left(\frac{4000}{T_0} - \frac{4000}{T}\right) \quad (99)$$

where,

T_0 = the reference temperature (293 ºK).

In the documentation provided by Westman, the necessary values for each of the parameters listed in this section are provided to allow the implementation of this model.[43] Based on the characteristics of the different mixtures tested by Westman, the mixture corresponding to a typical pavement mixture was selected. The characteristics of this mix is as follows: w/c = 0.40, 330 kg/m^3 cement, 5.6 percent air content, and a 28-day compressive strength of about 47.2 MPa. Based on the test results with this mixture design, it is recommended that the following parameters for the Extended Triple Power Law be used:

t_1	=	1.5 days	γ_1	=	10
t_3	=	1.5 days	γ_2	=	18
t_2	=	0.02 days	a_1	=	5
a_2	=	0.2	a_3	=	5

To obtain a reasonably accurate estimate of the stresses at early ages, the amount of relaxation that occurs must be taken into account. It is recommended that the Extended Triple Power Law be used to determine the creep compliance at early ages, as this model has been developed to characterize early-age response.

B.1.6.3 Implementation of Creep Model

In the implementation of creep compliance formulation, there are two possible approaches, and both methods have their advantages and disadvantages. The methods can briefly be described as follows:

- The simplest method "… is to assume the stress history is a series of sudden (discontinuous) stress increments and then solve the algebraic equations resulting from the superposition of creep responses due to all the individual stress increments."[46] (pp. 135 and 136) The error involved with this numerical procedure is of the second time step, however, the result obtained by Emborg[45] and others show good agreement with test data. The disadvantage of this method is that large storage space could be required to store the complete history of stresses for all the elements in the structure. However, it is believed that this problem is insignificant for early-age analyses, as few elements are considered in the finite-element analysis (FEA), and a period of only 72 hours typically is considered.

- The second method requires converting the creep compliance values into relaxation values. For this process, the Maxwell chain model is used most often in the conversion process. This procedure requires good selection of parameters for the Maxwell elements, and in some instances, convergence of the conversion could require user intervention. It is also reported that for very long load durations, negative relaxation values could develop, and adjustments of the creep curves are necessary to prevent this problem from occurring.[43] After the relaxation values are determined, further curve fitting also is required to obtain a smooth representation of the concretes behavior.

If this model is incorporated in future versions of HIPERPAV, it is recommended that the first method be used, since the approach is less likely to produce conversion problems during analysis. The following sections will provide further details on the solution to this procedure.

B.1.6.4 Algorithm for the Relaxation Formulation of Creep Deformations Based on the Principle of Superposition

Using the principle of superposition, the strain history $\varepsilon(t)$ caused by an arbitrary history of applied stress $\sigma(t)$ can be determined by assuming the stress history is composed of infinitesimal step functions as

shown in figure 16.[46] The total strain can be calculated as shown in equation 100.[45,46] This equation is a general uniaxial constitutive relation defining concrete as an aging viscoelastic material.

$$\varepsilon(t) = \int_0^t J(t,t_0)\cdot d\sigma(t_0) + \varepsilon_0(t) \tag{100}$$

where,

$J(t,t_0)$ = creep compliance defined as the response at time t after loading at time t_0,
$d\sigma(t_0)$ = stress increment at time t_0, and
$\varepsilon_0(t)$ = stress-independent strain increment at time t.

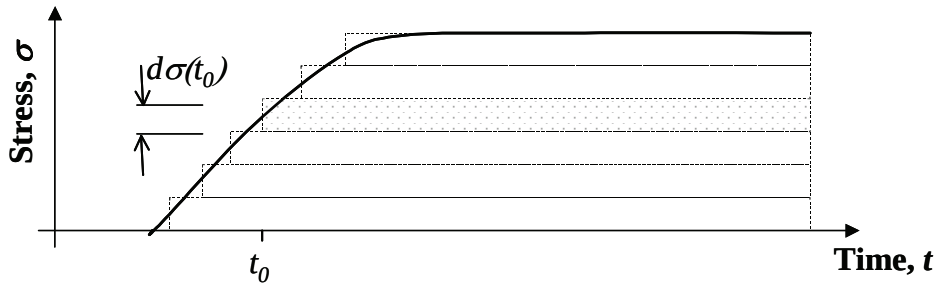

Figure 16. Decomposition of stress history into stress steps.

When the history of strain is prescribed, equation 100 can be solved by a step-by-step numerical solution, where time is subdivided into discrete time steps, t_r (r = 0,1,2, … n) with time steps, $\Delta t_r = t_r - t_{r-1}$.[46] A schematic for the numerical solution is shown in figure 17, and the steps for the algorithm are as follows:

Step 1: At time t_r, determine the equivalent age te_r, and the change in equivalent age as: $\Delta te_r = te_r - te_{r-1}$.
Step 2: Determine the applied strain, ε_r, and calculate the change in strain as: $\Delta\varepsilon_r = \varepsilon_r - \varepsilon_{r-1}$.
Step 3: Determine the incremental elastic modulus, $E''_r = 1/J(r,r-½)$. Subscript r, refer to the discrete time te_r, and $J(r,r-½)$ may be interpreted as $J(te_r, te_r - \Delta te_r/2)$.
Step 4: Determine the incremental strain, $\Delta\varepsilon''_r$, as shown in equation 101.

$$\Delta\varepsilon''_r = \sum_{s=1}^{r-1}\Delta J_r\cdot\Delta\sigma_s + \Delta\varepsilon_r^0 \tag{101}$$

where,

$\Delta\sigma_s$ = $\sigma_s - \sigma_{s-1}$, $\Delta\varepsilon^0_r = \varepsilon^0_r - \varepsilon^0_{r-1}$, and
ΔJ_r = $J(r,s-½) - J(r-1,s-½)$.

Step 5: Finally, the stress increment ($\Delta\sigma_r$) for the time step, Δt_r can be determined as shown in equation 102:

$$\Delta\sigma_r = E''_r\cdot(\Delta\varepsilon_r - \Delta\varepsilon''_r) \tag{102}$$

NOTE: Due to the nature of the summation required in equation 101, and the fact that the value *J(x,x)* is not singular, the start of the numerical iteration ($r = 0$, and $r = 1$) requires some initial calculations other than those presented above. Iteration interval $r = 0$, should be taken to occur at time, $t = t_0$, and $r = 1$ should be taken to occur at time, $t = t_o + 0.01$ (hours). The following calculations are necessary for $r = 0$ and $r = 1$ (equations 103 and 104, respectively):

At ***r* = 0**:

$$\Delta\sigma_r = 0, \text{ and } t = t_0 \text{ (days)} \tag{103}$$

At ***r* = 1**:

$$\Delta\varepsilon''_r = 0,\ t = (t_0 + 0.01)/24 \text{ (days)},\ E''_r = 1/J(r, r - 0.1), \text{ and } \Delta\sigma_r = E''_r \cdot (\Delta\varepsilon_r) \tag{104}$$

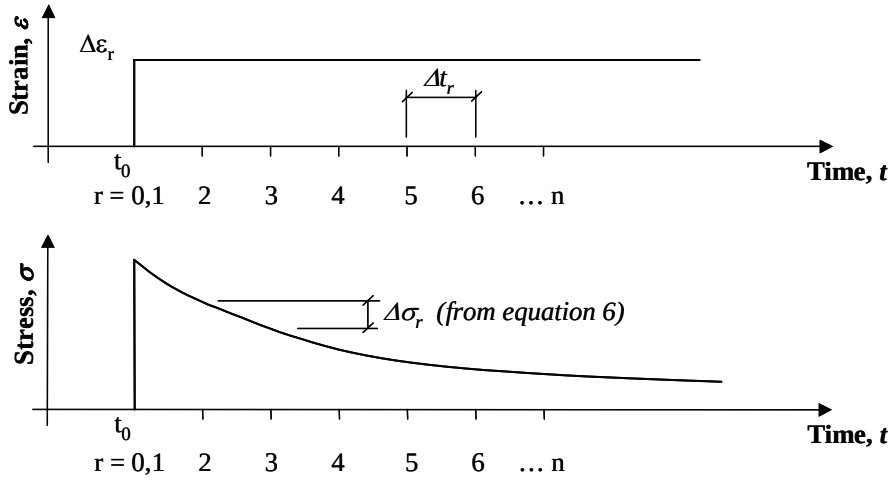

Figure 17. Discreet subdivision of time for numerical creep analysis.

Figures 18–20 show a schematic of how strains could be superimposed to model strain levels of varying intensities. Creep recovery at unloading could be overestimated by this principle, as the plastic flow component of the irrecoverable time-dependent deformation is not taken into accounted.(43)

Based on typical inputs, and the strains that were calculated with the HIPERPAV I program, the numerical procedure outlined above was programmed into mathcad™ to verify the results of the models. The results are shown in figure 21. With no relaxation modeled, the strains and the stresses cross the zero-stress level at the same time (approximately 22 hours). However, when the effects of relaxation are accounted for, the stress at ages less than 22 hours are significantly less, and the zero-stress level occurs earlier at an age of about 19 hours. Because much of the early tension has been relaxed, the magnitude of compressive forces between ages of 19 and 32 hours also is increased.

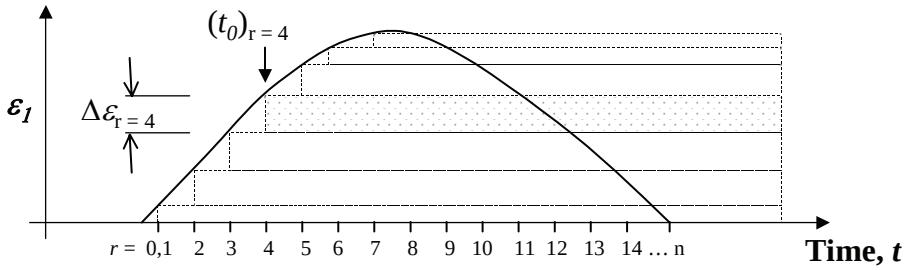

Figure 18. Superposition of various strains intensities: Loading.

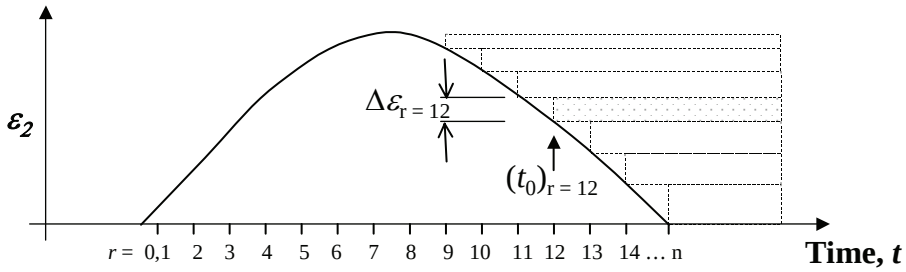

Figure 19. Superposition of various strains intensities: Unloading.

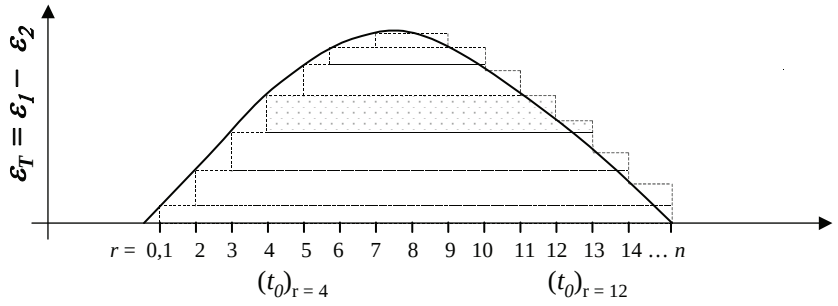

Figure 20. Superposition of various strains intensities: Net applied strains.

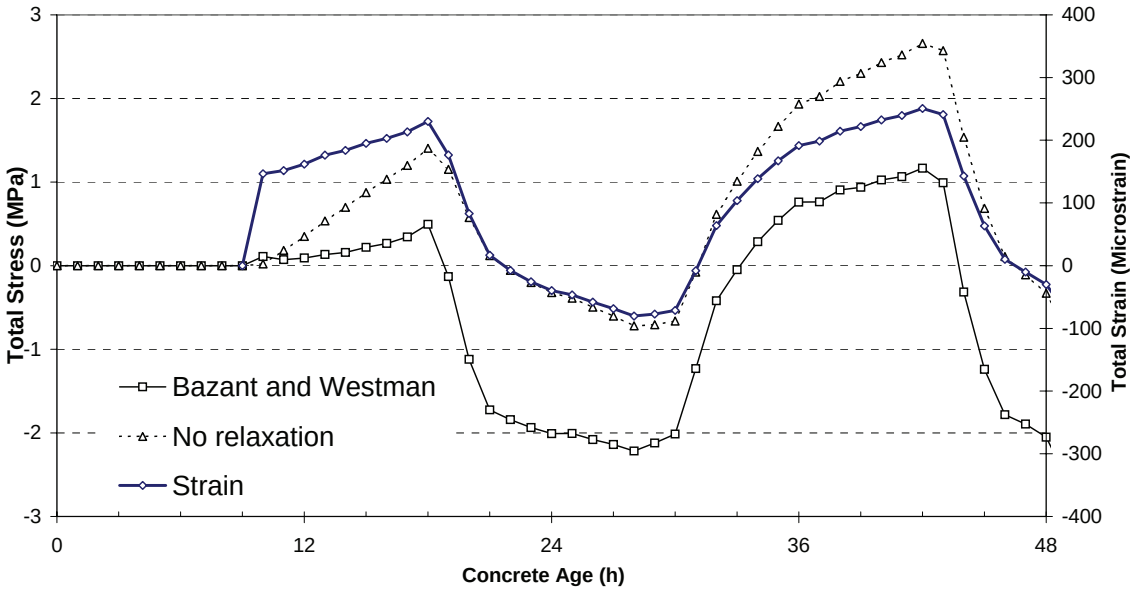

Figure 21. Comparison of the results of the relaxation model and model without relaxation.

B.1.6.5 Summary and Recommendations

To obtain a reasonably accurate estimate of the stresses at early ages, the amount of relaxation that occurs must be taken into account. It is recommended that the Extended Triple Power Law be used to determine the creep compliance at early ages, as this model has been developed extensively to characterize early-age response. A numerical technique to model the time-dependent response for concrete at early ages is also presented. The principle of superposition is used, where the strain history $\varepsilon(t)$ caused by an arbitrary history of applied stress $\sigma(t)$, is determined by assuming the stress history is composed of infinitesimal step functions.[46]

B.2 JPCP PERFORMANCE MODELS

A brief description of the primary JPCP long-term performance models incorporated in HIPERPAV II is provided in the following sections. These models are divided in the following categories:

- Environmental models.
- Long-term materials properties models.
- Structural models.
- Distress models.

Environmental models are used to predict the temperature and moisture gradient through the pavement structure. Long-term materials properties models are used to predict the development of strength and stiffness at ages beyond 28 days. Structural models are used to predict the pavement behavior in terms of stress, strain, and deflection due to environmental and traffic loadings. Finally, distress models are used to predict the distress progression as a function of environmental and traffic loads.

B.2.1 Environmental Models

B.2.1.1 Long-Term PCC Temperature Prediction Model

As stated in section B.1.2, the finite-difference method is used for prediction of long-term concrete temperatures in HIPERPAV II. A detailed description of this model is presented in that section. However, because pavement temperatures undergo seasonal changes in the long term, and because HIPERPAV II predicts PCC temperatures only at isolated periods of time for every season, the initial pavement temperature profile is required as an input in the finite-difference method for predicting the subsequent PCC temperatures for that season. HIPERPAV II uses the closed form solution developed by Barber described in section B.1.2.6 for this purpose.

B.2.1.2 Subgrade Moisture Model

This section summarizes the assumptions and limitations of the moisture model incorporated in HIPERPAV II. The model provides a simple method to predict the average monthly moisture content in pavement base materials using site-dependent climate conditions, soil data, and some pavement geometry.[18]

B.2.1.2.1 Inputs

The required inputs for the model are given below.

- Percent clay, *%Clay*, defined as the percent passing the #200 sieve.
- Saturation water content, w_{sat}.
- Plastic limit, *PL*.
- Liquid limit, *LL*.
- Plasticity index, *PI*.
- Difference in water content between the plastic limit and saturation, $w_{sat} - PL$.
- Suction at the plastic limit, Suc_{PL}.
- Monthly rainfall, $rain_{mo}$.
- Specific gravity of solids, G_s.
- Existence of paved shoulders.
- Thornthwaite moisture index (THMI).

The THMI is a correlation between rainfall and the potential for water loss through evaporation and transpiration.

High rainfall totals do not necessarily equate to a high THMI values because climatic conditions may dictate that the moisture is lost before it is absorbed into the soil.[47] A current practice is to group climate types according to moisture and winter temperature.[48] Table 14 gives a range of THMI values for specific locations in each of these climate types.

Table 14. Thornthwaite moisture index values.

City	THMI	Moisture	Winter Temperature
Chicago, IL	30	Wet	Cold
Fargo, ND	−5	Moderate	Cold
Reno, NV	−40	Dry	Cold
Washington, DC	60	Wet	Moderate
Oklahoma City, OK	0	Moderate	Moderate
Las Vegas, NV	−42	Dry	Moderate
Atlanta, GA	55	Wet	Warm
Dallas, TX	0	Moderate	Warm
San Antonio, TX	−18	Dry	Warm

Default soil characteristics that provided values for lesser known parameters were included with the model. Table 15 gives these values.

Table 15. Default soil characteristics.

USC	%Clay	$w_{sat} - PL$	Suc_{PL}	G_s
CH	70	26.2	3.5	2.68
CL	40	8.4	3.2	2.7
MH	30	5.3	3	2.7
ML	20	2.2	2.8	2.71
SC	30	4.4	2.9	2.65
SM	25	2.4	2.7	2.65
SP–SC	12	1.5	2.6	2.65
SW–SC	12	1.5	2.6	2.65
SP–SM	10	0.5	2.4	2.65
SW–SM	10	0.5	2.4	2.65
SP	5	0.3	2.4	2.64
SW	5	0.3	2.4	2.66
GW–GC	12	1.1	2.2	2.65
GP–GC	12	1.1	2.2	2.65
GW–GM	10	0.6	2	2.65
GP–GM	10	0.6	2	2.65
GP	5	0.2	1.8	2.65
GW	5	0.2	1.8	2.65

B.2.1.2.2 Calculations

The model makes a series of four calculations to predict the average monthly moisture content.

- Reference Suction: The reference suction, Suc_{ref}, is based on the *%Clay* and THMI. The magnitude of reference suction is determined as shown in equations 105 through 110:

If *%Clay* ≤ 6 percent:

$$\text{THMI} \geq -12.5\ Suc_{ref} = 1.86 \tag{105}$$

$$\text{THMI} < -12.5\ Suc_{ref} = -0.0141 * \text{THMI} + 1.69 \tag{106}$$

If 6 percent < *%Clay* < 40 percent:

$$\text{THMI} \leq -0.5\ Suc_{ref} = -0.0251 * \text{THMI} + 2.5 \tag{107}$$

$$\text{THMI} > -0.5\ Suc_{ref} = -0.0062 * \text{THMI} + 2.46 \tag{108}$$

If *%Clay* ≥ 40 percent:

$$\text{THMI} \leq -5.98\ Suc_{ref} = -0.043 * \text{THMI} + 3.23 \tag{109}$$

$$\text{THMI} > -5.98\ Suc_{ref} = -0.0118 * \text{THMI} + 3.4 \tag{110}$$

- Average Monthly Rainfall: The average monthly rainfall, $rain_{avg}$, is calculated by taking the average of the maximum, $rain_{max}$, and minimum, $rain_{min}$, monthly rainfall totals for the design year (equation 111).

$$rain_{avg} = (rain_{max} + rain_{min})/2 \tag{111}$$

- Suction Variation: The following steps in equations 112 through 114 are made to calculate the monthly soil suction, Suc_{mo}:

$$\text{If } rain_{mo} > rain_{avg} \quad Suc_{mo} = Suc_{ref} - ((rain_{mo} - rain_{avg})/(rain_{max} - rain_{avg})) * \Delta \tag{112}$$

$$\text{If } rain_{mo} < rain_{avg} \quad Suc_{mo} = Suc_{ref} + ((rain_{avg} - rain_{mo})/(rain_{avg} - rain_{min})) * \Delta \tag{113}$$

$$\text{If } rain_{mo} = rain_{avg} \quad Suc_{mo} = Suc_{ref} \tag{114}$$

where,

Δ = 0.25 for paved shoulders and
Δ = 0.50 for unpaved shoulders.

- Calculation of Moisture Content: The final step in the model is to correlate the monthly suction value to moisture content, as shown in equations 115 through 117.

If $Suc_{mo} \geq Suc_{PL}$:

$$w_{mo} = ((Suc_{mo} - 5.5)/(Suc_{PL} - 5.5)) * PL \tag{115}$$

If $Suc_{mo} < Suc_{PL}$:

$$w_{sat} < LL \; w_{mo} = PL + ((Suc_{mo} - Suc_{PL})/(1.0 - Suc_{PL})) * PI \tag{116}$$

$$w_{sat} \geq LL \; w_{mo} = PL + ((Suc_{mo} - Suc_{PL})/(1.0 - Suc_{PL})) * (w_{sat} - PL) \tag{117}$$

B.2.1.2.3 Sensitivity Analysis

A sensitivity analysis was performed on the continuity of the reference suction calculations and the influence of climate and rainfall.

B.2.1.2.3.1 Reference Suction

A quick analysis on the continuity of the reference suction calculation was performed by choosing values just above and below the calculation thresholds. This analysis is not included, but it indicated that the reference suction calculation is continuous. Six sets of values for *%Clay* and THMI were used to evaluate the six possible reference suction calculations. The effect of paved shoulders was also examined for each scenario. Constant monthly rainfall totals were used during this portion of the sensitivity analysis even though the THMI varied between runs. Table 16 shows the factorial for this portion of the experiment. The following sections summarize the results according to soil classification.

Table 16. Factorial for reference suction sensitivity analysis.

	Scenarios											
Variables	**1**	**2**	**3**	**4**	**5**	**6**	**7**	**8**	**9**	**10**	**11**	**12**
Thornthwaite	−15	−15	10	10	−15	−15	10	10	−15	−15	−10	−10
Soil class	CL	CL	CL	CL	GW-	GW-	GW-	GW-	GW	GW	GW	GW
%Clay	40	40	40	40	10	10	10	10	5	5	5	5
$w_{(PL)} - w_{(sat)}$	8.4	8.4	8.4	8.4	0.6	0.6	0.6	0.6	0.2	0.2	0.2	0.2
$w_{(sat)}$	23.4	23.4	23.4	23.4	15.6	15.6	15.6	15.6	10.2	10.2	10.2	10.2
Plastic limit	15	15	15	15	15	15	15	15	10	10	10	10
Liquid limit	40	40	40	40	21	21	21	21	15	15	15	15
Plasticity index	25	25	25	25	6	6	6	6	5	5	5	5
$\text{Suction}_{(PL)}$	3.2	3.2	3.2	3.2	2	2	2	2	1.8	1.8	1.8	1.8
Paved shoulder	Y	N	Y	N	Y	N	Y	N	Y	N	Y	N

Lean Clay (CL): Results for the CL soil are presented in figure 22 and table 17. Table 17 reports the monthly moisture content for scenarios 1–4 as outlined in table 15. The fifth (1–2) and sixth (3–4) columns examine the effect of paved shoulders on moisture content. The final two columns (1–3 and 2–4) examine the effect of changing the formula for reference suction calculation by a change in the THMI. The average and standard deviation for the effects of these changes are also given. Figure 22 shows the monthly variation in moisture content. The THMI value appears to control the general vertical location in this figure, while rainfall and paved/unpaved shoulders control variability. The presence of a paved shoulder appears to reduce moisture content variation throughout the year.

Table 17. Moisture contents for lean clay (CL) in scenarios 1–4.

		Scenario							
Month	**Rain (mm)**	**1**	**2**	**3**	**4**	**1–2**	**3–4**	**1–3**	**2–4**
Jan	81	10.31	10.02	14.18	13.89	0.29	0.29	3.87	3.87
Feb	93	10.56	10.53	14.43	14.39	0.04	0.04	3.87	3.87
Mar	64	9.95	9.31	13.82	13.18	0.64	0.64	3.87	3.87
Apr	89	10.49	10.37	14.35	14.24	0.11	0.11	3.87	3.87
May	173	12.23	13.86	16.91	19.75	1.63	2.84	4.68	5.89
Jun	59	9.85	9.10	13.72	12.97	0.75	0.75	3.87	3.87
Jul	155	11.85	13.11	16.26	18.45	1.26	2.19	4.40	5.34
Aug	108	10.87	11.14	14.74	15.01	0.27	0.27	3.87	3.87
Sep	17	8.97	7.34	12.83	11.20	1.63	1.63	3.87	3.87
Oct	129	11.30	12.00	15.29	16.51	0.70	1.22	3.99	4.51
Nov	168	12.12	13.65	16.72	19.38	1.52	2.66	4.60	5.73
Dec	83	10.35	10.11	14.22	13.98	0.25	0.25	3.87	3.87
					Average	0.76	1.07	4.05	4.37
					Std. Dev	0.61	1.02	0.32	0.81

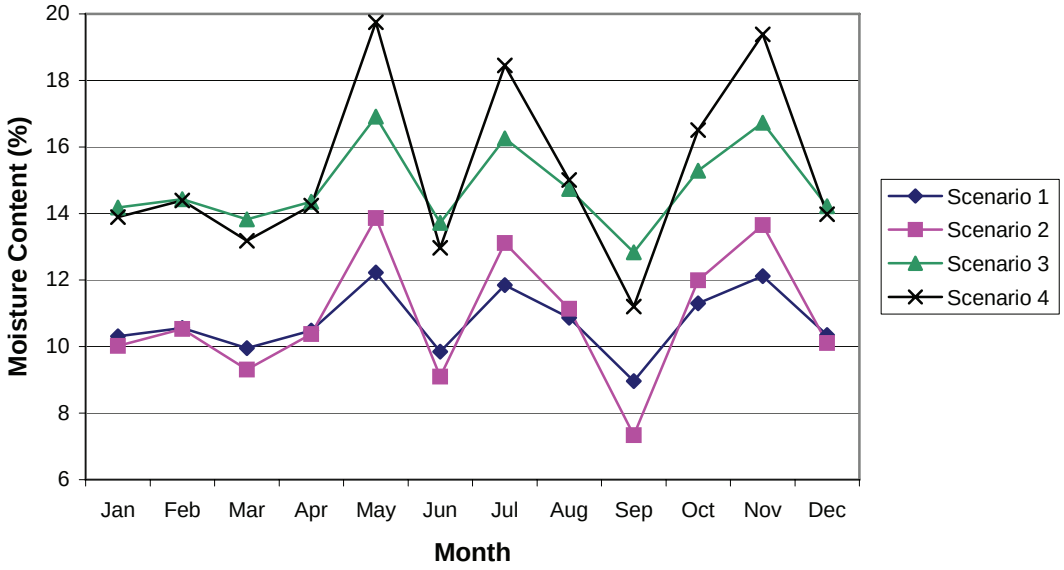

Figure 22. Monthly moisture content variation for lean clay (CL), scenarios 1–4.

Well-Graded Silty Gravel (GW–GM): Results for the GW–GM soil are presented in figure 23 and table 18. These scenarios also show that the moisture content value is dictated by the THMI, but the variability is dictated by rainfall and shoulder conditions. The variability of the GW–GM soil is noticeably less than the CL soil. This shows that the model accounts for changes in particle size, which directly affects the suction parameters used in the moisture content calculations. Smaller particle sizes or higher *%Clay* typically mean that the soil does not drain as well and is more susceptible to moisture content variation. As shown in figure 23 and in the previous section, the model predicts that a paved shoulder lessens the variability of moisture content throughout the year.

Table 18. Moisture contents for well-graded silty gravel (GW–GM) in scenarios 5–8.

		Scenario							
Month	**Rain (mm)**	**5**	**6**	**7**	**8**	**5–6**	**7–8**	**5–7**	**6–8**
Jan	81	11.05	10.86	13.10	12.91	0.19	0.19	2.05	2.05
Feb	93	11.22	11.20	13.27	13.25	0.02	0.02	2.05	2.05
Mar	64	10.82	10.40	12.87	12.45	0.42	0.42	2.05	2.05
Apr	89	11.17	11.10	13.22	13.15	0.07	0.07	2.05	2.05
May	173	12.32	13.39	14.37	15.60	1.07	1.23	2.05	2.21
Jun	59	10.75	10.26	12.80	12.31	0.49	0.49	2.05	2.05
Jul	155	12.07	12.90	14.12	14.95	0.83	0.83	2.05	2.05
Aug	108	11.42	11.60	13.47	13.65	0.18	0.18	2.05	2.05
Sep	17	10.17	9.10	12.22	11.15	1.07	1.07	2.05	2.05
Oct	129	11.70	12.16	13.75	14.21	0.46	0.46	2.05	2.05
Nov	168	12.25	13.25	14.30	15.42	1.00	1.12	2.05	2.17
Dec	83	11.08	10.92	13.13	12.97	0.16	0.16	2.05	2.05
					Average	0.50	0.52	2.05	2.07
					Std. Dev	0.40	0.44	0.00	0.06

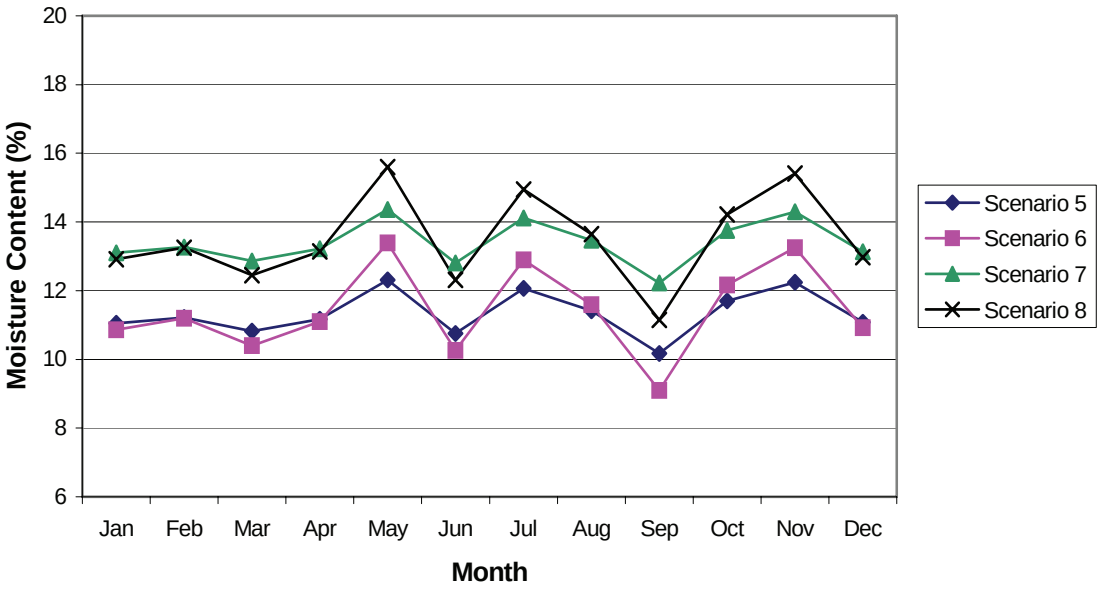

Figure 23. Monthly moisture content variation for well-graded silty gravel (GW–GM), scenarios 5–8.

Well-Graded Gravel (GW): Results for the GW soil are presented in figure 24 and table 19. The effects of THMI, paved shoulders, and rainfall are less pronounced for the GW soil. THMI changes did not alter the vertical placement in figure 24 as in the previous scenarios, which caused all four moisture contents to be in the same ranges throughout the design year. One explanation is that the model the GW soil contains only 5 percent clay and drains freely. Therefore, the evaporation and transpiration accounted for by the THMI does not have as great an affect as for soils with higher percentages of clay. In these scenarios, the presence of a paved shoulder reduces the moisture content variability, but not in the same range as in the previous scenarios.

Table 19. Moisture contents for well-graded gravel (GW) in scenarios 9–12.

		Scenario							
Month	**Rain (mm)**	**9**	**10**	**11**	**12**	**9–10**	**11–12**	**9–11**	**10–12**
Jan	81	9.61	9.49	9.72	9.60	0.12	0.12	0.11	0.11
Feb	93	9.71	9.70	9.82	9.81	0.01	0.01	0.11	0.11
Mar	64	9.46	9.19	9.57	9.30	0.27	0.27	0.11	0.11
Apr	89	9.68	9.63	9.79	9.74	0.05	0.05	0.11	0.11
May	173	10.20	10.20	10.20	10.20	0.00	0.00	0.00	0.00
Jun	59	9.42	9.11	9.53	9.22	0.31	0.31	0.11	0.11
Jul	155	10.20	10.20	10.20	10.20	0.00	0.00	0.00	0.00
Aug	108	9.84	9.95	9.95	10.14	0.11	0.19	0.11	0.19
Sep	17	9.05	8.37	9.16	8.49	0.68	0.68	0.11	0.11
Oct	129	10.04	10.20	10.20	10.20	0.16	0.00	0.16	0.00
Nov	168	10.20	10.20	10.20	10.20	0.00	0.00	0.00	0.00
Dec	83	9.62	9.52	9.74	9.63	0.10	0.10	0.11	0.11
					Average	0.15	0.14	0.09	0.08
					Std. Dev	0.19	0.20	0.06	0.06

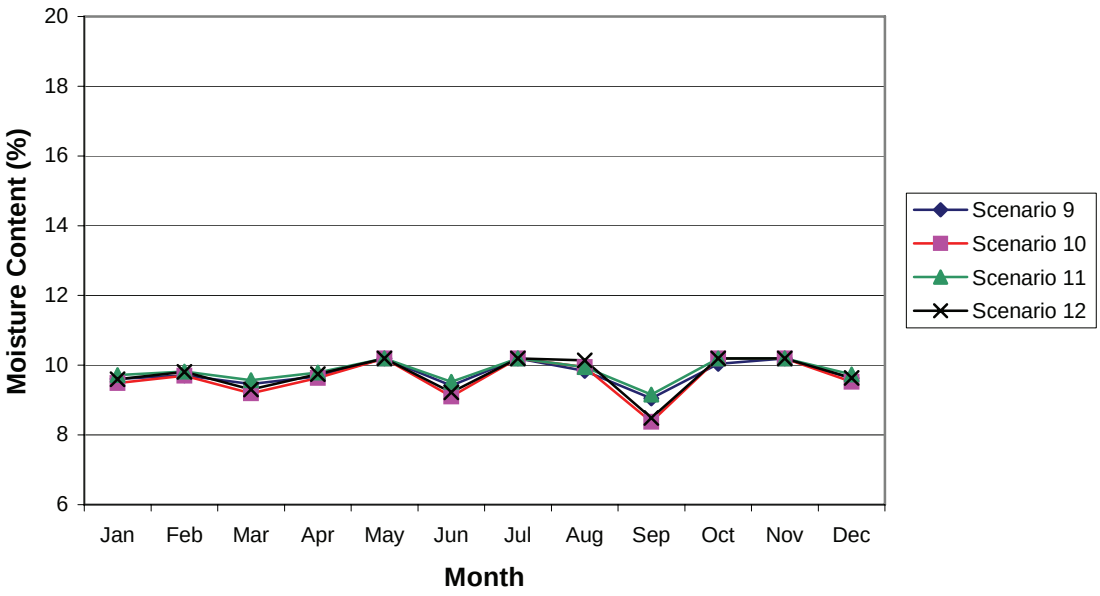

Figure 24. Monthly variation for well-graded gravel (GW), scenarios 9–12.

B.2.1.2.3.2 Climate and Rainfall

The second part of the sensitivity analysis evaluated two specific soils at five locations. The soil parameters used in this analysis were derived from Lytton's default values for CL and GW–GM soil types.[48] THMI and monthly rainfall values for each location were identified using historical climate data from the National Climate Data Center (NCDC).[49] Table 20 shows the factorial used for this aspect of the analysis.

Table 20. Factorial for climate and rainfall variation.

Location	City	THMI	Moisture	Winter Temperature
1	Chicago, IL	30	Wet	Cold
2	San Antonio, TX	−18	Dry	Warm
3	Oklahoma City, OK	0	Moderate	Moderate
4	Atlanta, GA	55	Wet	Warm
5	Reno, NV	−40	Dry	Cold

Table 21 gives the soil data for the CL and GW–GM soils used in the analysis.

Table 21. Soil data for climate and rainfall variation analysis.

Property	Soil 1	Soil 2
Soil class	CL	GW–GM
%Clay	40	10
$w_{(PL)} - w_{(sat)}$	8.4	0.6
$w_{(sat)}$	26.4	15.6
Plastic limit	18	15
Liquid limit	38	21
Plasticity index	20	6
$\text{Suction}_{(PL)}$	3.2	2
G_s	2.7	2.65

Table 22 gives the monthly rainfall totals for each of the five locations. Notice that the THMI value does not depend directly upon rainfall.

Table 22. Monthly rainfall totals for locations in the U.S in millimeters.[49]

Month	Chicago, IL	San Antonio, TX	Oklahoma City, OK	Atlanta, GA	Reno, NV
Jan	36.6	43.4	28.7	120.4	27.2
Feb	32.5	46.0	39.6	121.9	25.1
Mar	63.8	38.6	68.8	146.6	18.0
Apr	89.4	63.5	70.4	108.2	9.7
May	79.8	107.2	132.8	109.0	17.5
Jun	92.5	96.8	109.5	90.4	11.7
Jul	89.4	54.9	66.3	127.3	7.1
Aug	105.9	64.5	66.0	93.0	8.1
Sep	87.4	86.6	97.5	86.9	9.9
Oct	58.4	80.5	82.0	77.5	9.7
Nov	72.6	66.5	50.3	98.0	22.1
Dec	61.5	38.4	35.6	110.0	25.1
Total	869.7	787.1	847.1	1289.1	191.0

Lean Clay (CL): The results from the CL soil are given in table 23 and figure 25. This soil showed a large amount of variability between climate types. Atlanta, GA, and Chicago, IL, have the highest THMI values and have the highest predicted moisture contents. Reno, NV, has the lowest THMI and subsequently has the lowest predicted moisture content. These findings reinforce earlier observations that the vertical placement in figure 25 is directly related to THMI and the monthly variation is due to rainfall.

Table 23. Moisture contents for lean clay (CL) in five U.S. cities.

Month	Chicago, IL	San Antonio, TX	Oklahoma City, OK	Atlanta, GA	Reno, NV
Jan	17.46	10.04	14.48	22.64	6.26
Feb	17.25	10.20	14.89	22.73	5.84
Mar	19.06	9.77	15.99	24.35	4.47
Apr	20.64	11.19	16.04	21.83	2.82
May	20.05	13.66	18.45	21.87	4.34
Jun	20.84	13.08	17.52	20.66	3.20
Jul	20.65	10.69	15.89	23.08	2.35
Aug	21.67	11.25	15.88	20.82	2.53
Sep	20.52	12.51	17.06	20.43	2.86
Oct	18.73	12.16	16.49	19.81	2.83
Nov	19.61	11.36	15.29	21.16	5.28
Dec	18.92	9.75	14.73	21.94	5.85
Average	19.62	11.30	16.06	21.78	4.05
Std. Dev.	1.37	1.31	1.18	1.29	1.46

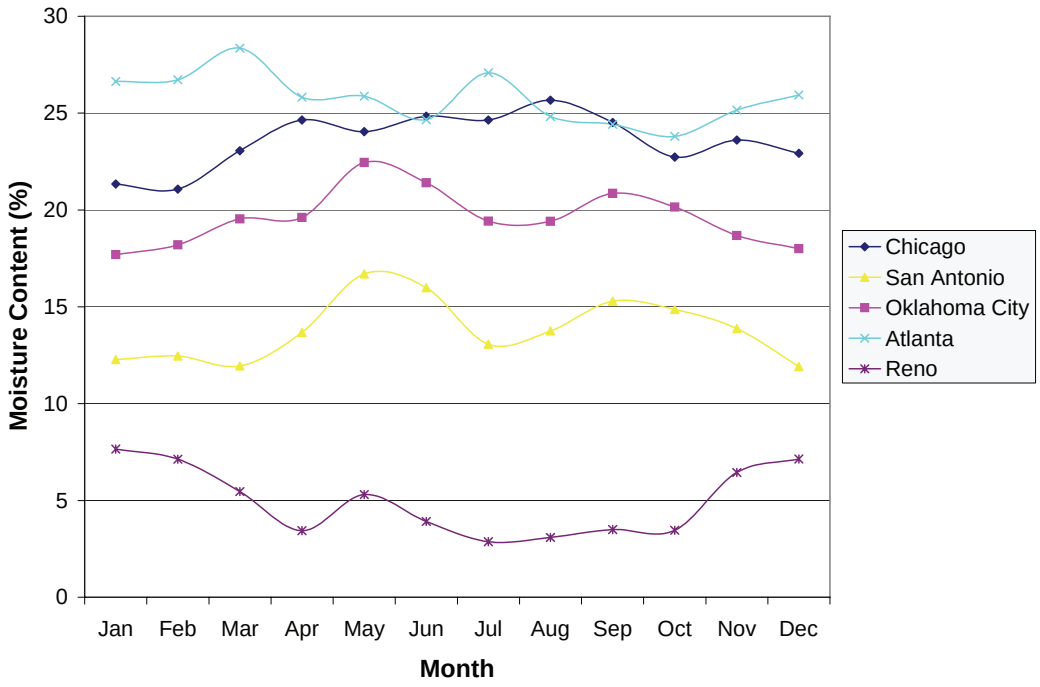

Figure 25. Monthly variation for lean clay (CL) in five U.S. cities.

Well-Graded Silty Gravel (GW–GM): The results from the analysis of the GW–GM soil type are shown in table 24 and figure 26. The prediction for this soil shows less variation than the CL soil. This also reinforces earlier observations that the model assumes soils with higher clay contents will fluctuate more than granular soils that drain more freely. Even with less variation, the moisture contents varied according to the THMI value at each location.

Table 24. Moisture contents for well-graded silty gravel (GW–GM) in five U.S. cities.

Month	Chicago, IL	San Antonio, TX	Oklahoma City, OK	Atlanta, GA	Reno, NV
Jan	10.04	10.01	11.96	14.75	9.63
Feb	10.20	10.09	12.18	14.79	9.40
Mar	9.77	9.86	12.78	15.60	8.64
Apr	11.19	10.64	12.82	14.37	7.74
May	13.66	11.99	14.10	14.39	8.58
Jun	13.08	11.67	13.62	13.82	7.95
Jul	10.69	10.36	12.73	14.96	7.48
Aug	11.25	10.67	12.73	13.90	7.58
Sep	12.51	11.36	13.37	13.71	7.76
Oct	12.16	11.17	13.06	13.42	7.75
Nov	11.36	10.73	12.40	14.05	9.09
Dec	9.75	9.85	12.10	14.42	9.40
Average	11.30	10.70	12.82	14.35	8.42
Std. Dev.	1.31	0.72	0.64	0.61	0.80

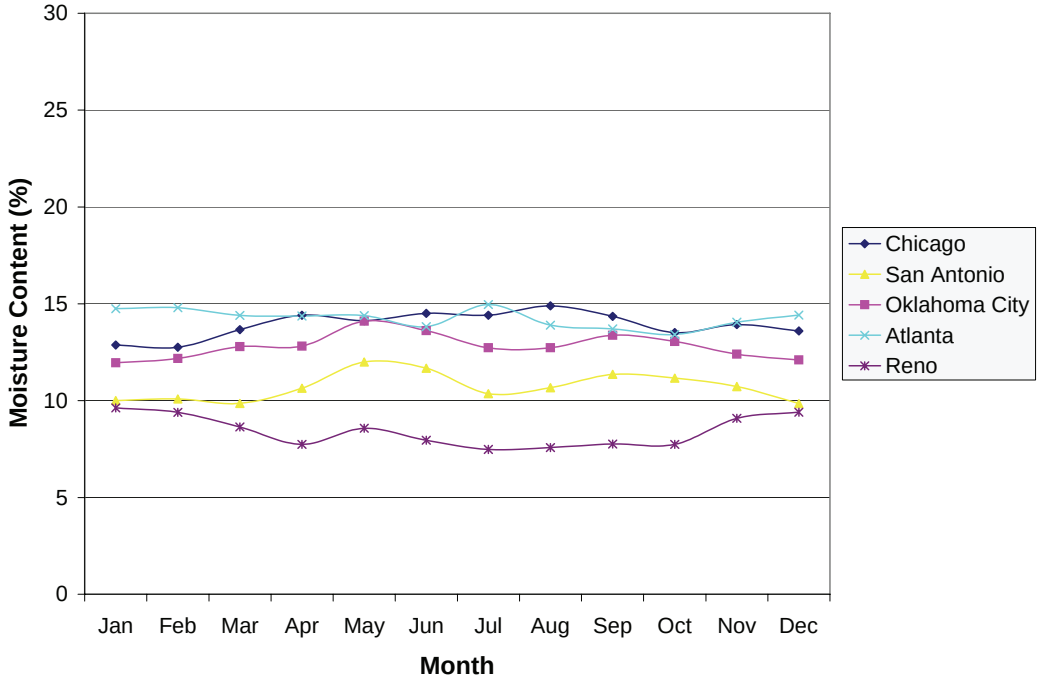

Figure 26. Monthly variation for well-graded silty gravel (GW–GM) in five U.S. cities.

B.2.1.2.4 AASHO Road Test

The model was evaluated using historical weather data from the NCDC and soil data from the American Association of State Highway Officials (AASHO) road test.[49,50,51] The pavement in loop 1 (untrafficked control lanes) was used for the analysis. Three layers of soil were compacted beneath the pavement. These are referred to as the embankment, subbase, and base layers. Published average spring and summer

moisture contents from the road test were compared to the results from the model.[51] Some problems may have occurred in estimating the parameters needed by the model from the given soil data. Table 25 shows the gradation for each soil layer.

Table 25. Gradation for AASHO road test soils.[50]

% Passing	Embankment	Subbase	Base
3.8 cm	100	100	100
2.5 cm	100	100	90
1.9 cm	100	96.9	81
1.3 cm	100	89.7	68
No. 4	99	71.2	48
No. 10	96.8	–	35
No. 40	91	27	20
No. 60	87.7	–	–
No. 100	–	–	13.5
No. 200	80.6	7.5	10

To run the model, soil parameters were estimated from the gradation and other data included in the AASHO road test reports.[50,51] The gradation was used to determine the soil type and the corresponding default values included with the model were then used. Table 26 gives the actual values used in the model.

Table 26. Soil parameters for AASHO road test soils.

Property	Embankment	Subbase	Base
Soil class	CL	SW–SM	GW–GM
%Clay	81	7	10
$w_{(PL)} - w_{(sat)}$	8.4	0.5	0.6
$w_{(sat)}$	24.9	7.5	7.6
Plastic limit	16.5	7	7
Liquid limit	29.4	10	9
Plasticity index	13.6	3	2
$\text{Suction}_{(PL)}$	3.2	2.4	2
G_s	2.71	2.65	2.65
Paved shoulder (Y/N)	Y	Y	Y

Figure 27 compares the predicted moisture content using the aforementioned soil data and average rainfall totals from the NCDC and the measured values during the AASHO road test. The predicted measurements were typically within 2 to 3 percent in moisture content from the measured values. The lack of rainfall data from the time of measurement and error in the estimated soil properties could lead to deviation from the measured values.

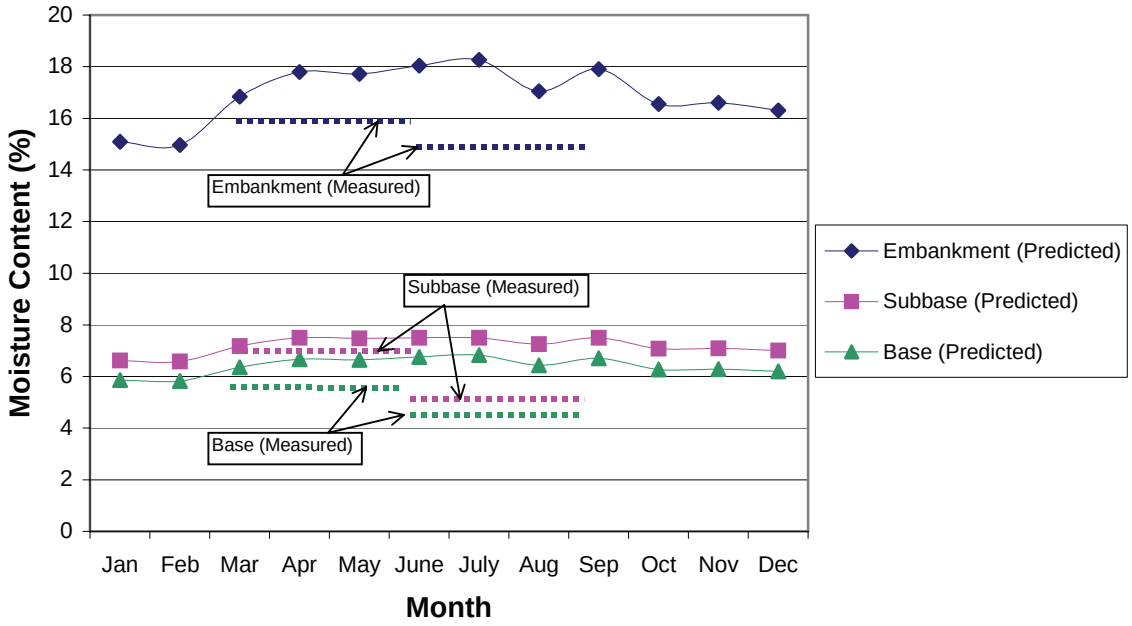

Figure 27. Comparison of predicted and measured values from the AASHO road test.

B.2.1.2.5 LTPP Sites

The model also was evaluated using soil and weather data from DataPave 2.0, Beta Version (April 1999) and compared with moisture contents calculated in a FHWA time-domain reflectometry study.[52,53] The sites used for this purpose were in Texas (48–1068) and Maine (23–1026). Table 27 gives the climatic data for each site.

Table 27. Climatic data for LTPP sites.

Location	THMI	Moisture	Winter Temperature
Texas	10	Moderate	Warm
Maine	80	Wet	Cold

As for the AASHO road test analysis, some soil properties had to be estimated from the given data. Missing soil data from the LTPP database had to be estimated to run the model. Soil types were recorded according to the AASHTO classification and had to be correlated to the Unified Soil Classification system to obtain certain properties. Figures 28 and 29 compare the predicted moisture contents and the values obtained from the FHWA study for the sites in Texas and Maine, respectively. The values from the FHWA study had to be estimated from charts and seemed to have questionable reliability.

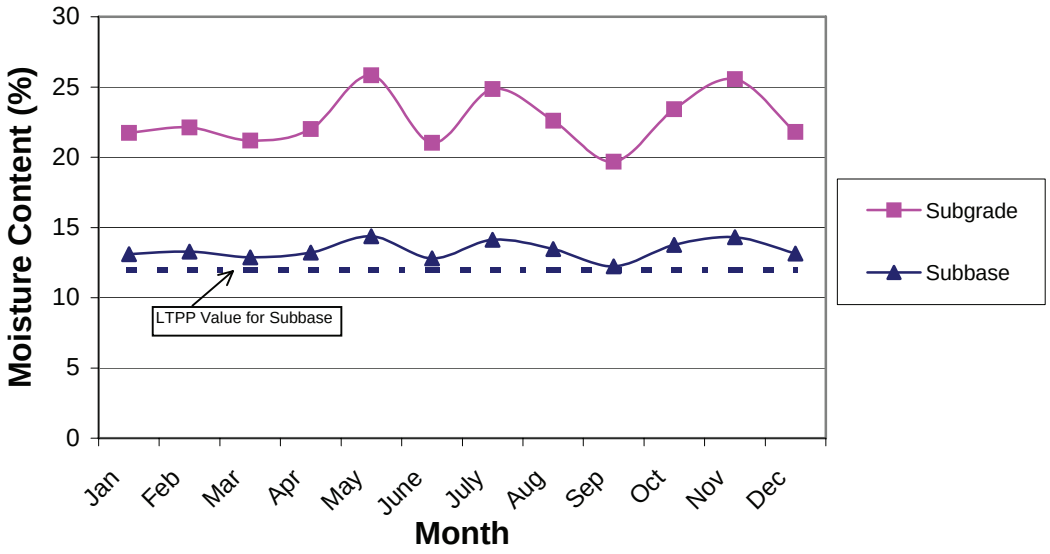

Figure 28. Texas LTPP site comparison.

The subgrade for the Texas site is a lean clay (CL, A–7–6) and the subbase is a well-graded silty gravel (GW–GM, A–2–4). For this location, the moisture content prediction compared very well with the data from the FHWA study, although no data for the subgrade was found in the database.

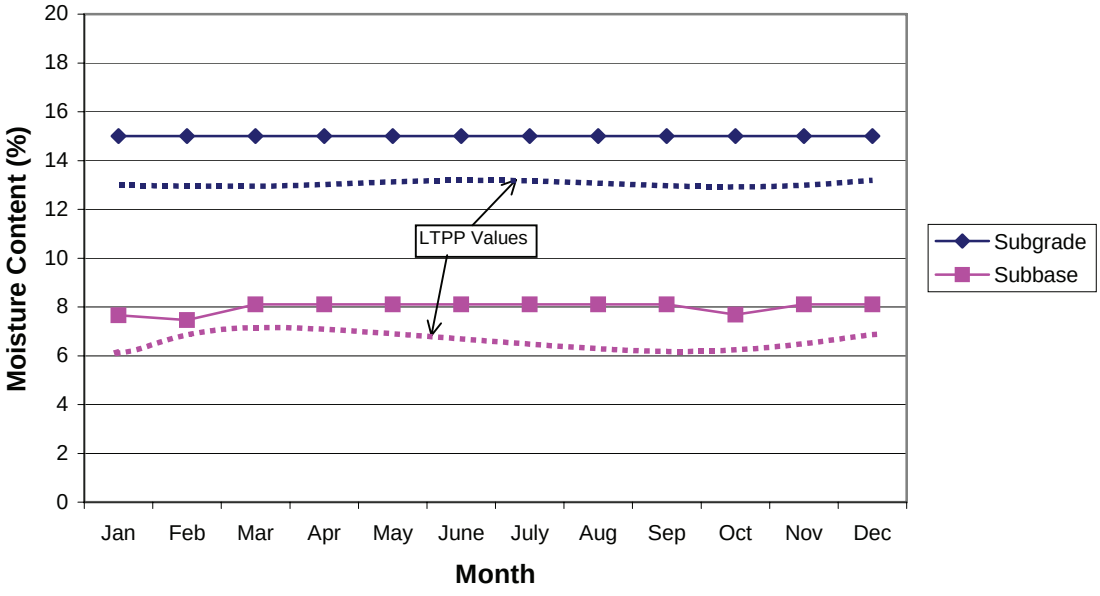

Figure 29. Maine LTPP site comparison.

The Maine site has a lean silty soil (ML, A–4) in the subgrade and a well-graded silty gravel (GW–GM, A–1–A) in the subbase. The model predicted the subgrade to be saturated throughout the year and the subbase to be saturated from March to September. The saturated water content was an estimated parameter for these soils, which signals the need for quality soil property assumptions to ensure the reliability of the model.

B.2.1.2.6 Summary and Conclusions

This model appears to be able to predict monthly moisture content based on a few simple assumptions regarding THMI, *%Clay*, and presence of paved shoulders. Since the model is fairly simple, estimated soil and weather parameters can directly affect the outcome and accuracy of the model, as indicated by the Maine LTPP site comparison. The following trends were noticed from evaluating the model and should be noted before the model is used further:

- Changing reference suction procedures due to changes in THMI does not greatly affect the moisture content calculation.
- Paved shoulders reduce variability in moisture content.
- Moisture content variability is related to clay content and rainfall.
- Average moisture content is related to THMI and rainfall.

The following items are not included in the model and can affect the moisture conditions beneath pavements:

- Surface infiltration through the pavement layers.
- Varying drainage conditions.
- Water table location.
- Layer thicknesses.
- Initial (compacted) moisture content.
- Intensity of rainfall.
- Horizontal and vertical variation of moisture content within layers.
- Freezing and thawing.

B.2.2 Long-Term Materials Properties Models

B.2.2.1 PCC Strength and Stiffness

Mechanical properties used in HIPERPAV II for long-term PCC characterization include modulus of elasticity and any of the following three strengths: tensile, flexural (modulus of rupture), or compressive. During the pavement life, the PCC slab is exposed to various stresses, such as curling and warping stresses, thermal axial stresses, and wheel load stresses. In the long term, one of the major failure modes is cracking due to fatigue. This generally has been found to be a function of the tensile stress to strength ratio at the bottom of the layer, implying that tensile strength is a significant characterization property. Unlike most concrete structures, JPCP does not rely on steel to withstand tensile stresses and is, therefore,

typically designed using a specified tensile strength. Because concrete is much weaker in tension than in compression, tensile strength is the most critical strength characteristic.

The elastic modulus is an estimate of the slope of the stress-strain curve in the elastic region and a good indicator of the overall structural stiffness of the concrete. Because stresses and strains are related through the elastic modulus under assumptions of linear elasticity, it is important that this property be characterized. The model incorporated in HIPERPAV II is described in reference 54.

The following test methods are used to characterize PCC strength and stiffness.

- Splitting tensile strength (f_{ST}): ASTM C 496.
- Modulus of rupture (f_R) : ASTM C 78 (third point loading).
- Compressive strength (f_c): ASTM C 39.
- Modulus of elasticity (E_c): ASTM C 469.

B.2.2.1.1 Relationship between Modulus of Rupture (f_R) and Splitting Tensile Strength (f_{ST})

In this section, recommended relationships between the different PCC pavement (PCCP) strength test methods are presented.

Melis et. al investigated the (f_{ST}/f_R) ratio with different mix properties that are representative of concretes normally used in concrete pavements in Texas.[55] Altogether, 720 beams and 1260 cylinders were tested during this study. For this study, centerpoint loading according to ASTM C 293 was used to determine the rupture modulus of the concrete. Hence, all the correlations with regard to the flexural strength determined in this study will have to be converted to incorporate the loading configuration's effect on the tested concrete strength. The correlation between the splitting tensile and flexural strengths were determined for different concrete mixes, and the following mix variables were investigated:

- Cement factor: 279 kg/m^3, and 335 kg/m^3.
- Cement type: Type I, II, and III.
- Air content: 1–3 percent, 4–6 percent, and 8–10 percent.
- Coarse aggregate type: River gravel and limestone.
- Coarse aggregate size: Grade Nos. 2 and 5.
- Coarse aggregate factor: 0.65, 0.75, and 0.80.
- Admixtures: Three combinations: None, water reducer and air entrainment, and accelerator and air entrainment.
- w/c: 0.4, 0.5, and 0.554.
- Curing age: 4, 7, 28, and 56 days.
- Slump: 0–25 mm, 25–76 mm, and 127–178 mm.
- Curing temperature: 10 °C, 24 °C, and 38 °C.

Table 28 provides a summary of the test results achieved. Based on the results summarized in table 28, it was concluded that the transformation equation from the centerpoint loaded modulus of rupture (f_{RC}) to the splitting tensile strength should be as shown in equation 118:

$$(f_{ST}/f_{RC}) \text{ ratio} = 0.62 \quad (118)$$

Table 28. Summary of strength test results obtained by Melis et. al.[55]

	Splitting Tensile (152-mm x 305-mm Cylinder)		Modulus of Rupture		(f_{ST}/f_{RC}) Ratio
	Average Strength (MPa)	C.V. (%)	Average Strength (MPa)	C.V. (%)	
4 days	2.69	6	4.34	6	0.62
7 days	2.86	6	4.62	6	0.62
28 days	3.24	6	5.31	6	0.62
56 days	3.52	6	5.38	5	0.66
Average	2.86	6	4.59	6	0.62

Melis et. al made the following final conclusions and recommendations based on their test results[55] (pp. 75–76):

- "The splitting tensile test is an effective test method for estimating the tensile strength of concrete. The cylinders associated with the splitting tensile test are easier to handle than those specimens used for the flexural beam test."
- "The variability and dispersion of the results from the 152-mm by 304-mm cylinder specimens tested by the splitting tensile test method did not differ significantly from the variability and dispersion of those from the flexural beam test method."

The recommendation from Melis et al. was based on centerpoint-loaded flexural beams, and to use their conversion formula, a conversion between the third point and centerpoint-loaded flexural specimens are required. Carrasquillo and Carrasquillo performed a study with more than 700 beam specimens cast from 14 different mixes to investigate the use of centerpoint loading versus the third point loading in determining the flexural strength of concrete.[56]

The correlation between a specimen loaded at its center as opposed to its third point, for coarse aggregate sizes normally used in concrete pavement construction, were determined to be as shown in equation 119:

$$f_R = 0.864 \text{ x } f_{RC} \quad (119)$$

The relationship found above is also of the same order of magnitude with earlier findings from Kellermann, which concluded that the third point loading strength of a beam is about 88 percent of that found when it is loaded at its centerpoint.[57] Based on the fact that the tests performed by Carrasquillo and Carrasquillo were done more recently on typical concrete mix designs used for concrete pavements, it is reasoned that their conversion between the two loading configurations should be used.

Based on the results obtained by Carrasquillo and Carrasquillo, the conversion presented in equation 118 can be modified to account for the reduced flexural strength obtained when the third point loading configuration is used as opposed to the centerpoint loading configuration. Using the conversion that the

third point flexural strength is 86.4 percent of the centerpoint loading, the following ratio (equation 120) between the splitting tensile strength and the third point-loaded modulus of rupture can be derived:

$$(f_{ST}/f_R) \text{ ratio} = 0.72 \tag{120}$$

B.2.2.1.2 Relationship between Modulus of Rupture (f_R) and Compressive Strength (f_c)

The fairly common relationship, shown in equation 121, between the modulus of rupture and compressive strength recommended by ACI is:[58]

$$f_R = 0.7\sqrt{f'_c} \quad \text{(in MPa)} \tag{121}$$

However, it has been shown that the ACI equation provides a lower bound estimate (5th percentile) of the flexural strength; on the conservative side when designing reinforced concrete structures against cracking. It is not appropriate to use the ACI equation, therefore, when a conversion between average pavement strength is necessary. It also has been recommended that the relationship between the compressive strength and modulus of rupture is better predicted with expressions as a function of ($f'_c{}^{2/3}$) as compared to those expressions as a function of ($f'_c{}^{1/2}$).[59]

Raphael investigated the relationship between the flexural and compressive strength of concrete.[60] In this study, 12,000 individual test results gathered by 4 independent researches were investigated together with the authors' own test results. The regression analysis that best fit the data can be seen in figure 30, and was determined to be, as shown in equation 122:

$$f_R = 2.3 \cdot \left(f_C\right)^{(2/3)} \quad \text{(in psi, 1 psi = 6.89 kPa)} \tag{122}$$

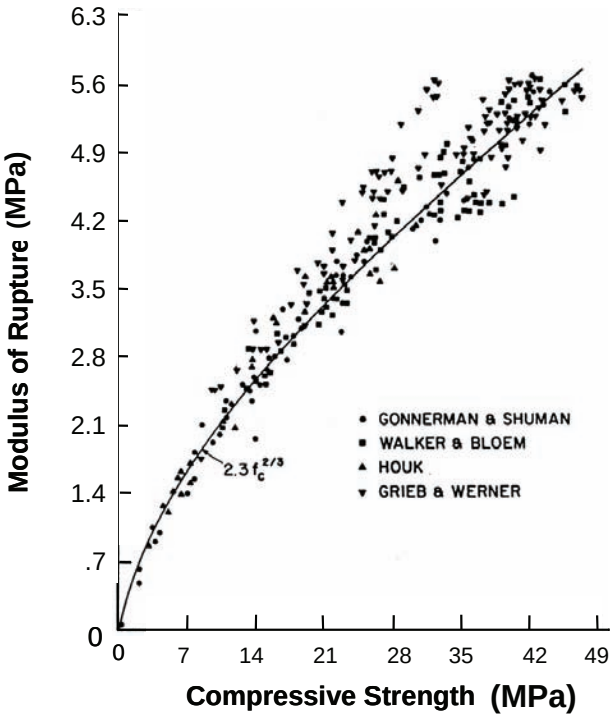

Figure 30. Comparison of test results with the correlation proposed in equation 122.[(60)]

In Texas, 306 compressive and 306 flexural test were performed on concrete specimens made from 5 different pavement mix designs. Two different aggregate types were used for these projects—limestone and river gravel. The relationship between the compressive and flexural strength as presented in equation 123 was determined to provide the best fit, and a r^2 value of 0.79 was obtained.

$$f_R = 2.28 \cdot \left(f_C\right)^{(2/3)} \quad \text{(in psi, 1 psi = 6.89 kPa)} \qquad (123)$$

Note that equations 122 and 123 are nearly identical and that they were developed from independent test results. Figure 31 shows the comparison of the equation developed by Raphael (equation 122) with regard to the test results measured in Texas. This figure demonstrates that Raphael's equation provides a good fit for the test data. This figure further shows the conservative nature of the ACI equation with regard to estimating the concrete's modulus of rupture. Based on the data presented in this section, it is recommended that equation 122 be used to describe the relationship between flexural and compressive strength.

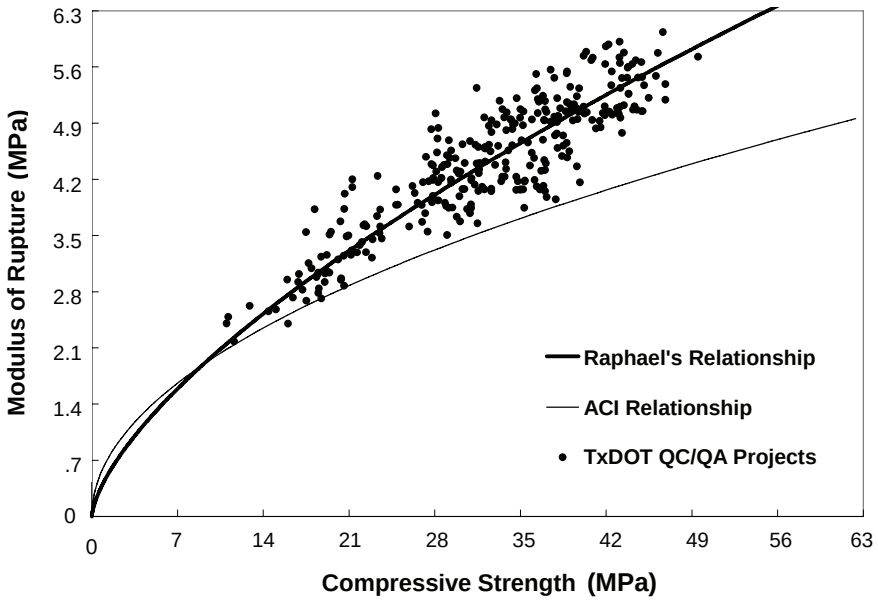

Figure 31. Modulus of rupture versus compressive strength for Texas data.

B.2.2.1.3 Relationship between Modulus of Elasticity (E_c) and Compressive Strength (f_c)

The well established relationship between modulus of elasticity (E_c) and compressive strength (f_c) as recommended by the ACI will be used in this project. The conversion is shown in equation 124, and it can be seen that it is a function of the unit weight of the concrete. As the coarse aggregate accounts for 50–70 percent of the concrete by volume, the unit weight of the mix is determined mostly by the type of aggregate used in the mix.

$$E_c = w_c^{1.5} \cdot 0.043\sqrt{f_c'} \tag{124}$$

where,

E_c = modulus of concrete in MPa and
w_c = unit weight of concrete in kg/m^3.

Note that equation 124 is only valid for values of w_c between 1500 to 2500 kg/m^3. To complete the conversion, the unit weight of the concrete must be determined. Popovics provides the following simplified equation (equation 125) to estimate the concrete unit weight.[61]

$$w_c = 16.02 \cdot (SG(45 - 0.6Air) + 33) \tag{125}$$

where,

w_c = unit weight of concrete in kg/m^3,
SG = average specific gravity of aggregate, and

Air = percent air content.

The average specific gravity of aggregate depends on the specific gravity of the mineral of which the aggregate is composed and also the amount of voids. The average specific gravity for different natural aggregates is presented in table 29.[62]

Table 29. Specific gravities for different aggregate types.[62]

Aggregate Type	Specific Gravity
Limestone	2.66
Sandstone	2.69
Granite	2.69
River gravel	2.72
Basalt	2.80

Based on a typical air content of 4 percent and the specific gravities listed in table 29, the unit weights of the different aggregate types are as presented in table 30.

Table 30. Specific unit weights for different aggregate types.[62]

Aggregate Type	Unit Weight (w_c) (kg/m^3)
Limestone	2344
Sandstone	2365
Granite	2365
River gravel	2385
Basalt	2440

B.2.2.1.4 Models for Characterization of Long-Term Concrete Properties

The long-term model forms recommended in the CEB-FIP Model Code 1990 are used HIPERPAV II.[54] The equations in the model apply to concrete with normal weight aggregates with no appreciable amount of entrapped air other than intentionally entrained air.

The model calculates the values for strength and elastic modulus relative to the desired 28-day value. Application of the equations provides reasonable values for ages beyond 28 days. Figure 32 shows the curves for tensile strength and elastic modulus from 0 to 20,000 days (50 years) based on 28-day values of 700 psi for tensile strength and 4000 ksi for elastic modulus, reasonable 28-day values for a concrete pavement. Using the CEB-FIP model, there is a 23 percent gain in tensile strength from 28 days to 3 years. Elastic modulus increases 11 percent during the same time period. After 50 years, the gains are 27 percent and 13 percent for tensile strength and elastic modulus, respectively, over the 28-day values.

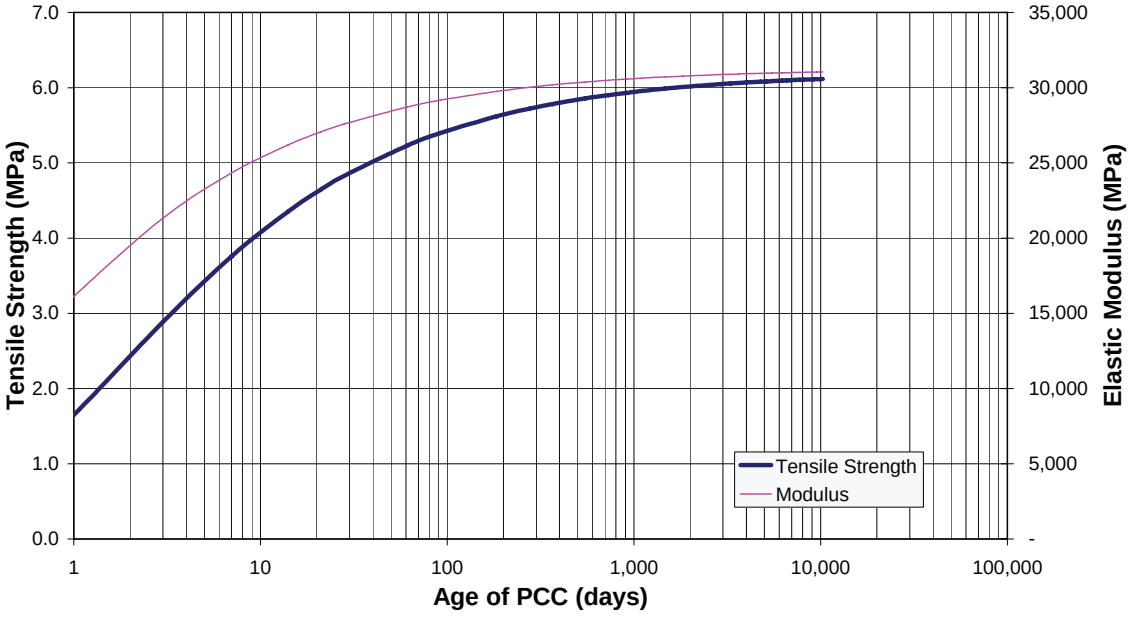

Figure 32. Tensile strength and elastic modulus values calculated using the CEB-FIP equation.

The development of strength with time depends on the type of cement, temperature, and curing conditions. The models assume a mean curing temperature of 20 ºC and curing in accordance with International Organization for Standardization (ISO) 2736/2. Equation 126 is used:

$$f_t(t) = f_t(28)\beta(t) \tag{126}$$

where,

$f_t(t)$ = the tensile strength at time t,
$f_t(28)$ = the desired 28-day tensile strength, and, as shown in equation 127,

$$\beta(t) = \exp\left\{ s\left[1 - \left(\frac{28}{t/t_1} \right)^{1/2} \right] \right\} \tag{127}$$

where,

s = coefficient that depends on the type of cement,
0.20 for rapid hardening high strength cements,
0.25 for normal and rapid hardening cements, and
0.38 for slowly hardening cements,
t = time in days, and
t_1 = 1 (for 1 day).

CEB-FIP recommends that the gain in other concrete properties, such as the modulus of rupture, compressive strength, and modulus of elasticity, be calculated using the same $\beta(t)$ factor. This is the approach used in HIPERPAV II to determine the concrete properties at ages other than 28 days.

The CEB-FIP model code provides general equations for concrete structures. The equations were developed from a compilation of available data and, as such, background and original references for the models are not provided in the CEB-FIP document. Although the equations are not specific to concrete pavements, they provide reasonable values for tensile strength and elastic modulus over the long term. However, the general nature of the equations dictates that the values calculated for curing times beyond 28 days be considered as only approximations to actual values.

The validation data for the tensile strength model was published in the *ACI Materials Journal*, by Ghafoori and Bucholc.[63] This validation shows an excellent correlation between the calculated and measured values with an r^2 of 0.995.

The validation data for the elastic modulus model was published in the *ACI Materials Journal*, by Khan, et al.[10] The measured values from the study at 14 different curing times during the first 100 days were compared to values calculated using the CEB-FIP model at the same ages and forced through the measured 28-day value. There was a good correlation between the calculated and measured values for most ages during the first 100 days of curing, with an overall r^2 value of 0.92. Although there is not a strong correlation between the measured and calculated values for the first 10 days, HIPERPAV II uses a maturity-based model for this purpose.[1]

B.2.3 Structural Models

B.2.3.1 LTE and Midslab Stress and Deflection Models

To predict the response of a rigid pavement due to external wheel loads accurately, a model is needed to assess the behavior of the pavement structure in the vicinity of discontinuities such as cracks and joints. This section describes the theoretical LTE model for both doweled and nondoweled JCP, and the midslab stress and deflection prediction models used along with the LTE model. These models were incorporated into HIPERPAV II.

The transfer of a wheel load across joints must be considered when mechanistically modeling the performance of a JCP. The LTE characterizes how traffic wheel loading is transferred from one section of JCP to the adjacent section. For a nondoweled JCP joint, load transfer can be attributed solely to aggregate interlock. If dowels are used, then both the dowels and the aggregate interlock contribute to the LTE of the joint. The theoretical LTE model presented here characterizes the load transfer across a joint as either a deflection transfer (LTE_δ), or as a stress transfer (LTE_σ).

If the deflection LTE of a joint is 100 percent efficient, both slabs will deflect the same amount. This is illustrated in figure 33, where both slabs deflect the same amount ($\delta/2$).

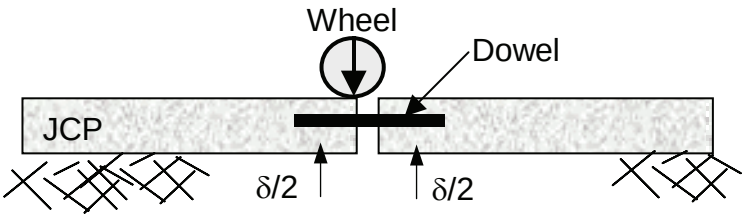

Figure 33. Schematic of deflection load transfer (LTE_δ) for a doweled JCP.

For the stress LTE (LTE_σ), the stress in the pavement due to wheel loading is transferred across the joint.

The following sections present the theoretical equations that can be used to calculate LTE for doweled or nondoweled sections of JCP. The model is based primarily on work conducted by Westergaard.[64,65] This model calculates LTE immediately after construction. The effect of repetitive loading on the joint and how this influences the LTE with regard to wearout and dowel looseness is discussed in subsequent sections.

B.2.3.1.1 Model Formulation

The following sections describe the detailed formulation of the LTE model. To present this formulation in a logical and straightforward manner, the model is divided into the following calculation components:

- Dimensional parameters.
- Dowel influence parameters.
- Aggregate interlock parameters.
- Joint stiffness parameters.
- Free edge deflection.
- Free edge stress.
- Unloaded edge deflection.
- Unloaded edge stress.
- Loaded edge deflection and stress.
- LTE parameters.

The dimensional parameters affect all of these components directly, except for the loaded stress and deflection, and the LTE, which are affected indirectly by these parameters. The remaining nine components work linearly, as illustrated in figure 34.

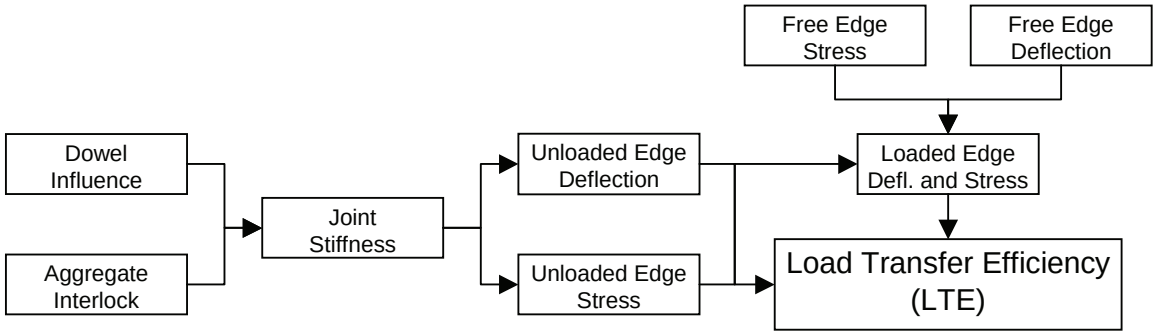

Figure 34. Schematic of LTE model logic.

B.2.3.1.2 Dimensional Parameters

These models identify dimensional parameters that are used in the majority of the remaining models. The first variable is the radius of the contact area (a). It is defined in equation 128 from basic geometry as:[64]

$$a = \sqrt{\frac{P}{\pi p_t}} \tag{128}$$

where,

a = radius of the contact area (m),
P = wheel load (N), and
p_t = tire pressure (MPa).

The radius of relative stiffness (l) of the pavement system is defined in equation 129 as follows:[64]

$$l = \sqrt[4]{\frac{E_c h^3}{12(1-\mu_c)^2 k}} \tag{129}$$

where,

l = radius of relative stiffness (m),
E_c = PCC elastic modulus (MPa),
h = PCC slab thickness (m),
μ_c = PCC Poisson's ratio (unitless), and
k = slab support reaction modulus (MPa/m).

A number of the following formulae will use the dimensionless ratio of these two parameters.

B.2.3.1.3 Dowel Influence Parameters

To determine the influence of dowels on the overall load transfer, a model based on the theory of Timoshenko and Lessels is used.[66] A summary of this theory can be found in a subsequent ACI publication.[67]

A number of variables are required for this characterization. The first is the bending moment of inertia (I_D) of the dowel. This is defined in equation 130 as:[68]

$$I_D = \frac{\pi \phi_D^4}{64} \tag{130}$$

where,

I_D = bending moment of inertia of a circular dowel (m^4), and
ϕ_D = diameter of the dowel (m).

The cross-sectional area of a circular dowel (A_D) is defined in equation 131 as:[68]

$$A_D = \frac{\pi \phi_D^2}{4} \tag{131}$$

where,

A_D = cross-sectional area of the dowel (m^2).

An adjustment is made of the cross-sectional area to account for its use in shear calculations.[69] The result is an effective cross-sectional area (A_{Dz}), defined in equation 132 as:

$$A_{Dz} = 0.9 A_D \tag{132}$$

where,

A_{Dz} = effective cross-sectional area of the dowel (m^2), and
A_D = cross-sectional area of the dowel (m^2) from equation 131.

The shear modulus of the dowel bar (G_D) can possibly be a user input. However, it is more practical to estimate this value based on the assumption that it is a homogeneous, isotropic material, as shown in equation 133:[68]

$$G_D = \frac{E_D}{2(1+\mu_D)} \tag{133}$$

where,

G_D = shear modulus of the dowel (MPa),
E_D = elastic modulus of the dowel (MPa), and
μ_D = Poisson's ratio of the dowel (unitless).

This formula should not be used when the dowels are constructed with anisotropic materials, such as fiberglass.

To calculate the contribution of dowel stiffness to the LTE, five additional parameters must be calculated. The first is a correction factor for deep-beam shear deformation (ϕ), defined in equation 134 as:[69]

$$\phi = \frac{12 E_D I_D}{G_D A_{Dz} w^2} \tag{134}$$

where,

ϕ = deep-beam shear deformation correction factor (unitless),
I_D = bending moment of inertia of a circular dowel (m^4), from equation 130,
G_D = shear modulus of the dowel (MPa), from equation 133,
A_{Dz} = effective cross-sectional area of the dowel (m^2), from equation 132, and
w = joint opening (m).

Secondly, the relative stiffness (or characteristic) of the dowel-concrete system (β) is calculated in equation 135 as:[69]

$$\beta = \sqrt[4]{\frac{K_D \phi_D}{4 E_D I_D}} \tag{135}$$

where,

β = characteristic of the dowel-concrete system (m^{-1}), and
K_D = effective modulus of dowel support (MPa/m).

The shear stiffness of the dowel (C) is then defined in equation 136 as:[69]

$$C = \frac{E_D I_D}{w^3 (1 + \phi)} \tag{136}$$

where,

C = dowel (beam) shear stiffness (N/m), and
ϕ = deep-beam shear deformation correction factor (unitless), from equation 134.

The dowel-concrete interaction parameter (DCI) is then calculated in equation 137 as:[69]

$$DCI = \frac{4 \beta^3 E_D I_D}{2 + \beta w} \tag{137}$$

where,

DCI = dowel-concrete interaction parameter (N/m), and
β = characteristic of the dowel-concrete system (m^{-1}), from equation 135.

Finally, the dowel shear stiffness (D') is calculated in equation 138 as:[69]

$$D' = \frac{1}{\frac{1}{DCI} + \frac{1}{12C}} \tag{138}$$

where,

D' = dowel shear stiffness (N/m),
DCI = dowel-concrete interaction parameter (N/m), from equation 137, and
C = dowel (beam) shear stiffness (N/m), from equation 136.

B.2.3.1.4 Aggregate Interlock Parameters

To characterize the joint stiffness contribution due to aggregate interlock, a new model has been developed. This model is based on data collected by the Portland Cement Association (PCA) on a controlled load transfer experiment.[70]

The LTE model described here was employed in developing the new aggregate interlock model. To accomplish this, the agg/kl parameter (to be described) was "solved" as an unknown variable. The remaining (known) variables first were fixed, and the agg/kl parameter was solved for a known (reported) joint transfer efficiency (JTE). The dowel and joint opening variables were not needed in this analysis, and the remaining known variables are given in table 31.

Table 31. LTE model variables used in developing the aggregate interlock model.[70]

Variable	Description	Units	Value(s)
E_c	PCC elastic modulus	MPa	30,337 *1
μ_c	PCC Poisson's ratio	none	0.15 *2
H	PCC slab thickness	mm	178 and 229
t_{saw}	Sawcut depth	mm	0
P	Wheel load	N	40,034
p_t	Tire pressure	MPa	0.31 *3
K	Slab support reaction modulus	MPa/m	24.2 (clay) 39.4 (sand-gravel subbase) 122.7 (cement-treated subbase)

Notes:
*1 – PCC modulus estimated from given compressive strength of 41.4 MPa
*2 – Assumed
*3 – Calculated from given load radius of 203 mm

JTE is a parameter that describes the percent of a load that is transferred from a loaded slab to an adjoining unloaded slab through load transfer. In the case of this experiment, aggregate interlock was the only mechanism. Additional information on this parameter will be given in a subsequent section. For the PCA experiment, JTE results for five combinations of the inputs in table 31 were reported. Within these five combinations, results for a number of crack openings were given. In total, 15 combinations of crack opening, slab thickness, and *k*-value were tested. From these combinations, agg/kl values were backcalculated using the LTE model. The results from these backcalculations are given in figure 35.

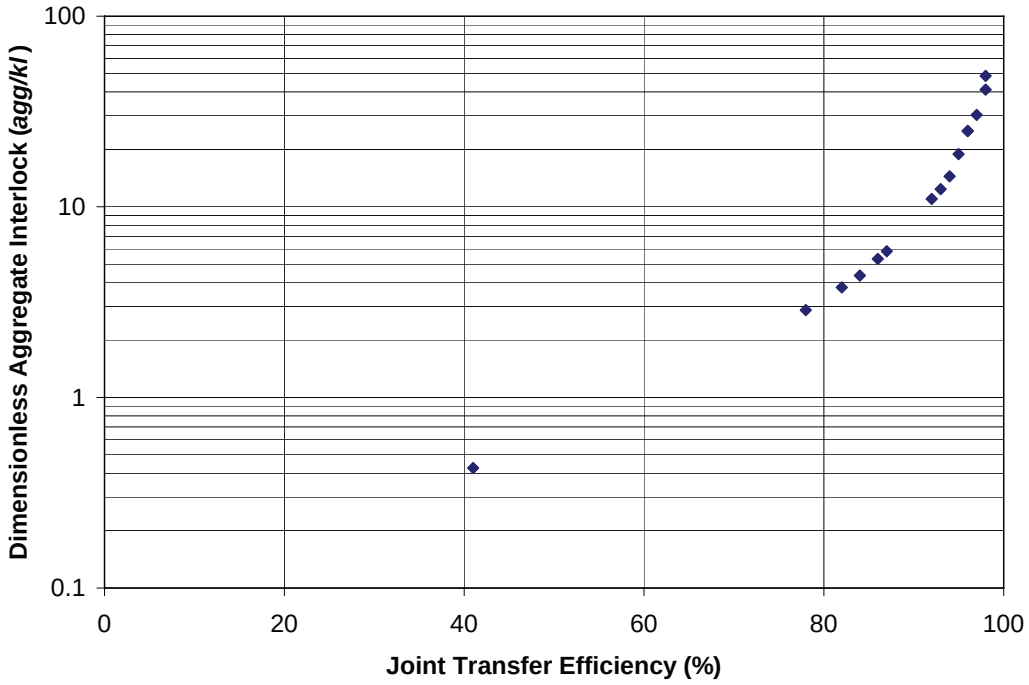

Figure 35. Relationship between the calculated agg/kl and measured JTE.

As can be seen from figure 35, the relationship between these two variables is quite pronounced. The next step in the development of an aggregate interlock characterization model was to identify a relationship between the backcalculated agg/kl values and the measured crack opening. Figure 36 illustrates the results of this comparison.

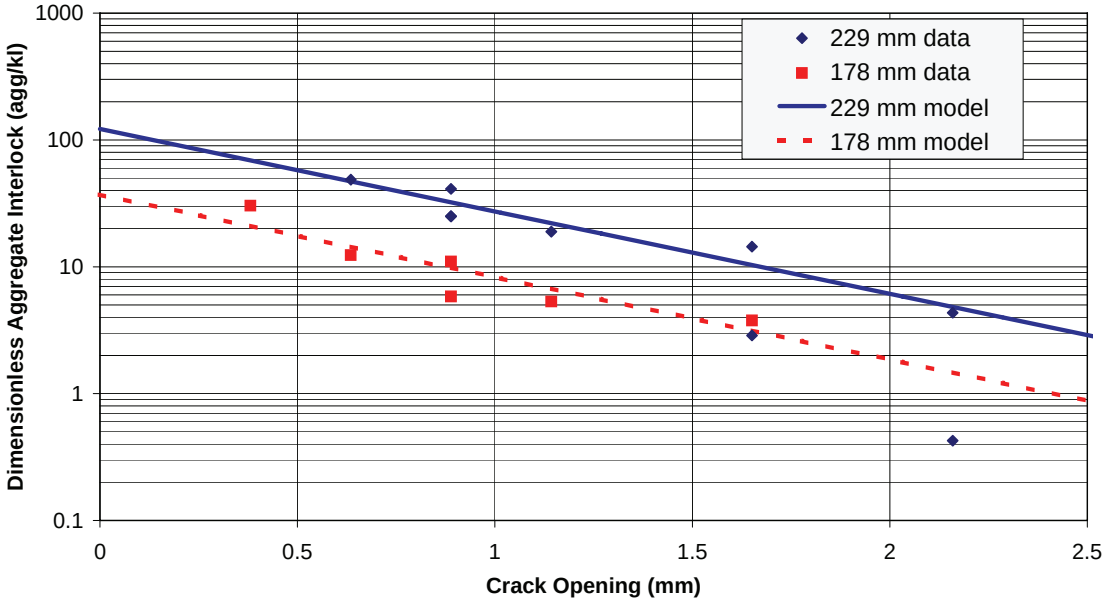

Figure 36. Relationship between measured crack opening and the calculated agg/kl.

From figure 36, two distinct relationships were identified corresponding to the two slab thicknesses used in the experiment. On a semilog scale, the relationships appear to be linear, and the two trends appear to be roughly parallel. As a result, a simple model form was selected with an exponential base, a constant slope, and a variable intercept. The final model is of the form shown in equation 139:

$$\frac{agg}{kl} = \gamma e^{-1.5w} \tag{139}$$

where,

agg/kl = the dimensionless aggregate interlock parameter (unitless),
γ = aggregate interlock model intercept (unitless), defined below,
e = base of natural logarithm (≈ 2.71828…), and
w = crack opening (mm).

Through calibration, the aggregate interlock model intercept (γ from equation 139) for the two known thicknesses was found to be 122 for the 229-mm slabs, and 37 for the 178-mm slabs. Based on engineering judgment, it is assumed that this intercept value would yield zero agg/kl as the thickness decreased in an exponential form and would increase linearly after an effective slab thickness of 178 mm. As a result of this assumption, the equations 140 and 141 were derived for the prediction of the intercept value as a function of the intact slab thickness (defined as the slab thickness minus the sawcut depth):

For $h - t_{saw} \leq 178$ mm:

$$\gamma = 1.388 \cdot 10^{-6} (h - t_{saw})^{3.5309} \tag{140}$$

For $h - t_{saw} > 178$ mm:

$$\gamma = 2.425 \cdot (h - t_{saw}) - 309 \tag{141}$$

where,

γ = aggregate interlock model intercept (unitless),
h = PCC slab thickness (mm), and
t_{saw} = sawcut depth (mm).

This model should be considered preliminary. One inherent deficiency in the model is the lack of a larger factorial of data for calibration. It is recommended that additional data be collected to conduct a more refined calibration. Subsequently, the model should be validated using an independent data set.

Although not required in the subsequent formulation, the variable defining the aggregate interlock (agg) can be calculated from the agg/kl value by simply multiplying by the slab support modulus (k) and by the radius of relative stiffness (l) as shown in equation 142:

$$agg = \frac{agg}{kl} kl \tag{142}$$

where,

agg = aggregate interlock (MPa),

agg/kl = the dimensionless aggregate interlock parameter (unitless),
k = slab support reaction modulus (MPa/m), and
l = radius of relative stiffness (m), from equation 129.

B.2.3.1.5 Joint Stiffness Parameters

To derive a common method to include the impacts of both dowels and aggregate interlock, a joint stiffness parameter is calculated. The joint stiffness parameter, or *J* value, is employed directly in a continuation of Westergaard's formulation for load transfer developed by Skarlatos, and reported subsequently by Ioannides and Hammons.[65,71,72]

For purposes of this model, the contribution to joint stiffness due to the presence of dowels (J_D) is defined in equation 143:[69]

$$J_D = \frac{D'}{s_D kl} \tag{143}$$

where,

J_D = dimensionless joint stiffness due to dowels (unitless),
D' = dowel shear stiffness (N/m), from equation 138,
s_D = dowel spacing (m),
k = Slab support reaction modulus (MPa/m), and
l = radius of relative stiffness (m), from equation 129.

The contribution of aggregate interlock to joint stiffness is simply defined as agg/kl, defined previously in equation 139. For nomenclature purposes, this variable is redefined in equation 144:

$$J_{agg} = \frac{agg}{kl} \tag{144}$$

where,

J_{agg} = dimensionless joint stiffness due to aggregate interlock (unitless), and
agg/kl = the dimensionless aggregate interlock parameter (unitless), from equation 139.

The sum of these two parameters is the overall joint stiffness (*J*), which is defined in equation 145:

$$J = J_D + J_{agg} \tag{145}$$

where,

J = overall dimensionless joint stiffness (unitless),
J_D = dimensionless joint stiffness due to dowels (unitless), from equation 143, and
J_{agg} = dimensionless joint stiffness due to aggregate interlock (unitless), from equation 144.

B.2.3.1.6 Free Edge Deflection

The free edge deflection for a JCP is defined as the critical concrete deflection induced by a wheel load when applied on a theoretically long pavement edge with no adjoining slab. This is illustrated graphically in figure 37. This stress is commonly calculated using Westergaard's classical formulation.[65] For

purposes of this model, a modified form is adopted here that has been enhanced by Ioannides and Hammons.[72] These authors have revisited the Westergaard solutions for pavement deflections and stresses, and have enhanced them using sophisticated numerical methods that were not available when the original solutions were developed.

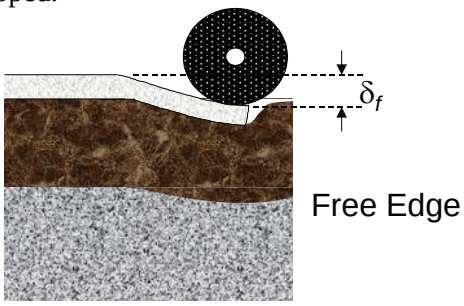

Figure 37. Free edge loading of JCP.

For edge deflections, a dimensionless free edge deflection (δ_f^*) is calculated as shown in equation 146:

$$\delta_f^* = B_3 - B_4 \frac{a}{l} + 0.5 B_5 \left(\frac{a}{l} \right)^2 \tag{146}$$

where,

δ_f^* = dimensionless free edge deflection (unitless),
B_3,B_4,B_5 = Westergaard coefficients for free edge deflection (unitless), defined below,
a = radius of the contact area (m), from equation 128, and
l = radius of relative stiffness (m), from equation 129.

The three Westergaard coefficients (B_3, B_4, and B_5) are defined in equations 147, 148, and 149:

$$B_3 = \frac{\sqrt{2 + 1.2\mu_c}}{\sqrt{12\left(1 - \mu_c^2\right)}} \tag{147}$$

$$B_4 = B_3\left(0.76 + 0.4\mu_c\right) \tag{148}$$

$$B_5 = \frac{B_4^2}{2B_3} \tag{149}$$

where,

B_3,B_4,B_5 = Westergaard coefficients for free edge deflection (unitless), and
μ_c = Poisson's ratio of the PCC.

The free edge deflection (δ_f) can then be calculated from the dimensionless free edge deflection (δ_f^*) as shown in equation 150:

$$\delta_f = \frac{\delta_f^* P}{kl^2} \tag{150}$$

where,

δ_f = free edge deflection (m),
δ_f^* = dimensionless free edge deflection (unitless), from equation 146,
P = wheel load (m),
k = slab support reaction modulus (MPa/m), and
l = radius of relative stiffness (m), from equation 129.

B.2.3.1.7 Free Edge Stress

The free edge stress is calculated in a manner similar to that of the free edge deflection. A dimensionless free edge stress (σ_f^*) is first calculated in equation 151 as the sum of two components:

$$\sigma_f^* = \overline{\sigma}^* + \sigma_c^* \tag{151}$$

where,

σ_f^* = dimensionless free edge stress (unitless),
$\overline{\sigma}^*$ = first component of the dimensionless free edge stress (unitless), defined below, and
σ_c^* = second component of the dimensionless free edge stress (unitless), defined below.

The two components of the dimensionless stress function are calculated in equations 152 and 153:

$$\overline{\sigma}^* = \frac{12(1+\mu_c)}{\pi(3+\mu_c)}\left[0.1159 - \ln\left(\frac{a}{l}\right) + \frac{1-\mu_c}{8}\right] \tag{152}$$

$$\sigma_c^* = \frac{12(1+\mu_c)}{\pi(3+\mu_c)}\left[\frac{3-\mu_c}{4} - 0.9544 + 0.3822\left(\frac{a}{l}\right)\right]\left[1.30259 + 2.98398\left(\frac{a}{l}\right)^2\right] \tag{153}$$

where,

$\overline{\sigma}^*$ = first component of the dimensionless free edge stress (unitless),
σ_c^* = second component of the dimensionless free edge stress (unitless),
μ_c = Poisson's ratio of the PCC (unitless),
a = radius of the contact area (m), from equation 128, and
l = radius of relative stiffness (m), from equation 129.

The constants employed in equation 153 are based on the assumption that the Poisson's ratio of the PCC is equal to 0.15. As a future enhancement to this model, it may be possible to rederive these constants for

other values of Poisson's ratio. However, due to the overall sensitivity of this parameter, this exercise may be of secondary importance.

Based on the dimensionless free edge stress, the actual free edge stress can be calculated in equation 154:

$$\sigma_f = \frac{\sigma_f^* P}{h^2} \tag{154}$$

where,

σ_f = free edge stress (MPa),
σ_f^* = dimensionless free edge stress (unitless), from equation 151,
P = wheel load (N), and
h = PCC slab thickness (m).

B.2.3.1.8 Unloaded Edge Deflection

The unloaded edge deflection is based on the same derivations previously described for the free edge deflection. In the case of the unloaded edge deflection, the value is equal to the deflection of the unloaded side of two adjoining slabs. Figure 38 illustrates this, where the unloaded and loaded edge deflections are defined graphically.

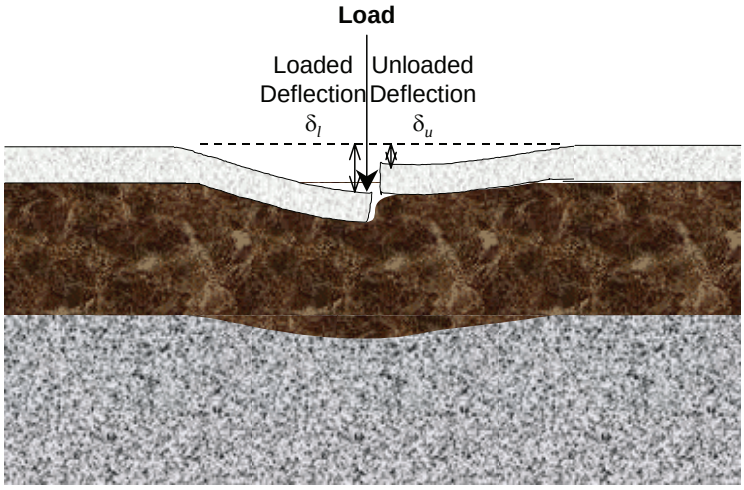

Figure 38. Loaded and unloaded deflections of a JCP.

The dimensionless unloaded edge deflection is given in equation 155:

$$\delta_u^* = B_3' - B_4' \frac{a}{l} + 0.008\left(\frac{a}{l}\right)^2 \left[1 + \log_{10}(J)\right] \tag{155}$$

where,

δ_u^* = dimensionless unloaded edge deflection (unitless),
B'_3,B'_4 = Westergaard coefficients for unloaded edge deflection (unitless), defined below,
a = radius of the contact area (m), from equation 128,
l = radius of relative stiffness (m) – from equation 129, and

J = overall dimensionless joint stiffness (unitless), defined in equation 145.

The Westergaard coefficients for this equation are defined in equations 156 and 157:

$$B'_3 = \frac{J - 0.6367 \log_{10}(1 + J)}{4.6516J + 1.8210} \tag{156}$$

$$B'_4 = B'_3\left[0.6984 + 0.0441\log_{10}(1 + J) - 0.00655J^{0.24}\right] \tag{157}$$

where,

B'_3,B'_4 = Westergaard coefficients for unloaded edge deflection (unitless).

The unloaded edge deflection (δ_u) can then be calculated from the dimensionless unloaded edge deflection (δ_u^*) in equation 158:

$$\delta_u = \frac{\delta_u^* P}{kl^2} \tag{158}$$

where,

δ_u = unloaded edge deflection (m),
δ_u^* = dimensionless unloaded edge deflection (unitless), from equation 155,
P = wheel load (N),
k = slab support reaction modulus (MPa/m), and
l = radius of relative stiffness (m), from equation 129.

B.2.3.1.9 Unloaded Edge Stress

The dimensionless unloaded edge stress can be calculated in equation 159:

$$\sigma_u^* = \frac{24\left(1 - \mu_c^2\right)}{\pi}\left[B'_1 - B'_2\left(\frac{a}{l}\right) + 0.5B'_9\left(\frac{a}{l}\right)^2\right] \tag{159}$$

where,

σ_u^* = dimensionless free edge stress (unitless),
B'_1,B'_2,B'_9 = Westergaard coefficients for unloaded edge stress (unitless),
μ_c = Poisson's ratio of the PCC (unitless),
a = radius of the contact area (m), from equation 128, and
l = radius of relative stiffness (m), from equation 129.

The Westergaard coefficients for this equation are defined in equations 160, 161, and 162:

$$B'_1 = 0.03316 + 0.07205\log_{10}(1 + J) + \frac{0.00773\sqrt{J} - 0.03360}{J + 1} \tag{160}$$

$$B'_2 = B'_1\left(0.08281J + 0.4790 - \frac{0.000149}{J}\right)^{\frac{1}{4.209}} \tag{161}$$

$$B'_9 = e^{\left[-5.0908+2.2805\log_{10}(J)-0.1577\log_{10}^2(J)\right]} \tag{162}$$

where,

B'_1, B'_2, B'_9 = Westergaard coefficients for unloaded edge stress (unitless), and
J = overall dimensionless joint stiffness (unitless), defined in equation 145.

Based on the dimensionless unloaded edge stress, the actual unloaded edge stress can be calculated as shown in equation 163:

$$\sigma_u = \frac{\sigma_u^* P}{h^2} \tag{163}$$

where,

σ_u = unloaded edge stress (MPa),
σ_u^* = dimensionless unloaded edge stress (unitless), from equation 159,
P = wheel load (N), and
h = PCC slab thickness (m).

B.2.3.1.10 Loaded Edge Deflection and Stress

The loaded edge deflection and stress can easily be derived based on the corresponding free and unloaded edge responses. The loaded edge deflection can be calculated as shown in equation 164:

$$\delta_l = \delta_f - \delta_u \tag{164}$$

where,

δ_l = loaded edge deflection (m),
δ_f = free edge deflection (m), from equation 150, and
δ_u = unloaded edge deflection (m), from equation 158.

The loaded edge stress can similarly be calculated as shown in equation 165:

$$\sigma_l = \sigma_f - \sigma_u \tag{165}$$

where,

σ_l = loaded edge stress (MPa),
σ_f = free edge stress (MPa), from equation 154, and
σ_u = unloaded edge stress (MPa), from equation 163.

B.2.3.1.11 LTE Parameters

Three LTE responses can be derived from the above referenced formulation: JTE, deflection LTE, and stress LTE.

JTE is defined as the percent of a load that is transmitted across a discontinuity (joint) due to the load transfer mechanisms present. Using the derived parameters, this can be calculated in equation 166:

$$JTE = \frac{2\delta_u}{\delta_l + \delta_u} \tag{166}$$

where,

JTE = joint transfer efficiency (often reported as a percent),
δ_u = unloaded edge deflection (m), from equation 158, and
δ_l = loaded edge deflection (m), from equation 164.

The JTE is the value that was reported by the PCA in the aggregate interlock experiment for which the new aggregate interlock model is presented.[70]

Deflection LTE (LTE_δ) is the ratio of the deflections of the unloaded to the loaded slabs. It is defined mathematically in equation 167:

$$LTE_\delta = \frac{\delta_u}{\delta_l} \tag{167}$$

where,

LTE_δ = deflection LTE (often reported as a percent).

Finally, the stress LTE is similarly calculated and is defined as the ratio of the stress induced in the unloaded slab to the stress in the loaded slab (equation 168):

$$LTE_\sigma = \frac{\sigma_u}{\sigma_l} \tag{168}$$

where,

LTE_σ = stress LTE (often reported as a percent),
σ_u = unloaded edge stress (MPa), from equation 163, and
σ_l = loaded edge stress (MPa), from equation 165.

The relationship between the various LTE indicators is of interest. For example, it can be demonstrated in equation 169 that the relationship between JTE and LTE_δ is:

$$LTE_\delta = \frac{0.5JTE}{1 - 0.5JTE} \tag{169}$$

where,

LTE_δ = deflection LTE (often reported as a percent), from equation 167, and
JTE = joint transfer efficiency (often reported as a percent), from equation 166.

Figure 39 illustrates this relationship. It can be seen, that the relationship does falls below the line of equity, demonstrating the nonlinear relationship in equation 169.

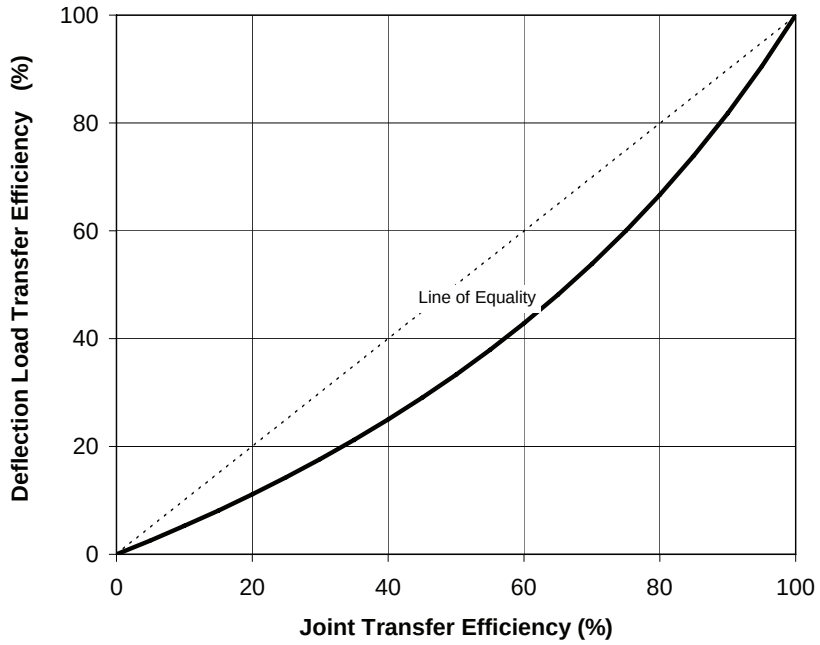

Figure 39. Relationship between JTE and LTE_{δ}.

As expected, the relationship between LTE_{δ} and LTE_{σ} is more complex. This is due to the complex nature of the formulation previously described. However, figure 40 illustrates that the relationship between these two parameters is a function of the *a/l* ratio, defined previously in equation 159.

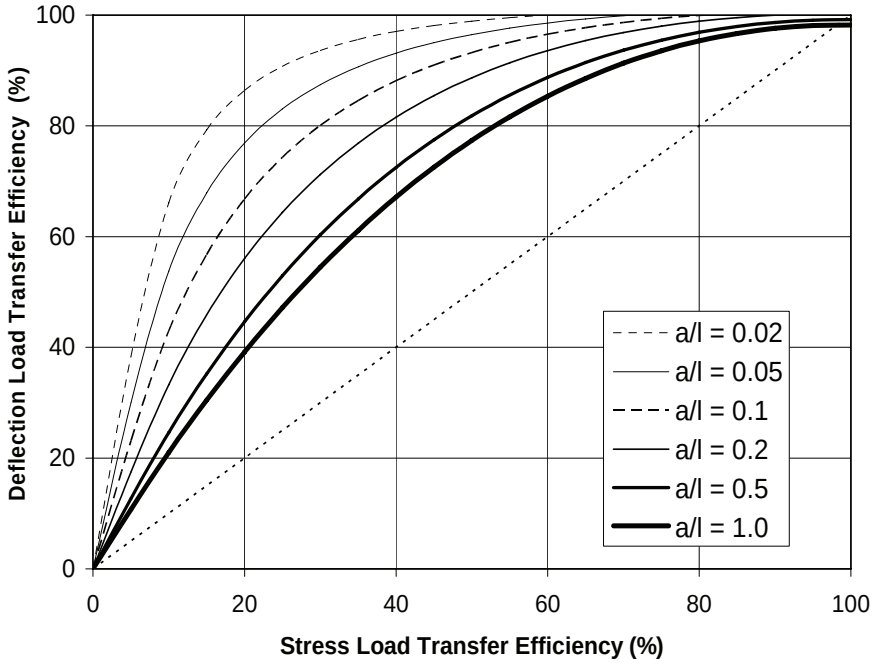

Figure 40. Relationship between LTE_{σ} and LTE_{δ}.

B.2.3.1.12 LTE Wearout Model

The wearout model takes into account the effect of traffic loading on LTE. The wearout model is based on experimental deflection testing evaluation of laboratory controlled slabs subjected to loading at a joint capable of transferring load through aggregate interlock only.(70)

Equation 139 models aggregate interlock at the beginning of the loading period. The LTE model depends on δ_u and δ_l that, in turn, depend on the joint stiffness for aggregate interlock.(73)

Figure 41 shows the JTE results obtained from the experimental work performed by Colley and Humphrey as a function of loading cycles of a 4086-kg load.(70)

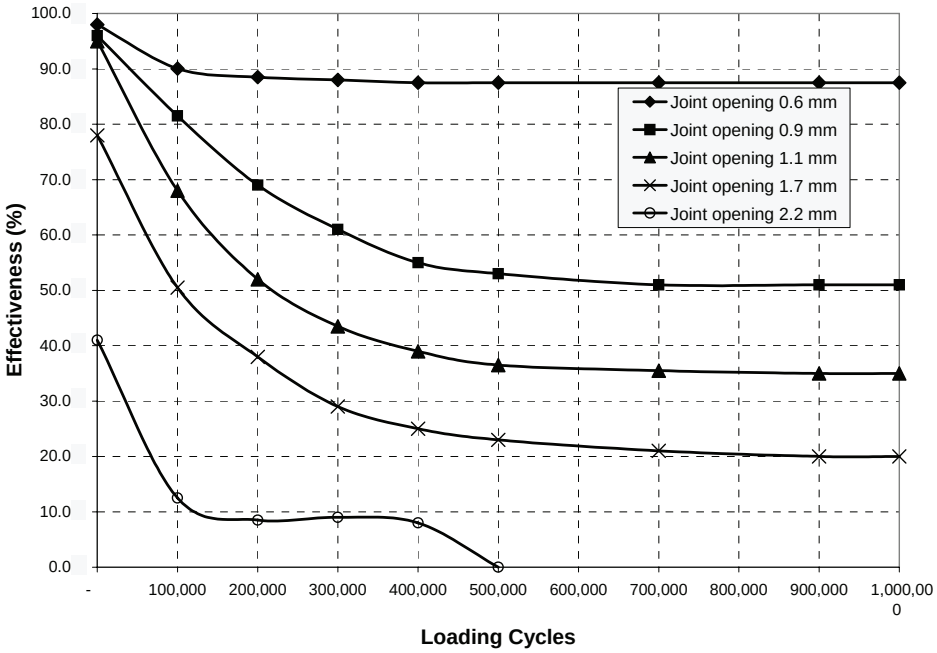

Figure 41. JTE results obtained from the experimental work performed by Colley and Humphrey as a function of loading cycles of a 4086-kg load.(70)

The initial JTE at the beginning of the loading period is modeled with the initial aggregate interlock previously developed. To model JTE as a function of loading cycles, an exponential function was fitted to the backcalculated agg/kl obtained for each one of the curves shown in figures 42 and 43. The resulting model for wearout is of the form shown in equation 170:

$$\frac{agg}{kl}_{wear} = \frac{agg}{kl}_{asymp} + \left(\frac{agg}{kl}_{init}\right) e^{-N/s} \quad (170)$$

where,

agg/kl_{wear} = Dimensionless aggregate interlock parameter at N loadings,

$agg/kl_{asymptote}$ = Dimensionless aggregate interlock parameter at an infinite number of loading cycles,
agg/kl_{init} = Dimensionless aggregate interlock parameter at the beginning of the loading period,
N = Noncalibrated cumulative traffic loading, and
s = Shape parameter, approximately 44,000 for the 229-mm slab and 91,000 for the 178-mm slab, on average.

To use the above model practically, the $agg/kl_{asymptote}$ parameter was estimated based on the backcalculated agg/kl values at the end of the experimental loading period from reference 70. Figure 44 shows the resulting $agg/ kl_{asymptote}$ as a function of joint opening for the two slab thicknesses evaluated.

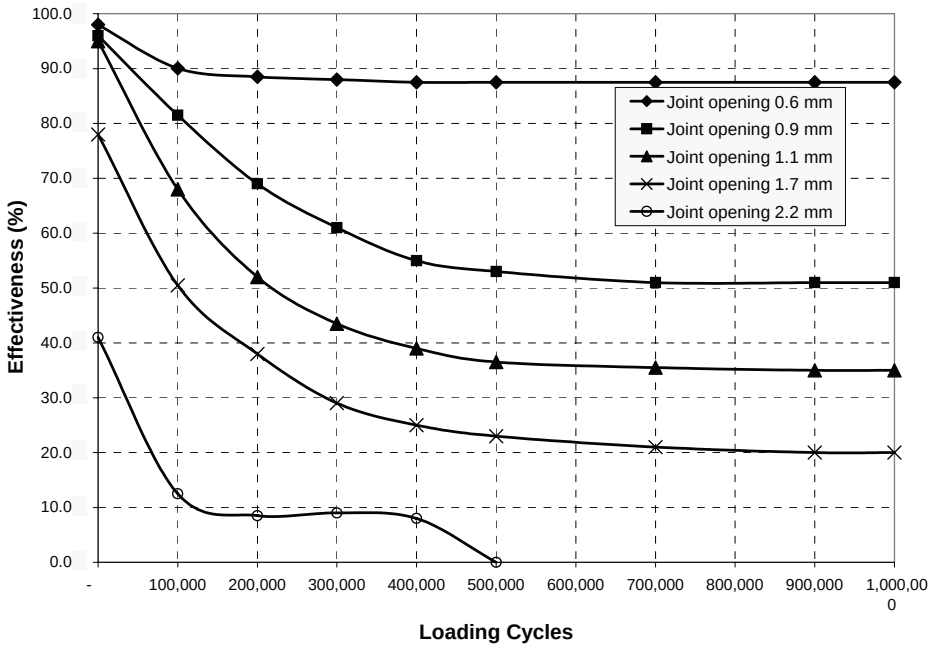

Figure 42. Influence of joint opening on JTE, 229-mm concrete slab, 152-mm gravel subbase.[70]

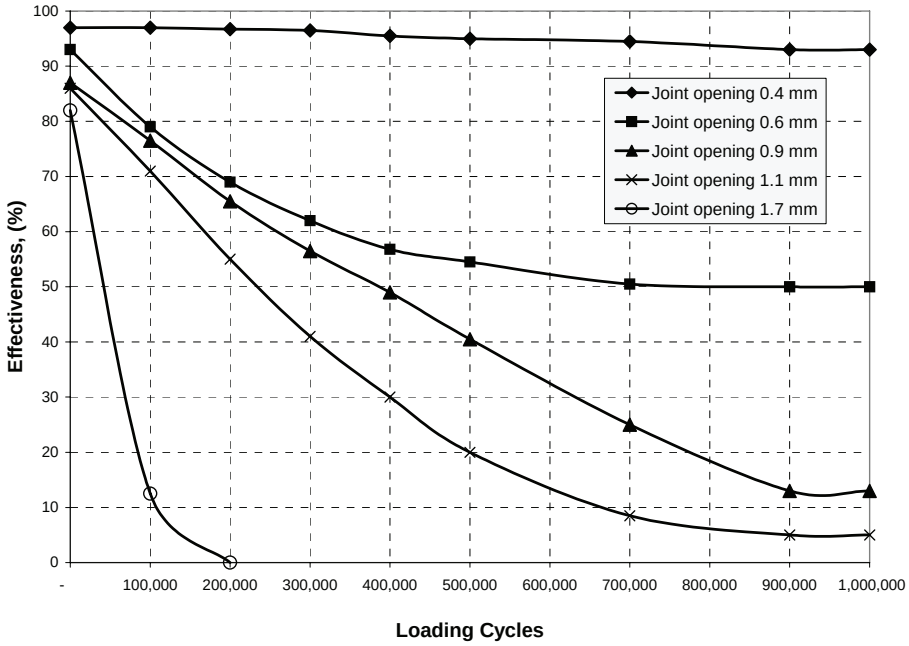

Figure 43. Influence of joint opening on JTE, 178-mm concrete slab, 152-mm gravel subbase.[70]

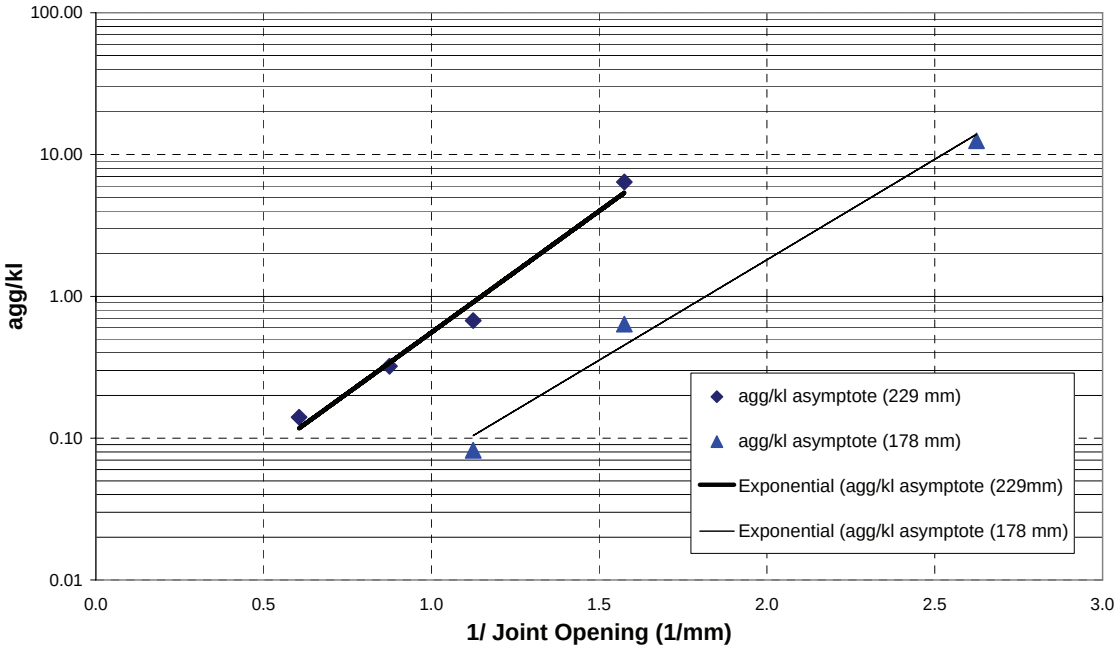

Figure 44. Asymptote dimensionless joint stiffness as a function of joint opening.

From the above data, a simple model was developed to predict the $agg/kl_{asymptote}$ parameter as a function of joint opening as shown in figure 171:

$$\frac{agg}{kl}_{asymptote} = \xi e^{3.63w} \tag{171}$$

where,

ξ = aggregate interlock asymptote model intercept (unitless), and
w = joint opening (mm).

The ξ intercept was found to depend on the slab effective thickness. The model was calibrated to have the same slope for both known thicknesses. This slope was assumed to have an exponential trend for $h - t_{saw} \leq 178$ mm and increase linearly thereafter. The resulting model for the ξ intercept is shown in equations 172 and 173:

For $h - t_{saw} \leq 178$ mm:

$$\xi = 1.935x10^{-8}\left(h - t_{saw}\right)^{6.9814} \tag{172}$$

For $h - t_{saw} > 178$ mm:

$$\xi = 0.01533\left(h - t_{saw}\right) - 0.092 \tag{173}$$

The data used to develop the above wearout model is based on laboratory controlled testing of experimental slabs. The following limitations are encountered in the application of the above model:

- Laboratory testing subjected the slabs to more severe conditions than normally encountered in the field. Higher deflections were observed for the laboratory experiment than for pavements evaluated in the field. In addition, while the support characteristics and joint opening were kept constant for the loading experiment, these conditions change in the field with time of day and season.[70]
- Only two thicknesses were investigated.
- The joint effectiveness results were not reported individually for the shape or hardness of the aggregates for the repetitive loading experiment. It is expected that differences in behavior would be observed for concrete with different aggregate properties as reported by Nowlen.[74]

It is therefore recognized that, although the above model provides a reasonable approach to characterizing LTE as a function of traffic loading and joint opening, investigation of a larger factorial of thicknesses, materials, and environmental conditions is required.

B.2.4 Distress Models

Several selection criteria were considered in selecting each individual JPCP distress model. One criterion included the preference for mechanistic models. Another selection criterion was that the model had been previously validated. Finally, the most important criterion (with respect to the HIPERPAV II effort), was that the model take into account early-age indicators for distress prediction such as joint opening, built-in curling, and/or delamination.

B.2.4.1 Faulting Without Dowels

The faulting model for JCPs without dowels at the joints incorporated into HIPERPAV II, was developed using the combined Concrete Pavement Evaluation System (COPES) and Performance/Rehabilitation of Rigid Pavements (RIPPER) databases.[75] The pavements are subdivided by their environmental regions of origin in the United States (wet-freeze, wet-no freeze, dry-freeze, and dry-no freeze) and by their design features in table 32.

Table 32. Distribution of pavement sections used in nondoweled faulting model.[75]

Climatic Region	None/AGG	CTB/ATB	LCB	PERM
Wet-freeze	5	5	2	2
Wet-no freeze	14	82	–	–
Dry-freeze	2	86	–	–
Dry-no freeze	3	127	14	–

NOTE: None: no base, AGG: aggregate, ATB: asphalt-treated base, CTB: cement-treated base, LCB: lean concrete base and PERM: permeable stabilized or permeable nonstabilized base.

A mechanistic-empirical faulting model has been developed for nondoweled JCPs. The faulting equation is provided in equation 174:

$$FAULT = ESAL^{0.2500} * \left[\begin{array}{l} 0.000038 + 0.01830(100 \cdot OPENING)^{0.5585} + 0.000619(100 \cdot DEFLAMI)^{1.7229} \\ + 0.0400\left(\frac{FI}{1000}\right)^{1.9840} + 0.00565 \cdot BTERM - 0.00770 \cdot EDGESUP - 0.00263 \cdot STYPE \\ - 0.00891 \cdot DRAIN \end{array} \right] \quad (174)$$

where,

FAULT = mean faulting across the transverse joint (inches), The primary reference is not clear in defining mean faulting across the transverse joint. However, because the *Distress Identification Manual for the Long-Term Pavement Performance Project* was used for performing the condition surveys in that study, mean faulting is understood as the average faulting for a pavement section at the transverse joints after a given number of ESALs,[15,72]

ESAL = cumulative 18,000-lb equivalent single-axle loads in traffic lane (millions),

OPENING = average transverse joint opening of the analysis pavement section, computed for the maximum climatic temperature drop throughout the year (inches), and

DEFLAMI = Ioannides' pavement corner deflection (inches) = equation 175:

$$\frac{P\left(1.2 - \frac{0.88 \cdot 1.4142 \cdot a}{\ell}\right)}{KSTAT \cdot \ell^2} \quad (175)$$

where,

ℓ = radius of relative stiffness (inches),

P = applied wheel load (~9000 lb),

a = radius of applied load (~5.64 inches, assuming a tire pressure of 90 psi),

KSTAT = modulus of subgrade reaction on top of base (psi/inch),
FI = freezing index (degree-days), and
BTERM = base type factor, which equals equation 176:

$$10\left[ESAL^{0.2076}\left(\begin{matrix}0.045456+0.05115\cdot GB+0.007279\cdot CTB+0.003183\cdot ATB\\-0.003714\cdot OGB-0.006441\cdot LCB\end{matrix}\right)\right] \quad (176)$$

where,

GB = variable for dense-graded aggregate base (1 if aggregate base, else 0),
CTB = variable for dense-graded cement-treated base (1 if cement-treated base, else 0),
ATB = variable for dense-graded asphalt-treated base (1 if asphalt-treated base, else 0),
OGB = variable for open-graded aggregate or asphalt-treated base (1 if open-graded base, else 0),
LCB = variable for lean concrete base (1 if lean concrete base, else 0),
EDGESUP = index for edge support (0 if no edge support exists, else 1),
STYPE = index for AASHTO subgrade soil classification (0 if A–4 to A–7 or 1 if A–1 to A–3), and
DRAIN = index for drainage condition (0 if no edge subdrain exists, else 1).

(1 inch = 25.4 mm, 1 lb = 0.454 kg, 1 psi = 6.894 KPa)

The r^2 statistic for this model is 0.81, and 398 slabs were used in its development.

Although this model is not truly mechanistic, it does contain a number of fundamental input parameters. In addition, the selected model has been validated using an extensive data set. Finally, the use of joint opening in this model, which is considered to be an important early-age indicator for distress prediction, was one of the primary factors for its selection.

B.2.4.2 Faulting of Doweled Pavements

The faulting model for JCPs with dowels incorporated in HIPERPAV II was also developed using the combined COPES and RIPPER databases.[75] The distribution of these pavement sections throughout the United States by climatic region and by subbase type is shown in table 33.

Table 33. Distribution of doweled pavement sections.[75]

Climatic Region	None/AGG	CTB/ATB	LCB	PERM
Wet-freeze	257	44	–	5
Wet-no freeze	11	35	4	–
Dry-freeze	141	10	–	1
Dry-no freeze	–	–	1	1

NOTE: None: no base course, AGG: aggregate, ATB: asphalt-treated base, CTB: cement-treated base, LCB: lean concrete base and PERM: permeable stabilized or permeable nonstabilized base.

The erosion of concrete from around dowels through repeated loading contributes to faulting in doweled pavements. In addition, pavement curling and warping increases deflection at the joint, further stressing

the dowels. It has been recommended that the bearing stresses at the joint be less than 10.4 MPa to limit faulting.[64] The mechanistic-empirical faulting equation (equation 177) is given as:

$$FAULT = ESAL^{0.5280} * \left[\begin{array}{l} 0.1204 + 0.04048\left(\frac{BSTRESS}{1000}\right)^{0.3388} + 0.007353\left(\frac{AVJSPACE}{10}\right)^{0.6725} - 0.1492 \cdot \\ \left(\frac{KSTAT}{100}\right)^{0.05911} - 0.01868 \cdot DRAIN - 0.00879 \cdot EDGESUP - 0.00959 \cdot STYPE \end{array} \right] \quad (177)$$

where,

FAULT = mean transverse joint faulting (inches),
ESAL = cumulative equivalent 18,000-lb single axle loads in lane (millions), and
BSTRESS = maximum dowel bearing stress on concrete using closed form solution (psi), shown in equation 178:

$$f_d \cdot P \cdot T\left[K_d\left(\frac{2 + BETA \cdot OPENING}{4E_s \cdot I \cdot BETA^3}\right)\right] \quad (178)$$

where,

BETA = relative stiffness of the dowel-concrete system,
f_d = a distribution factor (included in reference 75),
P = applied wheel load (~9000 lb),
T = percent transferred load (set to 0.45),
I = moment of inertia of dowel bar cross section (inches^4),
K_d = modulus of dowel support (~1,500,000 psi/inch),
OPENING = average transverse joint opening (inches),
E_S = modulus of elasticity of the dowel bar (set to 29,000,000 psi),
AVJSPACE = average pavement joint spacing,
KSTAT = effective modulus of subgrade reaction on top of the base (psi/inch),
DRAIN = index for drainage condition (0 if no edge subdrain exists, else 1),
EDGESUP = index for edge support (0 if no edge support exists, else 1), and
STYPE = index for AASHTO subgrade soil classification (0 if A–4 to A–7, else 1 if A–1 to A–3).

(1 in = 25.4 mm, 1 lb = 0.454 kg, 1 psi = 6.894 KPa)

The r^2 statistic for this model is 0.67, and 559 slabs were used in its development.

For the case of faulting with dowels, the use of bearing stress (related to joint opening) in the above model was one of the primary factors for its selection. In addition, although this model is not truly mechanistic, it contains a number of fundamental input parameters. Another factor influencing the selection of this model is that it has been validated using an extensive data set.

B.2.4.3 Joint Opening Model

The faulting models incorporated in HIPERPAV II (for both doweled and nondoweled JPCP) include inputs for joint opening. However, these faulting models were originally developed and calibrated based on a unique definition of joint opening.

The joint opening prediction made by HIPERPAV II is based on a different approach than the FHWA model. The FHWA model is closed form and rather simple prediction, while the HIPERPAV II model is based on a more sophisticated finite-difference-based analysis. Therefore, to use the joint prediction made by HIPERPAV II in predicting long-term faulting, a submodel was developed to convert from the HIPERPAV II-predicted joint opening to the joint opening parameter used in the FHWA faulting model.[75]

A parametric sensitivity analysis was performed on both the doweled and nondoweled faulting models. For the sensitivity analysis, joint opening was varied from 0.1 mm to 12.7 mm, and traffic loading from 0 to 50 million 80 KN ESALs. Plots of the results are in figures 45 and 46. As expected, these figures show that sensitivity to the faulting prediction exists as a function of both joint opening and traffic loading.

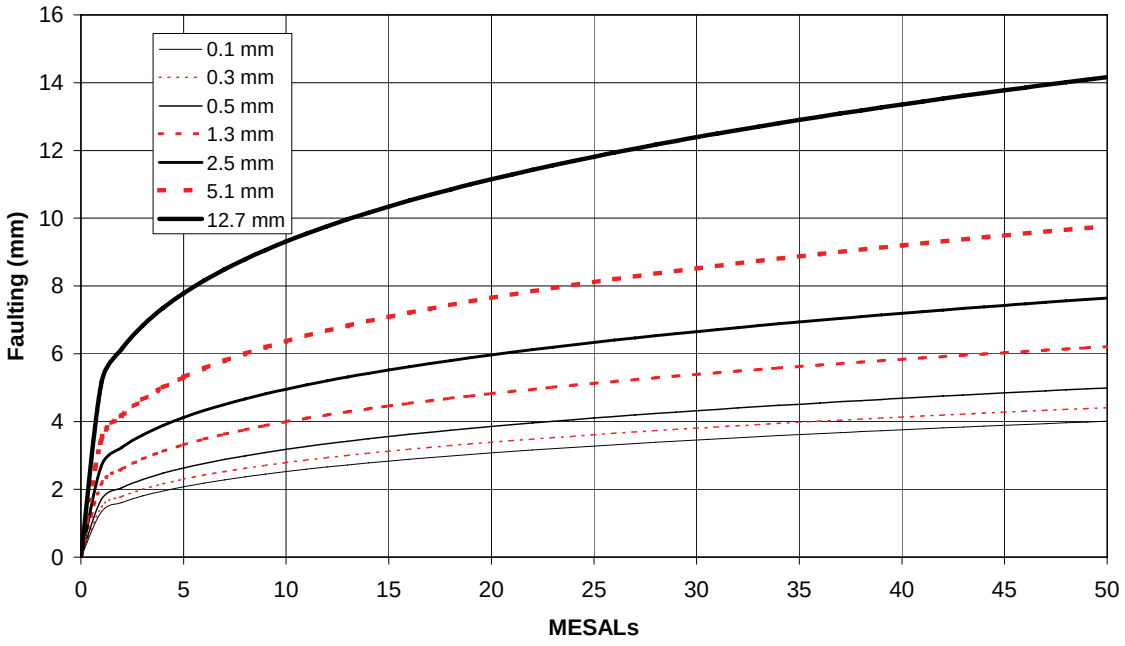

Figure 45. Sensitivity of faulting to joint opening and cumulative traffic loading for nondoweled JPCP (MESAL = 1,000,000 ESAL).

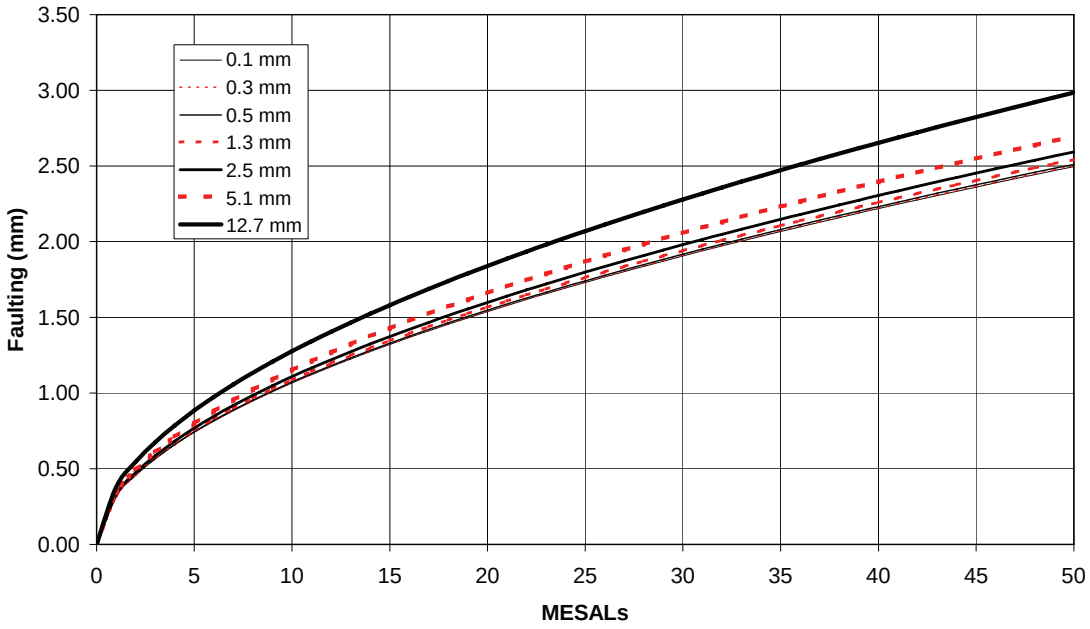

Figure 46. Sensitivity of faulting to joint opening and cumulative traffic loading for doweled JPCP (MESAL = 1,000,000 ESAL).

In the original FHWA report, joint opening is defined as in equation 179:[75]

$$OPENING = CON \cdot AVJSPACE \cdot 12\left(\frac{ALPHA \cdot TRANGE}{2} + \varepsilon\right) \quad (179)$$

where,

OPENING = joint opening, in inches (1 inch = 25.4 mm),
CON = frictional restraint adjustment factor (unitless) (0.65 for stabilized subbases, 0.80 for aggregate subbases),
AVJSPACE = average joint spacing in feet, (1 ft = 0.3048 m),
ALPHA = PCC CTE in inch/inch/°F, (1 inch/inch/degree Fahrenheit (°F) = 0.56 m/m/ºC),
TRANGE = annual temperature range in °F, (1 °F = 0.56 ºC), and
ε = PCC drying shrinkage coefficient (in microstrains).

Since the free strain of the PCC is defined in the last term, equation 179 can be simplified into equation 180:

$$OPENING = CON \cdot AVJSPACE \cdot 12 \cdot \varepsilon_{free} \quad (180)$$

The slab-base restraint model in HIPERPAV II is based on a finite-difference solution of the axial movement-restraint phenomenon.[1] It is currently one of the key models in predicting the critical stress in the concrete during the early-age period. However, this same model also can be used to predict the joint opening as a function of a number of variables, including those listed in table 34.

Table 34. HIPERPAV slab-base restraint model variables.

Variable	Definition	Typical Value
h	PCC slab thickness	305 mm
L	Average joint spacing	4.6 m
E_c	PCC elastic modulus	27,579 MPa
ε_{free}	Free strain	300×10^{-6} m/m
δ_{crit}	Movement at maximum friction	0.5 mm
F_{max}	Maximum friction force	27.6 KPa

The calculation of the joint opening in HIPERPAV II is not a closed form, as is that in the FHWA model (shown in equations 179 and 180), therefore the formulae for its calculation are not given here for brevity.(1)

Before even a cursory comparison of these two models for the prediction of joint opening, selecting "equivalent" inputs for the degree of slab-base restraint is required. The FHWA model includes a CON variable that is assigned a value of either 0.65 or 0.8, depending on the subbase type. The HIPERPAV II model is more sophisticated; it requires two parameters that define a bilinear relationship between the slab movement and corresponding force required for the movement. The intersection of the bilinear relationship is how the two parameters are defined. Extensive documentation on various subbase types was drawn upon to define equivalent values of subbase restraint that correspond to the two CON values given in the FHWA report. The final selection of these values, used in this analysis, is given in table 35.

Table 35. Definition of equivalent slab-base restraint values for joint opening models.

Subbase Type	CON Value for FHWA Model	δ_{crit} Value for HIPERPAV Model	F_{max} Value for HIPERPAV Model
Stabilized base	0.65	0.254 mm	55.2 KPa
Aggregate base or LCB with bond breaker	0.80	0.508 mm	27.6 KPa

To compare the predictive ability of the joint opening models, a factorial was established that consisted of 1920 combinations of the various model inputs. The variables and the ranges selected for this factorial are included in table 36.

Table 36. Factorial of joint opening model inputs.

Variable	Minimum Value	Maximum Value
Slab thickness	50.8 mm	406 mm
Average joint spacing	0.9 m	12.2 m
PCC elastic modulus	20,700 MPa	41,400 MPa
Free strain	50 με	2000 με
Slab-subbase restraint	CON = 0.65 δ_{crit} = 0.254 mm F_{max} = 55.2 KPa	CON = 0.80 δ_{crit} = 0.508 mm F_{max} = 27.6 KPa

The joint openings, using both the FHWA and the HIPERPAV II models, then were calculated for each of the factorial combinations. The results are given in figure 47. As can be seen in the figure, the predictions using the two models do not coincide. In all cases, the HIPERPAV II model predicts a greater joint opening than does the FHWA model. However, this is not surprising, due to the fundamental differences in the predictive methodology.

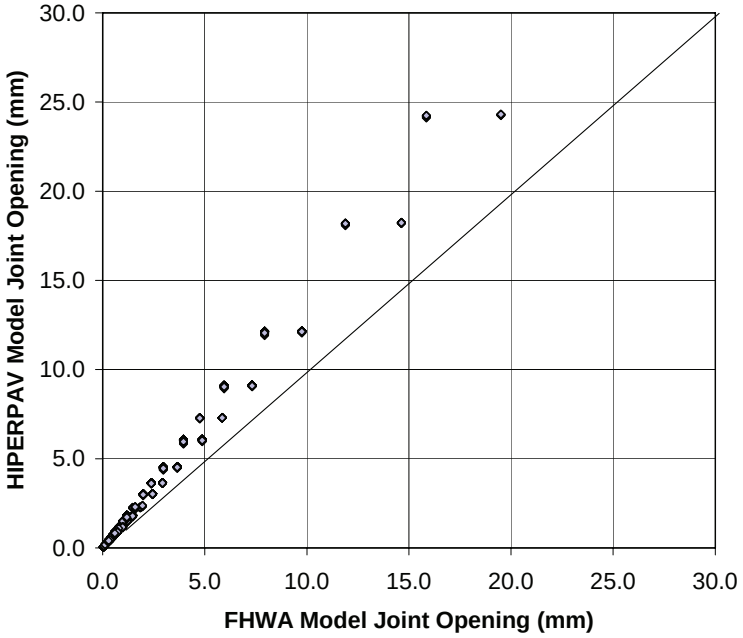

Figure 47. Relationship between joint opening model predictions.

Because the FHWA faulting model has been developed and calibrated based on a unique definition of joint opening, it is critical to the proper use of the model to find a relationship that can convert the HIPERPAV II prediction to the FHWA prediction.

It was decided that the most practical means of implementing a submodel to convert the HIPERPAV II joint opening to the FHWA joint opening is by calculating a ratio between the two. A nonlinear regression analysis was performed on the 1920 combinations given in the last section to predict the ratio of the FHWA to the HIPERPAV II joint opening. The result of this regression analysis is as shown in equation 181:

$$\frac{OPENING_{FHWA}}{OPENING_{HP}} = 0.84241 - \frac{0.018459}{h} - 2.3010 \times 10^{-4}\left(\frac{F_{\max}}{\delta_{crit}}\right) + \frac{57923.}{E_c} \quad (181)$$

Equation 181 has an r^2 of 0.926 and a Standard Error of the Estimate (SEE) of 0.020. Using this equation, the HIPERPAV II joint openings in figure 47 were converted to their equivalent HIPERPAV II joint opening predictions. The results are illustrated in figure 48.

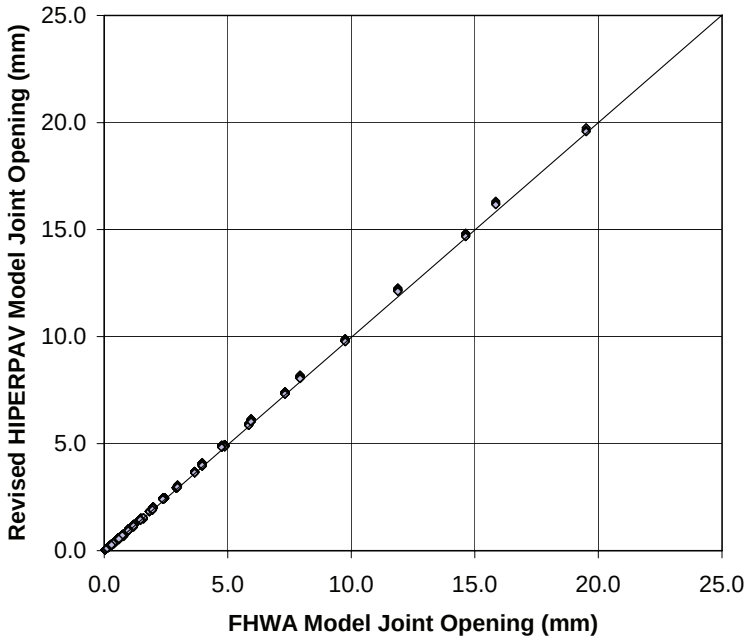

Figure 48. Relationship between revised joint opening model predictions.

B.2.4.4 Midslab Cracking Models

This section describes models for accumulating damage and models for predicting cracking in PCCP slabs. A short description also is given of three other models considered by the research team responsible for reference 76 in choosing appropriate fatigue damage and slab cracking models.

B.2.4.4.1 Fatigue Damage Model

The first type of model is concrete fatigue damage resulting from load applications that induce stresses in the pavement slab. The four proposed models in reference 76 regarding concrete fatigue damage are (references 77, 78, 79, and 80 are the original sources for each of these models):

Corps of Engineers and ERES Consultants, Inc. (ERES/COE) Model (equation 182):[77]

$$\log N = 2.13 \bullet SR^{-1.2} \tag{182}$$

NCHRP 1–26 Model (equation 183):[78]

$$\log N = \left[\frac{-SR^{-5.367} \log(1-P)}{0.0032} \right]^{0.2276} \tag{183}$$

Zero-Maintenance Model (equation 184):[79]

$$\log N = 17.61 - 17.61 \cdot SR \tag{184}$$

Austin Research Engineers, Inc. (ARE) Model (equation 185):[80]

$$N = 23{,}440 \bullet SR^{-3.21} \tag{185}$$

where,

N	= number of allowable load applications,
SR	= stress-to-strength ratio (σ/MR),
σ	= adjusted Westergaard critical stress in psi (1 psi = 6.89 KPa),
MR	= PCC modulus of rupture in psi (1 psi = 6.89 KPa), and
P	= probability of failure.

Figure 49 shows the four models' prediction of allowable loads as a function of stress-to-strength ratio. The figure shows the four models above, and includes the NCHRP 1–26 model based on both 50 percent and 5 percent probability of failure. The comparison in reference 76 fixed the probability term in the NCHRP 1–26 model at 50 percent.

The evaluation of the four models in reference 76 determined that the ERES/COE model was the best candidate, so it was chosen for use in the HIPERPAV II damage and cracking model. It should be noted, however, that the NCHRP 1–26 model is virtually identical to the chosen model when the probability term is set at 15 percent chance of failure, or an 85 percent reliability level.

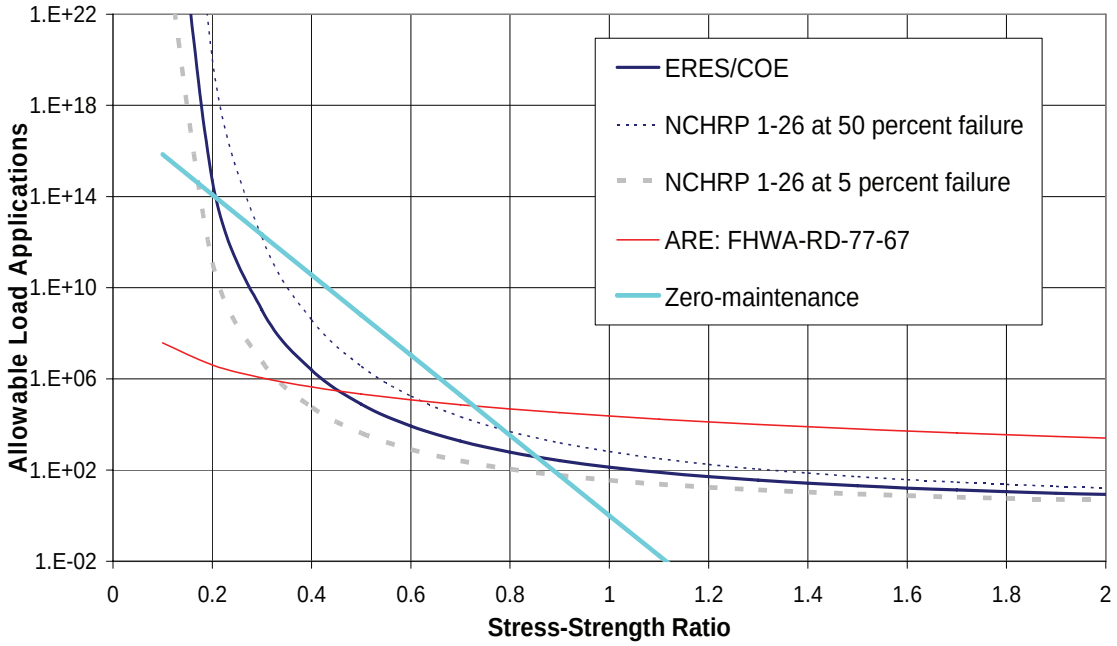

Figure 49. Allowable loads versus stress-to-strength ratio.

The following paragraphs are taken from the discussion and critique of models in reference 76.

ERES/COE model—this model was developed from U.S. Army Corps of Engineers data from 51 full-scale field sections. The edge load stress was calculated using H–51 program (computerized Pickett and Ray charts) and multiplied by 0.75 to account for the edge support in the sections.

NCHRP 1–26 model—this model was developed using the COE and AASHO road test data. This model is also based on edge load stress.

Zero-Maintenance model—this model is based on laboratory testing results of 140 beams.

ARE model—this model was developed based on the AASHO road test data. The actual loads were converted to 18-kip ESALs, and the maximum midslab stresses were calculated using elastic layer theory.

Yu et al. recognize that the first two models (ERES/COE and NCHRP 1–26) are very similar in form and that they give similar results at specific values of the probability term.[76] The report stated that the Zero-Maintenance model gave the most scatter, and that the ARE model gave the narrowest range of damage values but does not show a logical trend. Later, the report selects the ERES/COE model, stating that the damage results of the NCHRP 1–26 model were shifted to the left of the ERES/COE model by one magnitude. Results from the ERES/COE model are in a more conventional range (about 50 percent cracking at fatigue damage of 1.0).

The ERES/COE model was incorporated in HIPERPAV II. This model could be changed in the future as new developments (such as those under the NCHRP 1–37a study) become available.

B.2.4.4.2 Slab Cracking Model

The second model discussed in this section is the slab cracking model. Yu et al. developed a percent cracking model based on the accumulated damage.[76] This model was incorporated in HIPERPAV II and is given as equation 186:

$$\text{Percent Cracking} = \frac{100}{1 + 1.41 \cdot FD^{-1.66}} \tag{186}$$

where,

FD = accumulated fatigue damage. As shown in equation 187,

$$FD = \sum \frac{n_i}{N_i} \tag{187}$$

where,

n = actual number of loads for load group i, and
N = allowable number of loads for load group i.

In the classic damage model form, using Miner's law, damage from individual loads is accumulated to produce an aggregate damage value with which the level of cracking is predicted.

Figure 50 shows the fit of the data to the model in equation 186. As can be seen in the figure, when accumulated damage equals 1, the slab cracking approaches 40 percent. This is one of the reasons Yu et al. selected the model.[76]

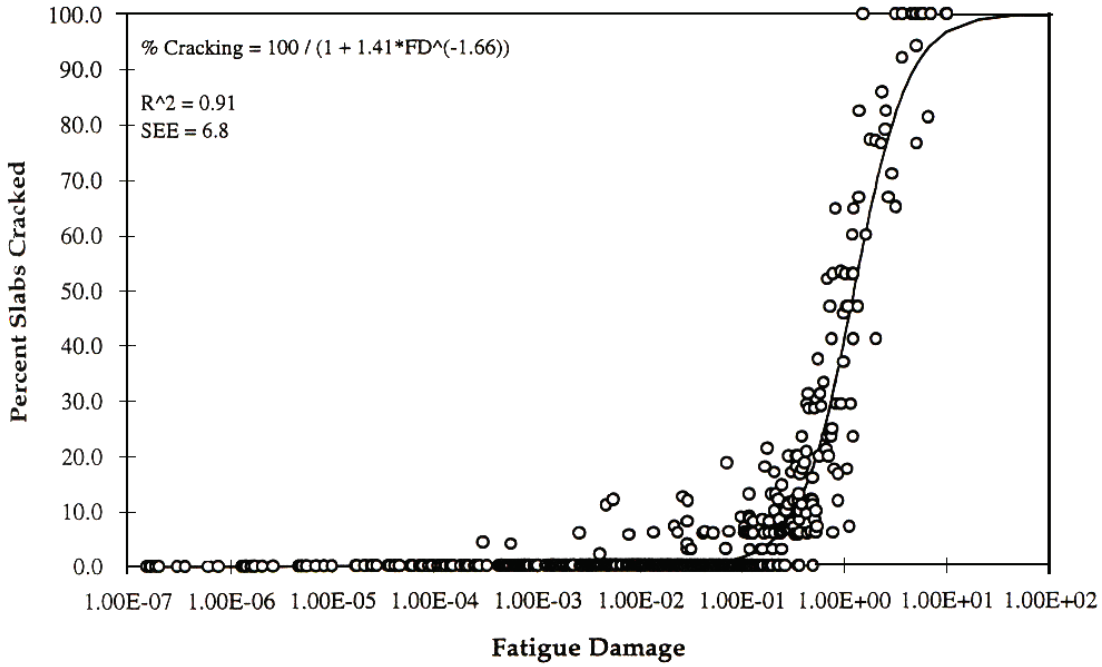

Figure 50. Fatigue cracking model with associated data.[76]

B.2.4.4.2.1 Assumptions

The form of the model was selected because it represents the theoretical characteristics of cracking progression in a PCC pavement section. Two theoretical boundary conditions are: 1) there will be 0 percent cracking when fatigue damage = 0, and 2) 100 percent of the slabs will be cracked as fatigue damage approaches infinity. This form of the model and the given boundary conditions ignore the possibility of environment-related cracking before any traffic-related fatigue damage, and the fact that 100 percent of the slabs may crack at a finite level of damage.

A good aspect of the model is that it seems to have been developed using sections both with and without cracked slabs. Some models can only consider sections with at least some cracking, and thus do not properly represent all possible data points in a set of data.

Other assumptions include the aggregate effects of curling and loading stresses and ability of the researchers to calculate stresses and fatigue damage accurately. The latter will be discussed in greater detail in the "Limitations" section below. The stress induced by traffic loads is adjusted for thermal curling, but other conditions such as drying shrinkage and other sources of curling and warping are not considered. Yu et al. state that climate can have a significant effect on cracking prediction due to the thermal and moisture gradients to which the slab is subjected.[76] The report references these effects, but other than the difference between temperature in the slab top and bottom, there is no way to account for these conditions.

B.2.4.4.2.2 Limitations

There are several limitations on this model, including the use of reliability, the necessity of calculating of fatigue damage rather than directly measuring it, the use of regression models rather than mechanistic-empirical models, and the use of the model without the curling component.

The first limitation mentioned above, the fact that reliability is not considered directly, is a drawback that the NCHRP 1–26 model does not have. In that model, as mentioned previously, the probability of failure is specifically included. This probability of failure can be considered analogous to the inverse of the probability of success. Given a 50 percent probability of failure, as the one considered in reference 76, the model also predicts a 50 percent probability of success. Given a 15 percent probability of failure, an 85 percent probability of success is implied (which is more reasonable for pavements on less important facilities). For this reason, the NCHRP 1–26 model was seriously considered for this project.

The need to calculate rather than measure fatigue damage directly is a limitation of this and any model. To validate a model, predictions of stress and accumulated damage must be made by other means. Perhaps a more reliable method of validating a combination of damage and cracking models could be made by comparing the inputs to the stress model described in the following section to the level of cracking predicted and observed. In that way, the entire stress-damage-cracking model system can be evaluated and validated.

A third limitation is the use of regression models. Although it is recognized that mechanistic models are much more difficult to develop, validate, and calibrate, new research should advance the state of the art so that such models are more reliable and accurate. As new models become available, the project team will evaluated them, and those that improve the predictive capability of the computer guidelines will be adopted.

The fourth limitation listed at the beginning of this section is the statement in reference 76 that "(w)hen this model is used without considering the built-in upward curling of slabs, the model is likely to predict an excessively high amount of cracking." (p. 78) Although it is not expected that this will be the case, it is a limitation of the model that should be considered.

B.2.4.4.3 Midslab Stress Adjustment Model

This section describes the model incorporated for midslab cracking prediction in HIPERPAV II. The model's background, characteristics, assumptions, and limitations, and a description of the validation efforts are included here.

B.2.4.4.3.1 Model Identification

The edge stress adjustment model is taken from a combination of papers submitted to TRB, ASCE, and the 6th International Conference of Concrete Pavements. (See references 81, 82, 83, and 84.) Each of the papers discussed in this section are based on the same principles, but contain different aspects of stress adjustment that the overall model addresses. This section combines the concepts and components of the various papers and demonstrates how they are all used together to modify the Westergaard free edge stress.

B.2.4.4.3.2 Model Characteristics

The model was derived from multiple runs of the ILLISLAB FEA program. The basis for this approach is that FEA can consider the effects of finite slab size and the possible loss of support due to linear temperature differentials. Theoretical (Westergaard) solutions that are based on infinite slab and full contact assumptions cannot consider the reality of slab size and temperature and moisture differentials.

The models presented in these papers were developed using multiple FEA runs with varying pavement designs and conditions. The resulting stresses predicted by the FEA were compared to the theoretical Westergaard solutions using the same conditions. Adjustment factors were developed to account for the differences in the two sets of solutions. In this way, a closed form solution was developed to represent the results of the FEA.

The papers claim that the models developed have been carefully validated and are readily implementable in spreadsheets or computer programs. They claim that the models are properly formulated to satisfy applicable engineering boundary conditions and that they are simple, easy to comprehend, and dimensionally correct. They further claim that the models can be extrapolated to wider ranges of input parameters.

One of the papers is an attempt to revise the PCA thickness design methodology and maintains adjustment factors for the placement of truck loads relative to the slab edge, and for the concrete's increased strength beyond 28 days.[82] Since HIPERPAV II includes strength gain prediction models beyond 28 days, this factor was omitted from this model. HIPERPAV II predicts this strength, eliminating the need to adjust the stress to account for increased strength.

The model developers reduced the Westergaard edge loading and deflection solutions to three dimensionless terms given by equations 188, 189, and 190:[81]

$$\frac{\sigma \cdot h^2}{P} \tag{188}$$

$$\frac{\delta \cdot k \cdot \ell^2}{P} \tag{189}$$

$$\frac{q \cdot \ell^2}{P} \tag{190}$$

where,

σ = Westergaard's edge stress, FL^{-2},
δ = Westergaard's edge deflection, L,
q = subgrade vertical stress, FL^{-2},
h = slab thickness, L,

P = single wheel load, F,
k = modulus of subgrade reaction, FL^{-3}, and
l = radius of relative stiffness of the slab-subgrade system, L.

The three dimensionless terms all depend on the normalized load radius a/l, assuming a constant Poisson's ratio of 0.15. Indeed, virtually all the models developed for these papers include an a/l term and other terms normalizing length dimensions to the radius of relative stiffness, such as W/l (slab width), L/l (slab length), and D_o/l (distance of wheel load to slab edge).

B.2.4.4.3.3 Logic

The term σ_{eq}, or equivalent stress, means the Westergaard edge stress adjusted for the specific design and conditions relating to the pavement in question. This stress is determined by equation 191:

$$\sigma_e = \left(\sigma_{we} \cdot R_1 \cdot R_2 \cdot R_3 \cdot R_4 \cdot R_5 + \sigma_{ce} \cdot R_T\right) \cdot f_1 \tag{191}$$

where,

σ_e = equivalent edge stress prediction, FL^{-2},
σ_{we} = Westergaard edge stress, FL^{-2},
σ_{ce} = Westergaard/Bradbury edge curling stress, FL^{-2},
R_1 = wheel configuration factor (single or dual tire and single, tandem, or tridem axle),
R_2 = finite slab length and width factor,
R_3 = tied concrete shoulder factor,
R_4 = widened outer lane factor,
R_5 = bonded or unbonded second layer factor,
R_T = adjustment factor for the combined effect of loading and thermal curling, and
f_1 = PCA adjustment factors for the effect of truck placement on the edge (see table 37).

Table 37. PCA edge adjustment factors.

Percent Trucks at Edge	Adjustment Factor f_1
1	0.825
2	0.855
3	0.870
4	0.880
5	0.890
6	0.894
7	0.901

The Westergaard closed form edge stress equation is given as equation 192, and the Westergaard/Bradbury curling stress equation is given in equation 193.

$$\sigma_w = \frac{3(1+\mu)P}{\pi(3+\mu)h^2}\left[\log_e\left(\frac{Eh^3}{100ka^4}\right)+1.84-\frac{4}{3}\mu+\frac{1-\mu}{2}+1.18(1+2\mu)\frac{a}{\ell}\right] \quad (192)$$

where,

μ = concrete Poisson's ratio,
E = concrete elastic modulus, FL^{-2}, and
a = radius of the applied load, L.

$$\sigma_c = \frac{CE\alpha\Delta T}{2} \quad (193)$$

where,

α = concrete CTE, T^{-1},
ΔT = temperature differential through slab thickness, T,
C = curling stress coefficient, which equals the formula shown in equation 194:

$$\left[1-\frac{2\cos(\lambda)\cosh(\lambda)}{\sin(2\lambda)\sinh(2\lambda)}\left(\tan(\lambda)+\tanh(\lambda)\right)\right] \quad (194)$$

λ = the formula shown in equation 195:

$$\frac{W}{\ell\sqrt{8}} \quad (195)$$

W = slab width, L.

These equations are used to determine a free edge stress, which is later modified by factors developed through the FEA performed by the authors of the referenced papers. (See references 81, 82, 83, and 84).

The researchers identified several dimensionless mechanistic variables with which they performed regression analysis on the ILLISLAB FEA results. The sets of variables are different under the loading-only condition and the loading-plus-thermal-curling analysis. The following variables (shown in equations 196 and 197) were identified:

Loading-only condition:

$$f\left[\frac{a}{\ell},\frac{L}{\ell},\frac{W}{\ell},\frac{s}{\ell},\frac{t}{\ell},\frac{D_o}{\ell},\frac{AGG}{k\ell},\left(\frac{h_{eff}}{h}\right)^2\right] \quad (196)$$

Loading-plus-thermal-curling analysis:

$$f\left[\frac{a}{\ell}, \frac{L}{\ell}, \frac{W}{\ell}, \alpha\Delta T, \frac{\gamma h^2}{k\ell^2}, \frac{Ph}{k\ell^4}\right] \tag{197}$$

where,

s = transverse wheel spacing, L,
t = longitudinal axle spacing, L,
D_o = offset distance between the outer face of the wheel and the slab edge, L,
AGG = aggregate interlock factor, FL^{-2},
h_{eff} = effective thickness of two unbonded layers, L, which equals the formula shown in equation 198:

$$\sqrt{h_1^2 + h_2^2 \frac{(E_2 \cdot h_2)}{(E_1 \cdot h_1)}} \tag{198}$$

h_1 = thickness of top slab, m, (also signified as h),
h_2 = thickness of second concrete slab, m,
E_1 = concrete elastic modulus of top slab, MPa, (also signified as E), and
E_2 = concrete modulus of second slab, MPa.

For the midslab (edge) stress, the daytime curling condition is critical. An early version of the model was developed to account for the edge stress under nighttime curling conditions, where the curling counteracts the effect of traffic loading.[81] However, the most recent version of the model omits the nighttime condition. Models for adjustment factors considering both conditions are included in reference 84. The model also includes equations for curling-only conditions. These components are not for use in a fatigue cracking model, but were developed for validation purposes. They are included in this section to maintain the integrity of the model as it appeared in the references.

B.2.4.4.3.4 Assumptions

The papers and models presented in this section take the original Westergaard stress equations, along with their assumptions of infinite slab size and medium slab thickness, and compare their results to stresses predicted by ILLISLAB, an FEA computer program. The FEAs were performed under various load configurations, slab sizes, and other conditions that alter the configurations assumed by Westergaard in his original work. The resulting stresses predicted by ILLISLAB were then compared to the Westergaard stresses, and appropriate adjustment factors were developed by the authors. A basic assumption the authors made is that of a constant concrete Poisson's ratio of $\mu = 0.15$, which greatly simplified the model development.

By using the FEA, the authors were able to eliminate the Westergaard assumption of full contact between the pavement slab and the subgrade. An important assumption in doing this, however, and one that is not mentioned by the authors of references 81 through 84 is that the nature of the stress model may change when a slab lifts off the subgrade, or when a void is otherwise present under the slab. The authors simply predict the adjustment factor for those conditions. This may be appropriate, but an addition to the model

may be necessary to predict slab liftoff and then calculate the stresses in a different way, possibly using beam theory or further FEA.

B.2.4.4.3.5 Limitations

These models have several limitations that are not discussed by the authors, but these may impact the models' validity. The first and easiest to correct is that many typographical errors were found in the presentation of these models in the various publications. In fact, each publication in which the models were presented has at least some errors that were identified, but it is not known if other errors exist in the presentation of the models and their coefficients. Another limitation is that some of the models in the different publications have entirely different coefficients or have differences in their construction. This means, for example, that the model for adjusting Westergaard edge stresses affected by the presence of a tandem axle (single wheel) configuration was changed after it was originally published in *Transportation Research Record No. 1568* to when it was published in the 6th International Conference of Concrete Pavement proceedings.[82,84] No explanation was given for this and other change, while other models in the same group were not changed.

Another limitation of these models is that each one has limits on the dimensions or configuration that can be analyzed with them. For example, the ratio of dual wheel spacing to radius of relative stiffness (l) cannot be less than 0.2 nor greater than 4.0. Similar restrictions are placed on slab length to l, axle spacing to l, etc. The restrictions arise from the limitations on the model development, but the authors seem to indicate that the models can be extrapolated beyond these limits.[81] It is not difficult to construct a set of conditions that violate the restrictions placed on the individual models, increasing the probability that the user of a design procedure may violate those same restrictions with a normal design problem. Further investigation should be made to determine the extent to which the restrictions may be violated safely.

A limitation on the validity of the entire set of models is maintained by the fact that the models were developed using ILLISLAB and that the same finite-element program was used to validate the models. The paper in reference 81 indicates that a series of ILLISLAB runs was performed to validate the models. It states that factorial runs were totally independent of previous modeling processes. It seems, however, that to use the same methods for model development and validation necessarily introduces bias in the results of the validation. To verify and validate these models further, the project team has performed FEAs by using LS-DYNA. The models have been compared to the results from LS-DYNA which, together with the ILLISLAB validation, have provided some confidence in the validation claims of the authors.

B.2.4.4.3.6 Slab Stress, Damage, and Cracking Model Integration

This section describes the integration of the midslab and corner stress adjustment models (section B.2.4.4.3) with the PCC fatigue damage and cracking model (sections B.2.4.4.1 and B.2.4.4.2) and with the overall long-term performance analysis module in HIPERPAV II. In general, the cracking module contains four embedded loops. The first two loops are for the time of day and the season of the year. Within these two loops a third loop over each axle configuration, from which the Westergaard free edge and free corner stresses are computed. The fourth loop adjusts the load group. For each combination, the edge and corner stresses are adjusted, midslab and corner fatigue damage is accumulated, and then cracking for each case is determined.

The stress and damage integration module is essentially a damage accumulation model. The appropriate damage for individual load groups, axle configurations, seasons, and times of day are accumulated, and at the end of each season, the total damage is used to calculate the level of cracking from the date of construction to the current time.

For midslab cracking, the stress adjustments are determined, as described in section B.2.4.4.3. The Westergaard stresses are determined for both the longitudinal and transverse free edge, given other conditions such as load, slab thickness, concrete elastic modulus, and the modulus of subgrade support. The stresses are then modified to account for load transfer to adjacent slabs (section B.2.3.1) and by applying the adjustment factors. Then, for each combination of season, time of day, axle, and load, the fatigue damage for both longitudinal and transverse cracking is accumulated. At the end of each season, the accumulated fatigue damage is used in the cracking model described above to predict the accumulated level of cracking, both in the transverse and longitudinal directions.

Figure 51 shows a flowchart describing the stress-fatigue-cracking integration module. The flowchart applies to each season for which the analysis is performed. For each season, the analysis is performed two times a day to capture the effects of upward and downward curling. Within each of the two times, the analysis loops over the axle and load groups, as described above. The total accumulated fatigue damage and percent slab cracking values are then returned to the main analysis routine.

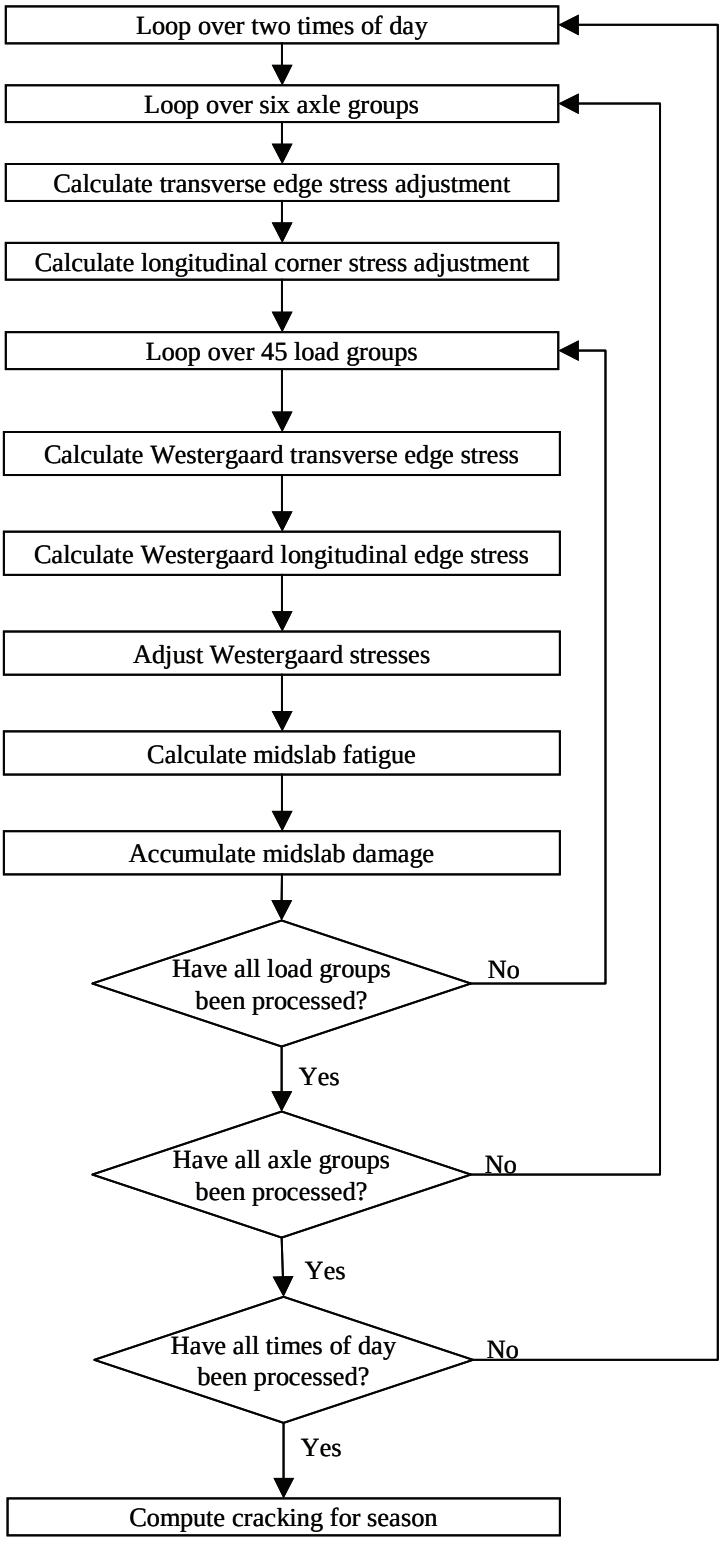

Figure 51. Flowchart of stress, damage, and cracking module.

The values that will be calculated and returned by this routine include the accumulated and incremental damage as well as the total cracking for the current season.

B.2.4.5 Roughness Model

Measuring the roughness of pavements is one of the most economical methods used to predict pavement serviceability. Two common roughness indicators are the present serviceability index (PSI) and the IRI. An evaluation of PSI and IRI models available in the literature and the models incorporated in HIPERPAV are presented in the following sections.

B.2.4.5.1 Present Serviceability Index

Present serviceability is defined as the ability of a specific section of pavement to serve high-speed, high-volume, mixed traffic in its existing condition.[64] The PSI originally was developed at the AASHO road test in 1960. PSI is a rating scale from 0 to 5, where 4 to 5 represent very good pavement, 3 to 4 is good, 2 to 3 is fair, 1 to 2 poor, and 0 to 1 is very poor. This rating is a function of the pavement's physical measurements of roughness and distress (e.g., cracking, faulting, patching). It depends on the pavement's longitudinal profile, where cracking, patching, and faulting are likely to contribute. The longitudinal profile can be expressed as the mean slope variance (deviation of the record from a baseline). These measurements are combined to formulate PSI.

The original equation (equation 199) for the PSI of rigid pavements is based on 49 rigid sections:[64]

$$PSI = 5.41 - 1.71\log(1 + \overline{SV}) - 0.09\sqrt{C + P} \tag{199}$$

where,

PSI = present serviceability index,
SV = slope variance measured using a profiler (10^{-6} rad),
C = cracking in ft/1,000 ft^2 (1 ft = 0.3048 m), and
P = patching (ft^2/1,000 ft^2).

The influence of faulting and spalling were also measured, but these did not have a statistically significant influence on the pavement serviceability. The r^2 for this model is 0.92.

This equation contains several limitations:

- The profiler that measured slope variance is no longer in use.
- Riders' perceptions of road serviceability have changed over the past 30 years because vehicles, highway characteristics, and speeds have changed.
- The rideability equation includes surface defects. Roughness and surface distresses do not necessarily correlate, because they are physically different attributes of the pavement condition.[64]

A 1990 study to predict PSI in JPCPs developed the following regression model, shown in equation 200:[85]

$$PSI = 4.536 - 0.0182(TFAULT) - 0.00313(SPALL) - 0.00162(TCRKS) - 0.00317(FDR) \quad (200)$$

where,

TFAULT = cumulative transverse joint faulting in inches per mile (1 inch per mile (inch/mi) = 15.8 mm/km),
SPALL = number of deteriorated (medium and high severity) transverse joints per mile (1 mi = 1.609 km),
TCRKS = number of transverse cracks (all severities) per mile (1 mi = 1.609 km), and
FDR = number of full depth repairs per mile.

For this model, the r^2 is 0.58 using 282 pavements. This model is a linear regression of multiple variables collected according to the *Distress Identification Manual for the Long-Term Pavement Performance Project.*[86] The intercept (4.536) is the maximum PSI allowed when all distresses equal zero. As the distresses accumulate, PSI decreases. Since the model sensitivity to FDR is relatively small and difficult to model, it can be omitted. The model incorporated in HIPERPAV II is shown in equation 201:

$$PSI = 4.536 - 0.0182(TFAULT) - 0.00313(SPALL) - 0.00162(TCRKS) \quad (201)$$

This model has some limitations, including:

- A longitudinal roughness term is not included in the model. Therefore, it does not account for long wavelength roughness due to subbase and subgrade settlement and heave. The distresses included only account for short wavelength roughness.
- The model cannot account for differences in construction quality, which can affect initial roughness.
- The model can output negative PSI. An error catcher is needed so that the minimum PSI output is 0.
- Care must be taken to ensure that the data input to the model is collected according to the LTPP distress manual regulations.[87]

Using the model presented in equation 201, the model's sensitivity to the faulting, spalling, and transverse cracking input parameters was assessed. An analysis was completed to calculate how each distress influences the PSI. To reduce PSI to 2.0 from the initial 4.536, each distress was increased while the other two distresses were kept at zero. As seen in figure 52, faulting has the greatest influence on PSI, spalling next, followed by transverse cracks. PSI depends on faulting 6 times more than spalling, and almost 12 times more than transverse cracking.

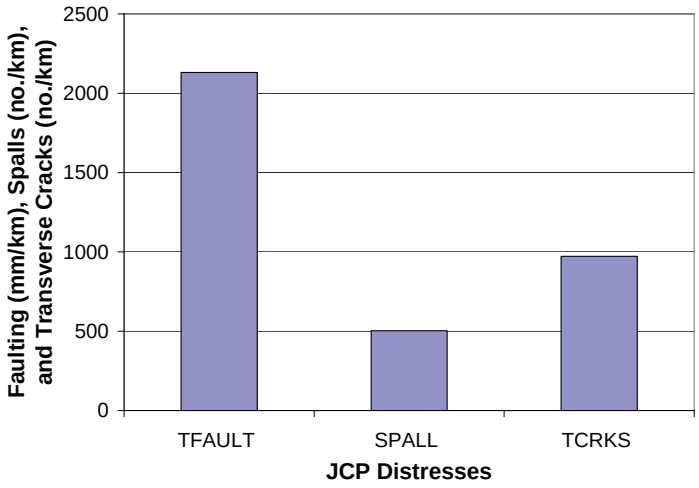

Figure 52. Amount of each individual distress required to reach a PSI of 2.0.

B.2.4.5.2 International Roughness Index

The IRI was developed at the International Road Roughness Experiment held in Brazil in 1982.[64] It is currently the standard for the FHWA Highway Performance Monitoring System database.[64] IRI describes the longitudinal surface profile in the wheel path, and it is defined as the average rectified slope (ratio of the accumulated suspension motion to the distance traveled) obtained from a mathematical model of a standard quarter car traversing a measured profile at a speed of 80 km/h. It is computed from surface elevation data collected by a topographical survey or mechanical profiler. The measurements should be calibrated to the measurement standard because roughness is sensitive to tire type, tire pressure, load, vehicle suspension system, and vehicle speed.

IRI can be estimated as a function of the PSI. Using linear regression, a contractor developed an IRI model using the LTPP GPS–3 sections. IRI is correlated to PSI as shown in equation 202.

$$IRI(m/km) = 1.0602(5 - PSI) \tag{202}$$

The r^2 is 0.76 for 3199 pavement sections. This equation only depends on PSI, so a sensitivity analysis is not needed. A plot of IRI versus PSI is shown in figure 53.

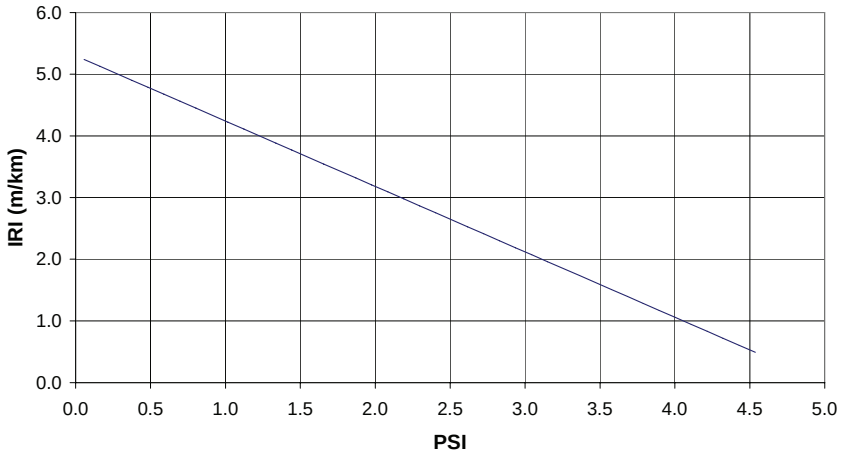

Figure 53. Shape of IRI versus PSI curve.

It may be necessary to develop a more sophisticated model that includes pavement design and location features in a later IRI calculation, as shown in equation 203.

$$IRI = (PSI, \text{Joint Spacing, Season, Location}) \tag{203}$$

The initial roughness (IRI_o) also can be incorporated into the relationship as shown in equation 204:

$$IRI = IRI_o + \Delta IRI \tag{204}$$

where,

ΔIRI = the change in *IRI* due to traffic loading and weather conditions.

B.2.4.5.3 Other IRI Relationships

Other relationships have been developed for IRI that use the JCP distress data as input. This section will compare these relationships, documented in FHWA–RD–97–147, FHWA–RD–00–130 and in the *Guide for Mechanistic Design of Pavements* developed under NCHRP study 1-37A to the one developed by the contractor, described above.[88,89,90]

B.2.4.5.3.1 FHWA–RD–97–147

For nondoweled JCP in the LTPP database, IRI is related to faulting as shown in equation 205.[88]

$$IRI\,(m/km) = 0.0098 * TFAULT + 1.268 \tag{205}$$

where,

TFAULT = total faulting (mm) per LTPP section.

This equation has an r^2 of 0.48 for 51 sections and is plotted in figure 54.

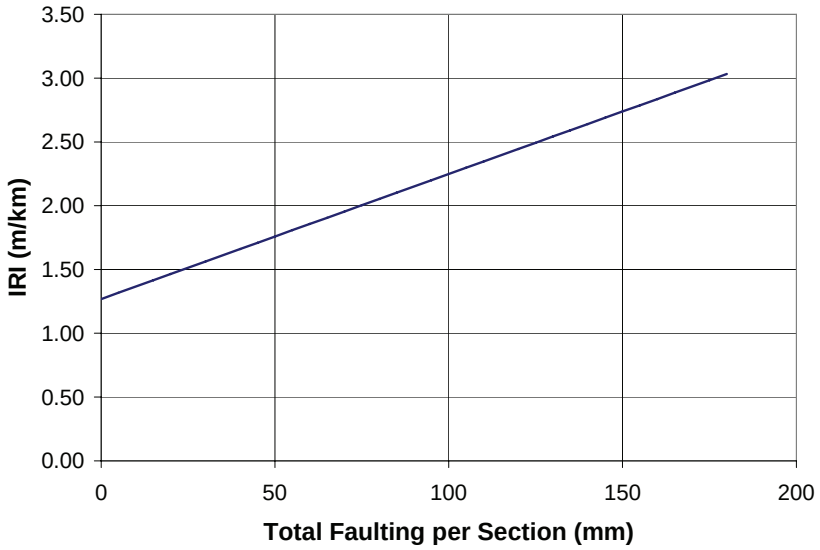

Figure 54. Effect of faulting on IRI.

B.2.4.5.3.2 FHWA–RD–00–130

This IRI model was developed to improve the prediction models for PCC pavement performance-related specifications.[89] This IRI model is based on pavement distresses and also a site parameter that accounts for climate, age, and other factors that influence IRI, as shown in equation 206.

$$IRI = IRI_0 + 0.013 * \%CRACKED + 0.007 * \%SPALL + 0.001 * TFAULT + 0.03 * SITE \quad (206)$$

where,

IRI = smoothness (m/km),
IRI_0 = initial smoothness measured as IRI (m/km),
%CRACKED = percent slabs with transverse cracking and corner cracks (all severities) (0–100 percent),
%SPALL = percent joints with spalling (medium and high severity) (0–100 percent),
TFAULT = total joint faulting cumulated per km (mm),
SITE = site factor, as shown in equation 207:

$$SITE = AGE * (1 + FI)^{1.5} * (1 + P_{0.075}) * 10^{-6} \quad (207)$$

AGE = pavement age,
FI = freezing index (°C-days), and
$P_{0.075}$ = percent subgrade material passing 0.075 mm (No. 200) sieve (0–100 percent).

The statistics for this model are $N = 183$, $r^2 = 0.70$ and SEE = 0.35 m/km. This model is compared to the others in figures 55 to 57.

B.2.4.5.3.3 1-37A Guide for Mechanistic Design of Pavements—TRB 2000 Presentation

An IRI model was presented at the 2000 TRB session for the *1-37A Guide for Mechanistic Design of Pavements*.[90] It is given in equation 208:

$$IRI = IRI_0 + 0.0337 * TransCk + 0.0083 * JtSPALL + 0.0997 * PATCH + 0.062 * CorBreak + 0.01255 * AGE + 0.001547 * TotFAULT \quad (208)$$

where,

IRI = smoothness (m/km),
IRI_0 = initial IRI (m/km),
TransCk = transverse cracking (all severities) (assumed to be 0–100 percent),
JtSPALL = percent joints with spalling (all severities) (0–100 percent),
PATCH = percent of area with flexible or rigid patching (all severities) (assumed to be 0–100 percent),
CorBreak = percent joints with corner breaks (all severities),
AGE = pavement age (years), and
TFAULT = total joint faulting (mm/km).

No information on the modeling statistics (i.e., *N* and r^2) was provided.

B.2.4.5.3.4 1–37A Guide for Mechanistic Pavement Design—TRB Presentation in 2001

In the 2001 TRB conference, the IRI (smoothness) model was modified from its past version presented at the 2000 TRB conference.[91] It more closely resembles the FHWA–RD–00–130 model, but it contains a term for patching. The general form of the equation is shown in equation in 209:

$$S(t) = S_0 + A_1 D(t)_1 + \ldots\ldots + A_n D(t)_n + B\,SF + C_j M_j \quad (209)$$

where,

$S(t)$ = pavement smoothness,
S_0 = initial IRI,
$D(t)$ = distress,
SF = site factor to address site conditions,
M = maintenance activities, and
A, B, C = regression coefficients.

The model regression coefficients are as shown in equation 210:

$$IRI = IRI_i + 0.0137\,CRK + 0.07\,SPALL + 0.005\,PATCH + 0.0015\,TFAULT + 0.04\,SF \quad (210)$$

where,

IRI = pavement smoothness (m/km),
IRI_i = initial IRI (m/km),
CRK = percent slabs with cracking (all severities transverse and corner breaks),
SPALL = percent of joints with spalling (medium and high severities),
PATCH = area with flexible or rigid patching (all severities) (m^2),
SF = site factor, as shown in equation 211:

$$SITE = AGE * (1 + FI)^{1.5} * (1 + P_{0.075}) * 10^{-6} \quad (211)$$

AGE = pavement age (years),
FI = freezing index (°C-days),
$P_{0.075}$ = percent subgrade material passing 0.075-mm sieve, and
TFAULT = total joint faulting (mm/km).

No information on the modeling statistics (i.e., *N* and r^2) was provided.

B.2.4.5.4 IRI Model Comparison

The five models are summarized below in table 38. The units and dependent variables included in the models are listed. In the following parametric studies, only the distress variables for faulting, cracking, spalling, patching, and the initial IRI_0 will be examined. The other variables will be held constant.

Table 38. Comparison between IRI models.

IRI Models	FHWA–RD–97–147	FHWA–RD–00–130	1–37A Guide (2000 TRB)	1–37A Guide (2001 TRB)	Contractor
Units	inches/mi	m/km	m/km	m/km	m/km and inches/mi
Initial IRI: IRI_0	Constant	Variable	Variable	Variable	Constant
Distress Variables	TFAULT	TFAULT	TFAULT	TFAULT	TFAULT
	–	Spalls	Spalls	Spalls	Spalls
	–	Cracks	Cracks	Cracks	Cracks
	–	–	Corner Breaks	–	–
	–	–	PATCH	PATCH	–
Other Variables	–	AGE	AGE	AGE	–
	–	FI	–	FI	–
	–	$P_{0.075}$	–	$P_{0.075}$	–

To perform the comparison, control variables for the models have been chosen. Because model FHWA–RD–97–147 only has a faulting term, faulting will first be varied in all four models between 0 to 1200 mm. For both the FHWA–RD–00–130 and 1–37A models, IRI_0 of 0.5 m/km is assumed, as is AGE of 10 years. Likewise, a freezing index of 300 °C-days and percent subgrade materials passing the No. 200 sieve of 40 percent are assumed. These are the control variables used in the model reference.[89] To convert the number of distresses per mile in the contractor's model to a percentage, an average joint

spacing of 5.1 m is used. This is the average joint spacing for all the GPS–3 sections in the LTPP database. The comparison is shown graphically in figure 55.

As can be seen in figure 55, the slope of the IRI versus faulting models tend to be similar for all the prediction equations. One of the major distinctions is the high initial IRI_0 of the FHWA–RD–97–147 model. The FHWA–RD–00–130 model and the contractor's model are very similar, as are the two 1–37A models.

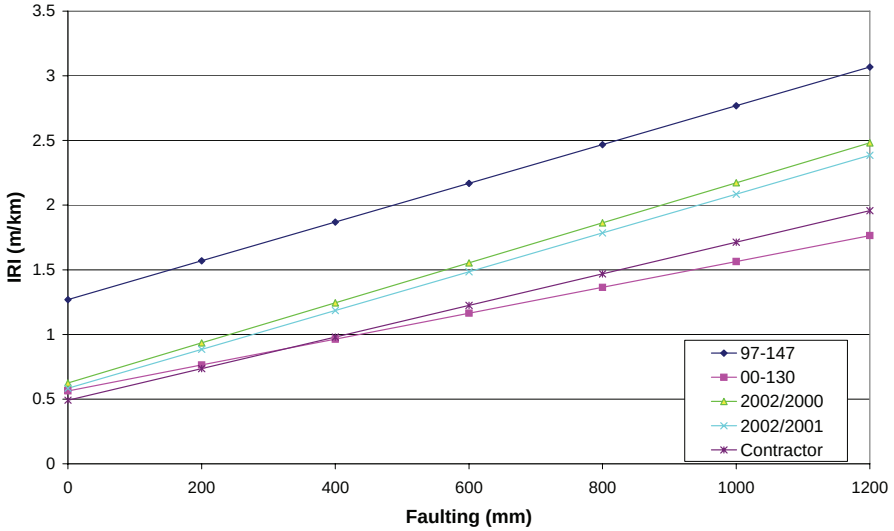

Figure 55. Comparison of faulting influence between the various IRI models.

Now the influence of cracking and spalling will be assessed using the IRI models. The FHWA–RD–97–147 model will not be included because it is dependent only on faulting. By varying the percent cracking between 0 percent and 100 percent, the plots for IRI versus percent cracking can be produced (figure 56). Similarly, the influence of spalling will be assessed; this is shown in figure 57. For both of these plots, the level of faulting is assumed to be 600 mm.

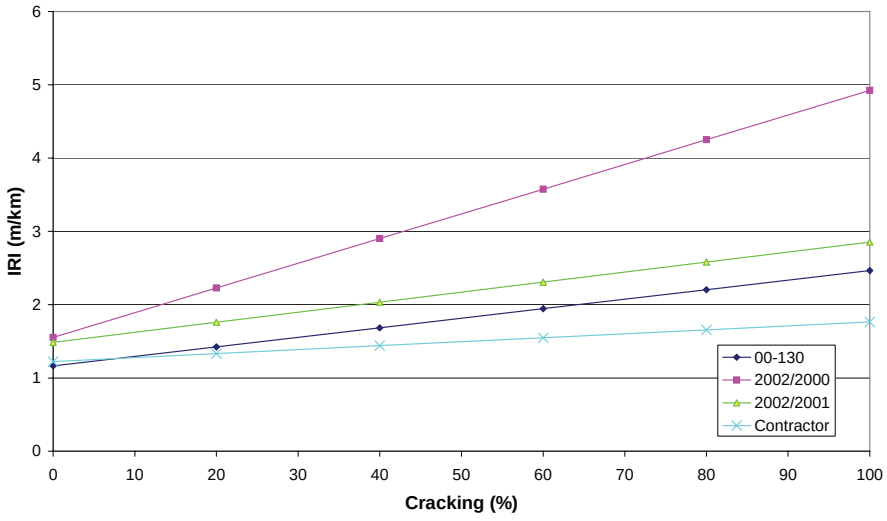

Figure 56. Effect of percent cracked slabs on FHWA–RD–00–130, 1–37A Guide, and contractor IRI models.

Increasing percent cracked slabs in figure 56 causes a marked increase in IRI according to the 1–37A model presented in 2000 at TRB. Its effect on the other three models is not as severe.

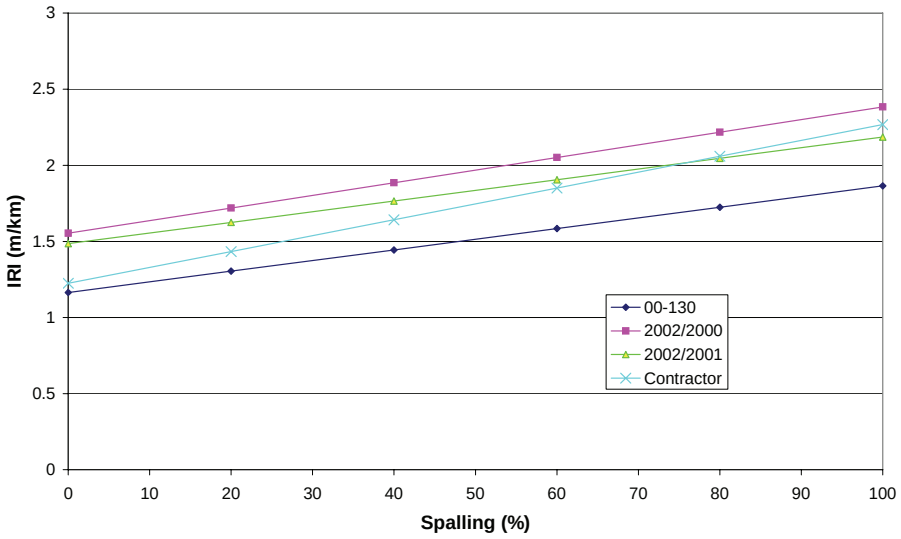

Figure 57. Effect of percent spalling on FHWA–RD–00–130, 1–37A Guide, and contractor IRI models.

Increasing the percent spalling causes a slight increase in IRI for all four models. The slopes of the FHWA–RD–00–130 and 1–37A IRI models are approximately the same.

Patching is only a factor in the 1–37A models. The other models do not account for it. Its influence on IRI is shown below in figure 58. The 1–37A model presented in 2000 is more sensitive to patching than is the one presented in 2001.

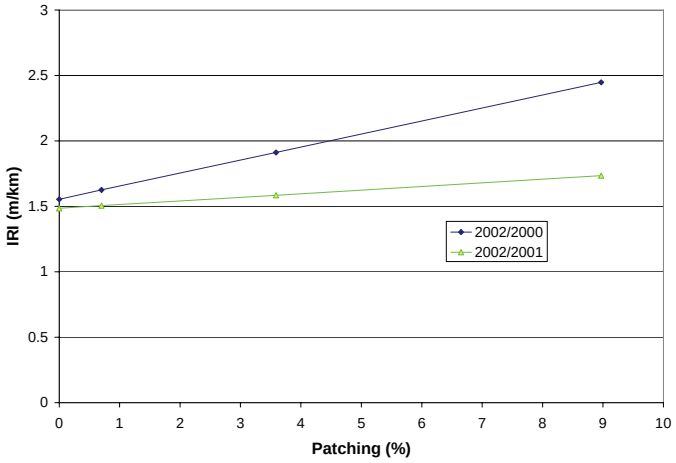

Figure 58. Effect of percent patching on IRI for the 1–37A models.

To assess the influence of initial roughness on the IRI models, IRI_0 is varied in the FHWA–RD–00–130 and 1–37A models in figure 59. It is apparent that the slopes of all the models are the same. This is expected because IRI_0 is an additive term. The contractor model cannot account for initial IRI, but it can be modified to do so in the future. In these modeling predictions, percent spalling and cracking are assumed to be 30 percent, and faulting is assumed to be 600 mm.

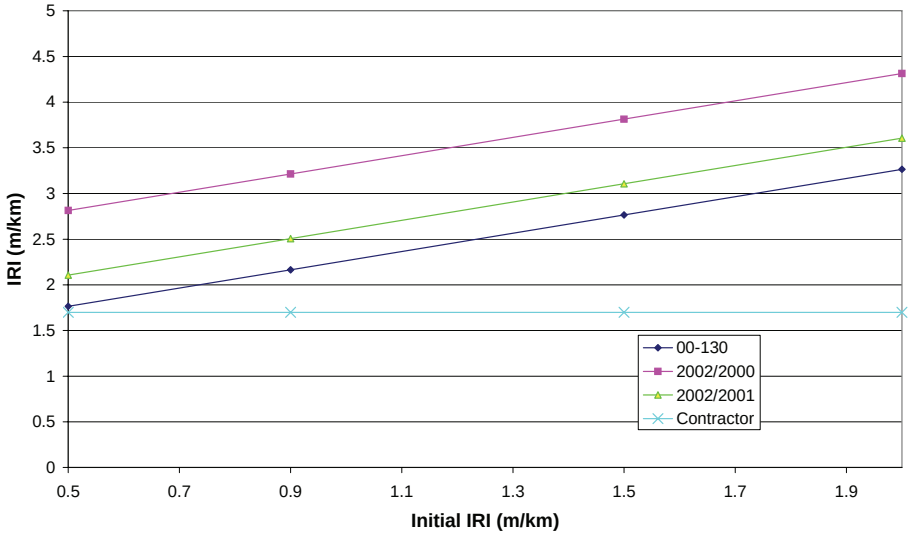

Figure 59. Effect of initial IRI_0 on FHWA–RD–00–130, 1–37A, and contractor IRI models.

It appears, based on the parametric analysis, that the FHWA–RD–00–130 and the 1–37A models are the most versatile. They account for the pavement distresses and also allow for an initial roughness (IRI_0). The simpler model by the contractor does not include an initial IRI_0 term. The two models that are the most similar are the FHWA–RD–00–130 model and the 1–37A model presented in 2001. Because documentation on the development of the latter model was scarce when the HIPERPAV II was developed, the IRI model described in FHWA–RD–00–130 was incorporated into HIPERPAV II for its versatility and validation.

B.2.5 Long-Term JPCP Model Assumptions and Limitations

The long-term JPCP module of the HIPERPAV II system was developed to optimize early-age strategies based on how they perform in the long term. With this objective in mind, two early-age strategies can be analyzed in the long term under the same long-term environmental and traffic conditions.

Accurate predictions of long-term performance require accurate and detailed information on pavement structural factors, materials characterization, environmental conditions, and traffic data. Because the HIPERPAV II long-term module is intended to help the user optimize early-age strategies rather than serve as a tool for pavement design, a number of considerations were made to simplify the data entry.

B.2.5.1 Pavement Support

No long-term input of seasonal adjustment factors for the *k*-value is required. The *k*-value used in the long-term module is the *k*-value input from the early-age analysis. This *k*-value represents the subgrade support conditions during construction. The *k*-value varies seasonally as a function of soil moisture and temperature, among other factors, and this may have a significant effect on pavement performance.

Loss of support is an important factor that affects the performance of the pavement. Loss of support depends highly on the erodibility of the subbase materials, presence of water, slab deflection, and magnitude and amount of traffic loads.[64] Available loss of support (pumping) models have limited applicability to mechanistic models such as the one used in HIPERPAV II to predict midslab cracking. For example, pumping models developed during the AASHO road test account for subbase materials highly susceptible to erosion and are thus not currently used. COPES models do not consider the subbase type as a factor.[64] Given the lack of a sound loss-of-support model, and considering that the HIPERPAV II long-term analyses are made to compare early-age factors, no loss-of-support model was incorporated. It is therefore important to emphasize that the effect of the structural support provided by the subbase must be evaluated with a pavement design procedure such as the one developed by the NCHRP 1–37A study.

Also, to minimize the number of inputs, no input for soil type is required. The soil type input required for the faulting prediction model has been hard coded to AASHTO classification A–2–6. Although the effect of soil type on faulting prediction for JPCP with no dowels is minimal, a significant effect on the faulting prediction for JPCP with dowels is observed. Given that the comparisons of early-age strategies are made under the same conditions of LTE in the long term, the results of the comparative analysis should be unaffected by this factor.

B.2.5.2 Structural Response

Loading position for analysis of longitudinal cracking is assumed at midslab along the transverse joint as required by the Westergaard stress model. No stress adjustment is made to account for the fact that the loading position rather than at midslab occurs at the wheel path.

No lift-off of the concrete slab from the subbase due to curling is considered, and the bond between the PCC slab and subbase layer is not taken into account.

B.2.5.3 Drainage

The model that is used to predict average monthly moisture content in the pavement layers underneath the slab is rather simplistic. This model uses site-dependent climatic conditions, soil data, and some pavement geometry, but does not consider information on the drainage system.

The faulting prediction models require input on whether edge subdrains are used. The condition for no subdrains is hard coded for this model.

B.2.5.4 Traffic

Input of accurate load spectra information requires of significant data entry time. To ease entry of traffic inputs, a number of assumptions are made:

- Daily and seasonal distributions are hard coded to be constant (no daily or seasonal variations in traffic are considered).
- Conversion from ESALs to traffic load spectra is based on findings from the NCHRP 1–37A study.[92] Load spectra is backcalculated based on an average load distribution per axle type. The percentage of single, tandem, and tridem axles is based on a weighted average of axles per truck for an average vehicle class distribution on rural and urban highways.

Early-age strategies are compared under the same traffic conditions in the long term. Therefore, it is assumed that the effect of traffic distribution on these comparisons is minimal.

B.2.5.5 Distress Models

A spalling model was not included in the long-term prediction module because of the complexity required to account for all possible factors that affect spalling distress. These include the moisture state in the pavement slab, concrete evaporation, sawcutting procedures, and dowel bearing stresses, among other factors.

Because no spalling distresses are predicted, serviceability and IRI may be underpredicted, as they are a function of the level of distresses present.

B.3 CRCP EARLY-AGE MODELS

The selected model for prediction of CRCP early-age behavior in HIPERPAV II is the CRCP–8 model developed by the CTR of the University of Texas at Austin, TX. CRCP–8 is a mechanistic model based on equilibrium of internal forces in the reinforced concrete for predicting concrete and steel stresses as a function of the concrete mechanical properties, temperature development, and restraint imposed by the subbase and the steel. Similar to the JPCP module in HIPERPAV II, stresses in the concrete are compared to the strength development at any time step for prediction of crack formation.

B.3.1 CRCP Stress Prediction

Figure 60 shows a schematic representation of the one-dimensional model for analysis of concrete and steel stresses in a CRCP basic analysis unit bounded by two adjacent transverse cracks and longitudinal joints.[93]

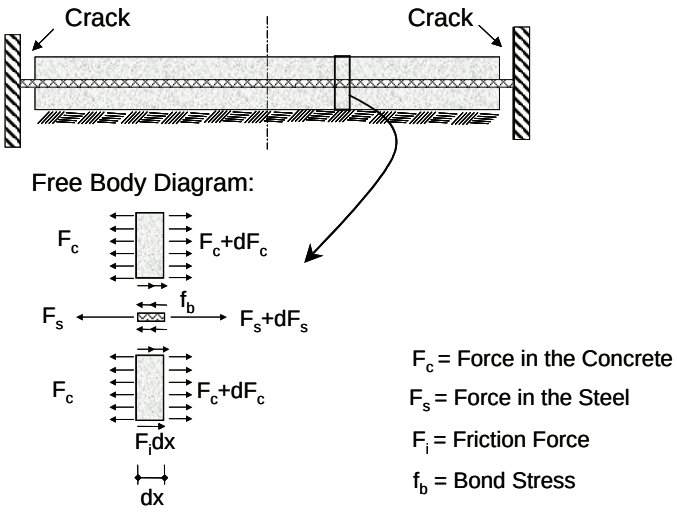

Figure 60. Schematic representation of analysis of concrete and steel stresses in CRCP–8.

The complete model derivation is described in detail in reference 93; only the primary governing equations are presented here. For derivation of the governing equations of the CRCP system, a number of assumptions are made:

- Concrete and steel properties are linearly elastic.
- Temperature variations and drying shrinkage are uniformly distributed throughout the slab depth.
- Friction at the slab-subbase interface is considered elastic.
- The effect of creep and warping are neglected.

Since concrete stress is zero at cracks, considering that the steel stresses that develop at the crack location must be in equilibrium with the subbase restraint and the stresses in the concrete at any point in the slab, the following relationship is derived in equation 212:[93]

$$\sigma_{sx} + \frac{\sigma_{cx}}{p_s} - \sigma_{sc} - \frac{\int_x^L F_i dx}{p_s D} = 0 \tag{212}$$

where,

x = coordinate distance from midslab,
σ_{sx} = stress in the steel at location x,
σ_{cx} = stress in the concrete at location x,
p_s = ratio of cross sectional area of steel (A_s) to area of concrete (A_c),
σ_{sc} = stress in the steel at a crack,
L = one-half of the slab segment length,
F_i = friction force per unit length along the slab, and
D = thickness of the concrete slab.

Equation 213 is used to determine the stresses in the concrete at any location along the slab.

$$\sigma_{cx} = \frac{\sigma_{sx}}{n} + E_c\left[(\alpha_c - \alpha_s)\Delta T + \varepsilon_{sh}\right] \tag{213}$$

where,

E_c = modulus of elasticity of the concrete,
n = E_c/E_s,
E_s = modulus of elasticity of the steel,
α_c = thermal coefficient of expansion of the concrete,
α_s = thermal coefficient of expansion of the steel,
ΔT = temperature change, and
ε_{sh} = drying shrinkage of the concrete.

Steel stress at the crack is determined as shown in equation 214:

$$\sigma_{sc} = \left(1 + \frac{1}{np_s}\right)\sigma_{sx} + \frac{Ec}{p_s}\left[(\alpha_c - \alpha_s)\Delta T + \varepsilon_{sh}\right] - \frac{\int_x^L F_i dx}{p_s D} \tag{214}$$

with terms as previously defined.

Depending on the relative displacements between the steel and the concrete, two zones are identified: 1) a fully bonded zone at the middle of the geometric model where concrete and steel displacement are zero, and 2) a bond development zone, in proximity to the cracks, where steel displacement is zero, but concrete displacement occurs, and is a function of the material properties and environmental conditions. With the above conditions, for the fully bonded zone, the rate of steel and concrete stress is primarily a function of subbase restraint as shown in equations 215 and 216. For the bond development zone, the rate of steel and concrete stress is primarily a function of the bond stress as shown in equations 217 and 218.

$$\frac{d\sigma_{sx}}{dx} = \frac{-F_i}{D\left(p_s - \frac{1}{n}\right)} \tag{215}$$

$$\frac{d\sigma_{cx}}{dx} = \frac{-F_i}{nD\left(p_s + \frac{1}{n}\right)} \tag{216}$$

$$\frac{d\sigma_{sx}}{dx} = \frac{4 f_b(x)}{\phi} \tag{217}$$

where,

$f_b(x)$ = bond stress at location x along the steel-concrete interface and
ϕ = diameter of steel bar.

$$\frac{d\sigma_{cx}}{dx} = -\frac{4 f_b(x) p_s}{\phi} - \frac{F_i}{D} \tag{218}$$

To solve the above system of equations, it is necessary to define a boundary condition for the steel stress at the crack location. It is assumed that the steel stress at cracks is the same regardless of the slab length. The steel stress is determined for a slab length with a mean crack spacing, X_{bar}, as shown in equation 219:

$$\int_0^X \sigma_{sx} dx = E_s \cdot \alpha_s \cdot \Delta T \cdot X_{bar} \tag{219}$$

In addition to the above boundary condition, relationships for the bond stress and bond development length are derived as a function of the steel stress at the crack location. A simplified coordinate system with origin at the location where bond slippage begins is used, as shown in figure 61, to derive the bond stress and bond development length relationships in equations 220–222.

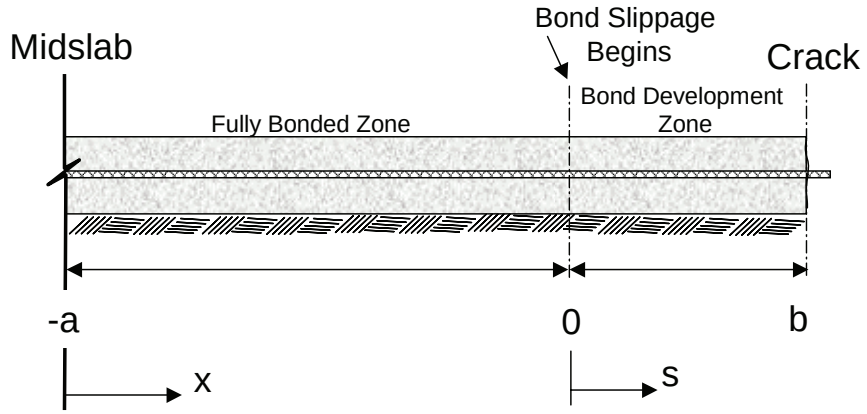

Figure 61. Simplified coordinate system for development of bond stress distribution functions.

$$f_b(s) = Kw(s) + Cs^2 + D + E\cos\left(\frac{\pi s}{2b}\right) \tag{220}$$

where,

s = coordinate distance from the location where bond slippage begins,
K = bond stiffness (bond stress per unit slip),
$W(s)$ = bond slip at location s,
C,D,E = constants that are functions of the boundary conditions (derived in reference 93), and
b = bond development length.

$$w(s) = Ae^{\frac{cs}{b}} + Be^{\frac{-cs}{b}} - \frac{1}{K}\left(Cs^2 + \frac{2C}{\alpha K} + D\right) - \frac{\alpha E}{\alpha K + \frac{\pi^2}{4b^2}}\cos\left(\frac{\pi s}{2b}\right) - \frac{\beta(s+a)}{\alpha K} \tag{221}$$

where,

c = $b(aK)^{0.5}$,
β = $\theta/(EcD)$,
θ = slope of the subbase frictional stress distribution,
A = constant that is a function of the boundary conditions (derived in reference 93), and
a = distance from the location where bond slippage begins to midslab.

$$-\frac{4}{\phi}\int_{-a}^{b}\int_{x}^{b} f_b(s)dsdx = \sigma_{sc}L - E_s\alpha_s\Delta TL \tag{222}$$

A second relationship between the steel stress at a crack and the bond development length is derived as shown in equations 223–225:

$$b = \frac{\phi}{4(266)}\left[\sigma_{sc}\left(1-\frac{1}{C_1}\right)+\left(\frac{C_2}{C_1}-\frac{\int_{-a}^{b}F_i dx}{p_s D C_1}+\frac{\int_{-a}^{0}F_i dx}{D\left(p_s+\frac{1}{n}\right)}\right)\right] \tag{223}$$

where,

$$C_1 = 1+\frac{1}{np_s} \tag{224}$$

$$C_2 = \frac{E_c}{p_s}\left[(\alpha_c-\alpha_s)\Delta T+\varepsilon_{sh}\right] \tag{225}$$

An iterative process is used to solve equations 222 and 223 that provides the same bond development length for a given σ_{sc}. With the bond development length and steel stress at the crack, concrete and steel stresses along the slab length are computed with the above relationships for both the fully bonded zone and the bond development zone. Initially, no subbase restraint is assumed, and an iterative process is used to solve for it. The subbase restraint stress distribution is approximated by a linear function of the distance from midslab.

B.3.2 CRCP Strength Prediction

In CRCP–8, the Monte Carlo method is used to simulate the PCC strength variability. By assuming a normal distribution for the PCC tensile strength, the Monte Carlo method is used to probabilistically assign different values of tensile strength along the pavement length. A comparison of the concrete stress and the simulated concrete tensile strength at any point is performed for prediction of crack formation. In this fashion, crack spacing is predicted with an inherent variability.[93]

As an enhancement to the CRCP–8 model, in this study, similar to the strength prediction for JPCP, the maturity method is used in the CRCP HIPERPAV II module to predict the early-age strength.

B.3.3 CRCP Temperature Prediction

In CRCP–8, the minimum and maximum PCC temperatures are an input for the days after construction until concrete reaches full strength (assumed to be 28 days) and for the coldest time of the year. As an enhancement to the CRCP–8 model, in this study the required PCC temperatures are predicted with the finite-difference temperature model described in section B.1.2.

B.3.4 CRCP Model Limitations

The CRCP model used in HIPERPAV II is a one-dimensional mechanistic model with the following limitations:

- No curling effects are considered. Although it has been hypothesized that, due to the short slab lengths in CRCP, curling is not a significant factor, new findings suggest that curling may lead to horizontal cracking due to the restraint imposed by the steel.
- The CRCP model does not account for creep-relaxation effects. Although creep-relaxation models are used in HIPERPAV for JPCP, no attempt to include this model in the CRCP module was made, because this could nullify the previous validation efforts made to this model.
- Because of the one-dimensional characteristics of the CRCP model, the steel is assumed to be at middepth. The effect of bar mats at different depths cannot be modeled.
- As identified from the validation results, the bond-slip relationships used have limited validity and may not predict properly the transfer of stresses from the concrete to the steel, possibly affecting the crack width predictions.
- Time of crack formation is not taken into account. This factor is believed to be of significant importance in determining crack width properly, since crack width is a function of the drying shrinkage and relaxation characteristics after cracks occur, among other factors.

B.4 MODELS USED IN THE COMET MODULE

Selection of the FHWA mix optimization study was described in Volume I of this report series. This study was incorporated in the HIPERAPV II system in the form of a module termed Concrete Optimization, Management, Engineering, and Testing (COMET). COMET is a simplified derivation of the Concrete Optimization Software Tool (COST) software originally developed by FHWA and the National Institute of Standards and Technology. A two-stage analysis process is involved.

Stage I: Trial Batches

A limited number of factors (or decision variables) are determined by providing bound values and a midpoint value. Specific gravity and unit cost of the constituents (e.g., cement, admixture, aggregate) are defined by the user. Desirability curves for responses or objective functions (e.g., cost, 28-day strength) are defined.

Trial batches, whose number is based on the number of factors plus replicates, then are generated. The predicted responses are obtained from default predictive models. However, the predicted responses may be overwritten using actual trial batch test results.

Stage II: Virtual Batches

A full quadratic model is fitted for each response based on the responses from the trial batches. Virtual mixes are then generated using a finer grid (i.e., adding more combinations within the operability region of the variable space). The responses of virtual mixes are subsequently predicted by the fitted quadratic models. Scores for all virtual mixes are calculated and ranked. The top *N* virtual mixes are then recommended as optimized mixes, where *N* is defined by the user.

B.4.1 Comments on COMET Features and Implementations

Since COMET is a simplified version of the FHWA COST software, its usability is enhanced while hiding the inherent complexity of the analysis. (See references 94, 95, 96, and 97.) This is not to deter users who have limited statistical backgrounds. However, flexibility and detailed statistical reports for all analysis stages are not available, nor is the more robust analysis that is provided by COST.

COMET uses FORTRAN in the back-end coding while it uses Microsoft® Visual Basic®/HTML in the front-end coding. COMET uses four fixed factors: percent coarse aggregate of total aggregate weight, cementitious content, percent pozzolan of total cementitious, and w/c. COMET uses three fixed responses: cost, early-age strength, and 28-day strength. Property desirability curves (with six data points) are user-defined for each response.

Face-centered design methodology is used to generate 29 trial mixes based on equation 226:

$$NB = 2^k + 2 \times k + x = FP + AP + CP \tag{226}$$

where,

k	= number of factors (four in this case),
x	= number of centerpoints (five in this case),
NB	= number of trial batches,
AP	= number of axial points,
CP	= number of central points, and
FP	= number of factorial points.

The trial batches may be increased if number of factors is increased. The current version of COMET utilizes eight evenly spaced design points between the limits of each factor. This generates a combination of 4096 virtual mixes (i.e., 8^4). A full quadratic model is used in model fitting. Fifteen terms are contained in this model. The 29 face-centered design points are used for model fitting, with predicted responses calculated for each of the 4096 points.

The central composite design (CCD) is a very efficient experiment design technique to fit second-order response models. It uses a two-level factorial or fraction combined with axial and centerpoints. The factorial points describe "a variance-optimal design for a first-order model or a first-order + two-factor interaction model".[98] (p. 322) The centerpoints capture the curvature in the system. If curvature exists, axial points will help in the approximation of quadratic terms efficiently. In summary, CCD is very efficient at providing information on variable effects and overall experimental error while minimizing the number of required runs.

B.4.2 Concrete Compressive Strength Model

To calculate concrete compressive strength as a function of w/c, Abrams' equation is used.[61] The most basic form of this equation (equation 227) relates compressive strength directly to w/c.

$$f_c = \frac{A_A}{B_A^{w/c}} + C_A \tag{227}$$

where,

f_c = compressive strength, in KPa,
w/c = water-to-cement ratio, and
A_A, B_A, and C_A = empirical coefficients that are independent of strength and w/c. C_A commonly is set to zero.

The empirical coefficients depend on the units, materials, test method used, age of testing, and the conditions of validity for Abrams' rule. Abrams' rule states that:

- Compressive strengths are lower with higher w/c's,
- Compressive strengths are higher with lower w/c's, and
- Compressive strengths are identical with the same w/c.

The strengths of comparable concrete depend solely on their w/c's regardless of their compositions. Abrams' rule is valid, provided that the following 10 assumptions hold:

1. The strength-developing capabilities of the cements used are identical.
2. The quantities and strength influencing effects of the admixtures used are identical.
3. The concrete specimens are prepared, cured, and tested under the same conditions.
4. The concrete ingredients are distributed evenly.
5. Air contents are the same, air voids are distributed uniformly, and none of the voids are too large for the specimen size.
6. Aggregate particles are stronger than the matrix.
7. The bonds between aggregate surfaces and the matrix are strong. The bond can transfer the stresses to the aggregate before loading crushes the matrix.
8. The strength affecting physical and chemical processes (drying, aggregate reactivity) are the same and are not overwhelming (hydration).
9. The composite nature of the concrete affects the strength of the compared concretes to the same extent.
10. The contribution of the aggregate skeleton is the same in the various concretes.

B.4.3 Development of the Compressive Strength Prediction Model Based on Mix Design

The compressive strength prediction model formulated for COMET must account for the influence of w/c, pozzolans, and aggregate contents, in addition to concrete age. The relationships between these inputs and compressive strength are listed below.

B.4.3.1 Effect of Water-to-Cement Ratio

A basic model for compressive strength at 28 days is given in equation 228: [61]

$$f_c\big|_{28-day}(ksi) = \frac{27.122}{23.07^{w/c}} \tag{228}$$

(1 ksi = 6.89 MPa)

An augmented model, which accounts directly for cement content, is given in equation 229:[61]

$$f_c\big|_{28-Day}(ksi) = \frac{51{,}290}{23.66^{w/c+0.000378c}} \tag{229}$$

where,

c = cement content in pcy (1 lb/yd^3 = 0.594 kg/m^3).

Figure 62 compares these two models. At low w/c's (w/c < 0.3), the compressive strength continues to increase according to the basic model. This relationship would be correct for fully compacted concrete, but at lower w/c's, it is difficult to achieve full compaction.[13] The augmented model, used in COMET, provides a more reasonable prediction of compressive strength.

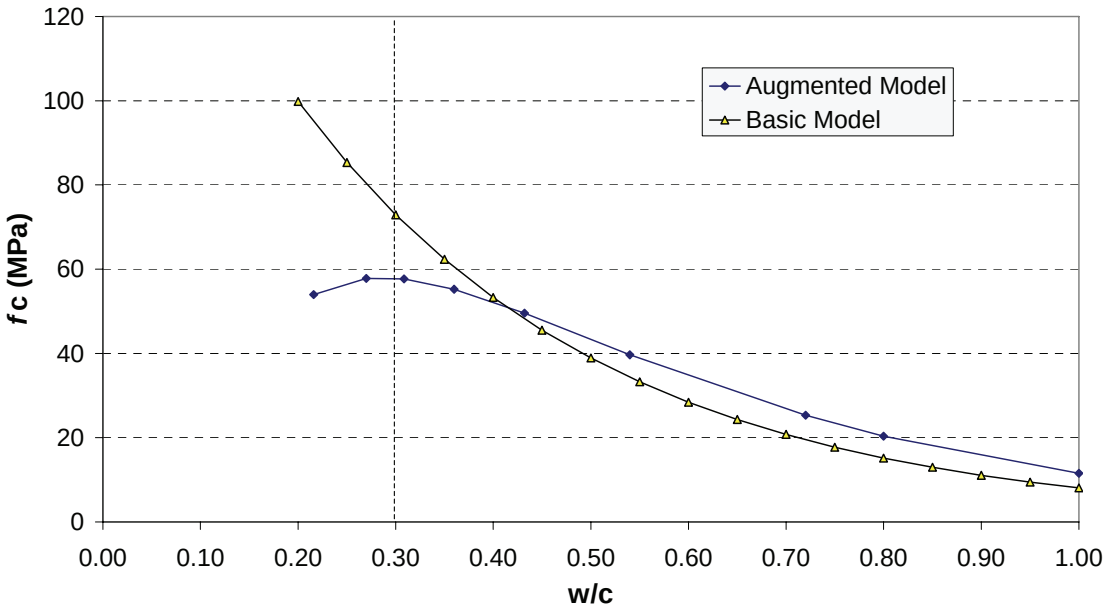

Figure 62. Compressive strength as a function of w/c and cement content.

B.4.4 Relative Strength

When investigating the effect of fly ash and age on the concrete's compressive strength, the relative change in strength (f_{rel}) can be calculated within the limits of Abrams' rule (equation 230).

$$f_{rel} = \frac{f}{f_1} = \frac{A_A}{A_{A_1}} \times \frac{B_{A_1}^{w/c_1}}{B_A^{w/c}} \tag{230}$$

where,

concrete strength f is related to w/c and
concrete strength f_1 is related to w/c_1.

Assuming $A_A = A_{A1}$, equation 231 follows:

$$f_{rel} = \frac{B_{A_1}^{w/c_1}}{B_A^{w/c}} = Ratio \tag{231}$$

B.4.4.1 Effect of Pozzolans

Abrams' rule is valid for blended cements. When a portion of the cement has been replaced by fly ash, the following approximation of B_A has been derived in equation 232.

$$B_A = 5.5 \times 6.3^{p/c} + 6 \tag{232}$$

where,

c = mass of cement and
p = mass of fly ash that has been added to the cement.

To use this equation to predict the 28-day compressive strength of concrete, the w/cm of $w/(c + p)$ applies. Also, it is only applicable for the range of $p/c = 0$ to 1. Although there is not a similar relationship for concretes containing silica fume, it is likely that Abrams' rule is still valid. Its effect on B_A has yet to be developed.

B.4.4.2 Effect of Age

It is also possible to relate the 28-day compressive strength to its early-age values at a specific time t using Abrams' rule. As given in Popovics:[61]

For Type I cement (equation 233):

$$B_A = \frac{46}{t} + 6 \tag{233}$$

For Type III cement (equation 234):

$$B_A = \frac{27}{t} + 6 \tag{234}$$

This hyperbolic function approximates the strength gain of the concrete well within the limits of 3 days and 1 year. The values, however, are too low at 1 day.

B.4.4.3 Effect of Aggregate Content

To develop the relationship between compressive strength and aggregate content, the importance of aggregate gradation was recognized. According to Gilkey, concrete strength is influenced by: 1) the ratio of cement to mixing water, 2) the ratio of cement to aggregate, 3) grading, surface texture, shape, strength and stiffness of aggregate particles, and 4) maximum size of the aggregate.[61] For concretes with identical w/c's, the compressive strength increases as the maximum particle size decreases.

The following ratio (equation 235) was developed to account for the effect of aggregate:

$$Ratio_{Aggregate} = \left(\frac{FA}{CA}\right)^{0.17} \tag{235}$$

where,

FA = fine aggregate content and
CA = coarse aggregate content.

Equation 235 was calibrated using the data provided by Ganju.[99]

B.4.5 Compressive Strength Prediction Model

Combining the effects of w/c, pozzolan content, aggregate content, and age on compressive strength yields the relationship shown in equation 236:

$$f_c' = Ratio_{Age} \times Ratio_{Pozzolan} \times Ratio_{Aggregate} \times f_c \tag{236}$$

where,

f'_c = compressive strength that includes the effects of age, pozzolan content, and aggregate content,
f_c = compressive strength calculated using only the w/c,
$Ratio_{Age}$ = factor that incorporates the influence of time on the compressive strength,
$Ratio_{Pozzolan}$ = factor that includes the effect of pozzolan content on compressive strength, and
$Ratio_{Aggregate}$ = factor that accounts for aggregate content on compressive strength.

This relationship is used in COMET to predict concrete compressive strength.

Limitations of this equation are:

- It is only valid for normal weight concrete in the ranges for which it was calibrated. Notably, w/c ranges from 0.3 to 1.0. Compressive strength ranges from 0 to 82.7 MPa.[61]
- The only pozzolan for which it is calibrated is fly ash.
- To account for the effect of pozzolan and age on compressive strength, it is assumed that A_A and A_{A1} values in Abrams' formulation are the same.
- It is assumed that all 10 conditions required to apply Abrams' rule hold.

B.5 MODELS USED IN THE HIPERPAV DOWEL-CONCRETE INTERACTION ANALYSIS MODULE

Dowel bars are subjected to combined environmental loading and dynamic traffic loading at the joint during the pavement's lifetime. The dowel bar module in HIPERPAV assesses how the dowel bars affect the early-age performance of JPCP. If the bearing stress is greater than the concrete's early-age compressive strength, then it is probable that the dowel will loosen over the lifetime of the pavement at a faster rate than if the bearing stress is less than the concrete's compressive strength. The model that predicts the early-age dowel bar bearing stress is summarized below.

B.5.1 Dowel Bar Bearing Stress Model

To calculate the dowel bar bearing stress, several inputs are needed in the model. These inputs are listed in table 39.

Table 39. Input to the dowel bar bearing stress model.

Input Category	Parameter	Units	Variable
Dowel bar	Diameter	m	d_D
	Poisson ratio	Unitless	ν_D
	Modulus	MPa	E_D
	Effective modulus of dowel support	MPa/m	K_D
Joint	Opening	MPa	w
Slab	Modulus	MPa	E_c
	Poisson ratio	Unitless	ν_c
	CTE	m/m/ºC	α_c
	Length	m	L
	Thickness	m	h
Load and support	Linear temperature gradient	ºC/m	ΔT
	Slab support reaction modulus	MPa/m	k

For the system, the radius of relative stiffness is calculated in equation 237:

$$\ell = \left[\frac{E_c h^3}{12\left(1-\nu_c{}^2\right)k} \right]^{0.25} \quad (237)$$

as are the dowel moment of inertia, I_D, in equation 238:

$$I_D = \frac{1}{64}\pi d_D^{\,4} \tag{238}$$

and the relative stiffness of the dowel-concrete system, β. Equations 237–239 can be found in Huang.[64]

$$\beta = \sqrt[4]{\frac{K_D d_D}{4E_D I_D}} \tag{239}$$

A dowel at the joint is subjected to moments M_o, as shown in figure 63.

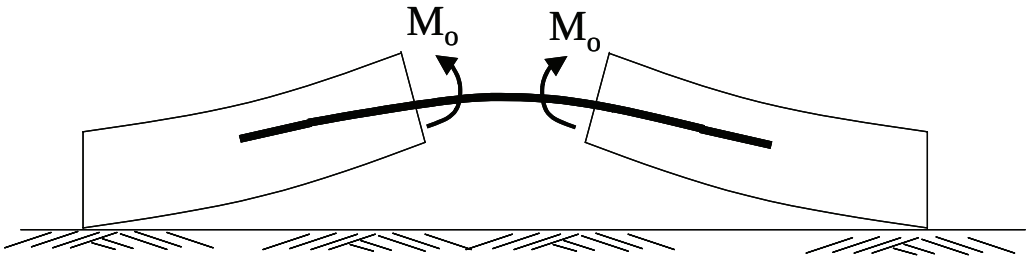

Figure 63. Schematic of dowel deformation and loading at the joint.

To model the behavior of the dowel at the joint, some assumptions are made. Two cases are shown in figure 64. In the first case, the gray dowel depicts behavior at the joint, assuming that the concrete underneath it does not deform, or that there is no concrete compliance. In the second case, the concrete has deformed under the black dowel.

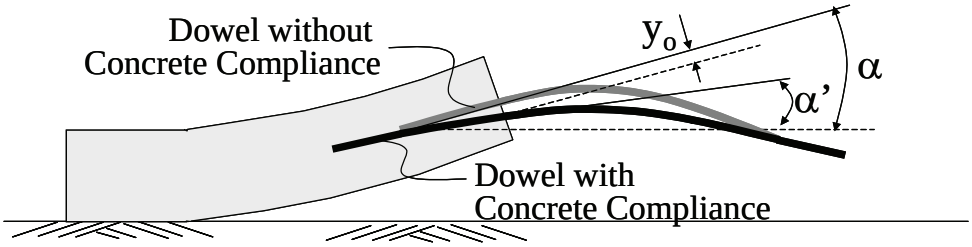

Figure 64. Schematic of dowel deformation without concrete compliance and with concrete compliance at the joint.

To relate the angles of the dowels as they leave the concrete to the deflection of the dowel at the slab face, y_o, the relationship in equation 240 is used:

$$\tan(\alpha - \alpha') = \frac{dy_o}{dx} \tag{240}$$

where,

α = slope of the dowel without concrete compliance,
α' = slope of the dowel with concrete compliance, and
y_o = deflection of the dowel at the slab face.

According to Timoshenko and Lessels, and as reported by Friberg, the deflection of the dowel at the slab face $y_o|_{x=0}$ when it is subjected to a moment is as shown in equation 241:[66,100]

$$y_o\big|_{x=0} = \left[\frac{-M_o e^{-\beta x}}{2\beta^2 E_d I_d}(\cos\beta x - \sin\beta x)\right]\Bigg|_{x=0} = \frac{-M_o}{2\beta^2 E_d I_d} \tag{241}$$

From Westergaard, the slope of the dowel without concrete compliance can be calculated. Westergaard solved for the deflection of a curled pavement, z.[101] Adjusted for the coordinate system presented here, it is shown in equation 242:

$$z = -z_o \frac{2\cos\lambda\cosh\lambda}{\sin 2\lambda - \sinh 2\lambda}\left[(-\tan\lambda + \tanh\lambda)\cos V\cosh V + (\tan\lambda + \tanh\lambda)\sin V\sinh V\right] \tag{242}$$

where, as defined in equations 243–246,

$$\lambda = \frac{L}{\sqrt{8}\ell} \tag{243}$$

$$z_o = (1 + \nu_c)\cdot\alpha_c\cdot\nabla T\cdot\ell^2, \tag{244}$$

$$V = \frac{x_{coord}}{\sqrt{2}\ell} \tag{245}$$

$$x_{coord} = \frac{-L}{2} \tag{246}$$

Taking the differential of the deflection with respect to x yields the slope. With the small angle assumption, the slope of the dowel approximates the angle of the dowel, α, under deformation when it leaves the slab (equation 247):

$$\alpha = \frac{-1}{\sqrt{2}\ell} \cdot z_o \cdot \frac{2\cos\lambda\cosh\lambda}{\sin 2\lambda - \sinh 2\lambda} \cdot \begin{pmatrix} [-\tan\lambda + \tanh\lambda] \cdot [-\sin V \cdot \cosh V + \cos V \cdot \sinh V] + \\ [\tan\lambda + \tanh\lambda] \cdot [\cos V \cdot \sinh V + \sin V \cdot \cosh V] \end{pmatrix} \quad (247)$$

To determine α', the dowel is modeled as a cantilever beam. The angle of the deflected dowel shape, α', at the center of the joint is given by equation 248, as derived by Timoshenko and Lessels.[66]

$$\alpha' = \frac{M_o w}{2E_D I_D} \quad (248)$$

M_o, the moment causing the dowel to deflect at an angle of α' now must be determined. Combining equation 248 with Friberg's (equation 241) and the geometric relationship (equation 240), equation 249 for the moment is derived as a function of α.

$$M_o = \frac{2E_D I_D \alpha}{\left(\frac{2}{\beta} + w\right)} \quad (249)$$

The resulting dowel bar bearing stress, from Huang, is shown in equation 250:

$$f_b = |y_o| K_D \quad (250)$$

The effect of varying nine of the model input are shown in figures 65 to 73 and is summarized in table 40.

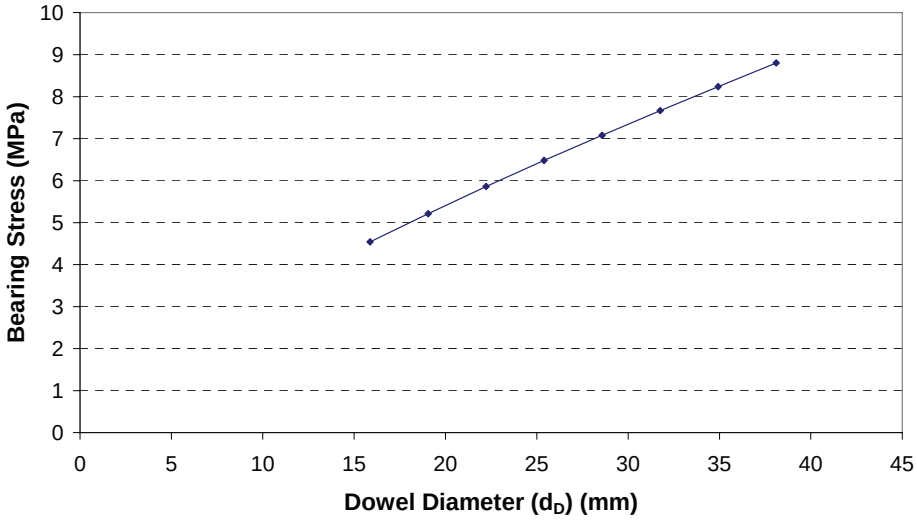

Figure 65. Effect of varying the dowel diameter (d_D) on the bearing stress.

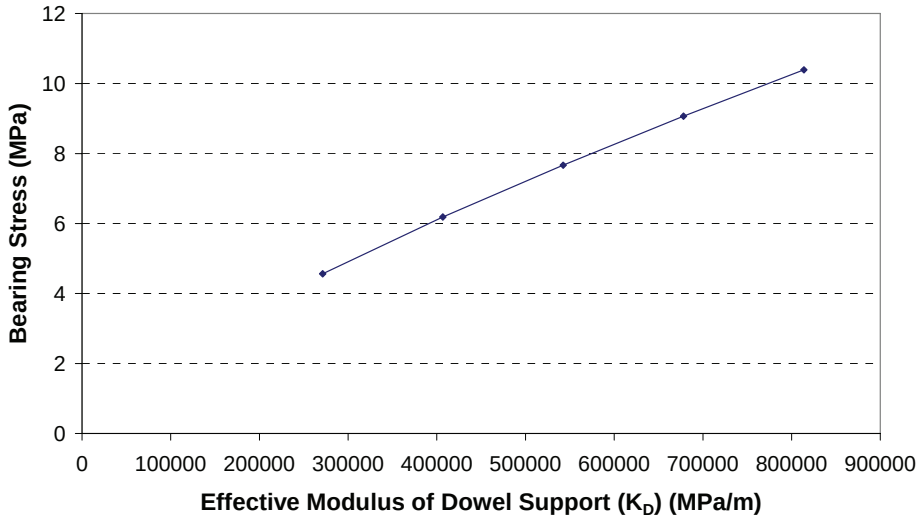

Figure 66. Effect of varying the effective modulus of dowel support (K_D) on the bearing stress.

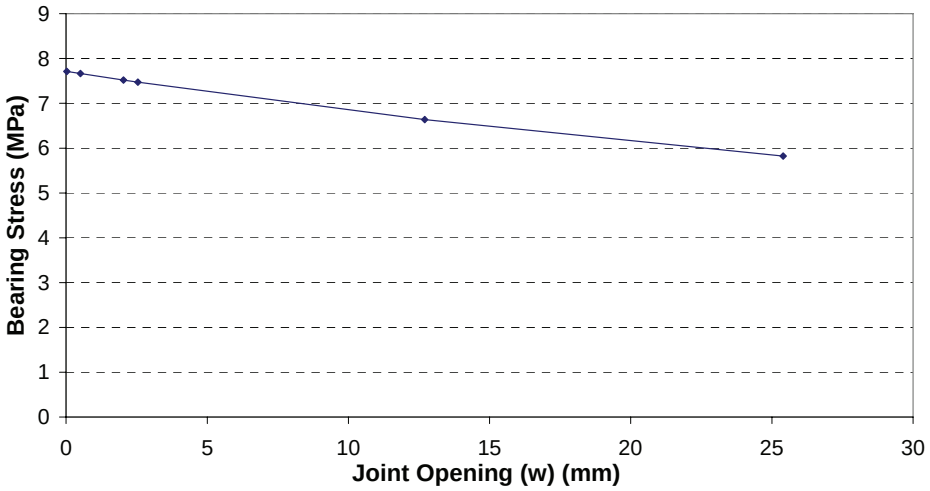

Figure 67. Effect of varying the joint opening on the bearing stress.

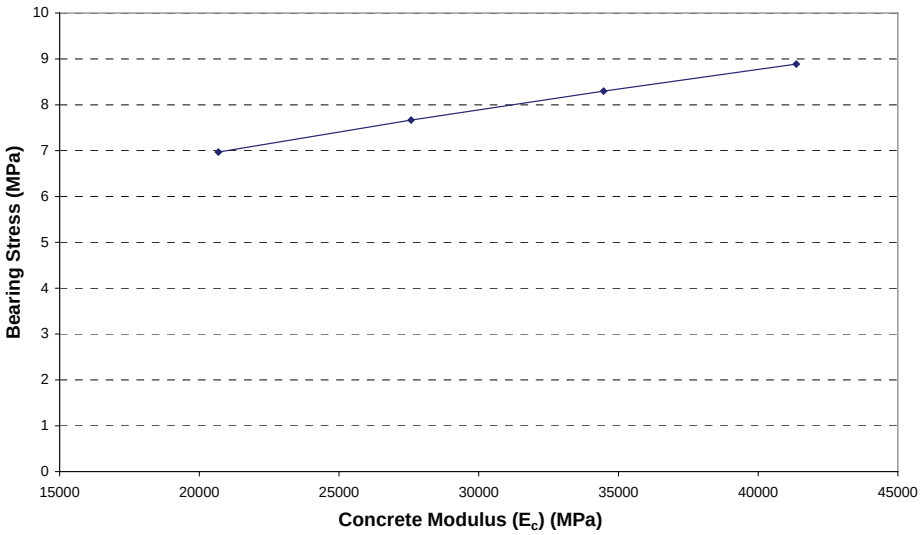

Figure 68. Effect of varying the concrete modulus (E_c) on the bearing stress.

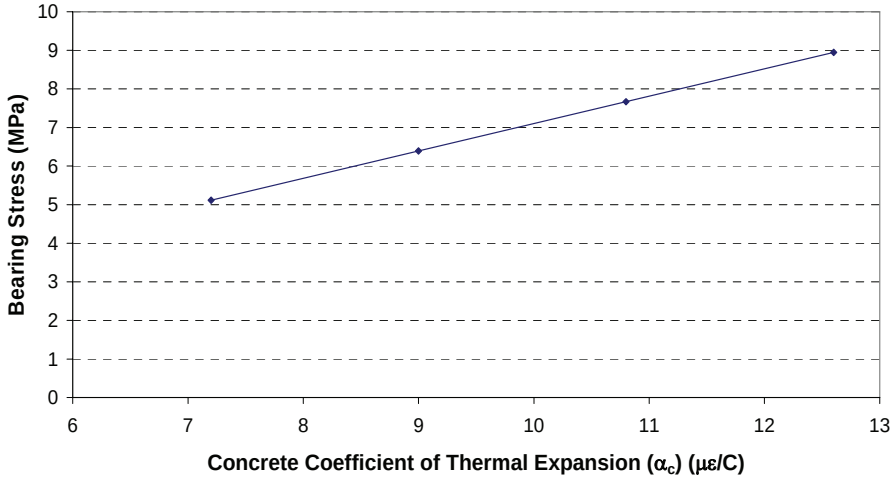

Figure 69. Effect of varying the concrete CTE (α_c) on the bearing stress.

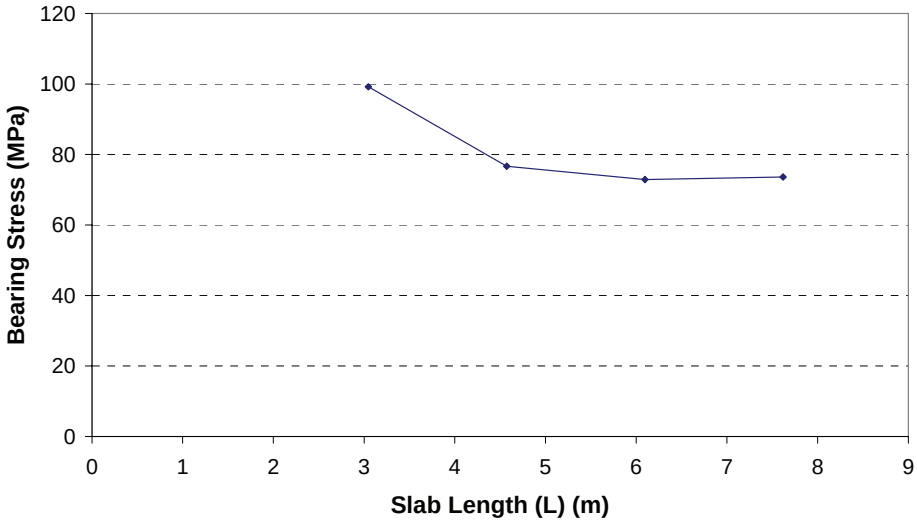

Figure 70. Effect of varying the slab length (L) on the bearing stress.

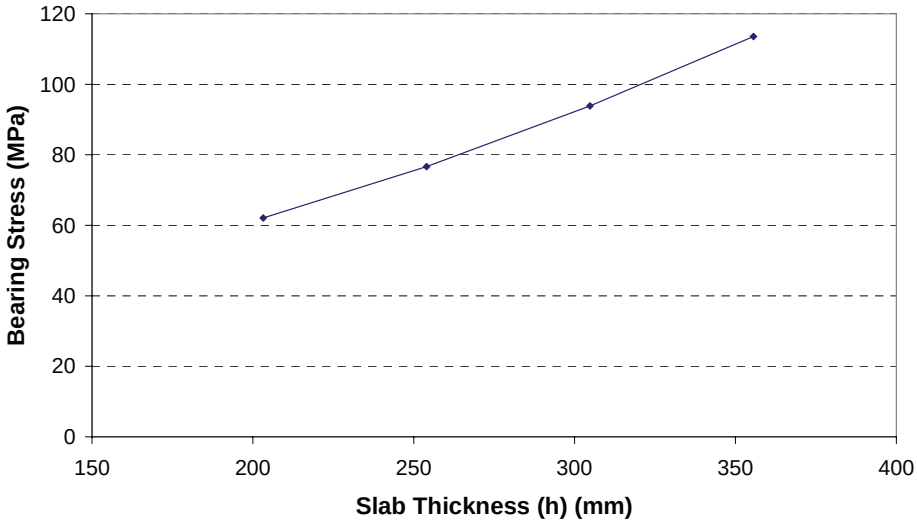

Figure 71. Effect of varying the slab thickness (h) on the bearing stress.

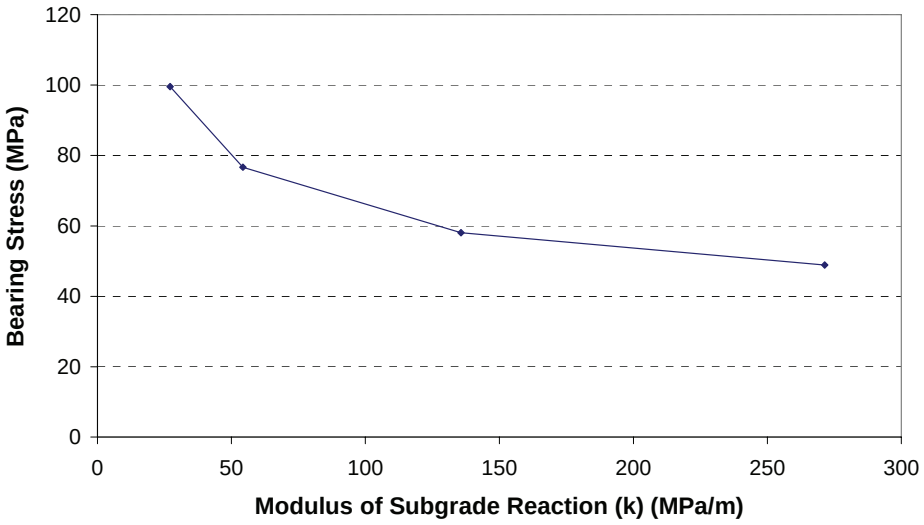

Figure 72. Effect of varying the modulus of subgrade reaction (k) on the bearing stress.

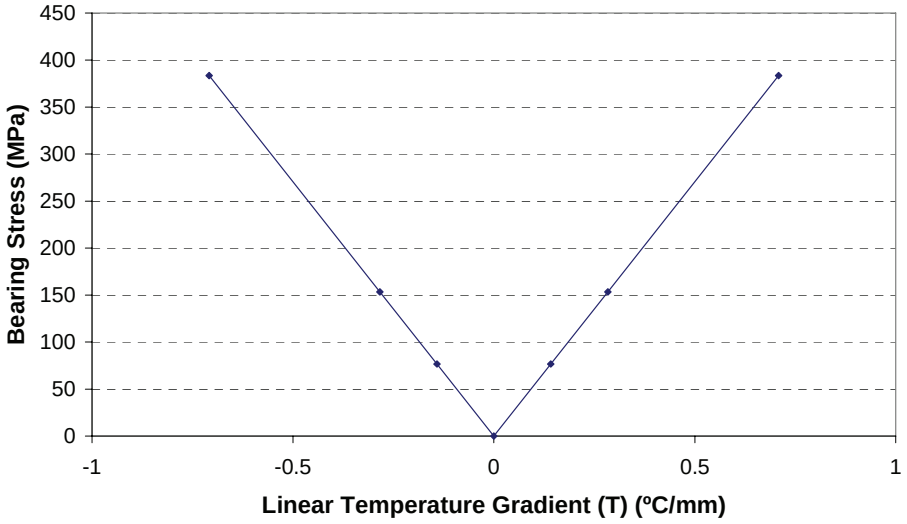

Figure 73. Effect of varying the linear temperature gradient (T) on the bearing stress.

Table 40. Summary of the sensitivity analysis of the dowel model.

Input Parameter	Influence on Bearing Stress	Influence on Bearing Stress According to Friberg[100]
Dowel diameter (d_D) ↑	↑	↓
Effective modulus of dowel support (K_D) ↑	↑	–
Joint opening (w) ↑	↓	↑
Concrete modulus (E_c)↑	↑	–
Concrete CTE (α_c) ↑	↑	–
Slab length (L) ↑	↓	–
Slab thickness (h) ↑	↑	–
Modulus of subgrade reaction (k) ↑	↓	–
|Temperature gradient| (∇T)↑	↑	–

B.5.2 Dowel Bar Stress Due to Shear Loading

When the joints in pavements are loaded in shear (P_{slab} in MPa/m) as illustrated in figure 74, the dowel bars resist this loading (P_{dowel} in MPa/m). The free edge deflection, y_o (in meters), is restrained by twice the value of y_1 (in meters) due to the dowels.

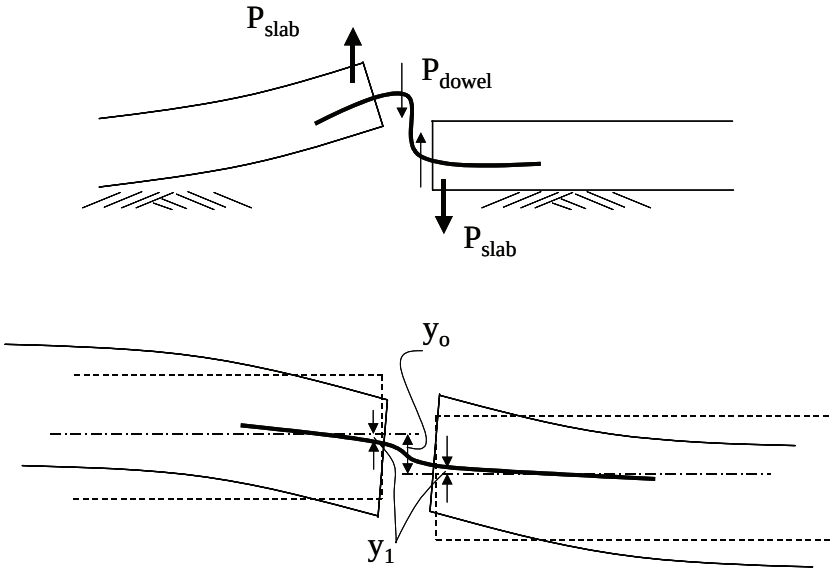

Figure 74. Schematic representation of slabs loaded in shear.

The resulting load on the dowel is shown in equation 251:

$$P_{dowel} = C\left(y_o - 2y_1\right) \tag{251}$$

where,

C = Huang's spring constant (MPa).[64]

Derived from Hetenyi's beam theory, the load on the slab is shown in equation 252:[102]

$$P_{slab} = 2\left[\frac{k}{2\lambda_b}\right] y_1 = \left[\frac{k}{\lambda_b}\right] y_1 = kl\sqrt{2}y_1 \text{ since } \lambda b = \frac{1}{l\sqrt{2}} \tag{252}$$

where,

k = slab support reaction modulus (MPa/m),
λ_b = beam characteristic (m^{-1}), and
ℓ = radius of relative stiffness (m).

Further proof of this derivation was provided by Skarlatos (equation 253):[71]

$$P_{slab} = 2\left(\frac{k\ell}{\sqrt{2}}\right)y_1 = k\ell\sqrt{2}y_1 \tag{253}$$

Equilibrium (equation 254) is achieved when:

$$P_{dowel} = P_{slab} \tag{254}$$

Solving for y_1 in term of y_o yields equation 255:

$$y_1 = \frac{Cy_o}{k\ell\sqrt{2} + 2C} \tag{255}$$

Since y_o is known from Westergaard theory, P_{dowel} can be calculated using equation 256:

$$P_{dowel} = C(y_o - 2y_1) \times Dowel\ \ Spacing\ \ (m) \tag{256}$$

Then the deflection of the dowel at the joint face (δ_{face} in m) can be determined by equation 257:

$$\delta_{face} = P_{dowel} \times \left(\frac{2 + \beta w}{4\beta^3 EI}\right) \tag{257}$$

where,

β, w, E, and I are previously defined.

The dowel bearing stress (σ_b in MPa) can now be calculated in equation 258:

$$\sigma_b\left(bearing\ stress\right) = \delta_{face} \times K_{dowel} \tag{258}$$

where,

K_{dowel} was previously defined in table 39.

This bearing stress is plotted in the HIPERPAV dowel bar module and compared to the concrete's compressive strength.

B.5.3 Dowel Analysis Module in HIPERPAV II

A screen capture of the dowel analysis module in HIPERPAV II is shown in figure 75. The calculated results are for the HIPERPAV II default input.

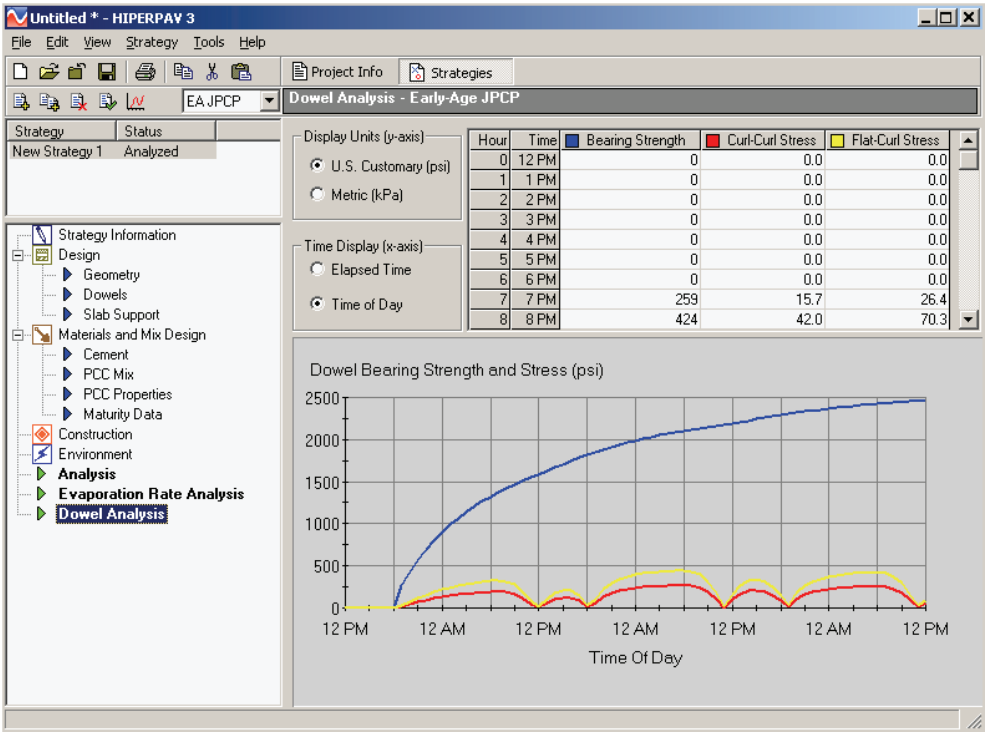

Figure 75. HIPERPAV II screen capture showing typical output from the dowel bar module.

APPENDIX C FIELD INVESTIGATION

Four field sites were investigated for validation of the HIPERPAV II system:

- Two inservice JPCP sections were evaluated to validate the long-term performance models in the JPCP module.
- Two newly constructed CRCP sections were instrumented to validate the CRCP early-age behavior module.

It is believed that the number of field sites evaluated will provide the minimum level of information necessary to meet the objectives of this effort successfully. However, future data from field sites could be used for local customization. This section describes the steps performed for validation of both the JPCP and CRCP pavement sites investigated.

C.1 JPCP SITES INVESTIGATED

JPCP sites investigated include a section on U.S. Highway 50 in Illinois and a bypass section of a farm to market road near Ticuman, Mexico. The selection of both sites was heavily weighted on the fact that extensive early-age and performance information is available for both of these sections.

C.1.1 JPCP Section on U.S. Highway 50, Illinois

A field investigation and monitoring of a JPCP test section on U.S. Highway 50 near Carlyle, IL, was performed from August 7–10, 2001. Following is some background information on this section.

C.1.1.1 Background Information

The test sections were constructed and instrumented from April to August in 1986 on U.S. Highway 50 just west of Carlyle, IL. Early-age monitoring was performed by researchers at the University of Illinois at Urbana-Champaign.[103] This data was used to develop mechanistic design procedures for the Illinois DOT. The following tables and figures provide a brief summary of the published data. Table 41 gives a brief description of the JPCP test sections.

Table 41. JPCP test section descriptions.[103]

Section	Design Thickness (mm)	Underdrains	Sealed Edge Joint	Section Length (m)
AA	241	Y	N	304
IA	216	N	Y	311
JA	216	N	Y	305
KA	216	Y	Y	305
LA	216	Y	N	335
MA	191	Y	Y	335
NA	191	Y	N	305

Section AA borders a bridge abutment on the west and is located 4.8 km from the other sections, which run continuously between IA to NA from west to east. The JPCP sections in this study were constructed with 6.1-m dowelled transverse joints. A 102-mm cement aggregate mixture (CAM) was used as the subbase. The concrete mix design was kept constant throughout the test sections and is shown in table 42.

Table 42. Concrete mix design—88PCC0710.[104]

Constituent	Description	Quantity
Cement	Continental cement	341 kg/m^2
Coarse aggregate	Falling springs quarry 022CAM07	1121 kg/m^2
Fine aggregate	Keyesport sand and gravel #2 027FAM01	666 kg/m^2
Water	–	148 kg/m^2
Air entrainment	Darex	–
Water reducer	Type A—WRDA® with Hycol	–
w/c	–	0.43
Mortar factor	–	0.80

Strength gain data was reported by Zollinger and Barenberg.[103] The reported centerpoint loading flexural strength at 28 days showed an average of 5.8 MPa, and the third point loading flexural strength at 28 days showed an average of 4.9 MPa. The average 28-day modulus of elasticity for all sections is 28,680 MPa.

Table 43 contains traffic data for each test section between 1987 and 1999 provided by Illinois DOT. This table shows the accumulation of ESALs for all sections. In this analysis, the traffic is divided into vehicular categories and factors to calculate ESALs.

Table 43. Accumulation of ESALs.

Year	Average Daily Traffic	Heavy Commercial Vehicles	Multiple Unit Vehicles	Single Unit Vehicles	Passenger Vehicles	MU Factor	SU Factor	PV Factor	Distribution Factor	ESALs (10^6)
1987	3400	461	340	121	2939	567.21	135.78	0.15	0.5	0.10
1988	4175	475	350	125	3700	567.21	135.78	0.15	0.5	0.11
1989	4950	594	338	256	4356	567.21	135.78	0.15	0.5	0.11
1990	4875	713	325	388	4162	567.21	135.78	0.15	0.5	0.12
1991	4800	831	313	519	3969	567.21	135.78	0.15	0.5	0.12
1992	4750	950	300	650	3800	567.21	135.78	0.15	0.5	0.13
1993	4700	900	350	550	3800	567.21	135.78	0.15	0.5	0.14
1994	4800	850	400	450	3950	567.21	135.78	0.15	0.5	0.14
1995	4900	800	450	350	4100	567.21	135.78	0.15	0.5	0.15
1996	5000	750	500	250	4250	567.21	135.78	0.15	0.5	0.16
1997	5100	773	515	258	4327	567.21	135.78	0.15	0.5	0.16
1998	5253	796	530	265	4457	567.21	135.78	0.15	0.5	0.17
1999	5411	820	546	273	4591	567.21	135.78	0.15	0.5	0.17
									Total	1.80

Table 44 compares the design ESALs versus the consumed ESALs as of 1999. All sections but section AA had surpassed the number of design ESALs by 1999. Sections MA and NA had nearly three times the number of design ESALs by 1999.

Table 44. Design and consumed ESALs.

Section	Design ESALS	1999 Cumulative ESALs	Percent Consumed
AA	2.60	1.80	69.1
IA	1.50	1.80	119.8
JA	1.50	1.80	119.8
KA	1.50	1.80	119.8
LA	1.50	1.80	119.8
MA	0.64	1.80	280.8
NA	0.64	1.80	280.8

Table 45 gives friction and ride quality data for the test sections at different times between 1990 and 1999, from Illinois DOT records.

Table 45. Historical ride quality data.

Year	Age (years)	IRI (m/km)
1994	8	1.53
1996	10	1.82
1998	12	1.78

Illinois DOT performed falling weight deflectometer (FWD) tests on the test sections in 1994 and 1998. Table 46 gives the results for D_0, deflection under the load, and LTE.

Table 46. Historical FWD data.

Section	Year	D_0 (microns)	Design Thickness	LTE, Transverse (%)	LTE, Shoulder (%)	LTE, Cracks (%)
AA	1994	86.4	241 mm	92.9	93.3	N/A
	1998	66.0		83.8	76.4	N/A
IA	1994	121.9	216 mm	85.1	70.8	N/A
	1998	106.7		83.9	61.7	N/A
JA	1994	127.0	216 mm	83.4	81.3	87.9
	1998	109.2		84.9	51.0	61.6
LA	1994	104.1	216 mm	91.7	89.8	N/A
	1998	104.1		85.4	68.1	N/A
NA	1994	139.7	191 mm	89.8	75.3	88.0
	1998	139.7		82.8	64.0	81.0

N/A = Not applicable (no cracks observed)

Before construction, the modulus of subgrade reaction was determined at several locations along the site and reported by Zollinger and Barenberg. An average static *k*-value of 130 psi was observed, although no test date was reported.[103]

In addition, historical condition survey data for the seven test sections was obtained from Illinois DOT and is presented in tables 47 through 53. In summary, each section remains intact, with the only visible distresses being a very small amount of transverse cracking and construction joint deterioration in several sections and some patching in section IA. The sections are performing well, considering the level of ESALs and the age of the pavements.

Table 47. Section AA—historical* and current condition survey.

Distress	Units	Severity	Year				
			1990	1992	1995	1997	2001
Corner break	Number	Low	0	0	0	0	0
		Medium	0	0	0	0	0
		High	0	0	0	0	0
Longitudinal cracking	Lane feet	Low	0	0	0	0	0
		Medium	0	0	0	0	0
		High	0	0	0	0	0
Random longitudinal cracking	Lane feet	Low	0	0	0	0	1
		Medium	0	0	0	0	0
		High	0	0	0	0	0
Spalling	Number	Low	0	0	0	0	17
		Medium	0	0	0	0	0
		High	0	0	0	0	0
Transverse cracking	Number	Low	0	0	0	0	0
		Medium	0	0	0	0	0
		High	0	0	0	0	0

* Data provided by Illinois DOT

Table 48. Section IA—historical* and current condition survey.

Distress	Units	Severity	Year				
			1990	1992	1995	1997	2001
Corner break	Number	Low	0	0	0	0	0
		Medium	0	0	0	0	0
		High	0	0	0	0	0
Longitudinal cracking	Lane feet	Low	0	0	0	0	0
		Medium	0	0	0	0	0
		High	0	0	0	0	0
Patching	Lane feet	Low	96	96	96	96	0
		Medium	0	0	0	0	0
		High	0	0	0	0	0
Random longitudinal cracking	Lane feet	Low	0	0	0	0	0
		Medium	0	0	0	0	0
		High	0	0	0	0	0
Spalling	Number	Low	1	1	1	1	2
		Medium	0	0	0	0	0
		High	0	0	0	0	0
Transverse cracking	Number	Low	2	2	0	0	0
		Medium	2	2	4	4	0
		High	0	0	0	0	2

* Data provided by Illinois DOT

Table 49. Section JA—historical* and current condition survey.

Distress	Units	Severity	Year				
			1990	1992	1995	1997	2001
Corner break	Number	Low	0	0	0	0	0
		Medium	0	0	0	0	1
		High	0	0	0	0	0
Longitudinal cracking	Lane feet	Low	0	0	0	0	0
		Medium	0	0	0	0	0
		High	0	0	0	0	0
Patching	Lane feet	Low	0	0	0	0	0
		Medium	0	0	0	0	0
		High	0	0	0	0	0
Random longitudinal cracking	Lane feet	Low	0	0	0	0	0
		Medium	0	0	0	0	0
		High	0	0	0	0	0
Spalling	Number	Low	0	0	2	0	1
		Medium	1	1	0	1	0
		High	0	0	0	0	0
Transverse cracking	Number	Low	0	0	3	2	0
		Medium	4	6	3	6	1
		High	0	0	0	0	5

* Data provided by Illinois DOT

Table 50. Section KA—historical* and current condition survey.

Distress	Units	Severity	Year				
			1990	1992	1995	1997	2001
Corner break	Number	Low	0	0	0	0	0
		Medium	0	0	0	0	0
		High	0	0	0	0	0
Longitudinal cracking	Lane feet	Low	0	0	0	0	0
		Medium	0	0	0	0	0
		High	0	0	0	0	0
Patching	Lane feet	Low	0	0	0	0	0
		Medium	0	0	0	0	0
		High	0	0	0	0	0
Random longitudinal cracking	Lane feet	Low	0	0	0	0	0
		Medium	0	0	0	0	0
		High	0	0	0	0	0
Spalling	Number	Low	0	0	0	0	5
		Medium	0	0	0	0	2
		High	0	0	0	0	0
Transverse cracking	Number	Low	1	1	0	0	0
		Medium	0	0	0	0	0
		High	0	0	0	0	0

* Data provided by Illinois DOT

Table 51. Section LA—historical* and current condition survey.

Distress	Units	Severity	Year				
			1990	1992	1995	1997	2001
Corner break	Number	Low	0	0	0	0	0
		Medium	0	0	0	0	0
		High	0	0	0	0	0
Longitudinal cracking	Lane feet	Low	0	0	0	0	0
		Medium	0	0	0	0	0
		High	0	0	0	0	0
Patching	Lane feet	Low	0	0	0	0	0
		Medium	0	0	0	0	0
		High	0	0	0	0	0
Random longitudinal cracking	Lane feet	Low	0	0	0	0	0
		Medium	0	0	0	0	0
		High	0	0	0	0	0
Spalling	Number	Low	0	0	0	0	5
		Medium	0	0	0	0	6
		High	0	0	0	0	0
Transverse cracking	Number	Low	7	7	0	0	0
		Medium	0	0	0	0	0
		High	0	0	0	0	0

* Data provided by Illinois DOT

Table 52. Section MA—historical* and current condition survey.

Distress	Units	Severity	Year				
			1990	1992	1995	1997	2001
Corner break	Number	Low	0	0	0	0	0
		Medium	0	0	0	0	0
		High	0	0	0	0	0
Longitudinal cracking	Lane feet	Low	0	0	0	0	0
		Medium	0	0	0	0	0
		High	0	0	0	0	0
Patching	Lane feet	Low	0	0	0	0	0
		Medium	0	0	0	0	0
		High	0	0	0	0	0
Random longitudinal cracking	Lane feet	Low	0	0	0	0	0
		Medium	0	0	0	0	0
		High	0	0	0	0	0
Spalling	Number	Low	0	0	0	0	5
		Medium	0	0	0	0	0
		High	0	0	0	0	0
Transverse cracking	Number	Low	0	2	0	0	0
		Medium	0	0	0	0	0
		High	0	0	0	0	0

* Data provided by Illinois DOT

Table 53. Section NA—historical* and current condition survey.

Distress	Units	Severity	Year				
			1990	1992	1995	1997	2001
Corner break	Number	Low	0	0	0	0	0
		Medium	0	0	0	0	1
		High	0	0	0	0	0
Longitudinal cracking	Lane feet	Low	0	0	0	0	1
		Medium	0	0	0	0	0
		High	0	0	0	0	0
Patching	Lane feet	Low	0	0	0	0	0
		Medium	0	0	0	0	0
		High	0	0	0	0	0
Random longitudinal cracking	Lane feet	Low	0	0	0	0	0
		Medium	0	0	0	0	0
		High	0	0	0	0	0
Spalling	Number	Low	0	0	0	0	17
		Medium	0	0	0	0	0
		High	0	0	0	0	0
Transverse cracking	Number	Low	3	6	5	5	0
		Medium	0	1	4	4	1
		High	3	3	2	3	7

* Data provided by Illinois DOT

C.1.1.2 Evaluation Activities

The monitoring included the following activities:

- Weather station installation to collect ambient temperature, relative humidity, and solar radiation.
- Visual inspection of each JPCP section.
- FWD measurements of slab deflection and load transfer.
- Mastrad® demountable mechanical strain gage (DEMEC) caliper measurements of joint movement.
- Face® Dipstick® profiling in longitudinal and diagonal directions.
- Coring to determine depths and provide specimens for laboratory testing.

The data collected from this experiment was used with early-age information available for this site to validate the long-term JPCP performance models in HIPERPAV II.

A condition survey with photo and video documentation for all seven test sections was performed during the afternoon of August 7, 2001. The location and severity of each distress was documented. As in the historical condition survey data, few distresses were evident in the sections. The major distresses included a few slabs with transverse cracking and some low severity transverse joint spalling. The

pavement has performed well, considering all sections except section AA exceeded the number of design ESALs by 1999, according to the original design.

Sections AA, IA, JA, KA, and LA were tested with FWD at midslab for backcalculation of the modulus of subgrade reaction (*k*) and at transverse and longitudinal shoulder joints for LTE. Each test consisted of a seating drop followed by drops at three increasing loads, typically near 9, 12, and 15 kips. The approach and leave sides of transverse joints were tested. Table 54 provides a summary of center slab deflection bowls that have been normalized to 9 kips and are compared to historical deflections in 1994 and 1998.

Table 54. Center slab deflections in microns, normalized to 4090 kg for Illinois JPCP evaluation.

Section	Statistic	0 mm (1994)	0 mm (1998)	0 mm	304.8 mm	609.6 mm	914.4 mm	1219.2 mm	1524 mm	1829 mm
AA	Mean	86.4	66.0	67.8	62.2	54.1	46.7	39.4	33.3	28.2
	St. Dev	–	–	5.6	4.8	3.6	2.8	2.0	1.5	1.0
IA	Mean	121.9	106.7	135.6	123.4	106.4	88.6	72.4	57.4	43.7
	St. Dev	–	–	26.7	23.1	17.3	12.7	9.1	6.6	4.3
JA	Mean	127.0	109.2	131.6	124.0	110.5	93.0	78.0	62.2	47.2
	St. Dev	–	–	4.3	4.3	5.1	5.1	5.1	4.6	3.8
KA	Mean	N/A	N/A	121.2	112.8	99.3	84.6	71.9	59.2	47.5
	St. Dev	–	–	16.3	14.2	9.9	5.1	2.0	2.5	2.3
LA	Mean	104.1	104.1	128.0	121.9	106.7	92.7	75.9	61.5	48.8
	St. Dev	–	–	16.0	13.7	9.7	6.6	3.0	2.0	1.0

Table 55 contains load transfer data and statistics for transverse joints for approach slabs.

Table 55. Approach slab load transfer data for Illinois JPCP evaluation.

Section	Avg. Load (N)	Load Transfer Efficiency					
		1994 (%)	1998 (%)	Mean (%)	St. Dev (%)	Median (%)	15th Percentile (%)
AA	39	92.9	83.8	77.3	1.41	77.2	76.1
	52			77.1	1.01	76.8	76.2
	66			77.1	1.08	77.0	76.3
IA	40	85.1	83.9	80.4	1.17	80.3	79.4
	53			80.2	1.44	80.3	78.8
	68			80.0	1.38	80.3	78.7
JA	39	83.4	84.9	81.2	1.32	81.6	80.0
	52			80.9	0.60	80.7	80.4
	67			80.6	0.74	80.7	79.9
KA	39	N/A	N/A	81.6	1.06	81.4	80.9
	51			81.7	0.89	81.6	81.0
	66			81.9	1.17	81.6	81.0
LA	38	91.7	85.4	82.5	0.56	82.6	82.0
	50			83.2	0.99	83.5	82.3
	65			82.7	0.78	83.2	81.8
Cracks (Section IA)	39	N/A	N/A	79.6	0.06	Not enough data (two values)	
	51			79.9	0.51		
	66			80.1	0.20		

Table 56 includes load transfer data for transverse joints and cracks for leave slabs. Statistical data is also included in the table. The values for the leave slabs are greater than the approach slabs.

Table 56. Leave slab load transfer data for Illinois JPCP evaluation.

Section	Avg. Load (N)	Load Transfer Efficiency					
		1994 (%)	1998 (%)	Mean (%)	St. Dev (%)	Median (%)	15th Percentile (%)
AA	39	92.9	83.8	89.5	2.72	91.1	87.3
	51			89.1	2.73	89.3	86.7
	65			88.9	2.98	89.9	86.3
IA	40	85.1	83.9	87.4	1.55	87.6	86.4
	53			87.9	1.38	87.7	86.8
	68			87.4	1.28	87.5	86.5
JA	39	83.4	84.9	87.4	1.86	88.4	85.5
	52			88.4	2.38	89.1	86.1
	66			87.7	2.03	88.0	85.8
KA	39	N/A	N/A	92.2	2.08	92.7	90.5
	51			93.5	2.53	94.1	91.1
	67			92.7	1.63	93.6	91.1
LA	38	91.7	85.4	92.3	1.34	92.7	91.5
	50			93.4	0.79	93.4	92.6
	64			92.7	0.68	92.6	92.2
Cracks (Section IA)	42	N/A	N/A	92.6	0.40	Not enough data (two values)	
	56			93.3	0.99		
	72			92.4	0.80		

T-type thermocouples were installed at three different depths (13, 76, and 127 mm) at sections AA, IA, and KA to monitor the temperature profile of the pavement. An additional thermocouple was installed at section AA at 241 mm to monitor the temperature at the bottom of the pavement. Measurements were taken manually to provide corresponding pavement temperature data during FWD and DEMEC testing. Figure 76 gives the temperature profile for section AA.

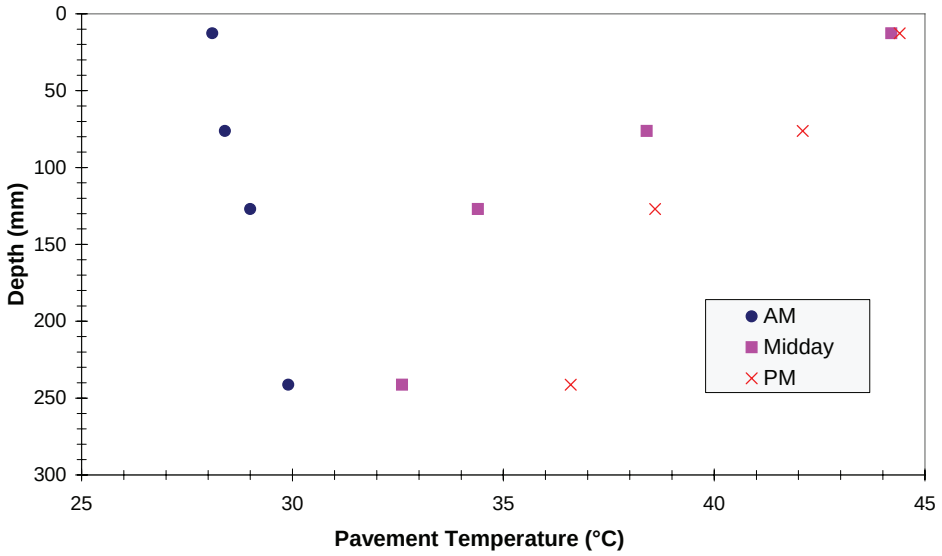

Figure 76. Pavement temperature profiles for Illinois JPCP evaluation.

The gradient moves from slightly negative and increases throughout the day. The results for sections IA and KA mirrored the trends of section AA.

A DEMEC caliper was used to measure the joint and crack movements by measuring the distance between metal studs epoxied to the pavement surface. Approximately five consecutive transverse joints were tested in each section. In addition, four longitudinal joints and all transverse cracks between the consecutive transverse joints were tested. Transverse cracks were included because they reduce the total movement at transverse joints by allowing expansion and contraction. Figure 77 shows the joint movement in section AA at different transverse joints.

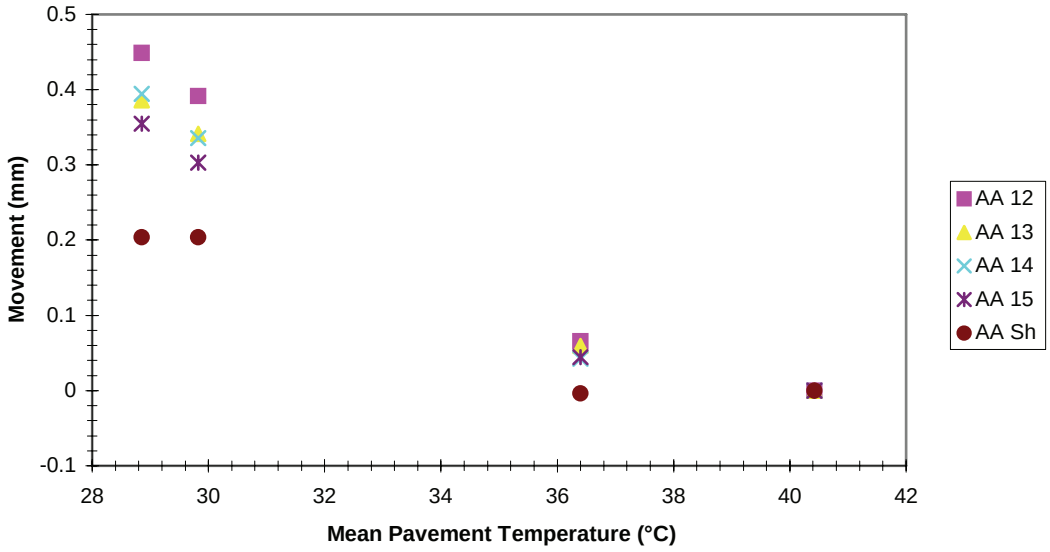

Figure 77. Joint movement for section AA in Illinois JPCP evaluation.

The downward trend indicates joints closing under higher temperatures and opening under cooler temperatures. All other sections showed the same trend. After 36 ºC, no further movement is observed, possibly because of joint closure after that temperature. Table 57 gives linear trendline data for all sections and includes transverse joints, transverse cracks, and longitudinal joints. High r^2 values show that the joint and crack movements follow a linear trend.

Table 57. Joint movement summary for Illinois JPCP evaluation.

Type*	Section AA		Section IA		Section JA		Section KA		Section LA		Section MA		Section NA	
	mm/°C	r^2	mm/°C	r^2	mm/°C	r^2	mm/°C	r^2	mm/°C	r^2	mm/°C	r^2	mm/°C	r^2
T.J.	−0.040	0.97	–0.026	0.99	–0.037	0.94	–0.034	0.98	–0.034	0.99	–0.080	1.00	–0.028	0.97
T.J.	–0.035	0.97	–0.054	1.00	–0.049	0.97	–0.024	1.00	–0.029	0.98	–0.041	0.97	–0.023	0.97
T.J.	–0.036	0.95	–0.035	0.99	–0.064	0.96	–0.047	1.00	–0.045	0.97	–0.053	0.96	–0.025	1.00
T.J.	–0.032	0.96	–0.026	0.99	–0.059	0.96	–0.020	1.00	–0.036	0.99	–0.030	0.96	–0.043	1.00
Mean T.J.	−0.036	–	–0.035	–	–0.052	–	–0.031	–	–0.036	–	–0.051	–	–0.030	–
Crack	–	–	–0.054	0.93	–	–	–	–	–	–	–	–	–0.080	0.86
Crack	–	–	–0.091	0.96	–	–	–	–	–	–	–	–	–	–
L.J.	–0.020	0.90	–0.059	0.98	–0.057	0.96	–0.024	1.00	–	–	–	–	–	–

*T.J. = Transverse Joint, L.J. = Longitudinal Joint

A Dipstick profiling device was used to establish longitudinal and diagonal surface profiles for pavement slabs and to compute IRI in each section. Profiles were measured during both the morning and afternoon to determine possible environmental effects of curling and warping on the pavement slabs. Figure 78 shows a typical longitudinal profile for section AA after correcting for slope. A curling pattern at every 6-m interval corresponding to the slab length for this section is evident from this figure.

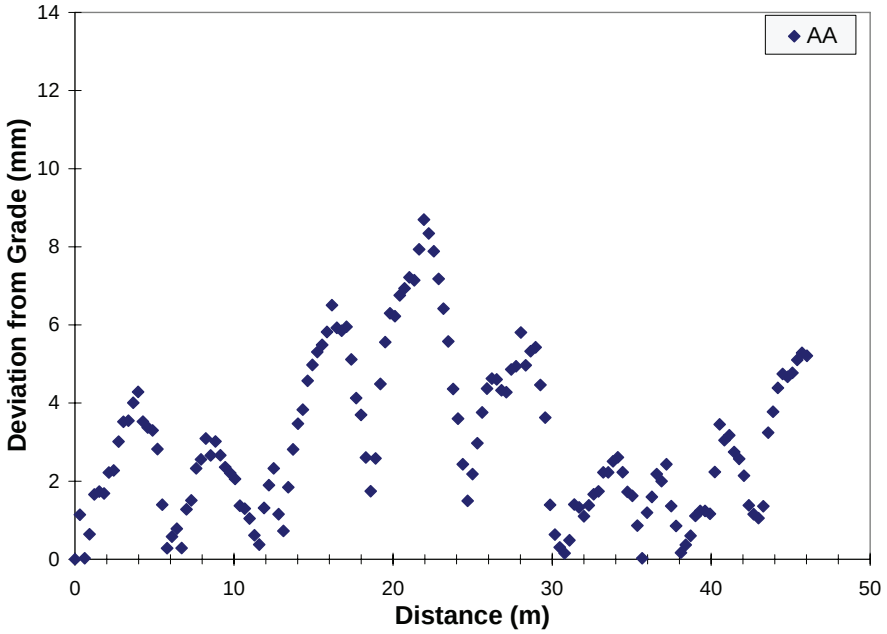

Figure 78. Longitudinal profiles for section AA, 253-mm thickness.

Six 152-mm and six 102-mm cores were drilled. The following list describes the size and locations of the cores:

- Section AA—five 102-mm cores.
- Section IA—one 102-mm and one 152-mm cores.
- Section JA—two 152-mm cores.
- Section KA—three 152-mm cores.

The 152-mm cores were tested for splitting tensile strength. The 102-mm cores were tested for Young's Modulus of Elasticity (*E*) and CTE. Thickness measurements were also taken from the cores and are compared to the design thickness in table 58.

Table 58. Summary of thickness measurements for Illinois JPCP evaluation.

Section	Design Thickness (mm)	Mean Measured Thickness (mm)
AA	241	253
IA	216	230
JA	216	220
KA	216	220

C.1.2 JPCP Section on Ticuman Bypass, Mexico

In the past, the project team has closely followed the design, construction, and interim evaluations of a JCP section in Mexico. This section was part of a demonstration project to promote the use of PCC for highways in Mexico. In 1993, a cement producer in cooperation with the Mexican Secretariat of Communications and Transports conducted this demonstration JCP construction project. The project entailed rehabilitating an existing asphalt pavement structure with a JCP overlay.

Pavement evaluation studies were initiated during and immediately after construction. Two years later, a performance evaluation was performed that included deflection testing, evaluation of the riding quality, and condition surveys. On the second evaluation, it was observed that the traffic patterns for that area of the country had changed drastically, subjecting the study section to an excessive increase in traffic loading. Some minor distresses were observed during that evaluation that later progressed as the traffic loads increased.

Given that the Ticuman bypass possessed many of the characteristics desired for validation of the JCP long-term pavement performance models in HIPERPAV II, the project team decided to evaluate this section further after approval from FHWA. This section, describes the Ticuman bypass JCP section and summarizes the design, construction, and post-construction evaluations to date.

C.1.2.1 Ticuman Bypass Preliminary Information

The Ticuman bypass section is located on the Yautepec-Jojutla farm-to-market road in the State of Morelos. The section serves as a bypass to the town of Ticuman. Figure 79 shows the general location and layout of the road. The Ticuman bypass is oriented to the north and south and services a resort area,

an aggregate quarry, and local farming and ranching operations. The project length is approximately 8.5 km that, for the most part, run along the edge of a ridge, down into a flood plain, and across a river.

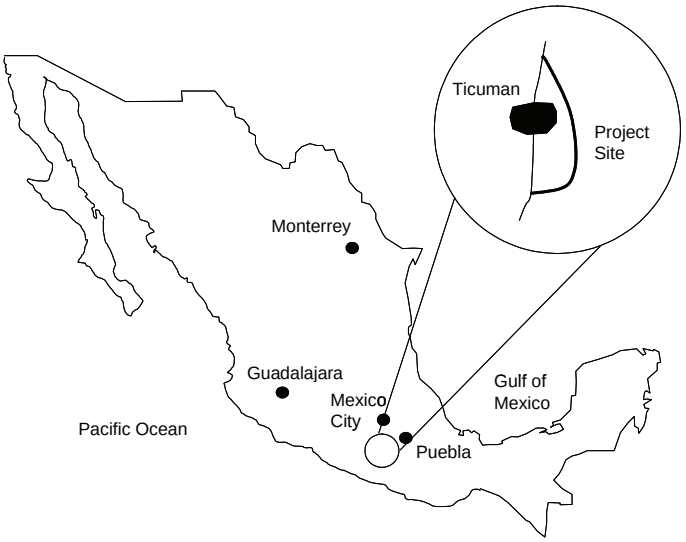

Figure 79. Ticuman bypass project location.

The Ticuman bypass is a two-lane road with 3.35-m wide lanes. The pavement structure is composed of a nondoweled JCP overlaying an existing HMA pavement. The slab thickness averages 233 mm and has a joint spacing of 4.5 m. The existing structure is composed of an HMA layer with an average thickness ranging from 50 to 80 mm. From a site inspection before construction, it was observed that the HMA was severely cracked in some areas. Cores extracted before construction showed an average thickness of 250 mm for the base layer. The base layer showed a plasticity index of 16.7 classified as GC under the unified classification system (UCS) or A–2–6 under the AASHTO classification system. The natural soil material showed a plasticity index of 17.6 with classification CL (UCS) or A–6 (AASHTO).

The mix design used for this project had the following proportions:

- Portland cement type I 280 kg/m^3
- Coarse aggregate 1,006 kg/m^3
- Fine aggregate 932 kg/m^3
- Water 158 liters/cubed meter (l/m^3)
- Air entrainer 115 millilters per cubed meter (ml/m^3)
- Water reducer 1,333 ml/m^3

Given that the existing HMA pavement was in very poor conditions, the traffic for this section was minimal. However, after construction of the JCP, the traffic patterns changed drastically, and significant traffic was generated. Table 59 summarizes the traffic conditions throughout the history of the road.

Table 59. Historical traffic data.

Year	Estimated Annual Average Daily Truck Traffic	Estimated Cumulative 18-kip ESAL (10^6)
1993	40	0
1995	299	0.09
2001	759	1.71

Annual temperatures for Ticuman were reported to range from 5 ºC to 38 ºC. Historic weather records for the days during construction were obtained from the meteorological center in Mexico (Comision Federal de Electricidad).

The JCP was constructed from September 23 to October 12, 1993, with slip form paving equipment. Construction proceeded as scheduled with minimal delays.

Table 60 shows the concrete compressive strength and stiffness statistics for the specimens taken at the Ticuman bypass (laboratory specimens from samples taken in the field, and core specimens extracted directly from the slab) tested after 28 days. Figure 80 shows the mean concrete compressive and flexural strength gain curves for the Ticuman bypass. This information is based on mean values from test results.

Table 60. Summary statistics for 28-day PCC compressive strength in Ticuman bypass.

Statistic	Laboratory (MPa)	Cores (MPa)	Modulus of Elasticity (MPa)
Mean	30.3	29.1	23,622
Standard deviation	4.7	5.8	3,300
Minimum	17.4	18.4	16,250
Maximum	37.7	35.8	27,294
Count	22	11	11
Coefficient of variation	15.50%	19.95%	13.97%

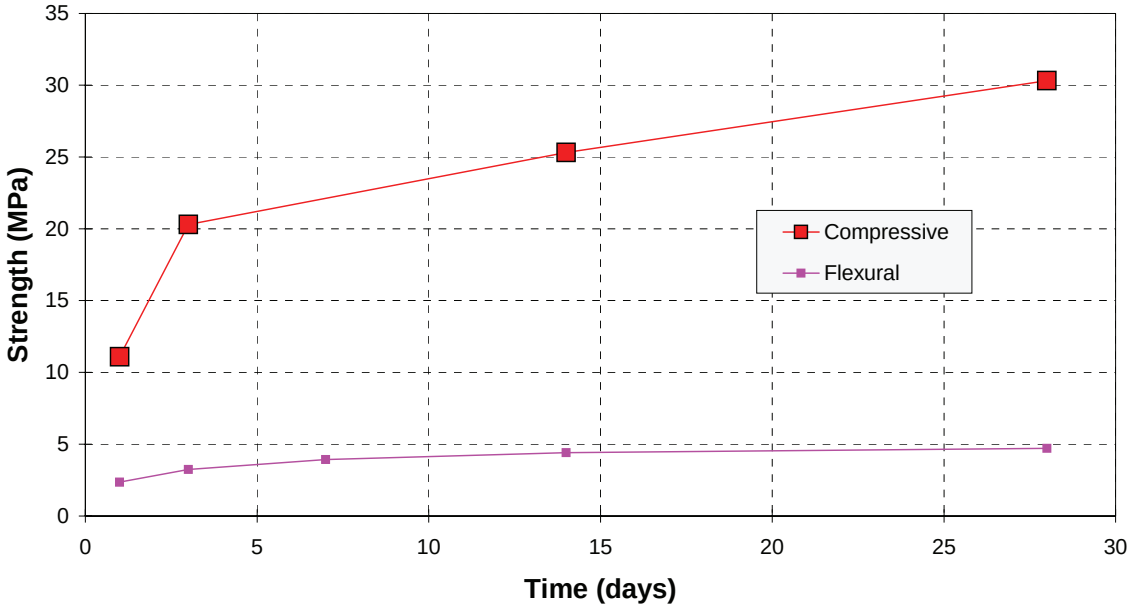

Figure 80. Mean concrete compressive and flexural strength gain curves for the Ticuman bypass.

Table 61 shows the statistics for the flexural strength and the splitting tensile test results at 28 days for the Ticuman bypass.

Table 61. Summary statistic for flexural strength and splitting tensile test results for the Ticuman bypass.

Statistic	Flexural (kg/cm^2)	Splitting (kg/cm^2)
Mean	48	30
Standard deviation	6	4
Count	22	15
Coefficient of variation	13.20%	12.50%

Table 62 shows the summary statistics of the slab thickness, as obtained from PCC cores.

Table 62. Summary statistics of core thickness for the Ticuman bypass.

Statistic	Thickness (cm)
Mean	233
Standard deviation	22.9
Minimum	185
Maximum	270
Count	28
Coefficient of variation	10.17%

The minimum thickness, as specified in the pavement design for the Ticuman bypass, was 200 mm. In the case of this particular project, since the existing asphalt structure was not leveled up, the variability in slab thickness seems reasonable for a JCP overlay, considering the high level of roughness of the existing asphalt structure.

C.1.2.2 Previous Evaluations

During and after construction, an extensive evaluation of the concrete pavement was performed, including joint cracking surveys and Dynaflect® deflection data collection. A cracking survey was performed on October 12, 1993. The survey consisted of making an inventory by visual inspection of those joints that were cracked. From this evaluation, cracks were observed to occur on average at every third joint (every 13.5 m). However, the spacing between cracked joints was reduced, as demonstrated in subsequent evaluations. During late December 1993 and early January 1994, pavement deflections were measured with Dynaflect equipment. These deflection measurements were taken at the midspan of the slab and at the joints to determine the pavement structural capacity and LTE between joints, respectively. In the case of the Ticuman bypass, load transfer between slabs is provided solely by aggregate interlock, since no load transfer devices were considered or installed during the pavement construction. The deflection measurements on which this analysis is based were taken during the winter, and although the temperature during measurement was not low, it was expected that during the summer this would be higher, and thus, joint openings would be smaller.

During July 1995, Dynaflect deflections were taken at the slab center and edge. In addition, a traffic survey and PSRs were obtained. A distress survey also was conducted in July 1995. That survey concluded that 3.3 percent of the slabs in the project were suffering from some type of cracking or spalling distress. Concurrent with the deflection data collection, 24-hour traffic information was collected over a 6-day period from a portable weigh-in-motion (WIM) station on the Ticuman bypass, which provided directional volumes and axle weights. From this traffic data, an average daily traffic of between 800 and 1200 vehicles was estimated.

C.1.2.3 JPCP Ticuman Bypass Evaluation in 2001

As part of this project, an extensive pavement evaluation was conducted for the Ticuman bypass during August 21 through 24, 2001. The pavement evaluation studies included testing deflection with Dynaflect equipment, determining PSI under morning and afternoon conditions, monitoring joint openings, conducting distress surveys, and extracting PCC cores for characterizing PCC properties. An initial data reduction of the above collected information is described in the following sections.

To perform detailed condition surveys, five sections were selected along the project. The stations for those sections are:

- Section 1—from km 0+000 to km 0+228.
- Section 2—from km 0+686 to km 0+869.
- Section 3—from km 1+655 to km 1+842.
- Section 4—from km 4+400 to km 4+569.
- Section 5—form km 8+076 to km 8+300.

Since limited traffic control was available for this project, the above sections were selected based on visibility conditions. A minimum representative sample of at least 40 slabs per section was evaluated (180 m), for a total of 1 km.

Other distresses observed included localized separation of the longitudinal joint. This was reportedly due to the fact that tie bars were not installed on some pavement sections, as was determined soon after construction. Some tie bar retrofitting also was observed on the areas with no tie bars. Some spalling problems that appeared soon after construction were repaired with PCC patches. Although some crack sealing was performed in 1995, no more maintenance was observed thereafter. The majority of the cracks had not been sealed at the time of this survey. In some localized areas, lane-to-shoulder dropoff also was observed. In addition to the detailed condition survey, a video documentation of the entire road was performed at a relatively low speed to capture the distress condition throughout the project. The distress survey indicates that 63 percent of the distresses are located on the northbound direction, with a total of 22.4 percent of slabs presenting some distress type, and 37 percent on the southbound direction, with 13.3 percent distressed slabs. The distress percentages on both directions agree with the load conditions for this road, which indicate a greater percentage of heavy vehicles on the northbound direction.

Figure 81 shows a compilation of the three distress surveys performed at different dates through the history of Ticuman bypass. This figure demonstrates that longitudinal cracking is the predominant distress type. In addition, a considerably large number of slabs have a mix of longitudinal, transverse, and/or corner cracking. These slabs were reported as shattered slabs. Researchers believe that the lack of preventive maintenance has contributed significantly to the distresses observed on this road.

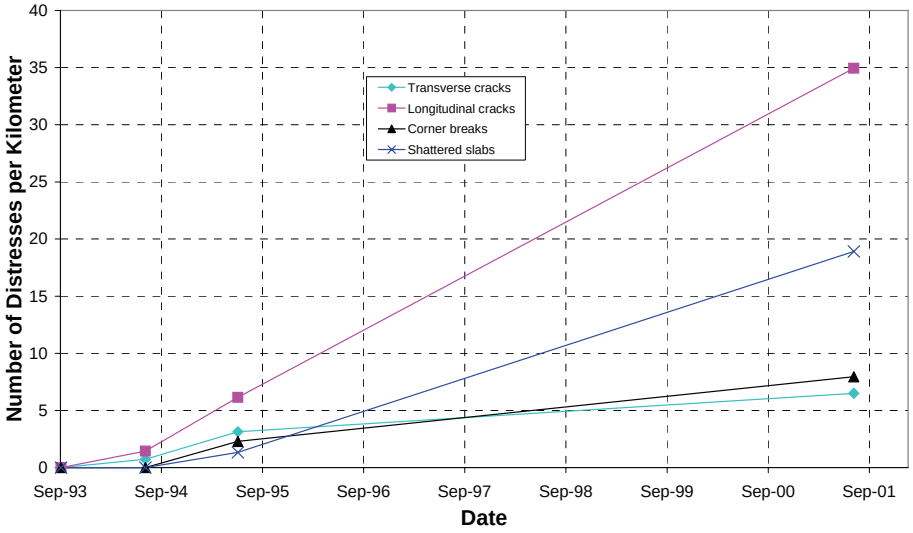

Figure 81. Number of distressed slabs per kilometer for the Ticuman bypass.

In addition to the above distresses, a faulting survey was performed on both lanes. Faulting was considered positive when the approach slab was higher than the departure slab. Figure 82 shows a distribution plot of the faulting recorded for all the sections investigated. Most of the faulting observed in this figure is between 0 and 2.0 mm and ranges between −2.5 mm and +4.0 mm. From this evaluation, section 1 showed slightly higher faulting readings than the rest of the sections. This section also presented a greater occurrence of sealant damage and spalling problems.

DEMEC studs were epoxied at an average of five to six joints and cracks to measure joint movement due to changes in temperature as a consequence of the diurnal cycle. Joint movement monitoring was performed in the morning and afternoon conditions during the days of August 22, 23, and 24. Monitoring of PCC temperature was achieved by installing thermocouple sensors at different depths throughout the slab depth. Figure 83 shows a distribution and cumulative plot of the joint opening at the Ticuman bypass. The average joint opening observed at the joints was in the order of 0.31 mm/ºC. This opening varied from 0.18 to 0.39 mm/ºC.

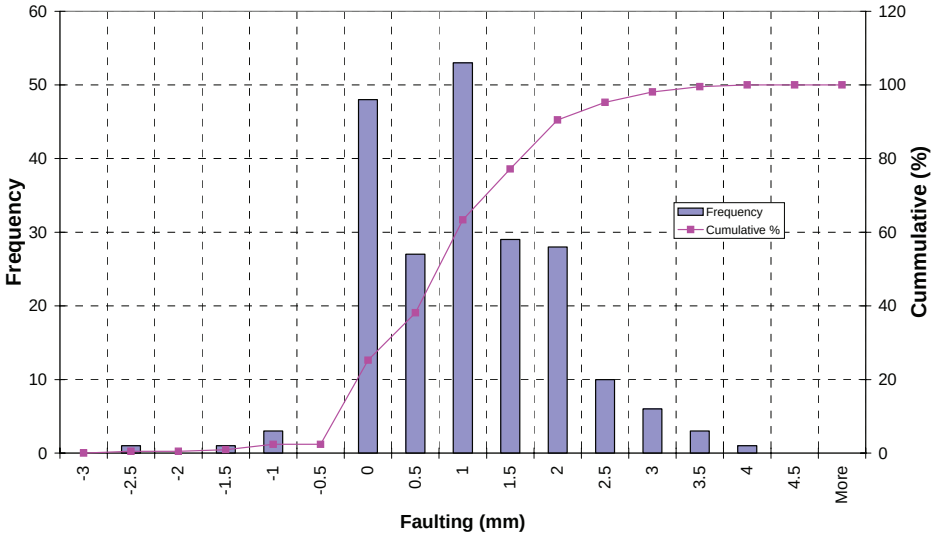

Figure 82. Faulting distribution for the Ticuman bypass.

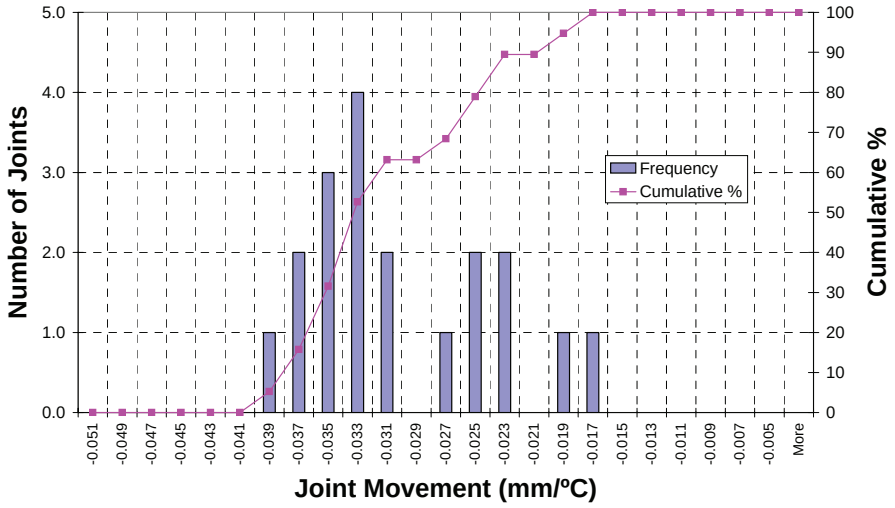

Figure 83. Measured joint opening during August 22 to 24.

Deflection testing was performed on August 22 from 2 p.m. to 6 p.m. on both lanes and under two loading conditions: at midslab to measure structural capacity, and at the joints to measure LTE. From this analysis, an average LTE of 93.0 percent was measured for the southbound direction; 90.2 percent was measured for the northbound direction. A comparison of the LTE analysis performed with 1993 data

shows that the LTE in 2001 was much higher than the LTE observed in 1993 (70 percent in average). The higher LTE values measured in 2001 initially were believed to be a difference in temperature conditions for each testing period. However, the range of temperatures observed for 1993 was from 22 ºC to 39 ºC, and those observed during 2001 ranged from 29 ºC to 32 ºC. Although a wider range of temperatures was observed during the spring of 1993, a comparison of LTE versus temperature for that period did not show any significant trend in LTE. During winter of 1993, a deflection analysis indicated an average effective joint spacing of 7.9 m. On the other hand, the joint movement analysis for summer of 2001 showed that all joints are working joints; thus the average joint spacing corresponds to the design joint spacing of 4.6 m. Since longer slab lengths result in larger joint openings and therefore reduced LTE, it is believed that the higher LTE values measured during summer 2001 are a result of the effective joint spacing observed.

Structural capacity for this road was performed in several occasions after construction of the JCP on the Ticuman bypass. The first evaluation was performed at the end of 1993. During that evaluation, extensive deflection testing was performed at midslab for most of the slabs. A second evaluation was performed 2 years later, in 1995. Finally, during the visit in 2001, Dynaflect deflections were taken again at midslab for this purpose.

Tables 63 and 64 compare the deflections taken in 1993, 1995, and 2001. Deflections correspond to the sensor under the load (D1) and the farthest sensor from the load (D5), which is believed to represent more closely the soil support conditions. Higher deflections were observed in 2001 than in the previous dates. No deflection data was obtained for the northbound direction in 1993.

Table 63. Deflection indicators for the southbound direction (microns).

Evaluation	Average D1	Average D5	Average D1–D5
1993	8.6	4.8	3.6
1995	9.1	5.1	4.1
2001	12.2	6.4	5.6

Table 64. Deflection indicators for the northbound direction (microns).

Evaluation	Average D1	Average D5	Average D1–D5
1995	9.1	5.1	4.1
2001	10.2	4.8	5.3

From a backcalculation analysis, a significant reduction in stiffness was observed in the HMA subbase layer after 1995. It is believed that lack of maintenance, along with the increasing traffic loads in this highway, may have contributed to reduced structural capacity.

To obtain a measure of the ride quality for the Ticuman bypass, Mays meter equipment was used for determination of PSI. A rather low riding quality was measured for this section, with no definitive difference between the southbound and northbound lanes. To detect any changes in the profile of the pavement slabs due to curling and warping, Mays meter measurements were performed in the morning (6:30 a.m.) and afternoon (1 p.m.) conditions. Figures 84 and 85 show the PSI measurements for the morning and afternoon conditions. For the southbound direction, the afternoon readings appear to be significantly higher than the morning readings. However, for the northbound direction, the opposite trend is observed on most of the readings. In these two figures, the PSI measurements taken on summer of

1995 are presented. The PSI measurements taken in 1995 on the southbound direction are slightly higher than the readings taken in the morning of summer 2001. However, they were very similar to those taken in the afternoon of 2001. The PSI results for the northbound direction did not show any definitive trend from morning to afternoon conditions. Furthermore, no difference in PSI readings was observed from summer of 1995 to summer 2001.

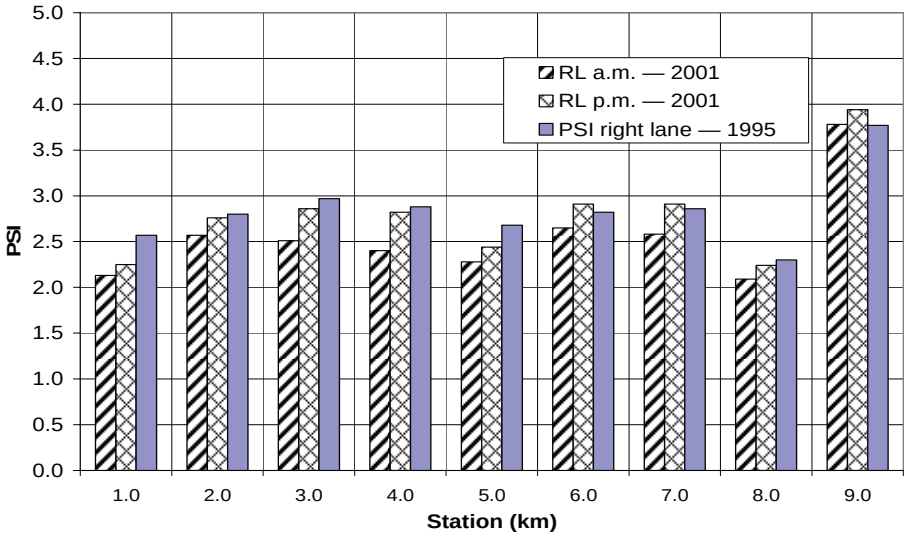

Figure 84. Comparison of PSI ratings on the southbound direction (summer 2001 versus summer 1995).

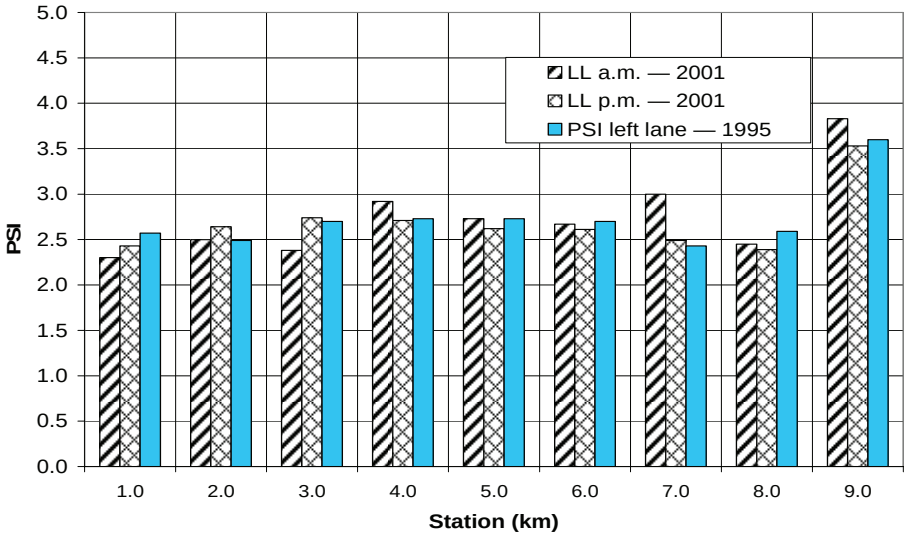

Figure 85. Comparison of PSI ratings on the northbound direction (summer 2001 versus summer 1995).

Twelve PCC cores were obtained for PCC strength, modulus of elasticity, and CTE testing.

The following findings are presented from the site inspection visit on August 2001:

- Extensive damage to the pavement structure was observed.

- The absence of maintenance to the drainage structures and a significant increase in the traffic loadings appear to be the primary factors contributing to the poor performance of this road.
- Lack of crack sealing allows the water to infiltrate into the pavement, which further contributes to the distress formation.
- A comparison of the LTE analysis performed with 1993 and 2001 data shows that the LTE measured in 2001 was much higher than that measured in 1993. The higher LTE values measured during summer 2001 are believed to be due to the fact that in 1993, not all joints had cracked, resulting in larger joint movements and therefore contributing to a reduction in LTE. In 2001, an evaluation of joint movement showed that every joint was cracked.
- The deflection analysis appear to indicate that reduced structural capacity is occurring, possibly due to striping in the HMA layer.
- Although the riding quality for this road is low, no significant reduction has been observed from previous evaluations.

C.2 CRCP SITES INVESTIGATED

C.2.1 CRCP Section at I–30 and I–35 Interchange in Fort Worth, TX

Because of its extensive network of CRCP pavements, the State of Texas was selected for identification of one of the two CRCP sites used for validation of HIPERPAV II. During the summer of 2001, TxDOT was undertaking the improvement of the U.S. Interstate (I)–35/I–30 interchange in Fort Worth, TX. As part of the improvement, a private contractor was constructing CRCP pavement on the approach to a bridge structure on the main lanes and on several access ramps. It was deemed this site could provide an excellent opportunity for validation of the HIPERPAV II module.

On July 16, 2001, a section of CRCP pavement was instrumented and monitored for 72 hours. This section was part of one of the access ramps on the I–35/I–30 interchange. Once at the site, all the preconstruction information was collected, including pavement design, mix design, and materials. The typical cross section at the construction site is shown in figure 86. The concrete was being placed in two stages. The right lane and monolithic curb were constructed first, and tie bars were installed to place the left lane and curb in a second stage.

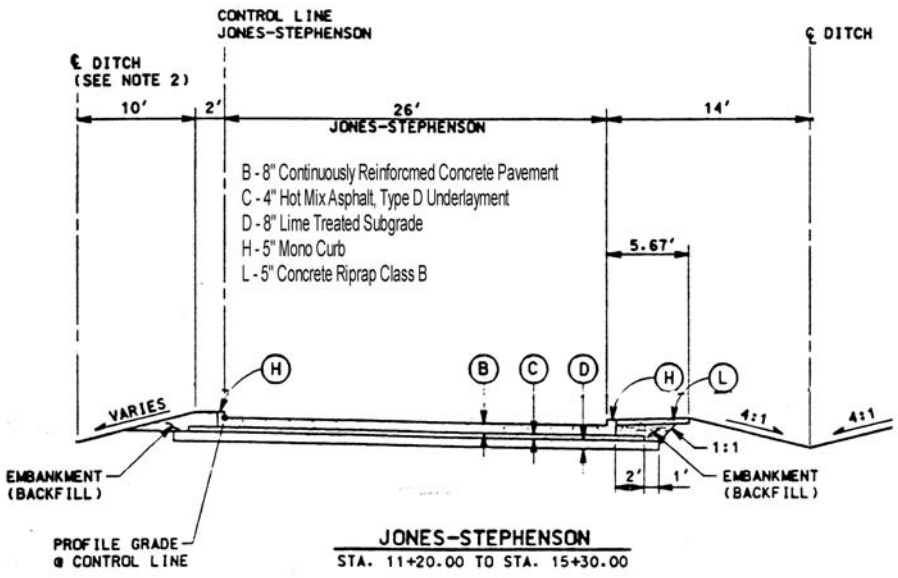

(1 ft = 0.3048 m, 1 in = 25.4 mm)

Figure 86. Typical cross section for the CRCP instrumented section.

To characterize the properties for the concrete at the site, information was collected on the mix design, admixtures, and additives used, as well as the coarse and fine aggregate properties and geological type. The mix design for this project is shown in table 65.

Table 65. Concrete mix design for CRCP on Jones-Stephenson access road, Texas.

Mix Design	Proportions
Water	138 kg/m^3
Cement type IP	309 kg/m^3
Fine aggregate	678 kg/m^3
Coarse aggregate, maximum aggregate size 38.1 mm, crushed limestone	1105 kg/m^3
Retarder	1082 ml/m^3
Air entrainer—(5%)	108 ml/m^3

C.2.1.1 Instrumentation Procedures

On July 12, 2001, the project team met with TxDOT and contractor representatives to identify the section to instrument. Due to repositioning of the paver, the next section to be placed was scheduled for Monday, July 16, 2001. During the days before placing the section to be monitored, the previously placed sections were surveyed to identify the typical crack spacing. In addition, a friction test was performed at the site (as described later in this section). From the previous sections placed, the average crack spacing measured was approximately 4.9 m. This survey helped determine the location for the crack inducers on the instrumented section. The crack inducers were spaced at approximately 4.9 m. Figure 87 shows the position of the crack inducers on the instrumented area.

Figure 87. Instrumented section delineated by crack inducers.

Roctest™ embedment vibrating wire gages type EM–5 were installed on the instrumented area at three different depths at midslab, edge, and corner (150 mm from the crack). Type T thermocouples were also installed at seven different depths throughout the pavement depth. The thermocouple located at the PCC surface was installed just after the slip form paver passed by the instrumented area. In addition, resistance gages type CEA–06–125UN–120 were epoxied to the steel rebar at different distances from the expected crack along with embedment gages to monitor the steel and concrete strain. After adhering the gage, mechanical protection was applied to avoid damage of the gage during the construction operations. Figure 88 shows the strain gages in concrete and on the reinforcing steel at the corner location.

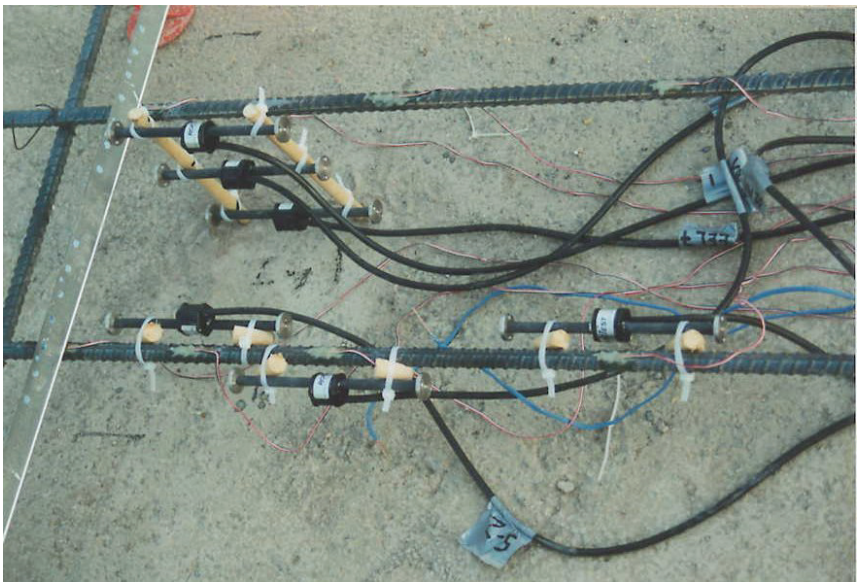

Figure 88. Strain gages in PCC and on reinforcing steel.

On the paving day, the instruments were doublechecked for position, elevation, and tightness. References were marked outside of the slab to determine the exact location of the instruments after the slabs were paved. Every detail in the construction operations was recorded. Shortly before the paver passed by the instrumented slab, the gages and thermocouples were protected with fresh concrete and vibrated with manual equipment. Testers ensured that the concrete used to protect the sensors was from the same batch to be used in the rest of the instrumented area. Some records from the placement activities are:

- Station at start of placement: 11+20.00.
- Stations at instrumented section: 13+55.
- Station at end of placement: 15+49 (the paver was repositioned and continued paving).
- Placement time at instrumented section: 11:05 h.
- Measured pavement thickness: 231 mm.
- Tinning: 11:45 h.
- Curing time: 12:30 h.
- Sky conditions: sunny.
- Mix temperature: 31.5 ºC.
- Subbase temperature during placement: 36.3 ºC.
- Transverse Soff-Cut® on instrumented section: 13:40 h.
- Linear variable displacement transducers (LVDT) installed: 20:50 h.

To measure CTE and free drying shrinkage in the field, two cylinder molds were instrumented with a vibrating wire strain gage and a thermocouple at the center of the specimen.

To ensure development of crack formation, green sawing was performed on the adjacent cracks to the instrumented area with Soff-Cut equipment approximately 2.5 hours after placement.

To measure the slab curling and warping, LVDTs were installed at the edge and at the corner of the test slab. These instruments were installed approximately 10 hours after placement and before the cracks had occurred.

After the concrete had set, DEMEC buttons were glued on the location of the crack inducers and 0.51 m toward the center of the slab along the edge from each crack. On the second day, after the first cracks appeared, DEMEC buttons were also glued at 20 additional cracks to monitor the crack movement due to temperature fluctuations and drying shrinkage.

A friction test also was performed to characterize the friction force developed at the concrete slab-subbase interface. The procedure consisted of casting a 0.9-m wide by 1.5-m long plain concrete slab, with the same thickness of the projected CRCP pavement, on top of the same subbase type. The slab was cast on July 13, 2001, and the friction test was performed 5 days later. For this test, a force was applied on one side of the slab with a hydraulic jack. A load cell was used to measure the applied load. Dial gages were installed at the opposite side to measure the slab movement. The friction force was determined from the applied load and the area under the slab. The history of friction force and slab movement during the pushoff procedure was recorded. The friction force at sliding also was identified. During the determination of the friction for this section, it was observed that the bond between concrete and asphalt

was so strong that shear forces developed in the asphalt. This originated a plane of failure in the asphalt along the border of the slab against which the load was applied, as illustrated in figure 89. Both the concrete slab and bonded asphalt slid together, originating the friction force underneath the asphalt subbase, between the asphalt layer and the lime-treated subgrade.

Figure 89. Shear failure as a result of pushoff test.

On the days following placement, pavement profiles were measured with Dipstick equipment to detect any changes in the profile of the CRCP slabs due to curling and warping. The pavement profiles were measured at several slab diagonals in between cracks at two different times during the day. The measurements were made early in the morning, when the pavement was at its coolest temperature at the surface, and in the afternoon, when the pavement surface had warmed up, to capture the maximum difference in shape of the CRCP slabs due to different thermal gradients. The climatic conditions at the site were monitored for the 72-hour period after placement. The air temperatures during the first days after construction ranged from 26.6 ºC to 40.0 ºC.

C.2.1.2 Monitoring Program

Dataloggers were used to constantly monitor the pavement. This equipment was programmed to retrieve concrete strains, concrete temperature, and vertical displacement every 10 minutes during the 72-hour period. Weather conditions were recorded every 15 minutes during the 72-hour period.

Condition surveys were performed for the entire section placed on July 16, 2001, to observe the cracking pattern in terms of crack spacing and crack width. During the same period, crack movement and PCC strain were monitored with DEMEC calipers twice a day.

During construction, the surface of the pavement was finished on two 76 by 76-mm squares 457 mm from the slab edge and separated 305 mm from each other, center to center. This was done to estimate the PCC set time with pulse velocity equipment. These areas were finished to leave a smooth surface. During monitoring of the test slab, the pulse velocity transducers were placed against both surfaces separated 305 mm apart, center to center, to obtain the transit time of the ultrasonic pulses traveling in the concrete from one transducer to the other. Although the reinforcing steel affected the pulse velocity measurements

(resulting in an overestimation of the elastic modulus), the rate of change in pulse velocity with time provided a good indication of when set time occurred. Analysis of this information indicates that set time occurred at approximately 3 hours, which seems to correlate well with the high placement temperatures observed.

C.2.1.3 Initial Observations

During the condition surveys, it was observed that a crack formed at the location of both crack inducers, as planned. The average crack spacing for the rest of the placement on that day was very close to the crack spacing observed in previous days. On the second and third day, additional cracks were observed at some areas with previously large crack spacings. However, for the instrumented section, no intermediate cracks were observed during the monitoring period. Figure 90 shows the sensor locations with respect to the observed cracks as constructed.

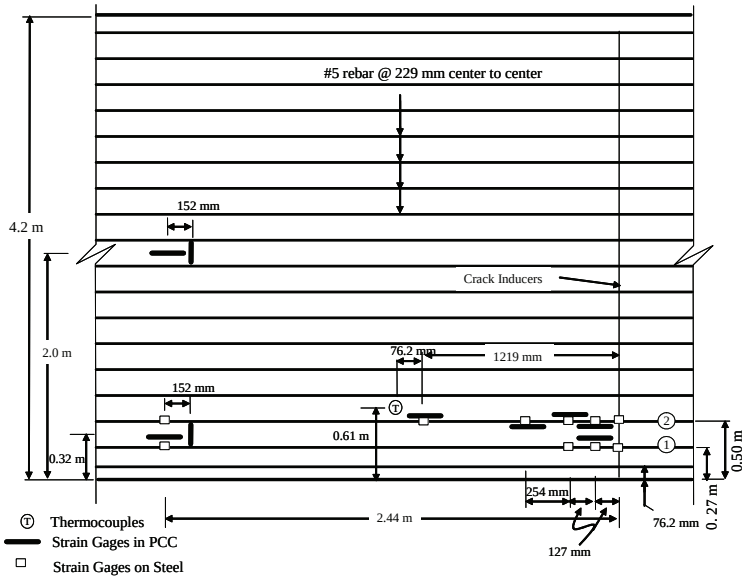

Figure 90. Position of strain gages and thermocouples as constructed.

C.2.1.4 Laboratory Tests

Concrete specimens were prepared at the site with the same batch of concrete delivered on the instrumented section. Personnel with the FHWA Mobile Concrete Laboratory helped prepare the concrete specimens. The specimens were cured in the field for the first 24 hours, then cured under laboratory conditions according to ASTM C 192. While at the site, sufficient materials to replicate the concrete mix in the laboratory were collected. The materials collected were used to perform adiabatic calorimetry, drying shrinkage, and set time tests.

C.2.2 CRCP Section on I–29 near Sioux Falls, SD

The second field section for the CRCP model validation was selected in the State of South Dakota. At the end of the summer of 2001, the South Dakota DOT was reconstructing I–29 south of Sioux Falls, SD, from approximately milepost 59 to milepost 70. In contrast to the CRCP instrumentation in Texas with air temperatures from 26.6 ºC to 40.0 ºC, the air temperatures in South Dakota ranged from 1 ºC to

24.4 ºC, providing a significant difference in terms of temperature and behavior under which the CRCP module will be evaluated and validated.

South Dakota DOT representatives and a member of the South Dakota Chapter of the American Concrete Pavement Association (ACPA) helped locate a CRCP construction job in South Dakota. Beginning on September 25, 2001, a section of CRCP pavement was instrumented and monitored for 72 hours. Once at the site, all the preconstruction information was collected, including pavement design, mix design, and materials. The typical cross section at the construction site on I–29 is designed to accommodate a four-lane divided road. Each direction is 12.2-m wide, with a 1.8-m left shoulder, two 3.65-m lanes, and a 3-m right shoulder as indicated in figure 91 (this figure shows the section in the opposite direction to traffic). The central portion of the pavement was being constructed with CRCP pavement to conform a 3.65-m wide right lane with 0.6-m PCC widened shoulder and a 3.65-m wide left lane. The rest of the shoulders were being paved with HMA. A longitudinal joint was being cut between lanes. The CRCP pavement is 279 mm thick on top of a 102-mm granular subbase.

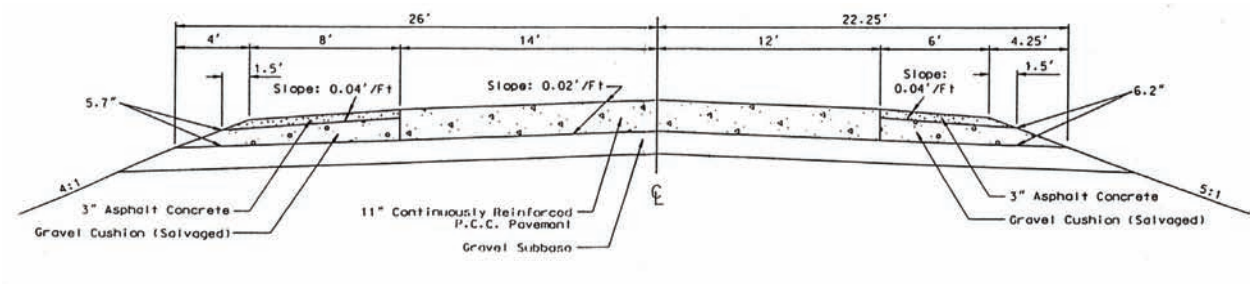

1 ft = 0.3048 m

Figure 91. Typical cross section for I–29, South Dakota (from opposite direction to traffic).

To characterize the properties for the concrete at the site, information was collected on the mix design, admixtures, and additives used, as well as the coarse and fine aggregate properties and geological type. The mix design for this project is shown in table 66.

Table 66. Concrete mix design for reconstruction project on I–29, South Dakota.

Mix Design (Saturated Surface Dry)	kg/m^3
Water	140
Cement type I/II	303
Fly ash class F	67
Fine aggregate	724
Coarse aggregate, maximum aggregate size 25.4 mm, crushed ledge rock (Sioux quartzite)	1043
Water reducer—WRDA 82	774–1160 ml/m^3, depending on weather conditions
Air entrainer—Daravair® R	690 ml/m^3 (6.5 percent air)

C.2.2.1 Instrumentation Procedures

The field crew arrived at the project the morning of September 24, 2001. After a briefing on the instrumentation procedures, the South Dakota DOT helped identify the section to instrument. The section that was placed on Friday, September 21, 2001, was surveyed to identify the average crack spacing. The

crack spacing observed varied from 4.3 m to 18.3 m, with an average spacing of 9.1 m. This survey helped determine the location for the crack inducers on the instrumented section. The crack inducers thus were spaced at approximately 9.1 m.

Similar to the instrumentation of the CRCP section in Texas, embedment gages type EM–5 were installed at midslab, edge, and corner at three different depths. Thermocouples were also installed at seven different depths throughout the pavement. Micromeasurements CEA–06–125UN–120 gages were also installed on the steel rebars at different distances from the crack. In addition, similar procedures were used to monitor climatic conditions, CTE and free drying shrinkage in the field, slab curling and warping, and cracking behavior.

To position the Roctest vibrating wire gages type EM–5, two wood dowels were driven into the subbase (granular subbase), separated approximately 102 mm for each set of gages, as indicated in figure 92. The gage then was fixed on the dowels at the proper height with plastic zip ties. Wood dowels were also used to install type T thermocouples at seven different depths throughout the pavement. The thermocouple located at the PCC surface was installed just after the slip form paver passed by the instrumented area.

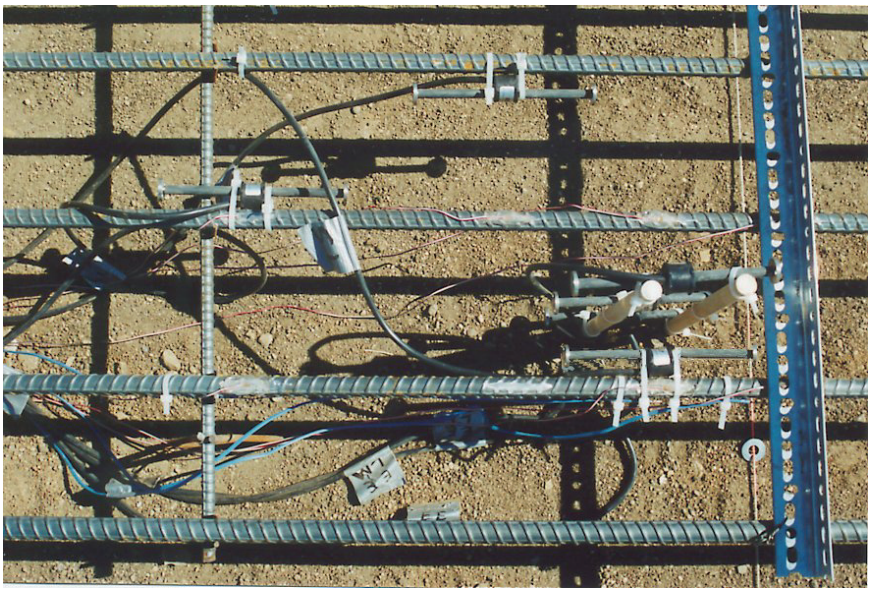

Figure 92. Strain gages in PCC and on reinforcing steel.

The procedure to install the micromeasurements CEA–06–125UN–120 steel gages consisted of grinding the rebar corrugations to leave a smooth surface. After the corrugations were ground, a file was used to smooth any surface indentations. The surface was smoothed even more with sandpaper grade 60, then with sandpaper grade 400. The grinding was done so as not to reduce the diameter of the rebar. Before adhering the resistance gage to the surface, isopropyl alcohol was used to clean and degrease the treated surface of the rebar. The gages with preattached lead wires were taped to the rebar. A conditioning solution was brushed on the surface of the rebar and on the area of the gage to be bonded to the rebar. After 1 minute of drying, M-bond 200™ adhesive was used to adhere the resistance gage to the rebar. After M-bond 200 was applied, the gage was held down against the surface of the rebar for at least 1 minute. After adhering the gage, researchers applied mechanical protection to avoid damage of the gage during the construction operations.

After all the gages were installed, a small trench was dug into the subbase on the area of the paver track to lead all the sensor wires out of the pavement and to the dataloggers.

Some records from the placement activities are:

- Stations at instrumented section: 536+65 to 536+95.
- Placement time at instrumented section: 13:05 h.
- End of placement approximately 15:00 h (due to paver breakdown).
- Measured pavement thickness: 279 mm (average of several points).
- Curing time: 14:15 h.
- Sky conditions: mostly sunny.
- Mix temperature: 21.2 ºC.
- Subbase temperature during placement (25.4 mm into subbase): 20.6 ºC.
- Saw cutting time (longitudinal joint): 9/25/01 (16:30–18:30 h).

C.2.2.2 Initial Observations

As discussed previously, the crack spacing initially estimated for this section was approximately 9.1 m. However, the cooling cycle after placement reached a low temperature of 1 ºC, which was beyond the forecasted low temperature of 4.4 ºC. This excessive temperature drop significantly reduced the crack spacing, and one intermediate crack occurred at the instrumented section on the first day. On the second day, two additional cracks were observed (see figure 93). However, the additional cracks in the instrumented section did not affect the main objective of the experiment, which was to determine the development of concrete and steel strains near the crack locations. In addition, the data collected for this site complemented the data collected for the Fort Worth, TX, section, where no intermediate cracks were observed. Figure 94 shows the sensor locations with respect to the observed cracks as constructed.

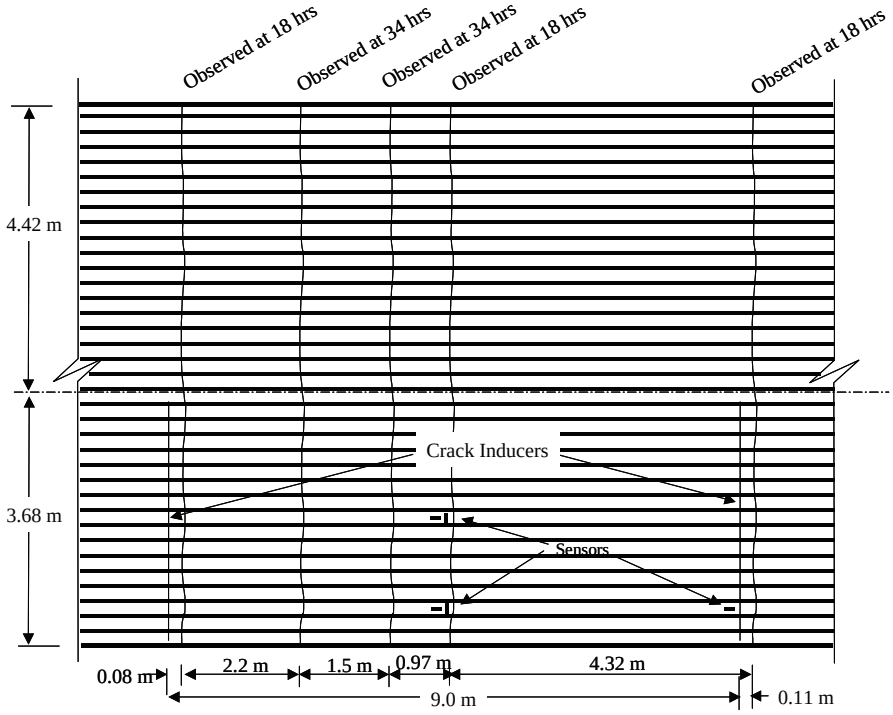

Figure 93. Cracking pattern on instrumented section.

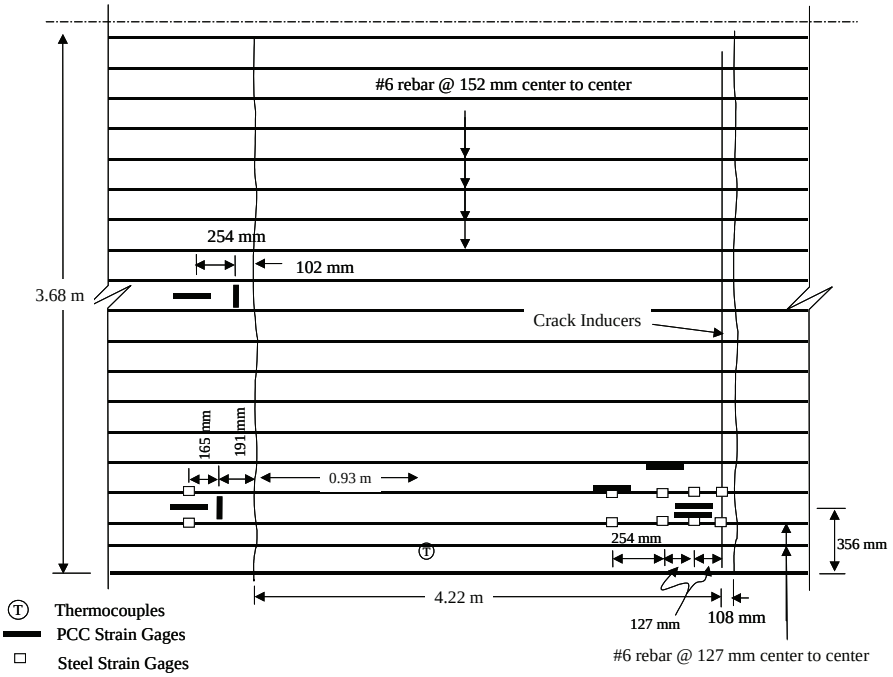

Figure 94. Location of the sensors with respect to the pavement edge and cracks as constructed.

C.2.2.3 Laboratory Tests

Concrete specimens were prepared at the site. These specimens were prepared to characterize the concrete properties under laboratory and field conditions. Two sets of laboratory concrete specimens were prepared as described in table 67. The first was cured under field conditions according to ASTM C 31, and the second set was cured under laboratory conditions according to ASTM C 192. The difference in curing procedures was done to verify the maturity properties for this specific concrete.

Table 67. Laboratory testing plan of PCC concrete specimens.

Test	Field Curing Conditions	Laboratory Curing Conditions
Splitting tensile	Three repetitions at 1, 2, and 3 days	Three repetitions at 1, 3, 7, and 28 days
Compression	–	Three repetitions at 3, 7, and 28 days
Modulus of elasticity	–	Three repetitions at 7 and 28 days
CTE	–	Two repetitions at 28 days
Temperature monitoring	One specimen	One specimen

C.2.2.4 Laboratory Results from Validation Field Sites

This appendix presents the laboratory testing data for the HIPERPAV II sites in Illinois, Mexico, South Dakota, and Texas. Laboratory testing included compressive strength, splitting tensile strength, modulus of elasticity, CTE, drying shrinkage, and set time. The testing matrix is provided in table 68.

Table 68. HIPERPAV II laboratory testing.

Site	Compressive Strength	Splitting Tensile Strength	Modulus of Elasticity	Drying Shrinkage	Set Time	CTE
Illinois	X	X	X	–	–	X
Mexico	X	X	X	–	–	X
South Dakota	X	X	X	X	X	X
Texas	X	X	X	X	X	X

The laboratory results are presented in the sections below, as are the concrete mix designs.

C.3 MIX DESIGNS

The concrete mix designs for the sites in Illinois, Mexico, South Dakota, and Texas are given in table 69.

Table 69. Concrete mix designs for the HIPERPAV II field sites.

	Illinois	Mexico	South Dakota	Texas
Cement type	I	I	II	IP
Cement content	341 kg/m^3	280 kg/m^3	303 kg/m^3	309 kg/m^3
Cementitious materials content	–	–	Fly ash class F 67 kg/m^3	–
Water content	148 kg/m^3	158 kg/m^3	140 kg/m^3	138 kg/m^3
Coarse aggregate content	1121 kg/m^3	1006 kg/m^3	1043 kg/m^3	1105 kg/m^3
Maximum aggregate size	–	38.1 mm	25.4 mm	38.1 mm
Aggregate type	–	–	Sioux quartzite	Limestone
Fine aggregate content	666 kg/m^3	932 kg/m^3	724 kg/m^3	678 kg/m^3
Water reducer	Type A WRDA with Hycol	1333 ml/m^3	WRDA 82 774–1160 ml/m^3	HPS–R 1082 ml/m^3
Air entrainer	Darex® AEA	115 ml/m^3	Daravair R 690 ml/m^3	AIR–INTX 108 ml/m^3

C.4 STRENGTH AND STIFFNESS FOR TEXAS SITE

At the Fort Worth, TX, I–35 West/I–30 interchange, a 203-mm thick CRCP was constructed on July 16, 2001. More details on the highway construction are given in section C.2.1. Several cylinders were molded to measure concrete material properties at 0.5, 1, 3, 7, and 14 days. The concrete specimens were cured in the field for the first 24 hours and then under laboratory conditions according to ASTM C 192. The compressive strength, splitting tensile strength, and modulus of elasticity as a function of time are shown in figures 95 to 97. All specimens were soaked until the time of testing. The individual data points are hollow, and the average is shown as a solid point.

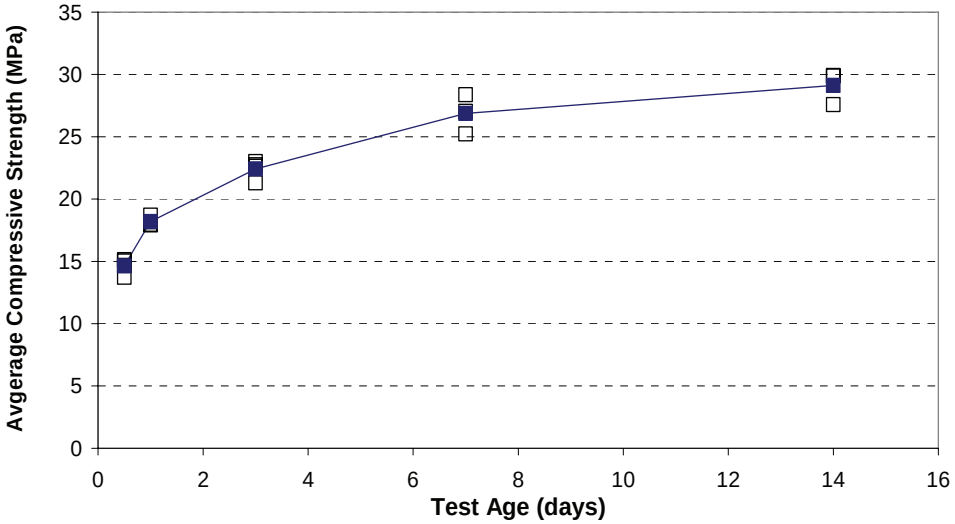

Figure 95. Time growth of Texas compressive strength.

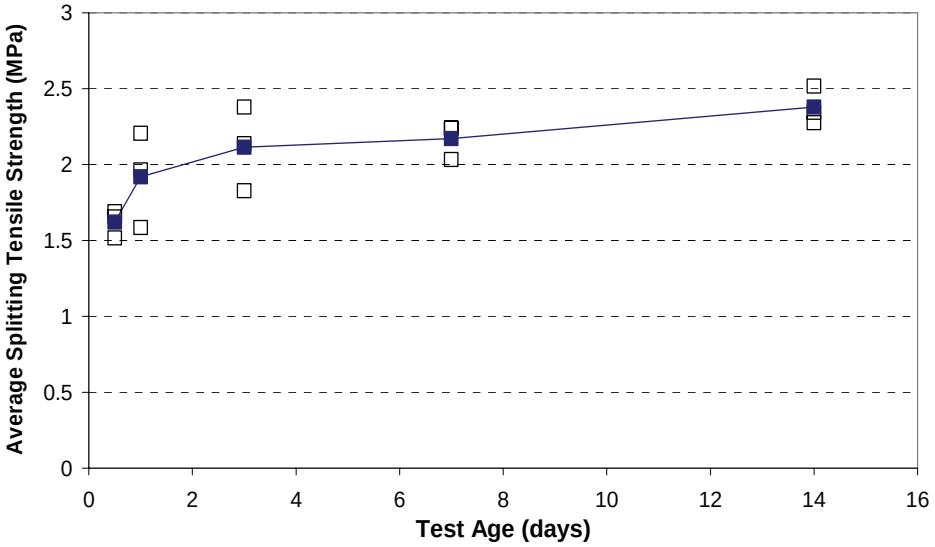

Figure 96. Time growth of Texas splitting tensile strength.

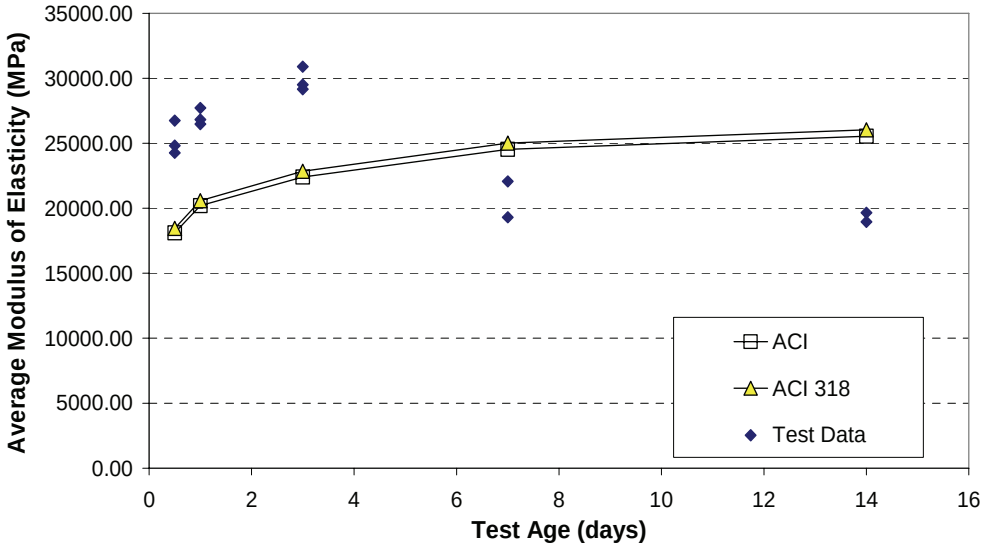

Figure 97. Time growth of Texas modulus of elasticity.

Because the compressive strength was measured on 102-mm and 152-mm diameter cylinders, it had to be adjusted for the different cylinder sizes.[61] All the splitting tensile tests were completed on 152-mm cylinders. The compressive strength and the splitting tensile strengths continue to increase from 0.5 to 14 days. Variability of the splitting tensile strength is high at early ages.

The modulus of elasticity data does not increase with time. The modulus increases from 0.5 to 3 days, and then drops at 7 and 14 days. The FHWA Mobile Concrete Laboratory tested the early-age concrete (0.5 to 3 days), and Construction Materials Research Group at the University of Texas at Austin tested the 7- and 14-day samples. Variability in testing and in data interpretation may have contributed to the

difference in modulus values. Using the ACI correlations between compressive strength and concrete modulus of elasticity shown in equations 259 and 260:[58]

ACI 318 Code (1):

$$E = 4{,}700\, f_c^{0.5}\,(MPa) \tag{259}$$

and

ACI 318 Code (2):

$$E = w_c^{1.5} \cdot 0.043\, f_c^{'0.5}\,(MPa) \quad (w_c = 2340 \text{ kg/m}^3) \tag{260}$$

It is apparent that the expected modulus of elasticity value lies below the high values at early ages, and above the low values at 7 and 14 days. The raw laboratory data for the Texas site are given in tables 71 to 74 in sections C.8 to C.10.

C.5 STRENGTH AND STIFFNESS FOR SOUTH DAKOTA SITE

The laboratory results for compressive strength, splitting tensile strength, and modulus of elasticity are presented here for the CRCP constructed in South Dakota on I–29. More details on the construction process and monitoring are provided in section C.2.2. It is apparent that the compressive strength, tensile strength, and modulus of elasticity increase with time in figures 98 to 100. Likewise, the modulus of elasticity for South Dakota is estimated from the compressive strength data using the ACI and ACI 318 models in figure 100. The model predictions are lower than the measured data.

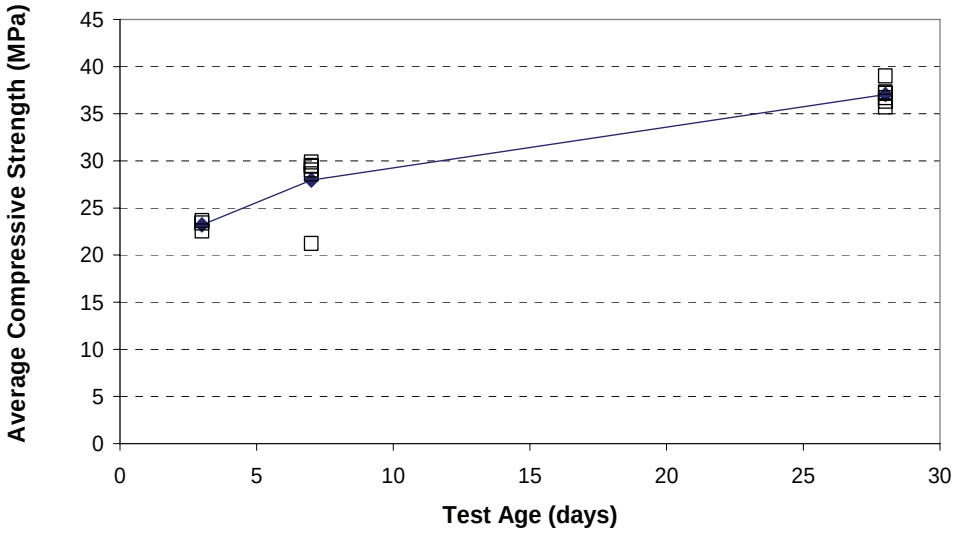

Figure 98. Time growth of South Dakota compressive strength.

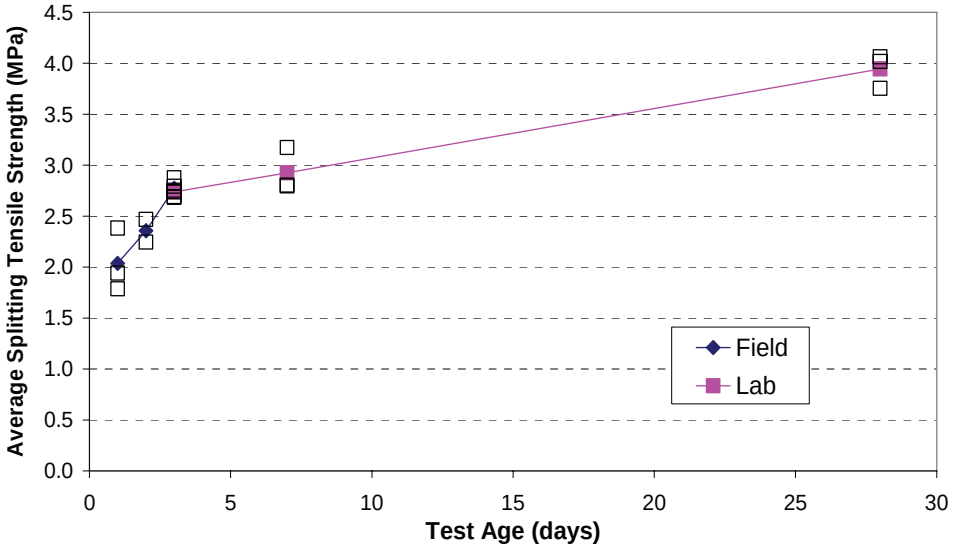

Figure 99. Time growth of South Dakota splitting tensile strength.

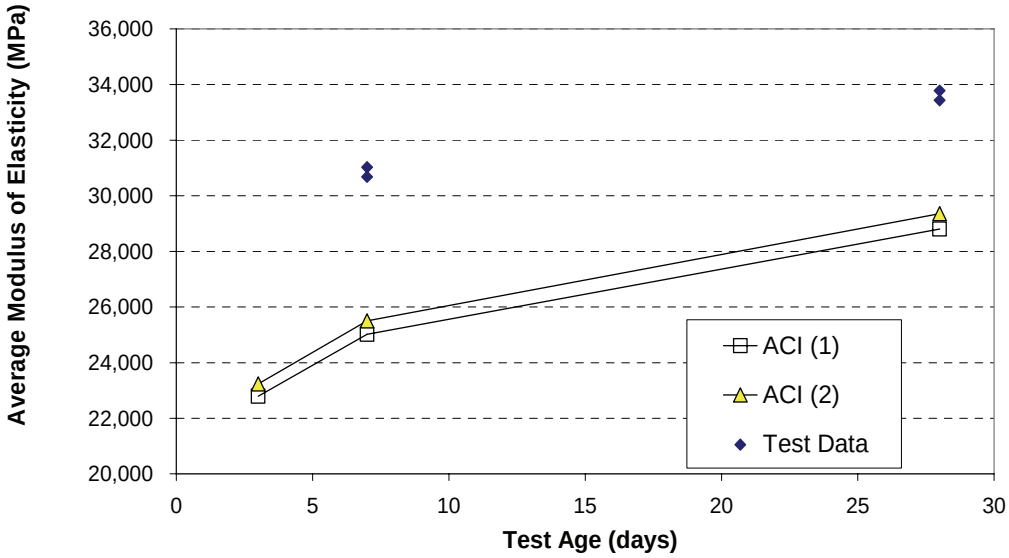

Figure 100. Time growth of South Dakota modulus of elasticity.

C.6 STRENGTH AND STIFFNESS FOR MEXICO SITE

An extensive pavement evaluation was conducted on the JCP section of the Ticuman bypass on August 21–24, 2001. This pavement was originally constructed from September 23 to October 12, 1993. The early-age laboratory data from 1993 are compared to the properties measured in 2001 in the figures below (figures 101 to 103). The concrete strength continued to increase over time, as expected, as does the splitting tensile strength and the modulus of elasticity. The modulus of elasticity is estimated using the ACI and ACI 318 models in figure 103. The predicted values are in the same range as the measured ones.

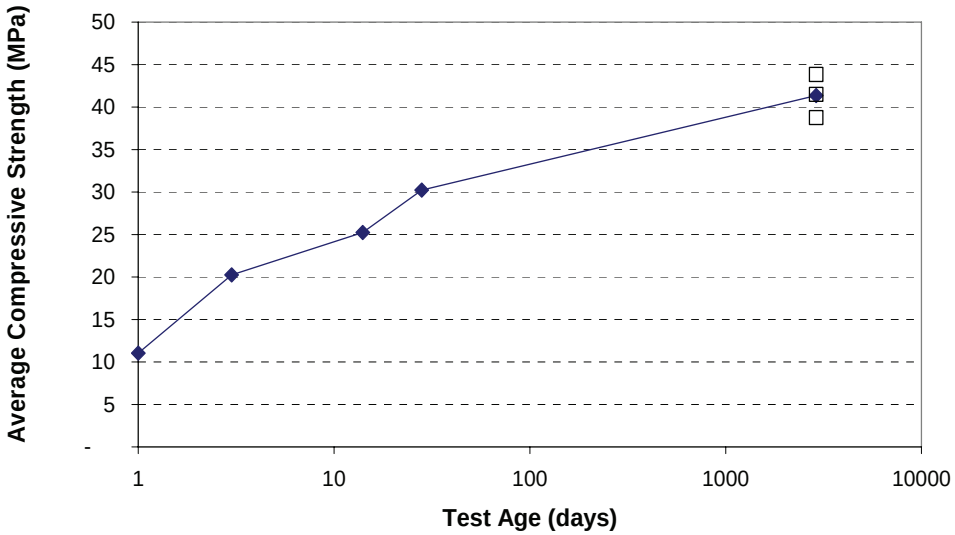

Figure 101. Time growth of Mexico compressive strength.

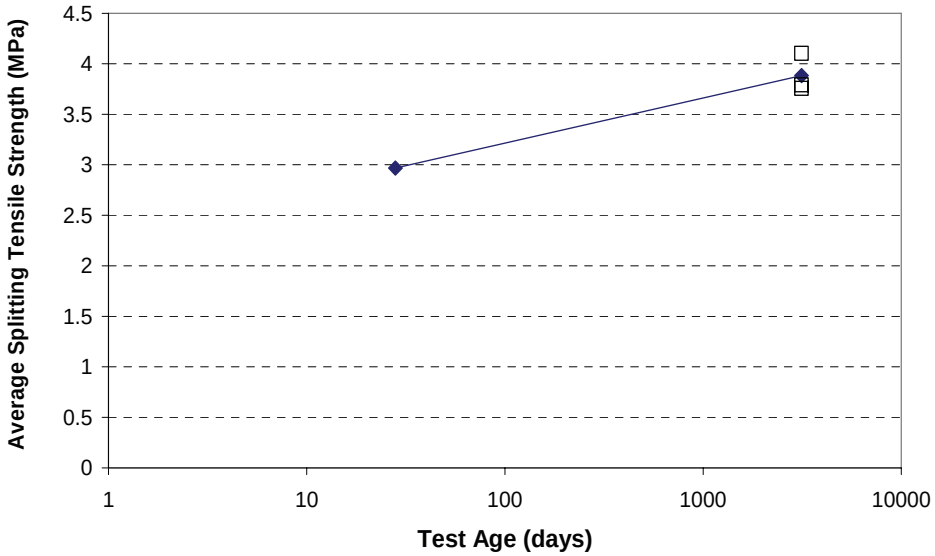

Figure 102. Time growth of Mexico splitting tensile strength.

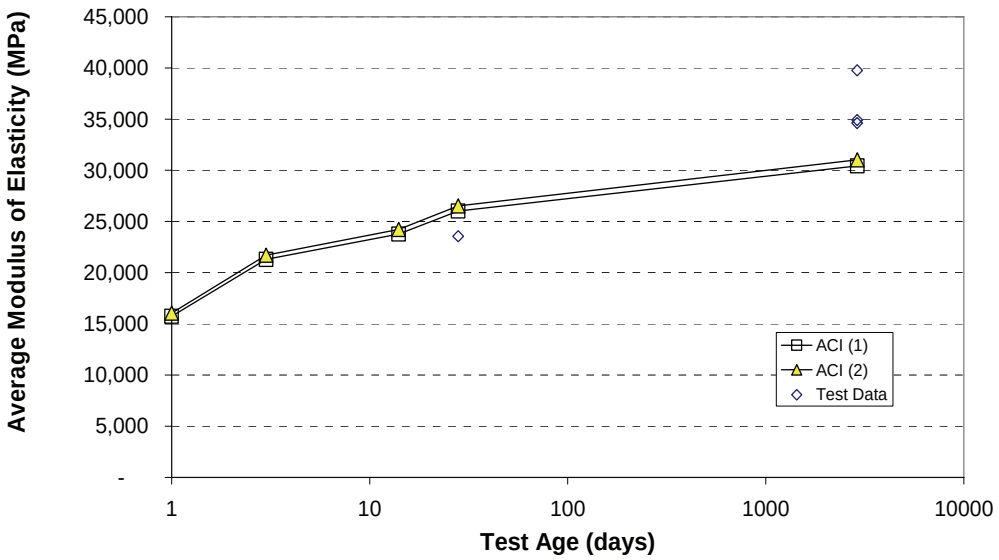

Figure 103. Time growth of Mexico modulus of elasticity.

C.7 STRENGTH AND STIFFNESS FOR ILLINOIS SITE

U.S. Highway 50, a JPCP near Carlyle, IL, was monitored from August 7 to 10, 2001. It was originally constructed from April to August of 1986. At that time, air content was 5.4 percent, slump was 51 mm, the 14-day flexural strength was 4.9 MPa, and the 28-day flexural strength was 492 MPa. Cores of the pavement were taken and tested in May 2002. The resulting concrete properties are listed in table 70.

Table 70. Average concrete properties for the Illinois site (tested May 2002).

Illinois	Concrete Properties (MPa)	CV (%)
Compressive strength	40.7	3.9
Splitting tensile strength	4.57	1.6
Modulus of elasticity	27,441	2.2

The flexural strength data, which is assumed to be measured under centerpoint loading, was also used to estimate the early-age compressive strength of this concrete using the following relationship shown in equation 261:

$$CS = \left[\frac{0.864 \cdot Cnt\ \ Pt\ \ Flex\ \ Str}{2.3} \right]^{1.5} \tag{261}$$

Its comparison to the compressive strength measured in May 2002 is shown in figure 104. After 14 days, the data shows a minimal increase in compressive strength, except for the 90-day calculated value.

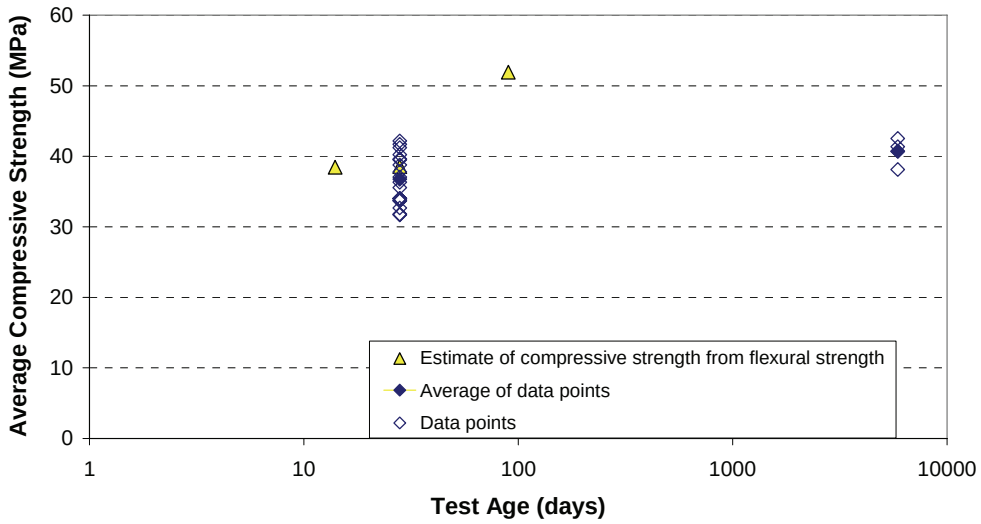

Figure 104. Time growth of Illinois compressive strength.

Likewise, the estimated compressive strength values are used to predict the modulus of elasticity (figure 105). They correlate well to the measured modulus of elasticity, except for the 90-day value as mentioned previously. Modulus of elasticity is relatively stable after 14 days.

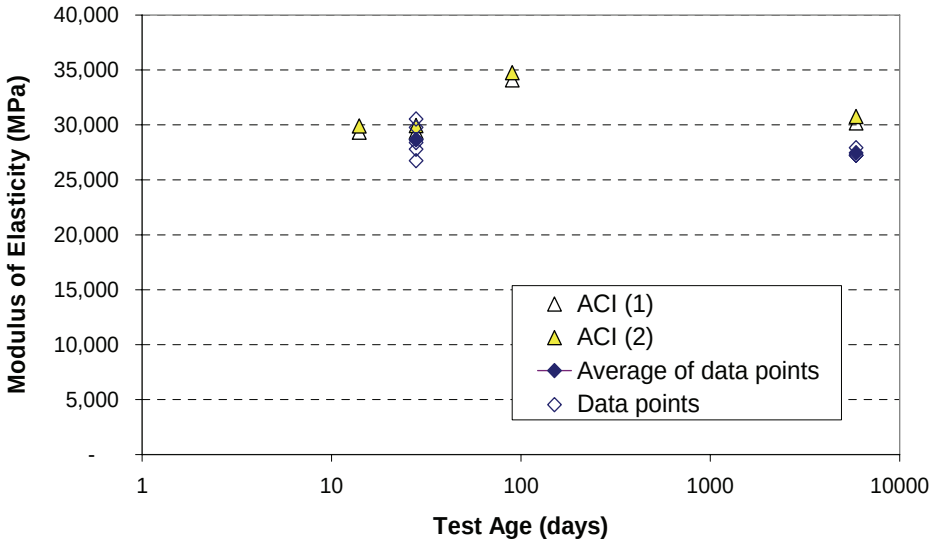

Figure 105. Time growth of Illinois modulus of elasticity.

C.8 DRYING SHRINKAGE FOR TEXAS AND SOUTH DAKOTA SITES

The drying shrinkage of the concrete placed in Fort Worth, TX, and South Dakota was measured in the laboratory using ASTM C 157, with minor modifications. The specimens were 102-mm prisms that were 286 mm long. The concrete mix quality control parameters are given in table 72. They were cured 24 hours at 100 percent RH and 23 °C, then were stored at 50 percent RH at 23 °C for the remaining period of time. Readings were taken every day for the first 7 days, and then at 14, 28, and 112 days. The time

growth of drying shrinkage is shown in figure 106 for South Dakota and in figure 107 for Texas. The Baźant-Panula drying shrinkage model is fit to the laboratory data, as shown (described in section B.1.3). If the ultimate shrinkage is known, it can be input to the model, or the Baźant-Panula model can predict ultimate shrinkage. A more accurate prediction is made if the ultimate drying shrinkage is known.

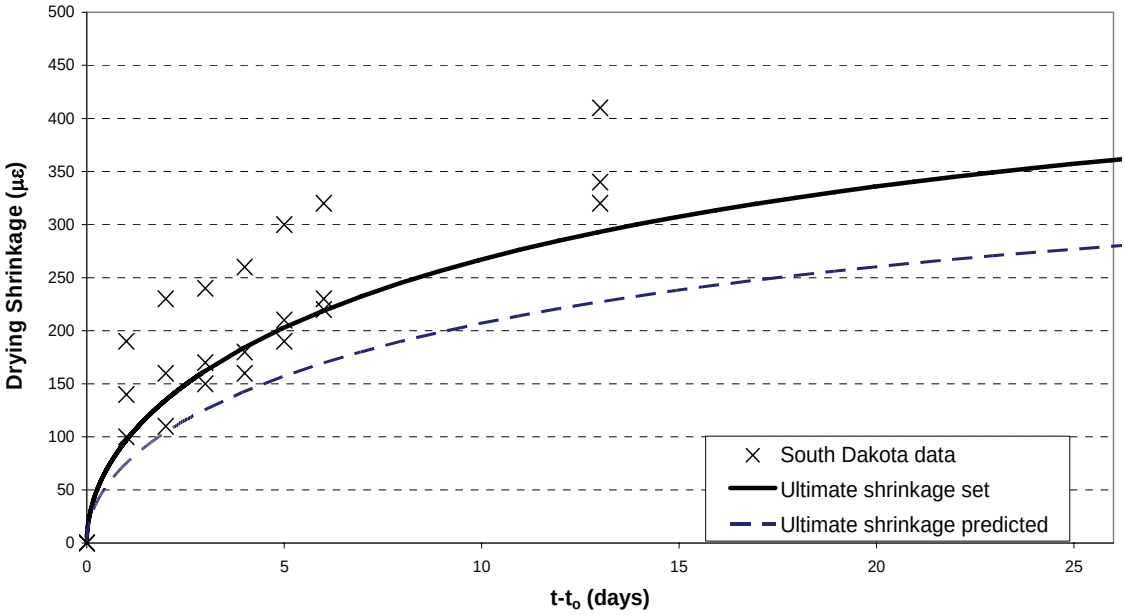

Figure 106. Drying shrinkage of South Dakota concrete.

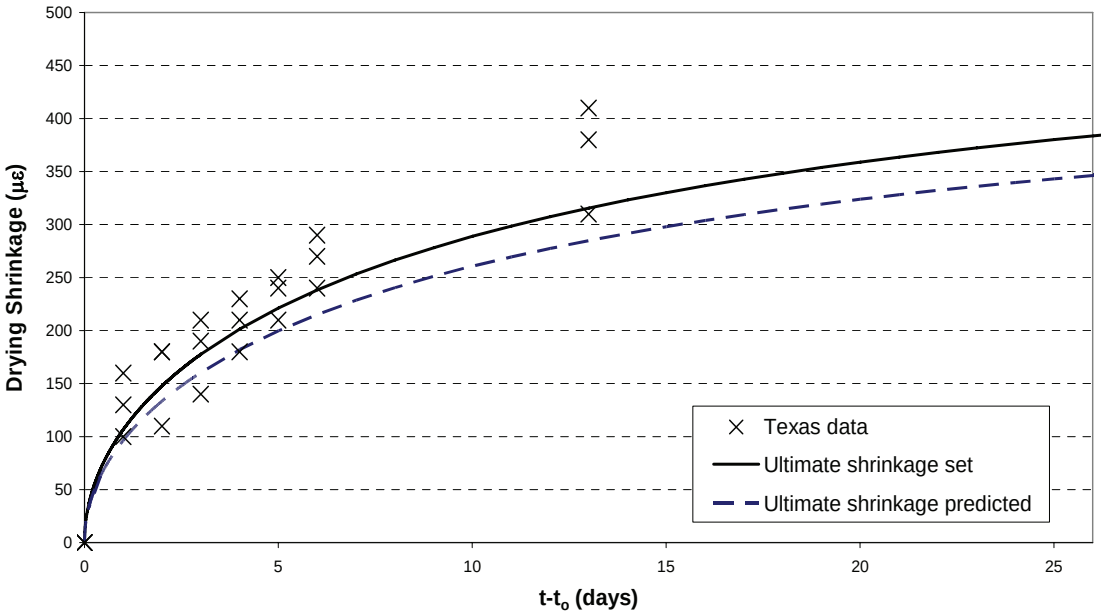

Figure 107. Drying shrinkage of Texas concrete.

The drying shrinkage input parameters for the Baźant-Panula model are listed in table 71. The concrete mix proportions that were input to the model were taken from table 69.

Table 71. Drying shrinkage model input.

Input	South Dakota	Texas
28-day compressive strength (MPa)	37.3	33.4
28-day modulus of elasticity (MPa)	33,784	27,580
Set time (days)	0.28	0.20
D (= 2 * volume/surface area) (mm)	46	46
k_s	1.28	1.28
α_1	0.85	1
α_2	1	1

The 28-day compressive strength and modulus of elasticity values were estimated from the measured laboratory data. Set time was taken from the data in the following section. Finally, k_s, the shape parameter, represents the shape of the laboratory produced drying shrinkage specimens.

C.9 SETTING TIME FOR TEXAS AND SOUTH DAKOTA

The set times for the concrete placed in Fort Worth, TX, and South Dakota were determined by following ASTM C 403. The quality control data for these mixes is given in table 72.

Table 72. Quality control data for Texas and South Dakota concrete mixes.

Concrete Property	South Dakota	Texas
Slump	45 mm	70 mm
Batching temperature	22.2° C	21.7° C
Batching date	10/26/2001	10/26/2001
Batching time	10:39 a.m.	11:27 a.m.
Air content (%)	4	5.5
Unit weight (kg/m^3)	2340	2262

The set time data for Fort Worth, TX was fit using a power function, with an r^2 of 0.99 (figure 108). The corresponding initial and final setting times are listed in table 73. The ambient temperature for measuring the Texas mix set time was 37.8 °C.

Using a regression analysis, the r^2 for the South Dakota data is 0.97. This is less than the 0.98 required by the specification for the set time analysis, so the data was hand fit, as shown in figure 108. The initial and final setting times are listed in table 73. The ambient temperature for the set time measurements using the South Dakota concrete was 18.3 °C.

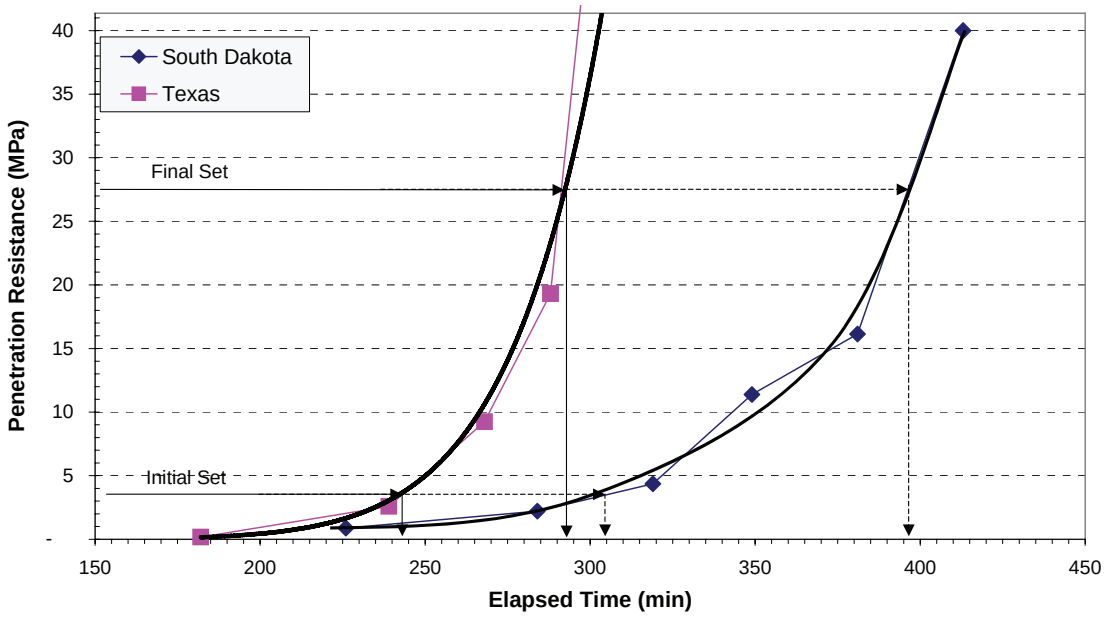

Figure 108. Setting times of concrete for Texas and South Dakota concretes.

Table 73. Setting times of the Texas and South Dakota concrete mixes.

Setting Time	Texas	South Dakota
Initial setting (min)	242	304
Final setting (min)	292	396

The concrete and air temperatures for the fresh concrete mixes from South Dakota and Texas are shown in figures 109 and 110.

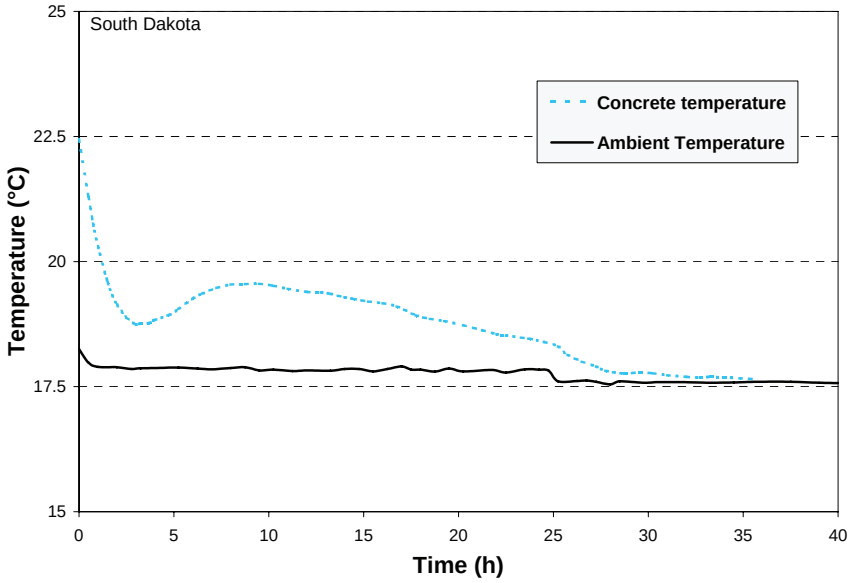

Figure 109. Concrete and ambient air temperatures for the South Dakota concrete.

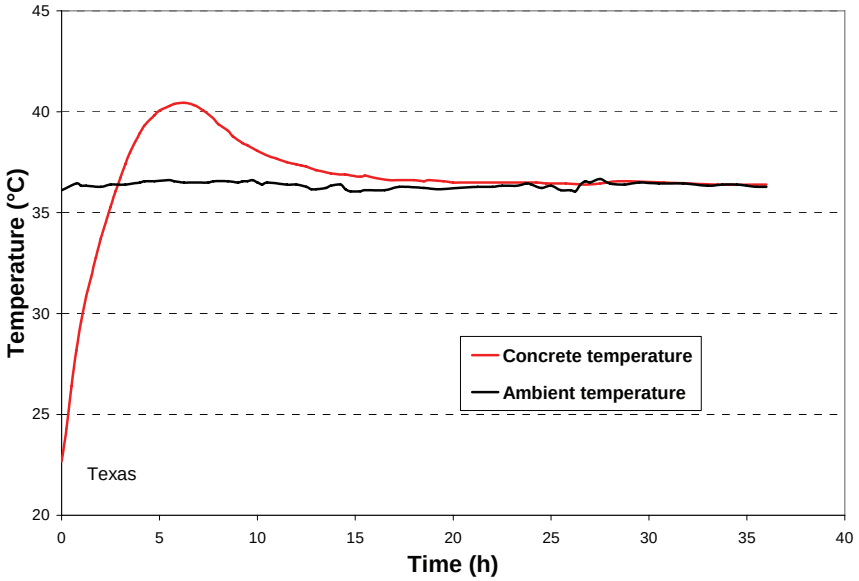

Figure 110. Concrete and ambient air temperatures for the Texas concrete.

C.10 COEFFICIENT OF THERMAL EXPANSION

CTE tests were also performed on concrete specimens for each field site on June 6, 2002. AASHTO test method TP–60–00 was followed. The average CTE values obtained for the PCC specimens tested are listed in table 74.

Table 74. CTE values determined according to AASHTO TP–60–00.

PCC Specimen ID	CTE ($\times 10^{-6}$ m/m/°C)
Fort Worth, TX	7.48
Illinois	6.85
Mexico	7.00
South Dakota	10.91

APPENDIX D VALIDATION OF THE ENHANCED GUIDELINES

Although the CRCP early-age behavior models and long-term JPCP models selected for use in this project have already undergone extensive validation efforts, modification to some of the models to reflect specific early-age conditions and to integrate well with the overall system warrant further validation.

Validation focuses on determining the reliability of the model. Model reliability determines if the model is a good one or a poor one. If there is significant scatter in the data as compared to the prediction, then the model is possibly poor. Less scatter implies that the model is reliable. The reliability of the individual models in the long-term JPCP and early-age CRCP modules in HIPERPAV II was assessed under this concept.

Two levels of validation were undertaken for both the long-term JPCP and early-age CRCP models incorporated into HIPERPAV II. The first level of validation was performed with the use of databases. The second level of validation consisted of selecting pavement sites and obtaining the necessary information for the validation analysis.

The database validation efforts are discussed in section D.1, and the field validation work is discussed in more detail in section D.2. Additional validation also was performed for general early-age behavior enhanced models such as the finite-difference temperature prediction model and the improved drying shrinkage model. Also, initial attempts to incorporate an improved relaxation-creep model were performed. Validation of each of these early-age behavior models is presented in section D.3.

D.1 DATABASE VALIDATION

The primary databases used for this purpose were the database maintained by LTPP and the Texas CRCP database.[105,106] The wider geographical distribution and variety of pavement sections in the LTPP database were determinant factors for its use, while the extensive amount of early-age data for CRCP in the Texas rigid pavement database was a major factor for its selection. Other databases, such as the COPES and the RIPPER databases, were investigated; however, lack of early-age information and monitoring records made the validation efforts difficult.[107,108]

D.1.1 Validation of JPCP Structural Response Models with LTPP Data

Information in the LTPP database was used exclusively for validation of the JPCP structural response models. Provided the LTE model has not been previously calibrated as a whole, pavement sections in the LTPP database were used for model calibration. Subsequently, validation of the JPCP long-term performance predictions was performed with information collected from existing field sites. Calibration of the LTE model is described in this section, and field validation of JPCP existing sites is discussed in section D.2.1.

As previously presented in section B.2.3.1, a model for the prediction of stress and deflection transfer across JPCP joints due to traffic loads was incorporated in HIPERPAV II. Prediction of LTE for JPCP is a function of a number of factors including the presence of dowels, aggregate interlock, pavement geometry, PCC mechanical properties, slab support, and environmental conditions.[69,70,73] The seasonal monitoring program (SMP) under the LTPP program includes monitoring of JPCP sections to observe the effects of temperature and moisture on the pavement structure and its response to loads.[109] Evaluation of LTE for SMP sections with enough information on the factors mentioned above was useful in better

understanding structural behavior of JPCP and provided the basis for calibrating the pavement response LTE model incorporated in HIPERPAV II.

D.1.1.1 Evaluation of Joint Opening

As part of the SMP study, joint movement is monitored along with PCC temperatures and deflections obtained with FWD equipment.[109] This information is believed to be useful in understanding the effect of joint opening on LTE. Lee and Stoffels reported several findings on analysis of joint movement information for the SMP sections.[110] The following observations from that study are of particular interest:

- An increase in PCC temperature causes a reduction in joint opening.
- Some joints appear to be locked, as joint opening does not appear to significantly change with a change in temperature.
- For some pavement sections, joint opening decreases with an increase in PCC temperature up to a given temperature, where the joint opening seems to close, or extraneous material is present at the joint that does not permit further reduction in joint opening.
- Some joints showed erratic large movements that appear to be associated with intermediate freezing joints.

Although joint opening is not directly measured in the SMP study, it is believed that monitoring of the joint movement during hot weather may capture the temperature of joint closure, as was the case for some of the sections analyzed by Lee and Stoffels.[110]

To determine the temperature of closure, an important parameter in the LTE analysis, the procedure developed by Lee and Stoffels was followed for this study.[110] JPCP LTPP sections were investigated and the effective ratio of joint movement to change in PCC temperature (ER) determined. The effective ratio is understood as a reduction in joint opening, in millimeters, for a 100 °C increase in PCC temperature. For this analysis, the information was obtained from the LTPP DataPave 3.0. Table 75 presents the ER statistics for each of the 12 sections investigated. From the analysis summarized here, although slight differences in the computed ER for a few sections were observed, similar findings were obtained to those presented by Lee and Stoffels. In addition to the JPCP sections previously investigated by Lee and Stoffels, SMP sections 39–0204 and 32–0204 were evaluated.

Table 75. Computed effective ratio of joint movement to change in temperature (ER) for SMP sections.

Section ID	Avg. ER (mm/100ºC)	Min. ER (mm/100ºC)	Max. ER (mm/100ºC)	Locked Joints	Closure Temp	Observations
04–0215	−5.82	−7.7	−3.9	1 of 8	32.3	–
06–3042	–	–	–	–	–	No correlation of PCC temperature to joint opening
13–3019	−5.35	−8.7	−3.4	2 of 6	13.8	–
18–3002	–	–	–	–	–	No PCC temperature records in DataPave 3.0 for joint opening dates
31–3018	−5.09	−6.8	−3.5	0 of 6	NR	–
32–0204	−11.72	−23.6	−3.8	3 of 6	NR	Many joints appear locked
37–0201	−2.84	−5.2	−1.8	2 of 6	NR	–
39–0204	−2.85	−6.6	−1.6	0 of 6	NR	–
49–3011	−5.25	−7.0	−3.3	0 of 8	30.5	–
53–3813	–	–	–	–	–	No correlation of PCC temperature to joint opening
83–3802	−9.99	−28.9	−1.4	1 of 6	4.8–14.5	Most joints with small ER
89–3015	−6.22	−12.1	−3.4	2 of 5	NR	–

ER = reduction in joint opening, in millimeters, for a 100 ºC increase in PCC temperature.
NR = temperature of closure not observed within range of temperatures monitored.

The following are some comments on the findings obtained:

- Sections 6–3042 and 53–3813 did not show a significant correlation of PCC temperature to joint opening. Although this could be attributed to joint freezing, a significant variability in joint movement readings (in some cases as high as 25 mm) indicates that the lack of correlation is probably due to measuring error.
- Although ERs are reported for section 18–3002 in reference 110, no PCC temperature records were found in the LTPP database.[110,111]
- Section 32–0204 shows an erratic and large ER for three of the six joints analyzed. Furthermore, the remaining three joints appear to be locked, since the ERs for this section are positive (increase in joint movement for an increase in PCC temperature). Since this is an SPS–2 section, it could be identified from the LTPP records that a dowel bar inserter was used for this section. This possibly could have contributed to dowel misalignment and the subsequent joint freezing.
- Section 83–3802 shows an erratic, large ER for at least two of the six joints investigated. For this section, the remaining joints show a small joint movement with only one of the six joints analyzed showing possible joint freezing.
- Sections 04–0215, 13–3019, 49–3011, and 83–3802 showed some evidence of reaching the temperature of closure for some of the joints analyzed. For sections 31–3018, 32–0204, 37–

0201, 39–0204, and 89–3015, the temperature of closure does not seem to be captured within the range of PCC temperatures monitored.

D.1.1.2 Prediction of Joint Opening

As part of this study, predictions with the HIPERPAV II joint opening model were made for the SMP sections evaluated. The HIPERPAV II joint opening model is documented elsewhere.[1,3]

For prediction of joint movement with the HIPERPAV II joint opening model, the following factors are required:

- Pavement thickness: obtained from DataPave tables TST L05B or SPS2_LAYER_THICKNESS.
- Slab length: obtained from INV_PCC_JOINT table.
- Modulus of elasticity of PCC: obtained from TST_PC04 table or estimated from INV_PCC_STRENGTH table.
- PCC CTE: obtained from TST_PC03 table, or estimated according to AASHTO recommendations from GEOL_CLASS_COARSE_AGGR field on SPS2_PCC_MIXTURE_DATA table or INV_PCC_MIXTURE table.
- Shrinkage strain of PCC: assumed to be negligible for long-term analyses.
- PCC set temperature: estimated to be temperature of closure obtained from ER analysis.
- Change in PCC temperature: a 100 ºC change according to the definition of the ER ratio was used.
- Movement at maximum friction and maximum friction force: estimated according to subbase type LAYER_NO, LAYER_TYPE, DESCRIPTION, and MATL_CODE fields on TST L05B table.

Figure 111 compares of the measured versus predicted joint movement for the investigated sections. In general, it can be observed that the HIPERPAV II joint opening model slightly overpredicted joint movement for most of the sections.

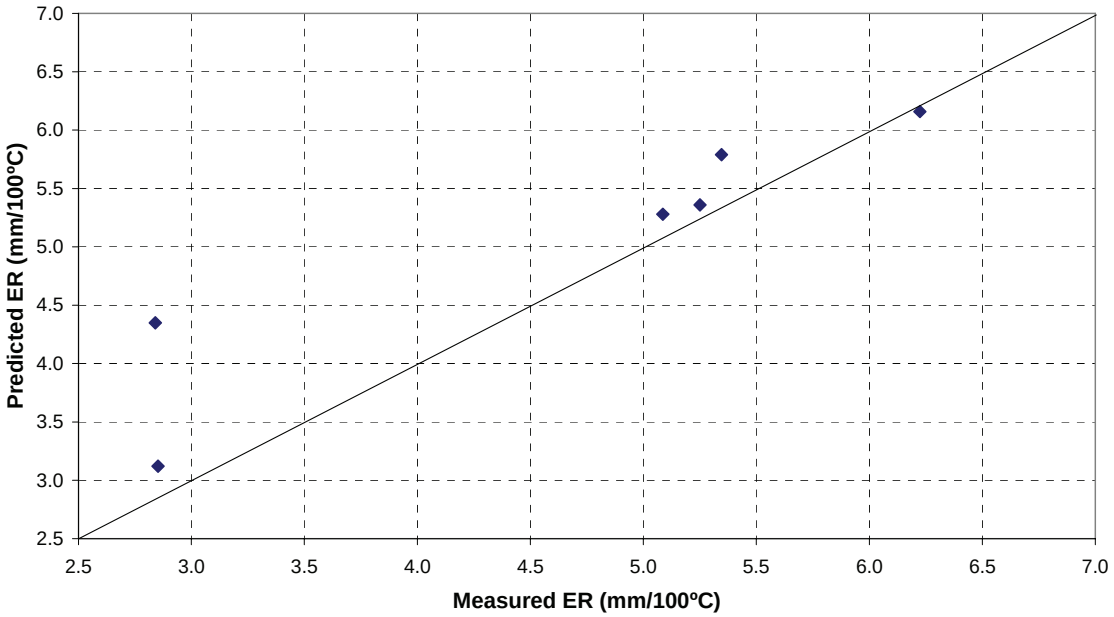

Figure 111. Measured versus predicted joint opening.

During this exercise, no attempt was made to predict the erratic and large joint movements measured for section 32–0204, since no CTE information for this section was found in DataPave 3.0. However, to match the measured average joint movement for section 83–3802, a 9.8-m joint spacing had to be assumed to account for the joint freezing effect observed for this section. The largest ER ratio for this section could be matched with a 28.4-m joint spacing. The last value would indicate that five joints were locked up, contributing to the large joint opening.

D.1.1.3 LTE Analysis

To perform the LTE analysis, information for the SMP sections in study was obtained from the following tables in DataPave 3.0:

- MON_DEFL_DROP_DATA: contains peak deflections for each of the seven to nine FWD sensors used, date and time the test was performed, specific point location, and type of test (i.e., midslab, wheel path, LTE test on approach slab, LTE test on leave slab, etc.). FWD tests were conducted at three load levels, approximately 40 kN, 53.4 kN, and 71.2 kN, with four drops at each load level.[(112)] The second drop for the load level at approximately 40 kN was selected for use in this analysis.
- MON_DELF_LOC_INFO: contains the FWD sensor configuration identification number for a specific testing date. Although the *LTPP Manual for Falling Weight Deflectometer Measurements* indicates that the sensor configuration for the LTPP tests was kept constant, the records in the DataPave 3.0 software indicate that the sensor configuration varied.[(112)] For the LTE testing, the distance from the load for sensors 1, 2, and 3 changed from 0 mm, 305 mm, and −305 mm to 0 mm, 203 mm, and 305 mm, respectively. For the first case, the deflection on the unloaded slab was recorded by the third sensor. In the later case, the deflection on the unloaded slab was recorded by sensor 9 at −305 mm from the load. To compute the LTE properly, this configuration information had to be known. Along with this information, the MON_DEFL_DEV_SENSORS table was used to obtain the sensor location for a particular configuration.

- MON_DEFL_TEMP_DEPTHS and MON_DEFL_TEMP_VALUES tables were used to obtain PCC temperatures manually measured at the time of FWD testing.[112]
- SMP_MRCTMP_AUTO_HOUR and SMP_MRCTMP_DEPTHS tables were used to obtain PCC hourly temperatures automatically obtained with thermistor sensors embedded in the concrete.[109,111]

In most cases, manual readings and automatic temperature readings differed for less than 3 °C. In cases when both manual PCC temperature measurements and automatic thermistor measurements were available, the PCC temperature reported by the thermistors was used. It was assumed that automatic monitoring would give less room to measurement error than manual readings.

A number of points were discarded for this analysis based on the following criteria:

- Only records with PCC temperature information available within 1 hour of the FWD testing were used in the current LTE analysis. This procedure minimizes the likelihood that PCC temperatures differ no more than 2 °C or 3 °C from the time the FWD testing was performed.
- Records with a lack of information on sensor configuration were discarded.
- A semiautomatic procedure with the use of regression techniques was used to identify illogical deflection basins. These records were filtered out of the LTE analysis.

Table 76 shows the total number of points used after the above filtering process was performed.

Table 76. Data points used for LTE analysis.

Section ID	Points in Database	Points Used for LTE Analysis	Points Used for LTE Analysis (%)	Points with Computed LTE > 100%	Points with Computed LTE > 100% (%)
04–0215	754	604	80.1	3	0.5
06–3042	660	597	90.5	14	2.3
13–3019	793	611	77.0	3	0.5
18–3002	383	329	85.9	0	0.0
31–3018	719	650	90.4	1	0.2
32–0204	405	404	99.8	6	1.5
37–0201	774	718	92.8	10	1.4
39–0204	422	381	90.3	12	3.1
49–3011	1038	971	93.5	3	0.3
53–3813	635	470	74.0	10	2.1
83–3802	868	845	97.4	35	4.1
89–3015	737	679	92.1	16	2.4

The LTE across joints was evaluated based on the deflection ratio using the procedure documented by Teller and Sutherland (equation 262):[113]

$$LTE = \left(\frac{2 \cdot W_u}{W_u + W_l} \right) \cdot 100 \tag{262}$$

where,

LTE = load transfer efficiency, percent,
W_u = deflection on the unloaded slab, and
W_l = deflection on the adjacent loaded slab.

Figure 112 shows a typical plot of PCC temperature versus joint LTE for a doweled section. It is observed that for high PCC temperatures the joint LTE remains high, typically above 80 percent. However, there is a threshold temperature below which LTE is significantly reduced, most likely due to the loss of aggregate interlock as the joint opens.

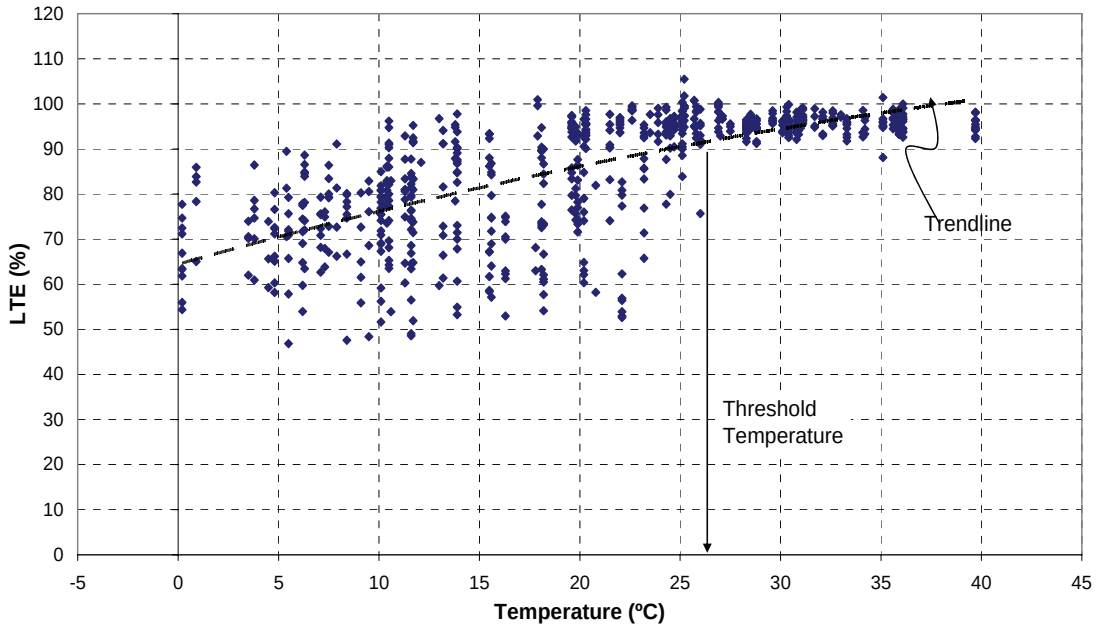

Figure 112. Typical plot of PCC temperature versus joint LTE, section 37–0201.

Table 77 shows some computed LTE statistics for the sections analyzed and some design and construction characteristics. In this table, the JPCP sections are sorted as a function of the average computed LTE, from lowest to highest. From this sorting procedure, the following observations are made:

- As expected, the sections with dowels show higher LTE than do the sections with no dowels. A lower average LTE is observed for sections with high threshold temperatures (temperature after which LTE > 80 percent). This LTE threshold temperature is believed to be related to the temperature of joint closure.
- In table 77, the temperature of joint closure computed during the joint opening analysis also is shown. Although this value could be computed only for a few sections, it appears to correlate to the computed average LTE.
- Other parameters examined include construction date, joint spacing, slab thickness, climate, and subbase type. None of these parameters seem to have as strong of an effect on LTE as is the case for the presence of dowels or the effect of PCC temperature (or joint opening).

Table 77. LTE statistics for SMP sections evaluated and some design and construction characteristics.

Section ID	Min. LTE (%)	Max. LTE (%)	Avg. LTE (%)	CV (%)	T after which LTE > 80%	T min.	T max.	Closure Temperature	Construction Date	Joint Spacing (m)	D (mm)	Climate	Dowels	Base
31–3018	18.6	100.0	58.6	33.0	30	−3.3	32.6	Not within range	May 1985	4.7	302	WF	No	Soil cement
49–3011	9.2	106.4	63.1	38.5	25	−4.2	41.6	30.5	May 1986	4.6	259	DF	No	CAM
06–3042	14.6	102.5	75.5	26.5	25	2.9	36.7	–	Jun 1979	4.7	224	DNF	No	CAM
83–3802	30.0	104.7	77.3	26.9	22	−16.0	31.6	4.8–14.5	Sep 1985	4.6	249	WF	No	Subgrade
53–3813	39.9	105.2	88.2	14.7	20	1.9	44.1	–	Aug 1966	4.6	203	WNF	No	Coarse soil agg. mixture
37–0201	46.8	105.5	85.9	15.0	26	0.2	39.7	Not within range	Nov 1993	4.6	229	WNF	Yes	Crushed stone
04–0215	45.2	104.7	86.3	12.8	36	12.3	48.4	32.3	Sep 1993	4.6	287	DNF	Yes	Crushed gravel
18–3002	63.1	99.1	90.5	7.6	17	−1.7	36.9	–	Aug 1976	4.7	241	WF	Yes	Crushed stone
13–3019	53.9	101.9	91.3	9.4	17	−0.5	43.0	13.8	Dec 1981	6.1	231	WNF	Yes	Crushed stone
32–0204	82.7	102.5	93.8	3.3	all	−0.9	34.4	Not within range	Jul 1995	4.6	300	DF	Yes	crushed gravel
89–3015	62.3	111.9	95.2	3.4	6	−17.0	32.7	Not within range	Sep 1984	6.0	208	WF	Yes	Crushed stone
39–0204	80.0	105.5	95.6	3.6	all	0.1	30.8	Not within range	Aug 1995	4.6	282	WF	Yes	Crushed stone

CAM – Cement-aggregate mixture, CV – Coefficient of variation, D – Thickness, DF – Dry freeze, DNF – Dry-no freeze, T – Temperature (°C), WF – Wet freeze, WNF – Wet-no freeze

*Random joint spacing

D.1.1.3.1 LTE Variability

For a number of sections, a large variability was found, as can be seen from the LTE CV in table 77. A large variability of LTE for JPCP sections in the LTPP database has been reported previously.[114] A more detailed analysis of section 49–3011 with the highest CV was performed to try to determine the reason for the large variability. Figure 113 shows a plot of PCC temperature versus LTE for that section. It is evident that several factors affect the variability of this section.

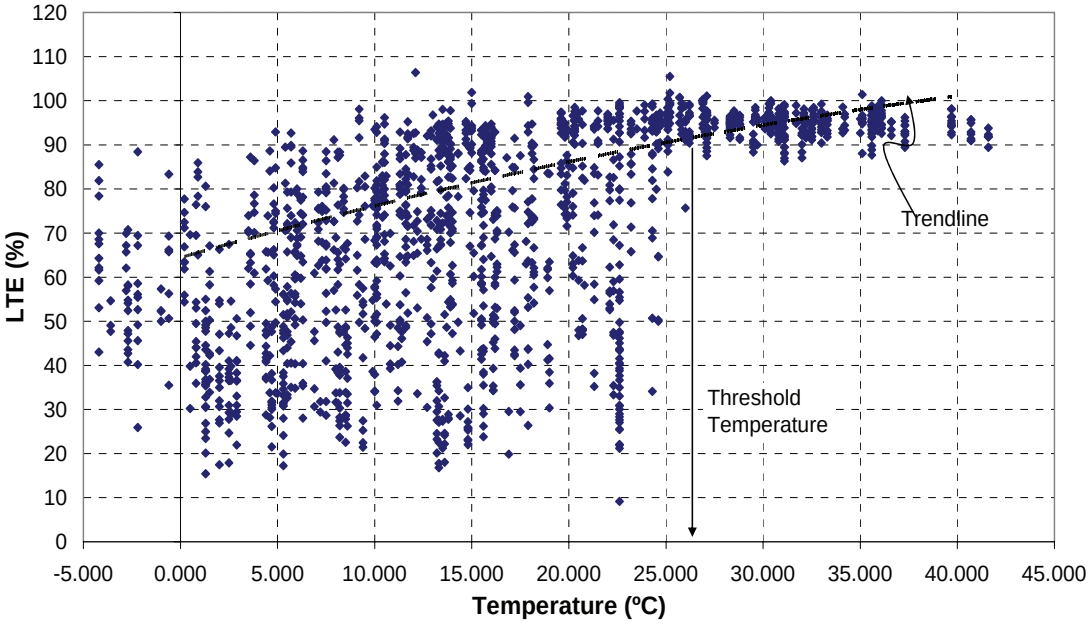

Figure 113. Computed LTE versus PCC temperature for section 49–3011.

The most remarkable factor from figure 113 is the effect of PCC temperature. As discussed before, above a certain threshold temperature (in this case, 25 °C), the LTE for this section remains above 80 percent. This is believed to be associated with the slabs expanding and causing a reduction in joint opening. Below that PCC temperature, the aggregate interlock is lost as the joint opens, and the LTE decreases significantly. It is also interesting to note that below freezing (PCC temperature < 0 °C), LTE is slightly higher than at PCC temperatures immediately above freezing. It is possible that the freezing effect provides higher soil support, therefore maintaining high LTE values. It is also hypothesized that ice in the joint can lead to a bridging effect. However, in figure 113, it is not quite clear why, for the range of temperatures above freezing and below 25 °C, a high variability occurs. Other factors that are believed to have an effect on LTE are pavement age, type of LTE test (load on approach slab or load on leave slab), variability in joint opening (figure 113 includes LTE tests for all joints monitored in that section), season of the year, and joint spacing (this section has random spacing).

D.1.1.3.2 Effect of Different Parameters on LTE

To further investigate the possible impact of the above factors, the LTE measurements for section 49–3011 were individually analyzed for each joint as a function of type of LTE test, and date LTE tests were performed. Figure 114 shows the average LTE computed for each joint. For each joint, the computed LTE was grouped into two categories: tests performed before 1996, and tests performed in 1996 and thereafter. The Joint ID in figure 114 includes the type of LTE test (load positioned on approach slab—

LTPP designation J4, or load positioned on leave slab—LTPP designation J5), distance from the start of the section to the joint in meters, and testing date group. An evident decrease in LTE is noted for the tests performed after 1996 as compared to the tests performed in previous years. It is also interesting to note that the approach slab tests show a lower average LTE than the leave slab tests for most of the joints, except for the joint located 8.95 m from the start of the section, where the trend is reversed.

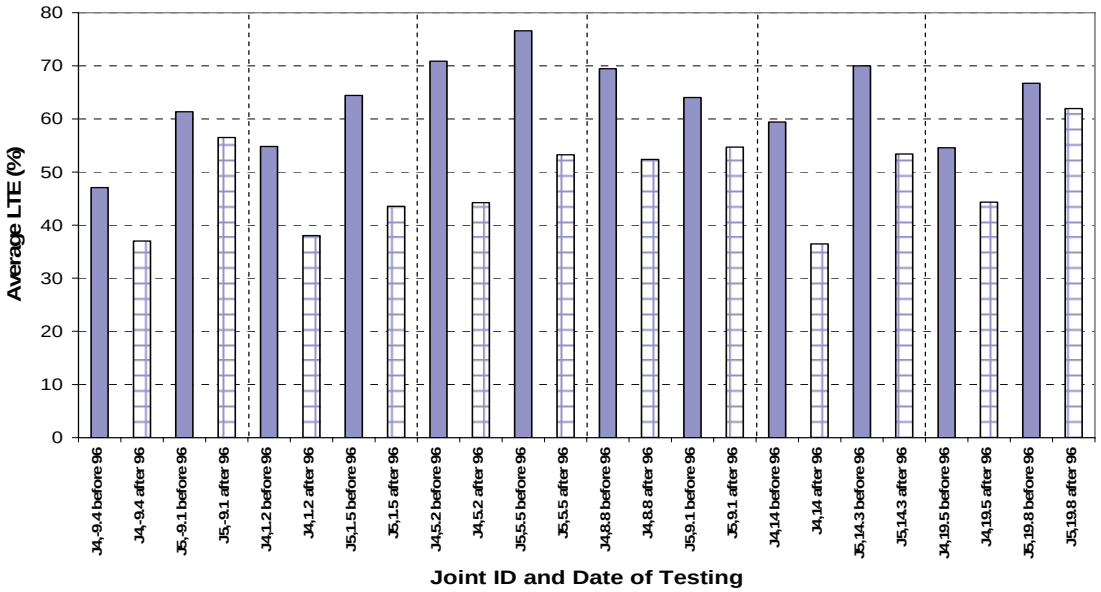

J4 – LTE on approach slab
J5 – LTE on leave slab
X.XX distance from start of section to joint location in meters
B–96 – LTE tests before 1996
A–96 – LTE tests after 1996

Figure 114. Average LTE above freezing and below 25 ºC, section 49–3011.

A statistical analysis for the average LTE is presented in table 78. The percent decrease in LTE for tests performed before 1996 and tests performed after 1996 is included along with a paired *t*-test to determine whether or not the means belong to the same population. It is observed that for most of the joints, except for joints −9.25 and 19.65 for the leave slab test, the null hypothesis that the mean LTE for tests performed before and tests performed after 1996 is the same is rejected at the 5 percent confidence interval. Therefore, quantitative evidence is obtained suggesting that age is a significant factor in joint LTE. The average decrease in LTE for tests after 1996 for all joints analyzed is 15.3 percent. The dates considered in the analysis range from November 1993 to September 1997.

Table 78 also shows the difference in LTE for approach slab tests and leave slab tests. For most of the joints, higher LTE values are observed for the leave slab test than for the approach slab test. On average, the leave slab tests show 9.8 percent higher LTE values.

A large variability in LTE also was noted between individual joints that also contribute to the overall LTE variability for that section. A typical example of the variability between joints is presented in figure 115. In general, lower values of LTE are noted for the joint located at −9.25 m from the start of the section than for the joint located at 8.95 m (for LTE tests below 25 ºC). In addition, the variability for the joint at 8.95 m is notoriously higher than that for the joint at −9.25 m, as implied by the lower coefficient of determination (r^2) for that joint, determined with a linear regression analysis.

Table 78. Summary statistics for effect of pavement age on LTE.

Type of LTE Test	Joint Location (m)	Date	Average LTE (%)	Standard Deviation	Coefficient of Variation	Change in Average LTE	*t*-test for Means	Difference in LTE (J5–J4)
J4	−9.25	before 96	0.471	0.173	36.6%	−10.1%	2.0%	–
		after 96	0.370	0.100	27.1%			
J5	−9.25	before 96	0.614	0.242	39.5%	−4.8%	10.1%	14.3%
		after 96	0.565	0.292	51.7%			19.5%
J4	1.35	before 96	0.548	0.140	25.4%	−16.8%	0.0%	–
		after 96	0.380	0.119	31.4%			
J5	1.35	before 96	0.644	0.159	24.7%	−20.9%	0.0%	9.6%
		after 96	0.436	0.183	42.0%			5.5%
J4	5.35	before 96	0.709	0.174	24.5%	−26.6%	0.0%	–
		after 96	0.442	0.119	26.9%			
J5	5.35	before 96	0.766	0.175	22.8%	−23.3%	0.0%	5.7%
		after 96	0.533	0.189	35.5%			9.0%
J4	8.95	before 96	0.695	0.177	25.5%	−17.1%	0.2%	–
		after 96	0.524	0.139	26.6%			
J5	8.95	before 96	0.640	0.220	34.4%	−9.3%	1.5%	−5.4%
		after 96	0.547	0.232	42.5%			2.3%
J4	14.15	before 96	0.594	0.222	37.3%	−23.0%	0.0%	–
		after 96	0.365	0.143	39.2%			
J5	14.15	before 96	0.700	0.251	35.9%	−16.6%	1.1%	10.6%
		after 96	0.534	0.280	52.5%			16.9%
J4	19.65	before 96	0.546	0.156	28.6%	−10.2%	3.7%	–
		after 96	0.443	0.187	42.1%			
J5	19.65	before 96	0.667	0.217	32.6%	−4.8%	38.0%	12.1%
		after 96	0.620	0.221	35.7%			17.6%
						−15.3%		9.8%

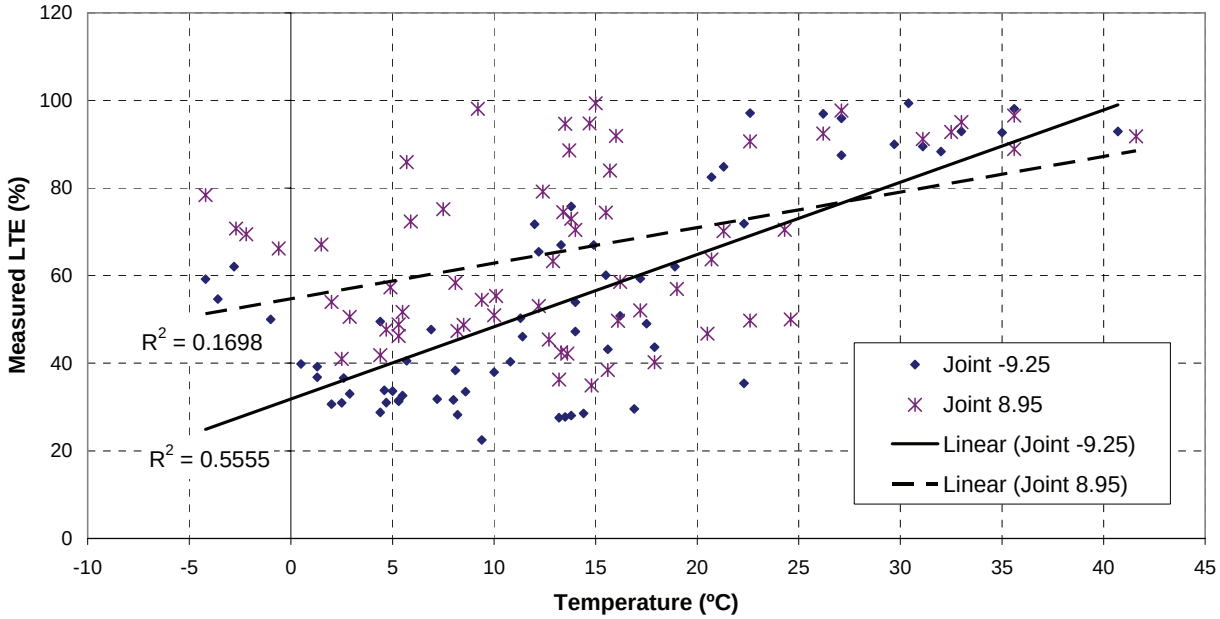

Figure 115. Variability of LTE for individual joints, section 49–3011.

In addition, as noted in table 77, section 49–3011 has a random joint spacing. Since the point location corresponds to the distance from the start of the section, and since most of these joints are consecutive to each other, individual joint spacings could be determined. Figure 116 shows the results of evaluating the effect of joint spacing on LTE for that section. Although a slight decrease in LTE is observed for larger joint spacings, a rather low r^2 is obtained. It must be noted that a similar variability between joints also was noted for sections with constant joint spacing. It is believed that the pavement age at which the crack formed at the joint may also play an important role on joint opening, and therefore on LTE. From previous experience, it has been noted that after construction, the joints that crack first tend to have larger joint openings than joints that crack later.

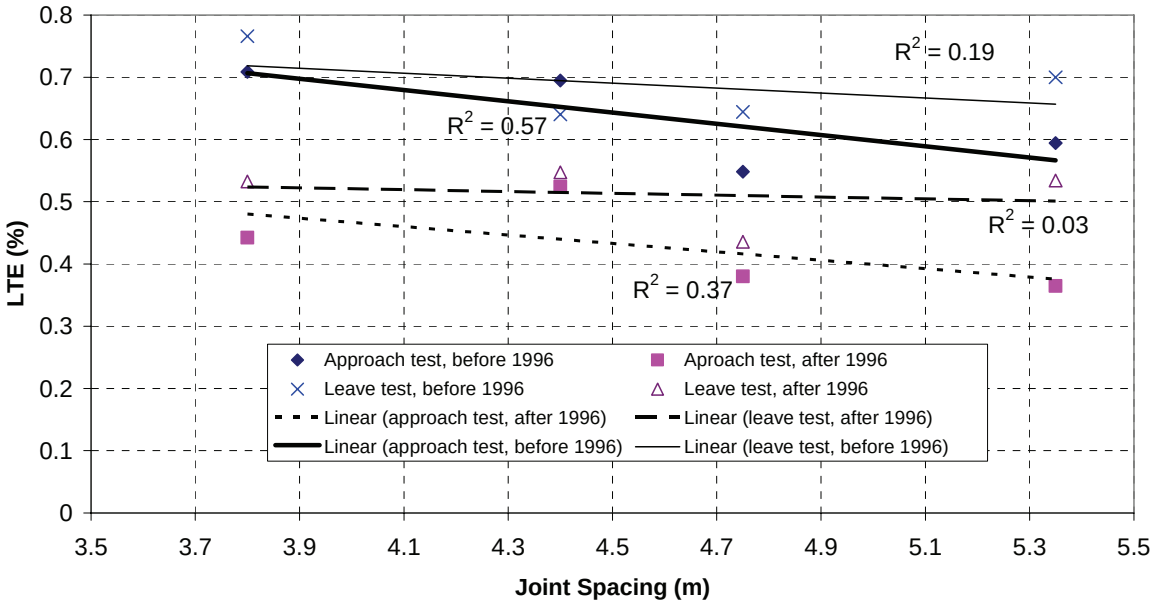

Figure 116. Effect of joint spacing on LTE, section 49–3011.

Figures 117 through 126 present the LTE computed for the remaining nondoweled and doweled sections in the SMP study, respectively. Individual analyses for each section showed similar trends in LTE, with testing date and type of LTE test, to those observed for section 49–3011. However, sections 04–0215 and 83–3802 showed reversed trends of LTE versus testing date. For these two sections, a higher LTE was observed for LTE tests after 1996. Although the increase in load transfer could be attributed to an improvement of the load transfer, records in DataPave 3.0 show no load transfer restoration for these sections nor any other rehabilitation activity of this sort.

D.1.1.3.3 LTE as a Function of Joint Opening

The temperature at joint closure and ER can be used to determine the joint openings at different temperatures for the sections in study.

Figure 127 shows a plot of LTE versus joint opening for an individual joint in section 49–3011. For this section, the temperature of closure could be clearly identified from the joint opening analysis. In figure 127, testing dates are split in LTE tests before and after 1996. A linear fit is used to differentiate between testing dates. This figure corroborates some of the findings previously presented.

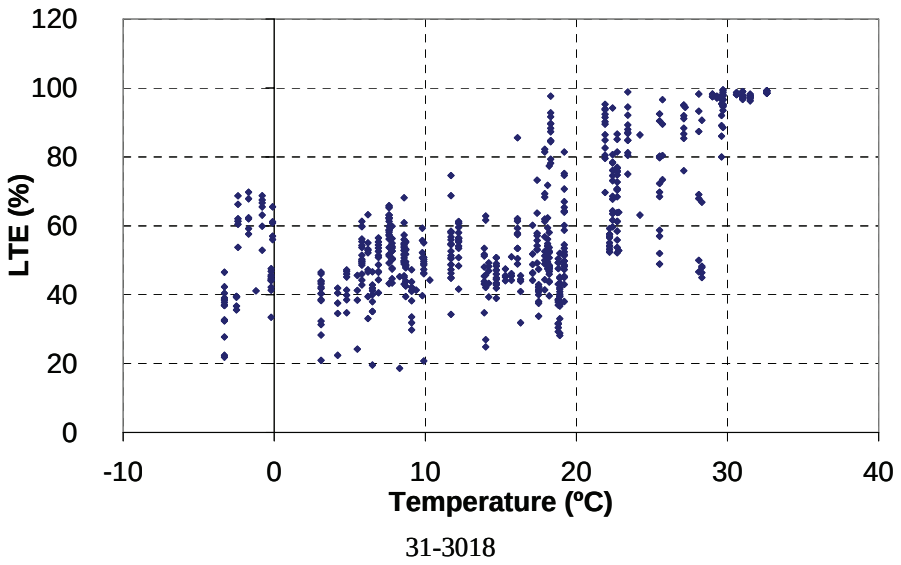

Figure 117. Computed LTE versus PCC temperature for nondoweled section 31–3018.

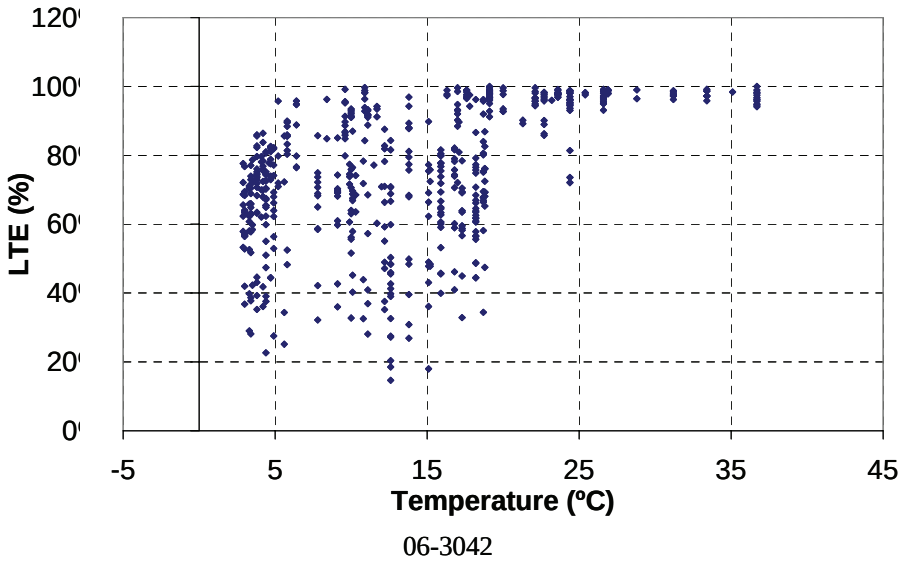

Figure 118. Computed LTE versus PCC temperature for nondoweled section 06–3042.

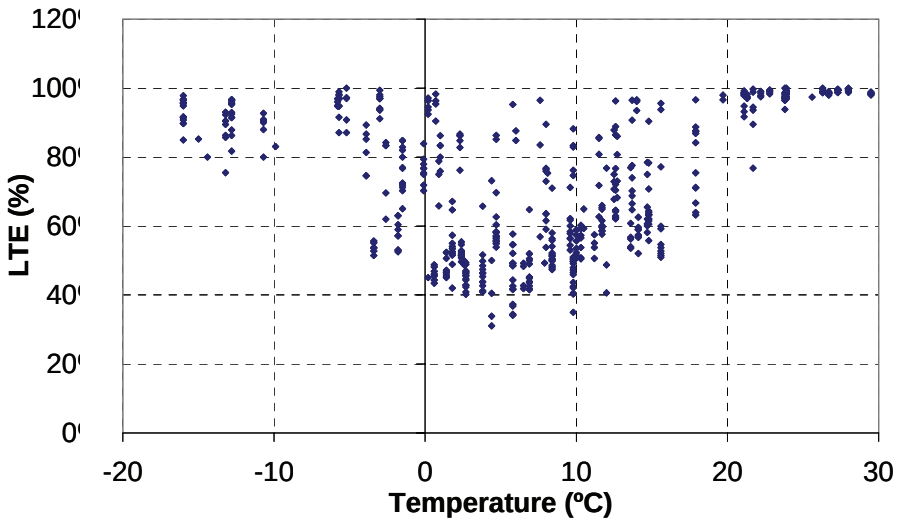

83-3802

Figure 119. Computed LTE versus PCC temperature for nondoweled section 83–3802.

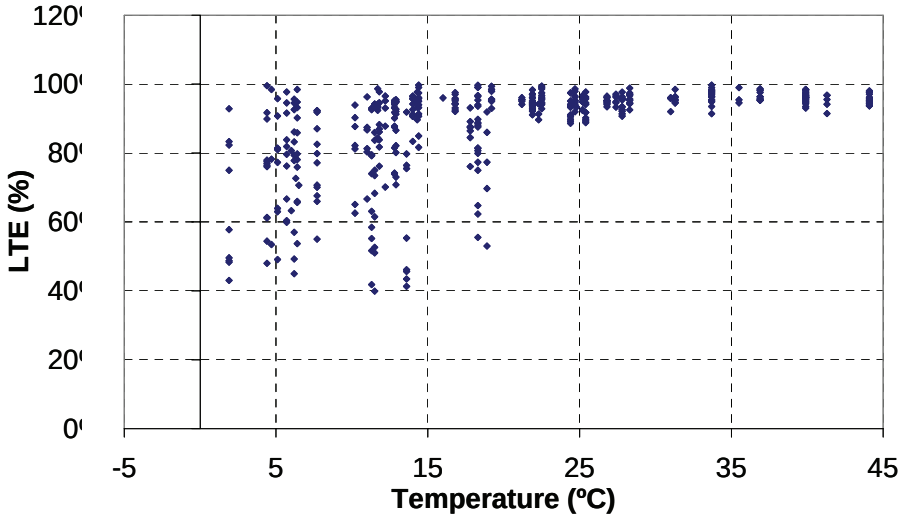

53-3813

Figure 120. Computed LTE versus PCC temperature for nondoweled section 53–3813.

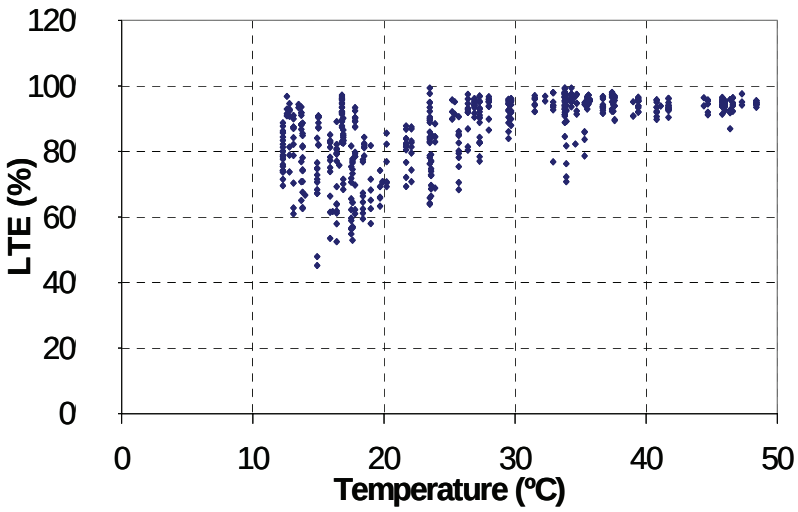

04-0215

Figure 121. LTE versus PCC temperature for doweled section 04–0215.

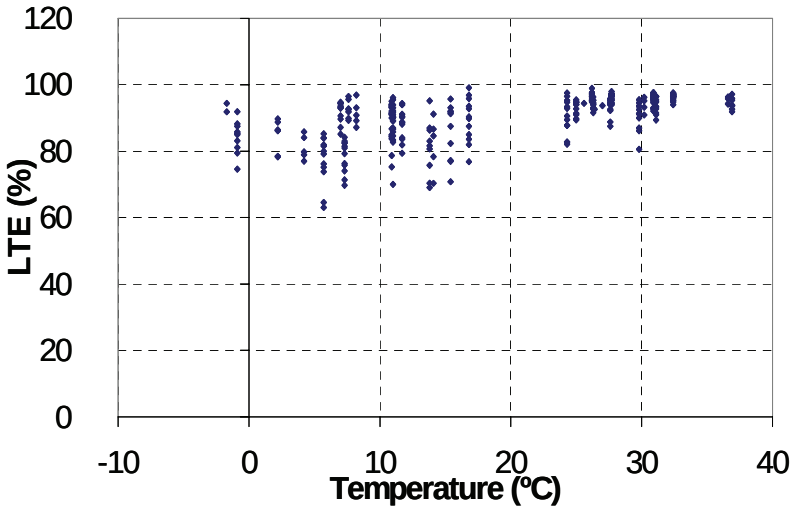

18-3002

Figure 122. LTE versus PCC temperature for doweled section 18–3002.

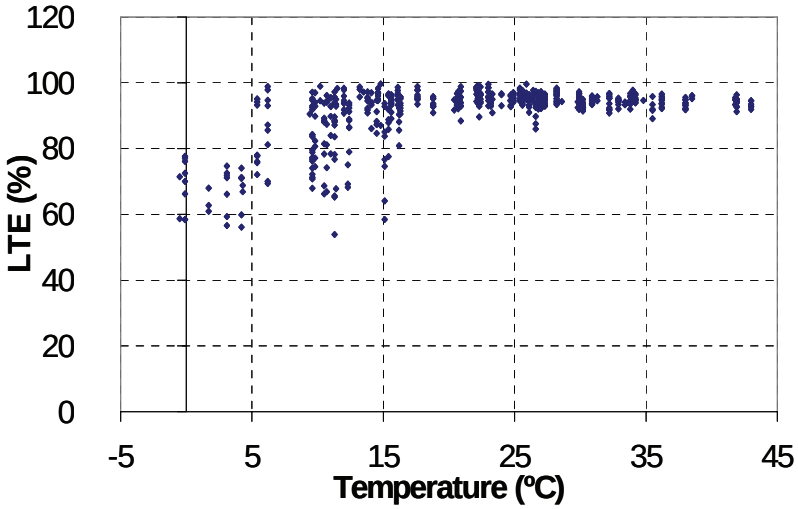

13-3019

Figure 123. LTE versus PCC temperature for doweled section 13–3019.

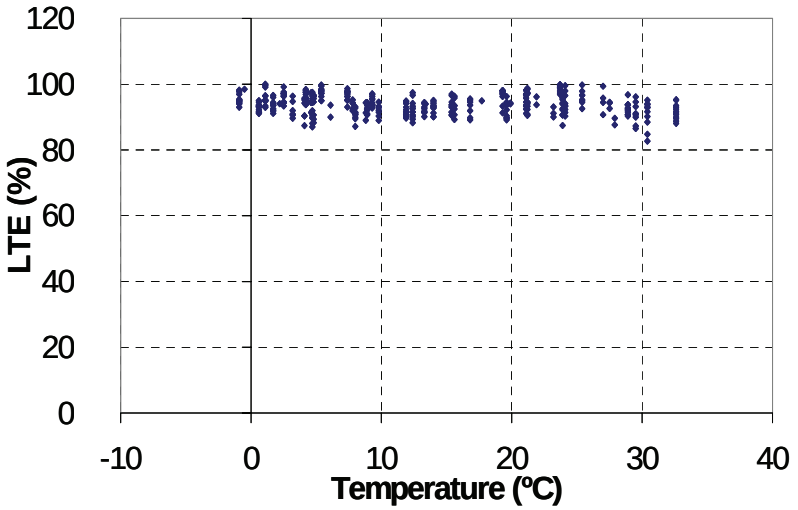

32-204

Figure 124. LTE versus PCC temperature for doweled section 32–0204.

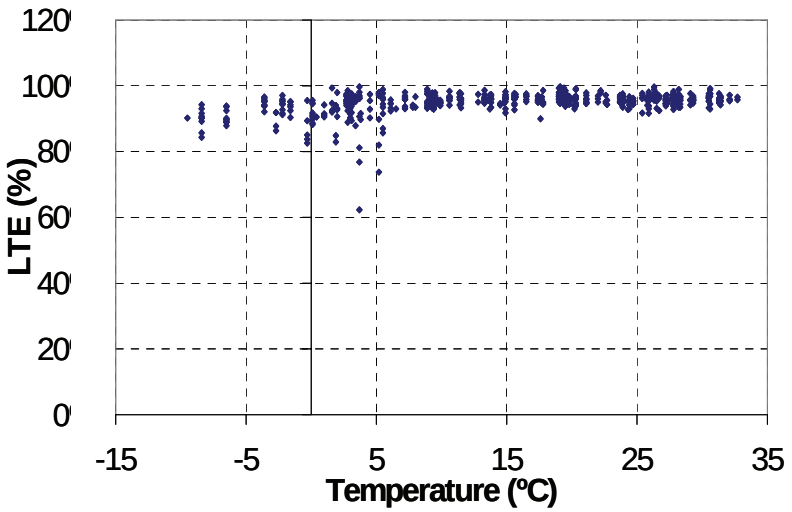

89-3015

Figure 125. LTE versus PCC temperature for doweled section 89–3015.

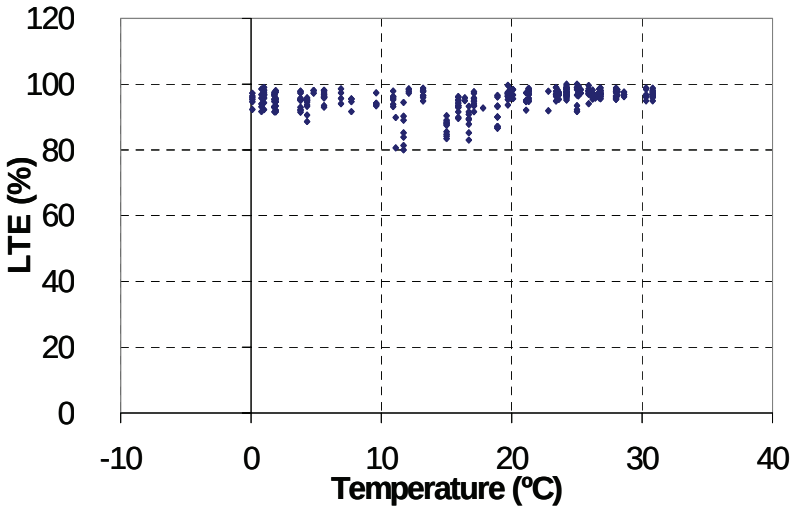

39-0204

Figure 126. LTE versus PCC temperature for doweled section 39–0204.

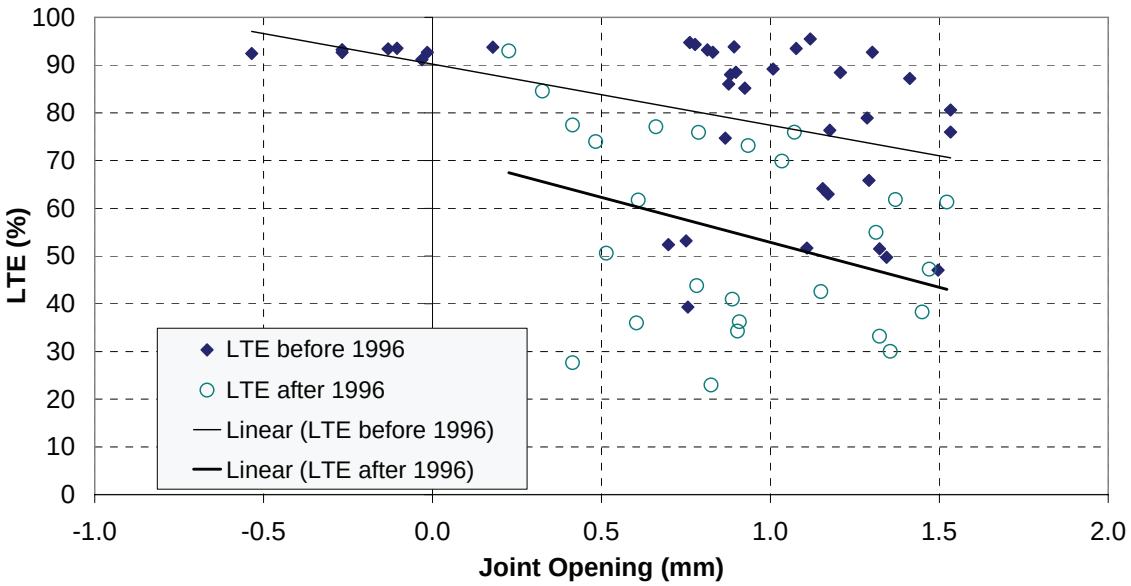

Figure 127. LTE versus joint opening for section 49–3011, joint at 5.5 m from start of section.

D.1.1.3.4 Summary of Findings

A number of analyses were performed to understand the effect of various parameters on joint LTE. An analysis was performed with LTPP data from SMP sections to determine the effect of temperature on joint movement and to identify the temperature of closure necessary in determining the joint opening. In addition, the computed LTE from the SMP sections was evaluated, and a number of factors were found to have a significant effect on LTE. These factors include:

- Doweled sections showed a higher LTE than nondoweled sections.
- The PCC temperature has a large effect on joint opening. Because the aggregate interlock is reduced for large joint openings, a decrease in temperature causes a reduction in LTE.
- High LTE values were observed for PCC temperatures above the temperature of closure at which the joint is tight.
- At freezing temperatures, higher values of LTE were observed from deflection testing.
- The type of LTE test (load on approach or leave slab) showed to be a significant factor in the computed LTE values. Higher LTE values were observed for the leave slab tests.
- Variability between joints also was a significant factor contributing to the overall variability of LTE. This variability is believed to be due to random joint spacing and time of crack formation at the joint after construction, among other factors.

It is believed that the procedures used in this investigation are effective in better understanding the effects of various factors on LTE.

D.1.1.4 Calibration of the LTE Model with JPCP Nondoweled Sections

For calibration of the LTE model, LTE was predicted as a function of joint opening and compared to the computed LTE from FWD tests. The temperature at closure and ER were used to determine the joint openings at different temperatures for the sections in study.

For sections where the temperature at joint closure could not be identified, this temperature was estimated based on a subjective assessment of the effect on LTE with change in temperature. It was noted that in most sections with information on temperature at joint closure, the LTE remained above 90 percent for joint openings smaller than 0.5 mm. Assuming this same behavior would hold true for the remaining sections with no joint closure information, the temperature at closure was backcalculated in such a way as to observe that drop below 90 percent on LTE at a joint opening of approximately 0.5 mm.

Figure 128 shows a plot of predicted versus computed LTE at a representative joint on section 31–3018. The LTE tests presented for this section date from 1995 to 2000. Because LTE prediction changes with load applications, the LTE tests were separated into two different periods: LTE tests on 1996 and before, and LTE tests after 1996. It can be observed in figure 128 that at the same joint opening, tests performed before 1996 show higher LTE values than those performed after 1996. However, a significant variability is noted, which makes it slightly difficult to determine a clear difference between testing dates.

The predicted LTE values are also shown in figure 128 at different load applications. LTE was predicted for the following loads: 0, 250,000, 500,000, and 12,400,000 ESALs. The last load level was obtained from traffic records in the LTPP database as the estimated cumulative ESALs at the end of 1996 for section 31–3018. Looking at figure 128 however, the predicted LTE at 250,000 ESALs seems to better match the computed LTE from tests at the end of 1996. After 500,000 ESALs, the predicted LTE seems to have very little variation with cumulative traffic.

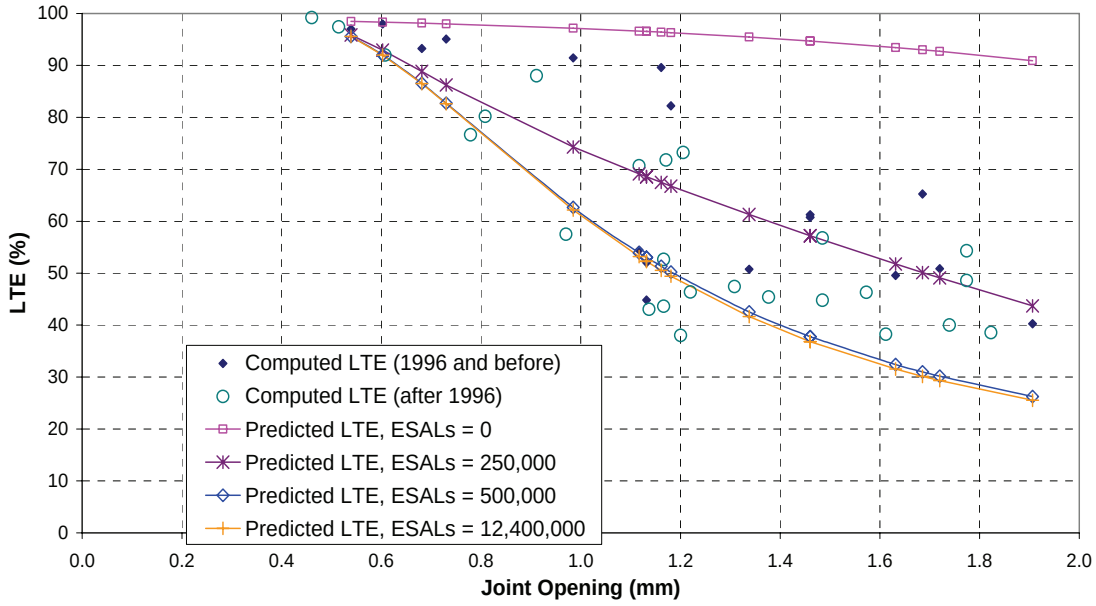

Figure 128. Predicted versus computed LTE for section 31–3018, joint 5.5 m from start of section.

It was mentioned in section B.2.3.1.12 that the laboratory testing data used to develop the aggregate wearout model is based on slabs of small dimensions to which 9-kip loads were applied. The 9-kip loads

subjected the slabs to higher deflections than normally observed in the field. It is possible that the 250,000 ESALs entered in the model represent the 12,400,000 ESALs actually applied to that section. That is, the model would need an ESALs multiplication factor of 0.02 to predict LTE properly.

The above exercise was repeated for all the sections in study to determine the number of load applications and ESALs correction factor that better matched the computed LTE in each case. Figures 129 through 132 present the LTE predictions at different levels of cumulative ESAL applications. A representative joint is shown with LTE tests for two different loading periods: before 1996 and after 1996.

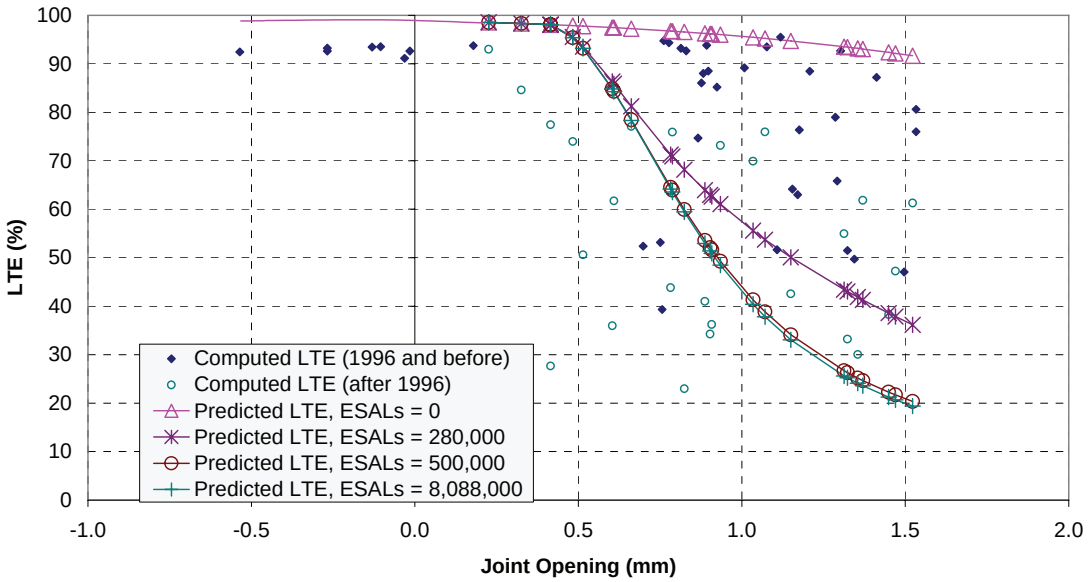

Figure 129. Predicted versus computed LTE for section 49–3011, joint 5.5 m from start of section.

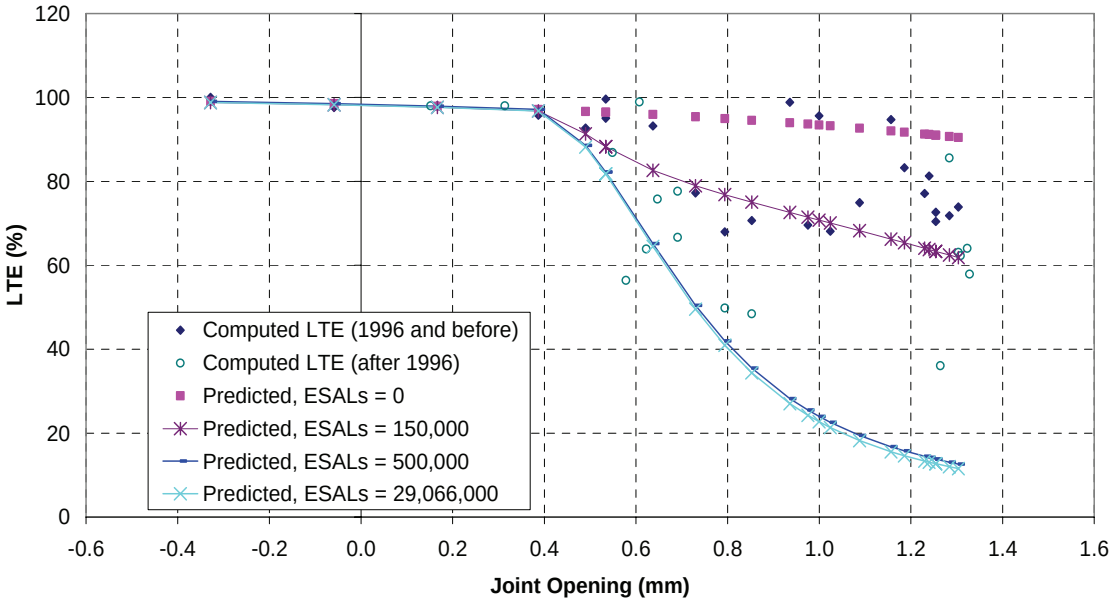

Figure 130. Predicted versus computed LTE for section 06–3042, joint 148.1 m from start of section.

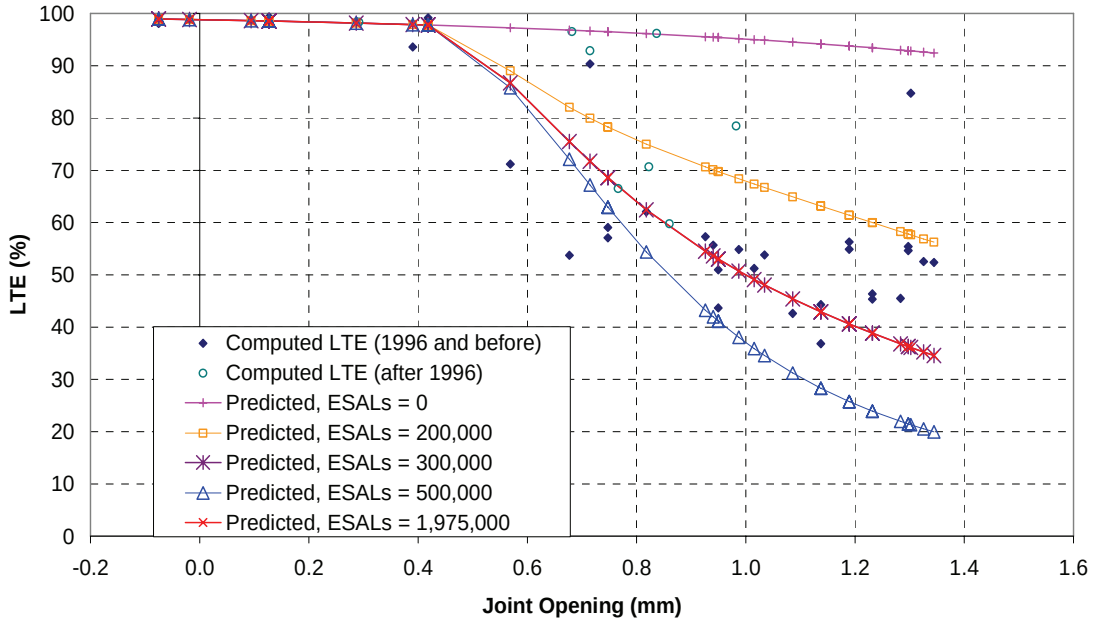

Figure 131. Predicted versus computed LTE for section 83–3802, joint 149.7 m from start of section.

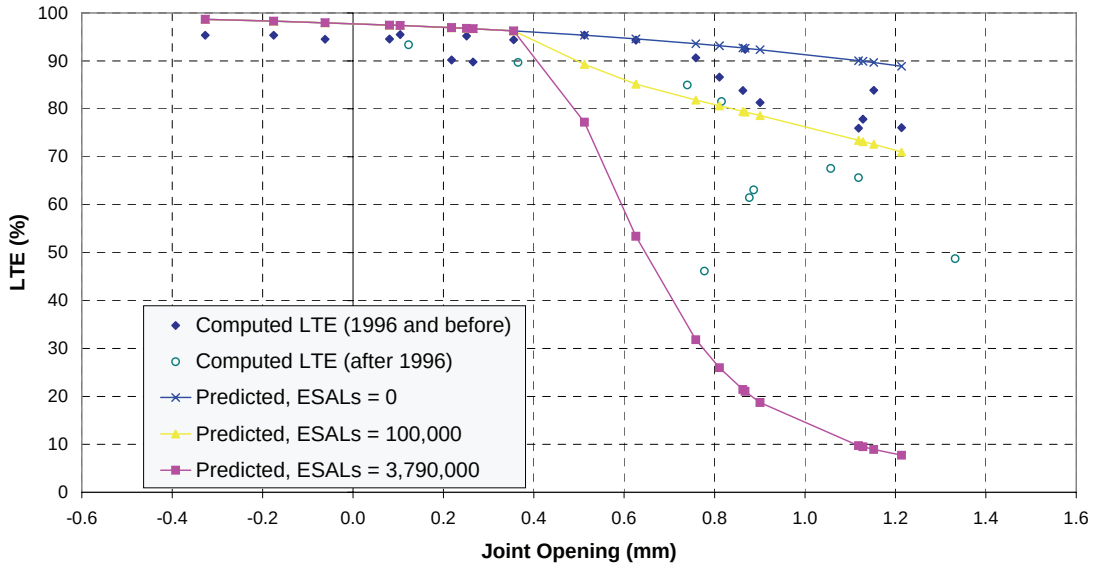

Figure 132. Predicted versus computed LTE for section 53–3813, joint 0.0 m from start of section.

Note from the above plots that, except for section 83–3802, the LTE test showed lower values for the period after 1996. Again, this seems to corroborate the effect of traffic loads on LTE. Although not indicated in the LTPP database maintenance records for section 83–3802, it is believed that some possible rehabilitation of this section could have been performed that resulted in the increased LTE after 1996.

As performed for section 31–3018, the number of ESALs that fit the LTE for 1996 was estimated with the LTE model in a rather subjective fashion. Table 79 presents the cumulative ESALs for every section on the analysis year along with the ESALs used in the model to fit the results from LTE tests. The last column presents the ESALs multiplication factor necessary to convert from the actual ESALs to the ESALs number required by the model to produce a good fit of the computed LTE. The average multiplication factor for all the sections analyzed was 0.048. However, a large variation of this factor was found among sections.

It is believed that although the LTE model is capable of producing the same trends in LTE as observed in the field, an accurate prediction will be possible only after a major investigation of the many factors that could affect these predictions such as aggregate type, aggregate shape, slab support conditions, and slab thickness is performed.

Table 79. Cumulative ESALs measured on design lane versus ESALs required to fit LTE model predictions.

Section	Year	Cumulative ESALs	ESAL fit	ESALs Multiplication Factor
31–3018	1996	12,409,440	250,000	0.020
49–3011	1996	8,088,833	280,000	0.035
06–3042	1996	29,065,803	180,000	0.006
83–3802	1995	1,973,712	300,000	0.152
53–3813	1996	3,792,431	100,000	0.026

Figure 133 shows the results of a sensitivity analysis of the LTE model for nondoweled joints. It is observed that, according to this model, the most predominant factors affecting LTE are joint opening, cumulative load applications, and slab thickness. No major effect from PCC stiffness, wheel load, pressure, nor *k*-value were observed on LTE. As previously mentioned, factors that are not included in the model but that are believed to somehow affect the development of load transfer at joints include the aggregate type and shape, as well as slab curling and warping.

It was found during the verification process that, although the LTE model predictions follow the general trends of LTE as computed from FWD tests, further investigation of a number of factors are necessary to be able to predict LTE with more accuracy.

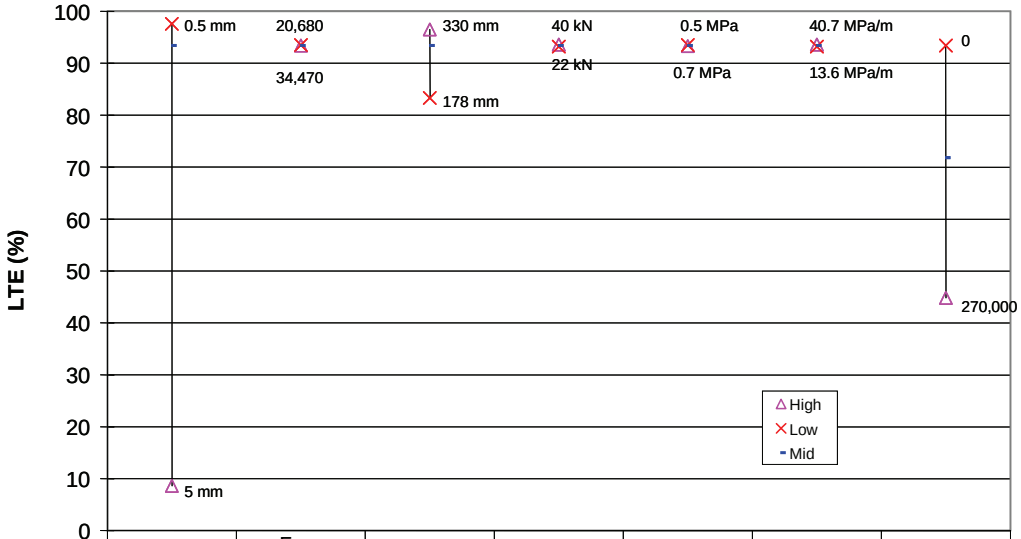

	JO	E_{pcc}	h	W	p	k-value	ESALs
△ High	8.6	93.4	96.5	93.6	93.3	93.6	44.8
× Low	97.6	93.5	83.3	93.2	93.5	93.2	93.4
- Mid	93.4	93.4	93.4	93.4	93.4	93.4	71.8

Parameter

Figure 133. Sensitivity analysis of LTE model for nondoweled pavements.

D.1.1.5 Calibration of JPCP Doweled Sections

In this section, an attempt to calibrate the LTE model for SMP doweled sections is performed. Similar to the nondoweled sections, LTE is predicted as a function of joint opening. The temperature at closure, and ER was used to determine the joint openings at different temperatures for the sections in study.

For sections where the temperature at joint closure could not be identified, this temperature was estimated based on a subjective assessment of the effect on LTE with change in temperature as described in the calibration of nondoweled sections.

For doweled sections, in addition to the PCC and support properties, the dowel characteristics are inputs to the LTE model. Among these characteristics, dowel looseness is one of the factors that has a significant effect on load transfer, as can be seen in the sensitivity analysis results presented in figure 134.

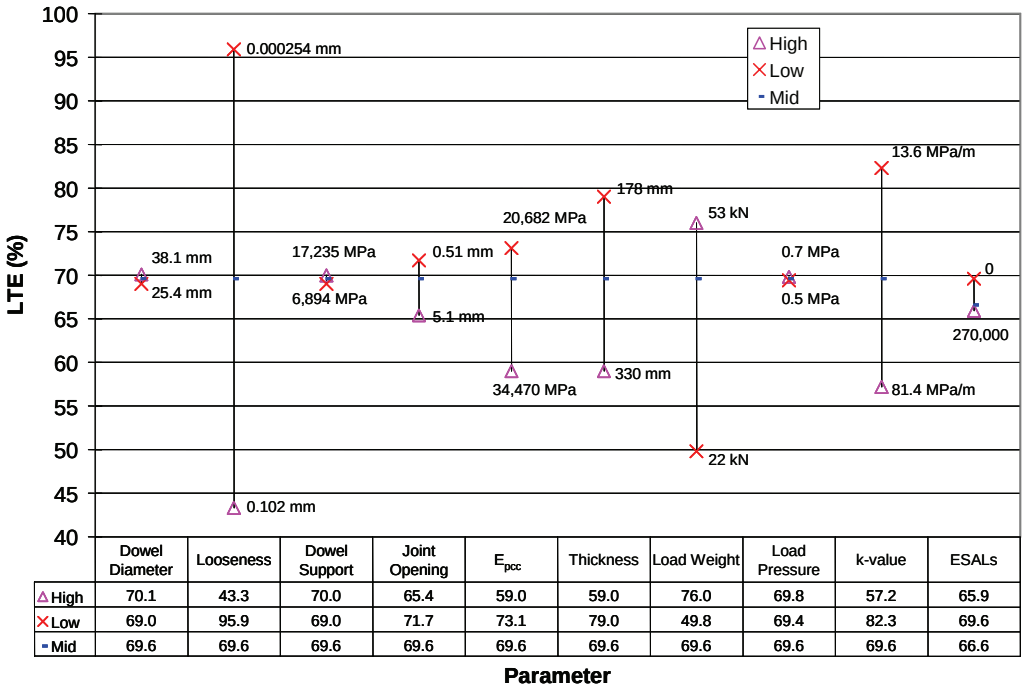

	Dowel Diameter	Looseness	Dowel Support	Joint Opening	E_{pcc}	Thickness	Load Weight	Load Pressure	k-value	ESALs
△High	70.1	43.3	70.0	65.4	59.0	59.0	76.0	69.8	57.2	65.9
×Low	69.0	95.9	69.0	71.7	73.1	79.0	49.8	69.4	82.3	69.6
-Mid	69.6	69.6	69.6	69.6	69.6	69.6	69.6	69.6	69.6	66.6

Figure 134. LTE model sensitivity for doweled sections.

Teller and Cashell explored the effect of dowel looseness under repeated loading.[115] They reported an increase in dowel looseness as a function of the load cycles. They also found some correlations of dowel diameter to dowel looseness. In this study, the correlations presented in equations 263 and 264 were made with the data reported by Teller and Cashell.

$$DL_0 = 0.0016 + \frac{0.0032}{1 + \left(\frac{\phi}{20.32}\right)^{6.4}} \tag{263}$$

where,

DL_0 = dowel looseness after construction and
ϕ = dowel diameter (mm).

$$DL_N = DL_0 + 0.00019(ESALS)^{0.185} \tag{264}$$

where,

DL_N = dowel looseness after N cumulative loading and
$ESALS$ = cumulative 8.2-ton single axle load applications.

Figure 135 shows a plot of predicted versus computed LTE at a representative joint on section 37–0201. The computed LTE presented for this section dates from 1994 to 2001. Because LTE has been observed to decrease with load applications, LTE tests were separated into two different periods: LTE tests in 1996

and before, and LTE tests after 1996. Although it can be observed that measurements after 1996 show lower LTE values, some variability is noted, which makes it difficult to determine differences between measurement dates clearly.

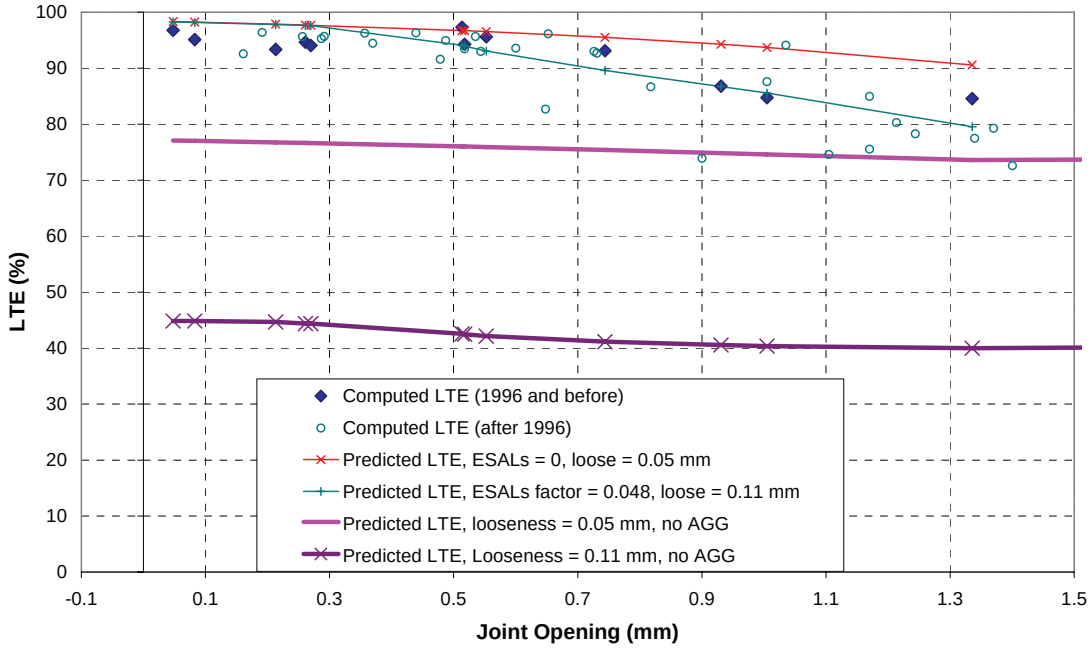

Figure 135. Predicted versus computed LTE for section 37–0201, joint 145.1 m from start of section.

The predicted LTE values at different load applications are also shown in figure 136. LTE was predicted for no loads and for 1593,467 ESALs (load level at the end of 1996 obtained from LTPP traffic records) adjusted by the multiplication factor of 0.048 previously determined for nondoweled sections. From equations 263 and 264, the predicted dowel looseness for those two load levels is 0.0018 and 0.0044, respectively. Figure 136 also includes the predicted LTE, assuming no aggregate interlock for the above looseness levels. For the looseness level with no traffic (0.0018), an LTE between 74 percent and 77 percent is obtained for the actual range of joint movement. For the looseness level at the end of 1996, the LTE varies between 40 percent and 45 percent. Given that the LTE for aggregate interlock is higher than the LTE for dowel support, it is difficult to verify the goodness of fit for the dowel looseness model in this LTPP section.

The above exercise was repeated for all the other sections in study to verify the accuracy of the ESALs multiplication factor for LTE determination and to verify the accuracy of the dowel looseness prediction model. Figures 137 through 140 present the LTE predictions at different levels of cumulative ESAL applications. For each section, a representative joint is shown with LTE measurements for two different loading periods: before 1996 and after 1996.

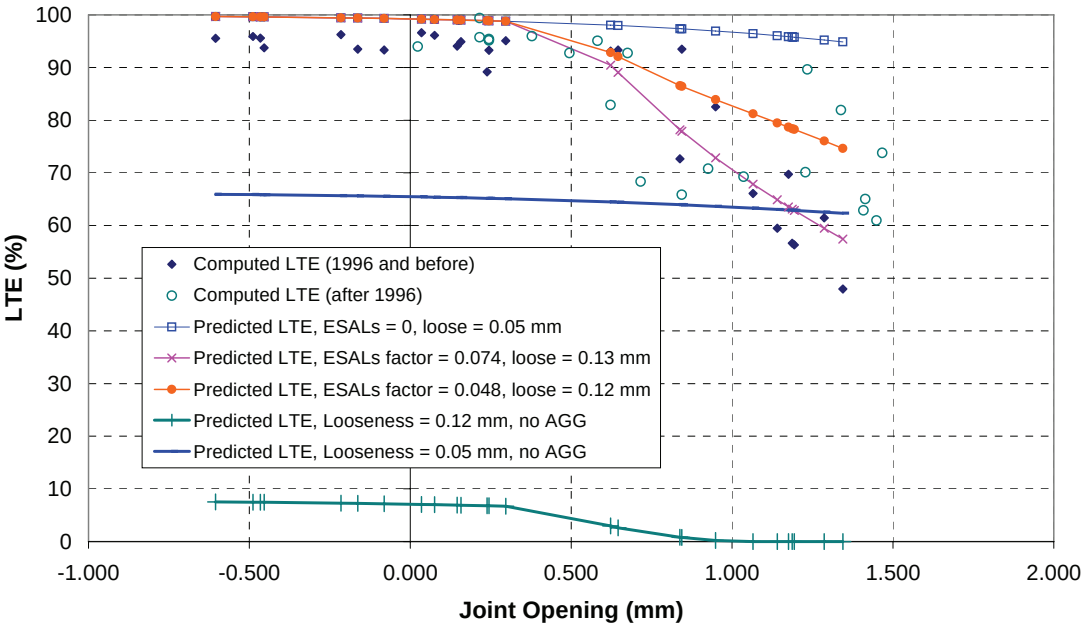

Figure 136. Predicted versus computed LTE for section 04–0215, joint 144.5 m from start of section.

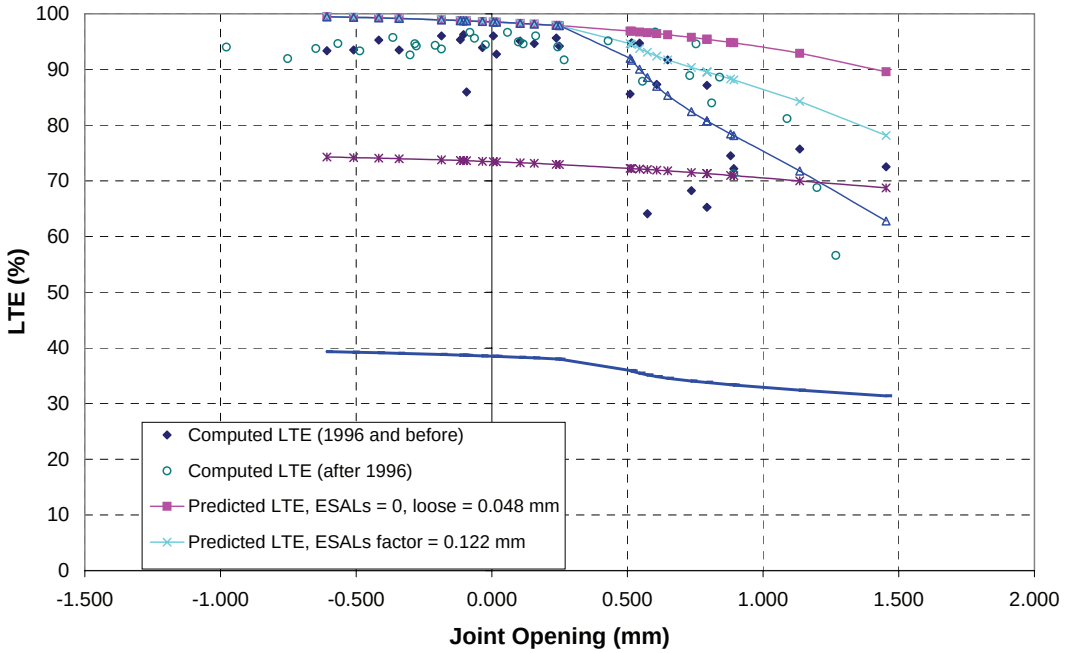

Figure 137. Predicted versus computed LTE for section 13–3019, joint 21.3 m from start of section.

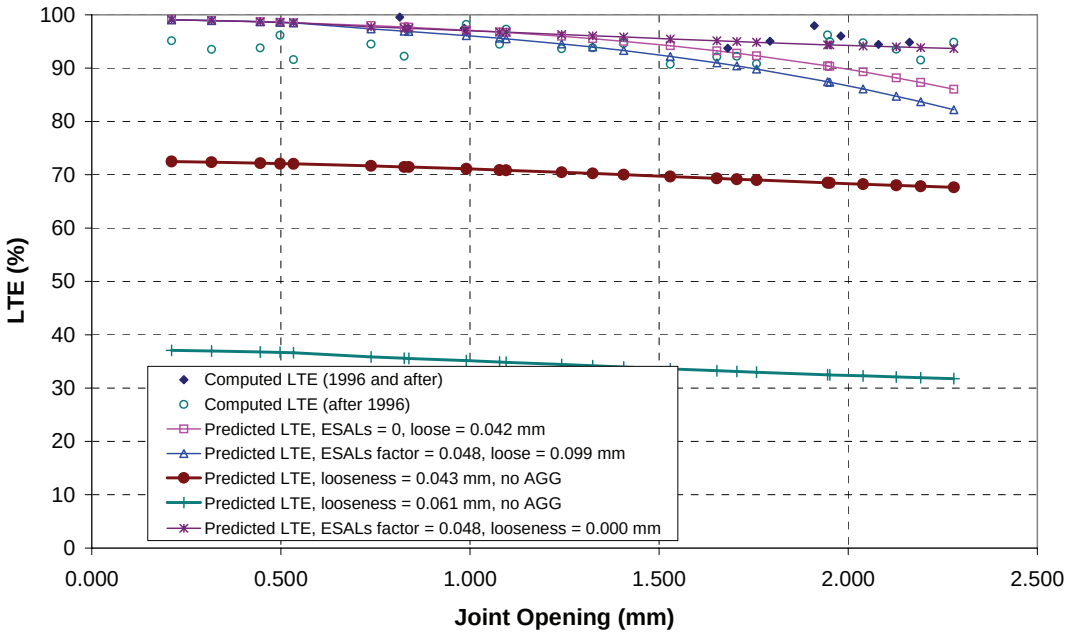

Figure 138. Predicted versus computed LTE for section 32–0204, joint 8.5 m from start of section.

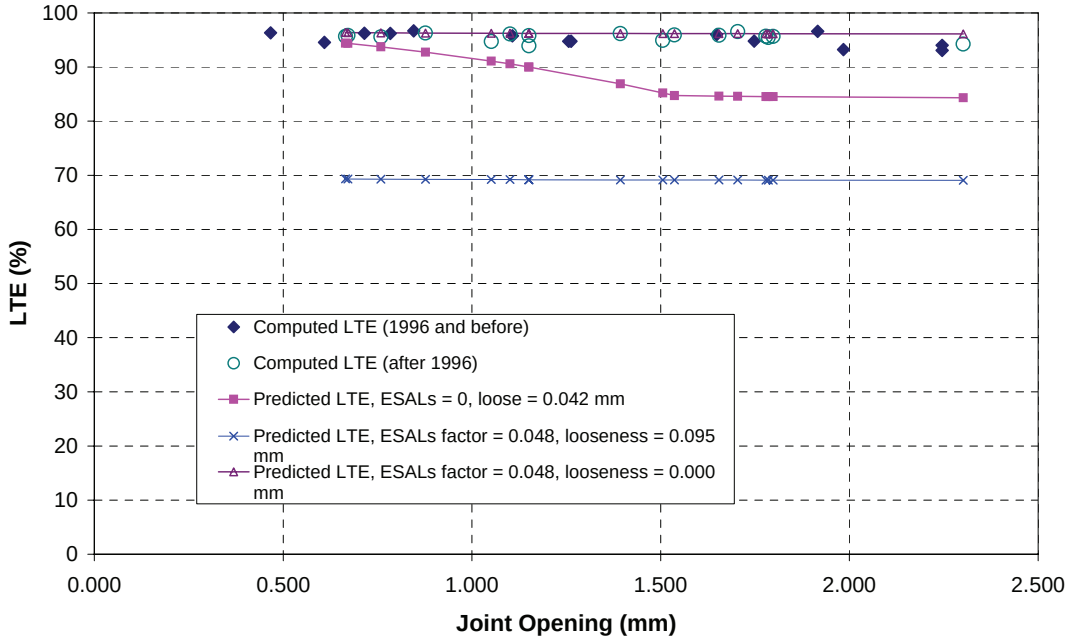

Figure 139. Predicted versus computed LTE for section 89–3015, joint 36.3 m from start of section.

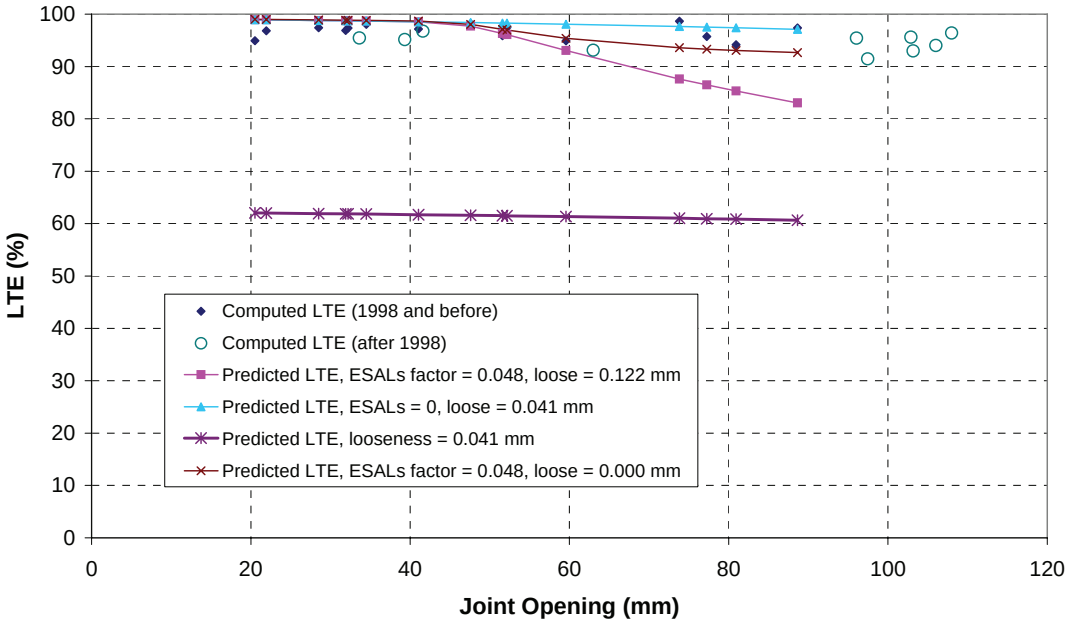

Figure 140. Predicted versus computed LTE for section 39–0204, joint 0.0 m from start of section.

Table 80 shows the cumulative ESALs for every section and the ESALs multiplication factor required to fit the computed LTE.

Table 80. Cumulative ESALs measured on design lane and ESALs multiplication factor required to fit LTE model predictions.

Section	Year	Cumulative ESALs	ESALs Multiplication Factor
37–0201	1996	1,593,467	0.048
04–0215	1996	3,395,341	0.074
13–3019	1996	1,553,000	0.090
32–0204	1996	559,708	0.048*
89–3015	1996	4,195,817	0.048*
39–0204	1998	1,967,539	0.048*

* Possibly biased due to no dowel looseness.

From a comparative analysis of the LTE predictions for the above pavement sections, the following findings are observed:

- ESALs factor for sections 04–0215 and 13–3019 seem to be higher than the average ESALs factor obtained for nondoweled sections. However, the ESALs factor for these sections fall within the variability range observed for the nondoweled sections.
- It appears that for sections 37–0201, 04–0215, and 13–3019, LTE is being provided mainly by aggregate interlock. For sections 32–0204, 89–3015, and 39–0204, LTE appears to be provided mainly by dowel support. It appears that to obtain an adequate prediction of LTE for the last three sections, dowel looseness must be very small or not present.

- None of the sections appear to show dowel looseness as high as that predicted by the dowel looseness observed by Teller and Cashell. Furthermore, it is likely that dowel looseness may be also a function of other variables not investigated by Teller and Cashell.

From this analysis, it was possible to verify the trend in LTE as a function of joint opening and load applications for a number of doweled LTPP SMP sections. The average ESALs multiplication factor previously found for nondoweled sections seems to work reasonably for the doweled pavement sections evaluated here.

For the sections evaluated, it was rather difficult to determine the level of dowel looseness, because for half of the sections, LTE appears to be provided by aggregate interlock with some dowel looseness, while the remaining sections appear to have very little or no dowel looseness. Therefore, further work is required to verify the dowel looseness models presented. It is recommended that factors such as aggregate characteristics, dowel coatings, and compressive stresses at the dowel location due to curling stresses in the early ages be investigated.

D.1.2 Validation of CRCP Early-Age Behavior Models

Validation of the CRCP early-age behavior models had two objectives: validation of cracking behavior during the early age and validation of cracking behavior in the long term. Although, as its name implies, the CRCP module in HIPERAV should predict cracking behavior at early ages, long-term performance can be better estimated based on the cracking characteristics after the lowest temperature (typically after 1 year). Therefore, validation was also performed on existing CRCP sections with crack spacing information. Validation of cracking characteristics for existing CRCP sections is described in the following section. Validation of early-age cracking behavior was performed with information collected on construction field sites and is described in section D.2.2.

The CRCP–8 model included in HIPERPAV II has been validated extensively in the past.[106,116,117] However, during its incorporation into the HIPERPAV II system, new enhancements were made. These enhancements consisted of using the capabilities for pavement temperature prediction and development of mechanical properties in the HIPERPAV II system. The above enhancements warranted an additional validation of this module.

Provided the mechanistic nature of the CRCP–8 model, extensive information on the input parameters for a few sections was desired as opposed to limited information on several sections. For this reason, 16 sections on State Highway (SH)–6 in Houston, TX, that have been monitored continuously since construction were selected for this effort. Other CRCP sections also were investigated, such as the GPS–5 sections of the LTPP database; however, only limited early-age information was available for validation of the CRCP–8 model.[118,119]

D.1.2.1 Description of CRCP Sections in Houston, TX

Reference 106 provides a detailed description of the section characteristics, construction, instrumentation, and testing procedures. A brief summary is presented below.

The test sections in study are located on SH–6 on two different segments, one placed during summer 1989 and other placed during winter 1990. For each segment, two different aggregate types were used with four different reinforcement designs for eight different design sections per construction season. Table 81 shows the factorial of designs used for both the summer and winter sections.

Table 81. Factorial design for CRCP test sections constructed in SH–6.

Section ID	A	B	C	D	E	F	G	H
Coarse Aggregate	SRG	SRG	SRG	SRG	LS	LS	LS	LS
Bar Size	#6	#6	#6	#7	#7	#6	#6	#6
Steel (%)	0.63	0.53	0.42	0.53	0.63	0.52	0.61	0.68

SRG – Siliceous river gravel
LS – Limestone

D.1.2.2 Instrumentation

To measure temperatures in the concrete, thermocouples were installed 25 mm from the surface, in the middle, and 25 mm from the bottom of the slab. In addition, DEMEC points were used to measure the magnitude of thermal changes in the concrete.

D.1.2.3 Condition Surveys

Condition surveys were performed during the month following construction to monitor crack spacing and crack width. In addition, long-term cracking characteristics have been monitored at different times throughout the pavement life.[106,116,117]

D.1.2.4 Laboratory Testing

A number of cylinders were cast at the job to measure concrete splitting tensile strength, compressive strength, elastic modulus, drying shrinkage, and CTE under field and laboratory conditions at different ages.

D.1.2.5 CRCP–8 Input Parameters

Validation of the CRCP HIPERPAV II module required collecting information on all the input parameters considered. This information and assumptions made are presented below.

D.1.2.5.1 Design Inputs

The CRCP design thickness for all sections was 279 mm. Since no construction information on thickness was reported, the design thickness was used in the analysis. A single layer of steel was used, with bar size and steel percentage as shown in table 81.

Slab support was provided by a 152-mm cement-treated base and 25-mm asphalt-stabilized base as a bond breaker. No restraint tests were reported. Typical restraint conditions for asphalt-stabilized bases were assumed for this exercise. A restraint stress of 41.4 kPa and movement at sliding of 0.63 mm were selected based on previous experiences by the authors.

D.1.2.5.2 Materials and Mix Design

As previously mentioned, the type of coarse aggregate used was SRG and limestone. The mix design information is reported by Suh et al. and is presented in table 82 below.[106]

Table 82. Mix design for SH–6 test sections.

Project	SH–6 Summer		SH–6 Winter	
Coarse aggregate type	SRG	LS	SRG	LS
Coarse aggregate—kg/m^3	1,204	1,127	1,236	1,127
Water—kg/m^3	139	134	125	133
Cement—kg/m^3	230	251	203	230
Fly Ash—kg/m^3	63	68	95	63
Fine Aggregate—kg/m^3	658	722	640	746
Entrained air (%)	5	5	5	5

D.1.2.5.3 Concrete Properties

Test results on concrete properties were reported by Suh et al. and are summarized in tables 83 and 84 for summer and winter placements, respectively.[106]

Table 83. Test results (SH–6—summer).[106]

Property	Agg. Type	Value (Lab/Field)
28-day splitting tensile (MPa)	SRG	3.9/4.1
	LS	3.6/3.4
28-day modulus of elasticity (MPa)	SRG	32884/37228
	LS	36125/38124
28-day compressive strength (MPa)	SRG	44.8/43.1
	LS	42.1/50.8
28-day shrinkage (με)	SRG	204.8/208.5
	LS	196.3/170.8
CTE (με/ºC)	SRG	8.6/9.9
	LS	5.2/5.6

Table 84. Test results (SH–6—winter).[106]

Property	Agg. Type	Value (Lab/Field)
28-day splitting tensile (MPa)	SRG	4/3.8
	LS	3.7/3.8
28-day modulus of elasticity (MPa)	SRG	37779/37848
	LS	34746/37159
28-day compressive strength (MPa)	SRG	40.5/38.2
	LS	47.4/46.5
28-day shrinkage (με)	SRG	90/115*
	LS	165/165
CTE (με/ºC)	SRG	–/11.9
	LS	–/6.8

* 30-day result

D.1.2.5.4 Construction

During construction, the placement temperature (temperature of the mix) was monitored, as was the time of day when construction began. This information is reported in tables 85 and 86, respectively.

Table 85. Mix temperature for test sections in SH–6 (ºC).[106]

Section	Summer	Winter
Section A	30	21
Section B	30	20
Section C	30	19
Section D	31	18
Section E	29	21
Section F	29	14
Section G	30	14
Section H	30	15

* Values in bold were reported, all other values were estimated.

Table 86. Time of placement for test sections in SH–6.[106]

Section	Summer	Winter
Section length (m)	70	70
Section A	6/16/1989 8:30	1/10/1990 13:00
Section B	6/16/1989 10:30	1/10/1990 15:00
Section C	6/16/1989 12:20	1/11/1990 10:00
Section D	6/16/1989 14:00	1/11/1990 12:30
Section E	6/19/1989 9:40	1/11/1990 16:00
Section F	6/19/1989 11:30	1/12/1990 10:00
Section G	6/19/1989 13:00	1/12/1990 11:20
Section H	6/19/1989 14:20	1/12/1990 14:00

* Values in bold were reported, all other values were estimated.

Curing method was not reported, and white curing compound was assumed; however, inconsistencies in the prediction of temperatures for sections G and H during winter placement lead to indications that polyethylene sheeting or cotton mats could have been used during the first few hours. This was based on the low temperatures observed during those days.

D.1.2.6 Environment

Historical air temperature, windspeed, relative humidity, and cloud cover data was retrieved from the National Oceanic and Atmospheric Administration (NOAA) database for the construction dates for every section. This information was obtained from the Houston Intercontinental Airport, the closest weather source to the site.

D.1.2.7 Measured Cracking Characteristics

Crack spacing and crack width information has been monitored continuously for the sections on SH–6. During construction, condition surveys were performed during the first 30 days. In addition, condition surveys have been performed at 180, 500, 1000, 2500, 2800, and 4700 days for the summer sections and at 300, 800, 2300, 2600, and 4700 days for the winter sections (data provided by CTR of the University of Texas at Austin). Average crack spacings for the above survey dates are presented in figures 141 and 142. A typical trend of reduced crack spacing with age can be observed; however, for most sections, higher average crack spacings were reported for the surveying date at 4700 days than for previous dates. Since no rehabilitation has been reported for those sections, it is believed that the higher average crack spacings at 4700 days possibly may be due to omitted cracks during crack spacings measurement (this may be possible if the measurements were taken during a hot summer day when concrete expansion closes the cracks, making some of them imperceptible to the human eye). During hot days, hairline cracks are difficult to identify, which may result in cracks not included in the condition survey. For this reason, the crack spacing at 2500 days for the summer sections and 2600 days for the winter sections was selected for validation of the long-term crack spacings.

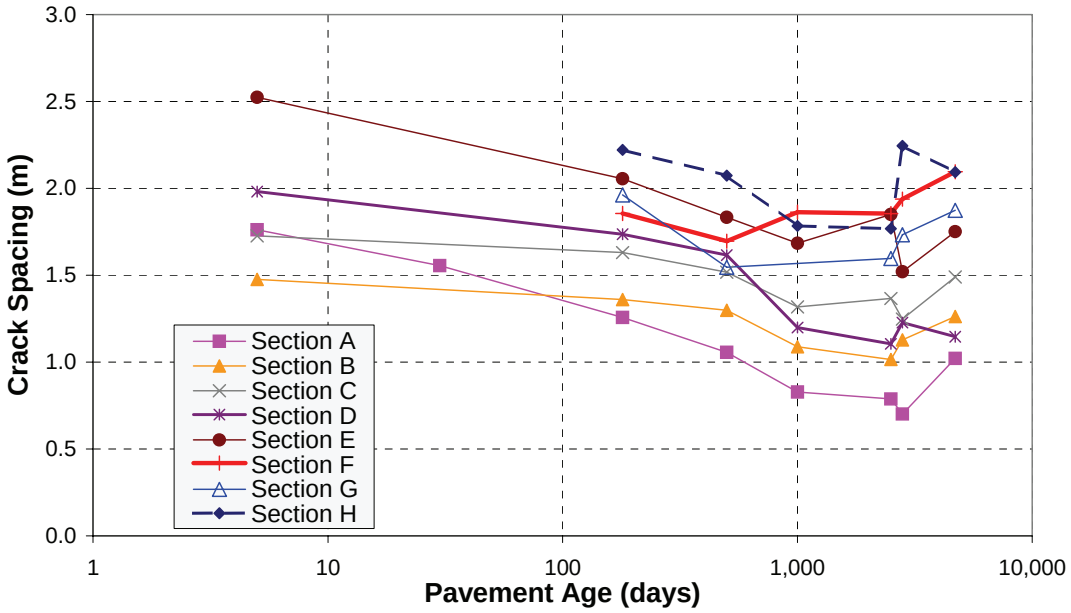

Figure 141. Crack spacing history for summer sections, SH–6.

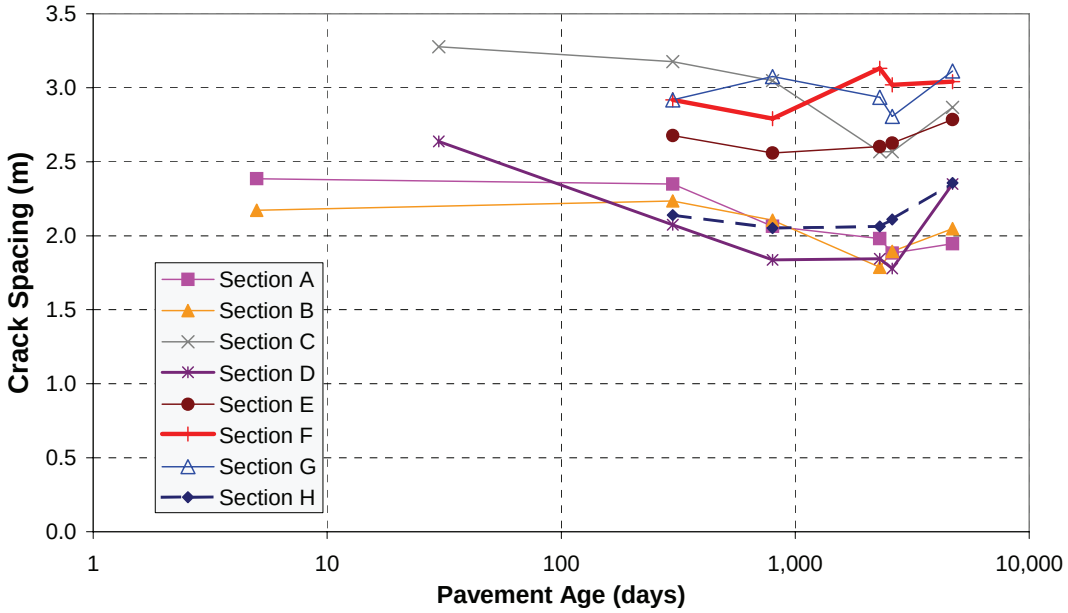

Figure 142. Crack spacing history for winter sections, SH–6.

D.1.2.8 Long-Term Crack Spacing Validation Results

With the above information, each section was analyzed with the CRCP HIPERPAV II module to compare the measured crack spacings to the predicted values. Figure 143 shows the comparison results using the above input parameters as reported. Although a general slight overprediction of crack spacing is observed, a reasonably good r^2 with respect to the 45º line was obtained (r^2 = 0.82).

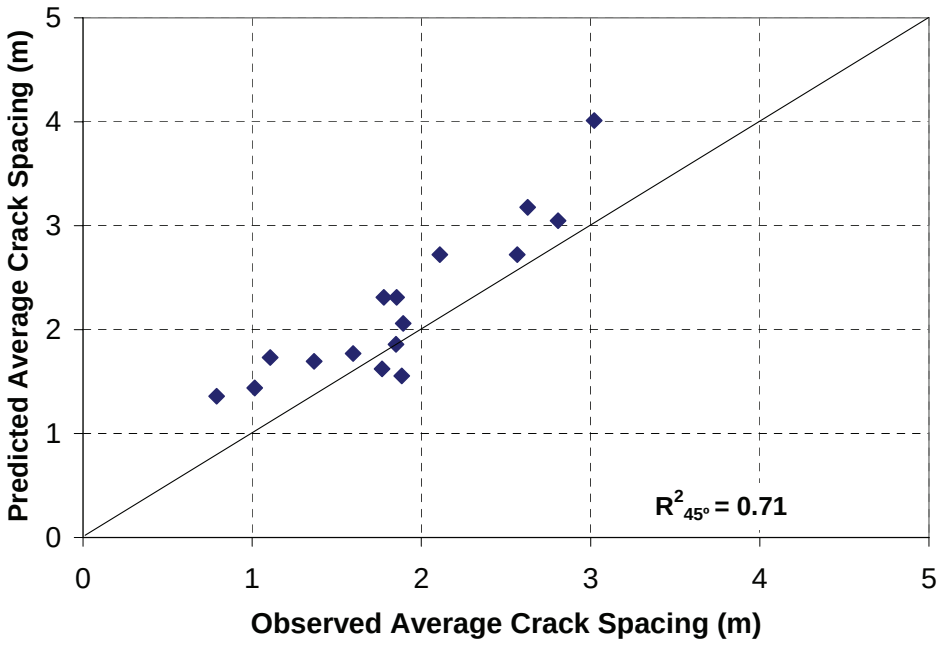

Figure 143. Preliminary long-term crack spacing prediction.

Given the reasonable fit obtained and because this validation effort was intended to determine if the differences in prediction are within reasonable limits rather than to calibrate the model, no model adjustments were performed.

D.1.2.9 Early-Age Crack Spacing Validation Results

Crack spacing during the early age was also compared to the predicted crack spacings with the CRCP HIPERPAV II module. Figure 144 shows the prediction results at 3 days from construction.

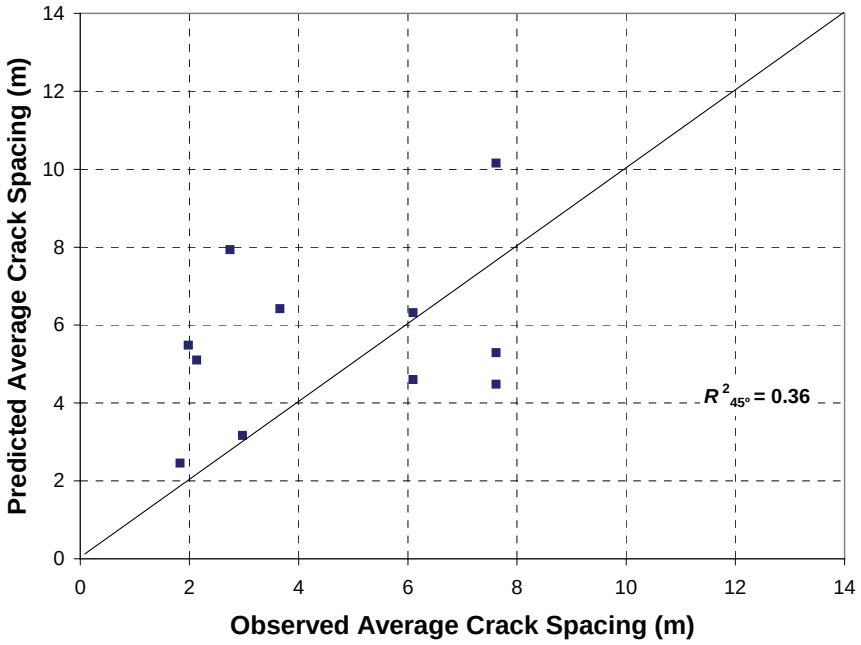

Figure 144. Crack spacing prediction at 3 days from construction.

For the early age, a generally poor prediction of crack spacings was observed. Similar results had been observed in previous validation efforts with this data set. Suh et al. had found good predictions for the first few months after construction; however, significant deviations were observed for the first 5 to 10 days.[106] This poor prediction may be attributed to a number of reasons:

- Monte Carlo Simulation: The stochastic nature of the crack spacing prediction model requires of a minimum number of data points to generate accurate predictions. Because the sections were relatively short (70 m long) and the crack spacings relatively large, it is possible that the data points generated were not sufficient to predict with accuracy.
- Inability to accurately predict early-age temperatures due to lack of curing information. It has been mentioned that no curing information was provided. In some cases, during winter, it is possible that curing with polyethylene sheeting or blankets might have been used due to the low temperatures. Information on this type of curing would be necessary for an accurate prediction.

Validation of the CRCP model during early ages is discussed further in section D.2.2.

D.1.2.10 Validation Results for Long-Term Crack Widths

Measurements of crack width 2 years after placement for the SH–6 test sections, were reported by Otero et al.[116] The HIPEPRAV CRCP module was used to predict crack widths at the temperature observed in the concrete during the crack width measurements. A comparison of the long-term crack width predictions against the measured values is presented in figure 145. Although a fair trend in crack width prediction is observed, all crack widths were largely overpredicted. This overprediction in crack widths had been observed in previous validation efforts.[116] Although Otero et al. proposed a new model for crack width prediction, the use of this model in this study did not show reasonable results. As has been previously reported, the overprediction may be because the CRCP–8 model does not account for the time when the crack forms, but rather depends on the predicted crack spacing, PCC thermal properties, and total shrinkage. As figure 146 illustrates, the drying shrinkage after crack formation depends on the concrete age when the crack occurs. It is believed that the residual drying shrinkage after the crack forms has a large effect on crack width.

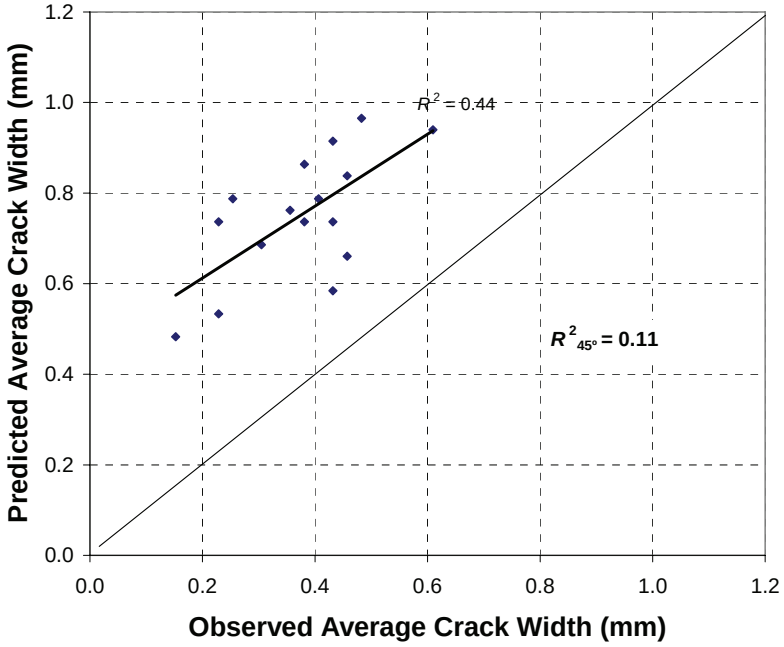

Figure 145. Measured versus predicted crack widths, SH–6.

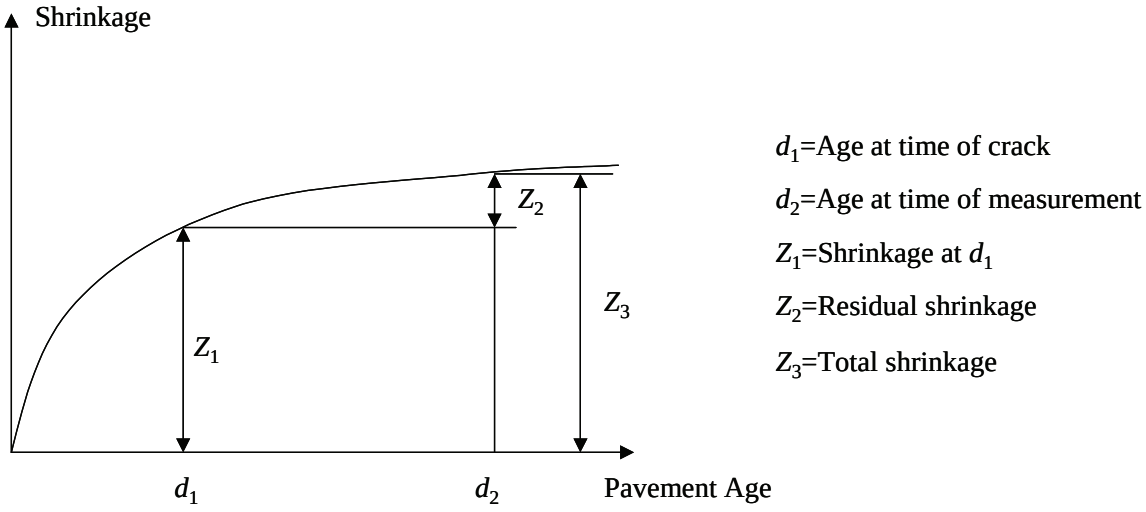

Figure 146. Conceptual representation of residual drying shrinkage effect (adapted from Otero et al.).[116]

The CRCP–8 crack width algorithm could be modified to account for the time of crack formation and residual drying shrinkage. However, such modification is out of the scope for this study, since additional data would be required for calibration and validation.

D.1.2.11 Validation Results for Early-Age Crack Widths

Only scattered information on crack widths during the early age was reported, and no attempt was made to perform validation with these data. It is believed that crack width information collected from the field sites evaluated in this study will shed some light on the accuracy of early-age crack width predictions.

D.1.2.12 Summary and Conclusions

During the database validation of the CRCP models in HIPERPAV II, good predictions of long-term crack spacing were observed. However, poor early-age crack spacing predictions were obtained. The inaccuracy in the early-age predictions is believed to be due to the nature of the stochastic algorithm used to predict crack spacings combined with the small length of the experimental sections (approximately 60 m) and the typically large crack spacings observed at early ages (from 2 to 8 m). Another possible reason contributing to the overprediction is the lack of information on curing procedures used. In the long term, the crack spacings were much smaller compared to the length of the experimental sections, with much better predictions achieved.

D.2 FIELD VALIDATION

Four field sites were investigated for validation of the HIPERPAV II system:

- Two inservice JPCP sections were evaluated to validate the long-term performance models in the JPCP module.
- Two newly constructed CRCP sections were instrumented to validate the CRCP early-age behavior module.

It is believed that the number of field sites evaluated will provide the minimum level of information necessary to meet the objectives of this effort successfully. However, additional data from field sites in the future could be used for local customization. The objective of this section is to describe the steps performed for validation of both, the JPCP and CRCP pavement sites investigated. The detailed data collection procedures and data reduction is presented in appendix C.

D.2.1 Validation of Long-Term Performance Models with Inservice JPCP Sites

The information collected from the pavement sections in Illinois and Ticuman, Mexico were used for validation of the long-term performance prediction models in HIPERPAV II. In this effort, the reliability of prediction for these two sites was evaluated. Several factors were considered in the validation of the long-term JPCP HIPERPAV II module for each field site. This validation included a comparison of measured and predicted mechanical properties, LTE, and long-term distresses. Validation of each factor is discussed in the following paragraphs.

D.2.1.1 Validation Results for JPCP Section on U.S. Highway 50, Illinois

As previously mentioned in section C.1.1, the Illinois site consisted of several pavement sections with different designs. Design features that were varied included the slab thickness, presence of longitudinal underdrain, and presence of sealant on longitudinal joint. Therefore, each of the sections evaluated was analyzed separately. In addition, to account for the effect of time of day of construction on performance, analyses for placement times at 2 a.m., 8 a.m., 2 p.m., and 8 p.m. were evaluated.

Information on pavement design, materials, and construction procedures was extracted from historical records for this site. Climatic information was extracted from NOAA records for the date of construction of every section for input into HIPERPAV II.

D.2.1.1.1 Mechanical Properties

Information on concrete flexural strength is available from records at 14, 28, and 90 days.[103] In addition, the flexural strength almost 16 years after construction was estimated based on the splitting tensile strength obtained from cores extracted during the field visit in 2001. Figure 147 shows the flexural strength for these ages along with the early-age and long-term strength predicted with HIPERPAV II.

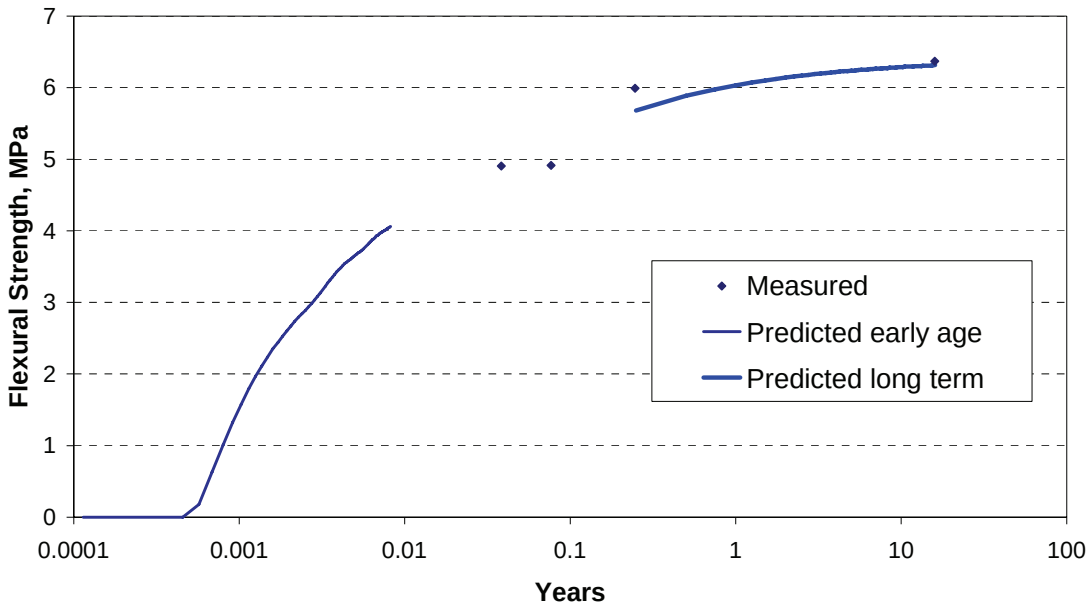

Figure 147. Comparison of measured and predicted strength, Illinois site.

In general, although the 90-day strength is slightly underpredicted, a reasonably good prediction of the measured long-term strength is obtained.

A similar analysis was performed for prediction of the elastic modulus. Figure 148 shows the measured modulus of elasticity at 28 days and the one obtained from concrete cores extracted from the field visit in 2001. While the predicted elastic modulus shows an increasing trend, the elastic modulus obtained from field cores in 2001 shows a slight decrease from the 28-day value. A significant difference in predicted versus measured elastic modulus is thus observed after 16 years. Although no further investigation was performed to determine the cause of the unexpected decrease in measured modulus of elasticity, possible reasons for this trend include variability in testing and in data interpretation, since the tests at 28 days and those in the long term were performed by different laboratories.

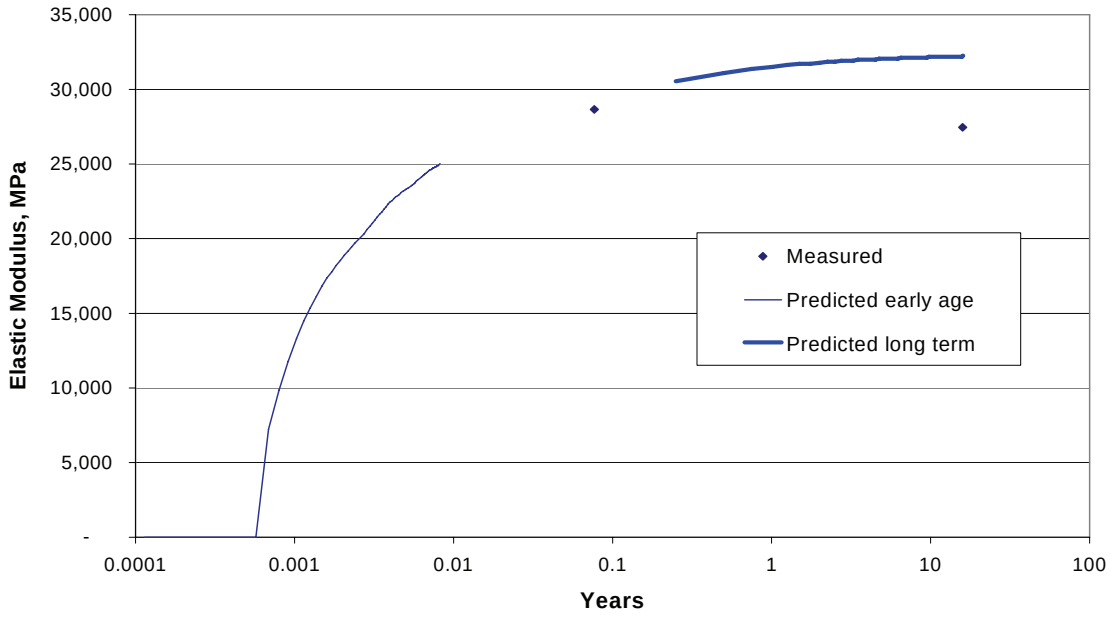

Figure 148. Comparison of measured and predicted modulus of elasticity, Illinois site.

D.2.1.1.2 LTE

LTE has been measured on this site at 8, 12, and 15 years of age. Figure 149 shows the measured and predicted LTE for the sections with 216-mm thickness. The predicted LTE is shown as continuous lines for four times of day: 2 a.m., 8 a.m., 2 p.m., and 8 p.m. The fluctuating trend observed is due to seasonal effects. Higher LTE values are observed for the summer months when the joints are tight due to the higher temperatures on those months. Both the approach and leave slab LTE is shown for the tests performed at 15 years. In general, a slight overprediction of LTE is observed for all testing ages.

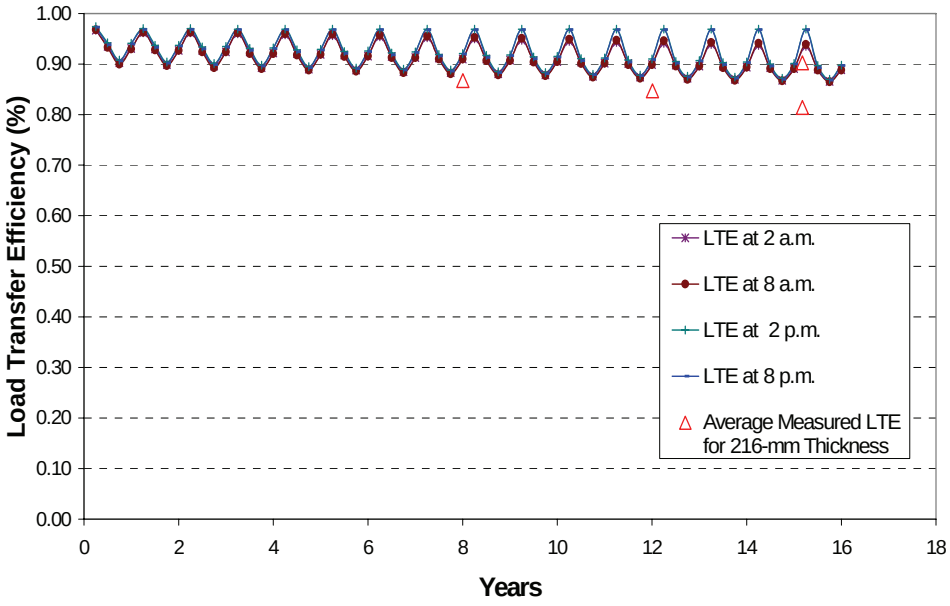

Figure 149. Comparison of measured versus predicted LTE.

D.2.1.1.3 Early-Age Analysis

Figures 150 to 152 show typical early-age results for these sections in terms of strength and stress development for the first 72 hours after construction. In these figures, the results for the placement time at 2 p.m. are shown for sections AA, IA, and NA. It is particularly interesting to observe the excessive stresses for section NA. As previously mentioned in section C.1.1, a cement-aggregate mixture base was used under the slab, which is believed to have induced high restraint conditions. In addition, higher air temperatures for that day were observed from historical weather records. These analysis results suggest that the transverse cracking observed from condition surveys on these sections possibly originated in the early age rather than from fatigue cracking.

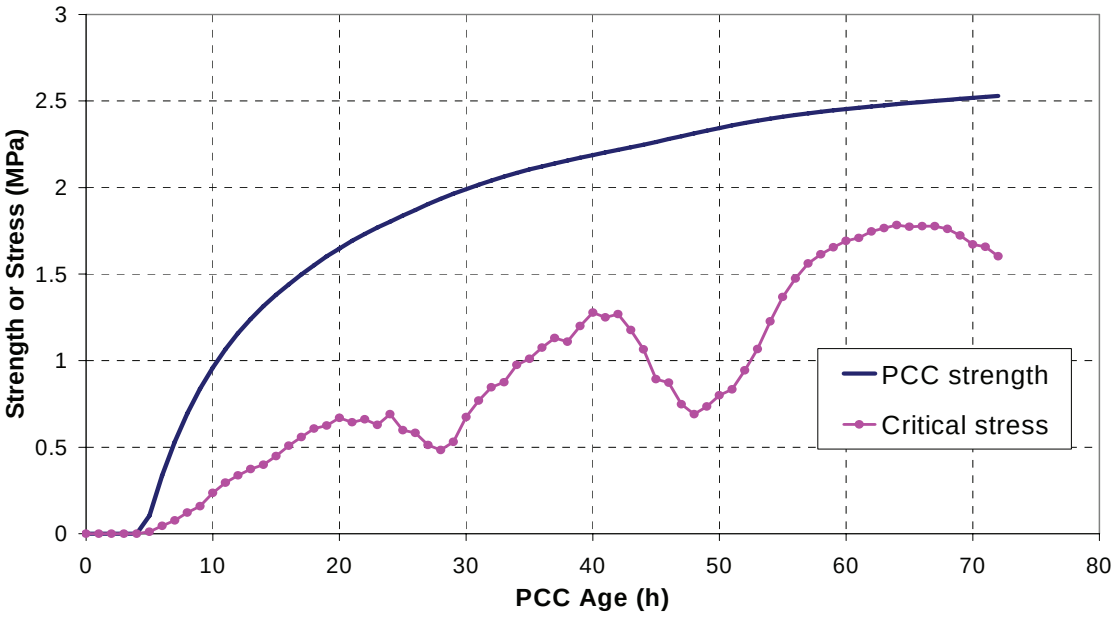

Figure 150. Early-age analysis for section AA, for placement at 2 p.m.

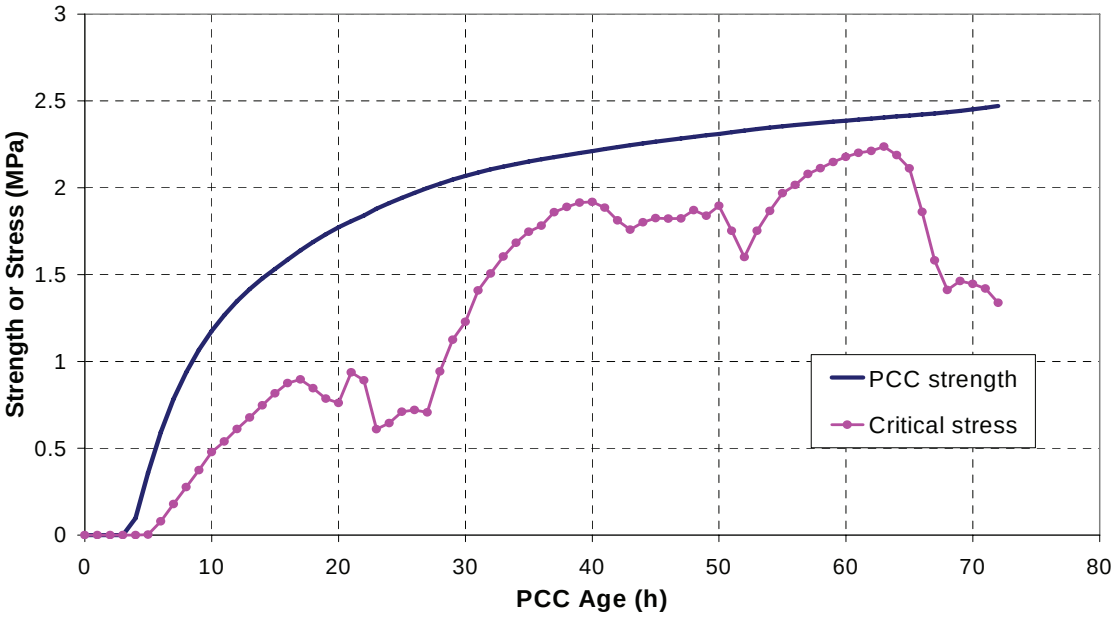

Figure 151. Early-age analysis for section IA, for placement at 2 p.m.

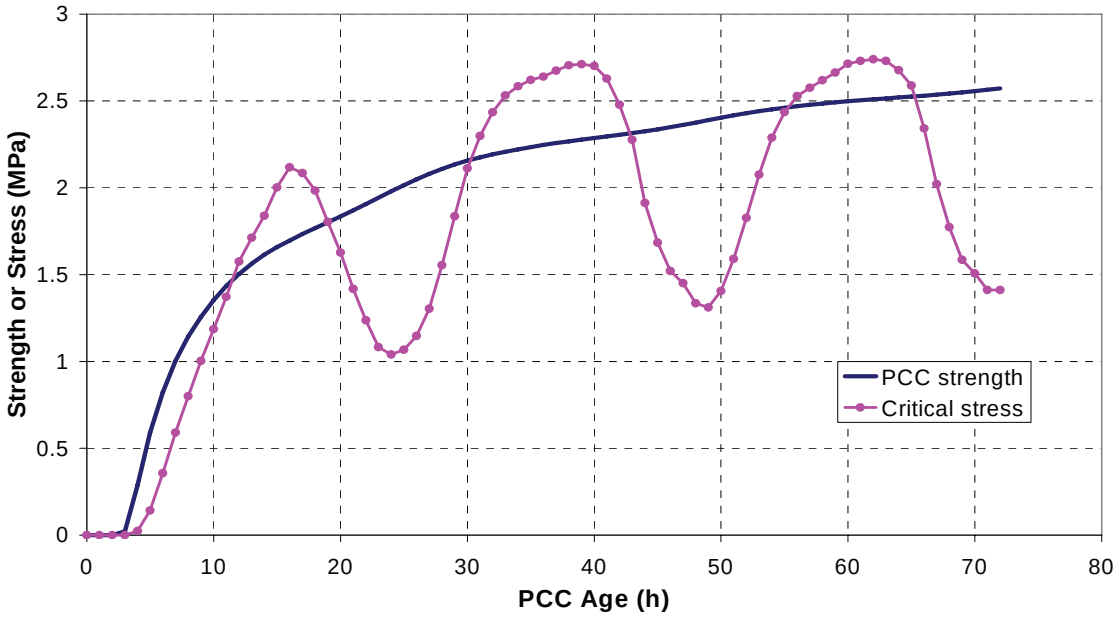

Figure 152. Early-age analysis for section NA for placement at 2 p.m.

D.2.1.1.4 Long-Term Distresses

In addition to the early-age analysis, materials characterization, and structural response evaluation above, a comparison of measured versus predicted long-term distresses was made to assess the accuracy of prediction of the HIPERPAV II long-term module. Individual runs were performed at 10 percent, 50 percent, and 90 percent reliability levels.

Figure 153 shows the predicted faulting for sections MA and NA with 191 mm of thickness. These predictions closely follow the observations made during the field visit in 2001, where no apparent faulting was reported.

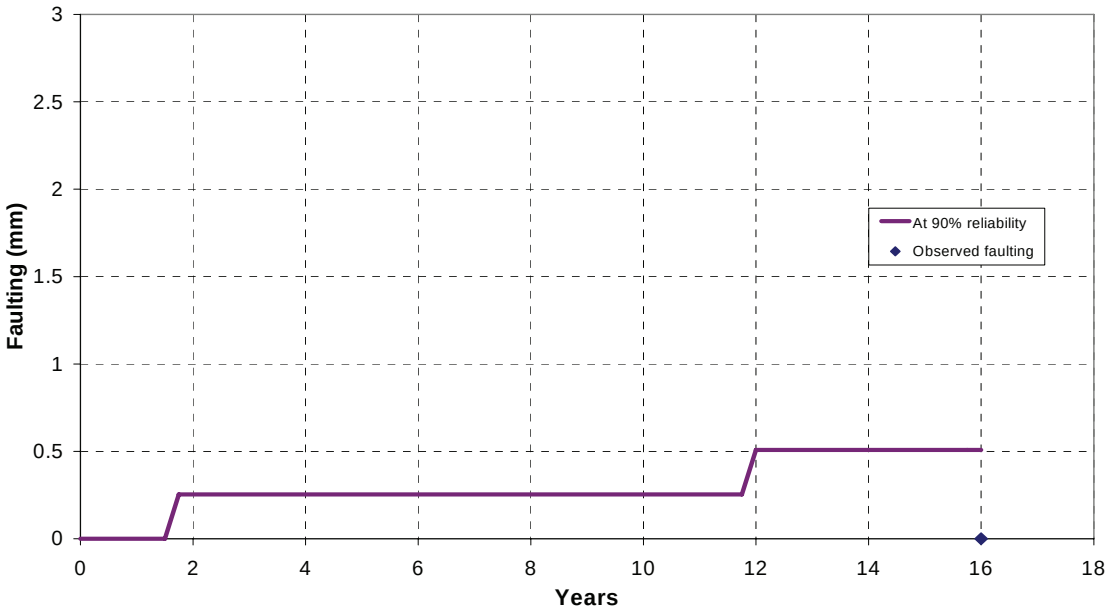

Figure 153. Predicted faulting for sections MA and NA (191-mm thick).

Figures 154 to 156 show a comparison of measured and predicted midpanel cracking in the transverse direction for the sections evaluated. As previously mentioned in the early-age analysis for this site, it is believed that the amount of transverse cracking present is due to early-age factors rather than to fatigue cracking. The predicted fatigue cracking observed for these sections is minimal compared to the transverse cracking observed from surveys.

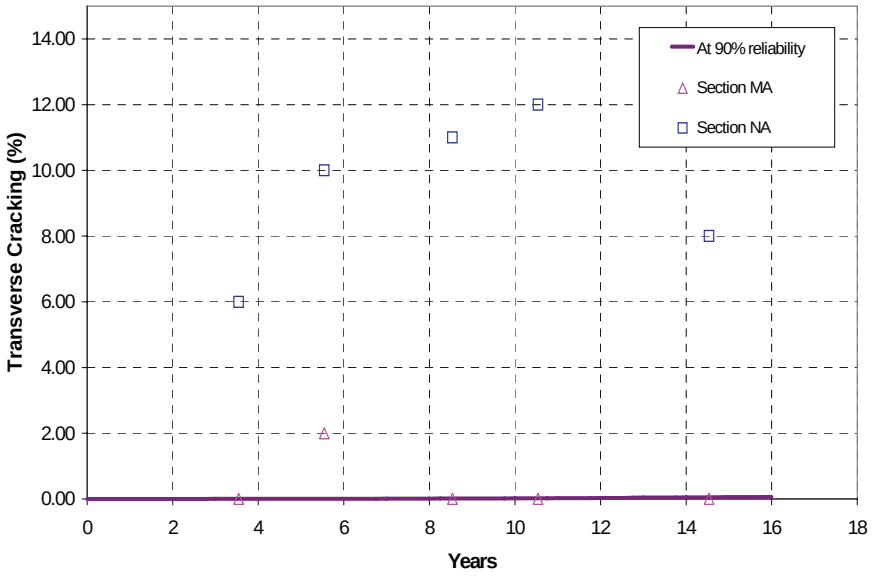

Figure 154. Comparison of measured and predicted transverse cracking (sections NA and MA).

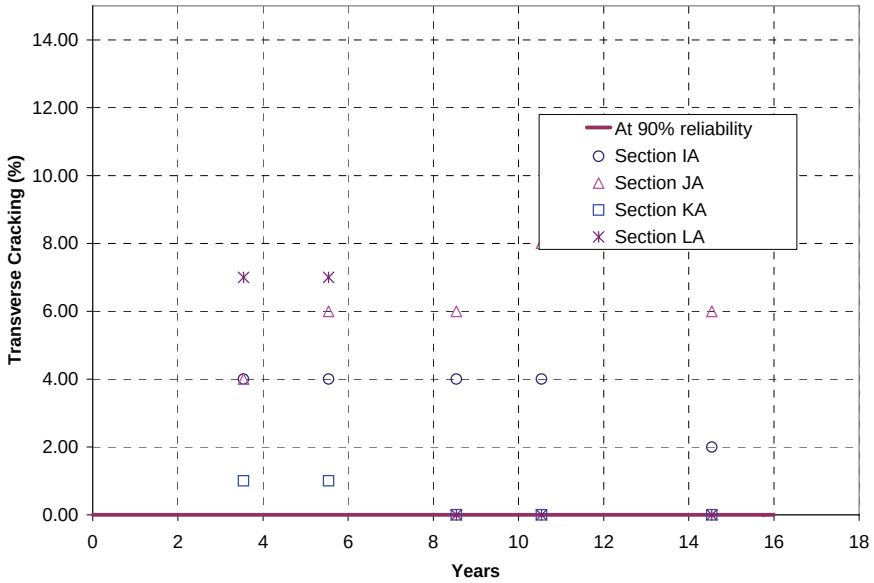

Figure 155. Comparison of measured and predicted transverse cracking for sections (IA, JA, KA, LA).

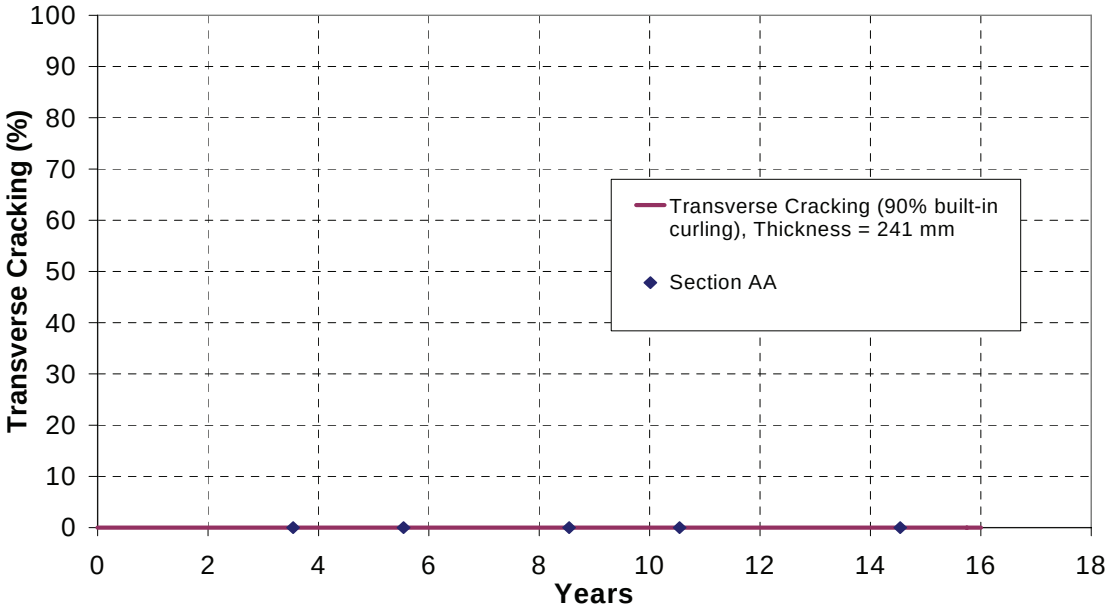

Figure 156. Transverse cracking for section AA, thickness = 241 mm.

Figure 157 shows a comparison of transverse cracking for sections MA and NA with 191-mm thickness. Only one low severity longitudinal crack was observed for section NA. Similar to the transverse cracking present in some of these sections, the longitudinal cracking observed is believed to be due to thermal effects and restraint conditions. No longitudinal cracking was either predicted or observed in the fields for all other sections.

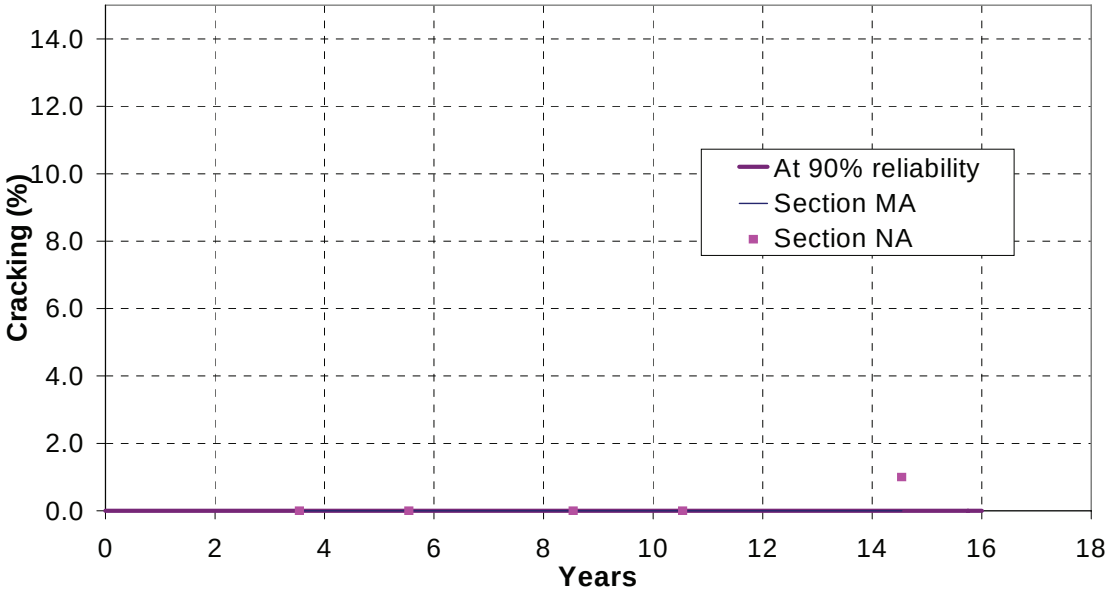

Figure 157. Comparison of measured and predicted longitudinal cracking (sections MA and NA)

No longitudinal cracking was observed for sections AA, IA, JA, KA, and LA. The model predictions for these sections showed no longitudinal cracking, either.

Figure 158 shows the IRI predicted for section NA. The average IRI for all sections for 1994, 1996, 1998, and 2001 also is shown in this figure. Because no data was available for the IRI after construction, an estimated IRI of 1.42 m/km was assumed for this analysis. From this figure, a high scatter in the measured IRI is observed.

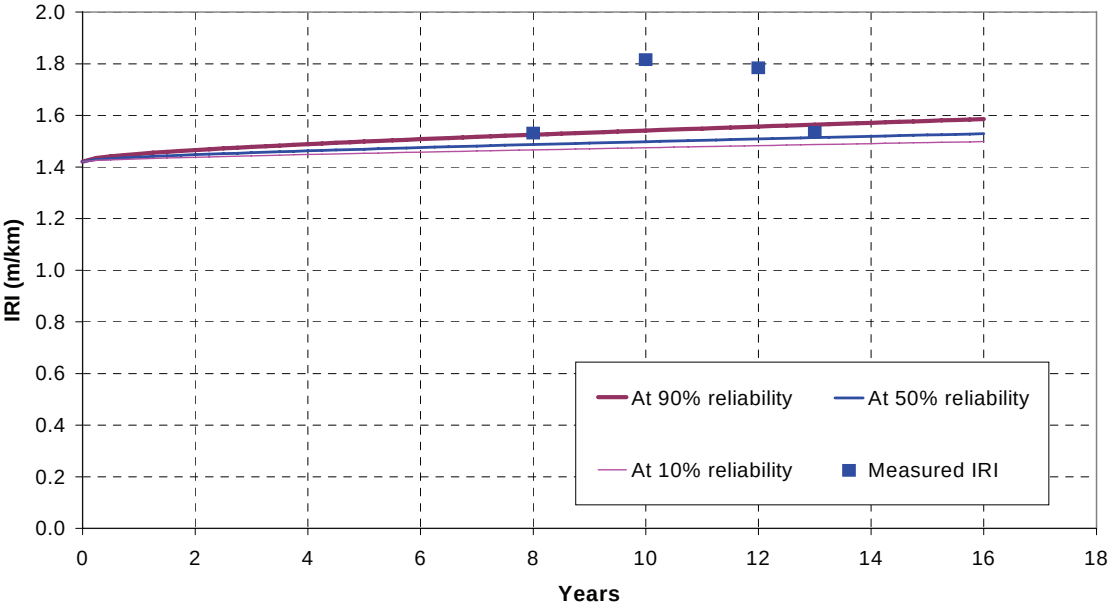

Figure 158. Comparison of measured and predicted IRI (section NA).

D.2.1.2 Validation Results for JPCP Section on Ticuman Bypass, Mexico

Similar to the Illinois site, a comparison of the measured and predicted mechanical properties, structural response, and long-term performance distresses was made for the Ticuman bypass.

D.2.1.2.1 Mechanical Properties

Figure 159 shows a comparison of the measured and predicted third-point flexural PCC strength for the Ticuman bypass. Flexural strength tests were performed at 1, 3, 7, 14, and 28 days of age. The long-term flexural strength value at 8 years of age was estimated from compressive and indirect tensile strength tests results obtained from cores extracted in the 2001 field evaluation. In general, a rather good prediction of the PCC strength was achieved.

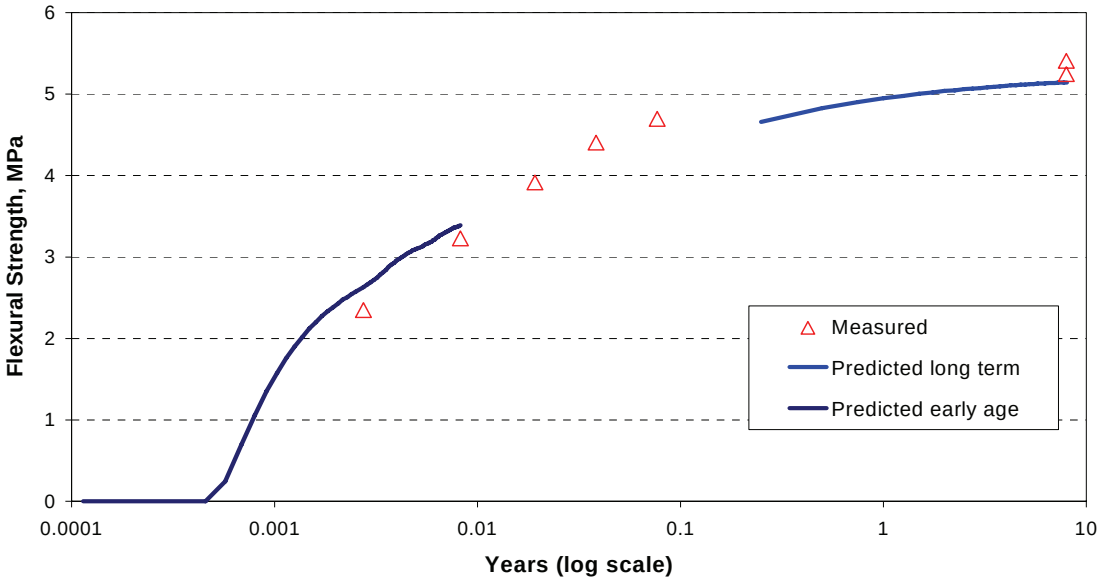

Figure 159. Comparison of measured versus predicted flexural strength, Ticuman, Mexico.

Figure 160 shows a comparison of the measured versus predicted modulus of elasticity. The measured values correspond to 28 days and 8 years of age. A significant underprediction of the elastic modulus at 8 years of age is observed. While the predicted modulus of elasticity shows an increase of 12 percent from 28 days to 8 years, the measured value shows an increase of 55 percent. This finding is opposite to the one observed for the Illinois site, where the elastic modulus was overpredicted.

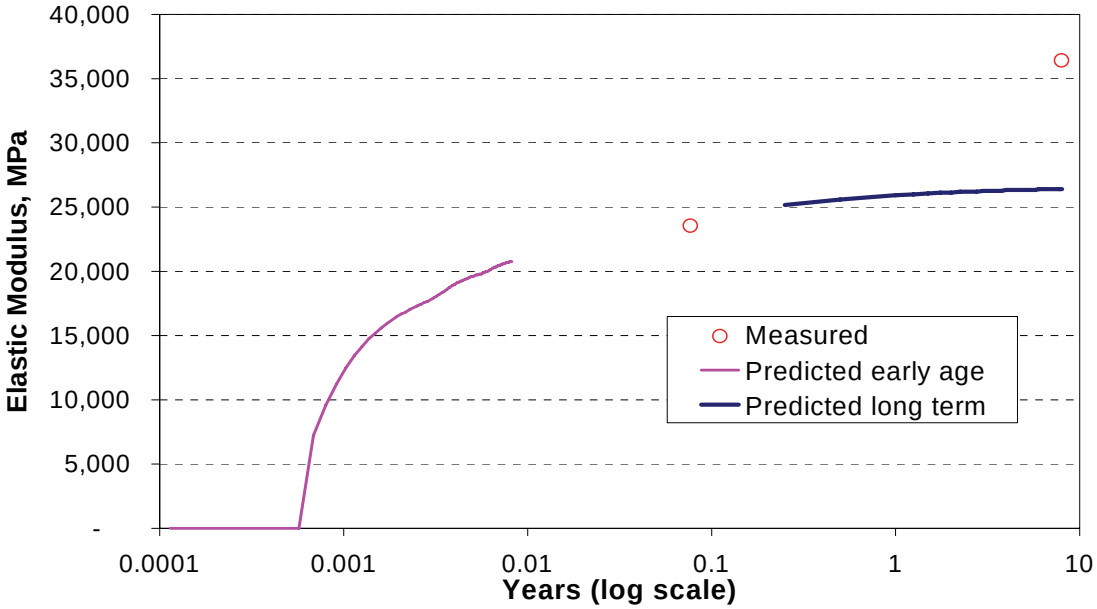

Figure 160. Comparison of measured versus predicted modulus of elasticity, Ticuman, Mexico.

D.2.1.2.2 LTE

LTE tests results are available for two instances: during the first few months after construction, and at 8 years of age. These results are compared to the model predictions in figure 161. As previously mentioned in section C.1.2.2, the low LTE test results observed in 1993 are attributed to the fact that some of the joints had not cracked, leading to wider joint widths and poor load transfer. In comparison, the LTE tests results at 8 years of age show a high LTE. Compared to the LTE predicted with HIPERPAV II, the LTE predicted is higher than the measured in 1993 and slightly lower than the one measured in 2001.

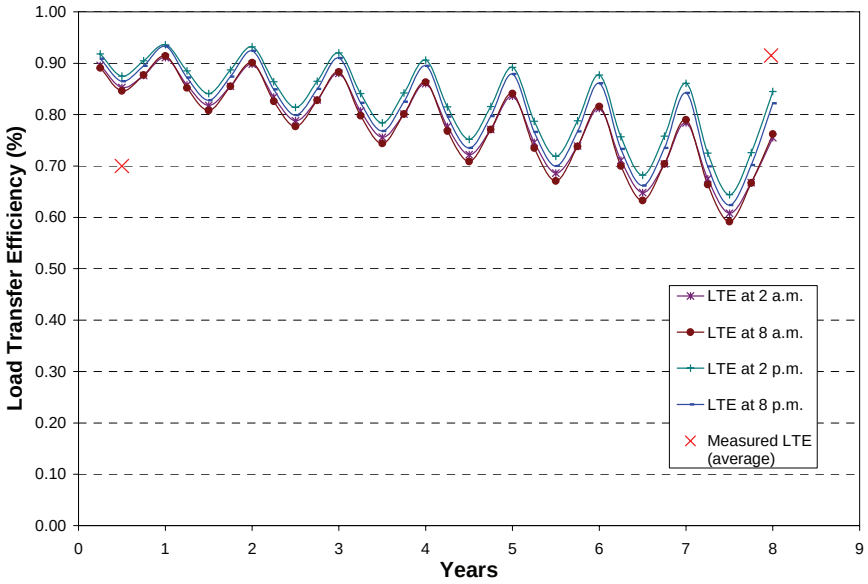

Figure 161. Comparison of measured versus predicted LTE, Ticuman, Mexico.

D.2.1.2.3 Long-Term Distresses

A total of 54 factorial runs were considered for analysis of the distresses at the Ticuman bypass. This factorial was to account for the variability on thickness observed at this site and the different times of placement. In addition, the factorial was expanded to account for different levels of reliability in the long-term analyses.

For the early-age scenarios, three different thicknesses were considered: 203, 229, and 254 mm. Each one of these scenarios was evaluated for placement times at 8 a.m., 2 p.m., and 6 p.m. For the long-term scenarios, three levels of reliability were considered: 10 percent, 50 percent, and 90 percent. Each strategy was analyzed under two conditions: curling stresses computed from thermal gradient at time of loading only, and curling stresses computed for the thermal gradient at time of loading plus built-in curling present at PCC set time.

Figure 162 shows the effect of built-in curling for longitudinal cracking on placement times at 10 a.m. and 6 p.m. For the 10 a.m. placement, the gradient at time of loading with no gradient built-in at set produces higher cracking than the condition with built-in curling. In contrast, the placement at 6 p.m. shows the opposite trend, with the condition with built-in curling showing higher longitudinal cracking. Further investigation into this effect shows that the slabs placed at 10 a.m. set with a positive built-in curling, while the slabs placed at 6 p.m. set with a negative built-in curling. In addition, the most critical loading condition in the long-term for both cases is found to be at 2 p.m., when the slab is being subjected to a positive thermal gradient. For the 10 a.m. placement, the positive thermal gradient built-in at set counteracts the positive thermal gradient during loading and thus reduces the total tensile stresses at the slab bottom for that condition. The opposite occurs for the placement at 6 p.m., where the negative built-in gradient adds to the positive thermal gradient at the time of loading, effectively increasing the stresses for this condition. Because the relaxation occurring on the curling shape of the slab with time, it is believed that the actual stress state at time of loading lies somewhere between these two conditions.

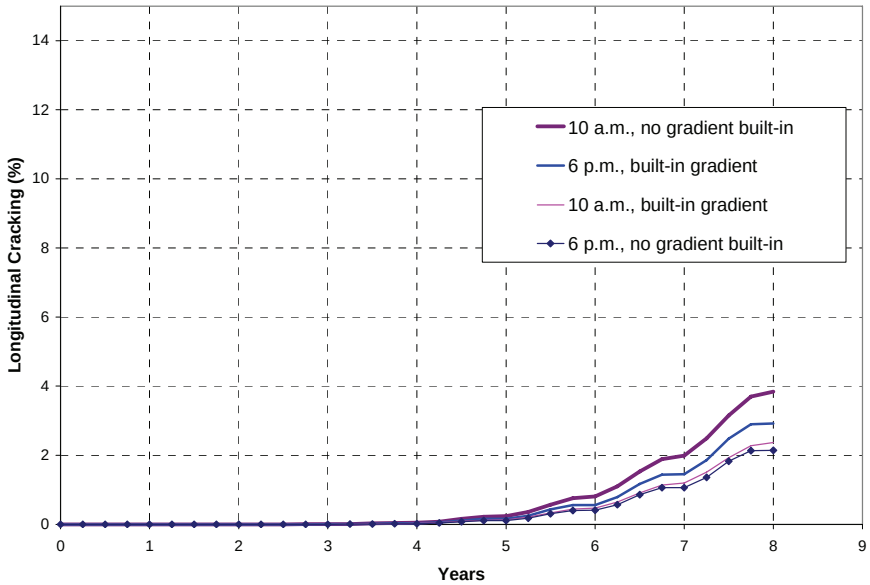

Figure 162. Analysis for 229-mm slab at different construction times and built-in gradient conditions, Ticuman bypass.

Faulting was measured for the Ticuman bypass on the field visit in 2001. Figure 163 shows a comparison of measured and predicted faulting for this site. The average measured faulting of 1.0 mm is lower than the faulting predicted at 50 percent reliability and above the faulting predicted at 10 percent reliability.

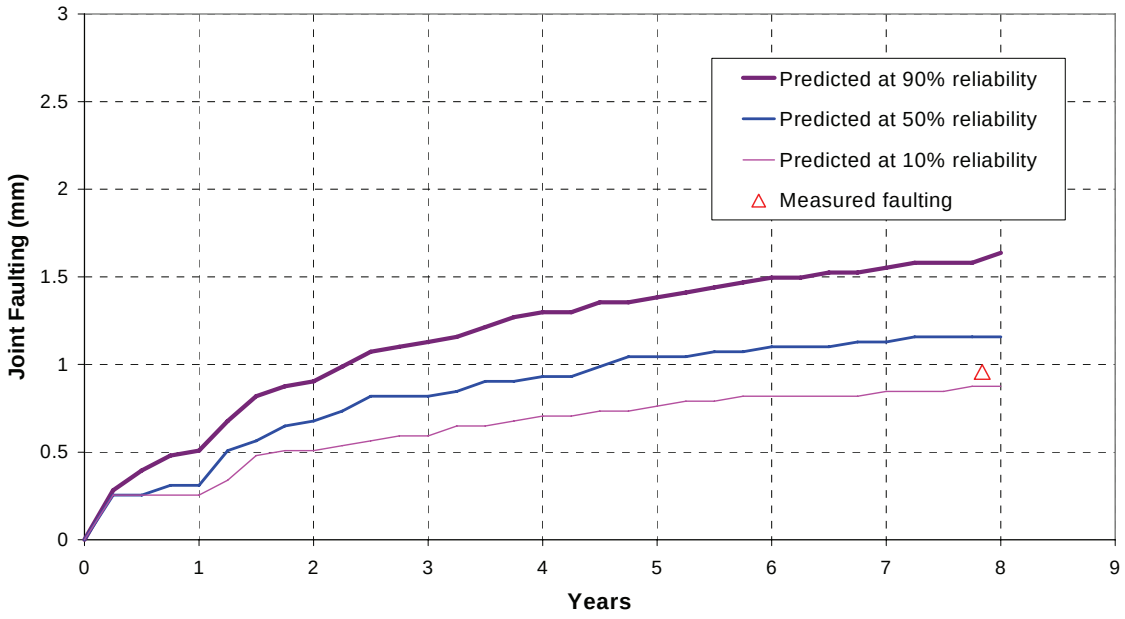

Figure 163. Comparison of measured versus predicted joint faulting, Ticuman, Mexico.

Figures 164 and 165 show the observed and predicted cracking in both, the transverse and longitudinal directions respectively. The amount of both, transverse and longitudinal cracking observed for this site is between the cracking predicted at 50 percent and 90 percent reliability.

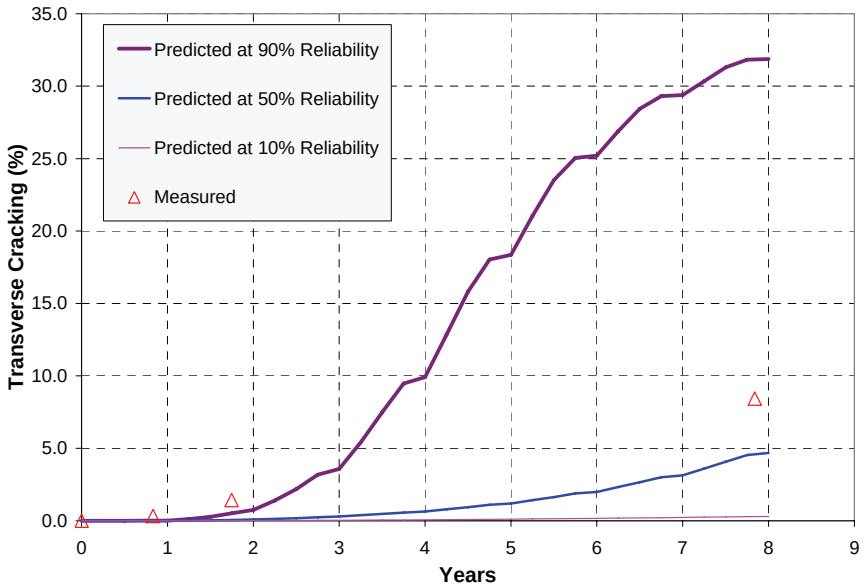

Figure 164. Comparison of measured versus predicted transverse cracking, Ticuman, Mexico.

As previously mentioned in section C.1.2.3, the significant amount of cracking is attributed to the lack of maintenance and the excessive traffic loading on this road.

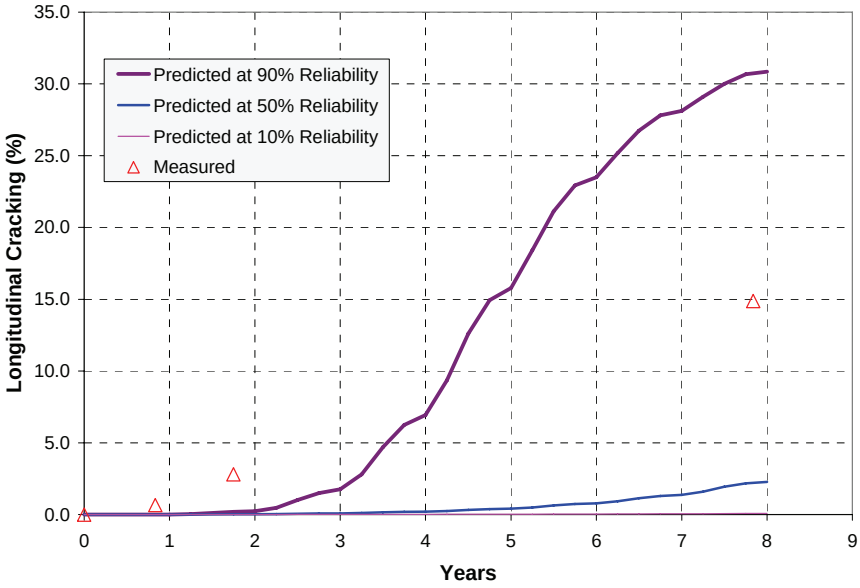

Figure 165. Comparison of measured versus predicted longitudinal cracking, Ticuman, Mexico.

Figure 166 show a comparison in terms of measured and predicted serviceability index. PSI measurements with Mays meter have been performed in 1993 just after construction, in 1995, and in 2001. The PSI in 2001 (after 8 years) is just above the PSI predicted at 90 percent reliability. However, this condition was also observed in 1995 (2 years after construction). While the predicted PSI shows a gradual decrease with time, the PSI measurements show a significant drop for the first few years, and then this condition is maintained.

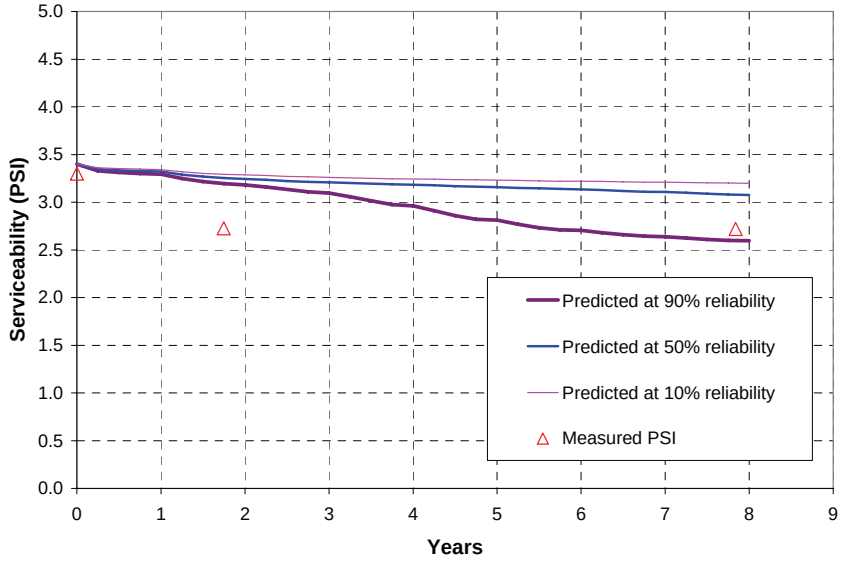

Figure 166. Comparison of measured versus predicted present serviceability index, Ticuman, Mexico.

In summary, it can be concluded that reasonable predictions were obtained in terms of long-term performance for both field sites. Although limited, this validation was done with extensive and quality data on pavement design, materials, climatic, and construction inputs. It is recommended that continued validation of the models be made as more sites are available with enough information on materials characterization and construction.

D.2.2 Validation of Early-Age Behavior Models with Newly Constructed CRCP Sites

D.2.2.1 Validation Results for CRCP Section in Fort Worth, TX

This section presents the data reduction and analysis of the information collected for the CRCP instrumentation in Fort Worth, TX. Measured responses in terms of steel stresses, crack widths, and crack spacings for this site and those predicted with HIPERPAV II also are presented.

D.2.2.1.1 Slab/Subbase Restraint

As documented in appendix C, a slab pushoff test was performed to determine the restraint conditions at the slab/subbase interface. Figure 167 shows a plot of the measured restraint values. The restraint curve observed was fitted with a nonlinear restraint power function with ultimate displacement of 3.8 mm, critical restraint stress of 58.6 kPa, and power coefficient of 3.5. The resulting fit is also shown in figure 167.

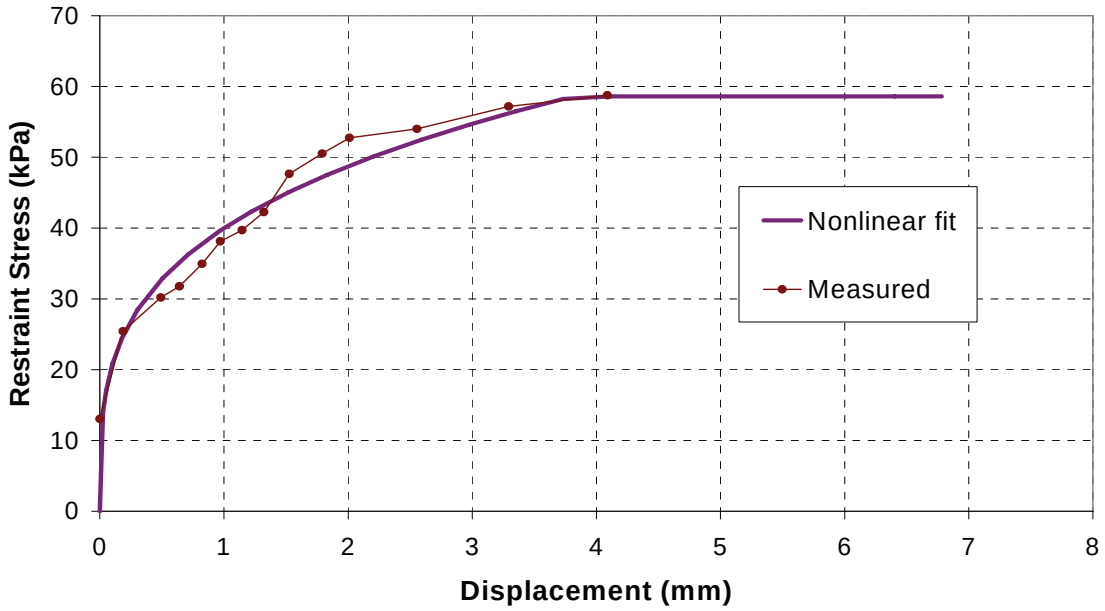

Figure 167. Restraint at the slab/subbase interface.

D.2.2.1.2 PCC Set Time

PCC set time is an important parameter, because the development of many concrete properties depends on it. It is anticipated that set time from laboratory testing and set time in the field will differ, since the aggregate matrix and environmental conditions are different. For determining PCC set time in the field,

information from three sources was considered: laboratory testing, pulse velocity testing, and analysis of PCC strains from an unconfined specimen.

PCC set time tests were performed under laboratory conditions with materials collected from the Fort Worth, TX, CRCP site. The procedure and results from these tests are presented in section C.9. Under laboratory conditions, initial and final set times of 4.0 hours and 4.9 hours were obtained, respectively. Although attempts were made to maintain the temperature of the sample under the same environmental conditions than those observed in the field, slight differences were noted. Therefore, the equivalent time at set was obtained to determine the set time at 20 ºC and determine the set time in the field corresponding to that equivalent time. Using the Arrhenius relationship for equivalent time, initial and final set times at 20 ºC would occur at 8.8 hours and 11.3 hours, respectively. For the temperatures observed in the field, initial and final set for those equivalent ages correspond to 3.5 hours and 4.4 hours real time, respectively.

To corroborate the lab results, the pulse velocity readings were analyzed. For CRCP, pulse velocity time is affected by the presence of steel in the concrete. However, the rate of change of wave travel time still depends on stiffening of the concrete and can be related to set time. In figure 168, a significant decrease in wave travel can be observed between 2.5 and 5.0 hours, which indicates a significant stiffening of the concrete and initial set time occurrence. The estimated set times are indicated in this figure to be within the transition zone between the plastic and hardened state of concrete.

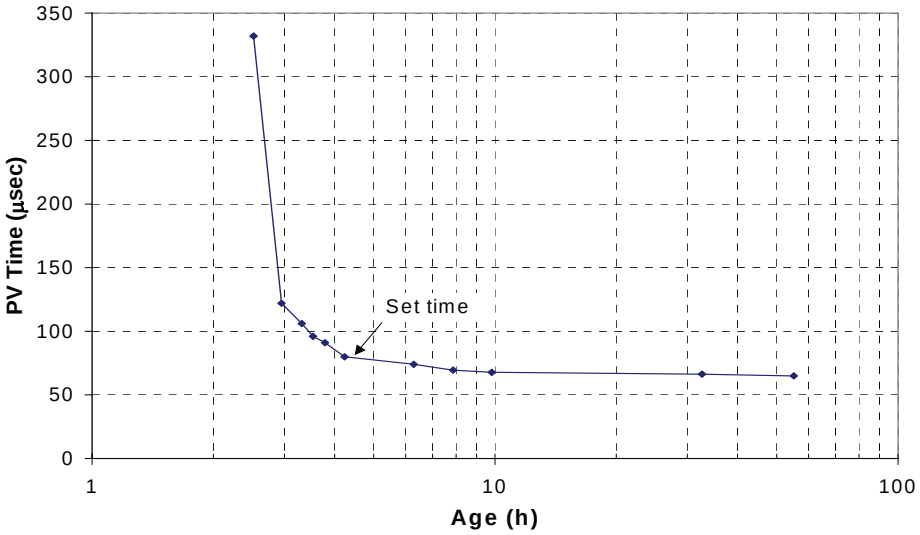

Figure 168. Determination of set time with pulse velocity equipment.

Analysis of the PCC strains in an unconfined concrete specimen also can be used to estimate PCC set time. Figure 169 shows a plot of observed PCC strain versus PCC temperature for an unconfined field concrete specimen instrumented with an embedded strain gage. When the strain gage is initially embedded in the concrete cylinder, relative strain readings do not follow a definitive trend with change in temperature, as the concrete is still plastic. As time progresses and the concrete stiffens, the strains tend to follow the temperature changes in the concrete. The transition, as observed in figure 169, occurs between 2.1 and 4.5 hours, corresponding to the set times from laboratory testing. After this time, the strains in the specimen follow a trend with temperature, fluctuating between contraction and expansion cycles.

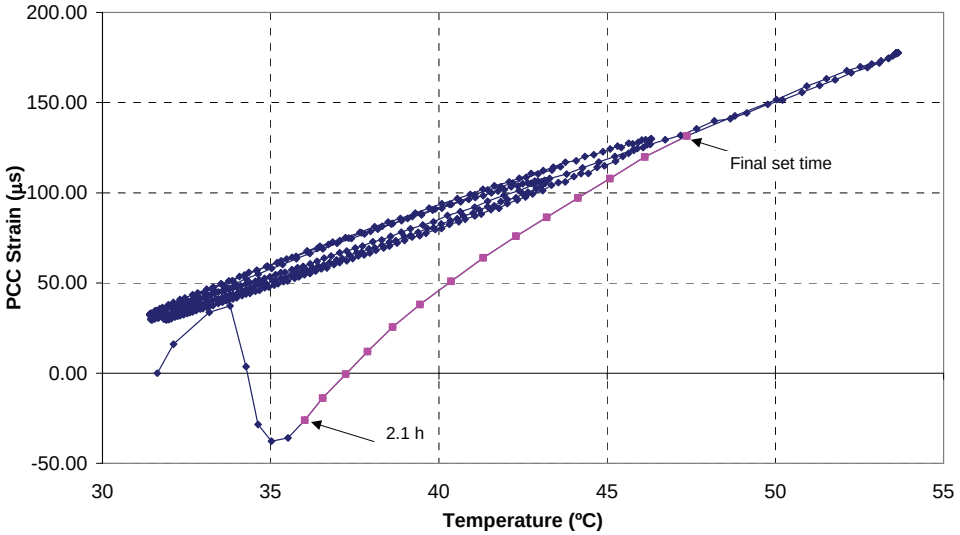

Figure 169. PCC strains during PCC set time as a function of temperature changes.

It most be noted that during construction, joint sawing of the instrumented slab was performed shortly after the slab was strong enough to withstand the Soff-Cut equipment. This occurred at 3.25 hours of age, which is before the measured final set time of 4.4 hours as determined from laboratory testing. According to the pulse velocity readings and the observations of joint sawing in the field, it is evident that initial set time for the instrumented slab occurred approximately at 3.0 hours after placement.

D.2.2.1.3 PCC CTE

The CTE was determined with two different procedures: laboratory testing according to AASHTO TP–60–00 and PCC strain analysis of a field unconfined concrete cylinder as a function of temperature. From laboratory testing, a CTE of 7.48×10^6 m/m/ºC was reported. From the analysis of strains versus temperature, a CTE of 6.6×10^6 m/m/ºC is determined (see figure 170). A slight difference is observed between testing procedures. It is believed that the difference in relative humidity conditions at which the CTE for each procedure was determined may have contributed to the difference in CTE.

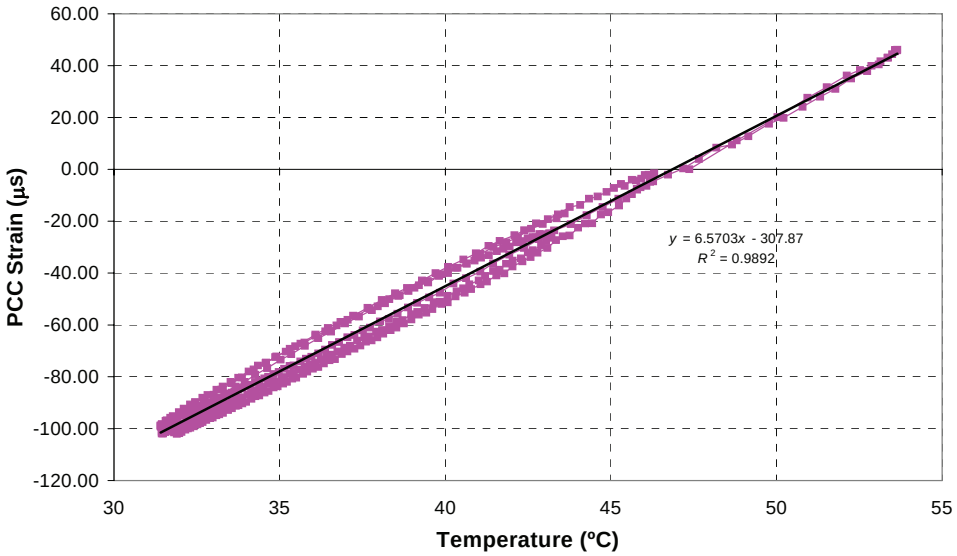

Figure 170. Determination of PCC CTE with the use of PCC strains on an unconfined concrete cylinder.

D.2.2.1.4 Validation Procedures

Validation of the CRCP HIPERPAV II module required collection of information on all the input parameters. With the above information, the CRCP monitored section was analyzed with the CRCP HIPERPAV II module to compare the measured and predicted cracking characteristics.

D.2.2.1.4.1 Analysis of Steel Strains

Steel strains were evaluated at different distances from the crack, as observed in figure 171.

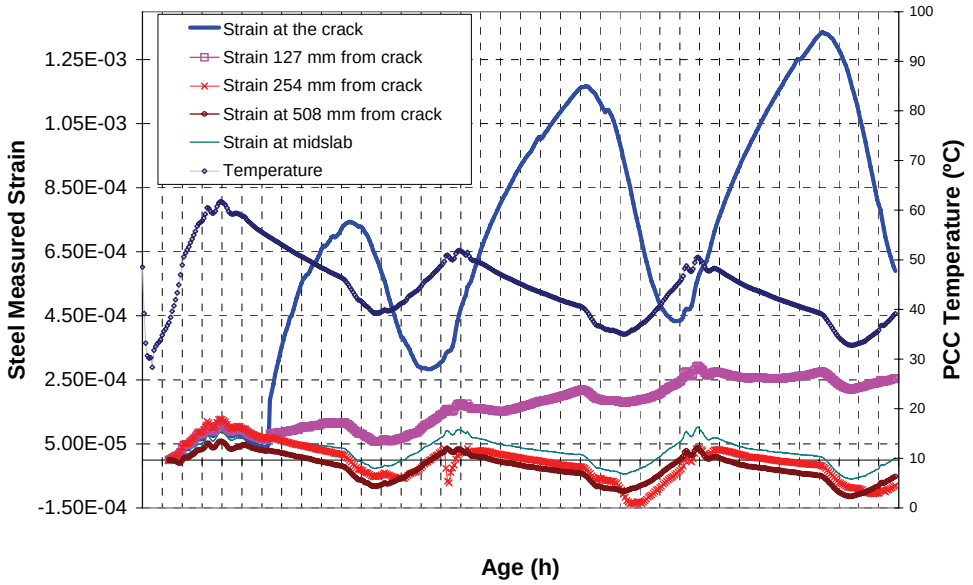

Figure 171. Steel strains at various distances from the crack location.

Note from this figure that steel strain increases at lower temperatures and also as a function of time. This last trend possibly is due to the increase in PCC drying shrinkage. Figure 172 shows a plot of steel strains along the slab length for the strain peaks observed at 21.0, 44.8, and 68.5 hours. The strain plotted is the average strain of the two strain gages installed at each distance.

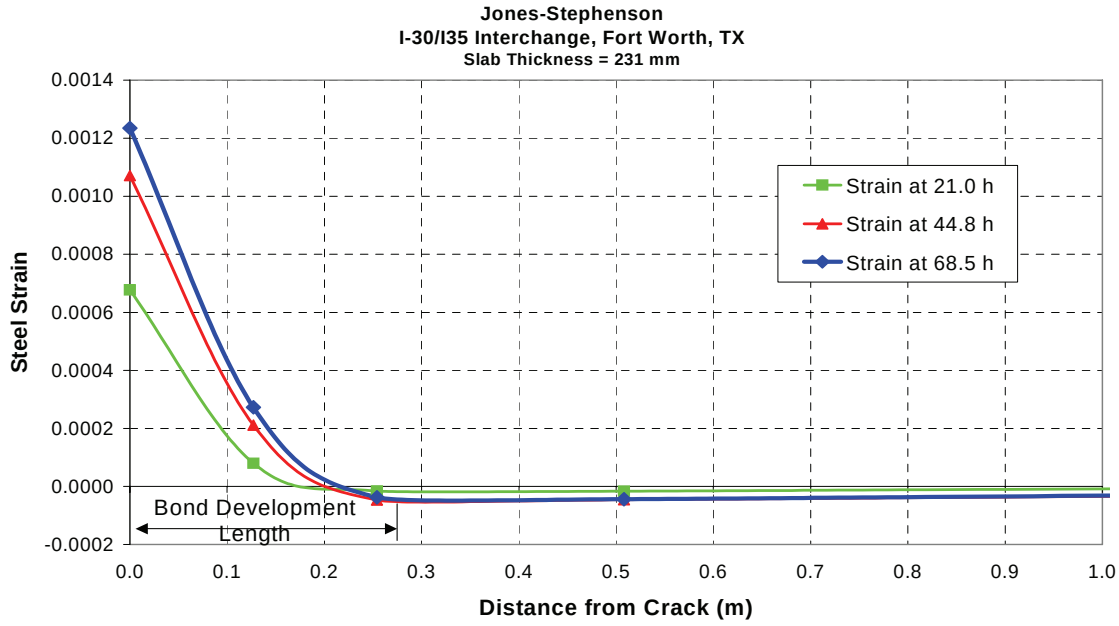

Figure 172. Steel strain along the slab length at different ages.

From figure 172, the bond development length can be identified; this is the slab segment from the crack location for which the steel strain is variable. In this case, a bond development length of approximately 279 mm is observed for these ages.

D.2.2.1.4.2 Analysis of Concrete Strains

Concrete strains were analyzed to determine their influence on the stress development in the steel. Figure 173 shows the strains observed in the concrete at different distances from the crack. The time of crack formation can be clearly identified by the sharp increase in strains on the gages at 127 mm from the crack. The crack is observed to occur close to 12 hours after construction, which also coincides with the significant development in steel strain at the crack seen in figure 171.

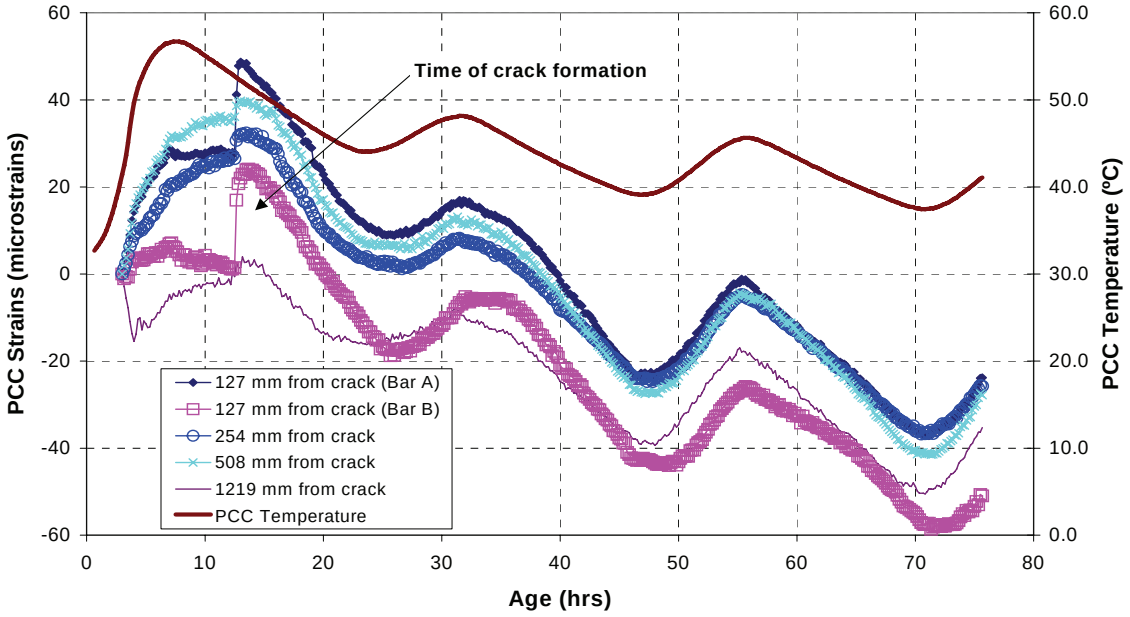

Figure 173. Concrete strains at middepth along slab length.

Comparing the individual ages of 21.0, 44.8, and 68.5 hours with steel strains, the average concrete strains for those ages are 4.4×10^{-6} m/m, -26.7×10^{-6} m/m, and -40.6×10^{-6} m/m. A negative trend in PCC strain is observed, which can be attributed to the decreasing temperature in the concrete and to drying shrinkage. The drying shrinkage observed on an unrestrained PCC cylinder in the field after subtracting temperature effects is presented in figure 174.

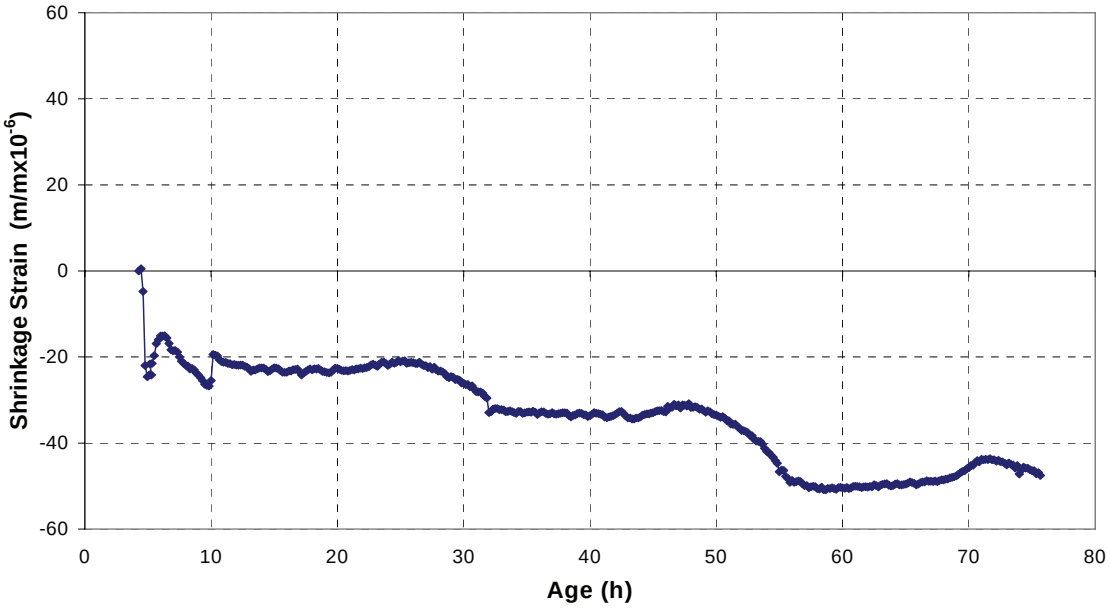

Figure 174. Drying shrinkage observed in the field on an unrestrained PCC cylinder.

Figure 175 shows the steel strains in the concrete and in the steel at 68.5 hours after construction. The strains in the concrete appear almost constant along the slab at approximately 40 microstrains. The strains in the steel also appear within the same order of magnitude along most of the slab, except near the crack, where they increase significantly.

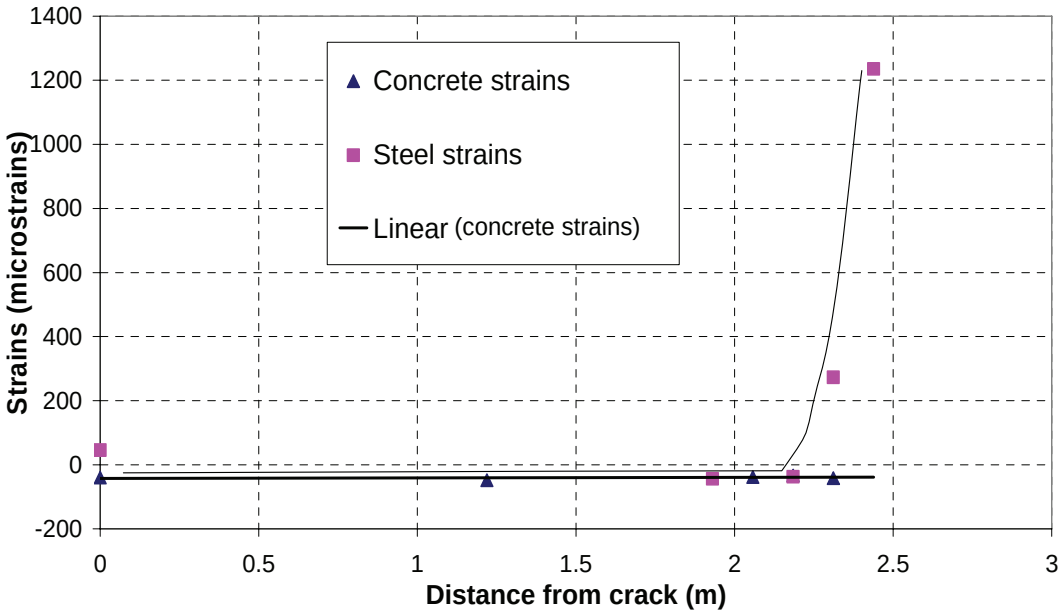

Figure 175. Strains in concrete and steel at 68.5 hours after construction.

Assuming a strain level in the steel similar to the one observed in the concrete at midslab and integrating the strains along the slab length, the displacement of concrete and steel is plotted in figure 176.

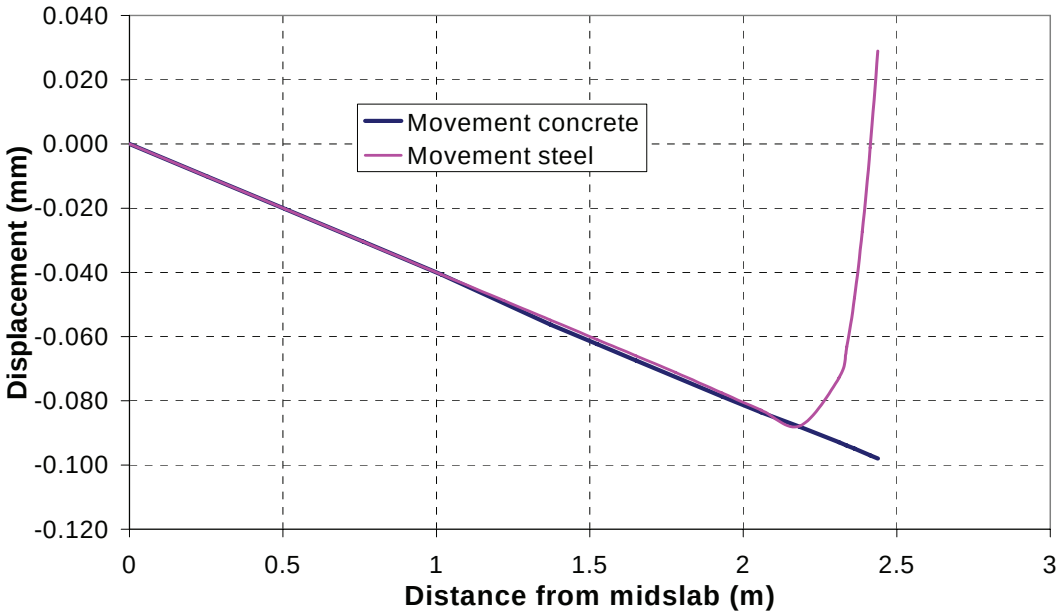

Figure 176. Displacements in steel and concrete along slab length at 68.5 hours.

D.2.2.1.4.3 Evaluation of Stress and Bond Development Length

The bond development length predicted with HIPERPAV II for this site for the first 3 days of age varied from 0.56 to 0.79 m. The bond development length predicted is significantly higher than the measured one of approximately 279 mm.

From the strains measured, the steel stress is computed and is shown in figure 177 for the age of 68.5 hours. The steel stress at the crack is 246.8 MPa. The steel stress computed by HIPERAV for that age is 392.3 MPa at the crack location. The predicted stress is also shown in this figure. It is believed that the difference in predicted and measured bond development length and steel stress is related to the limitations in the bond-slip relationships assumed in the CRCP–8 model. These limitations have been previously identified by Palmer et al.[120]

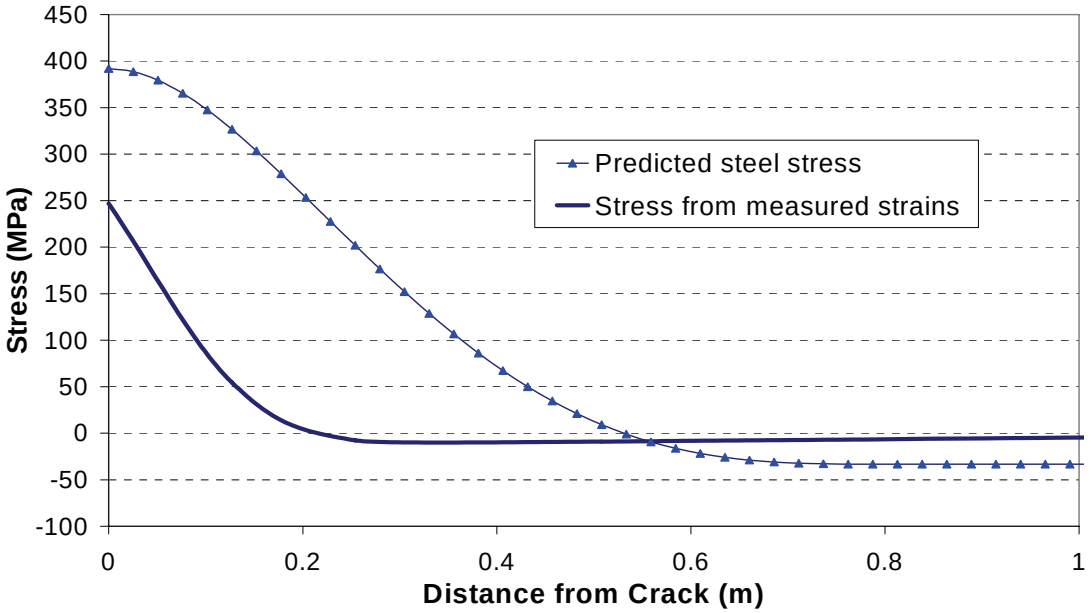

Figure 177. Steel stress along the slab at 68.5 hours.

D.2.2.1.4.4 Analysis of Crack Widths

Crack width data was evaluated as a function of pavement age and also as a function of pavement depth. Table 87 shows the crack widths observed during the first 3 days after construction for the top, middle, and bottom of the slab.

Table 87. Comparison of average crack width predicted and measured values.

Age	Measured Top	Measured Middle	Measured Bottom	Predicted Middle
Day 1	0.005	0.003	0.002	0.027
Day 2	0.009	0.004	–	0.042
Day 3	0.010	0.005	–	0.050

A large discrepancy in measured and predicted crack width is observed. The predicted crack width is overpredicted by a factor of 5 compared to the average crack width at the top, and by a factor of 10 compared to the crack width measured at middepth.

Crack width tends to increase as a function of time. In addition, larger crack widths are observed at the top of the slab compared to middepth and bottom; this is attributed to increased drying shrinkage at the slab surface. Crack width measurements were obtained at the slab edge. The crack width at the steel location was not measured. It is believed that, due to the steel restraint, the crack width near the steel is smaller than those reported here and therefore increasing the overprediction.

The limitations in crack width prediction have been discussed in section D.1.2.10. The differences in steel stress and bond development length found in this analysis also are believed to contribute to the overprediction of crack widths.

D.2.2.1.4.5 Crack Spacing Validation Results

Table 88 shows a comparison of measured versus predicted crack spacings for the first 3 days after construction. Although the measured crack spacings show a slight decreasing trend, the predicted crack spacing is constant for the early ages and is reduced to an average crack spacing of 1.55 m after 1 year. However, the average crack spacing predicted of 3.32 m matches very closely the measured average crack spacing of 3.59 m at 3 days of age. The predicted crack spacing at 1 year for this site is 1.55 m.

Table 88. Comparison of predicted and measured average crack spacings.

Age	Measured (m)	Predicted (m)
Day 1	4.36	3.32
Day 2	3.99	3.32
Day 3	3.60	3.32
After construction traffic	–	2.71
1 year	–	1.55

The crack spacing distributions are presented in figure 178. Although a reasonably good fit for the crack spacings observed after 3 days is achieved, it is believed that the bond slip relationships in the CRCP–8 program must be further investigated to predict steel stresses and crack widths accurately.

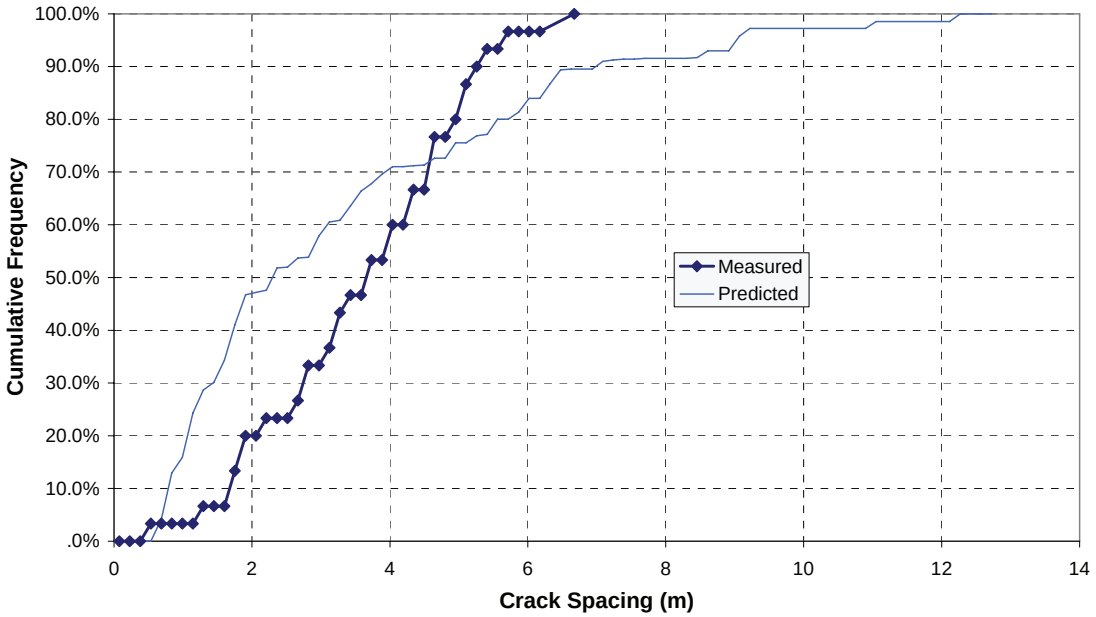

Figure 178. Measured versus predicted crack spacing at 3 days of age, Fort Worth, TX

D.2.2.2 Validation Results for CRCP Section on I–29, South Dakota

This section presents the data reduction and analysis of the information collected for the CRCP instrumentation in South Dakota. Measured responses in terms of steel stresses, crack widths, and crack spacings for this site and those predicted with HIPERPAV II also are presented.

D.2.2.2.1 Slab/Subbase Restraint

Although no pushoff test was performed for this site, the subbase restraint conditions were observed to be typical of an unbonded aggregate base. Default values for this subbase type were selected.

D.2.2.2.2 PCC Set Time

For determination of PCC set time in the field, information from two sources was considered: laboratory testing and analysis of PCC strains from an unconfined specimen.

PCC set time tests were performed under laboratory conditions with materials collected from the South Dakota CRCP site. The procedure and results from these tests are presented in appendix C. Under laboratory conditions, initial and final set times of 5.1 hours and 6.6 hours were obtained, respectively. However, given the inability to relate laboratory set time to the time set occurred in the field for the South Dakota site, set time was identified with the analysis of PCC strains from an unconfined specimen. With this procedure, a set time of approximately 6 hours was measured.

The equivalent time at set was obtained to determine the set time at 20 ºC and determine the set time in the field corresponding to that equivalent time. Using the Arrhenius relationship for equivalent time, initial and final set times at 20 ºC would occur at 4.9 hours and 6.4 hours, respectively. For the temperatures observed in the field, set times for those equivalent ages correspond to approximately 4.0 hours and 5.0 hours in real time, respectively.

Analysis of the PCC strains in an unconfined concrete specimen used can also be to estimate PCC set time. Figure 179 shows a plot of observed PCC strain versus PCC temperature for an unconfined field concrete specimen instrumented with an embedded strain gage. When the strain gage is initially embedded in the concrete cylinder, relative strain readings do not follow a definitive trend with change in temperature, as the concrete is still plastic. As time progresses and the concrete stiffens, the strains tend to follow the temperature changes in the concrete. The transition, as observed in figure 179, occurs between 2.8 hours and 6.5 hours. The initial and final set times from laboratory tests fall within this range. After this time, the strains in the specimen follow a trend with temperature, fluctuating between contraction and expansion cycles.

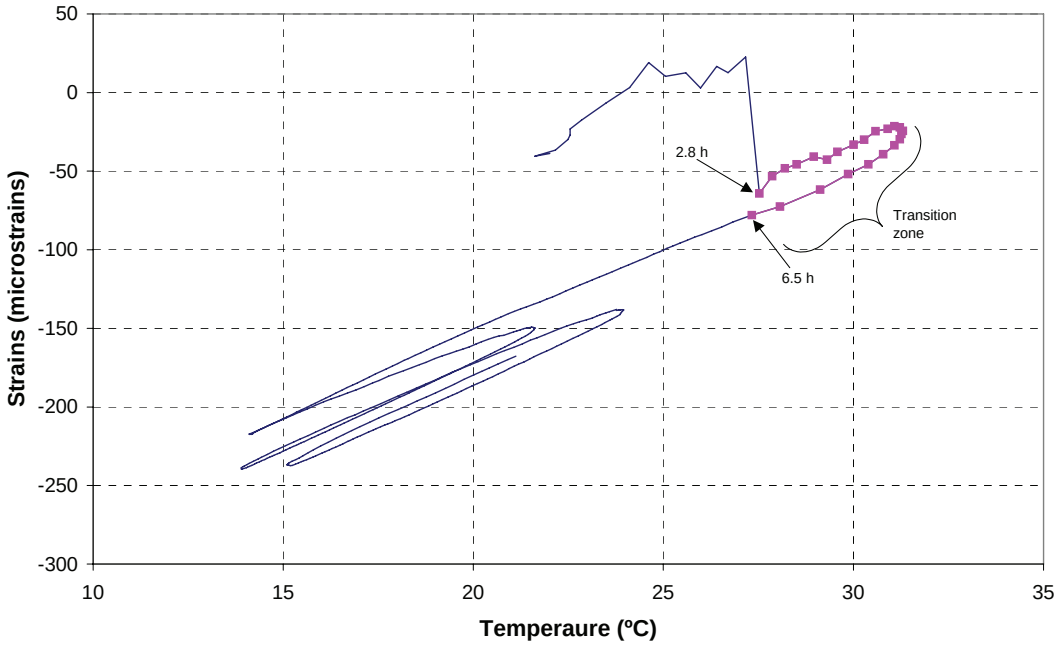

Figure 179. PCC strains during PCC set time as a function of temperature changes.

According to the above analysis, the initial and final set times of 4.0 hours and 5.0 hours, respectively, were used for analysis.

D.2.2.2.3 PCC CTE

The CTE was determined with two different procedures: laboratory testing according to AASHTO TP–60–00 and PCC strain analysis of a field unconfined concrete cylinder as a function of temperature. From laboratory testing, a CTE of 10.9×10^6 m/m/ºC was reported. From the analysis of strains versus temperature, a CTE of 11.6×10^6 m/m/ºC is determined (see figure 180). A slight difference is observed between testing procedures. It is believed that the difference in relative humidity conditions at which the CTE for each procedure was determined may have contributed to the difference observed.

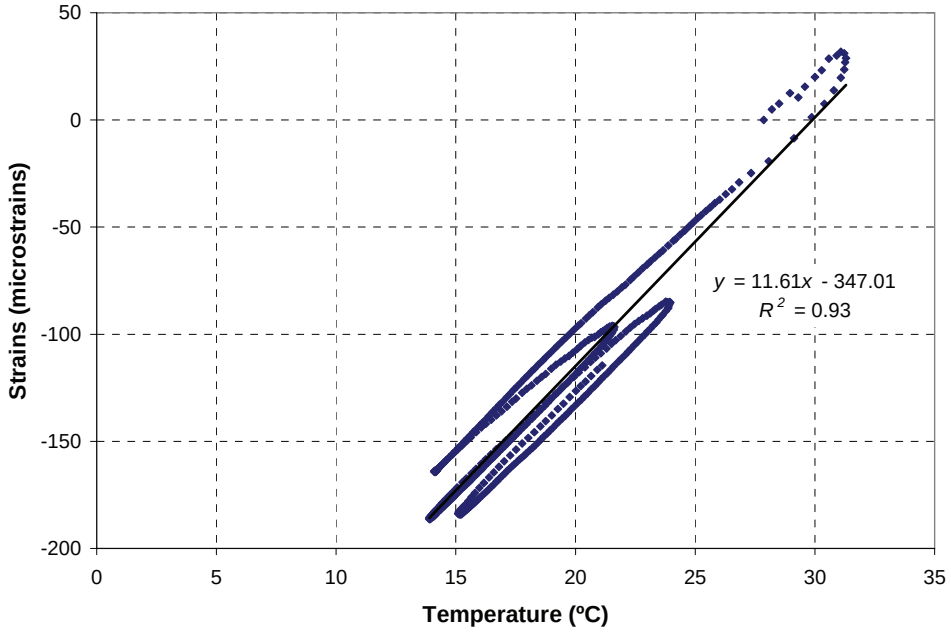

Figure 180. Determination of PCC CTE with the use of PCC strains on an unconfined concrete cylinder.

D.2.2.2.4 Validation Procedures

Validation of the CRCP HIPERPAV II module required collecting information on all the input parameters. With the above information, the CRCP monitored section was analyzed with the CRCP HIPERPAV II module to compare the measured and predicted cracking characteristics.

D.2.2.2.4.1 Analysis of Steel Strains

Steel strains were evaluated at different distances from the crack as observed in figure 181. Gages were installed on two different bars and are identified as either "A" or "B" in the figure. The crack occurred 108 mm from the expected location, thus shifting the location of the gages by that amount. In addition, a second crack was noticed later 356 mm from midslab, leaving the gages at that location at that distance from the new crack. Crack occurrences can be identified clearly by the sharp change in strain at approximately 19, 34, and 40 hours from placement.

Similar to the Fort Worth, TX, site, the strain gages closer to the crack recorded higher strains than those far from the crack. However, the gages at 356 mm from the second crack did not show a significant increase in strain after crack occurrence, as would be expected. However, it most be noted that, for the Fort Worth, TX site, the bond development length was smaller than 356 mm. Therefore, it is possible that the bond development length for the second crack could have been less than 356 mm.

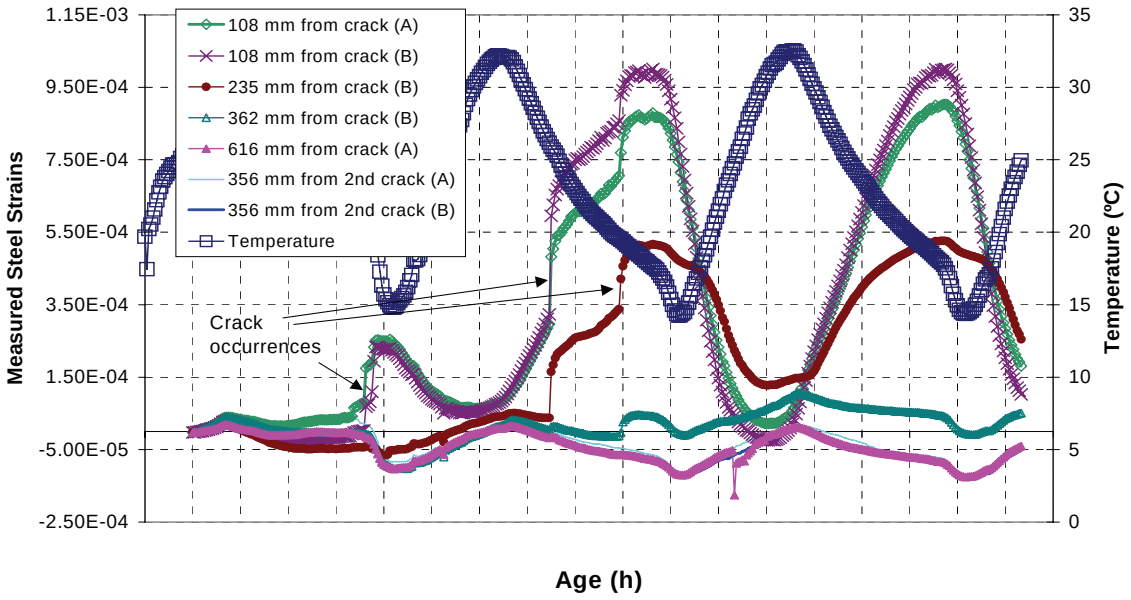

Figure 181. Steel strains at various distances from the crack location.

Figure 182 shows a plot of steel strains along the slab length for the strain peaks observed at 20.3, 43.2, and 67.2 hours. The strain plotted is the average strain of the two strain gages installed at each distance.

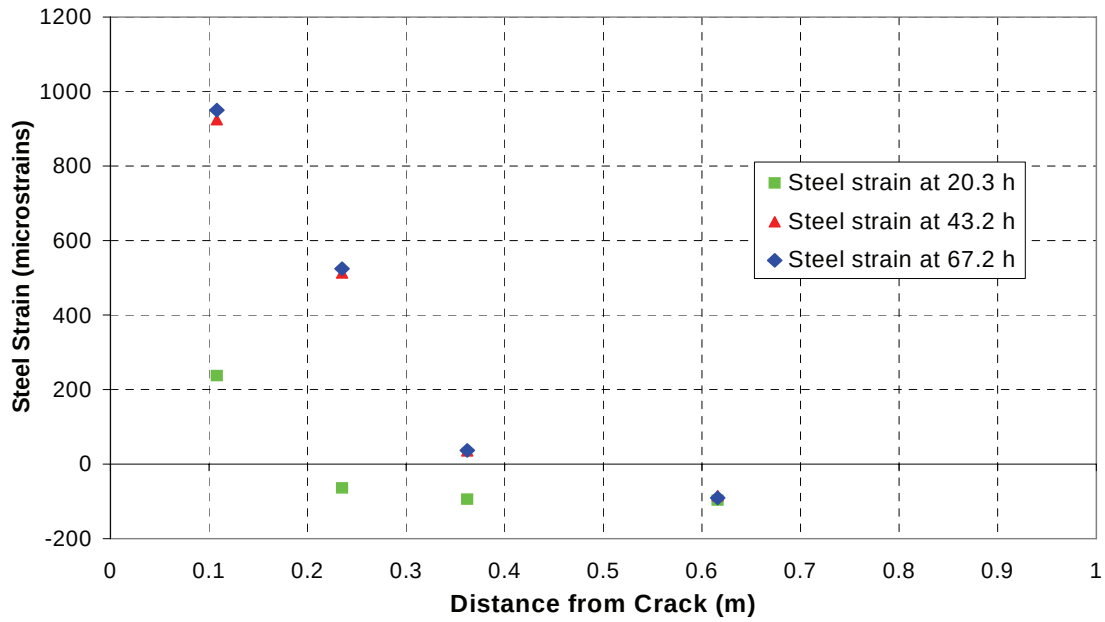

Figure 182. Steel strain along the slab length at different ages.

From figure 182, the bond development length can be identified; this is the slab segment from the crack location for which the steel strain is variable. In this case, a bond development length of approximately 0.5 to 0.6 m is observed for these ages. Extrapolating the steel strains to estimate the strain at the crack yields 550 microstrains at 20.3 hours and 1200 to 1500 microstrains for the other two ages.

D.2.2.2.4.2 Analysis of Concrete Strains

Concrete strains were analyzed to determine their influence on the stress development in the steel. Figure 183 shows the strains observed in the concrete at different distances from the crack. The time of crack formation can be identified clearly by the sharp increase in strains on the gages at 235 mm from the crack. The cracks are observed to occur close to 19, 34, and 40 hours after construction, which also coincide with the significant development in steel strain seen in figure 181.

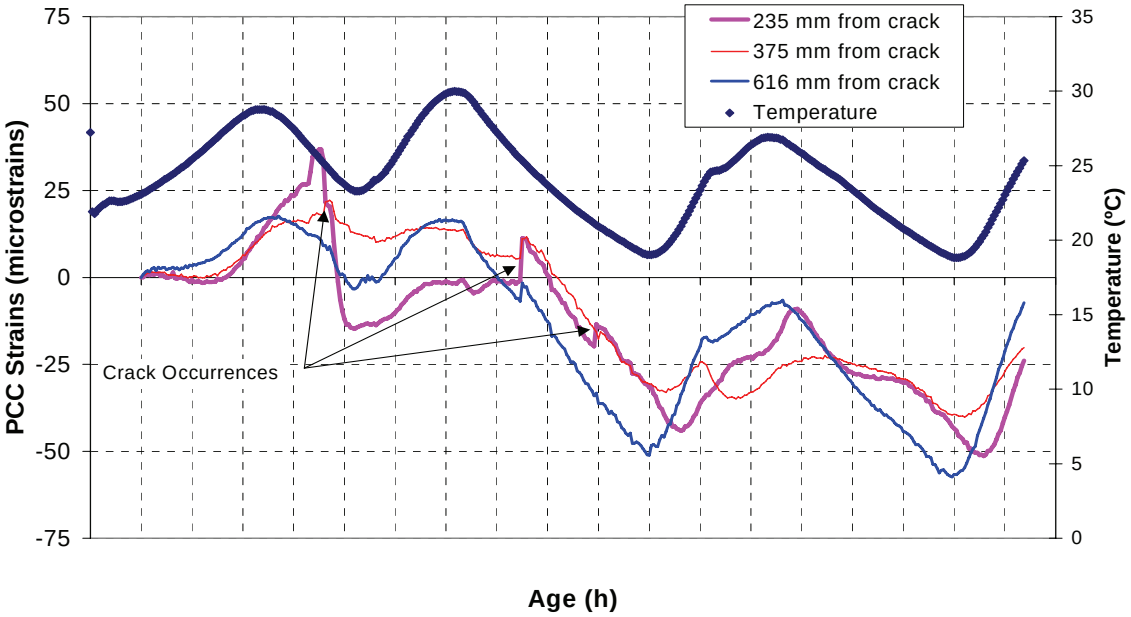

Figure 183. Concrete strains at middepth along slab length.

In the above figure, the concrete strains at 20.3, 43.2, and 67.2 hours are compared with the steel strains; the average concrete strains for those ages are 0.2×10^{-6}, -34.7×10^{-6}, and -44.3×10^{-6}. Similar to the Fort Worth, TX, site, a negative trend in PCC strain is observed. The drying shrinkage observed on an unrestrained PCC cylinder in the field after subtracting temperature effects is presented in figure 184.

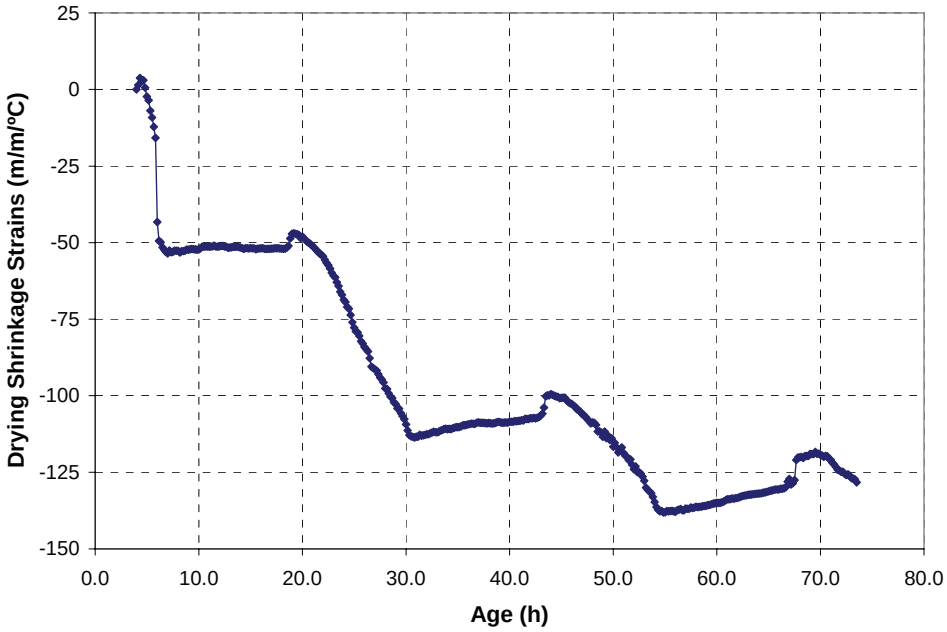

Figure 184. Drying shrinkage observed in the field on an unrestrained PCC cylinder.

Figure 185 shows the steel strains in the concrete and in the steel at 67.2 hours after construction. The strains in the concrete appear almost constant along the slab at approximately 40 microstrains. The strains in the steel also appear within the same order of magnitude along most of the slab, except near the crack, where they increase significantly.

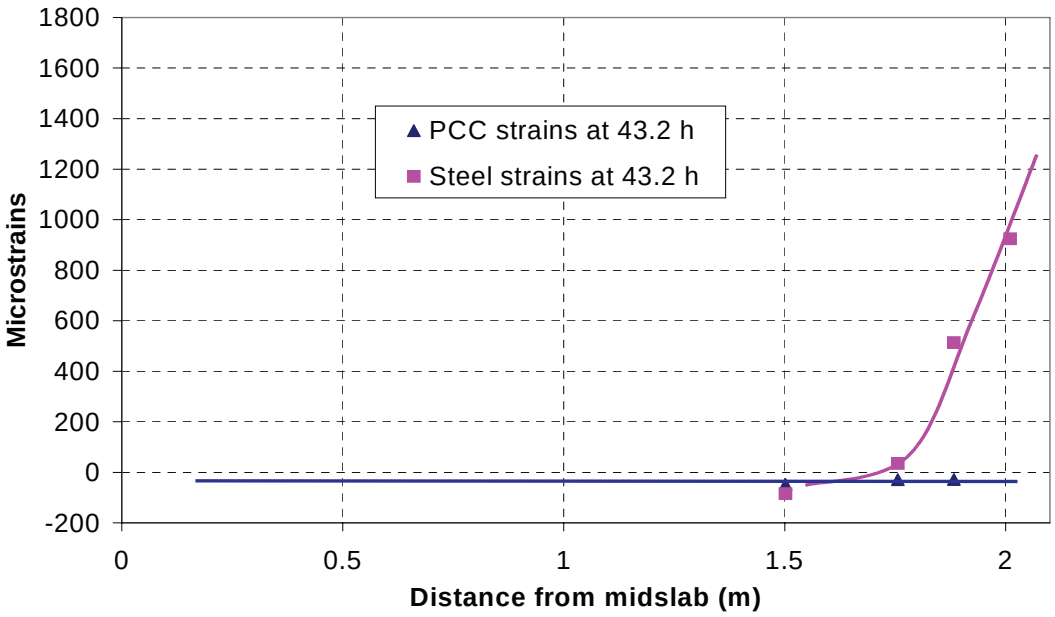

Figure 185. Strains in concrete and steel at 67.2 hours after construction.

D.2.2.2.4.3 Evaluation of Stress and Bond Development Length

A comparison of measured and predicted bond development lengths for this site is presented in figure 186. The bond development length predicted with HIPERPAV II for this site for the first 3 days of age varied from 0.48 to 0.66 m. A rather good prediction is observed on the bond development length for this site.

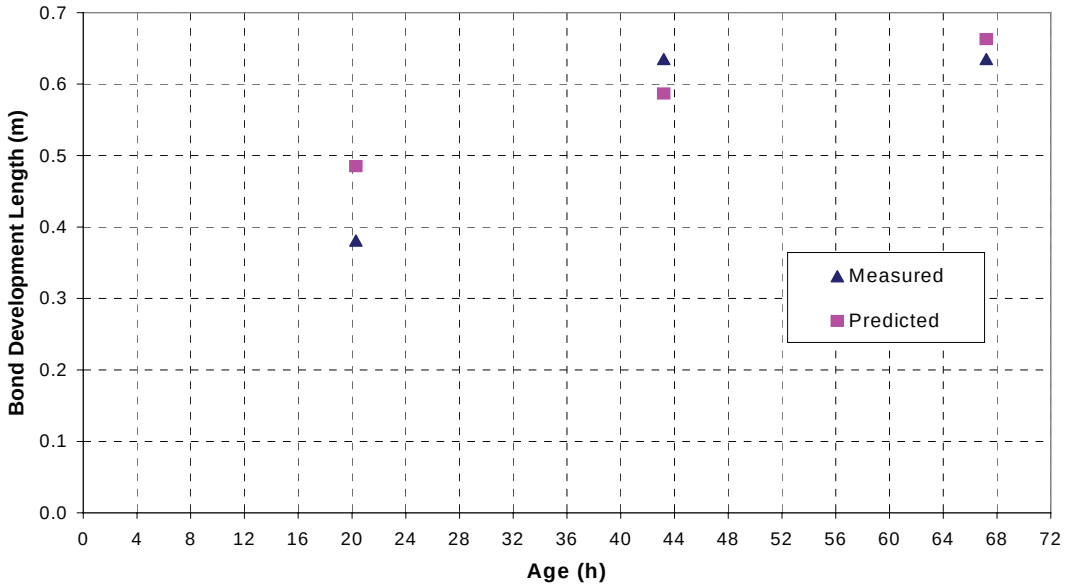

Figure 186. Comparison of measured and predicted bond development length.

From the strains measured, the steel stress is computed and is shown in figure 187 for the age of 67.2 hours.

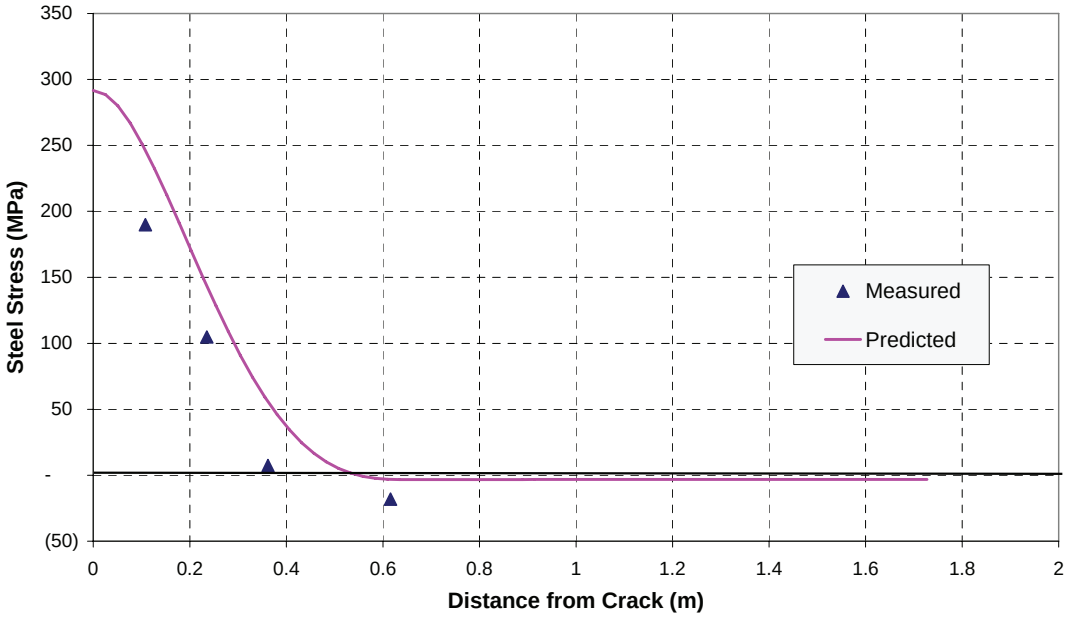

Figure 187. Steel stress along the slab at 67.2 hours.

In general, a rather good prediction of stresses at the steel were observed for this site.

D.2.2.2.4.4 Analysis of Crack Widths

Crack width data was evaluated as a function of pavement age and also as a function of pavement depth.

Table 89 shows the crack widths observed during the first 3 days after construction for the top, middle, and bottom of the slab.

Table 89. Comparison of average crack width predicted and measured values.

Age	Measured Top	Measured Middle	Predicted Middle
Day 1	–	0.002	0.018
Day 2	–	0.008	0.025
Day 3	0.010	0.008	0.029

A large discrepancy in measured and predicted crack width is observed. The predicted crack width is overpredicted by a factor of three compared to the average crack width measured at middepth.

Similar trends to the Fort Worth, TX site in terms of increasing crack widths with time also are observed for this site. Crack width measurements were obtained at the slab edge. The crack width at the steel location was not measured. It is believed that due to the steel restraint, the crack width near the steel is smaller than those reported here, therefore increasing the overprediction.

D.2.2.2.4.5 Crack Spacing Validation Results

Table 90 shows a comparison of measured versus predicted crack spacings for the first 3 days after construction. Although the measured crack spacings show a slight decreasing trend, the predicted crack spacing is constant for the early ages and is reduced to an average crack spacing of 1.25 m after 1 year. However, the average crack spacing predicted of 3.47 m matches very closely the measured average crack spacing of 3.08 m at 3 days of age. The predicted crack spacing at 1 year for this site is 1.25 m.

Table 90. Comparison of predicted and measured average crack spacings.

Age	Measured (m)	Predicted (m)
Day 1	5.33	3.47
Day 2	3.32	3.47
Day 3	3.08	3.47
1 year	–	1.25

The crack spacing distributions are presented in figure 188. Although a reasonably good fit for the crack spacings observed after 3 days is achieved, the predictions for earlier ages do not follow the measurements in the field. Inaccuracy to match earlier ages also was reported on the validation for the Fort Worth, TX, site.

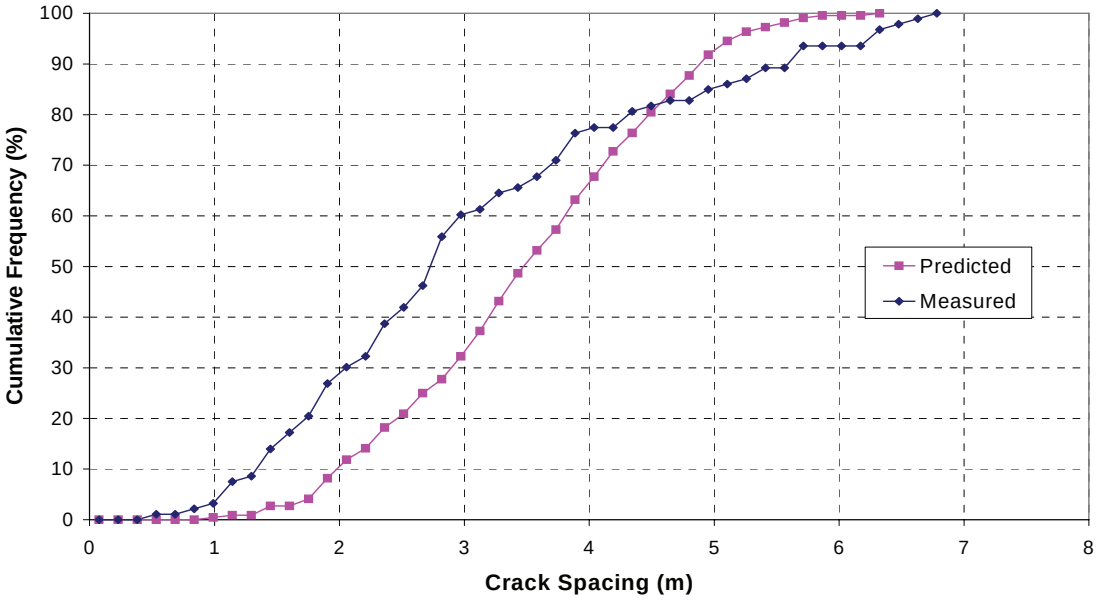

Figure 188. Measured versus predicted crack spacing at 3 days of age, Sioux Falls, SD.

D.3 VALIDATION OF GENERAL EARLY-AGE BEHAVIOR MODELS

Improvements to the concrete pavement temperature prediction, drying shrinkage, and creep-relaxation models were investigated in this study. Results of the validation efforts for this models are presented below.

D.3.1 Finite-Difference Temperature Prediction Model

Over the course of its development, HIPERPAV has employed two different temperature prediction models. Originally, the temperature prediction model was a transient two-dimensional FEM. However, this procedure had proven to require excessive solution times. The model has since been replaced by a one-dimensional finite-difference approach, which allows quicker execution without a compromise in accuracy. However, the accuracy of the finite-difference model needed to be verified by comparison with field data. Verification of the temperature predictions with the improved model is presented in appendix E.

D.3.2 Drying Shrinkage Prediction Model

D.3.2.1 Drying Shrinkage Calibration for JPCP Early-Age Predictions

Using the field data collected from the five early-age HIPERPAV I field sites, the calibration factor (D_{eff}) for the Bażant-Panula shrinkage model could be determined.[121] The vibrating wire strain gages placed at midslab 25 mm from the pavement surface and 152 mm from the edge, in the transverse direction, were used for the calibration. The restraint strains induced by the subbase would be small at this location, allowing the drying shrinkage strains to be modeled. Calibration results are presented below.

All of the slabs in field were cured with white curing compound (α_2 = 1.1), and the cement types varied between Type I and Type II (α_1 = 1 and 0.85). The coarse aggregate used at the sites had a relatively low CTE. In Minnesota, limestone and gravel were mixed. In Nebraska and Texas, limestone was used. In North Carolina, slate was used. In Arizona, a gravel basalt was used. The Baźant-Panula shrinkage model was developed for similar aggregate types to those found in the HIPERPAV I sites, so relatively good fits resulted. Fly ash content was not included in the mix components input to the model, since it does not greatly influence concrete shrinkage.[37]

The D_{eff} values determined for each site are listed in table 91. D_{eff} for Nebraska is 0.6; this is the highest value. The Nebraska mix was not typical; more sand/fine aggregate was used than coarse aggregate. Averaging all of the sites yields an average D_{eff} of 0.45 with a standard deviation of 0.09. A D_{eff} of 0.50 has also been reported by Persson, and it is used to account for specimen shape in HIPERPAV II drying shrinkage calculations.[36]

Table 91. Calibration of D_{eff} for the HIPERPAV I field sites.

Site Location	D_{eff} Without Fly Ash
Arizona	0.35
Minnesota	0.40
Nebraska	0.60
North Carolina	0.45
Texas	0.46

The fit of the Baźant-Panula shrinkage model to these five field sites is shown in the following plots (figures 189-193).

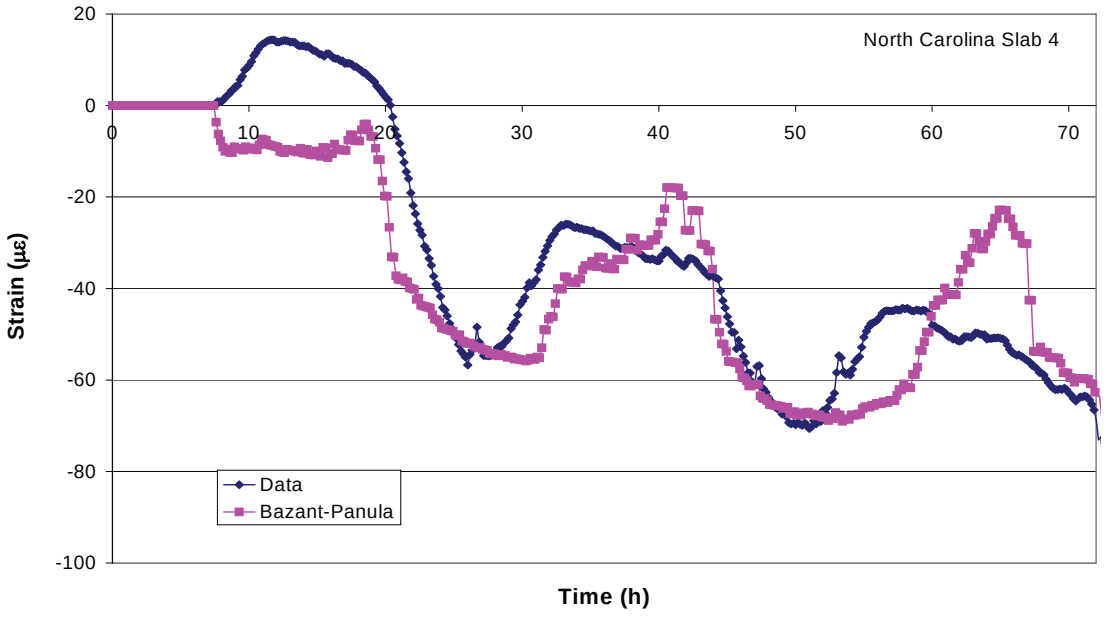

Figure 189. Drying shrinkage results for North Carolina site.

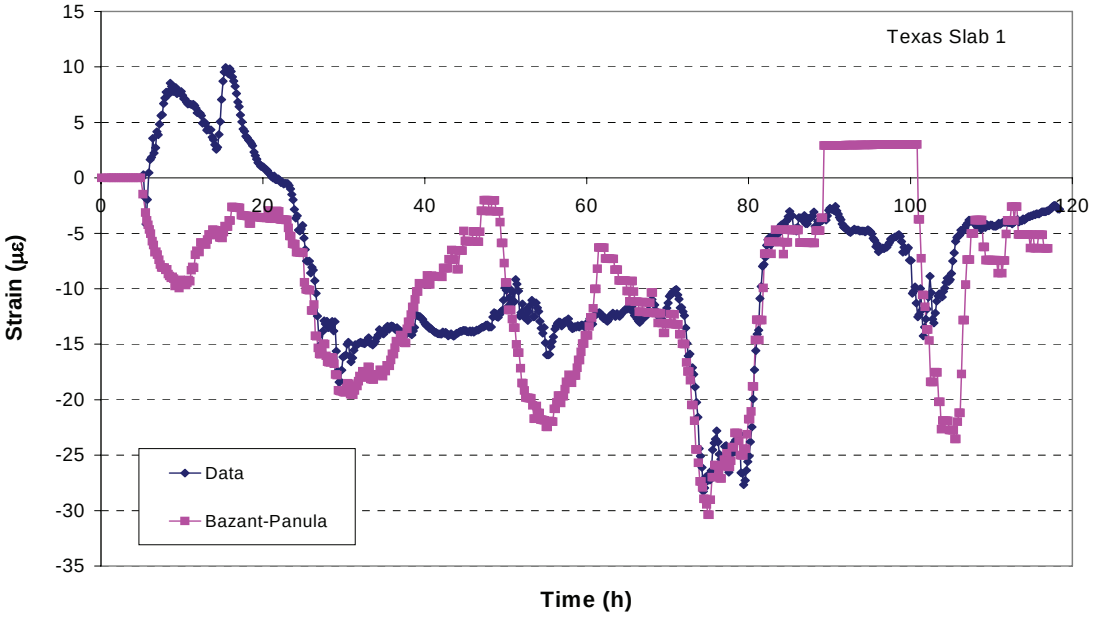

Figure 190. Drying shrinkage results for Texas site.

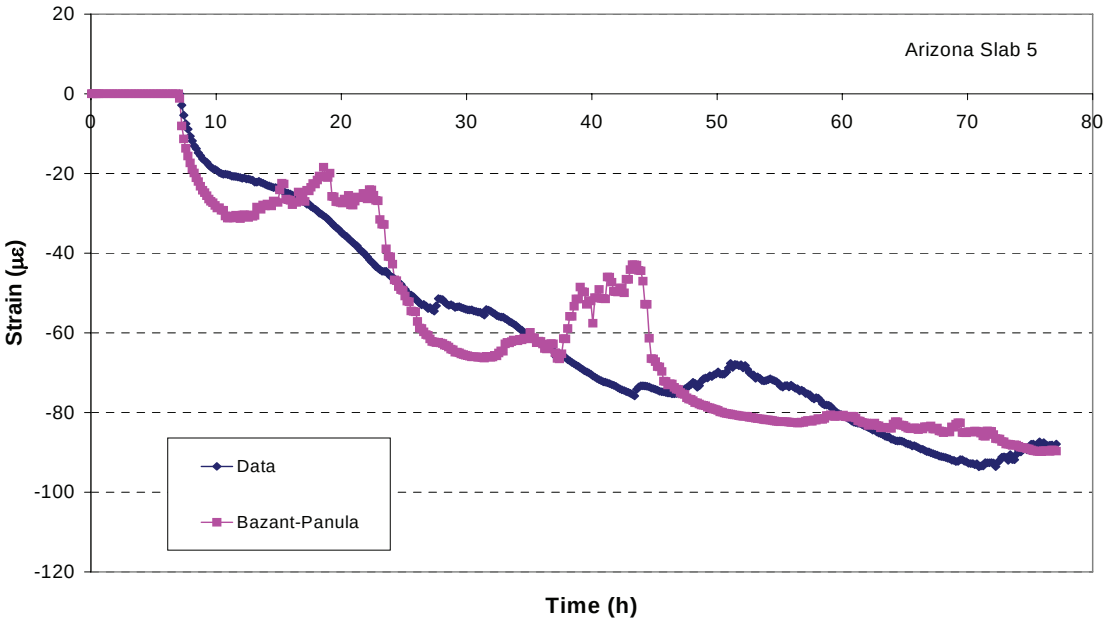

Figure 191. Drying shrinkage results for Arizona site.

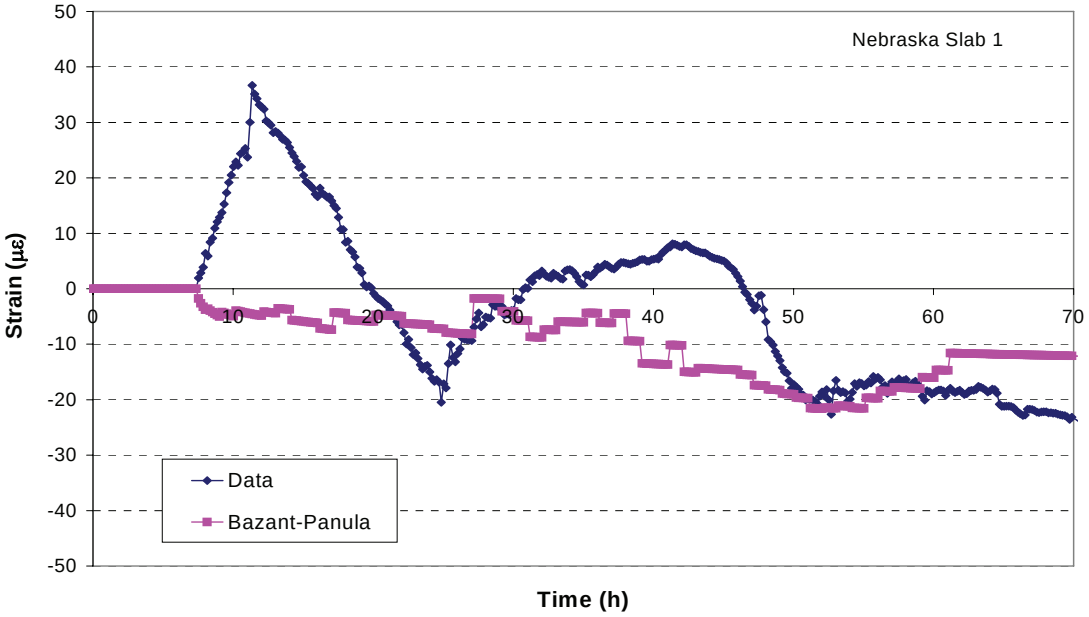

Figure 192. Drying shrinkage results for Nebraska site.

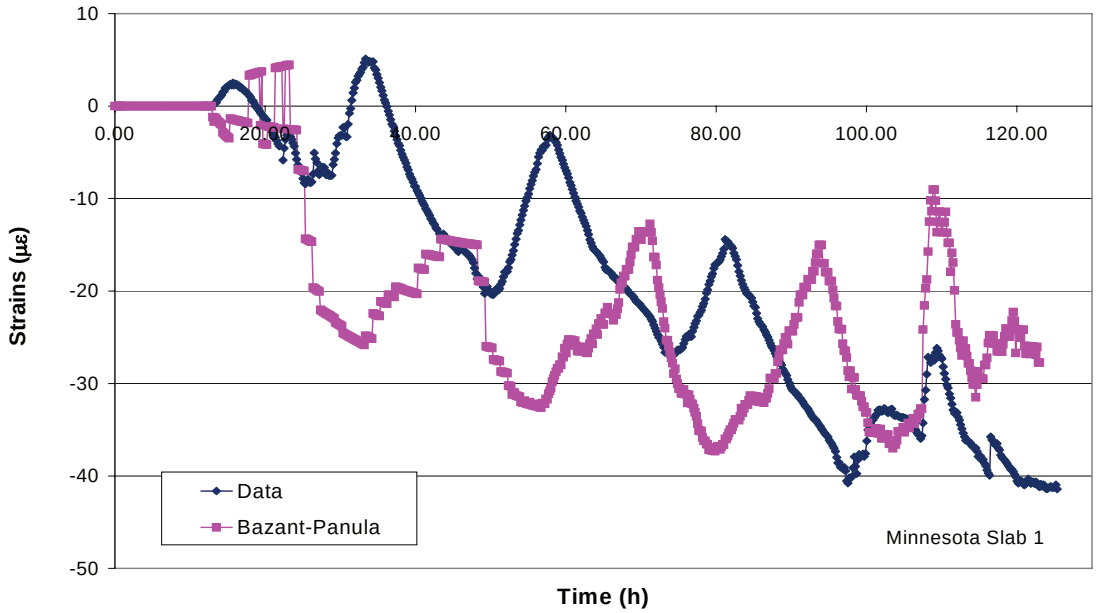

Figure 193. Drying shrinkage results for Minnesota site.

D.3.2.2 Drying Shrinkage Calibration for CRCP 28-Day Predictions

To calibrate the size factor D_{eff} for CRCP, 28-day drying shrinkage predictions from the Bażant-Panula model were matched to the experimentally measured drying shrinkage values taken in concrete placed on

SH–6 in winter and summer.[106] Limestone was the coarse aggregate. At 28 days, the drying shrinkage was 171 με in the summer and 165 με in the winter. These values were matched using an D_{eff} of 0.2. A comparison of drying shrinkage predictions at different ages are shown in figures 194 and 195 as a function of D_{eff}. The drying shrinkage measured for the Houston, TX, sections is presented in these figures with its corresponding calibration factor.

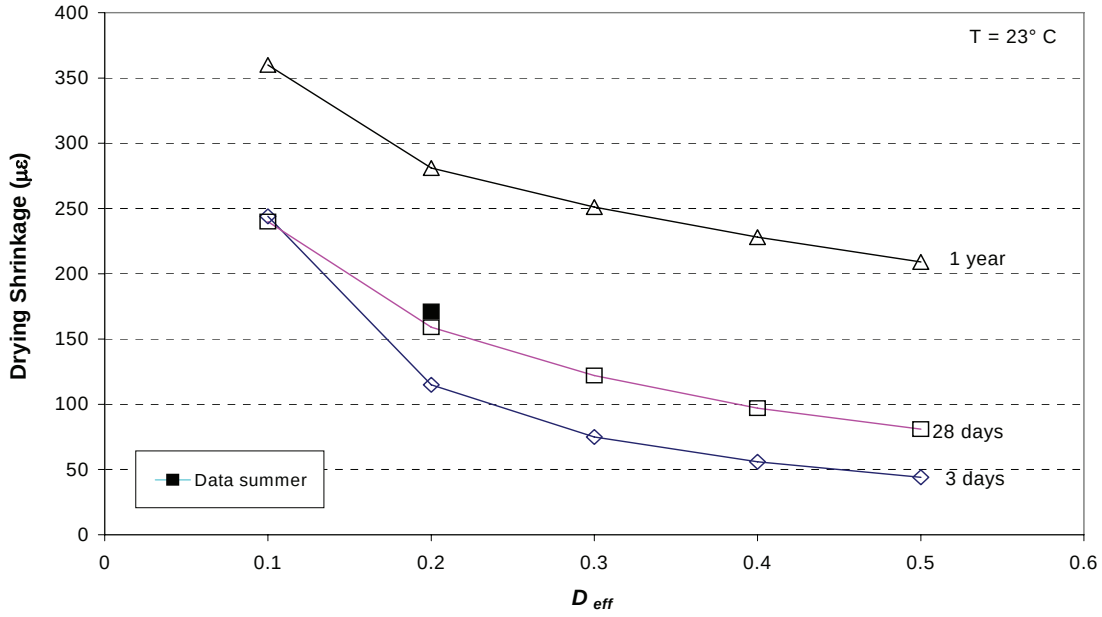

Figure 194. Calibration of drying shrinkage factor for Houston, TX, sections constructed in summer.

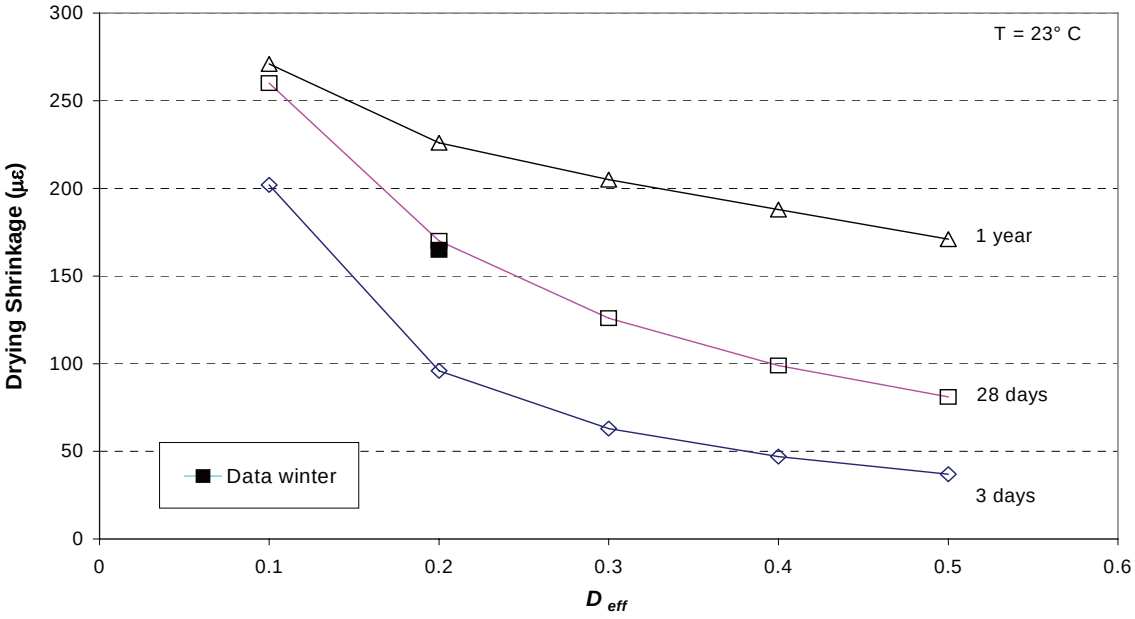

Figure 195. Calibration of drying shrinkage factor for Houston, TX, sections constructed in winter.

D.3.3 Relaxation-Creep Model

Attempts to validate the creep model based on the extended Triple Power Law presented in appendix B were made. However, preliminary sensitivity analyses showed that, in some instances, tensile stresses were being overpredicted significantly as compared to results from the previous validation efforts of the current prediction models in HIPERPAV II. Possible reasons for inaccuracy are:

- In this model, it is assumed that creep in compression is equivalent to creep in tension. Due to the cyclic stress state in the pavement between tension and compression, if this assumption does not hold true, it is possible that compressive stresses may be underpredicted while tensile stresses are overpredicted, or vice versa.
- In implementing creep compliance formulation, there are two possible approaches as outlined in appendix B: 1) with numerical integration; and 2) with the use of a Maxwell chain model for conversion of creep compliance into relaxation values. In this effort, both methods were explored. However, the required user intervention in the second method made it inappropriate for this effort. The first method was investigated further; however, the large matrix array required to store the stress history limited the minimum time step that could be implemented to 1 hour. It is believed that the large time step possibly contributed to the cause of the observed overpredictions of tensile stresses.

Further work is required to validate this method properly. It is believed that, after calibrated and validated, it will prove helpful in properly determining creep and relaxation effects for stress prediction, built-in curling prediction, and possibly determining the curled slab shape.

APPENDIX E FINITE-DIFFERENCE TEMPERATURE MODEL VALIDATION

The HIPERPAV II temperature model predicts the temperature development of concrete at early ages. The temperature development in the concrete structure is determined by the balance between heat generation in the concrete and heat exchange with the environment. This model includes the heat of hydration of the cementitious materials and the heat transfer mechanisms of thermal conduction, convection (including evaporative cooling), solar radiation, and irradiation. In section B.1.2, all the models and material properties necessary to predict the temperature distribution in the pavement structure were presented.

Over the course of its development, HIPERPAV has employed two different temperature prediction models. Originally, the temperature prediction model was a transient two-dimensional FEM. However, this procedure required excessive solution times. The model has since been replaced by a one-dimensional finite-difference approach, which allows quicker execution without a compromise in accuracy. However, the accuracy of the finite-difference model needs to be verified by comparison with field data.

The model was calibrated by comparing the predicted versus measured field temperatures. To validate the temperature model, the concrete temperatures measured in the field were compared to the concrete temperatures predicted with the temperature model. Early-age temperature data was collected from PCC paving applications located across the United States. Eighteen slabs were instrumented; nine of these were selected for calibration and nine for validation of the model. Table 92 provides a brief summary of the different sites, and it also indicates which slabs will be used for the model calibration and validation.

Table 92. Different construction sites and their use for calibration and validation.

Pavement Construction Site	Description	Calibration	Validation
Eden Prairie, MN, U.S. Highway 212	October 1998, 305-mm JPC	Slab 1 and 4	Slab 2 and 3
Tucson, AZ, I–10 Frontage	December 1998, 254-mm JCP	Slab 1, 3, and 6	Slab 4 and 5
Lufkin, TX, U.S. Highway 69	April 1999, 305-mm JCP	Slab 2 and 3	Slab 1 and 4
Surry County, NC, I–77	May 1999, 279-mm JPC	Slab 2 and 3	Slab 1 and 4
Fort Worth, TX, I–30/I–35	July 2001, 203-mm CRPC	–	Slab 1

E.1 FIELD INSTRUMENTATION SITES

Two separate mechanisms are considered to predict changes in pavement temperature: environmental effects and the PCC heat of hydration. Environmental conditions, including air temperature, solar radiation, windspeed, and relative humidity, were monitored by using a portable weather station. The heat of hydration over time of the cementitious materials was determined by adiabatic calorimeter testing. Concrete temperatures during the first 72 hours after concrete placement were measured with thermocouples installed at various depths: at 25 mm from the top, middepth, and 25 mm from the bottom of each slab. At some sites, concrete temperatures were recorded by free vibrating strain gauges located at the three depths described above.

Many parameters influence the development of concrete temperatures. During the field instrumentation, these parameters were measured or recorded in the field or obtained through laboratory tests, and these parameters are summarized in table 93. In addition to this information, the results of the cement heat of hydration tests and the properties used to model the boundary conditions and heat transfer for all the concrete mixes is listed in table 94.

Based on the data collected for these paving projects, the ranges of values covered during this calibration and validation effort are as follows:

- Pavement thickness: 200 to 305 mm.
- Subbase type: unbound granular, AC, and crushed concrete base.
- Cement type: I, IP, II, and I/II.
- Admixtures: 7 percent to 21 percent cement replacement with Class C fly ash and, 18 percent to 23 percent cement replacement with Class F fly ash.
- W/cm: 0.36 to 0.44 and w/c: 0.45 to 0.56.
- The air temperature during the instrumentation varied as follows: Minnesota 0.5 to 22 ºC, Arizona -1.1 to 23 ºC, Texas (Lufkin) 8 to 30 ºC, North Carolina 8 to 28 ºC, and Texas (Fort Worth) 25 to 37 ºC. In general, the paving conditions for Minnesota and Arizona were colder than for the rest of the States.
- Curing method: White liquid curing compound was used at most of the sites. However, due to cold weather conditions in Arizona, polyethylene sheets were used to retain concrete temperatures during the first and second days after placement.

E.2 MODEL CALIBRATION

The temperature model was calibrated by comparing the predicted versus measured concrete temperatures during the first 72 hours after placement. It was determined that some parameters had to be adjusted to calibrate the finite-difference model. After all the concrete temperatures from all the sites were evaluated against the predicted values, it is recommended that the following modifications be made to the temperature model:

- **Solar absorptivity constant:** The solar absorptivity of PCC is a function of the surface color, with typical values ranging from 0.5 to 0.6. An ideal white body would have a value of 0.0, and an ideal black body would have a value of 1.0. A solar absorptivity constant of 0.50 was found most appropriate for concrete pavements cured with white curing compound.
- **Heat transfer by convection/conduction:** The model outlined in section B.1.2.3 provides an accurate means to model the heat loss on the pavement surface. During the construction of the Arizona pavement, plastic sheets were used. Using the thickness of the plastic sheet and its thermal conductivity underestimated the amount of heat being retained by the pavement. However, when sheets are used, they are not in total contact with the slab, and the air void between the concrete and sheets act as additional insulation. An average air void thickness of 5 mm in addition to the plastic sheet provided an accurate account of the surface insulation for all the slabs where sheets were used. It is recommended that an additional air void thickness of 5 mm be used for all future cases where plastic sheets are used.
- **Heat transfer due to evaporative cooling:** When evaporation of the water from a surface occurs, the energy associated with the phase change is the latent heat of vaporization, which causes evaporative cooling. A preliminary model to account for heat transfer due to evaporative cooling was developed.[122] The use of the model depends on the interaction between curing, bleeding, and environmental conditions. These effects were noticeable only for some of the slabs in North Carolina. This is an area where further research is required to model the interaction between moisture movement, bleeding, concrete materials, curing compound effectiveness, and evaporation.

- **Solar radiation:** The amount of heat gain due to solar radiation varies with longitude, latitude, altitude, time of day, day of year, and the prevailing atmospheric conditions. Next to the heat of hydration, the flux due to solar radiation is the most important heat source to the pavement system and should be modeled. In HIPERPAV II, the environmental data for any location in the United States is generated based on averaged 30-year historical data obtained from a weighted average of nearby weather stations. It is recommended that the hourly values from this database be used for the temperature prediction. The maximum solar flux may be determined as the 99^{th} percentile of the 30-year average hourly global horizontal radiation.
- **Cloud cover:** During day times, cloud cover affects the intensity of the direct and diffuse solar radiation that reaches the pavement surface. During night times, the cloud cover also determines the amount of reradiation from surfaces, and affects the magnitude of the irradiation. To achieve accurate temperature predictions, the amount of cloud cover should be defined as accurately as possible by the user.
- **AE:** The AE determines the temperature sensitivity of the concrete's hydration process relative to that at the reference temperature. The AE model described in section B.1.1 is recommended for use.
- **Ultimate degree of hydration:** Complete hydration of all the cementitious materials is seldom attained in actual concrete structures. This depends on the amount of space available for the hydration products, and also on the need for sufficient free mix water, which ensures continued hydration.[123,124] The model described in section B.1.1 is recommended to determine the ultimate degree of hydration for saturated concrete.

Table 93. Summary of variables collected during instrumentation of some HIPERPAV field sites.[121]

	Variable Description	Arizona**					Minnesota**				North Carolina**				Lufkin, Texas**				Fort Worth, Texas***
General	Transverse joint spacing (m)	4.57					4.57				Variable from 4.88 to 6.71 m				4.57				None
	Pavement thickness (mm)	254					305				279				305				200
	Subbase type	HMA base					Granular				HMA leveling course				HMA base				HMA base
Concrete Mixture Proportions	Cement type	II					I/II				I/II				I/II				IP
	Aggregate type	River gravel					19 mm - Natural gravel 19 mm + Crushed limestone				Phyllite				Crushed limestone				Crushed limestone
	Cement content (kg/m³)	285					267				250				247				248
	Cementitious materials (kg/m³)	Fly ash Class F					Fly ash Class C				Fly ash Class F				Fly ash Class F				Fly ash Class C
	Cementitious materials content (kg/m³)	61					71				75				67				61
	Cementitious materials replacement	18%					21%				23%				21%				20%
	Water content (kg/m³)	128					122				141				113				136
	Coarse aggregate content (kg/m³)	1102					(19 mm +) 544 (19 mm -) 559				1149				1143				1,217
	Fine aggregate content (kg/m³)	802					776				836				588				670
	Chemical admixtures:	Water reducer-air entrainer					Water reducer-air entrainer				Water reducer-air entrainer				Water reducer-air entrainer				Water reducer-air entrainer
	Water reducer (ml/m³)	889.6					1,315				1,060				595.7				1083
	Air entrainer (ml/m³)	0-1482 (as needed)					213				106				139.2				108.3
	w/c	0.45					0.46				0.56				0.46				0.55
	w/cm	0.37					0.36				0.43				0.36				0.44
Construction	Slab number	1	3	4	5	6	1	2	3	4	1	2	3	4	1	2	3	4	1
	Curing method	Curing compound and plastic sheet					Curing compound				Curing compound				Curing compound				Curing compound
	Construction date	12/3	8 Dec 1998		11 Dec 1998		7 Oct 1998		14 Oct 1998		19 May 1999		22 May 1999		31 March		6 April 1999		7 July 2001
	Time of day of construction (hh:mm)	9:20	10:25	15:00	9:50	13:35	9:05	13:08	9:05	10:25	12:00	14:05	10:20	12:30	8:35	9:30	8:10	11:30	10:40
	Saw cutting time after placement (hh:mm)	16:40	23:10	21:30	26:25	26:35	20:00	17:30	18:00	17:30	7:00	6:55	8:40	9:30	14:15	12:50	12:30	9:50	-
	Initial concrete mix temperature (ºC)	17.2	13.3	17.2	12.8	16.7	13.9	15.0	10.0	11.1	27.8	28.9	27.2	27.2	20.6	20.0	22.2	26.7	32.2
	Initial subbase temperature (ºC)	15.6	11.7	15.6	8.9	11.7	15.5	14.4	11.1	11.7	30.6	28.9	25.6	26.1	18.3	18.3	18.3	22.8	36.1
	Measured pavement thickness (mm)	248	260	254	267	273	308	305	308	302	276	274	284	281	305	305	305	305	205
	Measured slab length (m)	4.6	4.7	4.6	4.6	4.6	4.5	4.5	4.5	4.6	6.4	6.8	5.2	5.2	4.5	4.5	4.3	4.5	-
Environment	Air temperature range (ºC)	-1.1-23					0.5-22				8-28				8-30				25-37
	Air temperature at placement (ºC)	7.8	5.6	12.8	7.8	13.9	8.9	11.1	3.9	5.6	16.1	22.2	12.2	22.2	13.9	15.6	9.4	8.3	30.5
	Relative humidity (%)	15-99					29-100				28-99				30-100				30-67
	Windspeed (kph)	0-52.29					0-25.7				0-24				0-27				0-9
	Overcast conditions at placement *	S	S	S	S	S	S	PC	PC	PC	S	S	C	OC	OC	OC	S	S	Sunny and hot

Notes: * S – Sunny, PC – Partly Cloudy, C – Cloudy, OC – Overcast ** - Collected under HIPERPAV I validation *** - Collected under HIPERPAV II validation

Table 94. Summary of hydration parameters for all the field sites.

Parameter [a]	Arizona	Minnesota	North Carolina	Fort Worth, TX	Lufkin, TX
Hydration parameters, λ_1	1.0	1.0	1.0	1.0	1.0
Hydration parameters, t_1 (h)	11.21	9.32	16.93	16.47	9.57
Hydration parameters, k_1	2.029	1.694	1.188	0.783	1.909
Total heat of hydration, H_u (J/g)	388	438	390	415	416
AE, E (J/mol)	27,910	40,004	35,350	39,260	37,995
Ultimate degree of hydration	0.75	0.70	1.00	1.00	0.65

[a] Hydration parameters were determined by adiabatic calorimeter tests

The measured temperatures and the predicted temperatures for all the calibration sites are presented in figures 196 to 231 in section E.5. The goodness of the temperature prediction was calculated in terms of the coefficient of determination (r^2 value). The calculation of the r^2 value was also performed to the 45º line (measured versus predicted temperature). Two r^2 values were computed for each instrumented section:

- An average r^2 value obtained after comparing the temperatures at 25 mm from the top, middepth, and 25 mm from the bottom of each slab.
- An r^2 value obtained after comparing the measured versus predicted temperature differential.

The r^2 values obtained for the calibration sites are summarized in table 95. The average r^2 values ranged between 0.750 and 0.866. The r^2 values obtained for the temperature gradient ranged between 0.539 and 0.909. The low r^2 values were obtained for the JCP section instrumented in Texas. From the r^2 values obtained during this analysis, it may be concluded that the modified finite-difference model incorporated in HIPERPAV II is calibrated sufficiently. The model should be validated to determine the accuracy of the temperature prediction for PCC paving applications.

Table 95. Summary of r^2 values obtained during the calibration of the temperature model.

Instrumented Site		Figure Numbers	Coefficient of Determination (r^2)	
State	Slab Number		r^2 for Temperature	r^2 for Temperature Gradient
Minnesota	1	196–199	0.854	0.890
	4	200–203	0.801	0.820
Arizona	1	204–207	0.852	0.794
	3	208–211	0.750	0.844
	6	212–215	0.853	0.821
Lufkin, TX	2	216–219	0.866	0.539
	3	220–223	0.844	0.654
North Carolina	2	224–227	0.858	0.909
	3	228–231	0.825	0.840

E.3 MODEL VALIDATION

The measured versus predicted temperatures were compared as outlined in the previous section. The measured temperatures and the predicted temperatures for all the validation sites are presented in figures 232 to 267 in section E.6. The goodness of the temperature prediction was calculated in terms of the two r^2 values documented in the calibration section. The r^2 values obtained for the validation sites are summarized in table 96. The average r^2 values ranged between 0.803 and 0.903. The r^2 values obtained for the temperature gradient ranged between 0.470 and 0.924. As was the case for the model calibration, the lowest r^2 values were obtained for the JCP section instrumented in Texas.

From the r^2 values obtained during this analysis, it may be concluded that the finite-difference model included in HIPERPAV II provides an accurate prediction of early-age concrete temperatures for PCC paving applications.

Table 96. Summary of r^2 values obtained during the validation of the temperature model.

Instrumented Site		Figure Numbers	Coefficient of Determination (r^2)	
State	Slab Number		Temperature	Temperature Gradient
Minnesota	2	232–235	0.815	0.848
	3	236–239	0.814	0.766
Arizona	4	240–243	0.820	0.788
	5	244–247	0.879	0.865
Lufkin, TX	1	248–251	0.864	0.470
	4	252–255	0.803	0.641
North Carolina	1	256–259	0.873	0.801
	4	260–263	0.903	0.924
Fort Worth, TX	1	264–267	0.859	0.748

E.4 SUMMARY AND RECOMMENDATIONS

The early-age temperature development of concrete can be estimated from knowledge of cement composition, cement factor, admixtures, thermal characteristics of the concrete, slab thickness, and the environmental conditions that occur during paving and curing. Based on the calibration of the temperature model, recommendations were made to adjust/modify some models. These include modifications to the solar absorptivity constant, heat transfer by convection when plastic sheet are used, heat transfer due to evaporative cooling, the maximum solar radiation intensity, AE, and the ultimate degree of hydration. Major findings from this investigation are as follows:

- Adiabatic calorimeter tests provide a means of characterizing concrete hydration with time. With the parameters determined through these tests, the temperature prediction model can account for the effects that different mixture proportions and constituents have on the heat of hydration of concrete.
- Heat transfer due to evaporative cooling may significantly reduce temperatures in hydrating concrete. A model to account for this effect has been developed, and it is recommended that this model be further developed to account for actual construction practices. Modeling of the moisture condition in the hardened cement paste will be beneficial for this purpose.
- From the high r^2 values shown in tables 95 and 96, and the temperature predictions shown in sections E.5 and E.6, it may be concluded that the finite-difference model is able to produce good predictions of the early-age concrete temperatures development in concrete paving applications.

.

E.5 TEMPERATURE PREDICTION RESULTS OBTAINED DURING CALIBRATION

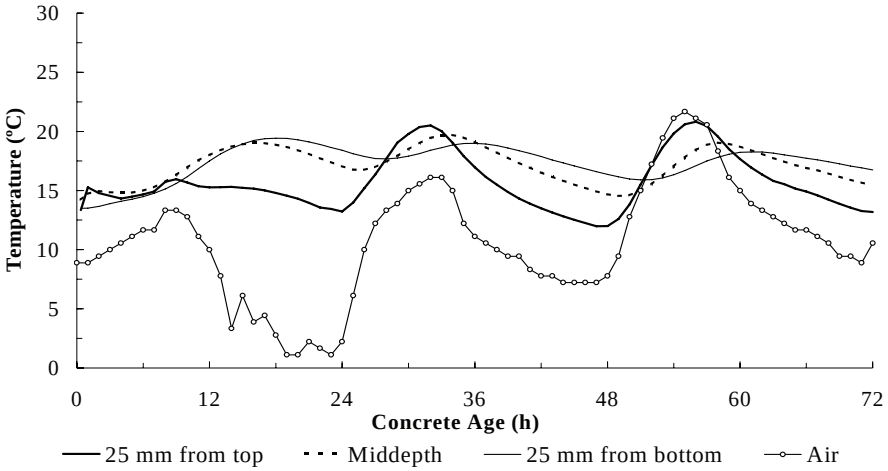

Figure 196. Measured concrete and air temperatures for Minnesota, Slab 1.

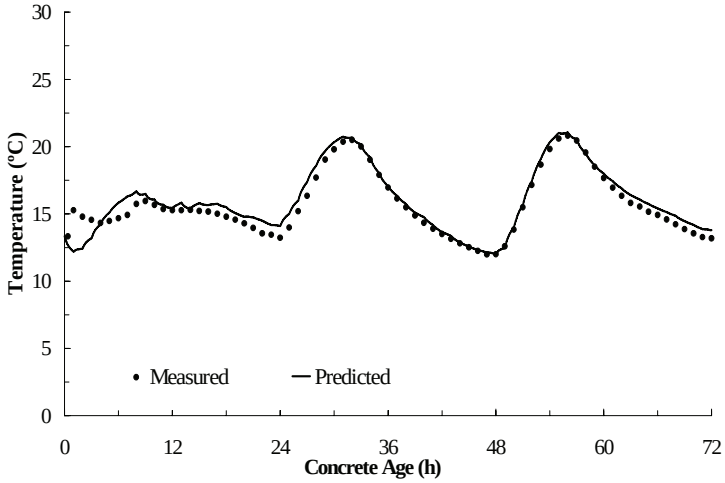

Figure 197. Measured versus predicted temperatures 25 mm from top of slab for Minnesota, Slab 1.

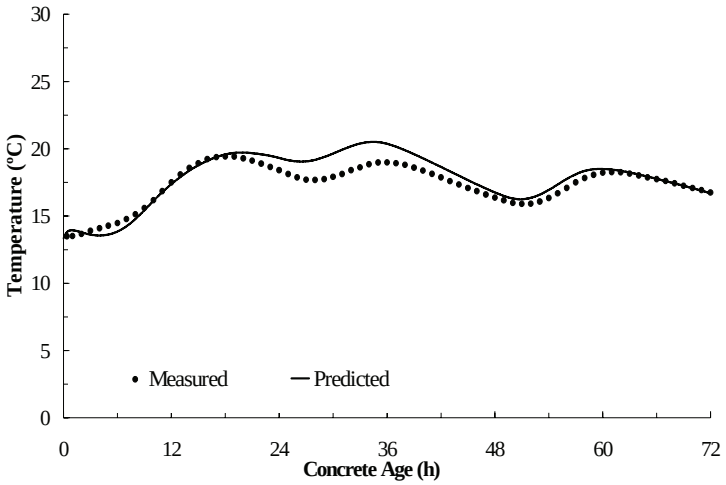

Figure 198. Measured versus predicted temperatures 25 mm from bottom of slab for Minnesota, Slab 1.

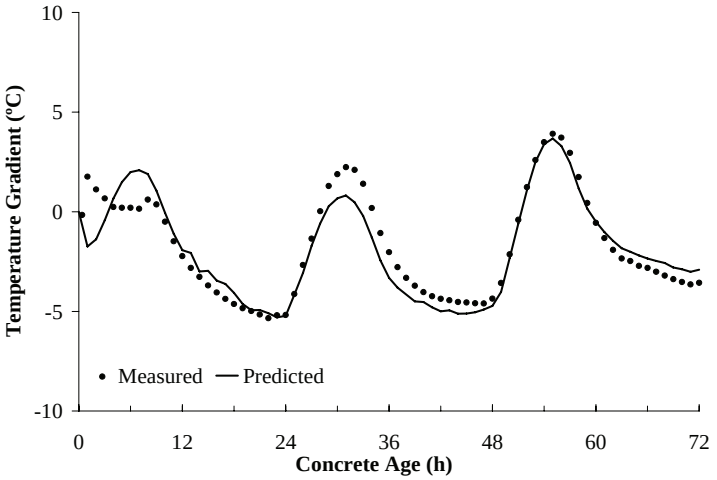

Figure 199. Measured versus predicted temperature gradient for Minnesota, Slab 1.

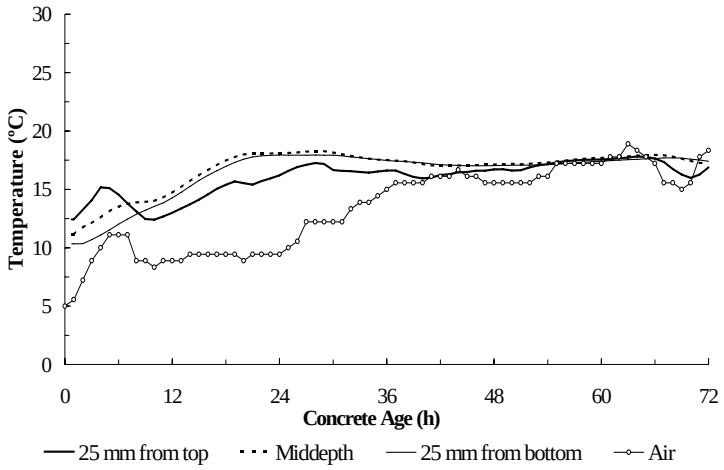

Figure 200. Measured concrete and air temperatures for Minnesota, Slab 4.

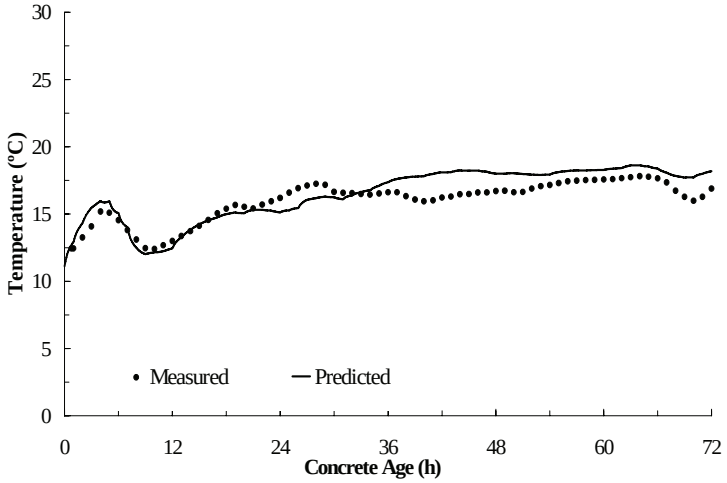

Figure 201. Measured versus predicted temperatures 25 mm from top of slab for Minnesota, Slab 4.

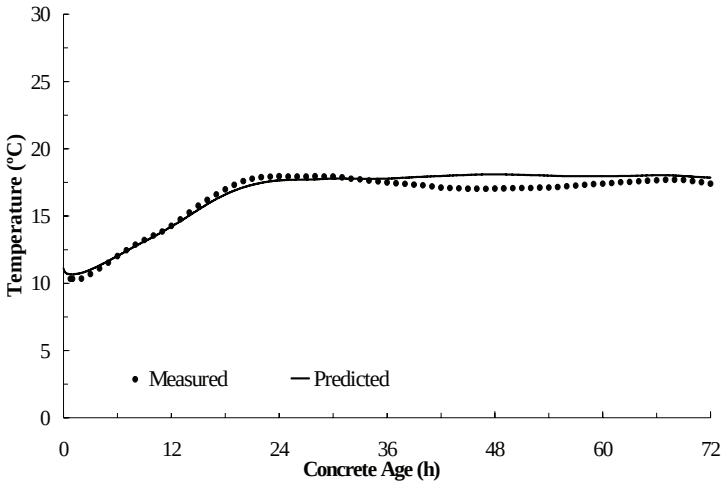

Figure 202. Measured versus predicted temperatures 25 mm from bottom of slab for Minnesota, Slab 4.

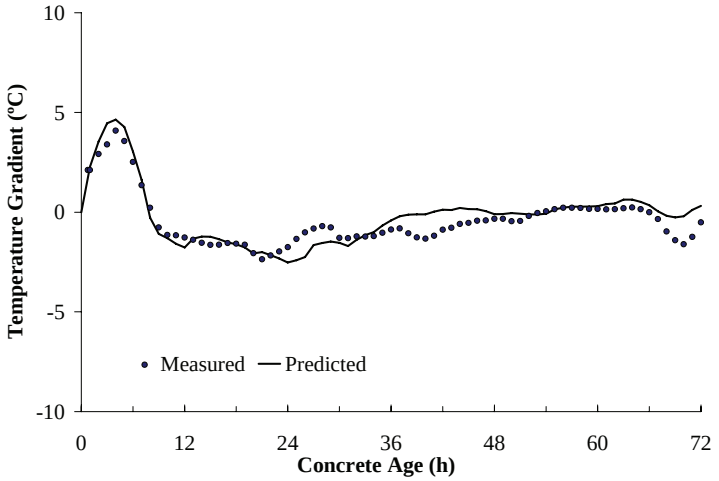

Figure 203. Measured versus predicted temperature gradient for Minnesota, Slab 4.

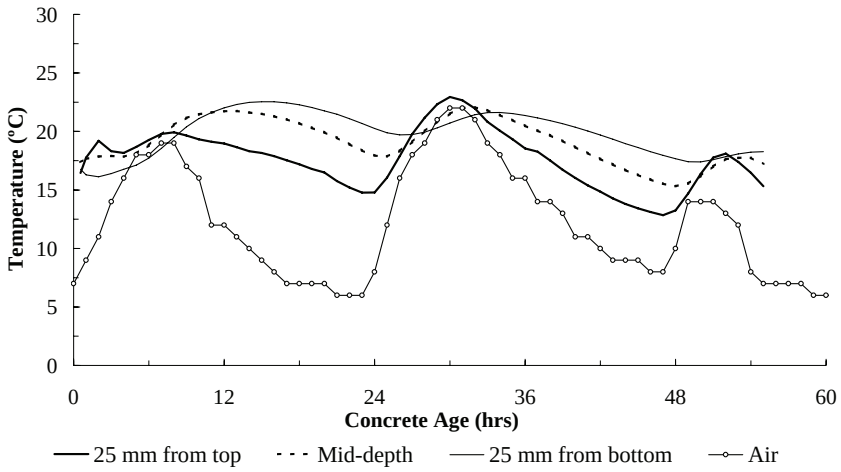

Figure 204. Measured concrete and air temperatures for Arizona, Slab 1.

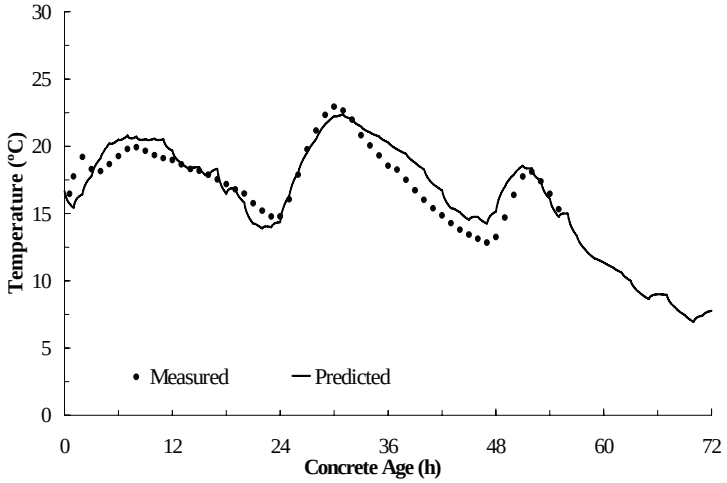

Figure 205. Measured versus predicted temperatures 25 mm from top of slab for Arizona, Slab 1.

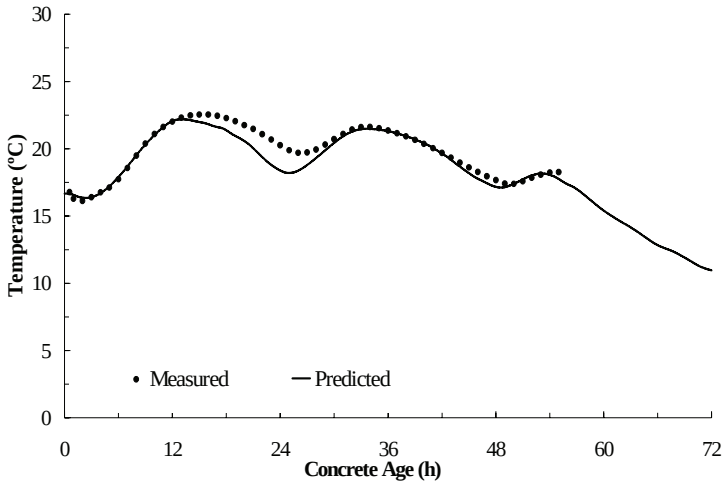

Figure 206. Measured versus predicted temperatures 25 mm from bottom of slab for Arizona, Slab 1.

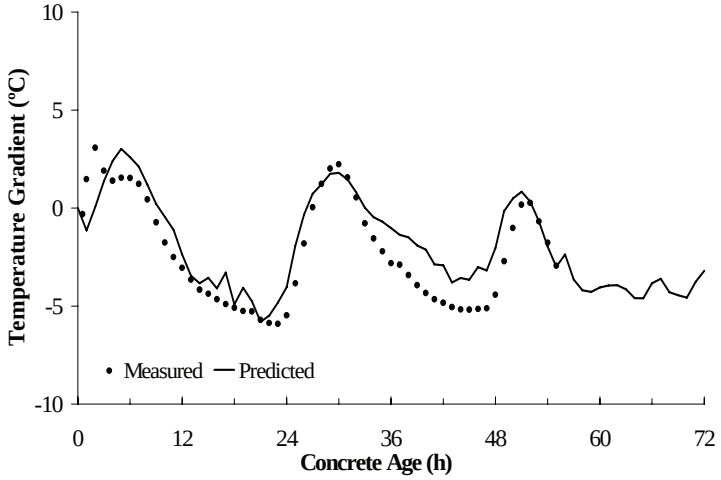

Figure 207. Measured versus predicted temperature gradient for Arizona, Slab 1.

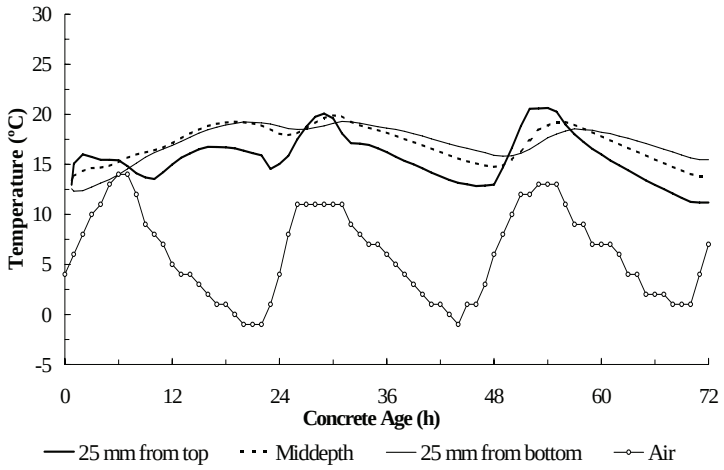

Figure 208. Measured concrete and air temperatures for Arizona, Slab 3.

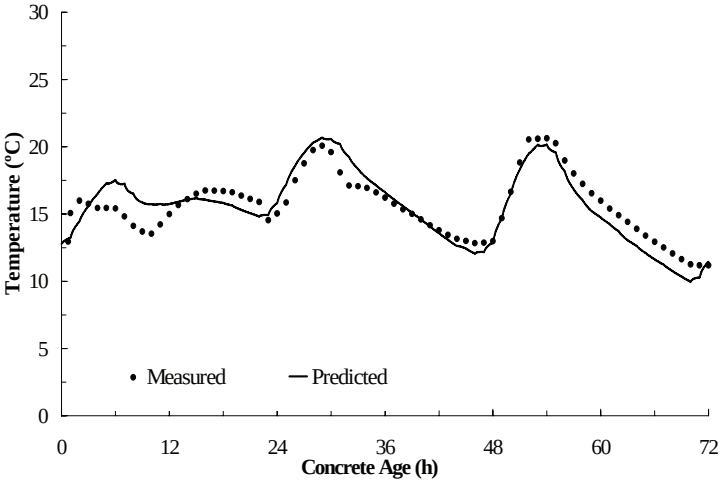

Figure 209. Measured versus predicted temperatures 25 mm from top of slab for Arizona, Slab 3.

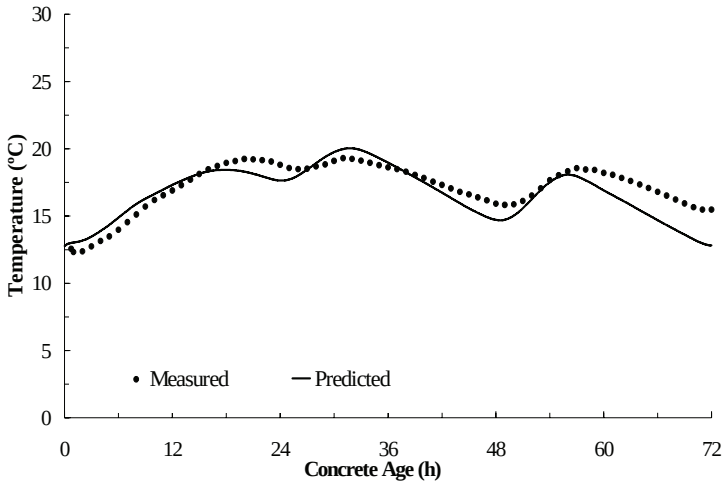

Figure 210. Measured versus predicted temperatures 25 mm from bottom of slab for Arizona, Slab 3.

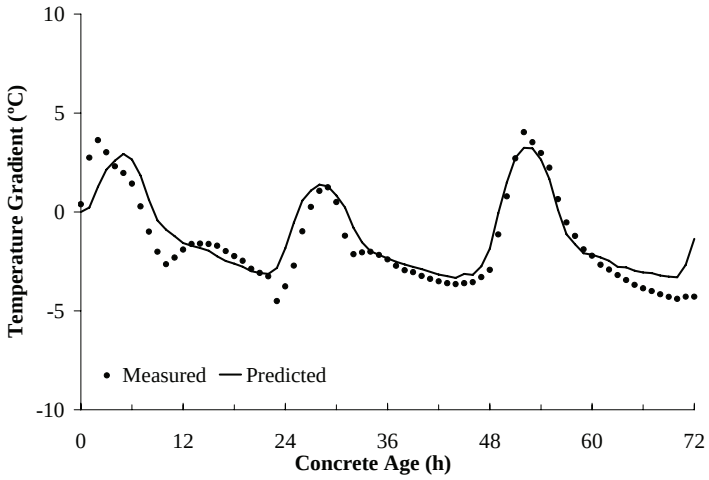

Figure 211. Measured versus predicted temperature gradient for Arizona, Slab 3.

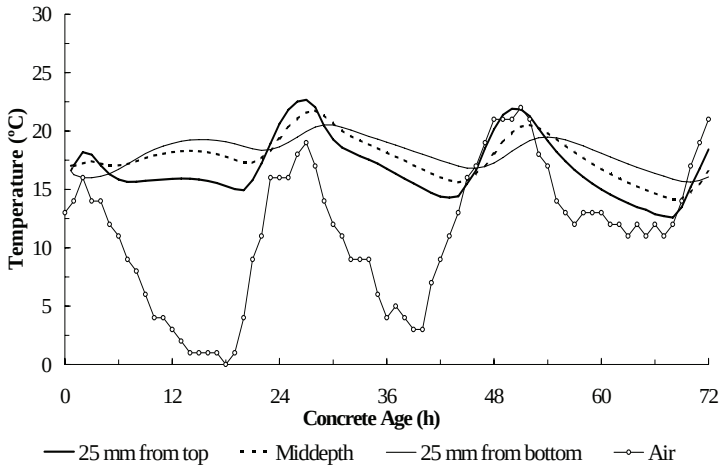

Figure 212. Measured concrete and air temperatures for Arizona, Slab 6.

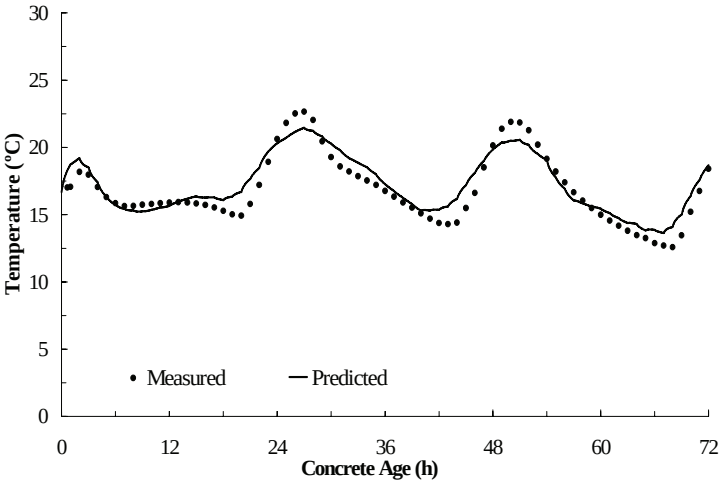

Figure 213. Measured versus predicted temperatures 25 mm from top of slab for Arizona, Slab 6.

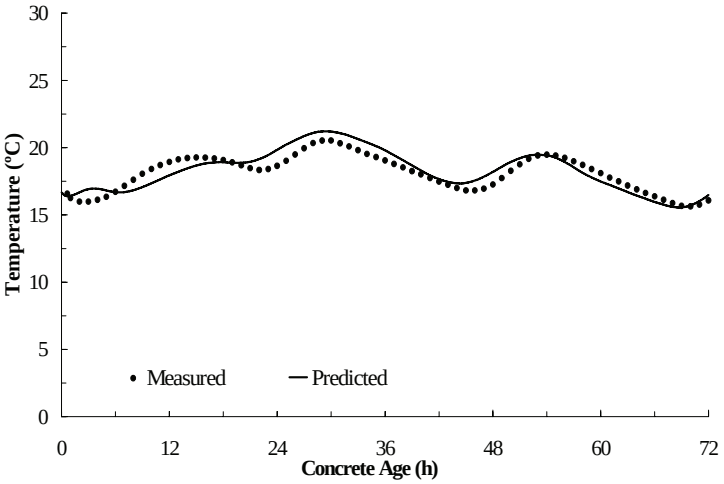

Figure 214. Measured versus predicted temperatures 25 mm from bottom of slab for Arizona, Slab 6.

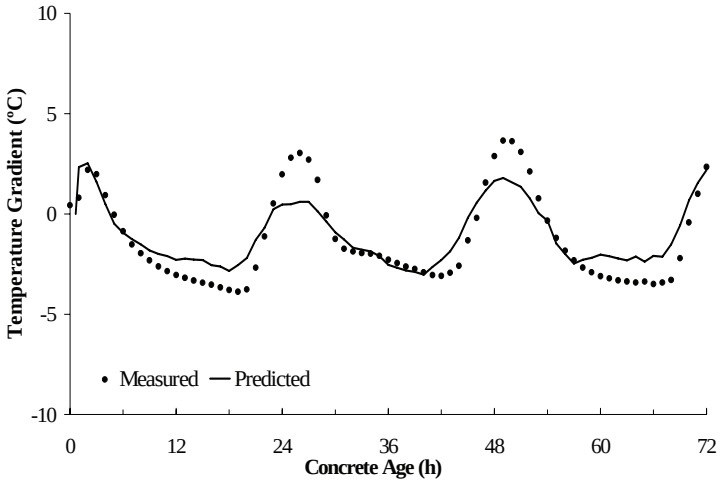

Figure 215. Measured versus predicted temperature gradient for Arizona, Slab 6.

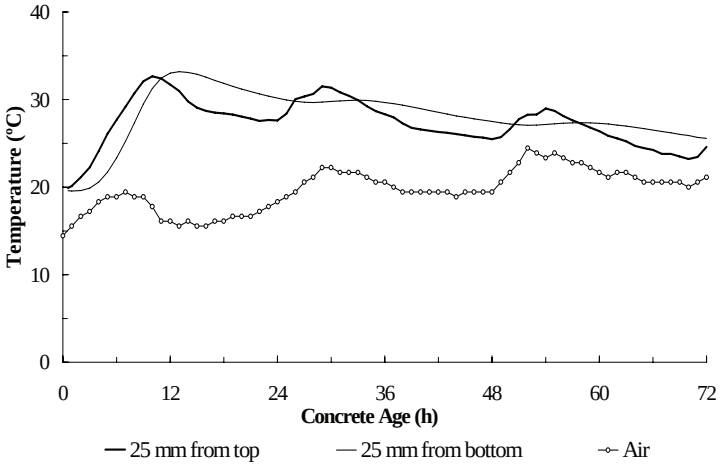

Figure 216. Measured concrete and air temperatures for Lufkin, TX, Slab 2.

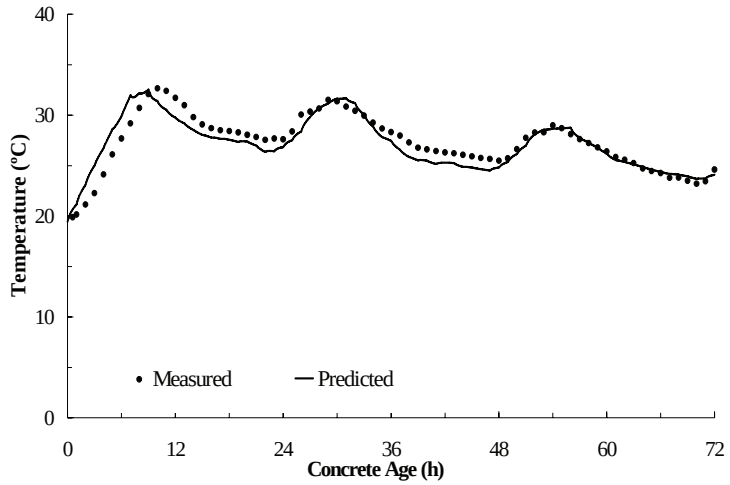

Figure 217. Measured versus predicted temperatures 25 mm from top of slab for Lufkin, TX, Slab 2.

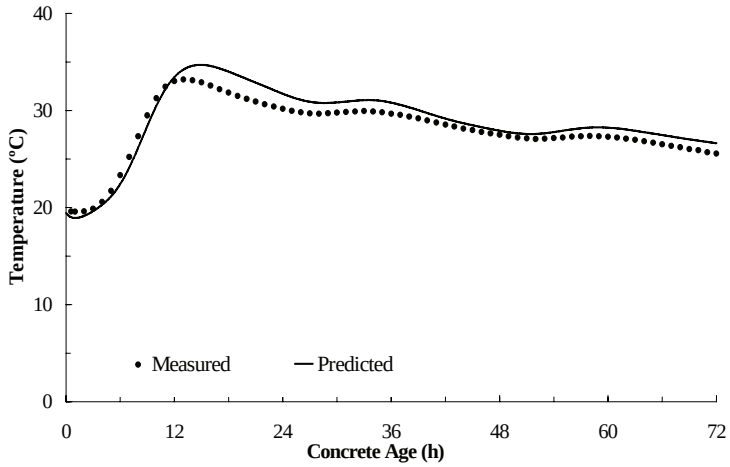

Figure 218. Measured versus predicted temperatures 25 mm from bottom of slab for Lufkin, TX, Slab 2.

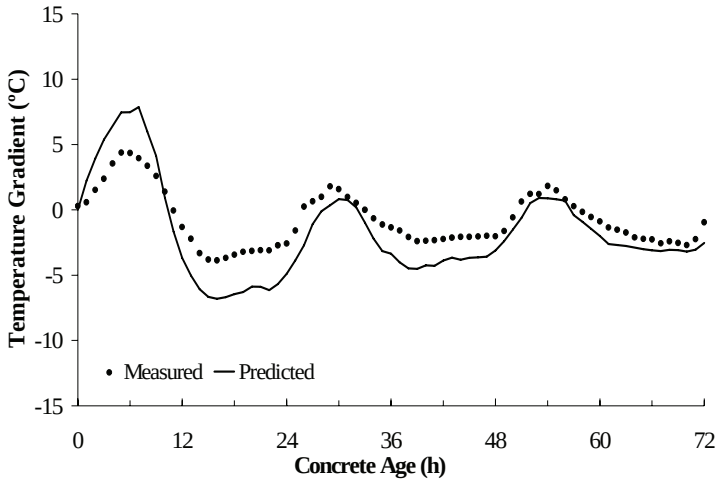

Figure 219. Measured versus predicted temperature gradient for Lufkin, TX, Slab 2.

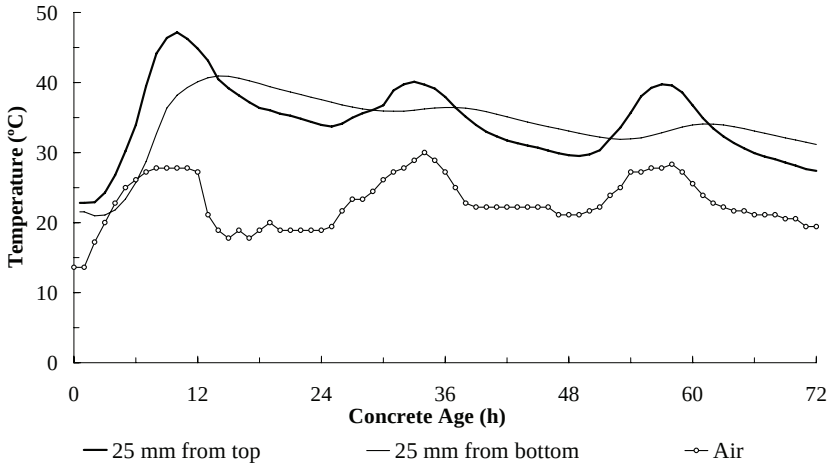

Figure 220. Measured concrete and air temperatures for Lufkin, TX, Slab 3.

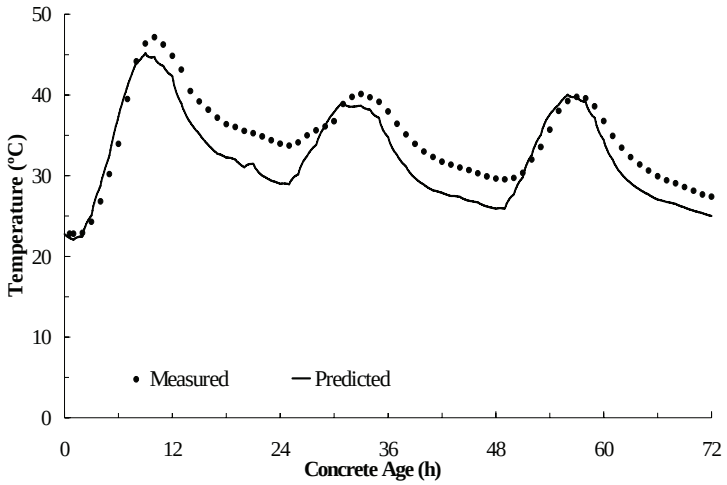

Figure 221. Measured versus predicted temperatures 25 mm from top of slab for Lufkin, TX, Slab 3.

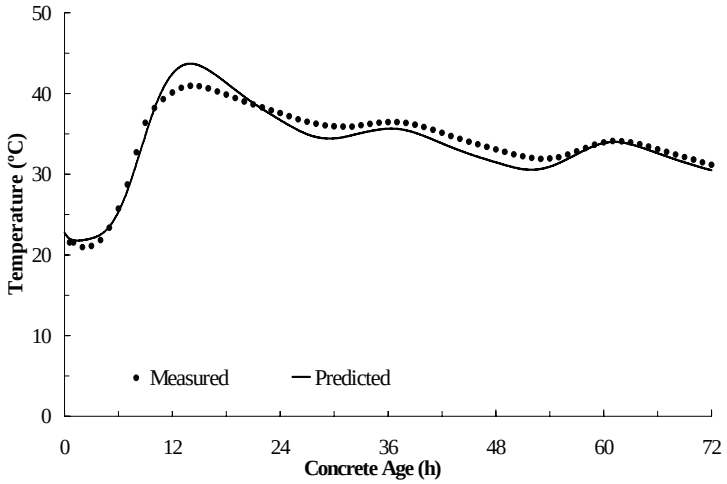

Figure 222. Measured versus predicted temperatures 25 mm from bottom of slab for Lufkin, TX, Slab 3.

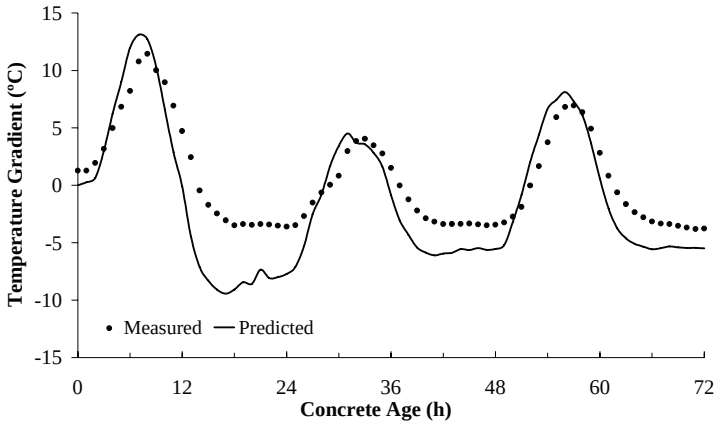

Figure 223. Measured versus predicted temperature gradient for Lufkin, TX, Slab 3.

Figure 224. Measured concrete and air temperatures for North Carolina, Slab 2.

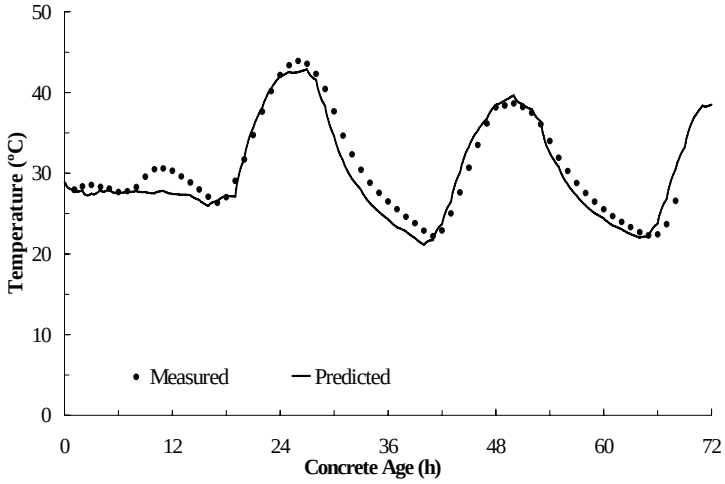

Figure 225. Measured versus predicted temperatures 25 mm from top of slab for North Carolina, Slab 2.

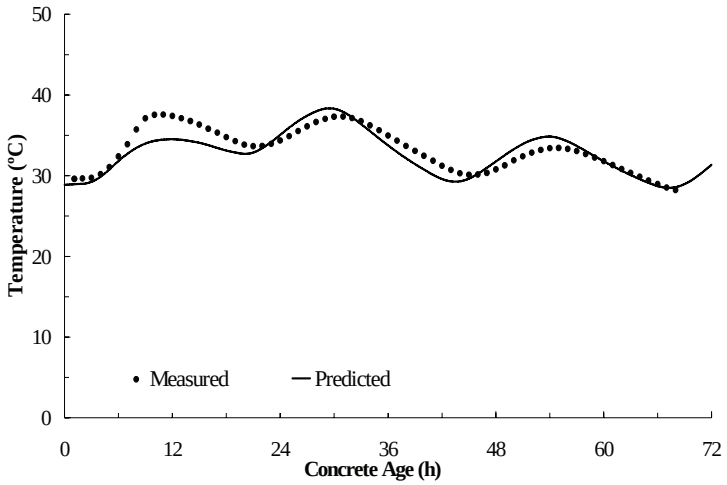

Figure 226. Measured versus predicted temperatures 25 mm from bottom of slab for North Carolina, Slab 2.

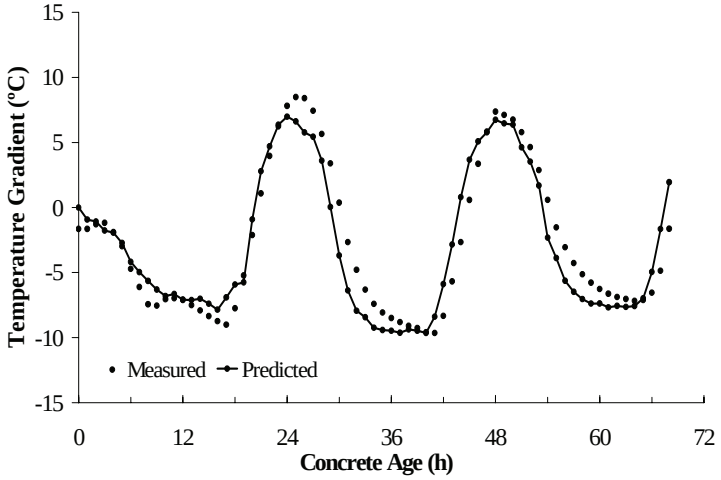

Figure 227. Measured versus predicted temperature gradient for North Carolina, Slab 2.

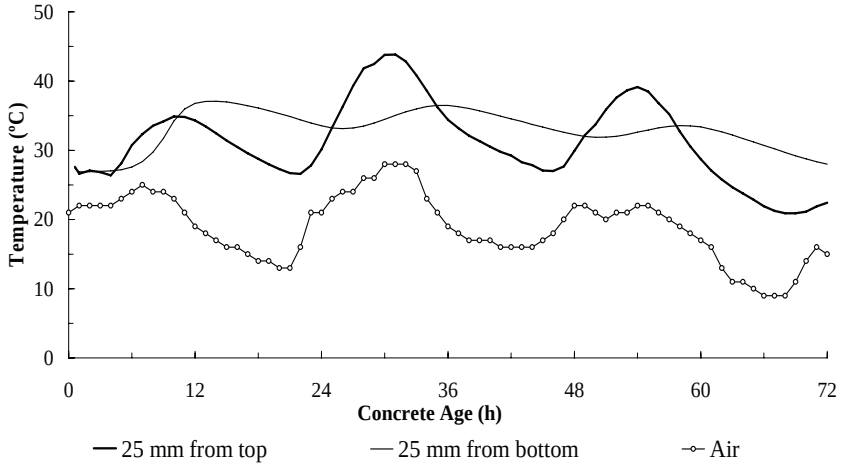

Figure 228. Measured concrete and air temperatures for North Carolina, Slab 3.

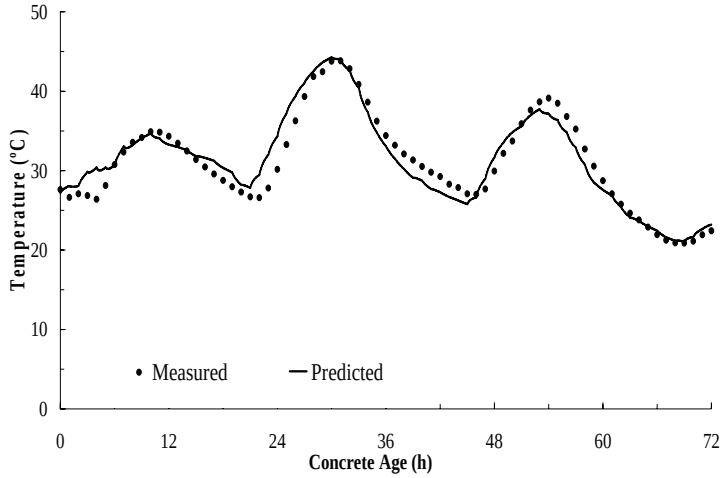

Figure 229. Measured versus predicted temperatures 25 mm from top of slab for North Carolina, Slab 3.

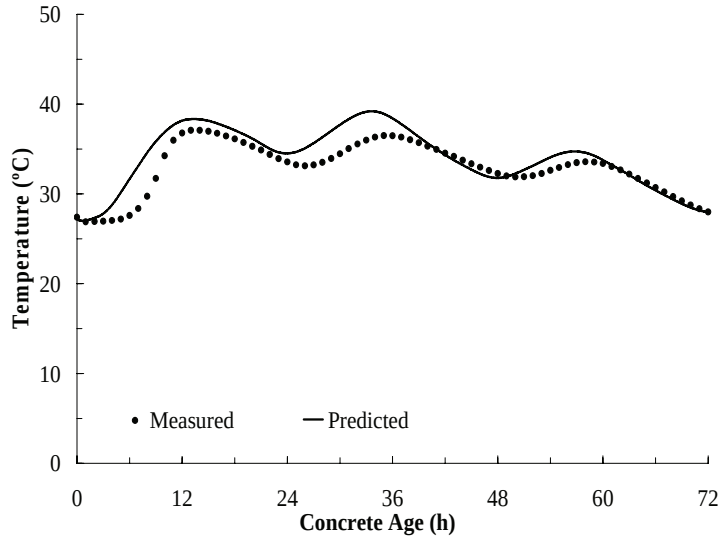

Figure 230. Measured versus predicted temperatures 25 mm from bottom of slab for North Carolina, Slab 3.

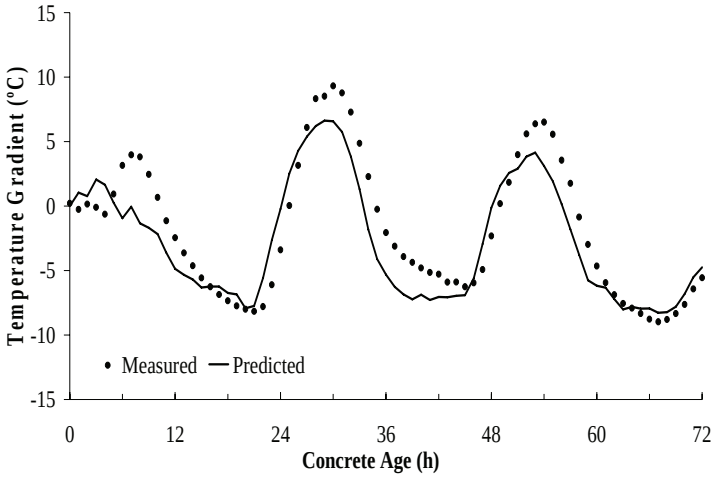

Figure 231. Measured versus predicted temperature gradient for North Carolina, Slab 3.

E.6 TEMPERATURE PREDICTION RESULTS OBTAINED DURING VALIDATION

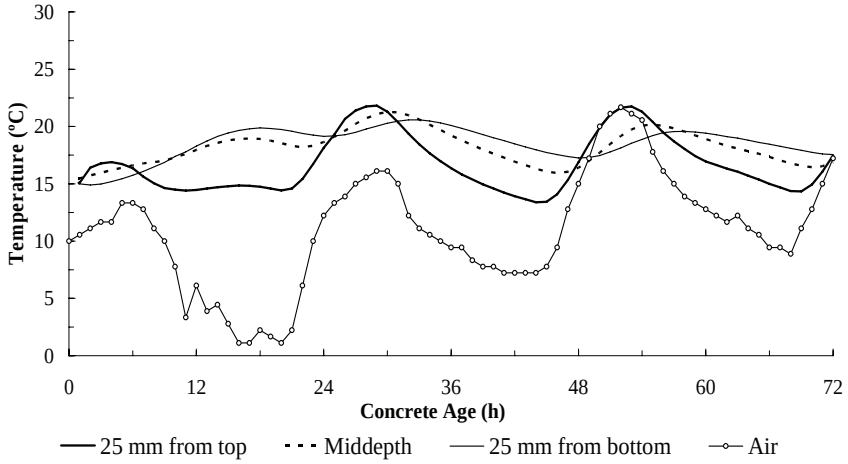

Figure 232. Measured concrete and air temperatures for Minnesota, Slab 2.

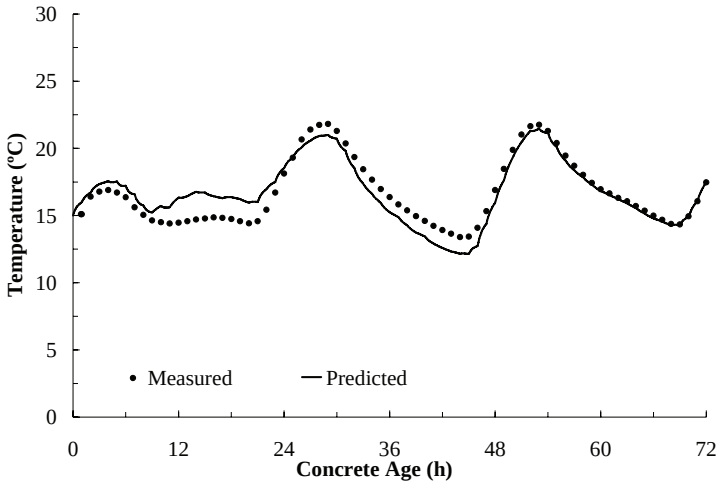

Figure 233. Measured versus predicted temperatures 25 mm from top of slab for Minnesota, Slab 2.

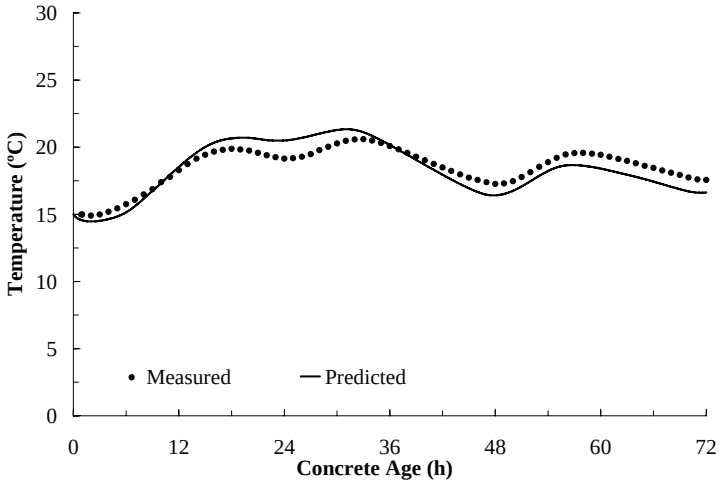

Figure 234. Measured versus predicted temperatures 25 mm from bottom of slab for Minnesota, Slab 2.

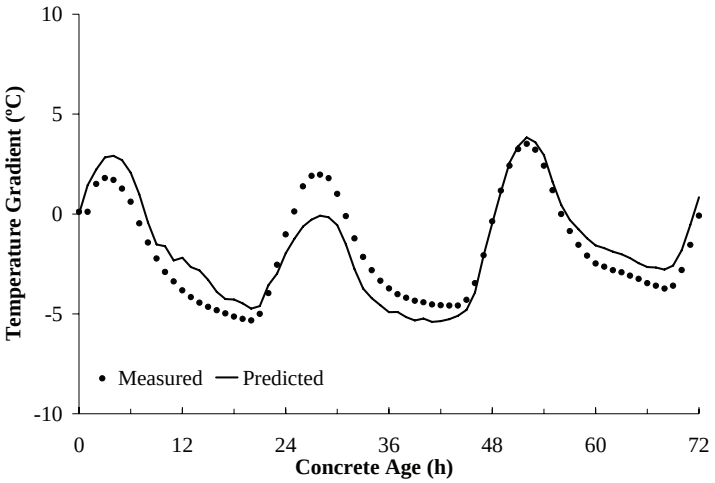

Figure 235. Measured versus predicted temperature gradient for Minnesota, Slab 2.

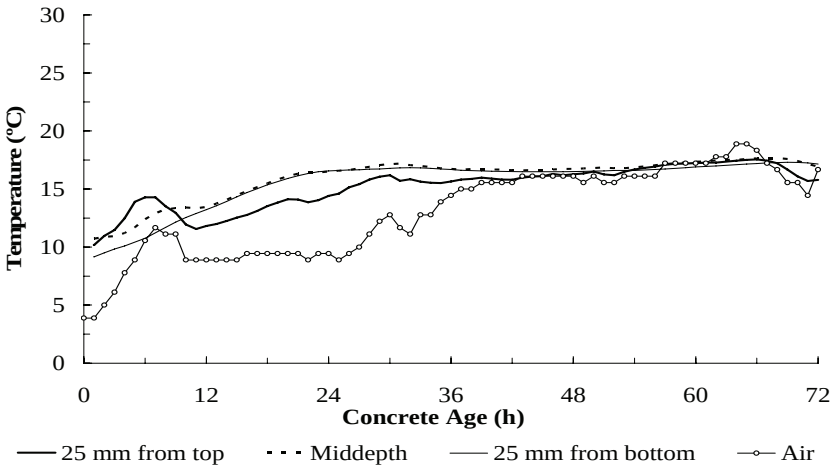

Figure 236. Measured concrete and air temperatures for Minnesota, Slab 3.

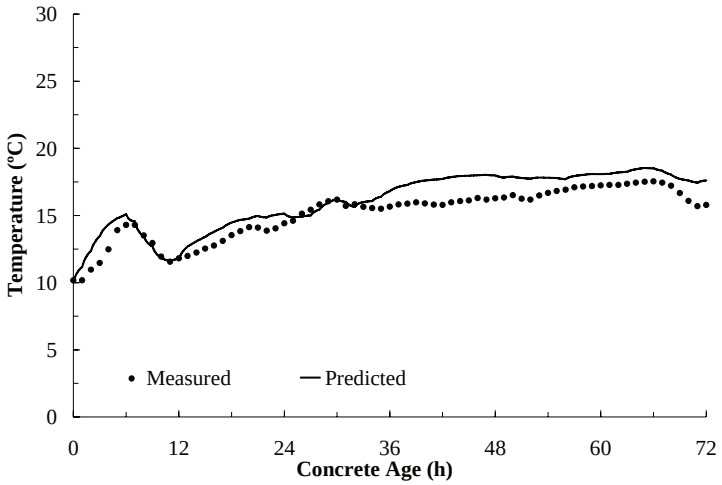

Figure 237. Measured versus predicted temperatures 25 mm from top of slab for Minnesota, Slab 3.

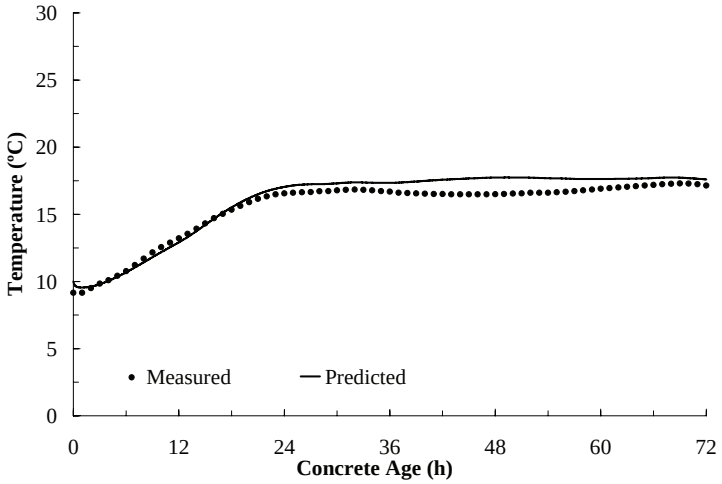

Figure 238. Measured versus predicted temperatures 25 mm from bottom of slab for Minnesota, Slab 3.

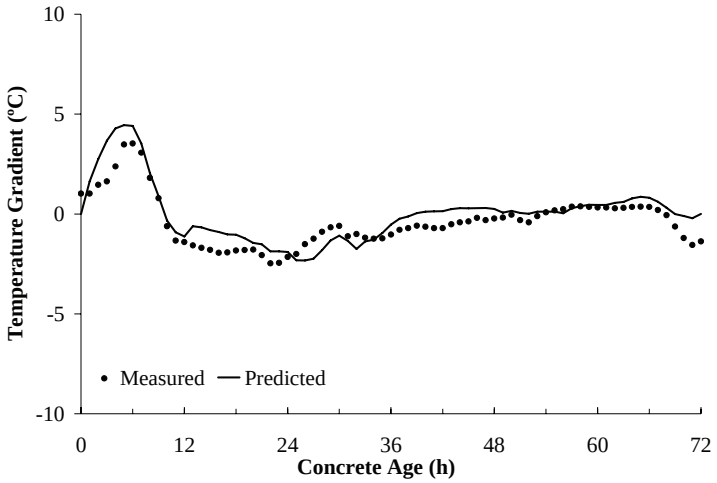

Figure 239. Measured versus predicted temperature gradient for Minnesota, Slab 3.

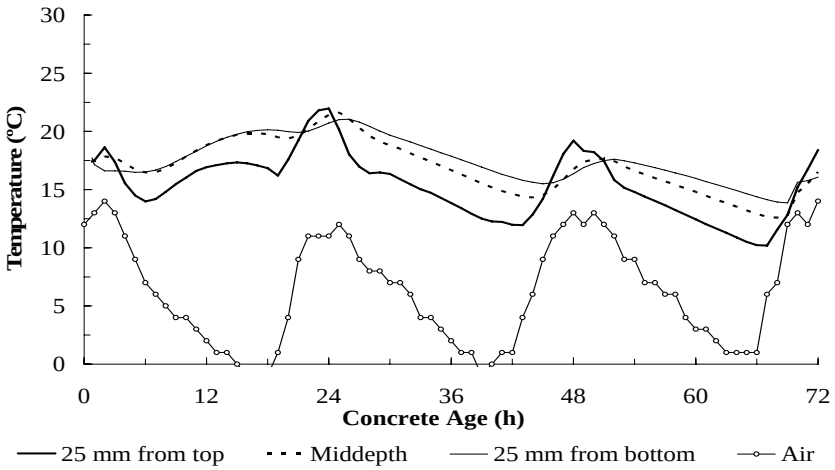

Figure 240. Measured concrete and air temperatures for Arizona, Slab 4.

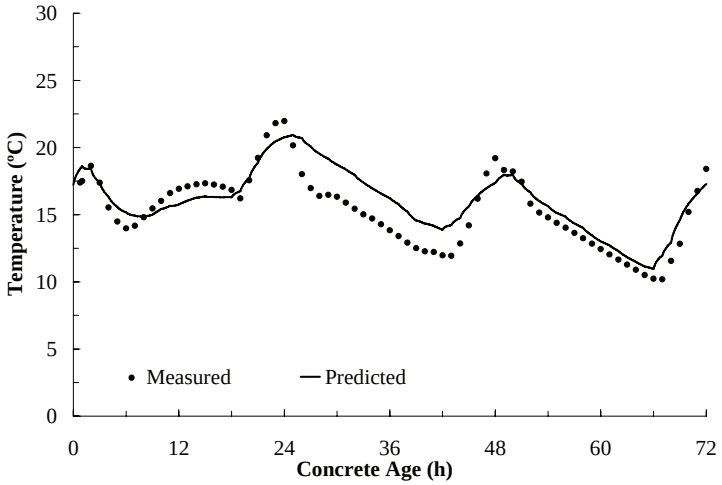

Figure 241. Measured versus predicted temperatures 25 mm from top of slab for Arizona, Slab 4.

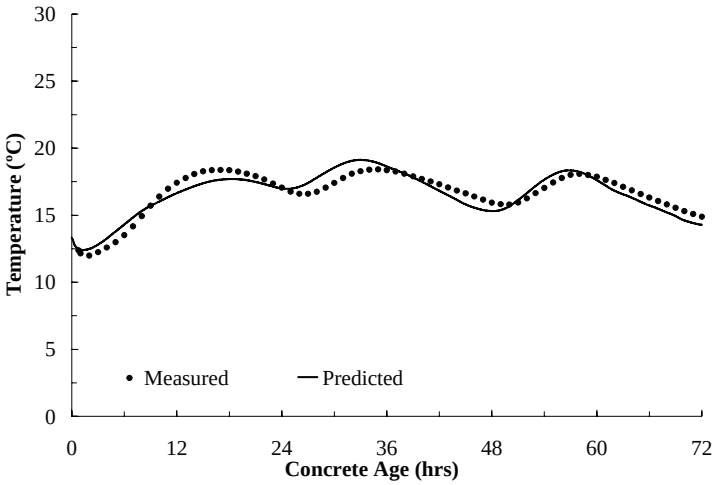

Figure 242. Measured versus predicted temperatures 25 mm from bottom of slab for Arizona, Slab 4.

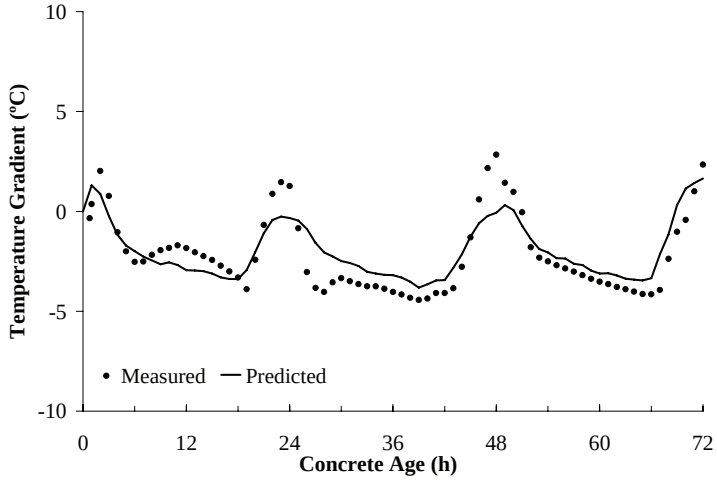

Figure 243. Measured versus predicted temperature gradient for Arizona, Slab 4.

Figure 244. Measured concrete and air temperatures for Arizona, Slab 5.

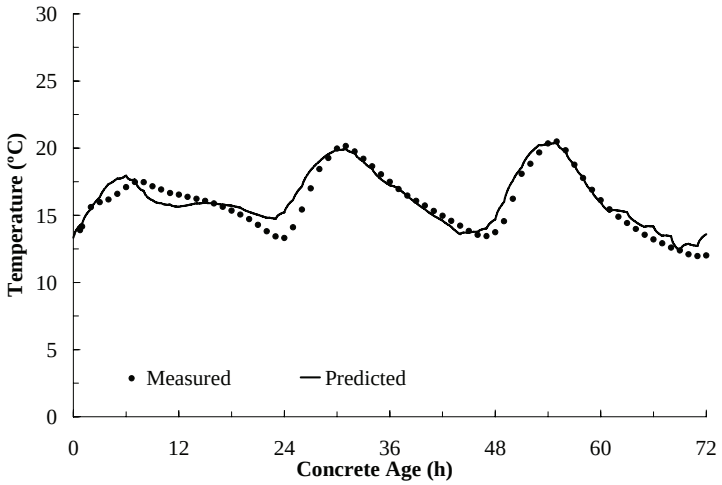

Figure 245. Measured versus predicted temperatures 25 mm from top of slab for Arizona, Slab 5.

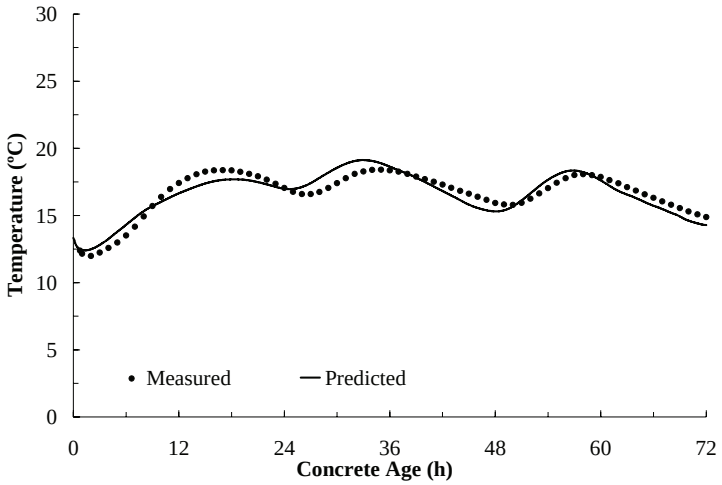

Figure 246. Measured versus predicted temperatures 25 mm from bottom of slab for Arizona, Slab 5.

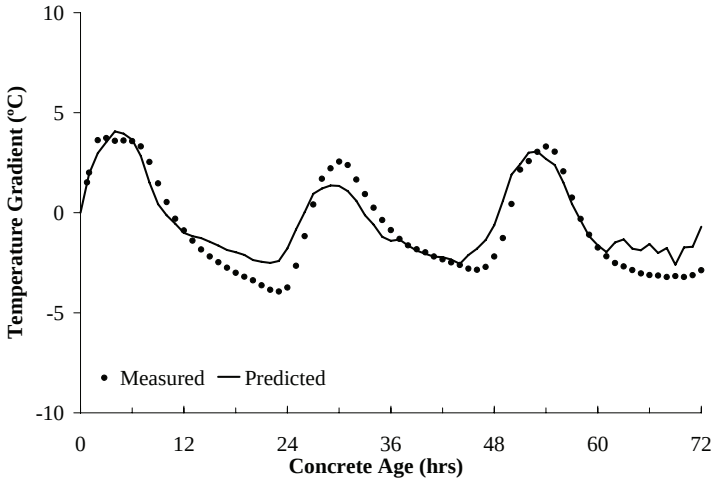

Figure 247. Measured versus predicted temperature gradient for Arizona, Slab 5.

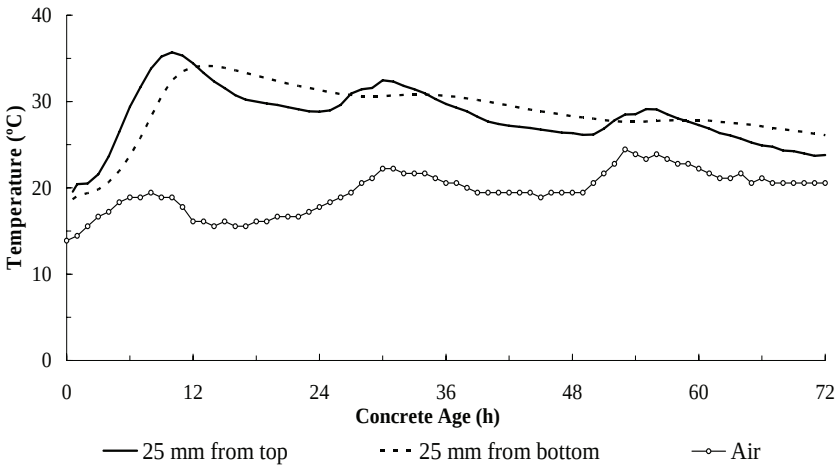

Figure 248. Measured concrete and air temperatures for Lufkin, TX, Slab 1.

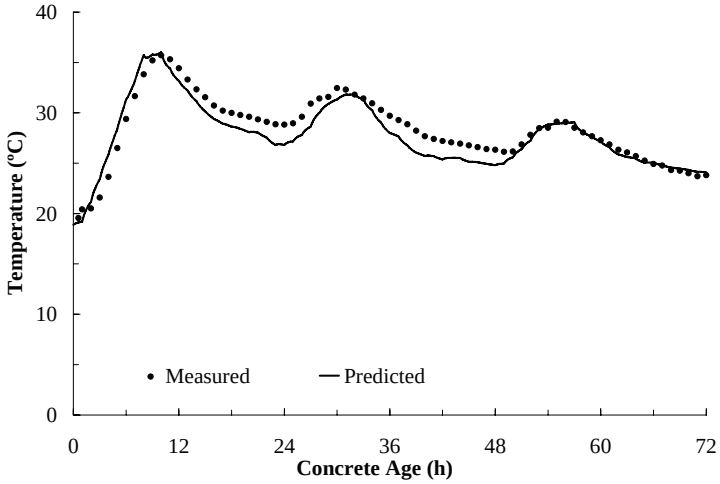

Figure 249. Measured versus predicted temperatures 25 mm from top of slab for Lufkin, TX, Slab 1.

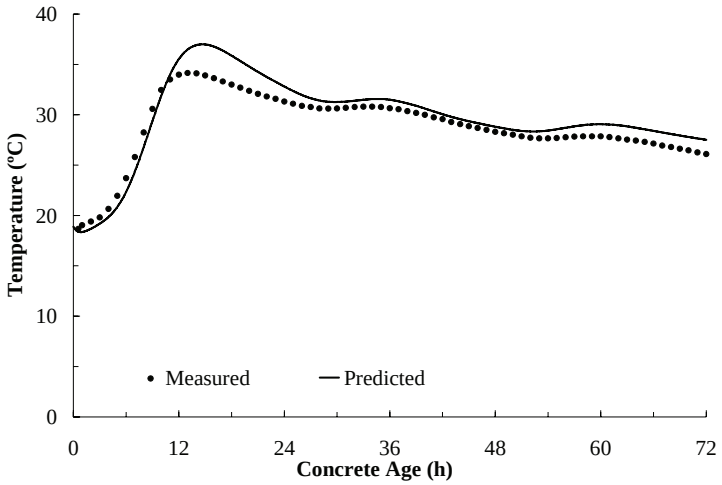

Figure 250. Measured versus predicted temperatures 25 mm from bottom of slab for Lufkin, TX, Slab 1.

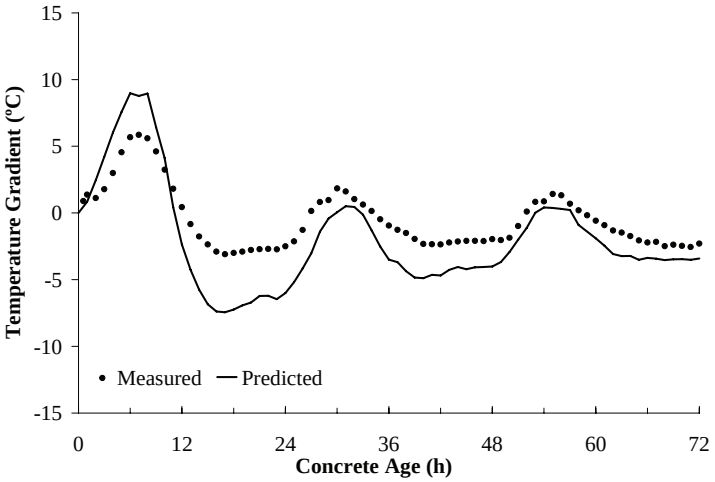

Figure 251. Measured versus predicted temperature gradient for Lufkin, TX, Slab 1.

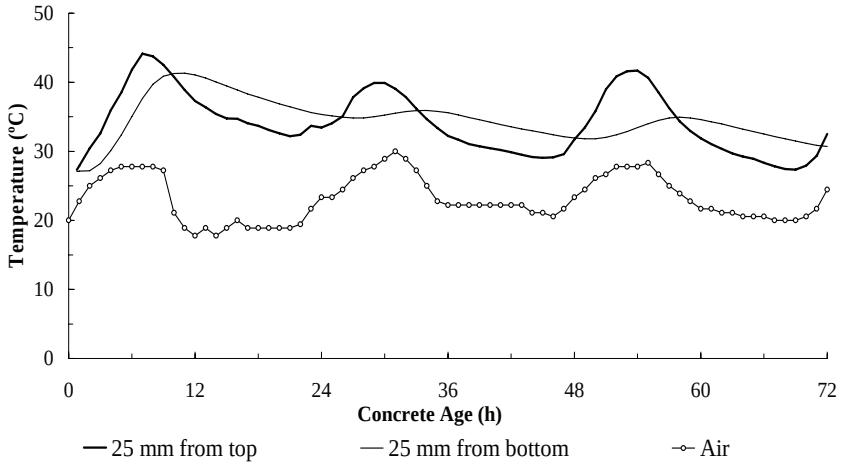

Figure 252. Measured concrete and air temperatures for Lufkin, TX, Slab 4.

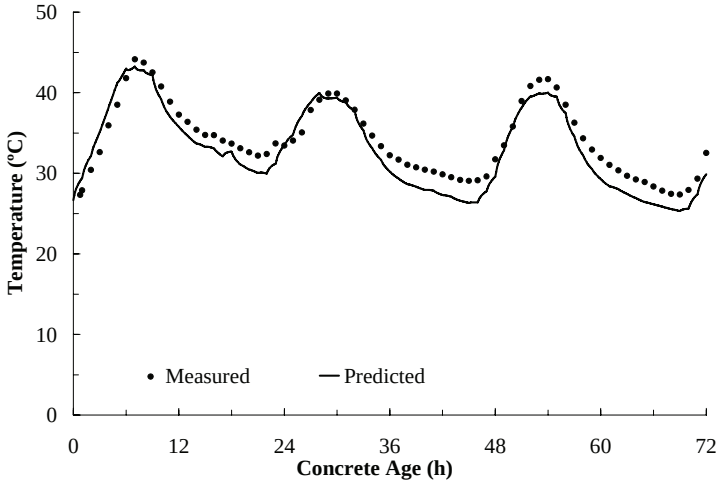

Figure 253. Measured versus predicted temperatures 25 mm from top of slab for Lufkin, TX, Slab 4.

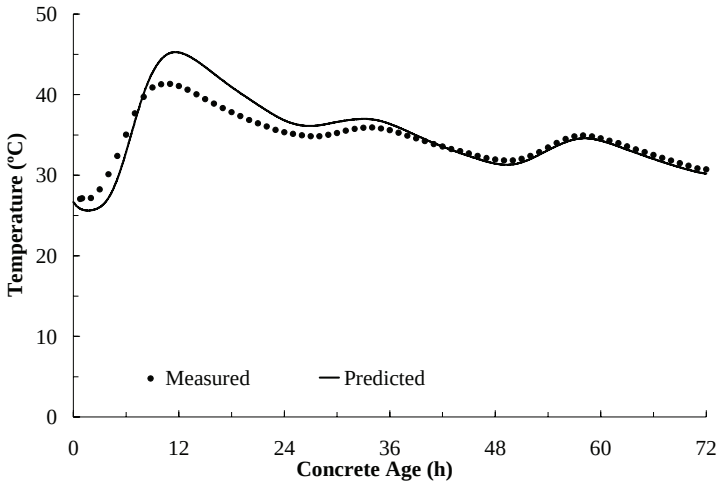

Figure 254. Measured versus predicted temperatures 25 mm from bottom of slab for Lufkin, TX, Slab 4.

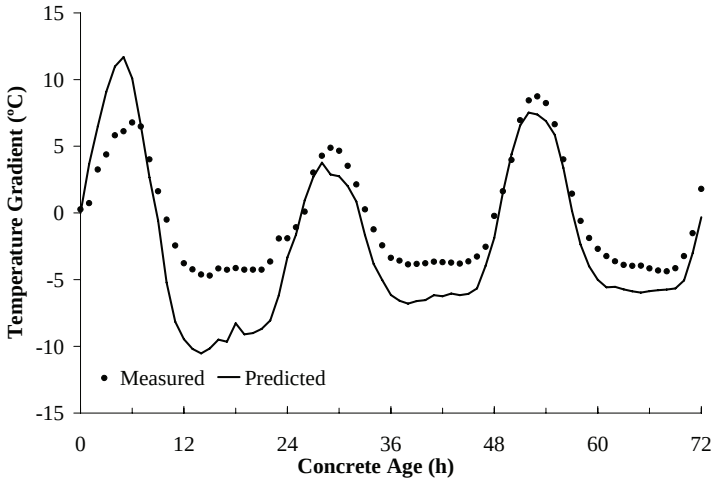

Figure 255. Measured versus predicted temperature gradient for Lufkin, TX, Slab 4.

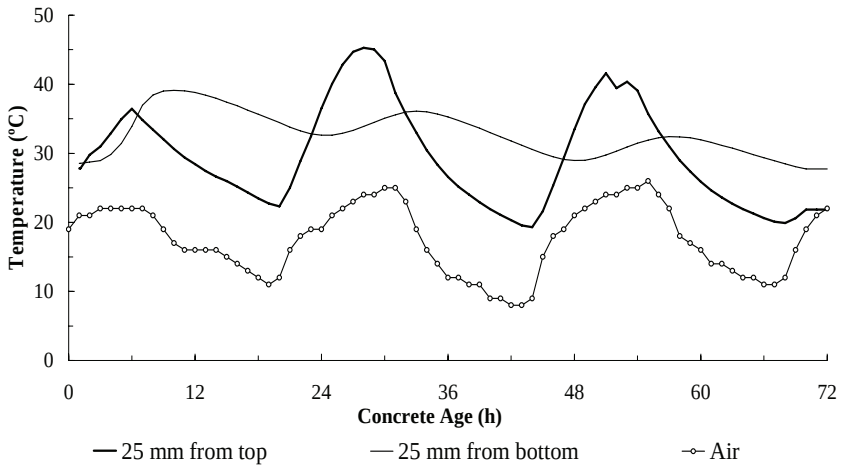

Figure 256. Measured concrete and air temperatures for North Carolina, Slab 1.

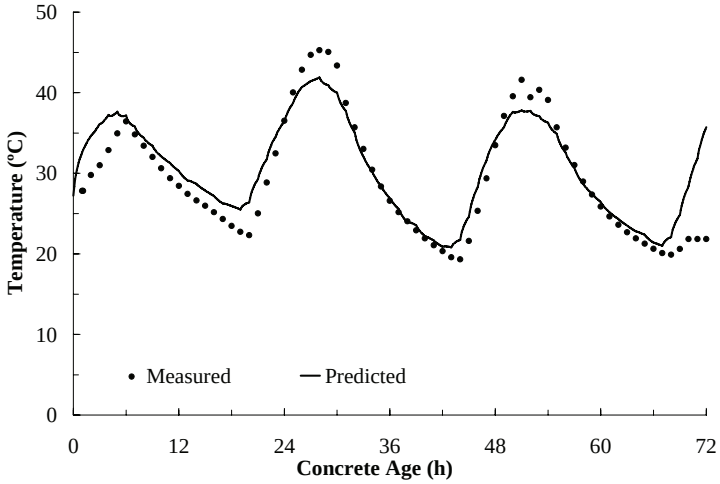

Figure 257. Measured versus predicted temperatures 25 mm from top of slab for North Carolina, Slab 1.

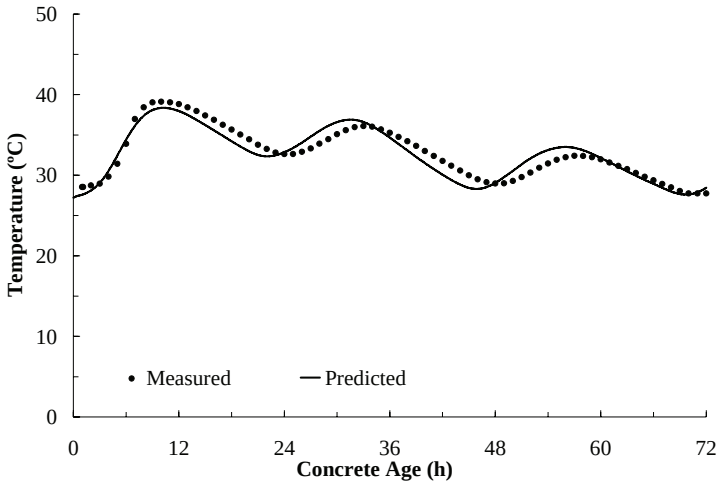

Figure 258. Measured versus predicted temperatures 25 mm from bottom of slab for North Carolina, Slab 1.

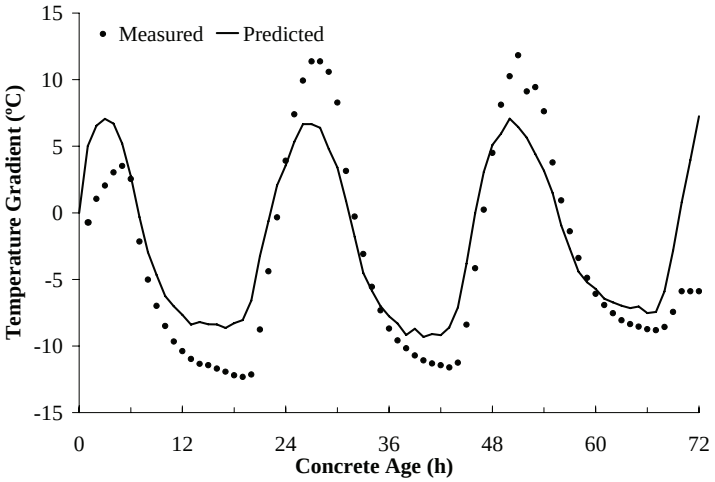

Figure 259. Measured versus predicted temperature gradient for North Carolina, Slab 1.

Figure 260. Measured concrete and air temperatures for North Carolina, Slab 4.

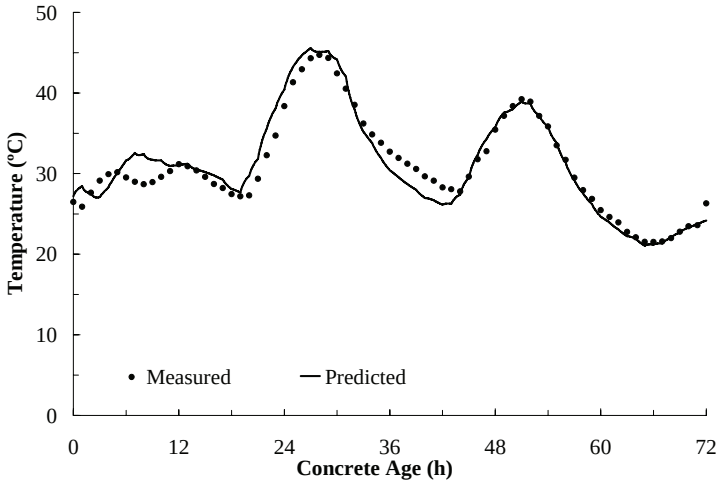

Figure 261. Measured versus predicted temperatures 25 mm from top of slab for North Carolina, Slab 4.

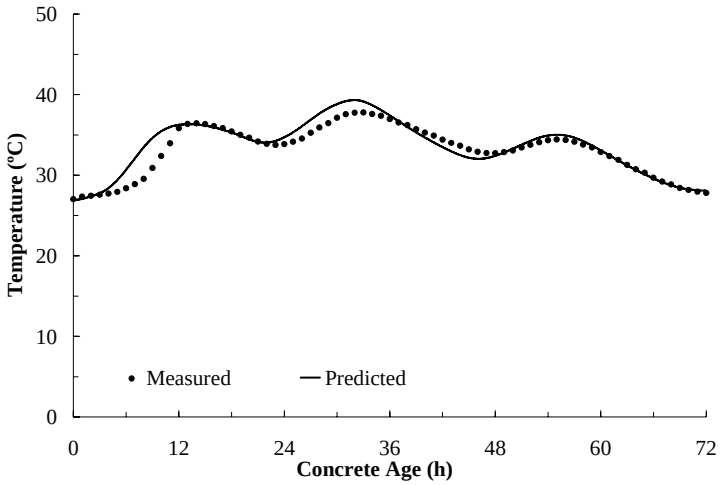

Figure 262. Measured versus predicted temperatures 25 mm from bottom of slab for North Carolina, Slab 4.

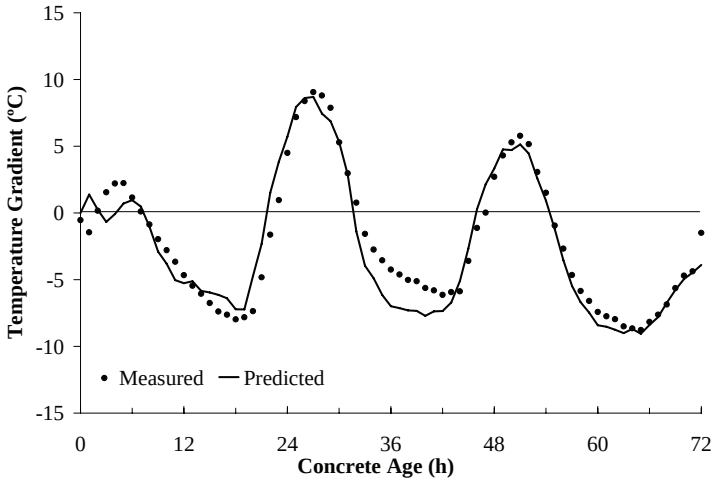

Figure 263. Measured versus predicted temperature gradient for North Carolina, Slab 4.

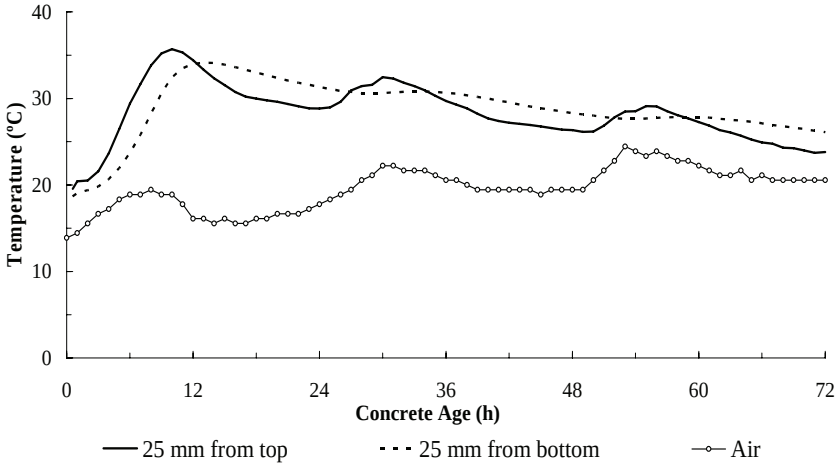

Figure 264. Measured concrete and air temperatures for Fort Worth, TX, Slab 1.

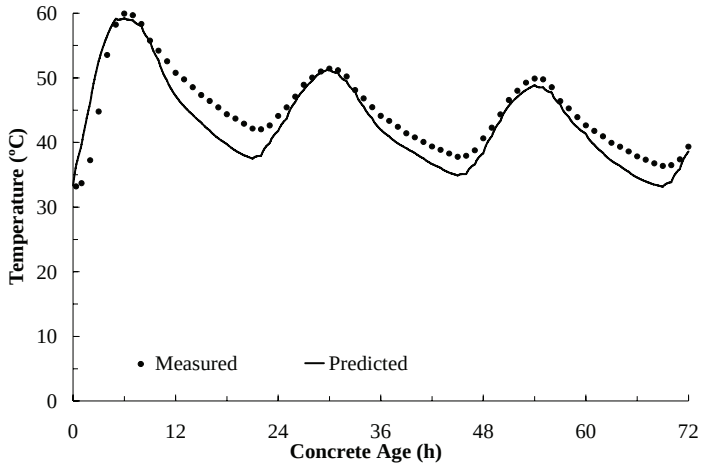

Figure 265. Measured versus predicted temperatures 25 mm from top of slab for Fort Worth, TX, Slab 1.

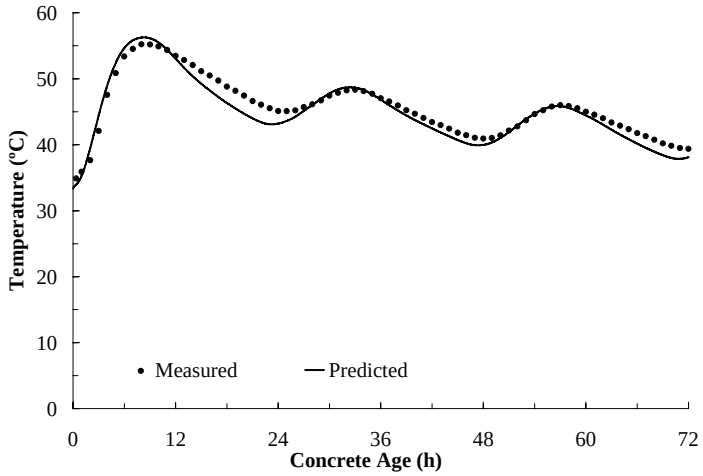

Figure 266. Measured versus predicted temperatures 25 mm from bottom of slab for Fort Worth, TX, Slab 1.

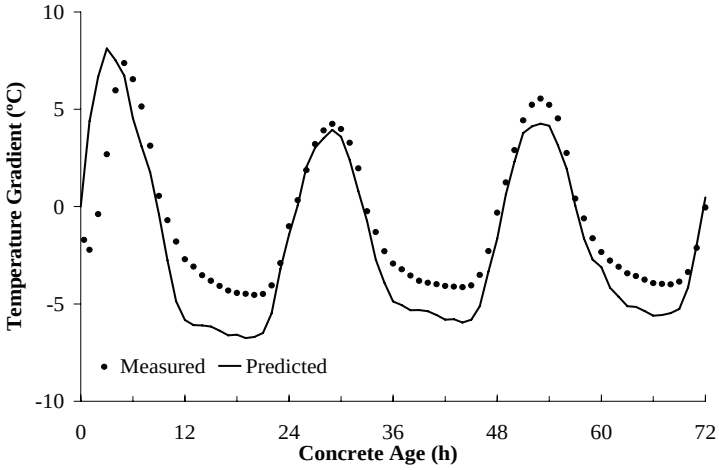

Figure 267. Measured versus predicted temperature gradient for Fort Worth, TX, Slab 1.

REFERENCES

1. McCullough, B.F. and Rasmussen, R.O. *Fast-Track Paving: Concrete Temperature Control and Traffic Opening Criteria for Bonded Concrete Overlays, Volume I: Final Report.* FHWA–RD–98–167. Federal Highway Administration, Washington, DC, 191 pp., October 1999.
2. Ruiz, J.M., Schindler, A.K., Rasmussen, R.O., Nelson, P.K., and Chang, G.K. *Concrete Temperature Modeling and Strength Prediction Using Maturity Concepts in the FHWA HIPERPAV Software.* CD Proceedings of the 7th International Conference on Concrete Pavements, Orlando, FL, September 9–13, 2001.
3. Rasmussen, R.O., Ruiz, J.M., Rozycki, D.K., and McCullough, B.F. *Constructing High-Performance Concrete Pavements Using the FHWA HIPERPAV Systems Analysis Software.* CD–ROM. Transportation Research Board, Washington, DC, 2002.
4. Schindler, A.K. Concrete Hydration, *Temperature Development, and Setting at Early Ages*. Doctoral Dissertation, the University of Texas at Austin, Austin, TX, May 2002.
5. Lerch, W. and Ford, C.L. "Long-Term Study of Cement Performance in Concrete: Chapter 3. Chemical and Physical Tests of the Cements." *ACI Journal*, Vol. 19, No. 8, pp. 745–795, 1948.
6. Kjellsen, K.O., Detwiler, R.J., and Gjørv, O.E. "Development of Microstructure in Plain Cement Pastes Hydrated at Different Temperatures." *Cement and Concrete Research*, Vol. 21, No. 1, pp. 179–189, 1991.
7. Bogue, R.H. *The Chemistry of Portland Cement*. Reinhold Publishing Corporation, New York, NY, 572 pp., 1947.
8. Byfors, J. *Plain Concrete at Early Ages*. Research 3:80, Swedish Cement and Concrete Research Institute, Cement och Betong Institutet (CBI), Stockholm, Sweden, 1980.
9. Scanlon, J.M. and McDonald, J.E. *Thermal Properties, Significance of Tests and Properties of Concrete and Concrete-Making Materials*. Edited by Klieger, P. and Lamonds, J.F., ASTM Special Technical Publication No. 169C, Philadelphia, PA, pp. 229–239, August 1994.
10. Khan, A., Cook, W., and Mitchell, D. "Early-Age Compressive Stress-Strain Properties of Low-, Medium-, and High-Strength Concretes." *ACI Materials Journal*, Vol. 92, No. 6, November–December 1995.
11. De Shutter, G. and Taerwe, L. "Specific Heat and Thermal Diffusivity of Hardening Concrete." *Magazine of Concrete Research*, Vol. 47, No. 172, pp. 203–208, September 1995.
12. Van Breugel, K. *Simulation of Hydration and Formation of Structure in Hardening Cement-Based Materials.* Second Edition, Delft University Press, Netherlands, 305 pp., 1999.
13. Mindess, S. and Young, J.F. *Concrete.* Prentice-Hall, Inc. Englewood Cliffs, NJ, 1981.
14. Trinhztfy, H.W., Blaawendraad, J., and Jongendijk, J. *Temperature Development in Concrete Structures Taking Account of State Dependent Properties.* Proceedings from RILEM International Conference on Concrete at Early Ages, Vol. 1, Paris, France, pp. 211–218, 1982.
15. ACI Committee 207, *Effect of Restraint, Volume Change, and Reinforcement on Cracking of Massive Concrete.* American Concrete Institute, Farmington Hills, MI, 1986.
16. *A Guide to Evaluating Thermal Effects in Concrete Pavements.* SHRP–C–321, Strategic Highway Research Program, National Research Council, Washington, DC, 104 pp., 1993.
17. Tompson, M.R., Dempsey, B.J., Hill, H., and Vogel, J. *Characterizing Temperature Effects for Pavement Analysis and Design.* Transportation Research Record 1121, pp. 14–22, 1988.
18. Lytton, R.L., Pufahl, D.E., Michalak, C.H., Liang, H.S., and Dempsey, B.J. *An Integrated Model of the Climatic Effects on Pavements.* FHWA–RD–90–033, Federal Highway Administration, 285 pp., November 1989.
19. *Accelerated Rigid Paving Techniques: State-of-the-Art Report (Special Project 201),* FHWA–SA–94–080, Federal Highway Administration, Washington, DC, 255 pp., December 1994.
20. McAdams, W.H. *Heat Transmission.* McGraw Hill Series in Chemical Engineering, McGraw Book Company, New York, NY, 532 pp., 1954.

21. Turner, W.C. and Malloy, J.F. *Thermal Insulation Properties.* McGraw-Hill Book Company, New York, NY, 629 pp., 1981.
22. *1993 ASHRAE Handbook*, American Society of Heating, Refrigerating and Air-Conditioning Engineers, Inc., Atlanta, GA, 1993.
23. Heilman, R.H. *Surface Heat Transmission.* Transactions of the Society of Mechanical Engineers, Vol. 51, Part 1, pp. 287–302, 1929.
24. 4C-Temp&Stress—*Temperature and Stress Simulation During Hardening.* User Manual, Germann Instruments, Evanston, IL, 1998.
25. *CIMS, Computer Active Maturity System.* Software and Hardware Manual, Digital Site Systems Inc., October 1988.
26. Sungchul Y. *A Temperature Prediction Model in New Concrete Pavement and a New Test Method for Concrete Fracture Parameters.* Dissertation, Texas A&M University, Austin, Texas, May 1996.
27. ASTM C 309. *Standard Specification for Liquid Membrane-Forming Compounds for Curing Concrete.* American Society for Testing and Materials, West Conshohocken, PA, 1998.
28. Incorpera, F.P and DeWitt, D. *Fundamentals of Heat and Mass Transfer.* Third Edition, J. Wiley & Sons, New York, NY, 919 pp., 1990.
29. Bliss, R.W. "Atmospheric Radiation Near the Surface of the Ground: Summary for Engineers." *Solar Energy*, Vol. 5, No. 3, pp. 103–120, 1961.
30. Hottel, H.C. and Egbert, R.B. *Radiant Heat Transmission from Water Vapor*. Transactions of the American Institute of Chemical Engineers, Vol. 38, New York, NY, pp. 531–568, 1942.
31. Barber, E.S. *Calculation of Maximum Pavement Temperatures from Weather Reports.* Highway Research Board, Bulletin 168, Washington, DC, 1957.
32. Jonasson, J.-E. and Hedlund, H. *An Engineering Model for Creep and Shrinkage in High Performance Concrete.* RILEM Proceedings PRO 17. Shrinkage of Concrete, Shrinkage 2000. Edited by Baroghel-Bouny, V. and Aitchin, P.-C., pp. 507–529, 2000.
33. Baźant, Z.P. and Baweja, S. "Creep and Shrinkage Prediction Model for Analysis and Design of Concrete Structures—Model B_3." *Materials and Structures*, Vol. 28, pp. 357–365, 1995.
34. Aïtcin, P.-C. "Demystifying Autogenous Shrinkage." *Concrete International*, Vol. 21, No. 11, pp. 54–56, November 1999
35. Baźant, Z.P. and Panula, L. "Practical Predictions of Time-Dependent Deformations of Concrete." *Materials and Structures*, Third RILEM, Vol. 11, No. 65, pp. 307–316, 1978.
36. Persson, B. *Shrinkage of Concrete. Early-Age Cracking in Cementitious Systems*. Edited by Bentur, A. pp. 102–114. RILEM 2001.
37. Brooks, J.J. "How Admixtures Affect Shrinkage and Creep." *Concrete International*, Vol. 21, No. 4, pp. 35–38., April 1999.
38. Rasmussen, R.O. and Rozycki, D. *Characterization and Modeling of Axial Slab-Support Restraint.* Transportation Research Record 1778, Washington, DC, pp. 26–32, 2001.
39. Friberg B. F. *Frictional Resistance Under Concrete Pavements and Restraint Stresses in Long Reinforced Slabs.* Highway Research Board Proceedings of the 23rd Annual Meeting, Vol. 33, Washington, DC, pp. 167–184, 1954.
40. Timms, A.G. *Evaluating Subgrade Friction-Reducing Mediums for Rigid Pavements.* Highway Research Record 60, pp. 28–38, 1963.
41. Chia, W.S., McCullough, B.F., and Burns, N.H. *Field Evaluation of Subbase Friction Characteristics.* Research Report 401–5. Center for Transportation Research, September 1986.
42. Mohamed, A. and Hansen, W. *Effect of Nonlinear Temperature Gradient on Curling Stresses in Concrete Pavements.* Transportation Research Record 1568, pp. 65–71, 1997.
43. Westman, G. *Concrete Creep and Thermal Stresses.* Doctoral Thesis, Luleå University of Technology, Division of Structural Engineering, 301 pp., 1999.
44. Baźant, Z.P. and Chern, J.C. "Strain Softening with Creep and Exponential Algorithm." *Journal of Engineering Mechanics Division*, ASCE, Vol. 111, No. 3, 1985.

45. Emborg, M., *Thermal Stress in Concrete Structures at Early Ages.* Doctoral Thesis, Luleå University of Technology, Division of Structural Engineering, 285 pp., 1989.
46. Bażant, Z.P. "Numerical Determination of Long-Range Stress History From Strain History in Concrete." *Materials and Structures*, (RILEM Paris), Vol. 5, No. 27, pp. 135–141, May–June 1972.
47. Thornthwaite, C.W. "An Approach Toward a Rational Classification of Climate." *Geographical Review*. Vol. 38, pp. 55–94, 1948.
48. Lytton, R.L., Pufahl, D.E., Michalak, C.H., Liang, H.S., and Dempsey, B.J. *An Integrated Model of the Climatic Effects on Pavements.* FHWA–RD–90–033. Federal Highway Administration, Washington, DC, November 1989.
49. National Climatic Data Center. *Solar and Meteorological Surface Observation Network, 1961–1990.* Vol. 1, 2, and 3, Version 1.0, September 1993.
50. *The AASHO Road Test, Report 2—Materials and Construction.* Special Report 61B. Highway Research Board. National Academy of Sciences. National Research Council. Washington, DC, 1962.
51. *The AASHO Road Test, Report 5—Pavement Research.* Special Report 61E. Highway Research Board. National Academy of Sciences. National Research Council. Washington, DC, 1962.
52. *DataPave 2.0. Beta Version.* Federal Highway Administration, Washington, DC, April 1999.
53. Jiang, Y.J. and Tayabi, S.D. *Analysis of Time Domain Reflectometry Data from LTPP Seasonal Monitoring Program Test Sections.* Final Report. FHWA–RD–99–115. Federal Highway Administration, Washington, DC, July 1999.
54. *CEB-FIP Model Code 1990*. Comité Euro-International Du Béton, Redwood Books, Trowbridge, Wilshire, Great Britain, 1991.
55. Melis, L.M., Meyer, A.H., and Fowler, D.W. *An Evaluation of Tensile Strength Testing.* CTR Project 432–1F, Center for Transportation Research, University of Texas at Austin, Austin, TX, 1985.
56. Carrasquillo, P.M. and Carrasquillo, R.L. *Improved Concrete Quality Control Procedures Using Third Point Loading.* CTR Project 1119–1F, Center for Transportation Research, University of Texas at Austin, Austin, TX, November 1987.
57. Kellermann, W.F. "Effect of Size of Specimen, Size of Aggregate and Method of Loading on the Uniformity of Flexural Strength Tests." *Public Roads*, Federal Highway Administration, Washington, DC, 1933.
58. ACI. "Building Code Requirements for Structural Concrete (ACI 318M–02) and Commentary (ACI 318RM–02)." *ACI Standards*. American Concrete Institute, Farmington Hills, MI, 2002.
59. Légeron, F. and Paultre, P. "Prediction of Modulus of Rupture of Concrete." *ACI Materials Journal*, Vol. 97, No. 2, pp. 193–200, March–April 2000.
60. Raphael, J.M. "Tensile Strength of Concrete." *ACI Journal*, Proceedings Vol. 81, pp. 158–165, March–April 1984.
61. Popovics, S. *Strength and Related Properties of Concrete, A Quantitative Approach.* J. Wiley & Sons, Inc., New York, NY, 535 pp., 1998.
62. Neville, A. *Properties of Concrete.* Fourth Edition, J. Wiley & Sons Inc., New York, NY, 535 pp., 1999.
63. Ghafoori, N. and Bucholc, J. "Properties of High-Calcium Dry Bottom Ash Concrete." *ACI Materials Journal*, Vol. 94, No. 2, March–April 1997.
64. Huang, Y.H. *Pavement Analysis and Design.* Prentice Hall. Englewood Cliffs, NJ. 1993.
65. Westergaard, H.M. "New Formulas for Stresses in Concrete Pavements of Airfields." *Transactions of the American Society of Civil Engineers*, Vol. 113, pp. 425–444, 1948.
66. Timoshenko, S. and Lessels, J.M. *Applied Elasticity.* Westinghouse Technical Night School Press, Pittsburgh, PA, pp. 133–141, 1925.
67. *Structural Design Considerations for Pavement Joints.* ACI Title 53–1 Report from ACI Committee 325, Subcommittee III, Journal of the American Concrete Institute, Vol. 28, No. 1, pp. 1–28, July 1956.

68. Gere, J.M. and Timoshenko, S.P. *Mechanics of Materials.* 3rd Ed. PWS–KENT Publishing, Boston, MA, 1990.
69. Ioannides, A.M. and Korovesis, G.T. "Analysis and Design of Doweled Slab-on-Grade Pavement Systems." *Journal of Transportation Engineering*, Vol. 118, No. 6, pp. 745–768, November–December 1992.
70. Colley, B.E. and Humphrey, H.A. *Aggregate Interlock at Joints in Concrete Pavements.* Proceedings of the Highway Research Board 46th Annual Meeting, Report HRR 189, pp. 1–18, 1967.
71. Skarlatos, M.S. *Deflections and Stresses in Concrete Pavements of Airfields with Continuous Elastic Joints.* Harvard University Research Report under contract W-33-107-eng-4240, U.S. Army Corps of Engineers, Ohio River Division Laboratories, Mariemont, OH, June 1949.
72. Ioannides, A.M. and Hammons, M.I. *A Westergaard-Type Solution for the Edge Load Transfer Problem.* Preprint from the Transportation Research Board 75th Annual Meeting, January 1996.
73. Ioannides, A.M. and Korovesis, G.T. *Aggregate Interlock: A Pure-Shear Load Transfer Mechanism.* Transportation Research Record 1286, Transportation Research Board, National Research Council, Washington, DC, pp. 14–22, 1990.
74. Nowlen, W.J. "Influence of Aggregate Properties on Effectiveness of Interlock Joints in Concrete Pavements." *Bulletin D139*, Vol. 10, No. 2, Portland Cement Association, 1968.
75. Smith, K. D., Mueller, A.L., Darter, M.I., and Peshkin, D.G. *Performance of Jointed Concrete Pavements. Volume II—Evaluation and Modification of Concrete Pavement Design and Analysis Models.* FHWA–RD–89–137, Federal Highway Administration, Washington, DC, July 1990.
76. Yu, H.T., Smith, K.D., Darter, M.I., Jiang, J., and Khazanovich, L. *Performance of Concrete Pavements Volume III—Improving Concrete Pavement Performance.* FHWA–RD–95–111, Federal Highway Administration, Washington, DC, 1995.
77. Darter, M.I. *A Comparison Between Corps of Engineers and ERES Consultants, Inc. Rigid Pavement Design Procedures.* Technical Report Prepared for the U.S. Air Force SAC, Urbana, IL, 1988.
78. Salsilli, R.A., Barenberg, E.J., and Darter, M.I. *Calibrated Mechanistic Design Procedure to Prevent Transverse Cracking of Jointed Plain Concrete Pavements.* Proceedings of the 5th International Conference on Concrete Pavement Design and Rehabilitation, Purdue University, West Lafayette, IN, 1993.
79. Darter, M.I. and Barenberg, E.J. *Design of Zero-Maintenance Plain Jointed Concrete Pavements Volume I—Development of Design Procedures.* FHWA–RD–77–111, Federal Highway Administration, Washington, DC, 1977.
80. Treybig, H.J., McCullough, B.F., Smith, P., and Von Quintus, H. *Overlay Design and Reflection Cracking Analysis for Rigid Pavements—Volume 2, Design Procedures.* FHWA–RD–77–67, Federal Highway Administration, Washington, DC, 1977.
81. Lee, Y.H. and Darter, M.I. *Loading and Curling Stress Models for Concrete Pavement Design.* Transportation Research Record No. 1449, Transportation Research Board, National Research Council, Washington, DC, 1994.
82. Lee, Y.H. and Darter, M.I. *Modified Portland Cement Association Stress Analysis and Thickness Design Procedures.* Transportation Research Record No. 1568, Transportation Research Board, National Research Council, Washington, DC, 1997.
83. Lee, Y.H. and Darter, M.I. *Mechanistic Design Models of Loading and Curling in Concrete Pavements, Airport Pavement Innovations: Theory to Practice.* Airfield Pavement Committee, Proceedings of the Conference, American Society of Civil Engineers, New York, NY, 1993.
84. Lee, Y.H., Yen, S.T., Lee, C.T., Bair, J.H., and Lee, Y.M. *Development of New Stress Analysis and Thickness Design Procedures for Jointed Concrete Pavements.* Proceedings of the 6th International Conference of Concrete Pavements, Purdue University, West Lafayette, IN,1997.
85. Smith, K.D., Peshkin D.G., Darter, M.I., and Mueller, A.L. *Performance of Jointed Concrete Pavements. Volume III—Summary of Research Findings.* FHWA–RD–89–138, Federal Highway Administration, Washington, DC, November 1990.

86. *Distress Identification Manual for the Long-Term Pavement Performance Project.* Strategic Highway Research Program. SHRP–P–338. Washington, DC, 1993.
87. Pilson, C.C. "JCP PSI Ride Model Summary." Aurora 2000 Technical Memorandum, The Transtec Group, Inc., May 1998.
88. Perera, R.W., Byrum. C., and Kohn, S.D. *Investigation of Development of Pavement Roughness.* FHWA–RD–97–147, Federal Highway Administration, Washington, DC, May 1998.
89. Hoerner, T.E., Darter, M.I., Khazanovich, L., Titus-Glover, L., and Smith, K.L. *Improved Prediction Models for PCC Pavement Performance-Related Specifications, Volume I: Final Report.* FHWA–RD–00–130, Federal Highway Administration, Washington, DC, December 2000.
90. *1-37A Guide for Mechanistic Design of Pavements.* Presented at the 79th Transportation Research Board Annual Meeting in Washington, DC, 2000.
91. *1-37A Guide for Mechanistic Design of Pavements.* Presented at the 80th Transportation Research Board Annual Meeting in Washington, DC, 2001.
92. *Determination of Traffic Information and Data for Pavement Structural Design and Evaluation, Interim Report*, NCHRP project 1–37A, Development of the 2002 Guide for Design of New and Rehabilitated Pavement Structures, December 1999
93. Won, M., Hankins, K., and McCullough, B.F. *A Twenty-Four-Year Performance Review of Concrete Pavement Sections Made with Siliceous and Lightweight Coarse Aggregates.* Research Report 472–3. Center for Transportation Research. The University of Texas at Austin, Austin, TX, April 1989.
94. Simon, M.J., Lagergren, E.S., and Snyder, K.A. *Concrete Mixture Optimization Using Statistical Mixture Design Methods*. Proceedings of the PCI/FHWA International Symposium on High Performance Concrete, pp. 230–244, 1997.
95. Simon, M.J., Snyder, K.A., and Frohnsdorff, G.J. *Advances in Concrete Mixture Optimization.* Concrete Durability and Repair Technology Conference, pp. 21-32, University of Dundee, Scotland, UK, September 1999.
96. Simon, M.J., Lagergren, E.S., and Wathne, L.G. *Optimizing High-Performance Concrete Mixtures Using Statistical Response Surface Methods.* Proceedings of the 5th International Symposium on Utilization of High Strength/High-Performance Concrete, Norwegian Concrete Association, Oslo, Norway, pp. 1311–1321, 1999.
97. Simon, M.J., *Concrete Mixture Optimization Using Statistical Methods: Final Report.* FHWA-RD-06-060, Federal Highway Administration, McLean, VA, September 2003.
98. Meyers, R.H. and Montgomery, DC, *Response Surface Methodology: Process and Product Optimization Using Designed Experiments.* Second Edition, J. Wiley & Sons, New York, NY, 2002.
99. Ganju, T.N. "Spreadsheeting Mix Designs." *Concrete International.* Vol. 18, No. 12, pp. 35–38, December 1996.
100. Friberg, B.F. "Design of Dowels in Transverse Joints of Concrete Pavement." *Journal of Transportation Engineering*, ASCE, Vol. 105, 1979.
101. Westergaard, H.M. *Analysis of Stresses in Concrete Pavements Due to Variations in Temperature.* Proceedings of 6th Annual Meeting of Highway Research Board. Vol. 6, pp. 201–217, Washington, DC, 1926.
102. Hetenyi, M. *Beams on Elastic Foundation.* University of Michigan Press. Ann Arbor, MI. 1946.
103. Zollinger, D.G. and Barenberg, E.J. Background for Development of Mechanistic Based Design Procedure for Jointed Concrete Pavements. FHWA/IL/UI 224. University of Illinois at Urbana-Champaign, IL, May 1989.
104. *PCC Mixture Report (12)—History Data for Contract 40456.* Illinois Department of Transportation—Bureau of Materials and Physical Research. Springfield, IL, September 2, 1987.
105. Dossey, T. and McCullough, B.F. *Updating and Maintaining the Rigid Pavement Database.* Center for Transportation Research. Research Report 1342–3F. The University of Texas at Austin, TX, November 1994.

106. Suh, Y.C., Hankins, K., and McCullough, B.F. *Early-Age Behavior of Continuously Reinforced Concrete Pavement and Calibration of the Failure Prediction Model in the CRCP–7 Program.* Research Report 1244–3, Center for Transportation Research, The University of Texas at Austin, Austin, TX, March 1992.
107. Darter, M.I., Becker, J.M., Snyder, M.B., and Smith, R.E.. *Portland Cement Concrete Pavement Evaluation System*, COPES, National Cooperative Highway Research Program Report 277, Transportation Research Board, National Research Council, Washington, DC, September 1985.
108. Yu, H.T., K.D. Smith, M.I. Darter, J. Jiang, and L. Khazanovich. *Performance of Concrete Pavements Volume III—Improving Concrete Pavement Performance.* FHWA–RD–95–111, Federal Highway Administration, Washington, DC, 1995.
109. Rada, G.R., Elkins, G.E., Henderson, B., Van Sambeek, R.J., Lopez, Jr., A. *LTPP Seasonal Monitoring Program: Instrumentation Installation and Data Collection Guidelines.* FHWA–RD–94–110, Federal Highway Administration, Washington, DC, April 1994.
110. Lee, S.W. and Stoffels, S.M.. *Analysis of In Situ Horizontal Joint Movement in Rigid Pavements.* Transportation Research Record 1778, Transportation Research Board, National Research Council, Washington, DC, 2001.
111. SMP_ATEMP_RAIN_HOUR and SMP_MRCTEMP_AUTO_HOUR Tables, LTPP (CD–ROM) NT 2.5, Data Release 9.9, September 10, 1999.
112. *LTPP Manual for Falling Weight Deflectometer Measurements, Operational Field Guidelines.* Federal Highway Administration, McLean, VA, August 2000.
113. Teller, L.W. and Sutherland, E.C. "The Structural Design of Concrete Pavements: Part 4: The Study of the Structural Action of Several Types of Transverse and Longitudinal Joint Designs." *Public Roads*, Federal Highway Administration, Vol. 17, Nos. 7 and 8, Washington, DC, September and October 1936.
114. Wu, C.L and Tayabji, S.D. *Variability of Concrete Pavement Load Transfer Efficiency Data.* Paper presented at the Transportation Research Board 81st Annual Meeting, Paper No. 02–2448, Washington, DC, January 2002.
115. Teller, L.W. and Cashell, H.D. "Performance of Doweled Joints under Repetitive Loading." *Public Roads*, Federal Highway Administration, Vol. 30, No. 1, pp. 1–24, April 1958.
116. Otero, M.A., McCullough, B.F., and Hankins, K. *Monitoring of Siliceous River Gravel and Limestone Continuously Reinforced Concrete Pavement Test Sections in Houston 2 Years After Placement, and Development of a Crack Width Model for the CRCP–7 Program.* Research Report 1244–4, Center for Transportation Research, The University of Texas at Austin, Austin, TX, March 1992.
117. Schindler, A.K., Henry, C.P., and McCullough, B.F. *Validation of CRCP–8 to Predict Long-Term Transverse Crack Spacing Distributions in Continuously Reinforced Concrete Pavements.* CD–ROM Proceedings, Transportation Research Board 79th Annual Meeting, Washington, DC, January 2000.
118. Tayabji, S.D., Zollinger, D.G., Vederey, J.R., and Gagnon, J.S. *Performance of Continuously Reinforced Concrete Pavements: Volume III—Analysis and Evaluation of Field Test Data.* FHWA–RD–94–180, Federal Highway Administration, Washington, DC, 1998.
119. Tayabji, S.D., Selezneva, O., and Jiang, J. *Preliminary Evaluation of LTPP Continuously Reinforced Concrete (CRC) Pavement Test Sections.* FHWA–RD–99–086, Federal Highway Administration, Washington, DC, 1999.
120. Palmer, R.P. Olsen, M.P.J., and Lytton, R.L. *TTICRCP—A Mechanistic Model for the Prediction of Stresses, Strains and Displacements in Continuously Reinforced Concrete Pavements.* Research Report 371–2F, Texas Transportation Institute, The Texas A&M University System, College Station, TX, 1988.
121. Ruiz, J.M., Kim, P.J., Schindler, A.K., and Rasmussen, R.O. *Validation of HIPERPAV for Prediction of Early-Age Jointed Concrete Pavement Behavior.* Transportation Research Record 1778, Transportation Research Board, Washington, DC, pp. 17–25, 2001.

122. Schindler A.K., Ruiz J.M., Rasmussen R.O., Chang G.K., Wathne L.G., "Concrete Pavement Temperature Prediction and Case Studies with the FHWA HIPERPAV Models," *Cement and Concrete Composites*, Vol. 26, No. 5, pp. 463-471, Elsevier, 2004.
123. Pantazopoulou, S.J. and Mills, R.H. "Microstructural Aspects of the Mechanical Response of Plain Concrete." *ACI Materials Journal*, Vol. 92, No. 6., pp. 605–616, November–December 1995.
124. Hansen, T.C. "Physical Structure of Hardened Cement Paste—A Classical Approach." *Materials and Structures*, Vol. 19, No. 114, pp. 423–436, November–December 1986.